THE UNIVERSITY OF HULL

CHINONYELUM MARY UDEMU

MODELLING AND SCALE-UP STUDIES OF SORPTION-ENHANCED STEAM REFORMING (SE-SR) OF METHANE FOR BLUE HYDROGEN PRODUCTION

SCHOOL OF ENGINEERING

PHD THESIS

THE UNIVERSITY OF HULL

MODELLING AND SCALE-UP STUDIES OF SORPTION-ENHANCED STEAM REFORMING (SE-SR) OF METHANE FOR BLUE HYDROGEN PRODUCTION

Being a Thesis submitted in partial fulfilment of the requirements for the Degree of Doctor of Philosophy (PhD) in Engineering

in the University of Hull

By

CHINONYELUM MARY UDEMU

Supervisor: Dr Carolina Font-Palma

May 2024

To my mum, Sweet Tonia.

Acknowledgements

I would like to express my deepest gratitude to my supervisor, Dr Carolina Font-Palma, for her guidance and support throughout this PhD journey. Her insights and feedback have been instrumental in directing my research. I also thank Chris Keily and Olga Dubinin of EDF Energy, UK for serving on the supervisory committee and for providing thoughtful suggestions that have helped strengthen this work.

I would like to acknowledge Dr Bjørnar Arstad of SINTEF, Norway for providing access to crucial data that enabled validation of the CPFD models developed in this work. Special thanks to the CPFD Software, LLC technical support team for their prompt assistance and expertise in resolving any technical challenges I encountered during the course of this research.

I am deeply indebted to my financial sponsors, the Net Zero Research (formerly Biomass and Fossil Fuels Research Alliance – BF2RA), UK and the Petroleum Technology Development Fund (PTDF), Nigeria, for their generous funding and belief in the significance of this work. Their support enabled me to pursue this research without financial constraints.

To my dear mother, Tonia Ejike, all my friends too numerous to mention individually, and to my beloved sisters – Stephanie, Nkem, and Chigozie, thank you for your unwavering love, encouragement and understanding throughout this demanding journey. Your belief in me and your constant presence have been a source of strength and motivation, even during the most challenging times.

Above all, I am eternally grateful to Almighty God for bestowing upon me the strength, resilience, and wisdom to embark on and complete this academic endeavour.

Publications and Conferences

Publications

- **Udemu C**, Font-Palma C. Modelling of sorption-enhanced steam reforming (SE-SR) process in fluidised bed reactors for low-carbon hydrogen production: A review. Fuel 2023;340:127588. https://doi.org/10.1016/J.FUEL.2023.127588.
- **Udemu C**, Font-Palma C. Potential cost savings of large-scale blue hydrogen production via sorption-enhanced steam reforming process. Energy Convers Manag 2024;302:118132. https://doi.org/10.1016/j.enconman.2024.118132.
- **Udemu, C**., & Font-Palma, C. Steam reforming process for conversion of hydrocarbons to hydrogen. In Handbook of Hydrogen Production and Applications: Hydrogen Production from Non-renewable Resources: First Edition. CRC Press; 2024.
- **Udemu C**, Font-Palma C. Computational simulation of SE-SR of methane in a bench-scale circulating fluidised bed reactor: Insights into the effects of bed geometry design and catalyst-sorbent ratios. Fuel 2024;377:132817. https://doi.org/10.1016/j.fuel.2024.132817.

Conferences: Poster and oral presentations

- **Udemu C**, Font-Palma C. Modelling of sorption-enhanced steam reforming (SE-SR) process in fluidised bed reactors for low-carbon hydrogen production: A review. Poster presented at the 24th Fluidized Bed Conversion Conference, May 8-11, 2022, Sweden.
- **Udemu C**, Font-Palma C. Computational simulation of SE-SMR process in a bench-scale circulating fluidised bed reactor: Effect of geometry design and solid ratio. Paper presented at the 2nd FERIA Conference, the European Conference on Fuel and Energy Research and Its Applications, September 4-6, 2023, United Kingdom.

Abstract

Rising concerns over climate change, largely driven by anthropogenic CO_2 emissions, have intensified research and development in low-carbon and carbon-neutral energy solutions. Hydrogen is increasingly gaining attention. Unlike fossil fuels, hydrogen combustion produces only water vapor, making it an environmentally attractive fuel source. This potential has spurred technological innovations in hydrogen production methods. Sorption-enhanced steam reforming (SE-SR) of methane is an emerging technology incorporating in-situ carbon capture that enables hydrogen (blue) production from natural gas. This study aims to advance this approach through mathematical modelling and scale-up within bubbling fluidised bed reactors. This is significant because SE-SR currently has a low technology readiness level (TRL). The aim was achieved by developing novel reactor and process models in Barracuda Virtual Reactor® and Aspen Plus® software, respectively, as well as applying scaling laws and methodologies to upscale SE-SR of methane for industrial applications.

A computational particle fluid dynamics (CPFD) reactor model was developed using Barracuda VR® and rigorously validated against experimental data from the literature. Comparisons showed close agreement, with deviations between simulated and literature values falling within a narrow range of 0.1-2%. The validated CPFD model was then employed to evaluate the reliability of two potential scale-up methodologies. One of the methodologies was later selected for scaling simulations, due to better preservation of hydrodynamic behaviours and chemical conversion rates at more conserved materials and reactor dimensions. It was applied, in conjunction with the CPFD model, to progressively upscale the SE-SR reactor - first from a bench-scale reactor to an industrial-sized 1 MWth unit, then further to commercial-scale reactors of 50 MWth and 150 MWth. This effort establishes a validated simulation-guided approach for methodically upscaling SE-SR reactor from bench-scale to full commercial scale.

Furthermore, the economic scalability of SE-SR was also evaluated. A rigorous process simulation in Aspen Plus® software and cost assessment was conducted comparing projected levelised cost of hydrogen (LCOH) for scaled-up SE-SR systems against more established blue hydrogen alternatives, including autothermal gas-heated reforming coupled with carbon capture and storage (CCS), as well as conventional steam methane reforming plus CCS. The analysis found SE-SR to have a competitive economic outlook at the 600 to 1000 MWth commercial scale assessed. This benchmarking suggests SE-SR can be scaled cost-effectively for industrial applications. As the technology continues to mature, capital requirements may see further reductions. SE-SR therefore demonstrates strong potential as an economically viable pathway to facilitate large-scale production of low-carbon hydrogen.

Contents

List of Figures

List of Tables

Nomenclature

Symbols

Symbol	Description	Unit
$A_{metal\ surface}$	Catalyst's metal surface area,	m^2
C_d	Drag coefficient	-
D	Diameter of reactor	m
E	Activation energy	kJ/mol
H	Height of reactor	m
K	Equilibrium constant	$(kPa)^2$
k_1, k_3	Rate constants of R_1 and R_3	$(kmol/kg_{cat}\ s)\ (kPa)^{0.25}$
k_2	Rate constants of R_2	$(kmol/kg_{cat}s)\ (kPa)$
k_{ad}	Adsorption coefficient	$(kPa)^{-1}$
k^0_{SMR}	Rate constant for SMR in NK model	$kmol/(kg_{cat}s\ atm^{0.404})$
k^0_{WGS}	Rate constant for WGS in NK model	$kmol/(kg_{cat}s\ atm)$
$m, \dot{m}$	Mass flowrate	kg/s
m	Magnitude of scale	-
M	Molecular weight	kg/mol
n	mole	mol
p	Pressure	atm
P_e	Electricity consumption	MWh
q_{CO_2}	CO_2 loading in adsorbent	$mol/(kg_{CO2})$
$q^*_{CO_2}$	Adsorbent CO_2 loading at equilibrium	$mol/(kg_{CO2})$
r_{ad}	Sorption rate	mol/(kg s)
R	Rate of reaction	$kmol/(kg_{cat}s)$
R_1	Steam methane reforming reaction in XF model	$kmol/(kg_{cat}s)$
R_2	Water-gas shift reaction in XF model	$kmol/(kg_{cat}s)$
R_3	General steam methane reforming reaction in XF model	$kmol/(kg_{cat}s)$
Sh	Sherwood number	-
$S\dot{m}_g$	Fluid mass source term	$kg/m^3\ s$
T	Temperature	K

u	Gas velocity	m/s
$\Delta w_{\max}$	Maximum CO_2 uptake	g CO_2/g absorbent
X_i	Conversion for component *i*	-
z	Vertical coordinate along the reactor	m
Greek		
β	Partial reaction orders for glycerol	-
γ	Partial reaction orders for steam	-
α	Transfer coefficient	-
ε	Porosity	-
ϵ	Voidage	-
δ	Sorbent grain diameter	m
ρ	Density	kg/m^3
η	Efficiency	%
ζ	Bulk viscosity	Pa.s
Subscripts		
a, *b*, *c*	Co-efficient of reaction	
ACD	Acetaldehyde decomposition	
e,eff	Electrical efficiency	
ETD	Ethanol dehydrogenation	
i	Gas species	
NG	Natural gas	
REF	Reference	

Abbreviations

1D	One-dimensional
2D	Two-dimensional
3D	Three-dimensional
a-MDEA	Activated Methyldiethanolamine
ATR	Autothermal reforming
BECCS	Bioenergy with carbon capture and storage
BAM	Blended acceleration model
BFB	Bubbling fluidised bed
CCS	Carbon capture and storage
C-S	Catalyst-to-sorbent ratio

CFB	Circulating fluidised bed
CSCM	Combined sorbent catalyst material
CFD	Computational fluid dynamics
CPFD	Computational particle fluid dynamics
CCA	Cost of CO_2 avoided
CFL	Courant–Friedrichs–Lewy
DDPM	Dense discrete phase model
DEM	Discrete element method
EMMS	Energy minimization multi-scale
E-E	Eulerian-Eulerian
E-L	Eulerian-Lagrangian
FBR	Fluidised bed reactor
GHR	Gas-heated reforming
GHG	Greenhouse gas
HyBECCS	Hydrogen from bioenergy with carbon capture and storage
ICFB	Internally circulating fluidised bed
IPCC	Intergovernmental Panel on Climate Change
IEA	International Energy Agency
KTGF	Kinetic theory of granular flows
LCHA	Low Carbon Hydrogen Agreement
LCOH	Levelised cost of hydrogen
LHV	Low heating value
MWth	Megawatt thermal
Model G	Model Glicksman
Model H	Model Horio
MEA	Monoethanolamine
MP-PIC	Multiphase particle-in-cell
NOAA	National Oceanic and Atmospheric Administration
NK	Numaguchi and Kikuchi
POX	Partial oxidation
ppm	parts per million
PSA	Pressure swing adsorber
PEM	Proton exchange membrane
SOEC	Solid oxide electrolysis cell

SE-SR	Sorption-enhanced steam reforming
SMR	Steam methane reforming
S/C	Steam-to-carbon ratio
TRL	Technology readiness level
TIC	Total direct installed cost
TPC	Total plant cost
VR	Virtual reactor
XF	Xu and Froment

1 Introduction

1.1 Background

Climate change is one of the defining challenges of our time that has garnered significant attention and concern. Significant changes to systems across the planet demonstrate the reality of climate change. One of the most visible manifestations of this change is the rise in sea levels, which threatens coastal environments through inundation, flooding and erosion [1]. Wetlands are being swallowed and coastal communities are facing increased storm surge damage. This existential challenge is particularly acute for island nations and low-lying coastal cities, as the immense polar ice sheets continue to respond slowly to the warming [2]. Warming seas are also causing significant disruptions to marine ecosystems, altering the distribution of marine life and acidifying the oceans at rates not seen for millions of years [3]. These changes are disrupting vital underwater ecosystems that billions of people rely on for sustenance and livelihoods. On land, shifting rainfall patterns linked to climate change are extending drought conditions in some areas while increasing the frequency and intensity of heavy rainfall events and subsequent flooding in others [4]. These changes are exacerbating wildfire risk and degrading soil fertility, posing a threat to crop and livestock production, as well as the availability of freshwater resources for human populations and natural habitats worldwide. The impacts of climate change are not limited to environmental disruptions. Unprecedented weather extremes, such as intensifying hurricanes and heatwaves, are also inflicting significant economic losses, providing an early glimpse of the future disruptions that await if warming persists unchecked [4].

The scientific consensus by the Intergovernmental Panel on Climate Change (IPCC), is that the Earth's climate change is driven primarily by human activities [5]. Other possible influences, including variations in solar activity and volcanic eruptions, could not explain the rapid rise in global surface and ocean temperatures over the past century and the ongoing increases that break successively warmer records. Figure 1.1 illustrates the proof of human influence on worldwide surface temperatures presented in the latest IPCC assessment, which aggregated findings from paleoclimate archives, present-day measurements, and computed climate simulations. As seen from Figure 1.1, the patterns of warming align with rising concentrations of human-emitted greenhouse gases and are inconsistent with natural factors alone.

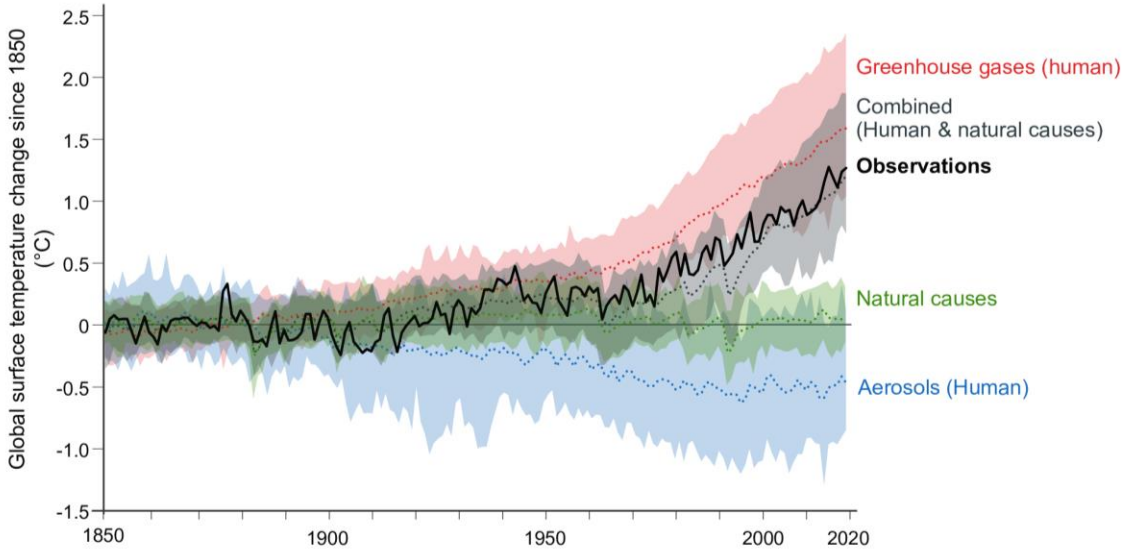

Figure 1.1: An updated assessment of human influences on broad-scale surface temperature from 1850 to 2019 [5].

Greenhouse gases (GHGs) like CO_2, CH_4 and nitrous oxide (N_2O) are emitted through industrial processes, transportation, energy production, agriculture and deforestation. However, a considerable portion of CO_2 emissions originate from those activities, compared to the other gases, as seen in Figure 1.2. Fossil fuel burning for activities such as generating electricity and powering vehicles, industrial processes and heating contributes the most to increased CO_2 emissions since preindustrial times. Coal, oil and natural gas contain carbon that produces CO_2 when burned, and emissions have risen sharply with industrialisation and global population growth.

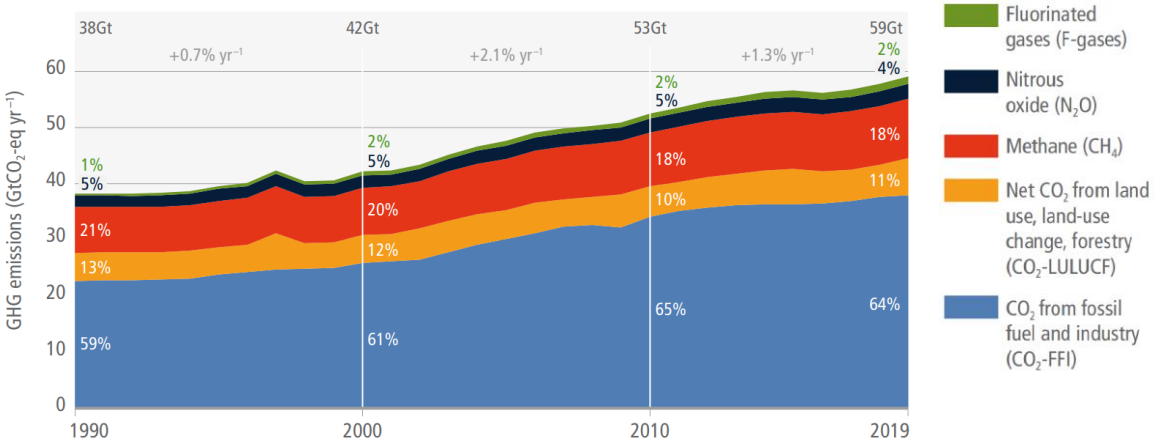

Figure 1.2: Global GHG emissions by gas from 1990 to 2019 [6].

Deforestation, primarily for cattle ranching and crop cultivation, is also a major driver of CO_2 emissions and additional warming through releasing carbon stored in trees and vegetation [6]. Agricultural activities including farming methods, fertilizer use and livestock production are key sources of non-CO_2

GHGs like CH_4 and N_2O. Methane, released during rice cultivation, livestock digestion and waste handling, has over 25 times the global warming potential of CO_2 over a 100 year period. Nitrous oxide emissions result from applied nitrogen fertilizers and manure being broken down by microbes in soils and oceans, with agricultural soil management responsible for around 60% of total N_2O emissions [5].

Clearly, climate change poses an urgent threat with irreversible environmental consequences due to the interdependence and vulnerability of living systems. Mitigation actions, such as the adoption of clean fuels, are expected to stabilise the climate balance. The role of hydrogen as a clean energy solution has gained significant attention. Hydrogen offers a versatile and promising pathway to mitigate the environmental impacts of energy production and usage [7]. Unlike fossil fuels, the combustion of hydrogen does not release carbon dioxide, making it a clean energy carrier that can be utilised across various sectors. Depending on the production method, hydrogen can have significantly lower greenhouse gas emissions compared to traditional energy sources.

The current use of hydrogen remains largely traditional. A major application of hydrogen is as an industrial feedstock in chemical and manufacturing processes. These industries rely on its chemical properties as a reducing agent to produce vital compounds such as ammonia and methanol. Additionally, hydrogen serves as a fuel in the refining process, converting crude oil into finished petroleum products like gasoline. Figure 1.3 depicts the global distribution of hydrogen applications between 2019 and 2023. The petroleum refining industry emerges as the primary consumer of hydrogen during this period. Following closely are industrial applications, comprising ammonia, methanol, and steel production. It is noteworthy that the vast majority of this hydrogen demand is satisfied through production methods that rely on unabated fossil fuel sources, highlighting the current dependency on traditional energy resources in hydrogen production.

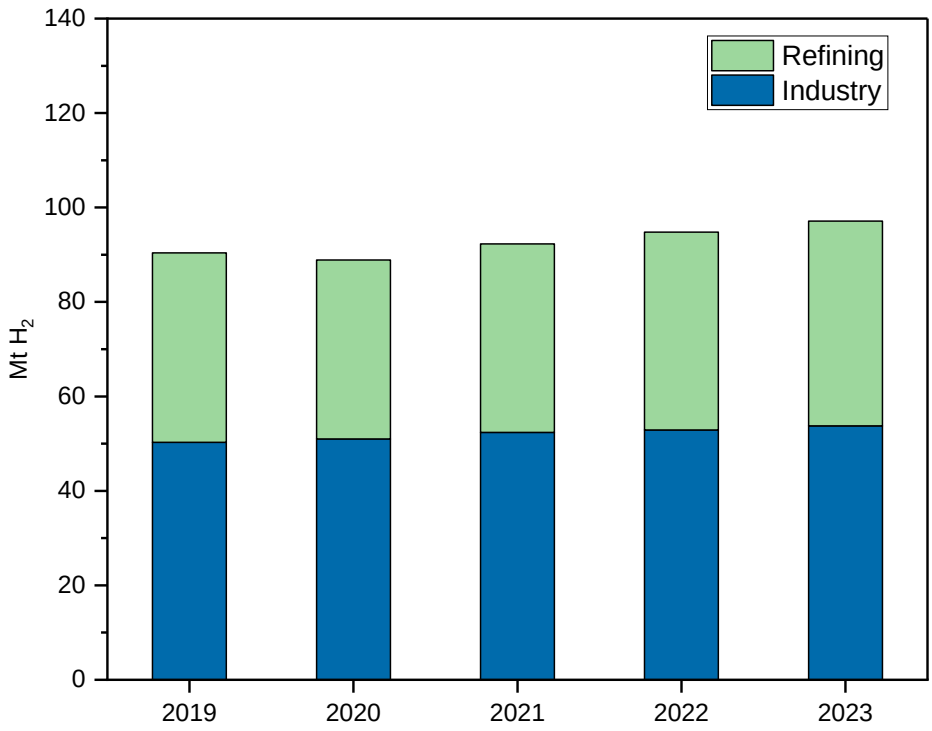

Figure 1.3: Distribution of hydrogen usage by sector from 2019 to 2023 [8]

The potential applications of hydrogen in the fight against climate change are extensive. In transportation, hydrogen-powered fuel cell electric vehicles (FCEVs) can replace conventional gasoline or diesel-powered vehicles, reducing tailpipe emissions and improving air quality in urban areas [7]. In power generation, hydrogen can be used to generate electricity through direct combustion or fuel cells. Furthermore, hydrogen can play a crucial role in decarbonising hard-to-abate industrial sectors, such as steel production, chemical manufacturing and refining, where traditional approaches are challenging. Hydrogen can also be utilised for heating and cooling buildings, displacing the use of fossil fuels in the residential and commercial sectors.

1.2 Motivation

As the world navigates the complexities of the climate crisis, the versatility and clean nature of hydrogen make it a promising solution that can contribute to a more sustainable and low-carbon future. Governments and private sector actors around the world are already taking steps to promote the adoption of hydrogen technologies, recognising the crucial role they can play in achieving global climate goals. However, unlocking the full potential of hydrogen in mitigating climate change will require significant development of enabling infrastructure and scale-up of production capacity to meet growing market demands.

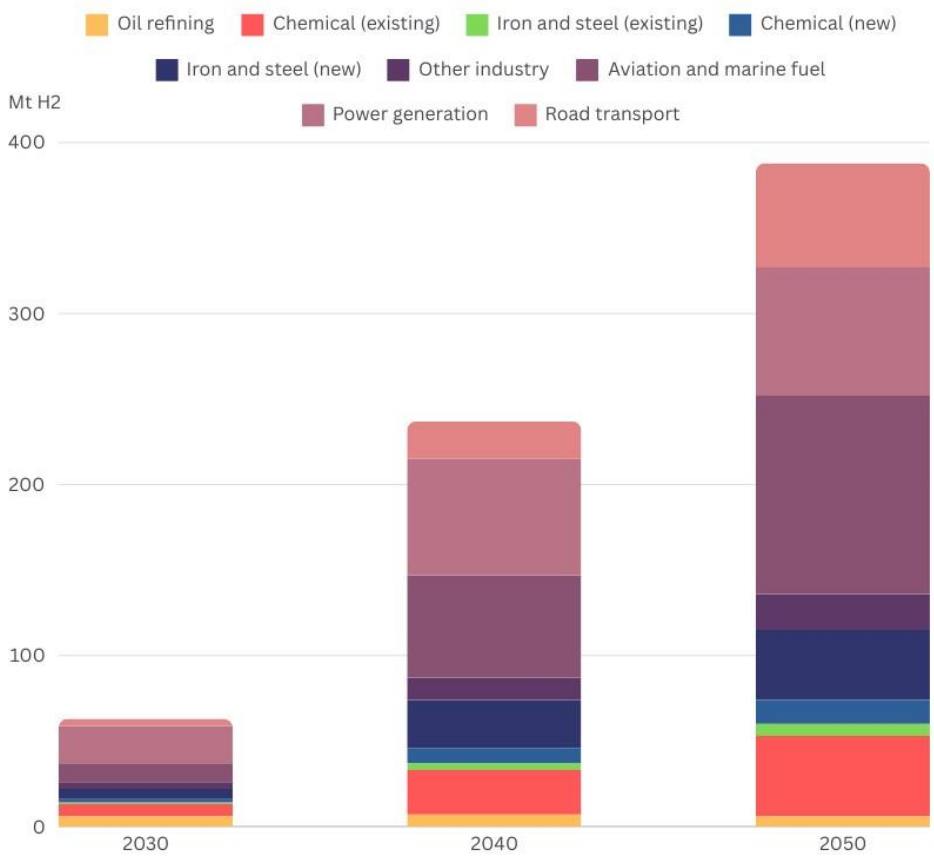

Figure 1.4: Projected low-carbon hydrogen demand from 2030 to 2050 net-zero scenario [9].

The demand for hydrogen is projected to increase substantially in the coming decades, with some demand still expected to be sourced from unabated fossil fuels, if additional low-carbon production is not scaled up [9]. As seen in Figure 1.4, projections indicate that low-emission hydrogen demand will increase more than fourfold by 2050 compared to 2030 levels, driven by its growing application in aviation and marine transport, heavy-duty transport such as freight trucks and buses, and manufacturing industries like steel, cement and chemicals. Thus, highlighting the urgent need to boost and expand the availability of competitively priced clean hydrogen.

Recent analyses suggest that fossil-based hydrogen integrated with carbon capture and storage (blue hydrogen) technologies, deployed at large scale, could help meet increasing hydrogen demand in the medium term [10]. Blue hydrogen exploits existing natural gas infrastructure while potentially capturing over 90-95% of emissions. The successful transition of emerging blue hydrogen production technologies, such as sorption-enhanced steam reforming (SE-SR) of methane, from laboratory-scale to commercial-scale operations is important for their widespread adoption. SE-SR of methane has been identified as a promising approach to produce high-yield blue hydrogen at lower costs, thanks to its compact nature and efficient carbon capture capabilities [11]. However, the technology is currently

at a low maturity level, and significant research is needed to overcome possible challenges that might be associated with its scale-up. Modelling and simulation techniques can play a vital role in this endeavour, providing insights into the complex physical and chemical phenomena occurring during the scale-up. In addition, literature on large-scale modelling of the SE-SR technology is limited. Thus, this work exploits opportunities to investigate SE-SR further.

1.3 Aim and objectives

The aim of this study is to investigate the behaviour and performance of sorption enhanced steam reforming (SE-SR) of methane for large-scale low-carbon hydrogen production, by developing high-fidelity models and validating a scaleup methodology. This was achieved through these objectives:

1. Conducting a general literature review to examine the current state of research and development in the wider field of low-carbon hydrogen production, with a particular focus on SE-SR technology.
2. Conducting a comprehensive review to understand the state-of-the-art in simulation and modelling approaches for SE-SR of methane in fluidised bed reactors (FBR).
3. Developing and validating a computational particle fluid dynamics (CPFD) model to simulate lab-scale SE-SR, benchmarked against published experimental data.
4. Extending the CPFD model to simulate a full-loop bench-scale SE-SR system and validating model predictions.
5. Developing and validating a scale-up methodology for SE-SR in bubbling fluidised bed reactors using the validated CPFD model.
6. Evaluating the performance of a 1 MWth SE-SR of methane system at varying operating conditions and extrapolating the model to assess behaviour at larger scales of 50 and 150 MWth.
7. Conducting a techno-economic analysis of SE-SR of methane production at commercial scales to benchmark against conventional blue hydrogen technologies, using validated process simulation models.

1.4 Novelty and scope of the study

1.4.1 Novelty

One of the major innovative elements of this research is the development and validation of a scale-up methodology for SE-SR of methane, leveraging high-fidelity computational particle fluid dynamics (CPFD) simulations.

Firstly, a CPFD model was developed and validated to accurately simulate a single lab-scale SE-SR reformer unit, which was then extended to the full-loop bench-scale system, rather than just the single reactor unit. This involved a rigorous validation process, where the model's predictions of both the hydrodynamics and chemical kinetics behaviour were benchmarked against published experimental data. This approach represents a significant advancement over previous work, which has often relied on simpler validation methods or modelling approaches.

Starting with the validated lab-scale CPFD model, a systematic scale-up methodology based on the principles of similarity, for SE-SR in bubbling fluidised bed reactors was developed. This scale-up approach, which was validated using CPFD simulations, allowed the prediction of the performance and behaviour of SE-SR technology at reactor scales that could be expensive to study experimentally.

This innovative combination of advanced CPFD modelling and scale-up criteria represents a unique contribution to the field, as it addresses one of the critical barriers to the commercialisation of SE-SR technology – the challenge of transitioning from lab-scale to large-scale commercial operations.

1.4.2 Scope of study

This research focuses on developing an advanced computational model to support the scale-up of SE-SR hydrogen production technology. No experimental testing is included in the scope of this project but data from published literature is used to validate the model [12,13].

Computational particle fluid dynamic models will be developed using the Barracuda VR® software platform. Barracuda VR® software is used as it will not only allow for a detailed simulation of the lab-scale systems and the entire bench-scale process loop, but also the simulation of the multiphase hydrodynamics within SE-SR reactors at larger scales.

A steady-state simulation of the technologies used for bench-marking SE-SR of methane process will be developed in Aspen Plus® software and validated using published literature data. Aspen Plus® was used because it has an extensive property database that ensures accurate modelling of the intricate behaviours of those processes, including the carbon capture units. Furthermore, it is integrated with

economic tools that will enable the estimation of costs associated with some of the components used in these technologies.

1.5 Thesis outline

The structure of this thesis is centred around the key research objectives outlined in section 1.3. It comprises ten chapters, with chapters 3, 5 and 8 based on the contributions extracted for publication in peer-reviewed journals. Chapter 1 (current chapter) introduces the background of study and establishes the motivation and objectives of this thesis.

Chapters 2 and 3 delve into the existing body of knowledge, first through a literature review on low-carbon hydrogen production methods, and then by critically examining the current simulation and modelling approaches used for SE-SR processes, particularly in the context of fluidised bed reactors. Chapter 2 also explores the recent advancements and the current state of research in the SE-SR field, identifying the critical knowledge gaps that the thesis aims to address.

Chapters 4 and 5 represent the core of the computational modelling work undertaken in this research. Chapter 4 presents the development and rigorous validation of a three-dimensional CPFD model for simulating the lab-scale SE-SR process. This detailed model serves as the foundation for the subsequent scale-up studies. Building upon this, Chapter 5 extends the CPFD model to a bench-scale circulating fluidised bed reactor, exploring the effects of reactor geometry and solids ratios on the performance of the SE-SR system.

The scale-up analyses are then addressed in Chapter 6, where a scale-up methodology for transitioning the SE-SR technology from lab-scale to commercial-scale operations is proposed and validated. This chapter provides a framework for designing and scaling-up larger-scale SE-SR in fluidised bed reactor.

Chapters 7 and 8 focus on evaluating the performance and economics of commercial-scale SE-SR systems, respectively. Chapter 7 investigates the parametric analysis of 1 MWth SE-SR reactor and the effect of scale, ranging from 1 MWth to 150 MWth, on the key performance indicators of SE-SR in bubbling fluidised bed reactors. This is complemented by Chapter 8, which presents a techno-economic analysis to assess commercial viability of large-scale blue hydrogen production via the SE-SR of methane and benchmarks it with other established blue hydrogen production technologies.

The final two chapters provide a broader perspective on the research. Chapter 9 offers a general discussion, synthesising the key findings and highlighting the overall contributions of the work to the advancement of SE-SR technology. The thesis concludes with Chapter 10, which summarises the main

conclusions and outlines the future research directions and opportunities to further enhance the deployment of SE-SR technology.

2 General Literature Review

2.1 CO_2 emissions and impact

Earth's natural temperature is regulated through a fine balance between incoming solar radiation and outgoing heat. Some of the sun's rays are reflected back into space by the Earth's surface and atmosphere, while others are absorbed and re-radiated as thermal energy. Certain gases in the atmosphere, called greenhouse gases (GHGs), which includes CO_2, methane, and nitrous oxide, play a vital role in this process. They act like a protective blanket, trapping some of the outgoing heat and preventing it from escaping back into space. This phenomenon, known as the greenhouse effect, is essential for sustaining a habitable planet [14].

However, problems arise when the concentrations of these greenhouse gases increase significantly above the levels that exist naturally in our atmosphere. When higher concentrations of greenhouse gases are present, they begin to trap more heat in the lower atmosphere, leading to a gradual warming of the planet. Among all greenhouse gases, CO_2 emissions make up the largest share of total emissions and have consequently been the focus of extensive scientific research due to their significant impact on anthropogenic climate change and global warming [15]. The combustion of fossil fuels, such as coal, oil and natural gas for energy production, transportation, and industrial processes, has been identified as the primary source of increased atmospheric CO_2 levels over the past century. This increase in CO_2 emissions has been linked to human activities, like industrialisation and urbanisation [15].

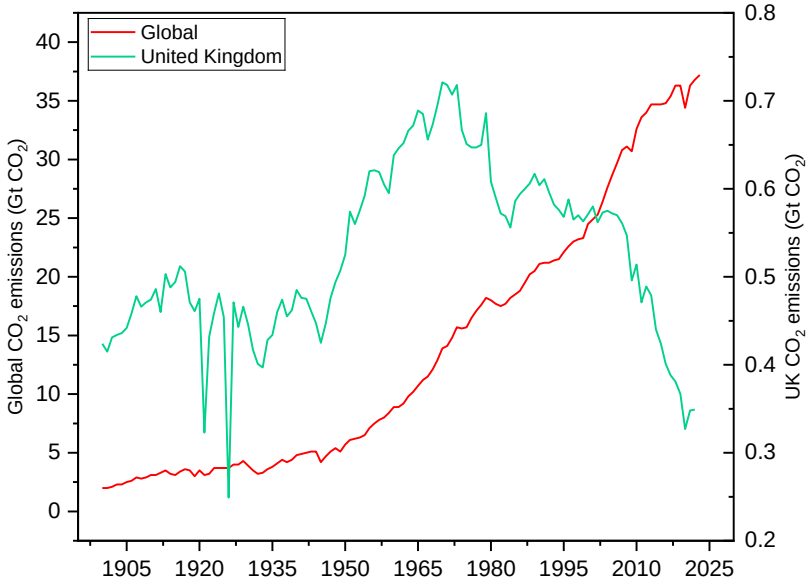

Figure 2.1: Growth of annual global CO_2 emissions from 1900 to 2023 [16].

While efforts have been made through clean energy initiatives and programs to reduce CO_2 emissions, concentrations in the atmosphere have continued climbing to new record highs. In 2023, global CO_2 emissions reached 37.4 Gt, according to the International Energy Agency (IEA) – the highest annual total ever recorded, as seen in Figure 2.1 [16]. This represents an increase of around 1 gigaton from 2022 levels. Human activities have raised the atmosphere's CO_2 content by 50% in less than 200 years. Data from the National Oceanic and Atmospheric Administration (NOAA) have revealed an alarming increase in the current CO_2 concentration, rising from 320 ppm recorded in 1960 to a concerning 425 ppm in recent times, a marked rise of over 30% in just over half a century [17]. These emissions and relatively high concentrations of CO_2 and other GHGs have also led to a measurable global warming of approximately 1 °C over the past 150 years [18]. Although a 1 °C increase may seem small, it represents a significant accumulation of heat in the atmosphere and oceans. Concerningly, the last decade was the warmest on record. In fact, 2023 is now considered the warmest year since systematic record keeping began, as the global average temperature was 1.18 °C above the 20th century average of 13.9 °C [18].

To prevent the most severe consequences of climate change, global leaders agree we must limit average global temperature rise to below 2°C through ambitious emissions reduction interventions. This is the internationally agreed upon goal as outlined in the 2015 Paris Agreement, signed by nearly every country [19]. Reaching this target will require global anthropogenic CO_2 emissions to fall by around 45% from 2010 levels by 2030, according to the IPCC [20].

2.2 Low-carbon hydrogen production technologies

Hydrogen is a promising energy carrier and a potential solution for decarbonising various sectors, including transportation, industry, and power generation. Today's hydrogen landscape is characterised by production methods heavily reliant on fossil fuels but this is changing as governments and industries worldwide recognise hydrogen's potential as a clean energy carrier. Looking to the future, hydrogen market is expected to undergo immense growth. This expansion will be driven by technological advancements, economies of scale, and supportive policy frameworks across the globe. Leading the way in hydrogen policies and initiatives are countries such as Canada, China, the United States, members of the European Union, and the United Kingdom.

The UK's Ten Point Plan places a strong emphasis on developing and scaling hydrogen production technologies as a key strategy for achieving net-zero emissions [21]. More recently, the country's previous target for low-carbon hydrogen production capacity was doubled, raising it to 10 GW by the year 2030, and mandating that 6GW be derived from electrolytic (green) hydrogen and 4GW from CCS-

enabled (blue) hydrogen [22]. To support the achievement of this 2030 production capacity target, the UK government introduced the Low Carbon Hydrogen Agreement (LCHA), which underpins the hydrogen production business model. The LCHA is structured as a private law contract between hydrogen producers and a government-appointed counterparty, and serves as a financial support mechanism designed to bridge the cost gap between low carbon hydrogen and high carbon fuels, thereby incentivising the production of low carbon hydrogen.

Furthermore, the UK's Balanced Net Zero Pathway, as seen in Figure 2.2, recognises the importance of diversifying hydrogen production methods to meet the country's ambitious targets for low-carbon hydrogen deployment. This approach acknowledges that different production routes will play varying roles over time as the hydrogen economy evolves and scales up. Initially, a significant portion of hydrogen production is expected to come from fossil fuel-based routes but will likely shift towards renewable-based production methods as the transition progresses.

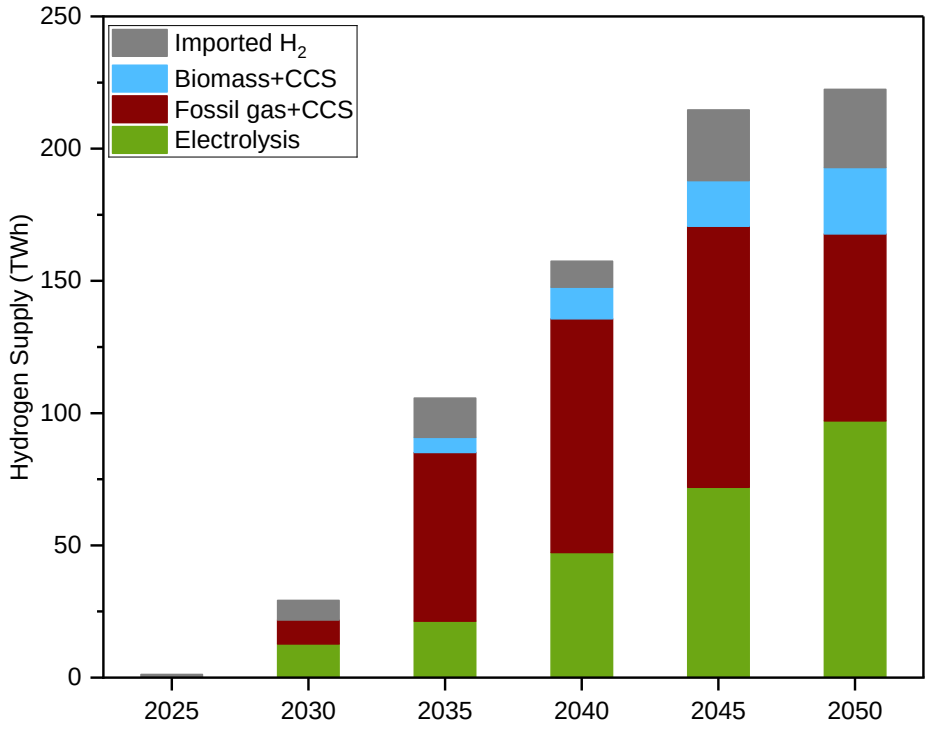

Figure 2.2: The UK's projected clean hydrogen supply mix by production technology: 2025-2050 [23].

The transition towards a low-carbon hydrogen economy has sparked significant interest and research into various production technologies that can minimise CO_2 emissions. A diverse range of methods have been proposed and explored, each with its own advantages and challenges. To better understand the landscape of low-carbon hydrogen production, it is essential to review the literature and examine the different technologies in detail. The classification of different hydrogen production technologies used here is based on the primary energy input required for the conversion of the feedstock materials:

electrolytic, biological/biochemical and thermochemical hydrogen production. The cost of hydrogen per kg and the Technology Readiness Level (TRL) of these technologies were also highlighted. The TRL scale is a measure used to assess the maturity of emerging technologies, with scale that runs from 1 to 9 [24]. A TRL of 1 represents the lowest level of technology maturity, while 9 represents the highest, most advanced state where a technology has been proven and adopted for full operational use.

2.2.1 Electrolytic hydrogen production technologies

This method of producing hydrogen involves using electricity to divide water molecules into their constituent parts of hydrogen and oxygen via a process called electrolysis [25]. The electricity required can be generated from low-emissions renewable energy sources such as solar, wind, hydropower or nuclear – which then powers the electrolysis. Some of the primary electrolytic techniques are alkaline electrolysis, solid oxide electrolysis and proton exchange membrane (PEM) electrolysis, all of which use electricity to split water into hydrogen fuel [26–29].

In the alkaline electrolysis process, an electrolytic cell contains an electrolyte solution made of alkaline chemicals such as potassium hydroxide or sodium hydroxide [30]. Two electrodes – a positive anode and negative cathode – extend into the cell. When an electric current flows through the electrodes, a redox reaction occurs at each one. At the negative cathode, water molecules are reduced. This means they gain electrons from the external power source, causing the molecules to split apart into hydrogen gas and hydroxide ions ($2H_2O + 2e^- \rightarrow H_2 + 2OH^-$). The hydroxide ions remain soluble in the alkaline electrolyte and diffuse across to the anode side of the cell. Meanwhile, at the positively-charged anode, the hydroxide ions undergo oxidation and generate oxygen gas as well as water molecules ($2OH^- \rightarrow 1/2O_2 + H_2O + 2e^-$) [30]. Although alkaline electrolysis is a mature technology, with a TRL of 9 and an efficiency of up to 80%, it faces certain limitations such as the requirement for a corrosive alkaline electrolyte and the potential for gas crossover between electrodes, reducing efficiency and purity [31–33]. Ongoing research efforts aim to address these challenges by developing advanced electrode materials, optimising cell designs, and integrating renewable energy sources to provide the necessary electrical input [34,35]. Its updated levelised cost of hydrogen (LCOH), calculated over the hydrogen plant operational lifetime, ranges from £2.08/kgH_2 to £7.42/kgH_2 (converted) but can go higher depending on the source of electricity used [36,37].

Unlike alkaline electrolysis systems that rely on liquid electrolyte solutions, PEM electrolysers use a solid polymer membrane as the electrolyte. A PEM electrolyser is made up of the membrane electrode assembly (MEA), which comprises a polymer electrolyte membrane sandwiched between two porous electrodes – the anode and cathode. The polymer membrane, usually made of a perfluorosulfonic acid (PFSA) material like Nafion, selectively allows the transport of protons (H^+) while blocking the passage

of electrons and gases. The electrodes are coated with catalysts, such as platinum, to facilitate the electrochemical reactions [38]. When an external electrical supply is connected to the electrodes, a series of reactions occur. At the anode, water molecules are oxidised, producing oxygen gas, protons, and electrons ($2H_2O \rightarrow O_2 + 4H^+ + 4e^-$). The protons generated at the anode are selectively transported through the polymer membrane to the cathode, where they combine with electrons to form hydrogen gas ($4H^+ + 4e^- \rightarrow 2H_2$) [39]. PEM electrolysis offers some advantages over alkaline electrolysis, including higher efficiency, compact design, and the ability to operate at higher current densities [40]. The solid PEM eliminates the need for corrosive liquid electrolytes and minimises gas crossover issues, enhancing overall performance. However, they typically have higher capital costs due to the use of expensive catalysts and membrane materials, with updated LCOH ranging from £2.31/kgH_2 to £9/kgH_2 [37,41]. PEM electrolysers are in the early stages of market adoption, with TRL of 8, and have efficiencies ranging from 67% to 82% [39]. Ongoing research efforts focus on developing cost-effective catalysts, improving membrane durability and efficiency.

Solid oxide electrolysis cell (SOEC) presents an innovative approach to hydrogen production through the electrolysis of water at elevated temperatures. Contrary to conventional alkaline and PEM electrolysis systems that can operate at relatively low temperatures, SOEC technology harnesses the unique properties of solid oxide ceramic materials as electrolytes, enabling high-temperature operation typically ranging from 600°C to 900°C [42,43]. The core component of an SOEC system is the solid oxide electrolyte, commonly composed of yttria-stabilized zirconia (YSZ) or other ion-conducting ceramic materials. This solid electrolyte facilitates the selective transport of oxide ions (O^{2-}) at high temperatures [42]. When an external electrical supply is applied across the electrodes, the high operating temperature enables the following reactions to occur: at the cathode, water vapor is reduced to produce hydrogen gas and oxide ions ($H_2O_{(vapor)} + 2e^- \rightarrow H_2 + O^{2-}$). Simultaneously, at the anode, the oxide ions are oxidised, generating oxygen gas and releasing electrons ($O^{2-} \rightarrow 1/2O_2 + 2e^-$) [39]. SOEC technology offers several advantages, including high efficiency, with potential to achieve up to 95% efficiency [44]. This high efficiency is attributed to the materials' ionic conductivity and the potential for co-production of steam or electricity by integrating with waste heat sources [44,45]. However, the high operating temperatures also present challenges, including material degradation, sealing issues, and the need for expensive high-temperature materials. Additionally, the start-up and shutdown processes for SOEC systems can be complex and time-consuming due to the high operating temperatures involved [44]. The TRL of SOEC technology is currently at 5 and is in the active research and development stage for commercialisation. The updated cost of hydrogen ranges from £2.38/ kgH_2 to £15.45/kgH_2 [41,44]. Ongoing research efforts in SOEC focus on improving the durability and lifetime

of the ceramic components, developing cost-effective materials and exploring integration with various heat sources.

2.2.2 Biochemical hydrogen production technologies

Biochemical hydrogen production involves using microorganisms like bacteria or algae to produce hydrogen gas through metabolic pathways. There are three main biological methods for producing hydrogen: dark fermentation, photo-fermentation and biophotolysis. These processes differ in their metabolic mechanisms and pathways for hydrogen production, as well as the components and designs of the bioreactors used.

Dark fermentation involves anaerobic bacteria breaking down a variety of organic substrates like sludge, bagasse and municipal wastes in the absence of oxygen and light, to produce hydrogen carbon dioxide [46,47]. Two popular types of anaerobic bioreactors that are commonly used for this reaction are continuous stirred-tank reactors and fluidised bed bioreactors. Continuous stirred-tank reactors provide homogeneous conditions through constant mixing, while fluidised bed bioreactors suspend the substrates using an upward flow of gas [48]. Although relatively simple and cost-effective, the hydrogen yield from dark fermentation alone is low, prompting researchers to explore hybrid systems that combine it with other techniques. When biomass is used as the substrate for hydrogen production, the energy efficiency typically ranges from 60-80% [49]. Additionally, the TRL of dark fermentation technology is 7 and is at early market stage. The updated cost of hydrogen production ranges from £1.53 to £2.34/kgH_2, which is lower than methods such as electrolysis [50]. Research into biologically produced hydrogen (bio-H_2) via dark fermentation has increasingly focused on optimisation strategies using continuous reactor systems.

Photo-fermentation uses anaerobic bacteria or algae that metabolise organic compounds, in the presence of light, to release hydrogen [51–53]. Photo-fermentation shows promise for hydrogen production from a wide range of substrates, with studies demonstrating maximum hydrogen yields of up to 80% but low conversion efficiencies of up to 9.3% [54]. Photo-fermentation technology is still in the emerging phase, primarily confined to research and development efforts, with TRL of 4 [50]. However, it offers several advantages, such as the ability to utilise a wide range of organic feedstocks, including waste materials, and the production of valuable byproducts like organic acids [53]. Additionally, the process does not require an external energy source, as it is driven by the metabolic activities of the microorganisms and the adoption of light energy. Nonetheless, photo-fermentation systems face challenges, including sensitivity to light intensity and the need for specialised photobioreactors, which can contribute to higher operational costs [55]. The updated cost of hydrogen

production via photo-fermentation ranges from £2.34 to £2.95/kgH_2 when using glucose as the feedstock [49].

Biophotolysis occurs in photobioreactors, where light interacts with microorganisms to drive the dissociation of water into oxygen, protons and electrons. These substrates are then recombined through microbial metabolic processes to yield molecular hydrogen gas [56,57]. The theoretical maximum efficiency of biophotolysis is around 10-16%, based on the conversion of solar energy into chemical energy stored in hydrogen [58]. However, in practice, the reported efficiencies are much lower, typically ranging from 1% to 2%, due to factors such as the requirement for specific light conditions. Biophotolysis is still considered an emerging technology and is primarily at the research and development stage, with a TRL of 4 [50]. While significant progress has been made in understanding the underlying mechanisms and optimising the process, further research is needed to address challenges related to scalability, efficiency and long-term stability before commercial viability can be achieved. The updated cost of hydrogen production from biophotolysis ranges from £2.59 to £12.49/kgH_2, depending on the energy source [59,60].

Although energy efficiency can be moderate, the low hydrogen yield and higher costs present drawbacks that need to be addressed for biochemical processes to be a competitive approach particularly for large-scale hydrogen generation.

2.2.3 Thermochemical hydrogen production technologies

Thermochemical hydrogen production technologies leverage high-temperature heat sources to drive chemical reactions that produce hydrogen from various feedstocks such as water, natural gas or coal. Some approaches under development utilise renewable heat from concentrated solar power or nuclear energy in innovative thermal-driven cycles referred to as thermochemical cycles. Others focus on biomass and fossil fuel feedstocks integrated with carbon capture techniques to minimise greenhouse gas emissions, in processes such as gasification, partial oxidation (POX), autothermal reforming (ATR) or steam methane reforming (SMR).

2.2.3.1 Thermochemical water-splitting technologies

Thermochemical water splitting uses high temperatures and carefully selected chemical compounds to dissociate water into hydrogen and oxygen through a series of thermochemical reactions. At the core of the process is a closed-loop series of chemical reactions known as a thermochemical cycle. Water serves as the sole feedstock and input, while select chemical compounds enable the reversible reactions and are continuously reused throughout repetitive turns of the cycle [61–63].

Solar collectors or nuclear reactors can be adopted to generate the intensive heat required, either delivering it directly or using thermal storage mechanisms to indirectly provide thermal power on demand. As each reaction in the sequence is catalysed by chemical agents under controlled thermal conditions, energy absorbed at one stage propagates the changes needed to drive the next. In this way, high-grade heat inputs are ratcheted down step-by-step until the bonding forces within water are overcome and its dissociation into gases is achieved.

Significant research has explored various thermochemical water splitting cycles, with over 300 cycles reported in scientific literature to date. Among the most prominent are the sulphur-iodine (S-I), copper-chlorine (Cu-Cl) and magnesium-chlorine (Mg-Cl) cycles. In the S-I cycle, the process begins with the endothermic dissociation of sulfuric acid (H_2SO_4) at temperatures of at least 850°C, followed by a series of chemical reactions involving iodine and water to produce hydrogen and oxygen [64]. The heat required for the initial dissociation step can be provided by concentrated solar power (CSP). The Cu-Cl cycle involves a series of chemical reactions between copper and chlorine compounds at high temperatures (around 550°C) to split water molecules. This cycle has the advantage of operating at lower temperatures compared to the S-I cycle, making it potentially more suitable for integration with nuclear and renewable heat sources [65].

However, these thermochemical approaches have not achieved widespread commercial adoption compared to more conventional hydrogen production methods. Some key challenges that have limited their cost competitiveness include material corrosion at high operating temperatures, complex solids handling during phase changes of reagents, and thermal efficiency losses. Continued engineering efforts aim to address these technological hurdles [66–68]. Reported thermal-to-hydrogen energy conversion efficiencies range from 14.1% to 82%, while updated costs for hydrogen production vary significantly from £2.19/kgH_2 to £8.72/kgH_2, depending on cycle design and the source of heat input [68].

2.2.3.2 Thermochemical conversion technologies

These technologies use thermal energy to break down fossil fuel or biomass feedstocks into gaseous components like CO, CO_2 and H_2 [69]. Approaches in thermochemical conversion of fossil fuels and biomass include partial oxidation, gasification, pyrolysis and reforming. In line with the UK's net-zero pathway and policy phasing out coal, feedstock options reviewed here are restricted to natural gas and biomass [23]. Also, all processes reviewed in this section can be integrated with carbon capture and storage (CCS) technologies to capture associated CO_2 and generate low-carbon hydrogen.

2.2.3.2.1 Partial oxidation (POX)

Partial oxidation fuel reforming method takes place in a reformer, where carbonaceous feed reacts with less oxygen than required to produce hydrogen and carbon monoxide [70]. The practical operating condition for this process occurs at 1150 – 1500°C, 25 – 100 bar and oxygen-to-carbon (O/C) ratio greater than 0.4, with an efficiency between 60% and 75%. In the presence of a catalyst, partial oxidation achieves a complete conversion of oxygen and almost complete conversion of hydrocarbon at high gas hourly space velocity and relatively low temperatures (800 – 900°C) [71–75]. This is referred to as catalytic partial oxidation.

Although partial oxidation is known to be compact, with good response time, as well as receptive to variety of fuels, it is marred with low hydrogen yield. There are also safety concerns associated with this process, owing to its high temperature operation. Additional drawbacks include carbon formation, system complexity due to compliance with exact O/C ratio and high capital cost due to post treatment of product gases or installation of air separation unit [71,76–78]. Currently, there are no published data on the hydrogen cost when this process is integrated with CCS. However, the adjusted hydrogen cost for POX without CCS is estimated to be £1.77/kgH_2 or less [79].

2.2.3.2.2 Reforming

Among the various hydrogen production technologies available at commercial scale, steam methane reforming (SMR) remains one of the most cost-effective for producing high yields of hydrogen. SMR process involves the reaction of hydrocarbons, commonly natural gas, with high-temperature steam in the presence of a nickel catalyst. This triggers a set of endothermic reforming and exothermic water-gas shift reactions. Initially, the methane and steam react at pressures of 15-30 atm and temperatures from 700-950°C to produce syngas (CO and H_2) [80]. Then, the water-gas shift reaction further converts some CO and H_2O into additional hydrogen. Typical SMR facilities can achieve hydrogen production efficiencies in the range of 70-85%, depending on design.

Although SMR benefits from efficient and low-cost hydrogen production at large scales, it currently results in relatively large volumes of CO_2 emissions during operations. SMR can be integrated with CCS technologies to mitigate these emissions and produce low-carbon hydrogen. Notable commercial-scale examples applying post-combustion capture to SMR include facilities in Port Arthur, Texas, and Port Jerome, France, which boast CO_2 capture rates upwards of 80-95% [81]. Estimates put the adjusted cost of low-carbon hydrogen via SMR integrated with CCS between £1.90/kgH_2 and £2.86/kgH_2, with a TRL of 4 to 9, depending on the type of CCS technology [59,82,83]. Overall, SMR remains one of the leading production routes but continues to be improved through carbon abatement technologies. Ongoing research in SMR include advancing catalysts, developing reactor designs,

devising concepts to integrate with carbon capture, improving modelling and simulation, and improving efficiency via process intensification techniques such as sorption-enhanced chemical looping steam reforming (SE-CLSR), steam plasma methane reforming, steam methane reformer-membrane reactors (SMR-MR) and sorption-enhanced steam reforming (SE-SR) [84–89].

Auto-thermal reforming (ATR) is another reforming process that has achieved greater commercial maturity. In ATR, partial oxidation and steam reforming reactions occur simultaneously through controlled addition of air and steam to produce syngas, which is shifted via water-gas shift reaction to convert CO to CO_2 and generate more hydrogen [80]. This yields a shifted syngas suitable for downstream CO_2 capture.

ATR is the combination of partial oxidation and steam reforming process, where the heat from oxidation is supplied for an endothermic steam reforming process in the presence of a catalyst, all in a single reactor. The hydrocarbon feedstock, steam and oxidant enter the reformer at the same time where the heat generation from oxidation process is used to drive the steam reforming reaction to produce syngas, which can be shifted to produce more hydrogen and carbon dioxide [90]. It is operated at a temperature range of 900 – 1500°C, pressure between 1 – 80 bar, with adjustable oxygen-to-carbon ratio and steam-to-carbon ratio [91,92]. Despite its easier start-up, high energy efficiency, fuel flexibility and better temperature control, ATR large scale deployment is hindered by nitrogen separation downstream, high explosion risks and investment cost for the oxygen production unit [80,93–95]. In order to maximise process output and improve carbon capture, various concepts of ATR technology have been developed such as; gas switching reforming (GSR), ATR with carbon capture and sequestration (ATR-CCS), sorption-enhanced ATR (SE-ATR), and membrane assisted autothermal reforming (MA-ATR), which selectively separates hydrogen produced in the reformer thereby bypassing water-gas shift or downstream hydrogen purification [96–98]. The methane conversion efficiency has been reported to reach 99% while the energy efficiency is between 60% and 75%, depending on the process configuration and operating condition [99–101]. Current research trends for this technology are geared towards catalyst development, process condition optimisation, and CCS integration [102–104]. There is currently no operational ATR with CCS hydrogen production facilities, instead projects have been announced and are presently in construction. As obtained from the International Energy Agency (IEA) database, these projects include H-Vision, Netherland; HyNet Northwest, UK; Acorn Aberdeenshire, with completion date set between 2024 – 2040 [105]. Regardless, techno-economic assessments for ATR with CCS have been conducted and LCOH is estimated at £1.88 – £3.26/kgH_2 [83,106].

A novel and improved design for ATR, called chemical looping reforming (CLR), uses a chemical looping concept to partially oxidise fossil gas, eliminating the need for direct feeding of air or oxygen to the reactor and improving hydrogen yield. In CLR, the oxygen carrier such as Fe_2O_3 and NiO, alternates between reduced and oxidised states as it transfers oxygen between the fuel and an air stream. During one half of the cycle, the oxidised oxygen carrier reacts with the fossil gas to produce syngas, aided by the oxygen captured on its surface from prior contact with air. In the second half of the cycle, the now reduced carrier is regenerated by reaction with air, replenishing its stored oxygen for the next reaction with fuel. This syngas can be further shifted to produce a concentrated CO_2 stream suitable for capture [107–109]. CLR has been integrated with CCS in a few relative processes termed chemical looping reforming carbon capture (CLR-CC), chemical looping reforming – sorption-enhanced water-gas shift (CLR-SEWGS) and sorption-enhanced chemical looping reforming (SE-CLR) for potential power plant applications [110,111]. Based on a techno-economic assessment conducted by Argyris et al. [106], the adjusted LCOH of blue hydrogen via CLR(-CC) ranges from £1.77/kgH_2 to £2.37/kgH_2, depending on the scale of production and capture rate [106]. Whilst chemical looping reforming shows promise as a means of producing concentrated CO_2 streams, it remains an immature technology that requires further research and development before commercial deployment.

2.2.3.2.3 Pyrolysis

Pyrolysis is an irreversible thermal decomposition of material at high temperature heat, in the absence of oxygen [112]. Pyrolysis can be applied to both gaseous and solid materials such as natural gas and biomass, as well as other hydrocarbon feedstocks, for hydrogen production [113–118]. This process results in the production of a diverse range of products present in the gaseous, liquid and solid phases, depending on factors like residence time, temperature, and heating rate. At very high temperatures, ranging from 1000°C to 3000°C, the pyrolysis process primarily yields gaseous products; whereas at lower temperature ranges of 500°C to 900°C, the production of liquid products, often referred to as pyrolysis oil, becomes more prevalent [119–121]. Unfortunately, the high energy requirements associated with pyrolysis at elevated temperatures can have adverse effects on the material properties and hydrogen yield, particularly when using biomass as the feedstock. To address these challenges, process modifications have been explored, such as the use of catalysts to improve the efficiency and product characteristics [69]. Catalytic pyrolysis has been applied to various feedstocks to produce char and hydrogen. Studies have reported energy efficiencies of up to 58% for catalytic pyrolysis processes [117,122–124]. Compared to other high-temperature reforming methods, pyrolysis produces less CO_2 per unit of hydrogen. However, residual emissions still occur that could potentially be abated.

The pyrolysis of biomass with CCS is gaining significant attention in the context of bioenergy with carbon capture and storage (BECCS) technologies [125–127]. If the integrated pyrolysis and carbon

capture system is designed specifically for hydrogen production from biomass, rather than electricity production, it can be termed HyBECCS [128,129]. In a biomass pyrolysis-CCS or HyBECCS system, the biomass feedstock is first subjected to the pyrolysis process. This leads to the production of a gas stream, a liquid bio-oil and a solid biochar residue [130]. The resulting gas stream contains a mixture of CO, CO_2, hydrogen, methane, and other light hydrocarbons. This gas stream undergoes further processing, including a water-gas shift reaction to increase hydrogen and CO_2 content. Subsequently, the gas is directed to a CO_2 capture unit where CO_2 is separated from the other components and prepared for storage. The biochar produced during the pyrolysis process can be used as a soil amendment, potentially improving soil fertility and sequestering carbon in the soil [131]. Additionally, the liquid bio-oil can be further refined and utilised as a biofuel or as a feedstock for the production of various chemicals. There are currently no published data on the hydrogen cost for HyBECCS. However, the adjusted cost of hydrogen from biomass pyrolysis, without CCS, ranges from £1.62/kgH_2 to £2.86/kgH_2 [132]. Although biomass pyrolysis technology is matured, its TRL for low-carbon hydrogen production is currently at 4 [133].

2.2.3.2.4 Gasification

Gasification converts carbonaceous solid materials like biomass into gaseous products (H_2, CO_2, CH_4, H_2O, CO), with reactions occurring at temperatures of 500°C – 1400°C and pressures of up to 33 bar, usually achieved using gasifying agents [134–136]. Gasifying agents, such as steam, air, and oxygen, have been strategically employed for oxidising or gasifying solid fuels. Several gasification techniques have been developed and demonstrated, including steam gasification, air and oxygen gasification, supercritical water gasification (SCWG), and chemical looping gasification (CLG). Each of these processes produces syngas, which can be further processed through the water-gas shift reaction to facilitate CO_2 capture [137–139].

Gasification of biomass occurs in four stages: drying, pyrolysis, oxidation and reduction [140]. These gasification reactions can be carried out in different types of gasifiers, which vary in terms of the flow direction of the solid fuel and oxidant, the mode of heat supply, and how the solid fuel is supported within the reactor vessel. Specifically, gasifiers are differentiated based on whether the solid fuel and oxidant move counter-currently or co-currently, how heat is supplied (e.g. indirectly via heated recirculated gases or directly via partial oxidation) and how the solid fuel is introduced and distributed, such as through gravity feed or fluidised beds [140,141]. When this gasification process using biomass as its feedstock is integrated with CCS, it can also be considered a HyBECCS system.

As reported by Pfeifer [142], the integration of this process with CCS has been demonstrated at pilot scale. However, pilot plants at a capacity of 8MW using biomass as feedstock, have been reported to

produce the lowest purity of hydrogen (48–52 H_2 vol%), compared to the lower scale plants (20kW to 200kW) with H_2 purity >70 vol.% [143]. Other operational gasification with CCS plants are retrofits, including the SINOPEC demonstration plant, Coffeyville facility and Great Plains Synfuel, and have been reported to produce blue hydrogen and syngas for industrial use such as fertilisers [144]. The major challenge associated with this process is the formation of tar and char, which can influence hydrogen yield and promote catalyst deactivation. The estimated cost (and updated £) of hydrogen produced via biomass gasification, without CCS, is at £2.30/kgH_2 to £18.48/kgH_2, depending on the type of biomass feedstock [50,59]. Additionally, the TRL of biomass gasification, without CCS, is currently at 9, whereas that of biomass gasification with CCS (HyBECCS) is at 3-5 [133,145].

Figure 2.3 summarises the various low-carbon hydrogen production technologies reviewed in this chapter, presenting their TRL and estimated hydrogen costs based on literature. It is important to note that the estimated costs reported are dependent on the models, assumptions and fuel types used in each study. The actual production costs could vary depending on location-specific factors such as fuel costs, resource availability, plant size, carbon pricing policies and other conditions not captured in the generic cost analysis. As low-carbon technologies continue to progress along their development curves, their estimated costs are likely to decline. Therefore, the costs shown here should be interpreted as preliminary estimates, subject to change as these technologies mature.

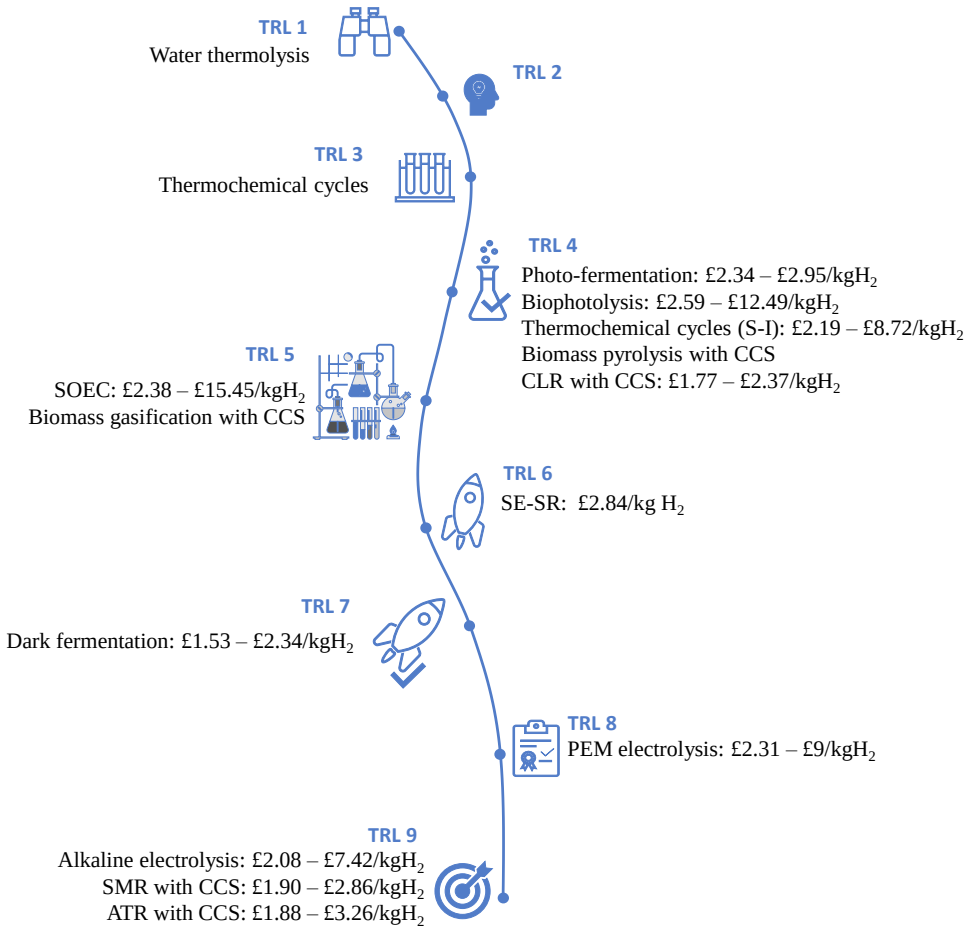

Figure 2.3: Summary of reviewed low-carbon hydrogen production technologies.

2.3 Carbon capture and storage (CCS)

The production of low-carbon hydrogen via thermochemical processes is closely tied to the implementation of effective carbon capture methods. Notwithstanding the fact that some thermochemical pathways, such as water splitting cycles, are inherently carbon-free, other routes involving hydrocarbon feedstocks like natural gas or biomass generate significant CO_2 emissions. To mitigate these emissions and achieve the desired low-carbon footprint, carbon capture technologies play a crucial role. CCS involves the separation and capture of CO_2 emissions from thermochemical processes like SMR, POX, ATR or gasification. The captured CO_2 is then compressed and transported for permanent storage in suitable geological formations, such as depleted oil and gas reservoirs or deep saline aquifers.

2.3.1 The CCS value chain

The main stages in the CCS value chain can be divided into capture, transport and storage, as shown in Figure 2.4. Several technologies are available for CO_2 capture and can be integrated into

thermochemical hydrogen production facilities, including post-combustion capture, pre-combustion capture, and oxy-fuel combustion.

Post-combustion capture involves separating CO_2 from the flue gas or shifted syngas (mainly CO_2 and hydrogen) after the combustion of the fossil fuel. This is the most mature and widely studied CO_2 capture technology and has been integrated in industrial hydrogen production facilities [146]. One advantage of this technology is its ability to be retrofitted to existing infrastructure without significant modifications. In post-combustion CCS, CO_2 can be separated from the flue gas using various techniques such as absorption, adsorption or cryogenic separation [147]. Many post-combustion processes employ cyclic separation and regeneration between two columns. One column separates the CO_2 from the flue gas stream via absorption or adsorption, depending on the specific separation method used. Meanwhile, the other column undergoes regeneration where the captured CO_2 is released, often through temperature or pressure changes [147]. This cyclic process allows for a steady capture process with the captured CO_2 available for further transport and storage or utilisation. However, the separation process can be energy-intensive and can reduce the overall production plant efficiency.

Pre-combustion CCS is aimed at capturing CO_2 from fossil fuels before they are burned for energy production. In this technology, solid or liquid fossil fuels are first converted into syngas via gasification or reforming, before it is shifted. The key aspect of pre-combustion capture is that the CO_2 is separated from the shifted syngas before the hydrogen fuel is used or combusted for energy generation [148]. In a combined cycle power plant, for instance, this separated hydrogen can then be used to fuel gas turbines for electricity production. The shifted syngas has high CO_2 concentration, which improves the efficiency of the subsequent CO_2 separation process. The separation can be achieved using methods similar to those employed in post-combustion capture systems.

Oxy-fuel combustion involves burning the feedstock in pure oxygen instead of air, resulting in a flue gas stream highly concentrated in CO_2, along with water vapor and minimal impurities like nitrogen [149]. The advantages of this approach include the high CO_2 concentration in the flue gas, simplifying CO_2 separation and reducing the energy penalty associated with capture. Additionally, the absence of nitrogen minimises the formation of nitrogen oxides, potentially reducing emissions and the need for additional flue gas treatment. However, challenges exist, such as the energy penalty from the air separation unit and the need for specialised boilers and burners designed for oxy-fuel combustion [149].

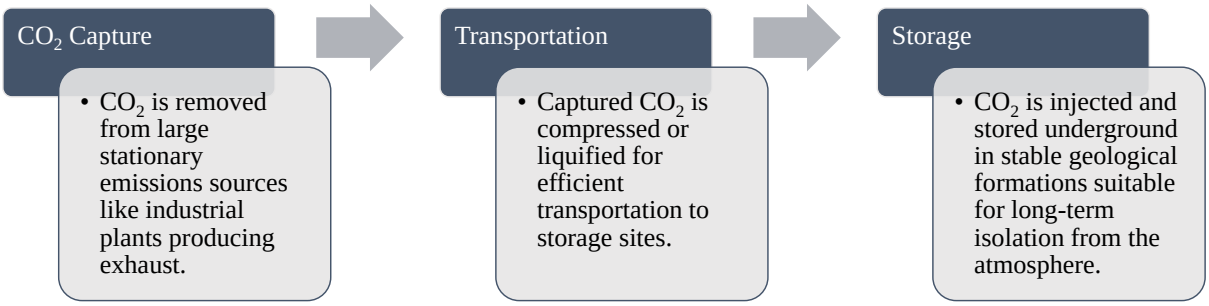

Figure 2.4: Carbon capture and storage value chain.

CO_2 transportation is important in the CCS value chain, as it facilitates the movement of the captured CO_2 from industrial sources to suitable storage sites. The choice of transportation method is influenced by factors such as the distance between capture and storage locations, the volume of CO_2 to be transported, regulation and associated costs [150].

One of the primary methods for CO_2 transport involves the use of pipelines. This approach is generally economical for transporting large volumes of CO_2 over long distances. The captured CO_2 is compressed into a dense phase, either liquid or supercritical state, before being pumped through the pipeline network. In some cases, existing natural gas pipelines can be retrofitted or new pipelines can be constructed specifically for CO_2 transportation [151].

Another option is ship transportation, which may be more suitable for offshore storage sites or when pipelines are not feasible. In this method, the captured CO_2 is liquefied and loaded onto specialised ships or barges for maritime transport [151]. Ship transportation can be cost-effective for shorter distances or smaller volumes of CO_2 [150].

For smaller-scale CCS projects or when pipelines and ships are impractical, CO_2 can be transported by trucks or railcars in pressurised tanks or containers. However, these modes of transportation are generally less efficient and more expensive than pipelines or ships for large-scale CO_2 transport [151]. Regardless of the transportation method employed, various factors must be considered, including pipeline or tanker design, materials compatibility, safety considerations and environmental impacts.

Conversely, the sequestration of captured CO_2 from industrial sources is an essential component of CCS system. Long-term containment of captured CO_2 involves injecting the gas deep underground through various geological sequestration techniques. Commonly evaluated storage approaches and projects comprise depositing CO_2 into depleted oil and gas reservoirs, saline aquifers, and un-minable coal deposits [151]. Prior to injection, the captured CO_2 is compressed into a dense, supercritical state

to maximise storage efficiency within the porous rock formations. The injection process involves drilling wells into the geological reservoir and pumping the CO_2 into the storage site.

Various trapping mechanisms contribute to the long-term storage security of CO_2 within these geological formations. These mechanisms include structural trapping, where the CO_2 is confined beneath low-permeability cap rocks or seals; residual trapping, where CO_2 becomes immobilised in the pore spaces of the rock; solubility trapping, where CO_2 dissolves in formation fluids; and mineral trapping, where CO_2 reacts with the rock matrix to form solid carbonate minerals over longer timescales [152]. To ensure the integrity and safety of CO_2 storage sites, comprehensive monitoring and verification techniques are employed. These include seismic surveys and satellite monitoring, among others [153]. Ongoing monitoring and management of the storage sites are essential to mitigate any potential risks and ensure the long-term containment of the stored CO_2.

2.3.2 CO_2 separation methods

Carbon capture technologies rely on efficient methods to separate and concentrate CO_2 from mixed gas streams. These separation methods can be incorporated into traditional thermochemical processes to enable lower-carbon hydrogen production. Leading separation methods under investigation include absorption, adsorption, cryogenics, and membranes.

2.3.2.1 Absorption

Absorption is one of the most widely used CO_2 separation techniques, particularly in post-combustion capture processes. It can be broadly classified into two categories: physical absorption and chemical absorption. Both methods involve the separation of CO_2 by dissolving or reacting it with a liquid solvent.

Physical absorption relies on the solubility of CO_2 in a non-reactive liquid solvent, governed by Henry's law. Common solvents include Selexol (dimethyl ethers of polyethylene glycol), Rectisol (methanol cooled to low temperatures) and Purisol (N-Methyl-2-Pyrrolidone) [154]. The process operates by contacting the gas stream with the solvent in an absorption column, where CO_2 dissolves. The CO_2-rich solvent is then regenerated by heating or depressurisation, allowing the captured CO_2 to be released and compressed for storage. In physical absorption processes, high pressure and low temperature favour increased absorption [155]. However, for flue gas streams with CO_2 partial pressures lower than 15 vol%, physical absorption becomes an economically unfavourable option for CO_2 separation [156].

Chemical absorption method involves the selective dissolution or reaction of CO_2 in a liquid absorbent, such as carbonates, amine-based solvents or ionic liquids. The CO_2-rich gas stream is brought into contact with the absorbent, where an intermediate compound is formed between the solvent and CO_2 [157]. The resulting CO_2-loaded absorbent is then regenerated through heat input, to release the

captured CO_2 for subsequent compression and storage. Chemical solvents using amines like monoethanolamine (MEA) have been extensively studied and employed as they can achieve 90%+ capture [158]. However, challenges such as solvent degradation, corrosion and high energy requirements for solvent regeneration have driven research into alternative absorbents and advanced absorption processes.

2.3.2.2 Adsorption

Adsorption is another widely employed technique for CO_2 capture, alongside absorption processes. It involves the selective accumulation of molecules on the surface of a solid adsorbent material, driven by intermolecular interactions between the adsorbent and the adsorbate [159]. In CCS, the gas stream is passed through a bed of adsorbent material, where CO_2 molecules are preferentially adsorbed onto the porous surface. Once saturated, the adsorbent is regenerated, through pressure or temperature swing processes, to release the captured CO_2 [156]. Just like absorption, adsorption process can also be classified into two main categories: physical adsorption and chemical adsorption.

Physical adsorption, also known as physisorption, is a reversible process driven by relatively weak van der Waals forces or electrostatic interactions between the adsorbent and the CO_2 molecules [159]. Commonly used adsorbents for physical adsorption of CO_2 include activated carbons, zeolites, and metal-organic frameworks (MOFs) [160]. As highlighted by Webley and Danaci [161], physical adsorption processes can operate at relatively low temperatures (as low as 25°C) and high pressures (up to 20 bar) to maximise the adsorption capacity. The regeneration of the adsorbent is achieved by reducing the pressure or increasing the temperature. In physical adsorption, the high pressures required to achieve sufficient adsorption capacity, increases energy consumption and operational costs but the process generally offer relatively lower energy requirements, typically having an enthalpy of less than 40 kJ/mol [162]. The adsorption capacity and selectivity of the adsorbent are usually influenced by surface area, pore structure or pore size distribution and surface chemistry [160]. Therefore, current research is focused on improving these properties.

In contrast, chemical adsorption or chemisorption, involves the formation of strong chemical bonds between the adsorbent and the CO_2 molecules [161]. However, the regeneration of the adsorbent often requires higher temperatures, making the process more energy intensive. Amine-functionalised adsorbents such as amine-grafted mesoporous silicas and amine-impregnated adsorbents, and metal oxides such as calcium oxides, are commonly employed for the capture of CO_2 [160]. Whilst, chemical adsorption processes can operate at lower pressures and offer higher CO_2 adsorption capacities and selectivity, they could require higher temperatures especially for regeneration, leading to increased energy consumption (more than 40 kJ/mol) and potential adsorbent degradation over time [161].

Adsorption processes for CO_2 capture offer advantages such as low energy requirements and the potential for high CO_2 selectivity than absorption processes. However, challenges include sorbent degradation, potential difficulties in scaling up the process, and solids handling.

2.3.2.3 Cryogenic CO_2 capture

Cryogenic CO_2 capture is usually operated at temperatures of between -50°C and -150°C, and leverages the distinct boiling points and phase behaviour of different gases, to enable the selective recovery of CO_2 in its liquid or solid form [163,164]. In operating this process, the gas stream is first cooled down below the critical temperature of CO_2 (approximately 31°C). This initial cooling step allows for the removal of water vapor and other condensable impurities, which can interfere with the subsequent cryogenic separation. Once the gas stream is sufficiently cooled, it is further chilled to cryogenic temperatures, causing the CO_2 to liquefy or solidify, while other gaseous components, such as nitrogen and oxygen, remain in the vapor phase [164]. The separation of the CO_2-rich liquid or solid phase from the remaining gas stream can be achieved through various techniques, including distillation columns and flash separators [163].

One of the advantages of the cryogenic process is its ability to produce a highly concentrated CO_2 stream, which can be directly compressed and transported for storage or utilisation, eliminating the need for additional purification steps [165]. However, the process can be energy-intensive due to the substantial cooling requirements and the need for efficient heat integration systems to recover the refrigeration energy.

Furthermore, the presence of impurities, such as water vapour, sulphur compounds or particulates, can adversely affect the performance of the cryogenic process by forming solid deposits or altering the phase behaviour of the gas mixture. Pretreatment steps may be necessary to remove these impurities and ensure reliable and efficient operation [165].

2.3.2.4 Membrane systems

Membrane systems use semi-permeable membranes to selectively separate gas mixtures based on their permeation rates [156]. The two main approaches for membrane-based CO_2 capture methods are membrane gas permeation and non-dispersive membrane contactors.

Membrane gas permeation uses selective polymer barriers to preferentially allow faster permeation of CO_2 over other gases from the flue gas. Multiple modules produce enriched and depleted streams. On the other hand, non-dispersive membrane contactors employ porous, hydrophobic barriers providing a large interface for highly efficient mass transfer of CO_2 directly from gas to liquid solvent without dispersion, via absorption [166,167]. Their key mechanisms – selective permeability versus

gas-liquid contact – influence process selection based on feed composition and project needs. Polymeric membranes, such as polyimides, cellulose acetate, and perfluoropolymers, are widely used due to their high CO_2 permeability and selectivity. Alternatively, inorganic membranes, such as zeolite or carbon molecular sieve membranes, offer higher thermal and chemical stability but may suffer from lower permeabilities and higher costs at larger scales. CO_2 membrane separation process has been tested at pressures, ranging from 10 to 60 bar, and temperature within a range of 25℃ to 60℃, as higher temperatures can adversely affect the membrane's performance and stability [166].

The selection of the right separation method often depends on the CO_2 concentration in the gas stream, volume of flue gas or shifted gas, and economic considerations. Sometimes, a combination of the different separation techniques may be employed to achieve optimal performance and cost-effectiveness. Membrane separation processes offer advantages such as simplicity, modularity, and potential for low energy consumption. However, challenges include membrane plugging due to impurities, limited flux, and the need for multi-stage separation processes to achieve high CO_2 purities [152,154].

2.4 Research trend in sorption-enhanced steam reforming (SE-SR) process

Traditional steam reforming with CCS operates as separate units for reforming and carbon capture. This separation can result in energy inefficiencies and heat losses due to heat duties crossing unit boundaries, thereby increasing the overall thermal requirements and costs. Research is therefore exploring techniques like process intensification to improve efficiency and capture rates. Process intensification seeks to improve process efficiency, economics, and performance through reactor design and process innovations [168]. SE-SR is a prime example of applying process intensification principles to help overcome challenges in conventional steam reforming, while improving CO_2 capture and hydrogen yield. Thus, this work focuses on SE-SR as it intensifies the process by combining reforming, water-gas shift and carbon capture simultaneously within a single reactor [83]. SE-SR process is described in more detailed in Chapter 3.

Though other thermochemical conversion processes, such as chemical looping reforming, offer alternatives for improving carbon capture, they remain in early stage with associated technical challenges. Moreover, SE-SR benefits from leveraging the commercial-scale design knowledge developed for traditional SMR. Research interest in SE-SR process has been growing and various aspects have been investigated for different purposes. However, the core research trend is focused on testing feedstocks, sorbents, catalysts, and reactor concepts, using mathematical models and experiments, as depicted in Figure 2.5. Furthermore, the methodology adopted to select research

articles for analysis is presented in Figure 2.6. About 121 articles majorly from Google scholar, were screened from 1956 to 2024, including conference proceedings and peer-reviewed publications. However, relevant articles between 1956 and 2006 were less than 20, and majority of the articles screened were between 2006 and 2024.

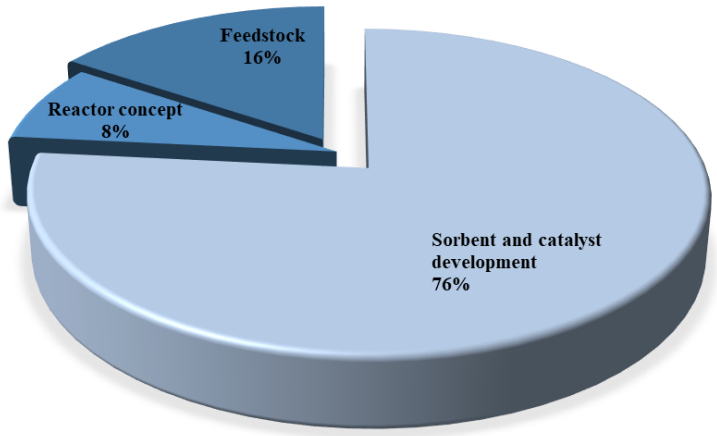

Figure 2.5: Distribution of core research trend for SE-SR process.

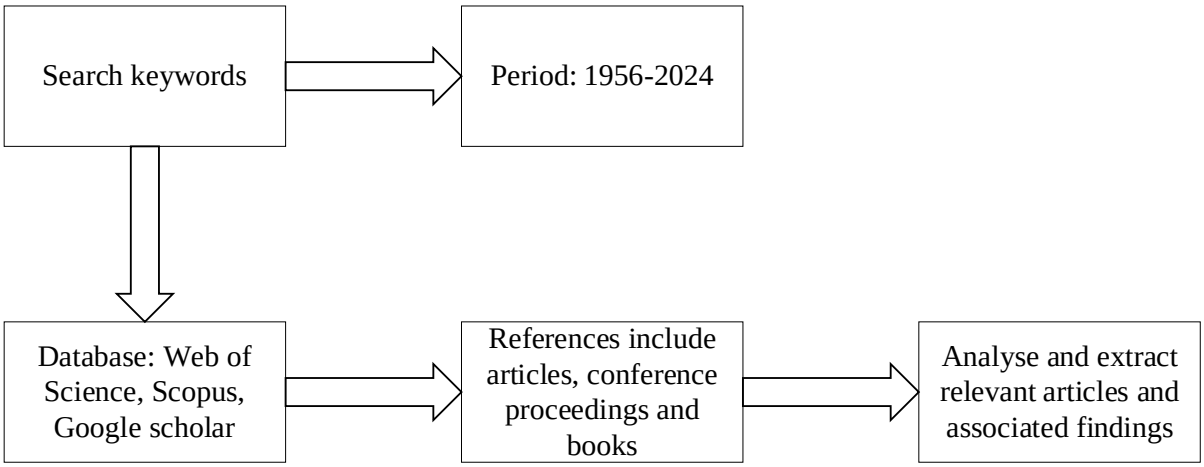

Figure 2.6: Block flow diagram of the methodology followed to select research articles.

2.4.1 Feedstock

A variety of alternative feedstocks beyond natural gas, represented in Table 2.1, have been proposed and investigated for use in SE-SR process to produce high-purity hydrogen. Individual studies conducted lab-scale tests and thermodynamic equilibrium modelling to evaluate the potential of reforming various feedstock compounds via SE-SR. In addition to examining thermodynamic feasibility,

these works also aimed to determine the effect of various operating conditions on the reforming process.

One noteworthy aspect is the ability to utilise byproducts and compounds present in waste streams as feedstocks. This includes materials such as glycerol, a byproduct of biodiesel production, coke oven gas and industrial waste streams containing compounds like phenol and acetic acid. Additionally, the process has been explored with a variety of liquid and gaseous feedstocks, such as alcohols (methanol, ethanol, butanol), hydrocarbons (propane, isooctane), bio-oils, and biogas.

The use of biogas and bio-oil as feedstocks for SE-SR is becoming increasingly popular due to their sustainable and renewable nature. The study by García et al. [169] compared the performance of biogas and pure methane feedstock for SE-SR. The results showed that the CO_2 in the biogas was removed by the dolomite sorbent at temperatures of 550-700°C, allowing the SE-SR process to produce high-purity, high-yield hydrogen from the biogas feedstock, with similar performance to pure methane. However, the study noted that at temperatures above 700°C, the CO_2 removal by the sorbent became less effective for the biogas feedstock compared to methane. As a result, the hydrogen yield was still slightly lower for biogas compared to methane at the higher temperatures, indicating that the presence of CO_2 in the biogas had a slight influence on the conversion to hydrogen.

Conversely, Xie et al. [170] conducted an experiment on SE-SR of bio-oil produced from corn cob pyrolysis, using calcium oxide (CaO) as the CO_2 sorbent. The results showed that using CaO significantly improved both the hydrogen yield and concentration, compared to experiments without sorbent. Over 75-85% hydrogen concentration and yields over 85% were achieved between 750-800°C, with a steam/carbon ratio of 12. However, these optimal conditions identified, such as the high steam/carbon ratio of 12, are more extreme compared to other biomass feedstocks. For example, in SE-SR of biogas, literature reported an optimal steam/carbon ratio between 4 and 6 [169]. The difference could be attributed to bio-oil having a more complex composition than biogas, requiring greater steam levels to drive reforming reactions to completion.

It is worth noting that while the SE-SR process has been studied with a wide range of feedstocks, methane remains the dominant choice, as it is widely available and has well-established conversion pathways.

Table 2.1: Alternative feedstocks investigated for SE-SR for hydrogen production and the purpose of related studies.

References	Feedstock	Type of Study
[171,172]	Glycerol	Experiment, thermodynamic modelling
[173,174]	Butanol	Experiment, thermodynamic modelling
[175,176]	Methanol	Experiment, thermodynamic modelling
[177–181]	Ethanol, bioethanol	Experiment, thermodynamic modelling
[182–184]	Coke oven gas	Experiment, thermodynamic modelling
[185,186]	Waste	Experiment
[170,187,188]	Bio-oil	Experiment, thermodynamic modelling
[189,190]	Propane	Thermodynamic modelling
[191,192]	Phenol	Experiment
[193,194]	Acetic acid	Experiment, thermodynamic modelling
[195]	Hydroxyacetone	Thermodynamic modelling
[196]	Isooctane	Experiment
[197]	Glucose	Experiment, thermodynamic modelling

2.4.2 Catalyst and sorbent development

In SE-SR system, the catalyst and sorbent are the key solid materials that enable the system to produce blue hydrogen. The catalyst facilitates the steam reforming of natural gas or other feeds to generate hydrogen, while the sorbent captures the generated CO_2 and prevents it from being released into the atmosphere.

The choice of solid sorbent for CO_2 capture in SE-SR has been reported to be dependent on a number of other factors, including kinetics of adsorption and desorption, adsorption capacity, cost, performance, and stability after multiple carbonation – regeneration cycles [198]. Sorbents are

generally classified as physical and chemical sorbents; where chemical sorbents allow for chemical reaction between the sorbate and sorbent and physical sorbents do not. Physical sorbents are suitable for relatively low temperature applications while chemical sorbents tend to find application in high temperature processes due to their high capacities at such temperatures. Chemical sorbents include metal oxide sorbents (CaO, MgO, NaO), alkali metal carbonates (including K, Na, Li and Al) and hydrotalcites, while zeolites and metal organic frameworks make up physical sorbents [199].

In SE-SR process, chemical sorbents employed can be grouped into natural and synthetic sorbents. Natural sorbents are derived from naturally occurring minerals such as limestone, dolomite and hydrotalcite and are usually calcined for CO_2 capture. Synthetic sorbents that have been widely tested include sodium zirconate (Na_2ZrO_3), lithium zirconate (Li_2ZrO_3), calcium aluminate ($CaAl_2O_4$), and lithium orthosilicate (Li_4SiO_4) [199,200]. Modifications of calcium, lithium and sodium-based sorbents are also considered as synthetic, and aim to resolve challenges such as sintering, attrition, and low number of carbonation-regeneration cycles encountered in the use of natural sorbents [201].

Natural sorbents are known to degrade after a few numbers of cycles even though they are characterised by high adsorption capacity at high temperatures. For instance, Johnsen et al. [13] studied the SE-SMR process using dolomite as a sorbent. A 98 – 99% hydrogen purity was achieved and remained so for up to four carbonation – calcination cycles of dolomite, followed by a reduced CO_2 sorption unto dolomite [202]. Current research is focused on the development and modification of new sorbents to improve cyclic performance of sorbents, without sintering.

In their research to produce high purity hydrogen, Broda et al. [203,204] prepared a CaO-based synthetic sorbent and compared its cyclic characteristics with a natural sorbent (limestone), in the presence of nickel catalyst. Under similar operating conditions, the synthetic sorbent demonstrated multicycle capability more than twice limestone, capturing more CO_2 and producing a higher amount of hydrogen. High purity hydrogen of 99% was produced at 500°C and steam-carbon ratio of 4. Similar research carried out using synthetic sorbents also proved increased cyclic performance, with an average cycle of 10 [205–207]. These are small number of cycles and will have to be proven for up to hundreds to thousands of cycles before they are deemed cost competitive at large scale when compared with natural and cheap sorbents such as limestone [208]. Comprehensive and recent reviews on state-of-the-art for CO_2 capture sorbents for SE-SR process can be found in literature [209,210].

The criteria for catalyst selection have been reported to include high thermal and mechanical stability, high activity at high temperatures, increased life-time and efficient heat transfer [211]. Nickel catalyst is the most widely adopted catalyst for steam reforming compared to other noble metals such as

platinum, iridium, and rhodium. However, due to its tendency to sinter at high steam – carbon ratio, research have been carried out towards the modifications of nickel catalyst. Ochoa-Fernandez et al. [212] prepared series of synthetic nickel–cobalt hydrotalcite catalysts and tested the effect of different loadings of the nickel–cobalt hydrotalcite compound on the performance of the SE-SR process. High nickel loading showed less deactivation tendencies whereas increased activity was observed for high cobalt loading. The best catalytic performance was found to be 30% nickel and 10% cobalt loading on hydrotalcite. Numerous studies have been carried out to develop and improve the properties of catalysts used for steam methane reforming [213–221]. These studies explored the addition of metal loads like Cu and Zn to create bimetallic catalysts, with the aim of enhancing activity and stability through synergistic effects between the active components. Addition of promoters such as lanthanum (La) and CeO_2 were also investigated to modify the catalyst surface and structural properties.

More recently, focus is shifting towards the development of single particle materials performing functions of both CO_2 capture and steam methane reforming [222–229]. The dynamics of the SE-SR process has led to increased interest in the development of a more compact material made from the combination of sorbent and catalyst, called bifunctional catalysts or combined sorbent catalyst materials [230,231]. They have been widely reported in literature for use in hydrogen production via SE-SR, due to their attractive benefits: elimination of particle sintering, low solid holdup in the reactor, no need for particle separation, better integration of exothermic and endothermic reactions and improved inter-particle flow [230].

In a recent study carried out by Di Giuliano et al. [232], a novel bifunctional catalyst was developed. The material made up of reforming catalyst – Nickel, and sorbent – CaO (in the form of CaO-Mayenite) – was proven to be stable after multicycles of reforming/carbonation and calcination, up to 205 cycles. At reforming operating condition of 650°C and 1 bar, and regeneration operating condition of 850°C and 1 bar, a stable continued uptake of CO_2 as well as reforming reaction were observed on a lab scale basis.

Bifunctional materials show promise for SE-SR but also face some technical hurdles. One challenge is that the sites absorbing CO_2 could expand during usage, which can potentially clog catalytic regions on the material surface over repeated cycles [210]. This swelling effect has the risk of reducing catalytic activity levels needed to drive the capture process.

2.4.3 Reactor design and process configuration

Limited work has explored improvements to reactor design and process configuration for SE-SR process. Some examples include reactor concepts that have been explored experimentally and computationally to analyse SE-SR performance.

Cherbański and Molga [233], and Obradović and Levec [234] investigated SE-SR of methane for hydrogen production using multi-stage trickle bed reactors. Cherbański and Molga [233] developed a model of their reactor and found that higher temperatures, higher sorbent loading and pressures below 0.4MPa improved performance. Obradović and Levec [234] conducted experiments using a 42mm diameter reactor, as shown in Figure 2.7, and validated a model showing their multi-stage design yielded hydrogen at higher purity than single-stage reactors. Both studies demonstrated that a multi-stage trickle bed configuration can efficiently capture CO_2 while producing hydrogen. However, poor heat and mass transfer as well as the formation of hotspots within the catalysts pose challenges. Additionally, scaling up the reactor design presents difficulties due to the complex phenomenon involved [235,236].

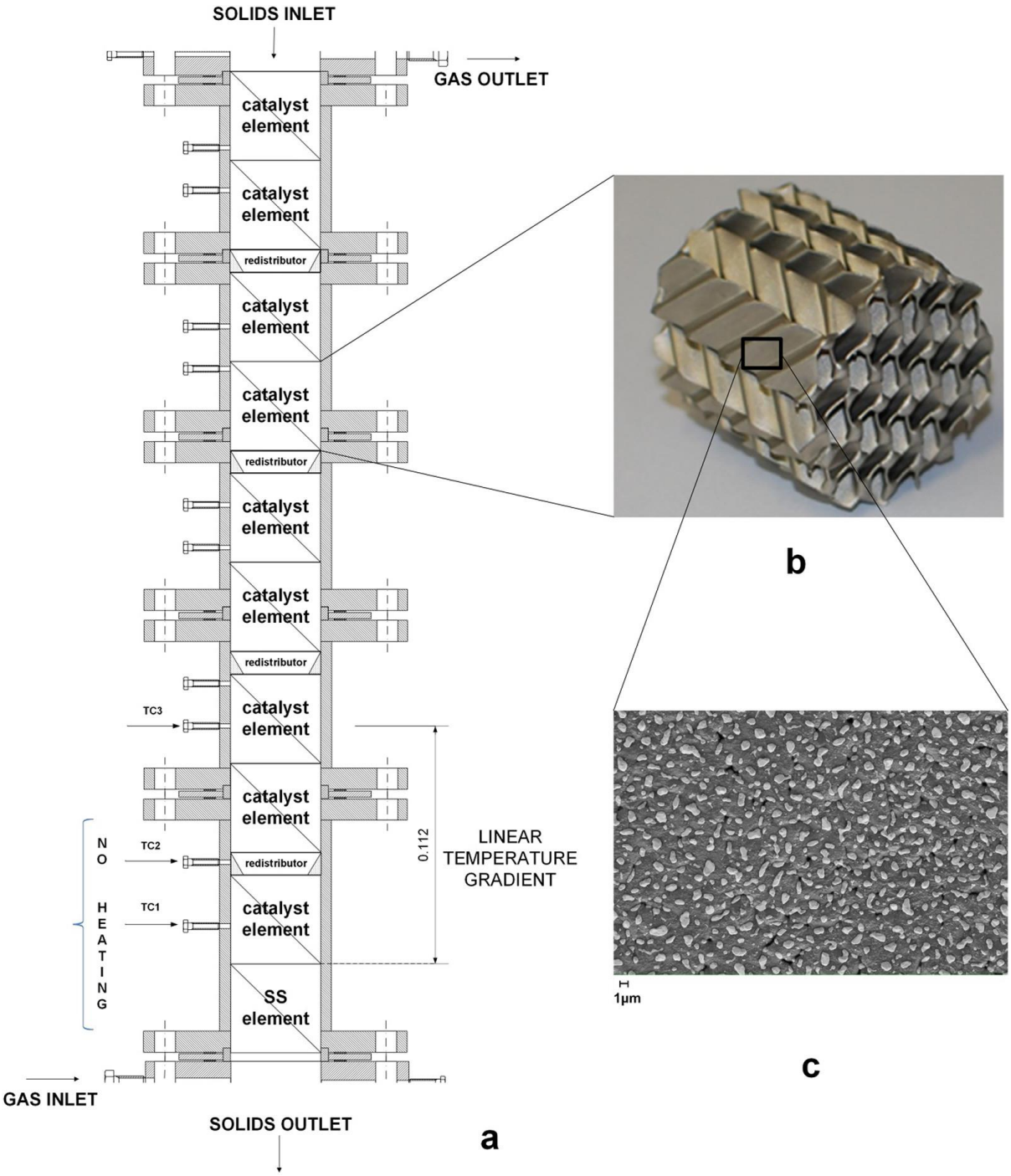

Figure 2.7: Schematic view of a (a) lab-scale multi-stage trickle bed reactor with (b) plate-type catalyst and (c) scanning electron microscopic image of the catalyst [234].

Fixed bed reactors were among the earliest designs tested for SE-SR. These reactors offer efficient gas-solid contacting and easy flow modelling but can suffer from rapid hot spot formation and high pressure drop [237,238]. Researchers have investigated both adiabatic and non-adiabatic, as well as multi-bed fixed bed configurations, exploring ways to improve process efficiency, sorbent development, and process integration [239–243]. Dual fixed beds operated cyclically allowed proof-of-concept

testing for continuous hydrogen production [244]. However, challenges regarding intermittent valve shutdown and switchover time for sorbent regeneration limited further development.

Fluidised bed reactor designs exhibit potential for continuous solids circulation for SE-SR, which eliminates the need for switchovers. The two main configurations that have been explored are dual bubbling fluidised beds and circulating fluidised beds, presented in Figure 2.8, both of which could enable continuous hydrogen production. Few studies have explored dual bubbling fluidised bed configurations to analyse the reforming and regeneration performance in circulating mode [12,245]. However, experimental testing using fluidised bed designs has been limited, especially for the circulating mode [146]. Whilst limited experimental studies have provided insights, modelling efforts have been the primary focus to understand the complex multiphysics and multiscale phenomena [246–248]. Yet, limitations exist in terms of closure approximations, model oversimplification, and the inability to fully capture particle-level interactions. Moreover, some of the studied SE-SR models in circulating mode require benchmarking against reproducible bench-scale experimentation. Alternately, interests are more intensified in the modelling of the single unit reforming/carbonator of the SE-SR, with a number of investigations reported in the literature [249–254]. Though the fluidised state enables uniform temperatures and easy solids circulation between reactors, challenges such as particle attrition and reduced performance due to poor gas-solid contact in certain flow regimes still need to be addressed [255–257].

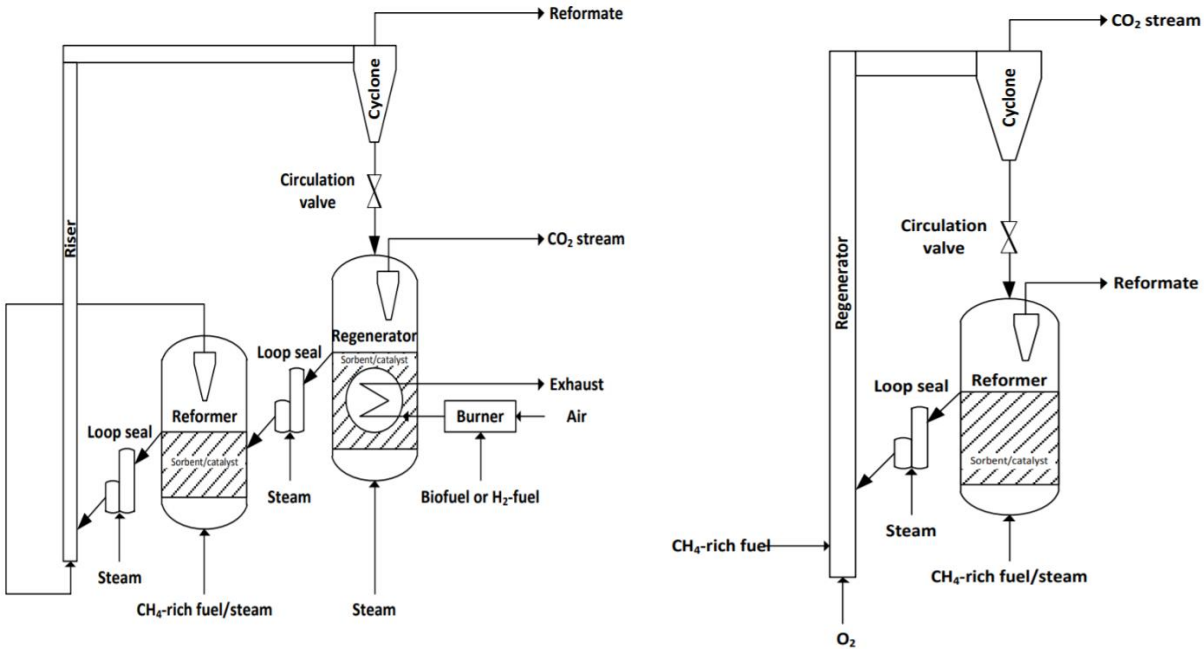

Figure 2.8: Schematic drawing of proposed dual bubbling fluidised beds (RHS) and circulating fluidised beds (LHS) for SE-SR process [258].

Membrane reformer design have the potential to improve hydrogen production from steam methane reforming by separating hydrogen selectively in-situ via a membrane [259–261]. This shifts the chemical equilibrium towards greater fuel conversion. However, incomplete conversion can still occur due to limited permeation through the membrane, for higher hydrocarbons [262]. Recently, combining membrane technology with SE-SR shows prospect to circumvent this issue. Few proof-of-concept studies have demonstrated the viability of this approach. Andres et al. [263] developed a novel reactor with a palladium membrane and limestone sorbent, achieving 78% thermal efficiency, 87% CO_2 capture and 99.99% hydrogen purity. Chen et al. [264] numerically modelled a SE-SR membrane fluidised bed reactor, finding over 91% methane conversion and 98% hydrogen purity could be achieved under optimal conditions. Wu et al. [265] experimentally validated thermodynamic models, achieving up to 91% conversion and 98.1% purity, at steam-to-methane ratio of 4, 1.3 atm and 600°C experimental operating condition. Of course, challenges remain in scaling the technology, improving membrane stability under reaction conditions, and identifying more cost-effective membrane materials.

Beyond reactor design, one study has explored the overall process configuration of the SE-SR system, to optimise the integration of various components such as the reformer, sorbent regenerator, hydrogen purification unit and heat recovery systems. This study performed a thorough assessment of six distinct SE-SR of methane configurations for generating low-carbon hydrogen, using Aspen Plus simulation software [266]. The main conclusions indicated that the configuration combining SE-SR reactors, pressure swing adsorption and chemical looping combustion heat source could realise nearly 100% CO_2 capture, while achieving the highest net efficiency of 75.5%. The process route incorporating SE-SR reactors, pressure swing adsorption and oxy-fuel combustion heat source also attained full CO_2 removal but with an approximately 2.7 percentage point reduction in net efficiency. Recycling hydrogen gas in the SE-SR system allowed for 94.2% carbon capture, though this came at the cost of decreased overall process performance.

2.4.4 Reactor model development

Accurate reactor models are essential for progress in SE-SR technology, as they allow researchers to gain a better understanding of the complex and coupled phenomena occurring within the reactor, optimise the process parameters and scale up the system. Fixed-bed and fluidised-bed reactor models have become quite popular in the literature for analysing SE-SR systems.

Depending on the level of complexity, fixed-bed reactor models can be classified as continuum or dispersion models, cell models, stochastic models, and Computational Fluid Dynamics (CFD) models [267]. The continuum and dispersion models treat the fixed-bed as a continuous medium, without considering the discrete nature of the packing. The cell model divides the system into discrete parts, which are then modelled as a combination of continuous stirred-tank reactors or plug-flow reactors. The stochastic model considers the random nature of the packing structure and flow distribution within the fixed-bed, while the CFD model takes into account the interior geometry of the reactor and solves the conservation equations, to provide a more detailed description of the flow and transport phenomena within the fixed-bed reactor [267]. Among these models, the continuum models are popularly adopted for modelling SE-SR in fixed bed reactors.

Pseudo-homogeneous and 1D heterogeneous continuum models are commonly used to simulate SE-SR in fixed-bed reactors [268–274]. Pseudo-homogeneous models assume ideal plug-flow reactor behaviour, incorporating an axial dispersion coefficient to account for deviations from this. They treat the catalyst and sorbent as a single, dispersed phase, with concentration and temperature gradients only in the axial direction [275]. This approach was initially applied and validated for lab-scale processes, assuming uniform particle properties. However, in real systems, heterogeneity exists between the catalyst and sorbent phases, as well as intra-particle concentration and temperature variations. Heterogeneous models address this by including separate solid-phase mass and energy balances, along with an effectiveness factor to account for resistance to heat and mass transfer within the pellets. Rusten et al. [276] found negligible differences between 1D pseudo-homogeneous and heterogeneous models for small (< 5 mm) particles, but discrepancies emerged at larger sizes due to diffusion limitations within the pellets, highlighting the importance of the heterogeneous approach.

2D heterogeneous models have also been developed and tested against experiments for SE-SR in fixed beds. These models capture radial variations in temperature, which can be significant in larger-scale reactors. Wu et al. [277] found close agreement between 1D and 2D heterogeneous models' post-breakthrough, but greater deviations pre-breakthrough and at the breakthrough point, suggesting 2D effects may be more prominent at larger scales. Moreover, Li and Cai [278] showed that the pre-breakthrough period, connected to the sorbent carbonation/calcination cycle, is sensitive to sorbent properties and should be carefully modelled.

Early studies on SE-SR reactor modelling for fluidised beds focused on the development of simple two-phase models to capture the basic principles of the process. For instance, Johnsen et al. [279] developed a non-linear algebraic fluidised bed model for a bubbling fluidised bed reactor, considering the kinetics of the steam reforming reaction, CO_2 sorption and sorbent regeneration. The model was

able to predict the reactor performance, including the hydrogen yield and CO_2 capture efficiency, under various operating conditions.

As the research for fluidised bed progressed, more sophisticated and comprehensive reactor models have been developed to better represent the complex multiphysics and multiscale phenomena involved in the reactive processes. These advanced models often employ CFD techniques to capture the detailed fluid dynamics, heat and mass transfer and chemical kinetics within the reactor. The majority of the CFD models used for the SE-SR process are based on the Eulerian-Eulerian two-fluid approach, which treats the solid and gas phases as interpenetrating continua [146]. While this modelling approach offers computational efficiency and the ability to capture the overall trends in the fluidised bed behaviour, it also comes with several drawbacks.

The Eulerian-Eulerian two-fluid model relies on empirical constitutive relations to describe the complex solid-gas interactions and particle-scale phenomena, which can introduce significant uncertainties and limit the model's predictive accuracy, especially in regions with high solid volume fractions or rapid changes in flow patterns [280]. Furthermore, the Eulerian-Eulerian approach typically employs a homogeneous description of the solid phase, overlooking the potential for heterogeneities in parameters such as sorbent conversion or catalyst deactivation within the fluidised bed. This simplification can lead to inaccuracies in the prediction of local reaction rates and product distributions, particularly in large-scale reactors where such heterogeneities are more pronounced. To address these limitations, some researchers have explored the use of more advanced modelling techniques, such as the coupling of the Eulerian-Eulerian approach with the discrete element method (DEM) to better capture the particle-scale dynamics [281]. However, the computational cost associated with these advanced models can be prohibitive, especially for the optimisation and scale-up of SE-SR reactor systems.

As the research in this field continues, further advancements in reactor modelling, including the incorporation of more detailed kinetic models, the coupling of multiphysics phenomena, and the integration of experimental data for model validation, are expected to be important in the optimisation and scale-up of SE-SR process.

2.4.5 Other activities

Other active areas of research on SE-SR involve thermodynamic modelling, energy and exergy analysis, and process integration. Thermodynamic modelling has been widely used to assess the feasibility and performance of SE-SR components such as sorbents and feedstocks, as well as its energy and exergy efficiencies. Ortiz et al. [282] used Aspen Plus® to model SE-SR of methane, finding it could produce

95% hydrogen while saving 20-25% energy compared to conventional SMR. Ochoa-Fernández et al. [283] developed an Aspen Plus® SE-SMR model to analyse CO_2 sorbents, determining yield and efficiency depended on sorbent properties.

The suitability of SE-SR for hydrogen-based power generation has been explored through system modelling. Cobden et al. [284] used Aspen Plus® to model hydrotalcite as a sorbent, finding 51% efficiency and 90% carbon capture. Zhang et al. [285] developed an Aspen Plus® conceptual design for hydrogen and combined heat/power generation via SE-SR of methane. Their thermodynamic analysis showed 83% energy and 74% exergy efficiencies, outperforming conventional SMR. Diglio et al. [286] proposed parallel fixed-bed reactor configurations in Aspen Plus® for continuous high-purity hydrogen. A six-stage cyclic process maintained 92% hydrogen production, with part powering SE-SMR and the rest fuelling a solid oxide fuel cell for self-sufficient power generation.

Additionally, exergy and energy efficiencies of SE-SR have been examined in some studies through appropriate thermodynamic modelling. Tzanetis et al. [287] modelled SE-SR of methane and conventional SMR to conduct energy/exergy analyses. Their steady-state Peng-Robinson thermodynamic model found SE-SR's exergy efficiency increased to 78% compared to SMR, while yielding 17.3% purer hydrogen. Similarly, Zhu et al. [288] integrated chemical looping combustion into SE-SR of methane for heat and conducted a process simulation to analyse the process advantages. The process achieved 14.4% higher exergy efficiency than SMR, with 92.6% hydrogen purity. Alam et al. [289] designed SE-SR of methane, integrated with a heat recovery steam generator. Their simulation showed 98% hydrogen purity, 95% carbon capture, and around 68% and 70% exergy and energy efficiencies, respectively.

2.5 Summary

This review evaluated multiple promising low-carbon hydrogen production methods, with a focus on thermochemical processes and their potential role in enabling a sustainable hydrogen economy. These thermochemical processes coupled with effective carbon capture could help reduce greenhouse gas emissions while supporting the large-scale deployment of clean hydrogen. Sorption-enhanced steam reforming (SE-SR) stands out as a compelling option for producing blue hydrogen due to its inherent ability to capture CO_2 during hydrogen generation, avoiding the need for separate carbon capture.

The various feedstocks, sorbent and catalyst materials, reactor design concepts and reactor model developments for SE-SR were also reviewed. Research into using different renewable feedstocks for SE-SR is advancing. Though natural gas currently dominates steam methane reforming commercially, exploring alternative inputs depending on regional resource availability and emission reduction

priorities, could increase interests in adopting SE-SR process. Advances in sorbent and catalyst materials likewise warrant reevaluating reactor designs to improve performance as properties evolve. More complex trickle multi-bed configurations showed promise but have seen limited real-world testing.

Furthermore, developing comprehensive kinetic models remains critically important. Therefore, notable progress has been made developing SE-SR reactor models, especial in fixed bed reactors. However, most models only address the steam reforming reactions and CO_2 sorption kinetics in isolation. For example, there is a need to represent the kinetics of interacting factors more comprehensively like CO_2 adsorption and desorption, and how changing conditions can affect the complex interdependence between sorption and reforming reactions over time. Additionally, incorporating deactivation mechanisms, like sintering and degradation, into kinetic models is also essential for accurate long-term performance prediction. Scaling up and optimising SE-SR reactor systems also presents an area of interest. Most research focuses on lab-scale models; more work is needed addressing scale-up issues involving larger particle handling, reactor geometry influences on flow and heat transfer, and commercial-scale operational optimisation. In summary, key research needs identified include more rigorous kinetics studies, long-term testing, larger pilot demonstrations and comprehensive lifecycle assessments to advance this promising hydrogen production pathway.

The current review has shown methane to be the most common carbonaceous feedstock for SE-SR. Additionally, CaO and nickel-based catalysts are widely used as the solid sorbent and reforming catalyst, respectively, in reported SE-SR systems. As the ultimate goal of this research is to scale-up an SE-SR design, CaO and Ni-based materials were selected for further investigation due to the significant kinetic and operational data available for these combinations. Exploring alternative sorbent-catalyst pairings was deemed less critical in this study, although, complementary studies employing new solid materials with enhanced properties may become valuable for future optimisation and commercialisation efforts. A detailed review of SE-SR mathematical models, presented in Chapter 3, informed the selection of appropriate mathematical models to simulate the intended laboratory-scale and subsequent scaled-up SE-SR system.

3 Review of mathematical models for sorption-enhanced steam reforming (SE-SR) process in fluidised bed reactors

This chapter is based on the peer-reviewed publication:

- Udemu C, Font-Palma C. Modelling of sorption-enhanced steam reforming (SE-SR) process in fluidised bed reactors for low-carbon hydrogen production: A review. Fuel 2023;340:127588. https://doi.org/10.1016/J.FUEL.2023.127588.

3.1 Introduction

Sorption-enhanced processes have been reviewed in literature, as seen in Table 3.1, on a broader scope. However, no review has been devoted to modelling studies concerning SE-SR in fluidised bed reactor at the reactor level. Therefore, this chapter not only focuses on highlighting the status of SE-SR models, but also its modelling approaches and reliability, while providing guidance for future modelling of SE-SR process in fluidised bed reactors. In this chapter, the sorption-enhanced process by steam reforming of methane is mainly described, but also includes steam reforming of other raw materials. The first section gives an overview of the technology and provides a brief review of experimental and pilot studies conducted in fluidised bed reactors. The second section focuses on the models, modelling activities and approaches implemented to study SE-SR process. It is worthy to note that this review does not consider feedstocks employing solid fuels such as coal and biomass.

Table 3.1: Highlights of review studies concerning SE-SR process

Authors	Review focus
Harrison [290]	General overview of research activities in sorption-enhanced process with emphasis sorbent adoption and durability.
Voldsund et al. [291]	General review of fossil-fuel based hydrogen production technologies with carbon capture such as absorption, adsorption, membrane, cryogenic separation technologies
Hanak et al. [292]	Review of progress and application of calcium-looping technologies in power generation systems including the application of sorption-enhanced process in power generation
Wang et al. [293]	Detailed review of sorbents for carbon capture including techno-economic assessment and sorbent application technologies.
Giuliano and Gallucci [294]	Review of SE-SR of methane with focus on the adoption and progress of CaO-based sorbent and Nickel-based catalyst in SE-SR of methane.
Barelli et al. [295]	Overview of methods to improve hydrogen production by SMR. Review of operating parameters for SE-SR of methane including performance of commonly used SMR and carbonation kinetic models.
Wu et al. [296]	Brief review on materials and thermodynamic studies of SE-SR with focus on developments in adsorptive reactor configuration.
Romano et al. [297]	Brief review of calcium-looping technologies modelling studies.
Soltani et al. [298]	Reviewed the impact of different process configurations of SE-SMR and the application of artificial intelligence in optimisation of SE-SMR
Sikarwar et al. [299]	Explored the various dimensions of in-situ CO_2 capture including sorption-enhanced – gasification of solid fuels, reforming of gaseous hydrocarbons, and water-gas shift of various feedstock.

3.2 SE-SR technology

3.2.1 Process overview

The concept of sorption-enhanced reaction for hydrogen production was earlier proposed by Gluud et al. [300], in which the steam reforming and shift reactions occur in a such a manner that the produced CO_2 is removed immediately, thereby shifting the equilibrium towards more hydrogen and CO_2

production, according to Le Chatelier's principle. As shown in Figure 3.1, the steam reforming and carbonation reactions mentioned, occur in the reformer/carbonator in the presence of a catalyst and sorbent. To reduce the cost of replacing fresh sorbent after each capture cycle, the sorbent is regenerated in a calciner or regenerator. In the calciner, the sorbent is regenerated by reducing the partial pressure of CO_2 below its equilibrium either by pressure swing [301] or temperature swing [302]. Various reactor concepts have been proposed and reported for SE-SR, including trickle bed [303,304], fixed bed [223,305–312] and fluidised bed reactors.

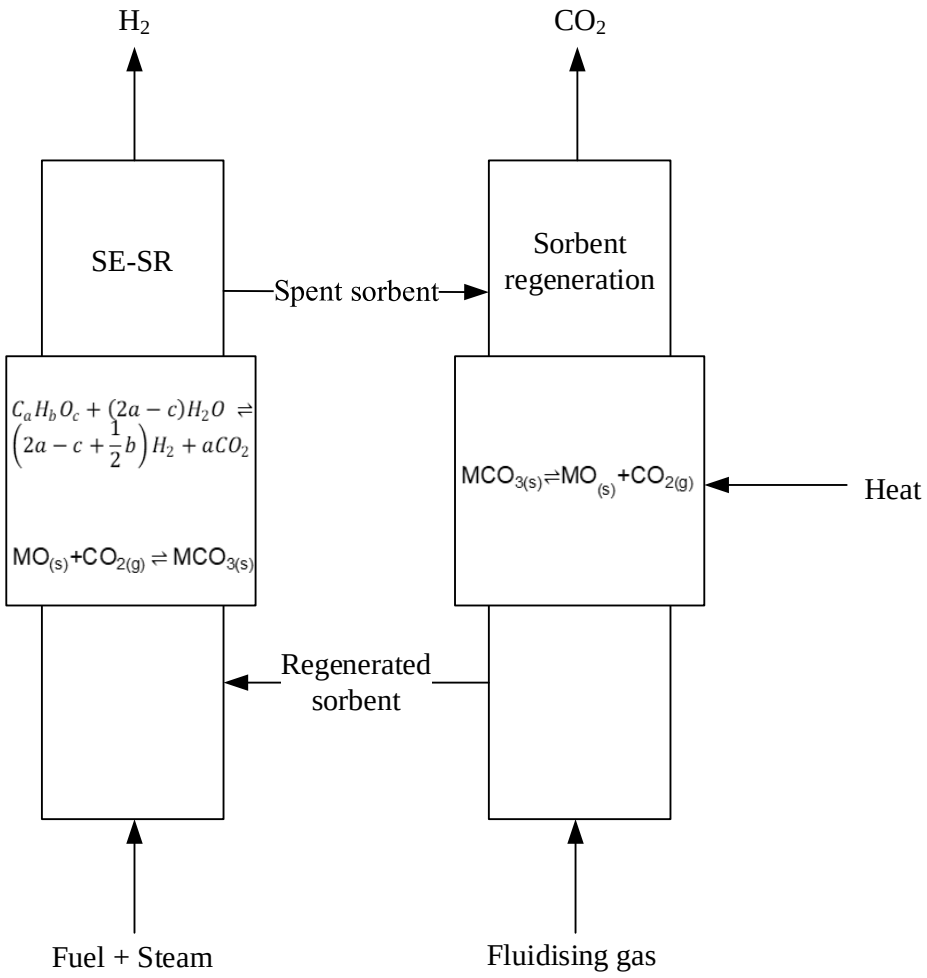

Figure 3.1: Schematic diagram of the sorption-enhanced steam reforming process.

Existing pilot scale configurations for SE-SR usually involve single or two interconnected bubbling fluidised bed (BFB) reactors. In SE-SR occurring in fluidised bed reactors, the fuel and steam are usually introduced through the bottom of the reactor at a specified steam-to-carbon ratio, and a flowrate above the minimum fluidisation velocity for the binary particles (catalyst and sorbent). The reforming and water-gas shift reactions occur inside the reactor alongside the sorption reaction, with reaction temperature ranging between 550°C and 650°C under atmospheric conditions [308,313–316]. This

combined reforming/carbonation reaction is considered to be thermally neutral, which means that the exothermic carbonation reaction provides just enough heat for the reforming reaction in the reactor [290]. Accordingly, the carbonation reaction produces $CaCO_3$ solids that are regenerated in the calciner operated at or above 900°C to produce pure CO_2 stream, with heat provided directly or indirectly. The combined reforming reaction is represented in equation 1, while the carbonation/regeneration reaction is given in equation 2.

$$C_aH_bO_c+(2a-c)H_2O \rightleftharpoons \left(2a-c+\frac{1}{2}b\right)H_2+aCO_2 \quad (1)$$

$$MO_{a(s)}+CO_{2(g)} \rightleftharpoons MCO_{3(s)} \quad (2)$$

M denotes alkali or alkaline-earth metals such as potassium, calcium, sodium, lithium, and aluminium – based materials. Zeolites, metal organic frameworks, and hydrotalcites also make up the sorbents [317]. Hydrogen concentration at the outlet stream of SE-SR can reach as high as 99.31%, as observed in the work of Wu et al. [318] using methanol as feedstock and hydrotalcite as sorbent, or much lesser at ~94% [319], depending on the feedstock, sorbent and operating conditions.

Catalysts and sorbents play a crucial role in the performance of SE-SR. The development and use of solid sorbents is popular due to their lower regeneration temperature which reduces the energy penalty for CO_2 separation [320]. The choice of solid sorbent for CO_2 capture in SE-SR has been reported to be dependent on a number of other factors including kinetics of adsorption and desorption, adsorption capacity, cost, performance and stability after multiple carbonation – regeneration cycles [295]. On the other hand, the criteria for catalyst selection include high thermal and mechanical stability, high activity at high temperatures, increased lifetime and efficient heat transfer [321]. Nickel catalyst is the most widely adopted catalyst for steam reforming compared to other noble metals such as platinum, iridium and rhodium. However, due to the tendency of these catalysts and sorbents to sinter at high steam-to-carbon ratio, a great deal of development is being made towards the improvement of these materials. A more compact material made by the combination of sorbent and catalyst is found to be feasible for application in SE-SR. These materials are referred to as bifunctional catalysts or combined sorbent catalyst materials [294,322], and have been widely reported in literature for use in hydrogen production via SE-SR. They benefit from the minimisation of particle sintering, low solid holdup in the reactor, little or no particle separation, better integration of exothermic and endothermic reactions and improved inter-particle flow [294].

3.2.2 Thermodynamics and effect of operating conditions

A thermodynamic analysis of SE-SR of methane using a calcium-based sorbent shows that an equilibrium hydrogen content of >95% can be attained at steam-to-carbon molar ratio of 4, pressure of 15 atm, and temperatures below 750°C [323]. Figure 3.2 illustrates how hydrogen composition changes under this condition, at varying temperatures. A maximum hydrogen content of 96% can be obtained at 650°C, in addition to a highly efficient carbonation reaction. Although hydrogen purity increases with temperature due to high methane conversion, the CO_2 separation efficiency is highly reduced at temperatures above 850°C and desorption occurs. It has also been reported that even higher pressures up to 30 bar for SE-SR reduces the hydrogen purity and methane conversion but improves the carbonation reaction [324].

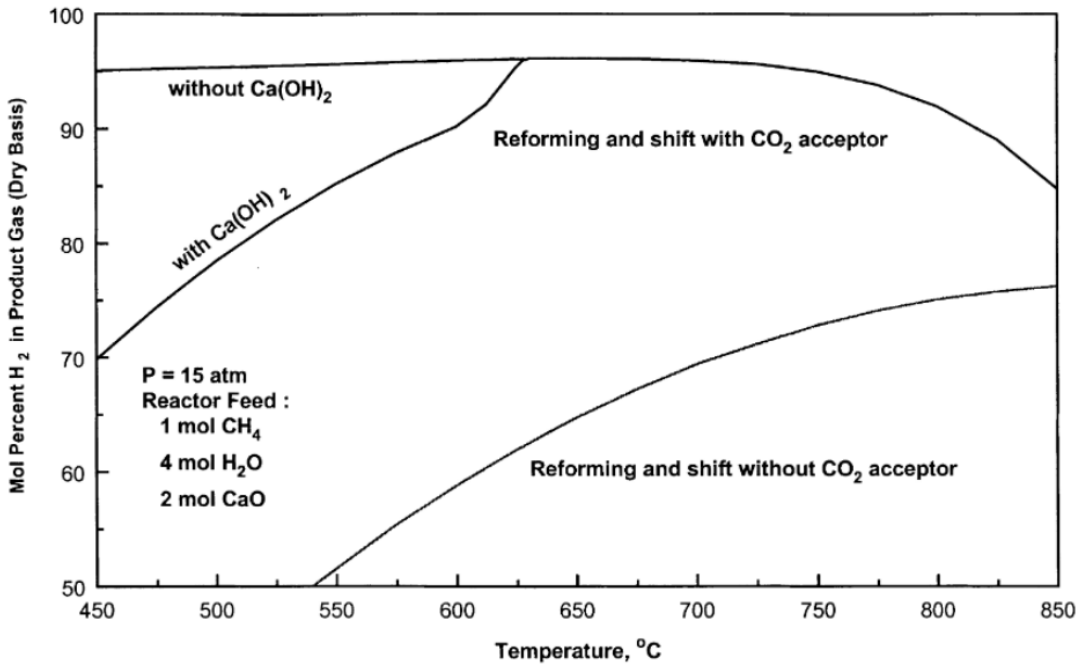

Figure 3.2: Hydrogen yield at equilibrium with and without CO_2 sorbent (reused from Balasubramanian et al. [323], with permission from Elsevier).

Factors such as temperature, pressure, steam-to-carbon ratio are known to affect hydrogen production by SE-SR processes in similar ways as described by thermodynamics. Temperature is a fundamental quantity that affects hydrogen purity and yield, as well as efficiency. At higher temperatures, fuel conversion is favoured due to endothermic steam reforming reaction, whereas CO_2 removal is inhibited due to the exothermic carbonation reaction [308]. Thus, CO_2 and hydrogen are relatively increased and reduced, respectively, in the prebreakthrough periods. Therefore, an optimum temperature at which hydrogen purity is improved whilst reducing outlet CO_2 composition, must be determined. Barelli et al. [295] divided the typical response (see Figure 3.3) from a sorption-enhanced reactor into start-up

region – period of catalyst reduction and activation; prebreakthrough period – equilibrium for SE-SR is reached and maximum concentration can be obtained for all components; breakthrough period – all sorbent has been converted and H_2 begins to reduce; and post-breakthrough period – corresponding to the absence of adsorption and dominance of steam reforming.

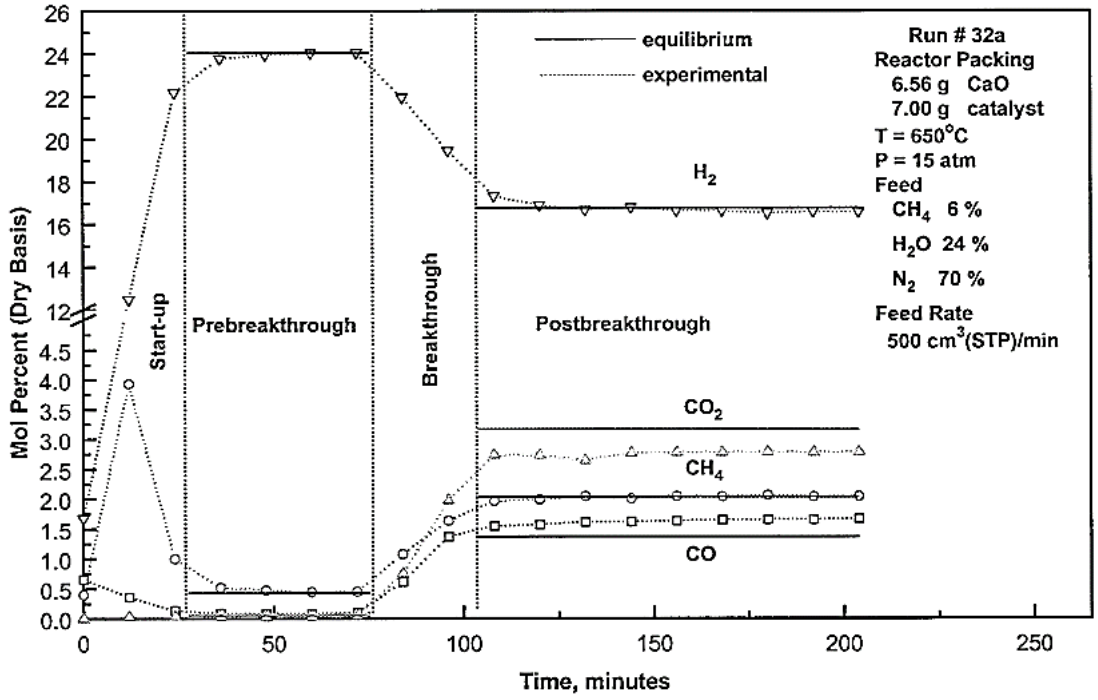

Figure 3.3: Reactor response profile for SE-SR of methane (reused from Balasubramanian et al. [323], with permission from Elsevier).

High steam-to-carbon (S/C) ratio has also been known to improve hydrogen concentration in the product stream [308]. Experimental trends for SE-SR show that the average S/C ratio used in experiments is 3 for methane but up to 6 for ethanol and glycerol. This implies that steam-to-fuel ratio is entirely subject to the type of feedstock adopted and will increase with the carbon content of the feed. However, due to increased plant cost imposed by higher steam-to-carbon ratios, an optimum is advised.

Conversely, the trend in published works shows that almost 80% of the experiments are carried out in fixed bed reactors, possibly due to ease of operation at lab scale while a few are performed in bubbling fluidised bed reactors. However, it is important to perform more SE-SR experiments in fluidised bed reactors, as these are more appropriate for large scale applications. This will also improve modelling and validation studies and enable understanding the challenges associated with continuous operation mode for the process, even at large scale.

3.3 Review of experimental and pilot tests in fluidised bed reactors

Experiments are important in model validation, to ensure the reliability and accuracy of the model in process analysis. Few experiments have been conducted for SE-SR in fluidised bed reactors and main achievements are described here.

3.3.1 Lab-scale fluidised bed reactors

An experiment conducted by Johnsen et al. [325] is popularly employed in model validation of SE-SR of methane in BFB reactors. In their work, a lab scale BFB reactor of height (without the expansion section) – 0.66m and inner diameter of 0.1 m was used to study the performance of SE-SR of methane within the bubbling regime. Sorbent regeneration was also carried out sequentially in the same reactor at 850°C. Under a catalyst/dolomite mass ratio of 2.5, S/C ratio – 3, reforming temperature and pressure of 600°C and 1 atm respectively; hydrogen composition reached 98-99 vol.% dry basis for up to 180 minutes, after 4 carbonation–calcination cycles. The duration reduces because of reduced sorption capacity of the dolomite sorbent caused by the increasing number of cycles. Similar results showing reduced sorption capacity with increasing carbonation–calcination cycles have also been reported by Hildenbrand et al. [326].

In the experiment by Hildenbrand et al. [326], the performance of natural dolomite sorbent during SE-SR of methane was examined in a fluidised bed reactor of inner diameter 25 mm. They reported the existence of an induction period, during which calcium hydroxide ($Ca(OH)_2$) is produced by the reaction of CaO with water vapour. This induction period is found to be dependent on temperature and steam-to-carbon ratio, with elevated temperatures and steam-to-carbon ratios reducing the induction time. Low hydrogen yield was observed during this period, due to the subsequent reduction in steam, following the formation of $Ca(OH)_2$.

Martínez et al. [327] compared the performance of a separate synthetic CaO-based sorbent and reforming catalyst particles with a combined sorbent catalyst material (CSCM), under relevant operating conditions. An SE-SR experiment was conducted in a batch fluidised bed reactor of length – 853 mm, internal diameter – 53.1 mm and distributor plate located 586 mm from top reactor. The same reactor was adopted for the calcination of the sorbent in a steam-rich environment and in the presence of small hydrogen. The CO_2 sorption capacity of the CSCM was found to be the same as that of the separate sorbent particles, and H_2 purity reached 96%. The presence of at least 4 vol% H_2 within the calciner was recommended to prevent the deactivation of the catalyst due to oxidation.

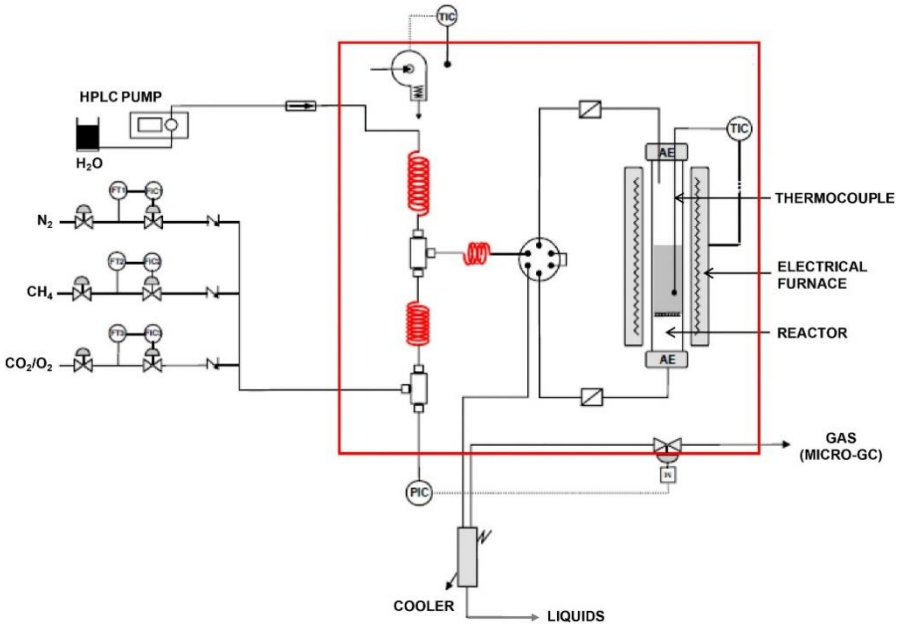

Figure 3.4: Laboratory set-up for SE-SR of biogas (reused from García et al. [328], with permission from Elsevier).

More recently, García et al. [328] experimentally investigated the performance of SE-SR of biogas in an updraft fluidised bed reactor (see Figure 3.4) and compared the results with the conventional biogas reforming. The reactor, which has an inner diameter of 27mm, was loaded with dolomite sorbent and nickel-based hydrotalcite catalyst materials at a sorbent-to-catalyst ratio of ≥ 5 g/g for the experimental runs. Hydrogen purity of 98.4 vol% was obtained at 550–600℃ before it reduced with an increase in temperature, whereas the hydrogen yield obtained at 650℃ was 93.2% for methane and 92.7% for biogas.

3.3.2 Pilot test facilities for SE-SR

SE-SR is still transitioning to TRL 6; therefore, few pilot test facilities are in existence. For example, a 1.5MWth pilot plant is currently being developed at Cranfield University, UK to produce blue hydrogen, with the major aim of demonstrating SE-SR under high pressure conditions (up to 30 bar), while improving the process economics [329]. A brief review of the pilot operations performed in currently existing pilot plants will be provided below, with the goal of identifying key operating parameters and results, useful for modelling studies and validation.

3.3.2.1 Institute for Energy Technology, IFE Hynor

IFE, Hynor operates the Hydrogen Technology Centre consisting of a high temperature solid oxide fuel cell (SOFC) technology integrated with a hydrogen reformer pilot plant, shown in Figure 3.5. The reformer system is a dual bubbling fluidised bed prototype that produces hydrogen by sorption-

enhanced steam reforming of methane [330]. The 30kW$_{H2}$ pilot plant has a reformer/carbonator, which is a bubbling fluidised bed with freeboard height, freeboard inner diameter and bed diameter of 1.20 m, 0.348 m and 0.2545 m respectively, interconnected to a bubbling bed calciner and a riser unit for transport. To enhance heat integration, a high-temperature heat exchanger was installed inside the calciner. Its surface area was sized to provide sufficient heating surface for driving the endothermic decarbonation reaction that occurs within the calciner. A riser with height, 4.5 m, and inner diameter, 0.067 m, transports the solids from the reformer to the calciner using the reformate gas (contains minor quantities of CO_2, CO, unconverted CH_4 and N_2). The operating conditions for the reformer/carbonator and the calciner are 600°C and 850°C, respectively, at near atmospheric pressure and using dolomite sorbent and nickel catalyst.

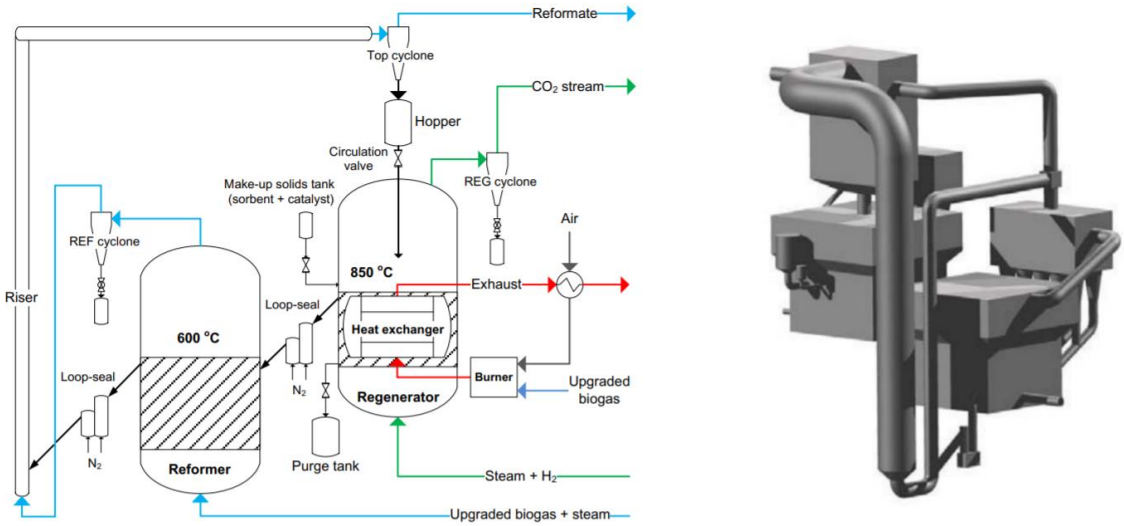

Figure 3.5: Design of the dual bubbling fluidised bed SER plant at IFE (reused from Meyer et al. [331], with permission from Elsevier).

A first batch test of the plant was run at reformer condition – 600°C, fluidisation velocity – 0.29m/s, steam to carbon ratio – 4 and sorbent to catalyst mass ratio of 2.8, using upgraded biogas as the feedstock. A stable hydrogen concentration of 95% vol. and high carbon capture rate was obtained. Temperature distribution across the reactor bed was reported to be uniform, validating the feasibility of operating the process under such conditions. The regeneration batch test, first powered up by electricity before stabilizing with the burner, exhibited a linear and even temperature increase across the bed. However, tests are ongoing to operate these reactors as a loop, coupling the solid circulation in continuous mode.

3.3.2.2 Gas Technology Institute (GTI) Hydrogen Technology

GTI has piloted an SE-SR process termed the compact hydrogen generator (CHG), with hydrogen production capacity of 20 MSCFD (~48 kg/day) and located at the Energy and Environment Research Centre (EERC) in Grand Forks, North Dakota [332]. The pilot plant, with flow diagram presented in Figure 3.6, consists of reformer/carbonator fluidised bed reactor, loaded with ~11 kg of nickel-based catalyst and CaO sorbent that is elutriated through the bed, a standpipe, which temporary stores the $CaCO_3$ to be regenerated, and an indirectly fired rotary kiln calciner. The reformer is operated at 700°C, steam to carbon ratio of 3, and 1-3 atm pressure, whereas the calciner temperature is maintained at 850-900°C. Sorbents of small particle sizes (<10 microns) is adopted for rapid release of CO_2 within a short residence time in the calciner, to mitigate sorbent decay and sintering caused by high temperature exposure. The standpipe is also controlled at hydraulic head of about 0.14 – 0.2 atm to prevent pressure differences between the reactor system as well as separate hydrogen product gases and burner gases, coupled with a rotary valve at the bottom to direct solids into the calciner.

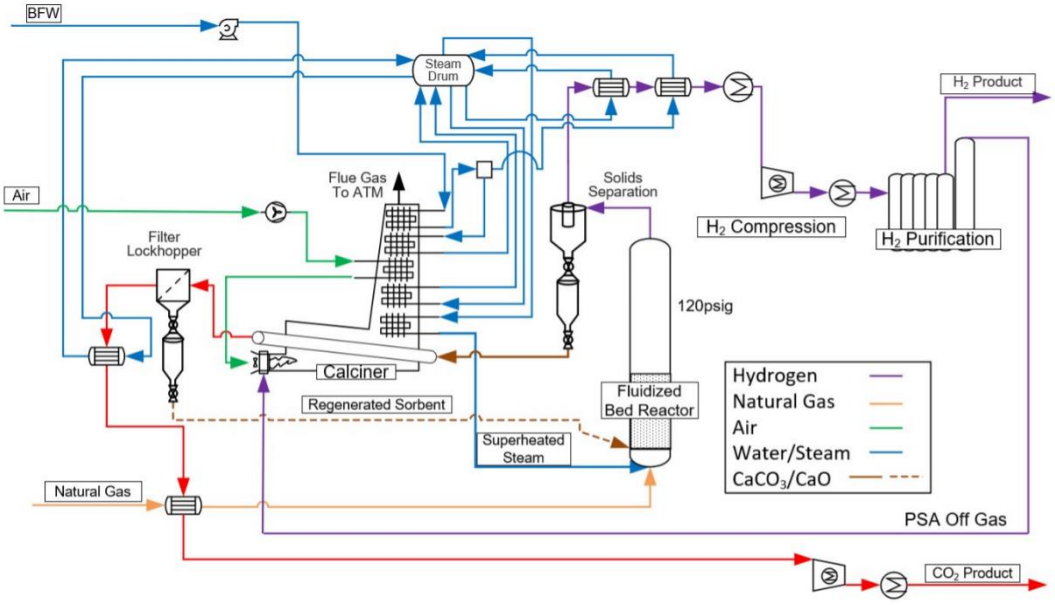

Figure 3.6: Process flow diagram of GTI's compact hydrogen generator pilot plant (reused with permission from Mays et al. [333]).

Four tests were carried out in the plant in 2016, with the first test riddled with challenges arising from design and installation such as rotor damage and the inability to seal the burner hat. However, subsequent tests proved successful, culminating in ~80-90% hydrogen purity, 90% CO_2 capture rate and minimisation of catalyst degradation. The fourth test to increase the feed rate to design rate was successful, but hydrogen purity was reduced due to low sorbent activity. Finally, the total pilot plant

operational time reportedly reached 88+ hours of SER operation and more than 200 hours of solids handling operation, achieving >92% hydrogen purity and 90% carbon capture rate [334].

3.4 Models for SE-SR process

Modelling studies are incredibly useful in developing an understanding of chemical processes, especially modern technologies like SE-SR. Rigorous modelling work will accelerate the deployment of SE-SMR technology, as these studies will expose complications and bottlenecks, as well as provide solutions, associated with the process at large scale. This section aims to provide insights on the status of SE-SR models and modelling approaches, highlight model reliability, drawbacks, and provide guidance for future modelling works, in order to advance SE-SR technology. The increasing interest in SE-SR as a technology for low carbon hydrogen production is the main driver for this section.

The overall mathematical model can vary depending on the scale (lab to large), spatial dimension (1D, 2D and 3D) and state (steady and dynamic). Modelling of reactive flows like SE-SR in fluidised bed reactor incorporates bed fluid dynamics (hydrodynamics) and the chemical reaction kinetics models. The hydrodynamic models are categorised into the conventional fluidisation models and CFD models, while the kinetic models depend on the type of sorbent and feedstock employed, which is different for each feed and catalyst type.

3.4.1 Kinetic models

In SE-SR, kinetic models are developed for the reforming, carbonation/sorption and decarbonation reactions as described here.

3.4.1.1 Steam reforming reactions

SE-SR of methane using nickel-based catalyst and calcium oxide (CaO) as sorbent are predominant in literature, due to their natural abundance and well-established kinetics. Several kinetic models have been developed to describe steam methane reforming (SMR) kinetics using elaborate reaction mechanisms, different kinetic approaches and over various catalysts. The intrinsic kinetics of steam reforming of the hydrocarbons were mostly developed by conducting experiments in fixed-bed or tubular reactors. One of the earlier kinetic studies performed for steam methane reforming over nickel reported that the reaction of steam with methane is first order relative to methane, with methane decomposition being the rate-determining step [335]. This model neglects diffusion limitation of the gases in the derivation of the rate equation and could be difficult in its prediction of product distribution. A subsequent kinetic model proposed that the desorption of carbon monoxide and

carbon dioxide is the rate determining step [336]. The complexities and conflicting description of SMR kinetic models resulted in the development of more exhaustive models by other researchers.

In SE-SR of methane over nickel catalyst, kinetic models by Numaguchi and Kikuchi (NK) [337], and Xu and Froment (XF) [338] are commonly applied. The NK model considered the Langmuir-Hinshelwood and power law type approach to develop a hybrid rate equation for SMR, while assuming surface reaction as the rate-controlling step. The model was studied for reaction temperatures and pressure up to 1160K and 25 bar, respectively. Conversely, Xu and Froment [338] presented a number of possible chemical reactions and generated 21 set of rate equations from developed reaction schemes, in their kinetic study of SMR over $Ni/MgAl_2O_4$ catalyst. They used the Langmuir–Hinshelwood approach to describe and formulate the reaction step and rate equation. Their mechanism indicated that CO and CO_2 are formed in parallel out of the methane adsorbed onto the catalyst, with the predicted rate reported to be dependent on the partial pressure of hydrogen. Although this model has been criticised for being complex and misrepresenting the mechanism of methane dissociation [339], it is widely adopted to model processes involving SMR on Ni-based catalysts. This is probably because all the possible reaction mechanisms involved in SMR, as well as the diffusion limitations, were considered in the determination of the intrinsic rate equation. A summary of the reforming reaction applied to SE-SR is presented in Table 3.2.

Table 3.2: Rate equations for steam reforming reactions applied to SE-SR

Ref.	Reactions	Rate equations (kmol.$kg_{cat}^{-1}s^{-1}$)	Equation
Methane [338]	R_1: $CH_4 + H_2O \rightleftharpoons CO + 3H_2$	$R_1=\frac{\frac{k_1}{P_{H_2}^{2.5}}\left[P_{CH_4}P_{H_2O}-\frac{P_{H_2}^3P_{CO}}{K_1}\right]}{DEN^2}$	3
	R_2: $CO + H_2O \rightleftharpoons CO_2 + H_2$	$R_2=\frac{\frac{k_2}{P_{H_2}}\left[P_{CO}P_{H_2}-\frac{P_{H_2}P_{CO_2}}{K_2}\right]}{DEN^2}$	4
	R_3: $CH_4 + 2H_2O \rightleftharpoons CO_2 + 4H_2$	$R_3=\frac{\frac{k_3}{P_{H_2}^{3.5}}\left[P_{CH_4}P_{H_2O}^2-\frac{P_{H_2}^4P_{CO_2}}{K_3}\right]}{DEN^2}$	5
		$DEN = 1 + K_{CH_4}P_{CH_4} + K_{CO}P_{CO} + K_{H_2} + \frac{K_{H_2O}P_{H_2O}}{K_{H_2}}$	6
Methane [337]	SMR: $CH_4 + H_2O \rightleftharpoons CO + 3H_2$	$r_{SMR}=\frac{k_{SMR}^0\cdot\exp(-\frac{E_{SMR}}{RT})(p_{CH_4}p_{H_2O}-\frac{p_{CO}p_{H_2}^3}{K_{SMR}})}{p_{H_2O}^{1.596}}$	7
	WGS: $CO + H_2O \rightleftharpoons CO_2 + H_2$	$r_{WGS}=\frac{k_{WGS}^0\cdot\exp(-\frac{E_{WGS}}{RT})(p_{CO}p_{H_2O}-\frac{p_{CO_2}p_{H_2}}{K_{WGS}})}{p_{H_2O}}$	8
Ethanol [340]	r_1: $C_2H_6O \rightleftharpoons C_2H_4O+H_2$	$r_1=\frac{k_{ETD}P_{C_2H_6O}}{DEN}\left(1-\frac{1}{K_{ETD}}\cdot\frac{P_{C_2H_4O}P_{H_2}}{P_{C_2H_6O}}\right)$	9
	r_2: $C_2H_4O \rightleftharpoons CO+CH_4$	$r_2=\frac{k_{ACD}P_{C_2H_4O}}{DEN}\left(1-\frac{1}{K_{ACD}}\cdot\frac{P_{CO}P_{CH_4}}{P_{C_2H_4O}}\right)$	10
	r_3: $CH_4 + H_2O \rightleftharpoons CO + 3H_2$	$r_3=\frac{k_{SMR}P_{H_2O}P_{CH_4}}{DEN^2}\left(1-\frac{1}{K_{SMR}}\cdot\frac{P_{CO}P_{H_2}^3}{P_{H_2O}P_{CH_4}}\right)$	11
	r_4: $CO+ H_2O \rightleftharpoons CO_2 + H_2$	$r_4=\frac{k_{WGS}P_{H_2O}P_{CO}}{DEN^2}\left(1-\frac{1}{K_{WGS}}\cdot\frac{P_{CO_2}P_{H_2}}{P_{H_2O}P_{CO}}\right)$	12
		$DEN = 1 + K_{CH_4}P_{CH_4} + K_{EtOH}P_{EtOH} + K_{H_2O}P_{H_2O}$	13
Glycerol [341]	$C_3H_8O_3(g)+3H_2O(g)\rightleftharpoons$ $3CO_2$ g $+7H_2$ g $+345kJ/mol$	$R_i=(\nu_i)Ae^{-E_a/RT}p_{C_3H_8O_3}^{\beta}p_{H_2O}^{\gamma}A_{metalsurface}$	14

(ν_i = −1 or +1, if species i is being consumed or produced, respectively)

Different kinetic models are developed for different catalyst systems because the variation of catalyst composition affects the parameters obtained and mechanisms in the kinetic model, thereby creating difficulty in the derivation of a general rate equation applicable for different catalysts [342]. Other kinetic models with associated rate expressions for SMR on various catalyst systems have been proposed using different kinetic modelling approaches. Power law approach was used to develop kinetic models for SMR on Rh–Ni/$MgAl_2O_4$ catalyst and Ni-YSZ (yttria-stabilized zirconia) cermet, by Katheria et al. [343] and Sugihara et al. [344], respectively. Other kinetic models employing Langmuir-Hinshelwood approach have been developed for Ni/a-Al_2O [345], Nickel/Calcium Aluminate [342] and $LaNiO_3$ perovskite-type oxide [346] catalyst systems.

In Table 3.2, the rate expression for ethanol steam reforming (ESR) catalysed by nickel catalyst, is based on Langmuir-Hinshelwood-Hougen-Watson kinetic model developed by Wu et al. [340], which

considers four reaction pathways – ethanol dehydrogenation, acetaldehyde decomposition, steam reforming, and water gas shift. Other rate expressions for ESR often used combine the power rate law-based ethanol decomposition developed by Mas et al. [347] with the SMR rate expressions of Xu and Froment [338]. In the case of glycerol steam reforming, the reaction rate is derived using the power law approach, with the main reactions being glycerol decomposition and SMR.

3.4.1.2 Carbonation reactions

Carbonation involves the reaction of CO_2 with alkali or alkaline-earth metal oxides-based sorbents or any other material such as layered double hydroxides, hydrotalcite, zeolites, capable of adsorbing CO_2 [293,348]. Rate expressions for these reactions can be developed based on a typical gas-solid heterogenous kinetic models [349]. The generic model for carbonation is expressed as [349];

$$\frac{dx}{dt} = kf(P_a)F(x) \qquad 15$$

Where $f(P_a)$ represents the driving force in terms of CO_2 partial pressure and depends on the order of reaction. The definition of $F(x)$ is a function of conversion and is based on any of the particle kinetic models such as the shrinking core, grain and pore models. According to the shrinking core model, the reaction progresses from the surface to the middle of the particle, leaving behind a thin product layer. It separately describes the surface reaction and product layer diffusion, leading to separate equations developed for both regions [350]. This model has been used to describe the kinetics of dolomite, as presented in Table 3.3 [351]. A parameter, *n* was introduced to account for the nonlinear driving force.

Alternatively, the grain model considers how grain size distribution changes with the reaction [350]. Stendardo and Foscolo [352] used the grain model to describe the behaviour of dolomite carbonation, while accounting for the dramatic decrease in the rate of carbonation that the shrinking core model was unable to explain. Similarly, Sun et al. [353] established an intrinsic rate expression for the carbonation of limestone and dolomite using a grain model. The rate constants were determined for each driving force (based on CO_2 partial pressures) less than and greater than 10kPa. Grain models have also been developed by a few authors for bifunctional pellets, assuming a constant volume and spherical pellets [312,354]. Aloisi et al. [354] successfully validated with experimental data, a pellet model developed for a new multifunctional catalyst for SE-SR of methane. The model was proven to describe the catalytic and sorption considering sorbent decay, with sensitivity analysis of sorbent grain size performed to account for sintering.

Pore models assume that the reaction proceeds by initially filling small pores before the diffusion process occurs [350]. Its variation, a three-dimensional random pore model (RPM), imagines the reacting solid surface to be the result of randomly overlaid cylindrical surfaces with specified pore size

distribution, and has been modified for applications in SE-SR. The RPM for fluid-solid reactions originally proposed by Bhatia and Perlmutter [355] has taken on a variety of forms to account for sorbent multi-cycling in SE-SR process [356].

Furthermore, apparent kinetic models that describes reaction kinetics in a simple and transparent way without the use of morphological measurements, can also be employed to describe carbonation in SE-SR [357]. Other sorption diffusion kinetics models such as the linear driving force (LDF) model have also been proposed [358]. LDF model features a driving force based on the linear difference between the equilibrium and actual adsorption amounts, as well as a proportionality constant, taking into consideration the adsorbent's intraparticle diffusional resistance. It is worthy to note that the conversion for CaO-based sorbent is usually assumed to be below 28% due to reduced sorbent usage and degradation during CaO multi-cycling.

Table 3.3: Rate equations adopted for carbonation in SE-SR

Sorbent [Ref.]	Kinetic models	Rate equations	Equations
Dolomite [351]	SCM	$r_c = \frac{\frac{3}{R_P}(1-X_{CaO})^{\frac{2}{3}}\frac{1}{RT}\left(P_{co_2}-P_{co_{2,eq}}\right)^n}{\frac{1}{k_4}+\frac{R_P\left[(1-X_{CaO})^{\frac{1}{3}}-(1-X_{CaO})^{\frac{2}{3}}\right]}{D_e}+\frac{(1-X_{CaO})^{\frac{2}{3}}}{k_g}}$	16
Dolomite [352], Bifunctional catalyst [354]	GM	$r_c = \frac{\sigma_{0,CaO}k_s(1-X_{Carb})^{2/3}(C_{CO_2}-C_{CO_2,eq})}{1+\frac{k_s N_{Ca}}{2D_{PL}}\delta_{CaO}\sqrt[3]{1-X_{Carb}}\left(1-\sqrt[3]{\frac{1-X_{Carb}}{1-X_{Carb}+X_{Carb}Z}}\right)}$	17
		$r_c = \frac{dX}{dt} = k_C\left(P_{co_2}-P_{co_{2,eq}}\right)^n S(1-X_{CaO})$	18
Dolomite [353]	GM	$k_C = \begin{cases} 1.04\times10^{-4}exp\left(\frac{-E}{RT}\right) \ at\ P_{CO_2}-P_{CO_2,eq}\le 10kPa\ ;\ n=1 \\ 1.04\times10^{-3}exp\left(\frac{-E}{RT}\right) \ at\ P_{CO_2}-P_{CO_2,eq}>10kPa\ ;\ n=0 \end{cases}$	19
		$r_c = \frac{dX}{dt} = k_C\left(P_{co_2}-P_{co_{2,eq}}\right)^n S(1-X_{CaO})$	20
Limestone [353]	GM	$k_C = \begin{cases} 1.67\times10^{-3}exp\left(\frac{-E}{RT}\right) at\ P_{CO_2}-P_{CO_2,eq}>10kPa;\ n=0 \\ 1.67\times10^{-4}exp\left(\frac{-E}{RT}\right) at\ P_{CO_2}-P_{CO_2,eq}\leqslant 10kPa;\ n=1 \end{cases}$	21
Limestone [359]	Apparent	$\frac{dX}{dt} = k_C\left(C_{co_2}-C_{co_{2,eq}}\right)^{0.37}\left(1-\frac{X_{Carb}}{X_U}\right)^{2.61}$	22
Limestone, dolomite [356]	RPM	$\frac{dX}{dt}=k_C\left(C_{co_2}-C_{co_{2,eq}}\right)^{(P/P_o)^{0.083}}\left(1-\frac{X_N}{X_{U,N}}\right)^{2/3}$	23
Hydrotalcite [358,360]	LDF	$\frac{\delta q_{CO_2}}{\delta t} = K_{LDF}(q^*_{CO_2}-q_{CO_2})$	24
LiO-based [349]	Apparent	$\frac{dX}{dt}=K\left(P_{co_2}-P_{co_{2,eq}}\right)^n\left(1-\frac{q}{q_{max}}\right)$	25
Lithium zirconate [361]	Apparent	$r_{ad} = \frac{\Delta w_{max}}{M_{CO_2}}k_{ad}C^n_{CO_2}(1-\frac{\Delta w}{\Delta w_{max}})$	26

(n = order of reaction; U = Ultimate; N = Number of cycles; Z = molar volume ratio of sorbent)

3.4.1.3 Decarbonation/calcination reactions

SE-SR is ideally operated in a cyclic manner, where regenerated sorbent is recycled back to the carbonator. This affects the texture of the sorbent, and in turn the kinetics of the carbonation and calcination. Under this cyclic condition, Okunev et al. [362] analysed decarbonation rates data obtained from experiments for a CaO-based sorbent. A rate expression for decarbonation of CaO was formulated in terms of CO_2 pressure, sorbent texture, Sherwood number and temperature. For SE-SR process employing CaO-based sorbent, the decarbonation model by Okunev et al. [362] is popularly employed and is presented in equation 27.

$$r_{decay} = \frac{1}{M_{CO_2}} \frac{2.46\times10^4 S_{sp} exp\left[\frac{-20474}{T}\right]}{\left[16\frac{d_p^2 S_{sp}\rho_p}{\varepsilon^2 Sh}\right]^{2/3} + exp\left[7.8\left(\frac{PCO_2}{PCO_{2,eq}}\right)\right]} \left(1 - \frac{PCO_2}{PCO_{2,eq}}\right) \quad (27)$$

3.4.2 Hydrodynamic models

Hydrodynamic models delineate the behaviours and interactions between the gas-solid and solid-solid flows, for the various fluidisation regimes characterised by variations in gas velocity. The original hydrodynamic model developed by Toomey and Johnstone [363], and later improved by Kunii et al. [364], describes bed dynamics using bubble action. Though, hydrodynamic models for fluidised bed reactors have been expanded to include the rising CFD models.

3.4.2.1 Conventional fluidisation models

In bubbling fluidised beds, the conventional fluidisation models are the two-phase model postulated by Toomey and Johnstone, which was later improved by Davidson and Harrison [365], and the three-phase model developed by Kunii-Levenspiel [364]. These models use bubble motion to describe the behaviour of fluidised beds, thus limiting its application to bubbling fluidised bed reactor, and are usually empirical or non-predictive [366]. Several modifications to the originally proposed two and three phase models have gone on to be developed. One of such models is the Orcutt model which has been applied to SE-SR of methane [351]. A schematic of such model is presented in Figure 3.7.

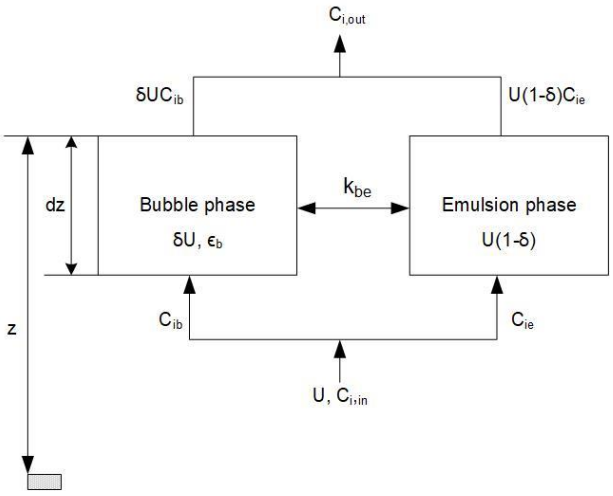

Figure 3.7: Schematic of the differential slice for a two-phase fluidisation model.

In this modelling approach, a differential slice is taken across any height of the reactor (reformer/carbonator) for the bubble and emulsion phases. Mass and energy balances are then written for each phase (gas and solid) in the bubble and emulsion phases, with an interphase mass transfer coefficient (k_{be}) used to represent the mass exchange between both phases. The resulting

equations are partial differential equations which must be solved numerically along with their constitutive correlations. Whilst some of the hydrodynamic parameters including minimum fluidisation velocity, bubble rise velocity, bubble size and bed voidage are presented in Table 3.4, more details on these variables are available in literature [364–366].

Table 3.4: Relevant constitutive correlations in conventional fluidisation model

Parameters	Equations	Unit	Equation No.	Ref.
Minimum fluidisation velocity	$u_{mf} = \mathrm{Re}_{p,mf}\frac{\mu_g}{d_p\rho_g}$;	m/s	28	[367]
	$\mathrm{Re}_{p,mf} = \sqrt{33.7^2 + 0.0408\mathrm{Ar}} - 33.7$;			
	$\mathrm{Ar} = \frac{1.75}{(\varepsilon_{mf}^3\phi)}\mathrm{Re}_{p,mf}^2 + \frac{150(1-\varepsilon_{mf})}{(\varepsilon_{mf}^2\phi^2)}\mathrm{Re}_{p,mf}$			
Bubble voidage fraction	$\epsilon_b = \frac{u - u_{mf}}{u_b}$	-	29	
Bubble rise velocity	$U_b = 0.711\sqrt{gd_b}$	m/s	30	[365]
Bubble size	$d_b = d_{bm} - (d_{bm} - d_{b0})\,exp\left(\frac{-0\cdot 3z}{d_t}\right)$	m	31	[368]
Interphase mass transfer coefficient	$k_{be} = 0\cdot 75U_{mf} + \frac{0\cdot 975g^{0\cdot 25}D^{0\cdot 5}}{d_b^{0\cdot 25}}$	1/s	32	[364]

Other fluidisation models have also been postulated to describe flow structures and transition from the various existing fluidisation regimes. For circulating fluidised beds which mostly operate in the fast fluidisation regime, these models have been classified into three types: (1) models capable of predicting the axial variation in density of solids suspension only, (2) models that assume two or more phases to predict radial variations, and (3) models that describe gas-solid flow using the principles of fluid dynamics [369]. While the Type 2 models have been loosely adopted to model SE-SR in a CFB [370], Type 3 models (including CFDs) are commonly used in the modelling SE-SR process in fluidised bed systems.

3.4.2.2 CFD models

CFD approach employs the conservation law of fluid dynamics to predict gas-solid flow behaviour in fluidised beds. This approach has been proven to depict bubble formation, growth and decay for a continuous flow [371], and can be used for a wide range of fluidisation regimes. Modelling of the

conservation equations (mass, momentum and energy) for the solid and gaseous phases requires that the phases be described using any of the following approaches, depending on the level of detail sought; Eulerian-Lagrangian (E-L) or Eulerian-Eulerian (E-E) [372]. E-L approach treats gas phase as a continuum, whereas solids are treated as discrete phase and particle motion is tracked. Two classes of Eulerian-Lagrangian approach exist: discrete element method (DEM) and dense discrete phase model (DDPM) [373], where the latter has recently been used to model the sorption-enhanced process. The Eulerian-Eulerian (multi-fluid or two-fluid model) approach is widely applied in the literature for the modelling of the SE-SR process, due to its low computational cost. In the E-E approach, both phases are described as interpenetrating continua, with individual conservation equations written and solved for the fluid and/or solid phases. The resulting averaged equation produces a set of unknowns that are solved using closure laws such as the constant particle viscosity (CPV), particle and gas turbulence (PGT), particle and gas turbulence with drift velocity (PGTDV), particle turbulence (PT), and kinetic theory of granular flows (KTGF). Majorly, the concept of kinetic theory of dense gases is applied to the granular solid flows to estimate the necessary constitutive correlations for the solid interfaces such as interphase momentum transfer, internal heat and mass transfer, solid pressure, stress tensors (see Table 3.5) [374]. Detailed description of these multiphase flow model equations and other corresponding parameters can be found in literature [375].

The conservation equations of mass, momentum and heat each contain the term, S, which can be a sink or source of these quantities. For instance, S in the mass conservation equation accounts for the mass transfer between the gas and solid phases due to the production and consumption of gas species from reforming and carbonation. The balanced rate of formation and consumption are derived for each of the gas components using the reforming and carbonation reaction rate expressions and inserted into their respective transport equations.

Table 3.5: Governing equations for a CFD model in the Eulerian framework, and some constitutive correlations and drag models

Principles	Equations	Equation No.	Ref.
Continuity	$\frac{\partial}{\partial t}\ \varepsilon_k\rho_k\ + \frac{\partial}{\partial x_i}\ \varepsilon_k\rho_k u_k\ = S_{con}$	33	[375]
Momentum	$\left[\frac{\partial}{\partial t}\left(\varepsilon_k\rho_k u_{k_i}\right) + \frac{\partial}{\partial x_j}\left(\varepsilon_k\rho_k u_{k_j} u_{k_i}\right)\right] = -\varepsilon_k \frac{\partial P_k}{\partial x_j} + \frac{\partial \tau_{kij}}{\partial x_j} + \varepsilon_k\rho_k g_i - \boldsymbol{M} + S_{mom} u_{k_i}$	34	[375], [376]
Species composition	$\frac{\partial}{\partial t}\ \varepsilon_k\rho_k X_{kn}\ + \frac{\partial}{\partial x_i}\ \varepsilon_k\rho_k X_{kn} u_{ki}\ = \frac{\partial}{\partial x_i}\left(D_{kn}\frac{\partial X_{kn}}{\partial x_i}\right) + S_{sp}$	35	[375]
Energy conservation	$\frac{\partial}{\partial t}(\varepsilon_k\rho_k H_k) + \nabla\cdot(\varepsilon_k\rho_k \boldsymbol{u}_k H_k) = \nabla(\lambda_k \nabla T_k) + \Delta H_k + S_{en}$	36	[375]
Granular temperature	$\frac{3}{2}\varepsilon_m\rho_m\left[\frac{\partial \Theta_n}{\partial t} + u_{mj}\frac{\Theta_{\partial m}}{\partial x_j}\right] = \frac{\partial}{\partial x_j}\left(\kappa_n\frac{\partial \Theta_m}{\partial x_j}\right) + \tau_{mij}\frac{\partial U_{m_i}}{\partial x_j} + \Pi_m - \gamma$	37	[375]
Solid pressure	$P_s = \varepsilon_s\rho_s\Theta_s + 2\varepsilon_s^2\rho_s\Theta_s g_{0,ss}\ 1+e_{ss}$	38	[377]
Interfacial momentum force	$\boldsymbol{M} = \beta\ u_s - u_k$	39	
Wen and Yu drag model	$\beta = \frac{3}{4}C_{\mathrm{d}}\frac{\varepsilon_{\mathrm{p}}\varepsilon_{\mathrm{g}}\rho_{\mathrm{g}}\lvert \boldsymbol{v}_{\mathbf{p}} - \boldsymbol{v}_{\mathbf{g}}\rvert}{d_{\mathrm{p}}}\varepsilon_{\mathrm{g}}^{-2.65};$ $C_{\mathrm{d}} = \frac{24}{\varepsilon_{\mathrm{g}}Re_{\mathrm{p}}}\left[1+0.15(\varepsilon_{\mathrm{g}}Re_{\mathrm{p}})^{0.687}\right]$	40	[378]
Gidaspow drag model	$\beta = 150\frac{\varepsilon_{\mathrm{p}}(1-\varepsilon_{\mathrm{g}})\mu_{\mathrm{g}}}{\varepsilon_{\mathrm{g}}d_{\mathrm{p}}^2} + 1.75\frac{\rho_g\lvert \boldsymbol{v}_{\mathbf{p}} - \boldsymbol{v}_{\mathbf{g}}\rvert}{d_{\mathrm{p}}}, \varepsilon_{\mathrm{g}} \le 0.80;$ $\beta = \frac{3}{4}C_{\mathrm{d}}\frac{\varepsilon_{\mathrm{p}}\varepsilon_{\mathrm{g}}\rho_{\mathrm{g}}\lvert u_{\mathbf{p}} - u_{\mathbf{g}}\rvert}{d_{\mathrm{p}}}\varepsilon_{\mathrm{g}}^{-2.65}, \varepsilon_{\mathrm{g}} > 0.80;$ $C_{\mathrm{d}} = \begin{cases}\frac{24}{\varepsilon_{\mathrm{g}}Re_{\mathrm{p}}}\left[1+0.15(\varepsilon_{\mathrm{g}}Re_{\mathrm{p}})^{0.687}\right], Re_{\mathrm{p}} < 1000; \\ 0.44, Re_{\mathrm{p}} \ge 1000\end{cases}$	41	[379]
Syamlal-O'Brien drag model	$\beta = \frac{3\varepsilon_{\mathrm{p}}\varepsilon_{\mathrm{g}}\rho_{\mathrm{g}}}{4\boldsymbol{v}_{\mathbf{r},\mathbf{p}}^{\mathbf{2}}d_{\mathrm{p}}}C_{\mathrm{d}}\left(\frac{Re_{\mathrm{p}}}{\boldsymbol{v}_{\mathbf{r},\mathbf{p}}}\right)\ u_{\mathbf{p}} - u_{\mathbf{g}}\ ;$ $u_{\mathbf{r},\mathbf{p}} = 0.5\left(A - 0.06Re_{\mathrm{p}} + \sqrt{(0.06Re_{\mathrm{p}})^2 + 0.12Re_{\mathrm{p}}\ 2B - A\ + A^2}\right);$	42	[380]
Gibilaro drag model	$\beta = \left(\frac{17.3}{Re_p} + 0.336\right)\frac{\rho_g\ u_g - u_s\ }{d_p}\epsilon_s\epsilon_g^{-1.8}$ $Re_P = \frac{1-\epsilon_s\ \rho_g\ u_g - u_s\ d_p}{\mu_g^m}$	43	[381]

Conversely in the momentum equation, the pressure, viscous and interfacial forces are accounted for in the solid and gaseous phases. To complete the momentum equation for the solid phase, a solid pressure, P_s, is included to the right-hand side of the equation. The interphase momentum force includes a drag function, β – an important parameter for describing hydrodynamics in fluidised bed reactors. This can be described by various drag models such as the Syamlal-O'Brien, Gidaspow, Energy minimization multi-scale (EMMS) and Gibilaro drag models; that have been applied to model SE-SR in fluidised bed reactors, as presented in Table 3.5. The energy conservation equation is written in terms

of specific enthalpy, H, and solved for phase k, where ΔH_k represents the heat of reaction. The mathematical models for SE-SR have been popularly solved using numerical techniques such as finite volume and finite difference methods in Ansys FLUENT, MFIX and MATLAB respectively.

3.5 Status of modelling activities for SE-SR in fluidised bed reactors

This section highlights and analyses the state-of-the-art in modelling works applied to SE-SR, and discusses the challenges and limitations associated with the models. Different models and modelling approaches have been employed to predict the performance of SE-SR in fluidised bed reactors. A summary of these modelling studies available in literature, including their kinetic model used and modelling approach, is presented in Table 3.6.

3.5.1 Two-phase models

One of the earliest models of SE-SR in fluidised bed reactors was developed using the conventional fluidisation model. Johnsen et al. [351] applied Orcutt's two-phase model to simulate SE-SR of methane in a bubbling fluidised bed reactor, as described in section 3.4.2. The bubble phase was assumed to be without reaction and in plug flow regime, whereas the dense phase contains gases that are perfectly mixed. Their model applied the SMR kinetic model of Xu and Froment [338], the shrinking core model for carbonation/calcination, and was implemented in MATLAB. Both reactors were solved in an iterative manner by guessing the initial temperature of solids input to the reformer, until steady-state was achieved. Although this model is simple and was able to simulate SE-SR of methane, the assumption of stagnant solids, the inability to account for flow details such as particle size distribution and internal circulation, and the complex solution procedure restricts the use of this model, especially for scaleup studies.

Johnsen [370] also applied this conventional approach to model CFB riser for SE-SR of methane, based on the slip-factor criterion. He assumed a steady state plug flow for the catalyst, gas and sorbent in the reformer and determined the solid fraction, using the correlation proposed by Pugsley and Berruti [369]. Though the results obtained were not validated by any experiments, solid fraction was found to be the key parameter influencing the performance of SE-SR of methane, as seen in equation 44. Equation 44 represents the design equation for a riser model, assuming a constant solid fraction along the height of the reactor; where $1-\epsilon$ is the solid fraction, F and r are the solid molar flow and the rate of reaction for species i, respectively. Increasing the solids flow rate increases the solid fraction, which inadvertently leads to an increase in the reaction rate.

$$\frac{\mathrm{d}F_i}{\mathrm{d}z} = A_c \ 1-\epsilon \ r_i \qquad 44$$

The two-phase model has not been considered for a while in SE-SR process modelling. Moreover, technological advancement has accelerated the adoption of computer-based models such as CFD.

3.5.2 Two-fluid CFD models

Current modelling works for SE-SR in fluidised bed reactors, using a wide range of feedstocks and sorbents, are dominated by CFD models. In the two-fluid model, conservation equations are written and solved for two phases: one gas phase and one particulate phase (for both sorbent and catalyst) based on the Eulerian framework. This is different from the multi-fluid/three-fluid model where conservation equations are solved for all the phases involved in the process – one gaseous phase and two solid phases (catalyst and sorbent). However, in most cases, the sorbent and catalysts are assumed to have the same properties and constant size [382–389]. CFD simulation of SE-SR in fluidised bed reactors have been carried out based on different levels of model complexities; usually based on phase description and spatial dimensions (1D, 2D and 3D) of the computational domain. The phase description mentioned here depends on whether it is a two-fluid, three-fluid or E-L model.

A close inspection of literature reveals that majority of the modelling activities originate from a research group in the Norwegian University of Science and Technology, Norway. Their central research theme was on improving reactor models using codes developed inhouse. Transient behaviour studies have been led by Solsvik et al. [386,387,390], which was focused on developing a transient 1D two-fluid model and applying it to SE-SR process. The 1D two-fluid model was applied to the simulation of SE-SR of methane in a BFB reactor to investigate its performance compared with a 2D two-fluid model [390]. Granular temperature, which is the kinetic energy that describes the random velocities of the particles, was not considered in the model. The finite volume method was implemented to solve the model equation in MATLAB and FORTRAN programs. Model validation was performed using simulation results of species outlet composition obtained for a formulated 2D model. However, this 1D model was unable to accurately predict internal flow behaviours such as bed expansion and gas bypassing compared to the 2D model, and relatively small errors in the outlet CO_2 composition, compared with experimental data, were also observed. Figure 3.8 shows the disparity in bed expansion between the 1D and 2D models. Larger bed expansion was predicted by the 1D model compared with the 2D model. The 1D model was also extended to the simulation of SE-SR of methane in a CFB reactor, where they discovered that reactor performance is largely impacted by the reactor temperature.

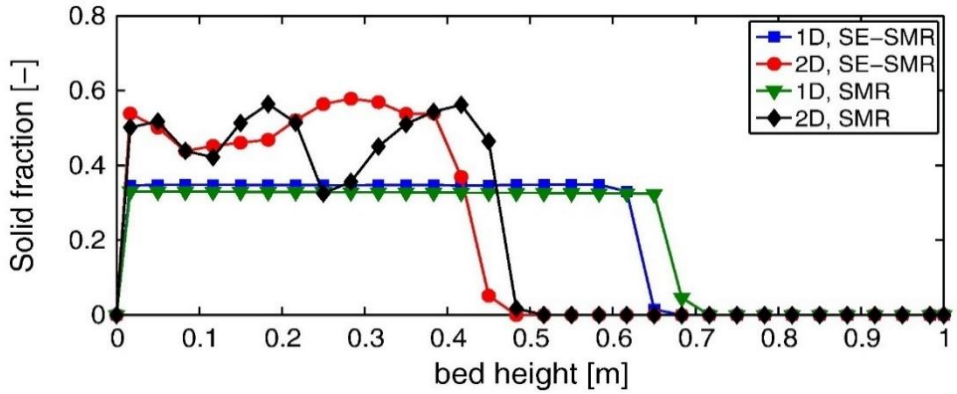

Figure 3.8: Comparison of solid fractions in 1D and 2D modelling of SE-SR of methane in a BFB reactor (reused from Solsvik et al. [390], with permission from American Chemical Society).

Compared to the one-dimensional model, a two-dimensional models can provide a more accurate prediction of gas-solid behaviours. Lindborg and Jakobsen [391] applied an axisymmetric 2D two-fluid model to investigate the performance of SE-SR in fluidised bed reactor, under varying heat supply conditions and reactor widths. The kinetic models were incorporated via a user defined function (UDF) to a CFD software, employing a finite volume method, to solve the set of governing equations. In their work, an ozone decomposition reaction occurring in a BFB reactor was first modelled to compare simulation results of the gas-solid reaction with laboratory experiments (model validation), before applying the model to SE-SR of methane. Though slightly deviating results for the in-bed concentrations were obtained during model validation, the impact of different bed diameters on reactor performance was successfully demonstrated (see Figure 3.9). Figure 3.9 shows relatively low temperatures as bed diameter increases, whereas decreasing hydrogen concentration is observed up to a bed diameter of 0.91 m. However, this axisymmetric 2D may not sufficiently provide a very good prediction of reactor performance. This is because the resulting flow pattern can depict large concentration of catalyst-sorbent particles at the central axis, since particles are unable to pass through the axis, thus negatively impacting on the hydrogen output result.

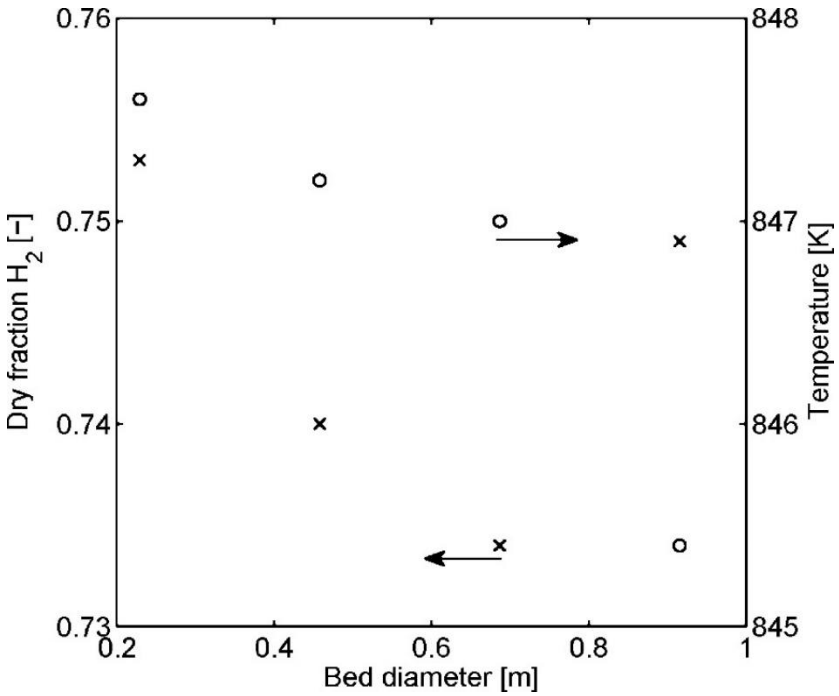

Figure 3.9: Influence of bed diameter on outlet hydrogen concentration and temperature (reused from Lindborg and Jakobsen [391], with permission from American Chemical Society).

In a study conducted by Herce et al. [384], 2D two-fluid model based on KTGF, combined with the Taguchi method was used to perform a sensitivity analysis on variables including bed expansion, CO_2 concentration, methane conversion, hydrogen production, pressure drop and solid fraction for SE-SR of methane. The model predicted that hydrogen production is very sensitive to temperature. Also, increased gas-solid residence time, influenced to a great extent by hydrodynamics, was also observed to significantly affect hydrogen production. Carbonation reaction was also established to be the rate limiting step of SE-SR of methane, with hydrogen purity reaching 92%.

Similarly, Phuakpunk et al. presented a simple 2D two-fluid model to simulate SE-SR of methane [383] and ethanol [392] in the riser of a CFB reactor. As with some other works, model validation was comparable for hydrogen output but showed great deviation for CO_2 concentration – about 40%. The model was used in conjunction with a 2^k factorial design method to perform a sensitivity study and explore the relationship between process variables like catalyst-to-sorbent ratio, temperature and gas velocity, and the response variables: hydrogen flux and purity. While inlet temperature was reported to greatly affect hydrogen flux, overall hydrogen performance – hydrogen flux and purity – was shown to be significantly influenced by solid flux, gas velocity and riser diameter. Further, the response was optimised, and the hydrodynamics of the optimum case investigated. Their work represents the first attempt at optimising hydrogen production in a newly designed riser reactor for SE-SR process. Although, their work did not present considerable information on sorbent performance, it has been established that only a part of sorbent's capacity is being utilised during SE-SR process in fluidised bed

reactors [393]. Therefore, the use of riser may impact on equipment size and cost, as the problem of low residence time affecting sorbent utilisation in a riser is solved by increasing the riser height. Conversely, a more elaborate 3D two-fluid model formulated by Wang et al. [394] and applied to the same process and particle properties, revealed behaviour slightly distinct from the 2D two-fluid model simulation. The steady-state model also presented a more uniform temperature distribution across the bed, indicating complete mixing as shown in Figure 3.10. In another work using the same model, they successfully investigated how hydrodynamic parameters, such as the restitution coefficient and gas flow rates, affect the reactions of SE-SR of methane [395]. It was pointed out that the effect of restitution coefficient was less significant compared with gas flow rate, as this variable is more apparent and dependent on the condition of the gas flow rates.

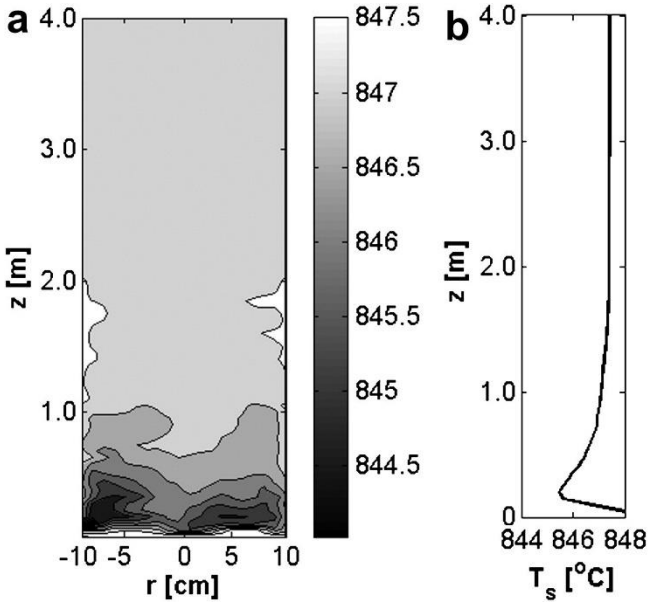

Figure 3.10: Vertical cross-sectional (a) and axial (b) distributions of temperature in the reactor (reused from Wang et al. [394], with permission from Elsevier).

Nevertheless, the simplification of the catalyst-sorbent particle in the two-fluid model neglects the internal transport phenomena occurring at the particulate level, and could impact results of hydrogen evolution and carbon capture. Moreover, Chen et al. [382] have revealed that assuming the same properties for both catalyst and sorbent particles generated a high error percent between simulation and experiments in the prediction of CO_2 concentration (see Figure 3.11).

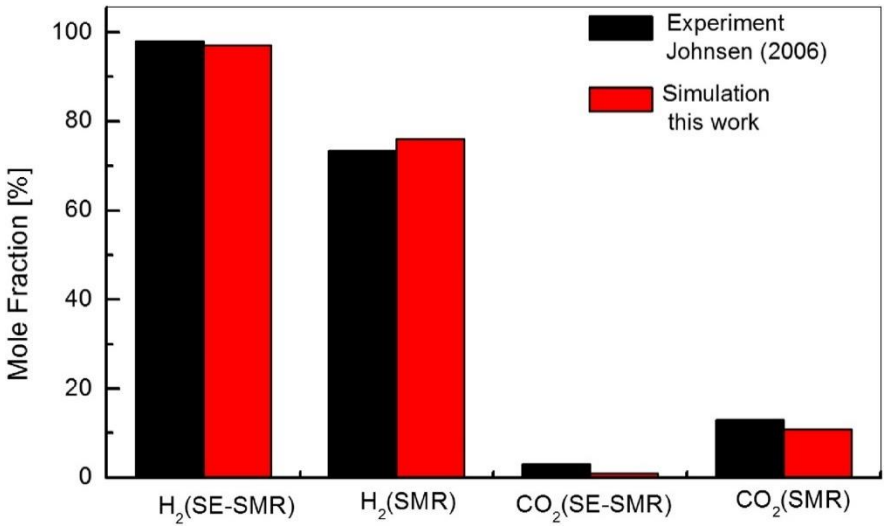

Figure 3.11: Comparison of gas products (H_2 and CO_2) of SE-SMR and SMR obtained from experiment and 2D two-fluid model (reused from Chen et al. [382], with permission from Elsevier).

3.5.3 Three-fluid CFD models

Accordingly, a three-fluid approach, in which the catalyst and sorbent particles are considered as separate phases and a particle-particle drag term is introduced to couple both particles, is more suitable [20]. Such approach can enable the study of phenomena such as particle segregation – an indication of mixing behaviour– or separation, since for such two-pellet system, catalysts need to be separated from sorbent, for sorbent regeneration under high-temperature condition. With this approach, it is also possible to explore the impact of phenomena such as diffusion limitation on the particle scale, which is often neglected in SE-SR modelling. Though, in some steam reforming kinetic models, intra-particle diffusion limitation is usually accounted for using effectiveness factor. Chao et al. [397] presented a multifluid model for polydisperse particles, introducing a semi-empirical frictional particle-particle drag term to account for the long-term frictional contact of particles, combined with the collisional particle-particle drag. The model was able to demonstrate the segregation of catalyst and sorbent particles under varying operating conditions, as well as its impact on reactor performance for SE-SR of methane. The authors noted that segregation occurs at the start of the process due to the large density difference and heavier catalyst particles but becomes well-mixed as reaction proceeds, due to sorbent conversion. Also, solids were reported to blend when the bed is run at 0.2m/s, below which they segregate, with this velocity showing no direct impact on the purity of the hydrogen produced.

In an earlier study conducted by Di Carlo et al. [389], this modelling approach was employed to investigate the hydrodynamics of SE-SR of methane in a lab-scale BFB reactor and compare results with the conventional SMR process. The 2D model considered intra and external mass transfer resistances

in the development of the kinetic models for both catalyst and sorbent, and included a collisional particle-particle drag, which accounts for short term frictional contact of particles. However, model validation results appeared to underpredict bubble diameter and overestimate experiment data, with a relatively large error (24%) reported for CO_2 molar fraction in the output gas. The authors emphasised the need for a model to be further validated at a higher superficial gas velocity. The same multiscale reaction approach applied to the carbonation model was integrated by Chen et al. [319]. They formulated a 2D three-fluid model resembling Di Carlo et al.'s [389], to simulate SE-SR of coke oven gas in a BFB reactor. The model explored the two types of pellets designs applicable to SE-SR process: monofunctional pellets or two-pellet design, where the sorbents and catalysts are modelled as separate particles, and bifunctional pellets or one-pellet design, which integrate the sorbents and catalysts as a single particle. Modelling of sorbent pellets for SE-SR in fluidised beds was achieved by applying the shrinking unreacted core kinetic model, which incorporates the three resistance terms – chemical reaction, intra-particle diffusion and external mass transfer, in its rate equation. Meanwhile, for the bifunctional pellet, the external diffusion term is excluded, since it is being accounted for by the effectiveness factor assigned to the catalysts. Simulation results were comparable to the experimental results generated by the authors.

An upgraded 3D version of the three-fluid model has also been applied for the simulation of SE-SR process. In their work, Wang et al. [396,398] presented this 3D model to simulate SE-SR of biodiesel by-product and crude glycerol in BFB reactors. The model integrated a heterogenous bubble-based drag model to resolve the mesoscale effect on the bubbling bed and was implemented in MFIX commercial program. Particle properties were assumed to have a mean density and diameter, and the multiscale approach for the chemical reactions was not considered. The result was also able to reveal the segregation behaviour between the highly dense sorbent particles and catalyst solids, and the effect of their mixing behaviour on temperature distribution. In addition, they were able to study the behaviour of each of the solids (catalysts and sorbents) involved in the process, as well as the gas distribution, using contour plots. Figure 3.12 shows the species and solids distribution in the reactor after 20 s simulation time.

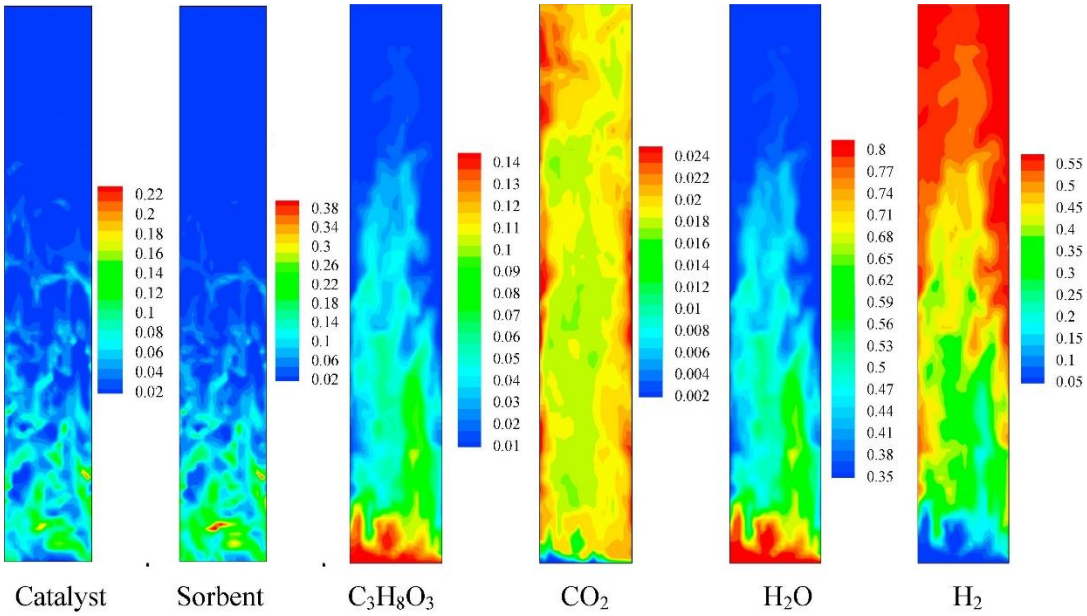

Figure 3.12: Distribution of gas and solid concentrations (reused from Wang et al. [398], with permission from Elsevier).

3.5.4 Eulerian-Lagrange (E-L) CFD models

E-L modelling approach solves for each individual particle using the Newton's second law of motion, easily accounting for particles of different size distribution and densities. Wang et al. [399] formulated a 3D DDPM model, which is an E-L hybrid model, in Fluent commercial code to study the performance of SE-SR of ethanol in a fluidised bed reactor. With the model, the particle size distribution was successfully used to analyse the bed expansion. Figure 3.13 shows the difference in solids concentration and bed expansion when particle sizes distribution is considered. The influence of hydrogen distribution, outlet gas composition, temperature distribution, effect of catalyst to sorbent ratio, and operating pressure on both CO_2 sorption and hydrogen production was also studied.

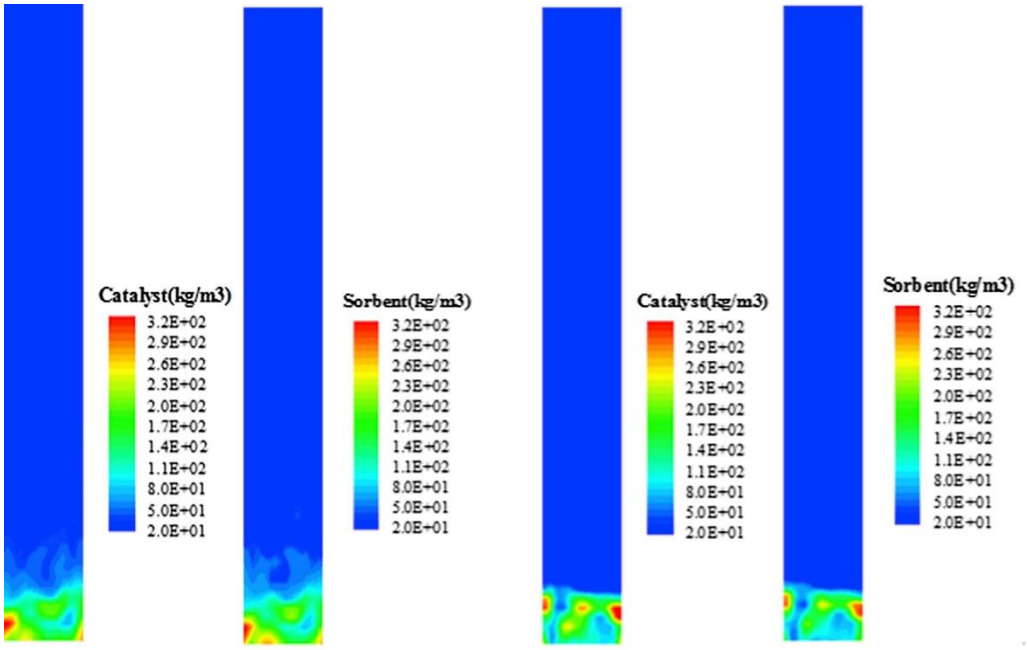

(a) With particle size distribution (b) Without particle size distribution

Figure 3.13: Catalyst and sorbent distribution with and without particle size distribution (reused from Wang et al. [399], with permission from Elsevier).

DDPM model is limited to reactors with small number of particles or dilute particle flows, due to the computational power required for simulation. For larger loadings and process scale, the multiphase particle-in-cell (MP-PIC) model is more fitting and has recently been applied to simulate SE-SMR in a BFB reactor. In MP-PIC, particles are grouped as parcels, thus reducing the number of particles, and are modelled in the Lagrangian framework. Wan et al. [400] adopted this model to simulate SE-SR of methane, where they analysed the impact of particle behaviours and bubble characteristics on the process performance. Figure 3.14 shows the species distribution across the bubbles in the reactor. The concentrations of product gases are seen to increase along the bed height, with lower concentration observed for CO_2.

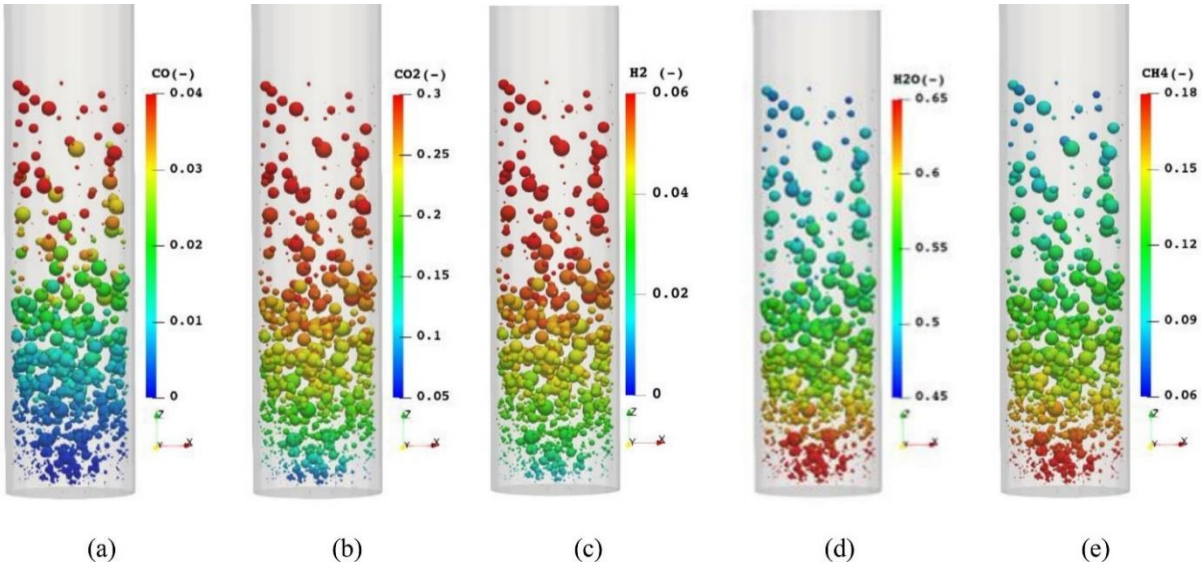

Figure 3.14: Bubble distribution in the reactor described by gas species (reused from Wan et al. [400], with permission from Elsevier).

Table 3.6: Summary of modelling activities for SE-SR in fluidised bed reactors

References	Reactor concept	Operating conditions	Kinetic models			Modelling approach	Research outcome
Johnsen et al. [351]	Dual BFB D = ~0.1 m	P = 1 bar; T = 873K; S/C = 3-4; Gas velocity = 0.1 m/s	**SMR** Ref. [338]	**Carbonation** Ref. [351]	**Calcination** Ref. [351]	Steady-state two-phase model of Orcutt et al. [401]	To achieve >90% capture efficiency, reformer temperature between 540°C and 630°C is recommended.
Solsvik et al. [386,387,390]	BFB, CFB Small D = 0.1 - 0.2m; H = 1 m Large D = 0.6m; H = 4 m	T = 900K; P = 1 and 10 bar; S/C = 3; Gas velocity = 0.2 m/s	Ref. [338]	Ref. [353]		CFD: 1-D Eulerian-Eulerian (two-fluid) model based on KTGF.	• Model validation showed wide deviations when internal flow details were compared. • Performance of SE-SR largely depends on reactor temperature.
Sanchez et al. [402]	CFB D = 1 m	T = 873 K; Gas velocity =0.10 m/s; S/C = 4	Ref. [338]	Ref. [353]	Ref. [362]	CFD: 1-D Eulerian-Eulerian two-fluid model based on Constant Particle Viscosity (CPV); Gidaspow drag model	Low reformer temperature and high hydrogen yield was observed at low solid circulation rates.
Di Carlo et al. [389]	BFB ID = 0.25 m; H = 2 m; Bed height = 0.4m	T = 923 K; P = 1 bar; gas velocity = 0.2 - 0.5 m/s; S/C ratio = 3	Ref. [337]	Ref. [352] and Ref. [354]	-	CFD: 2-D Eulerian-Eulerian two-fluid model based on KTGF; Gibilaro drag model.	At 100% calcined sorbent condition, up to 95% hydrogen purity can be obtained for all superficial velocities whereas at 50% calcined sorbent, less than 85% purity is obtainable.

Herce et al. [384,385]	BFB H = 1 and 4 m; D = 0.1 and 1 m	T = 600, 800 & 900 K; P = 1 & 7 bar; Superficial gas velocity = 0.1, 0.2 & 0.5 m/s; S/C ratio = 4	Ref. [338]	Ref. [352] and Ref. [353]	-	CFD: 2-D Eulerian-Eulerian two-fluid model based on KTGF; Syamlal-O'Brien drag model and Modified-Wang drag model	• The effect of heat and mass transfer on SE-SR reaction is more apparent at large scale compared to the use of different sorbent. • Carbonation reaction is the rate limiting step of SE-SMR process.
Phuakpunk et al. [383,403]	CFB Riser H = 7 m; ID = 0.05 and 0.2 m Regenerator D = 1.2 m; Bed height = 0.8m	Riser T = 848 and 938K; P = 1 bar; S/C = 4; Gas velocity = 4 and 6 m/s; Regenerator Gas velocity = 1 m/s	Ref. [338]	Ref. [353]	Ref. [362]	CFD: 2-D transient Eulerian-Eulerian two-fluid model based on KTGF; Gidaspow drag model	• Hydrogen purity is influenced by design parameters other than reaction parameters, with gas velocity, the riser diameter and the solid flux having the most impact. • Solid preheating to 950°C is required to achieve CaO conversion of ~0% when regenerator was scaled up to a double-stage bubbling bed.
Lindborg et al. [391]	BFB H = 0.687–5.496 m; D = 0.229–0.916 m	P = 10 bar; T = 848 K; Superficial velocity =0.10 m/s; S/C = 5	Ref. [338]	Ref. [361]	-	CFD: 2-D Eulerian-Eulerian two-fluid model based on KTGF; Gibilaro drag model	• Bed diameters have little effect on hydrogen production, therefore wide reactors are the best choice for high mass throughputs. • Performance by heat supply through CFB exceeds the batch reactor wall heating.

Chen et al. [319,382]	BFB H = 1 m; D = 0.1 m	T = 773 K; P = 1 bar; Inlet velocity = 0.08–0.3 m/s	Ref. [338]	Ref. [349] and Ref. [360]	-	CFD: 2-D transient Eulerian-Eulerian two-fluid model; three-fluid models based on KTGF; Syamlal–O'Brien drag model and Gidaspow drag model	• Under high velocities, large bubble sizes reduce CO_2 capture efficiency for the hydrotalcite sorbent, not necessarily gas residence time. • High content of CO and H_2 in COG feed reduces methane conversion • For the three-fluid approach, modelling SE-SR of COG with separate sorbent-catalyst system predicts product yield more accurately, compared with bifunctional catalysts system.
Di Carlo et al. [404]	BFB H1 = 0.6 m and 4 m; ID = 10 cm	T = 900 K; Superficial gas velocity = 0.3 m/s; S/C ratio = 4	Ref. [338]	Ref. [351]	-	CFD: 2-D Eulerian-Eulerian three-fluid model based on KTGF; Gidaspow drag model and Syamlal-O'Brien drag model.	• Considered intra and external mass transfer across the particles. • With a dolomite/catalyst ratio greater than 2, a dry hydrogen mole fraction of more than 0.93 is predicted.

Wang et al. [398]	BFB H = 1.5 m; D = 0.3 m	T = 873 K; P = 1 bar; Gas velocity = 0.4 - 0.6 m/s	Ref. [341]	Ref. [359]	-	CFD: 3-D Eulerian-Eulerian multi-fluid model based on KTGF; EMMS drag model	• Model considered the bubble impact on gas-solid drag force. • Decreasing both sorbent diameter and operating velocity improve hydrogen yield and conversion.
Dat Vo et al. [405]	CFB Reformer H = 4 m D = 0.2 m Regenerator H = 3 m D = 0.2 m	Reformer T = 873–973 K; P = 1–10 bar; Gas velocity= 0.3 m/s S/C = 4.0–5.0 Regenerator T = [1163+(P-1)*15] K; P = 1–10 bar; Gas velocity= 2 m/s	Ref. [338]	Ref. [353]	Ref. [406]	CFD: 1-D dynamic Eulerian-Lagrange model.	• Temperature has a significant impact on SE-SMR performance, cost and efficiency. • In comparison to the SMR process, SESMR was found to achieve a high energy efficiency of 82.2% and a 12% decrease in the cost of producing blue H_2.
Wang et al. [399]	BFB H = 1.0 m; ID = 0.063 m	T = 673 K; P = 1 bar; Gas velocity = 1 m/s	Ref. [340]	Ref. [358]	-	CFD: 3D Eulerian-Lagrange (DDPM) model; Gidaspow drag model	• Considering particle size distribution enhanced prediction of bed expansion height. • High pressure favours CO_2 sorption over hydrogen production.

Yang et al. [407]	ICFB Reformer H = 0.7 m; D = 0.05 m; Regenerator H = 1.4 m; D = 0.05 m	T = 673 K; P = 1 bar; Gas velocity= 1 m/s Regenerator T = 673 K; P = 1 bar; Gas velocity = 2 m/s	Ref. [340]	Ref. [358]	Ref. [358]	CFD: 2D Eulerian-Lagrange (DDPM) model	Increasing the regenerator's velocity and solid loading promotes solids circulation but causes gas leakage.
Wan et al. [400]	BFB H = 1 m; D = 0.1 m	T = 823 – 973 K; P = 1 bar; Gas velocity= 0.15 – 0.3 m/s	Ref. [338]	Ref. [352]	-	CFD: 3D Eulerian-Lagrange MP-PIC; Gidaspow drag model	• Studied the interaction and behaviour of flow characteristics including bubble evolution and thermal parameters. • Bed temperature and gas velocities influence product yields.

3.6 Challenges and future perspectives

A major challenge in modelling the SE-SR process reactors remains the development of models that couple both reactor units in CFB configuration. CFB reactors allow for continuous circulation of sorbent particles between the reformer and regenerator, which is ideal for largescale SE-SR process. To date, limited work has been made towards the extensive modelling and studying of a full-loop system (reforming/carbonation and calcination) for SE-SR, though this is usually attributed to the computational challenge of coupling both reactor units in the solution procedure.

For instance, Wang et al. [408] ran separate simulations of reforming/carbonation occurring in the downer (operating in bubbling flow regime) and regeneration in a riser using a 3D two-fluid model, without considering the solid flux between the reactors. Instead, the sorbent regenerator was investigated as a continuous operation where solids are allowed to leave and enter the boundaries at the outlet and inlet, respectively. Modelling the full-loop system is useful in studying the interactions between solid circulation rates and reaction parameters, since the conditions of the recycled solids from the calciner change. Influence of pressure drops across the reactors, entrainment, sorbent attrition and recovery can also be studied. Nonetheless, different strategies to achieve this coupling have been tried. One example is the 3D Eulerian two-fluid model based on KTGF, developed to model the carbonation/reforming of methane in a downer and sorbent regeneration in the riser of a CFB reactor by Wang et al. [409]. In their study, two sets of coordinates were used to simulate both reactors simultaneously in a CFD software using the same solid flux and time steps. Simulation results obtained at the outlets and inlets of both reactors are exchanged for each time step. Clearly, this simulation approach is prone to errors for a large simulation time due to its complexity. Alternatively, a simpler 1D two-fluid model has been applied to the simulation of SE-SR coupled in CFB reactors. Sanchez et al. [388] developed a 1D two-fluid model, based on Constant Particle Viscosity closure, to analyse SE-SR process in a CFB reactor. Both reactor units were coupled with the source terms for the solid phase species and energy conservation equations, and same pressure level was assumed for both units. This model was used to assess heat integration and solids flux, under steady state conditions. However, the model was also reported to overestimate hydrogen yield and CO_2 sorption when compared with experimental data. Although simple, the use of the 1D model meant inability to study certain flow properties, as this model neglects performance along the radial direction.

There is also a challenge of 1D modelling for the transition zone between the dense bed and freeboard regions. Solsvik et al. [386] tried to resolve this in their dynamic 1D model of SE-SR in CFB reactors by introducing a tolerance condition for void fraction in the governing equation. Regardless, the model

did not accurately predict bed expansion and other hydrodynamics and larger temperatures were recorded, when compared with the base 2D model. Alternatively, Dat Vo et al. [405] applied the principle of coordinate transformation, where the bed height variable is converted to the different coordinates, using the coordinate transformation equations. They simulated methane reforming/carbonation and regeneration in a CFB consisting of bubbling bed and fast fluidised bed reactors, respectively, using a dynamic 1D Eulerian-Lagrangian two-phase model. Loss of flow details associated with this 1D model still makes it undesirable for purposes such as analysing flow behaviours, reactor design and scaleup.

The low sorbent utilisation observed in fluidised bed reactors creates opportunities for studies into new reactor designs for SE-SR. Recently, a modelling study on a new reactor design coupling reforming/carbonation and regeneration processes was conducted by Yang et al. [407], who simulated SE-SR of ethanol in an internally circulating fluidised bed reactor using a 3D DDPM approach. Solid circulation was achieved by the transport of carbonated solids influenced by difference in pressure between both compartments, and the solids return from the regenerator section influenced by the descending velocity of the solids. However, it was found that while increased calciner velocity and solid loading favours solid circulation, gas leakage between the reactors increases, thereby reducing hydrogen yield.

From the literature reviewed, it can be deduced that the different models and modelling approaches applied to SE-SR process can affect the prediction of process performance, although extensive modelling to compare these approaches is yet to be conducted. For one, drag models have been shown to affect the prediction of bed hydrodynamics. Chen et al. [382] applied two drag models – modified Syamlal-O'Brien and Gidaspow drag models – to simulate SE-SR of methane in a bubbling fluidised bed reactor and reported that the modified Syamlal-O'Brien overpredicted the bed expansion by 6%, whereas the Gidaspow model gave a more accurate prediction at 2% difference but overpredicted the minimum fluidisation velocity. Further validation of other drag models applied to the simulation of SE-SR process should be considered.

Some of the experiments used to validate the CFD models do not necessarily depict the conditions of the reactor being modelled. For instance, Shuai et al. [398] developed a CFD model for SE-SR of glycerol in a fluidised bed reactor and validated it with the experiment performed by Dou et al. [410] in a fixed bed reactor. Their model, although attributed to the negligence of catalyst deactivation in the model, overestimated the hydrogen volume fraction. Additionally, the percentage error between the simulated and experimental data for outlet methane composition was around 83%. Therefore, more

experimental works conducted in fluidised bed reactors are needed to enable validation of SE-SR reactor models.

Due to the high capital cost associated with carbon capture plants, it is more cost-effective to operate SE-SR at high pressure conditions, to reduce the energy penalty of compressing hydrogen downstream. This condition has recently been considered and modelled by few authors [411,412], but will still require validation with a much larger-scale test data. Modelling and validation of the process in fluidised bed reactors under such industrial conditions is crucial.

Solid materials involved in SE-SR in fluidised bed reactors will be subject to continuous multi-cycling, implying the need to consider decay and sintering of these materials, as well as loss in sorption activity over time. However, information on bifunctional materials under this condition is scarce in literature. It is necessary to develop correlations that represents the decline in sorbent activity during cycling, specific to these kinds of materials.

Furthermore, with the current advancement in computational capability and performance, opportunity lies in developing high-fidelity models for full-loop SE-SR process. This will allow further studies into the improvement strategies of heat transfer between both reactors.

Finally, this chapter has provided a focused review of modelling studies for SE-SR in fluidised beds, addressing the need for a thorough evaluation and guidance on reactor-level modelling of SE-SR within fluidised bed, to support design and scale-up. As no such review had been conducted previously, it summarises the current status of SE-SR models and the various modelling approaches/techniques employed. This is important as fluidised beds also present a complex multiphase modelling at the reactor scale.

3.7 Summary

This chapter first explores the concept of SE-SR technology, then the experimental activities and pilot tests performed for this technology, followed by the review of progress made on SE-SR modelling. It was found that the Eulerian-Eulerian two-fluid model is the most popular approach widely adopted for modelling SE-SR in fluidised bed reactors. However, the averaging method used to close equations ignores flow details at particle level and simplifies the particle system. Moreover, while hydrogen purity and yield have been predicted within an acceptable error, larger errors for CO_2 gas output relative to experimental data have been reported for this model type.

More work remains to be done in modelling the full-loop SE-SR unit, comprising the reformer/carbonator and calciner. That way, it is possible to investigate and optimise heat transfer and

thermal efficiency between both reactors, sorbent circulation rate required to improve CO_2 capture efficiency, and overall system performance. Investigation of SE-SR modelling in circulating fluidised bed reactors showed that low usage of sorbent sorption capacity is observed, hence, opportunity lies in the design and improvement of different designs for the reformer/carbonator and calciner. In this thesis, the challenge of full-loop simulation was met by applying computational particle fluid dynamics (CPFD) modelling in Barracuda VR® , a leading computationally-efficient CPFD software. But firstly, this CPFD was applied to simulate a stand-alone SE-SR of methane reformer/carbonator. The CPFD model results were validated against literature data, followed by parametric analysis of the SE-SR process. This validation exercise and process analysis is presented in the following chapter.

4 A three-dimensional computational particle fluid dynamic model for sorption-enhanced steam reforming of methane

4.1 Introduction

This chapter is aimed at developing a validated reactor model to improve the description of reactor performance in fluidised beds for SE-SR process. Fluidised beds provide good heat and mass transfer characteristics, essential for the endothermic steam reforming reactions and efficient contact between catalyst, sorbent, and reactant gases. However, the hydrodynamics of fluidised beds are complex, and characterised by the chaotic motion of bubbles and solid particles. This multiphase flow behaviour and solids motion dictated by fluidised bed hydrodynamics influence critical performance factors like mixing, conversion rates, selectivity, attrition, and scalability [413]. High fidelity mathematical modelling can provide insights into the detailed flow behaviour and reactor performance, to enable optimal design, operation, and scaling.

CFD models are powerful modelling tools for understanding how fluids and particles interact in fluidised bed reactors, and for designing reactors that operate efficiently. Depending on the desired level of flow details aimed to be resolved, three modelling strategies have been described: Eulerian-Eulerian approach, and Eulerian-Lagrangian approach [281]. In the Eulerian-Eulerian model, the different phases are treated mathematically as interpenetrating continua, described by volume fractions, conservation equations, and constitutive relations obtained through empirical correlations [414]. This approach is computationally efficient for large scale simulations but relies on empirical closure models and cannot account for particle-scale phenomena. The Eulerian-Lagrangian approach combines Eulerian representation of the fluid phase with a Lagrangian description of the particulate phase [414]. Individual particle trajectories are computed, enabling the modelling of particle-scale phenomena. The particle-in-cell (PIC) method is a sub-category of this approach, where computational particles represent a collection of physical particles. This reduces computational cost while retaining an accurate representation of hydrodynamics. The computational particle fluid dynamics (CPFD) model adopted in this work is based on the multiphase-PIC (MP-PIC) method, which is the multiphase extension of PIC to dense gas-solid flows.

MP-PIC has been applied to study the hydrodynamics of gas-solid fluidised beds and validated against experimental data. Early work by Andrews and O'Rourke [415] demonstrated the MP-PIC model's capabilities for simulating complex dense particulate flows across dilute to dense loading, with multiple particle sizes and differential settling. For batch settling of a tertiary particle mixture, the MP-

PIC model showed good agreement with the experimental data over the full range of volume fractions tested. The model accurately captured the differential settling of the three particle sizes, making it suitable for studying segregation and mixing in binary fluidised beds. Snider et al. [416] expanded the MP-PIC modelling approach to two-dimensional simulations of fluidised beds, while Snider [417] further extended the method to three dimensions. In their works, improvements were made to the grid-to-particle interpolation techniques used to transfer relevant field quantities from the Eulerian grid to the Lagrangian particles, and the particle stress model. These enhancements to the interpolation methods and the sub-grid particle normal stress model helped improve the prediction of essential fluidisation characteristics like bed expansion, and solved problems associated with complex reactor geometries.

Up until recently, the MP-PIC modelling approach had not been applied to simulations of SE-SR occurring within fluidised bed systems. However, Wan et al. [418] applied this MP-PIC technique for the first time to study SE-SR of methane in fluidised beds, pioneering a new application for this numerical model. This OpenFOAM software-based model incorporated a homogeneous drag model (Gidaspow) and SMR kinetic model (Xu and Froment), alongside a spherical grain carbonation model. Subsequently, Di Nardo et al. [419] applied the MP-PIC to SE-SR of methane using a CPFD software. Their model featured a heterogeneous EMMS drag model, Xu and Froment's SMR kinetics, and a shrinking core carbonation model. Both studies parametrically analysed SE-SR of methane via variables like velocity, temperature, as well as bubble behaviour studies.

In this present study a high-fidelity 3D CPFD model was developed, by combining the two sub-models: 1) a hydrodynamic model describing gas and binary catalyst-sorbent particle behaviour, and 2) kinetic models for SMR and carbonation reactions. Three drag models - homogeneous and heterogeneous - were tested, alongside an SMR formulation (Numaguchi) and changing grain size carbonation model. The developed model was applied to the simulation of SE-SR in a bubbling fluidised bed reactor and will be a significant tool in the subsequent scale up of the process. The results from the model simulations were first compared with experimental data obtained from reliable literature, before parametric analysis was conducted. The validated CPFD model was able to predict the effect of velocity, pressure, and steam-to-carbon ratio on the performance of SE-SR of methane.

4.2 Methodology

A numerical model for SE-SR of methane was developed using CPFD software, an Eulerian-Lagrange method that draws on the MP-PIC approach, in Barracuda Virtual Reactor® v23.0.1. Barracuda VR® is a specialised fluidised bed reactor software focused on simulating chemically reactive multiphase flow

systems at low computational cost. It has been employed to study the kinetic and hydrodynamic interactions in fluidised bed reactors for chemical processes such as biomass gasification [420,421], and is one of the solutions to the drawback of other widely used modelling approaches, such as the Eulerian-Eulerian multi-fluid and discrete particle models. Certain drawbacks such as the inability to fully capture particle-scale interactions can easily be resolved using the CPFD method implemented in Barracuda VR®, especially for highly-dense beds.

4.2.1 Hydrodynamic model

In the MP-PIC approach, the computational domain is divided into a finite number of Eulerian cells to form a fixed mesh. The fluid phase variables, such as density, velocity and pressure, are defined on this stationary mesh. The particulate phase is modelled using computational particles that are free to move within the domain. Each particle represents a collection of physical particles and tracks their properties in a Lagrangian framework. As the particles traverse the cells over time, their properties are interpolated from the particle locations onto the stationary Eulerian mesh, using an interpolation operator. Likewise, the fluid phase variables defined on the fixed grid, such as hydrodynamic forces – pressure and drag, are interpolated back to the particle positions to update their motion. This coupling between the discrete Lagrangian particle phase and continuous Eulerian fluid phase facilitates multiphase interactions while reducing the computational cost, compared to fully resolving each individual physical particle.

The governing multiphase equations incorporate the conservation of mass, momentum and energy for both phases. Constitutive models describe stress and viscosity relationships. Additional terms account for the exchange of properties between phases via interpolation, as well as interphase forces like gas-solid drag. Together, these equations provide a numerical framework to simulate multiphase flow dynamics efficiently in Barracuda VR® [422].

i. Gas phase

The mass, momentum and energy conservation equations for the gas phase, assuming incompressible fluid phase, are expressed in equations 45, 46 and 47, respectively [415,423].

$$\frac{\partial(\theta_g \rho_g)}{\partial t} + \nabla \cdot (\theta_g \rho_g \boldsymbol{u}_g) = S m_g \quad (45)$$

$$\frac{\partial(\theta_g \rho_g \boldsymbol{u}_g)}{\partial t} + \nabla \cdot (\theta_g \rho_g \boldsymbol{u}_g \boldsymbol{u}_g) = -\nabla p + \boldsymbol{F} + \theta_g \rho_g \boldsymbol{g} + \nabla \cdot (\theta_g \tau_g) \quad (46)$$

$$\frac{\partial(\theta_g \rho_g \mathrm{h}_g)}{\partial \mathrm{t}} + \nabla \cdot (\theta_g \rho_g \mathrm{h}_g \mathbf{u}_g) = \theta_g (\frac{\partial \mathrm{p}}{\partial \mathrm{t}} + \boldsymbol{u}_g \cdot \nabla \mathrm{p}) - \nabla \cdot (\theta_g \boldsymbol{q}) + S_h + q_D \quad (47)$$

Where $\theta_g, \rho_g, \boldsymbol{u}_g, \mathrm{h}_g$ and τ_g are the gas volume fraction, density, velocity, enthalpy, and stress tensor, respectively, for the gas phase. $\boldsymbol{F}$ is the interface momentum transfer and couples the gas phase momentum with the particle motion. The stress tensor is given as:

$$\tau_{\mathrm{g}} = \tau_{\mathrm{g},ij} = \mu_{\mathrm{g}} \left(\frac{\partial u_i}{\partial x_j} + \frac{\partial u_j}{\partial x_i} \right) - \frac{2}{3} \mu_{\mathrm{g}} \delta_{ij} \frac{\partial u_{\mathrm{k}}}{\partial x_{\mathrm{k}}} \quad 48$$

In addition, the species continuity equation shown in equation 49 are solved to determine the mass fraction, $Y_{g,i}$, for each individual gas species, *i*, present in the multiphase mixture. The species continuity equations describe the conservation of mass for each gas component at every point in space and time. By finding the localised mass fractions, $Y_{g,i}$, the composition of the gas mixture is known at any given location.

$$\frac{\partial(\theta_g \rho_g Y_{g,i})}{\partial t} + \nabla(\theta_g \rho_g Y_{g,i} u_g) = \nabla(\rho_g D_t \theta_g \nabla Y_{g,i}) + Sm_{i,chem} \quad 49$$

The term D_t in the species transport equation represents the turbulent mass diffusivity, which accounts for turbulent mixing effects, while $S\dot{m}_{i,chem}$ is the species source term due to chemical reactions occurring in the system.

ii. Particle phase

The particulate phase is defined by the particle distribution function (PDF). The PDF, denoted as ϕ, provides a statistical representation of the particulate phase. It depends on particle properties such as position x, time t, velocity $\boldsymbol{u}_p$, and density ρ_g. To analyse the time evolution of the particulate phase distribution, the Liouville equation shown below, is commonly solved.

$$\frac{\partial \phi}{\partial t} + \nabla \cdot (\phi \boldsymbol{u}_p) + \nabla_{\boldsymbol{u}_p} \cdot (\phi \boldsymbol{a}_p) = 0. \quad 50$$

This Liouville equation accounts for changes in the PDF due to particle motion via $\boldsymbol{u}_p$, as well as acceleration of particles, $\boldsymbol{a}_p$, via external forces acting on each particle, such as fluid drag and pressure gradient forces. Integration of the PDF over all particle properties yields locally averaged particulate quantities, such as the number density and velocity. Solving the equation also advances the statistical description of the dispersed particle phase in a manner coupled to the fluid phase, defined on the grid.

iii. Gas-particle interphase coupling

In multiphase simulations, modelling the interaction between the dispersed particulate phase and the continuous carrier fluid is essential. This interaction is represented through coupling terms that account for momentum transfer in both directions. These two coupling terms are important for consistent two-way momentum exchange between the gas and solid phases.

Firstly, the particle acceleration ($\boldsymbol{a_p}$), which depends on the forces exerted by the surrounding gas on the particles as they move through the flow. This particle acceleration term couples the particle phase to the gas phase in the particle motion equations. This also accounts for drag and other factors that make the particulate motion deviate from pure inertia. The particle acceleration in the Liouville equation is expressed as [415]:

$$\boldsymbol{a}_p = D_p(\boldsymbol{u}_g - \boldsymbol{u}_p) - \frac{1}{\rho_p}\nabla p + \boldsymbol{g} - \frac{1}{\theta_p \rho_p}\nabla \tau_p \qquad 51$$

D_p is the drag function, whereas τ_p and θ_p are the interparticle normal stress and particle volume fraction described in equations 52 and 53, respectively. The right-hand side of the acceleration equation represents the following terms: aerodynamic drag, pressure gradient, gravitational acceleration, and gradient in the interparticle stress, τ_p. This stress is based on the particle volume fraction, θ_p, and is given as [417]:

$$\tau_p = \frac{10 P_s {\theta_p}^{\beta}}{max[\theta_{cp} - \theta_p, \varepsilon(1-\theta_p)]} \qquad 52$$

P_s and θ_{cp} in equation 52 represent pressure constant and close-pack volume fraction, respectively, while ε is a very small number included to prevent the occurrence of singularity as the solid fraction approaches close pack. θ_p is given by

$$\theta_p = \iiint \phi V_p dV_p d\rho_p d\boldsymbol{u}_p \qquad 53$$

V_p is the particle volume and changes in pressure and density are computed using the ideal gas equation.

Secondly, interphase momentum transfer (**F**) represents the rate of change of gas phase momentum due to the presence of particles. It couples the gas phase motion to particle loading and distribution. The interphase momentum transfer in the gas phase momentum equation is given by

$$\boldsymbol{F} = \iiint \phi V_p \rho_p \left[D_p(\boldsymbol{u}_g - \boldsymbol{u}_p) - \frac{1}{\rho_p}\nabla P \right] dV_p d\rho_p d\boldsymbol{u}_p \qquad 54$$

iv. Drag models

When modelling multiphase flows involving solid particles dispersed in a gas, an accurate representation of drag force is crucial. Drag function, D_p, significantly impacts the momentum exchange between phases through the particle acceleration and interphase momentum transfer terms. Several empirical drag models have been developed to calculate the drag coefficient based on particle and flow properties. Ideal selection depends on the flow regime and desired predictive accuracy. In

this study, three widely used drag models were evaluated: heterogenous modified energy minimization multiscale (EMMS) drag, and homogeneous Gidaspow and Wen-Yu drags.

The EMMS-Yang model is suitable for bubbling and turbulent fluidised beds as it accounts for variations in voidage. Gidaspow model smoothly blends formulas for both dense and dilute regions, making it applicable over a range of solid loadings, whereas Wen-Yu drag model is being tested for its simplicity while still incorporating relative velocity [424]. Moreover, these three drag functions have been successfully applied in previous simulations of similar SE-SR fluid bed systems using various CFD models. Those studies demonstrated predictive ability within the flow regime of interest and suggests they constitute appropriate options to carry out tests.

In this work, the goal was to identify which model best captures the fluid dynamics of the binary gas-solid system and enables reliable prediction of solids flow patterns using the CPFD method. This comparison aims to provide guidance for future modelling studies of SE-SR using CPFD method.

a. Modified energy minimization multiscale (EMMS) drag

The modified EMMS model, based on the works of Yang et al. [425] and Li and Kwauk [426], reflects the heterogenous structure of a gas-solid system. Rather than using an empirical drag law, EMMS solves for forces by minimising the total energy of the system, including contributions from potential, kinetic and interfacial energies [426]. This allows the model to account for the complex flow patterns within the voids and drag forces arising from frictional interactions between fluid and solid phases across finite contact areas. It avoids empirical constants and applies over a wide range of operating conditions using only particle properties and volume fraction, Θ, as inputs. Yang et al. [425] derived an analytical solution for the EMMS drag law that is more computationally efficient. Thus, the modified EMMS or EMMS-Yang model is adopted. The constants, c, in equations 56 and 57 were generated from the experiment of Li and Kwauk [426].

$$D_p = \frac{9}{2}\frac{\mu_f}{\rho_p r_p^2} C_d \tag{55}$$

$$C_d = \begin{cases} \frac{1}{18\theta_f}\left(c_0 \frac{\theta_p}{\theta_g} + c_1 \mathrm{Re}\right) & \theta_g < 0.74 \\ c_2 + c_3 \mathrm{Re}^{n_0}\ \omega & \theta_g \geq 0.74 \text{ and } \mathrm{Re} < 1000 \\ c_4 \frac{\mathrm{Re}}{24}\omega & \theta_g \geq 0.74 \text{ and } \mathrm{Re} \geq 1000 \end{cases} \tag{56}$$

$$\omega = \begin{cases} c_5 + \frac{c_6}{4(\theta_g + c_7)^2 + c_8} & 0.74 \leq \theta_g < 0.82 \\ c_9 + \frac{c_{10}}{4(\theta_g + c_{11})^2 + c_{12}} & 0.82 < \theta_g \leq 0.97 \\ c_{13} + c_{14}\theta_g & 0.97 < \theta_g \leq 1 \end{cases} \tag{57}$$

b. *Gidaspow drag*

At the core of the Gidaspow model is the recognition that the drag force experienced by a particle in a multiphase flow is heavily influenced by the local volume fraction of the dispersed phase [280]. The model combines two well-established drag correlations, the Wen and Yu correlation [427] for dilute systems and the Ergun equation [428] for dense systems, to provide a smooth transition between the two regimes. It incorporates particle Reynolds number and solid volume fraction as variables.

In dense regions, the Wen & Yu equation is used:

$$D_{p,1} = C_d \theta_g^{-3.65} \tag{58}$$

Where,

$$C_d = \begin{Bmatrix} (1 + 0.15\mathrm{Re}^{0.687}) & \mathrm{Re} \leq 1000 \\ 0.44\frac{\mathrm{Re}}{24} & \mathrm{Re} > 1000 \end{Bmatrix} \tag{59}$$

In dilute regions, the Ergun equation is applied:

$$D_{p,2} = \frac{2\mathrm{Re}+180(1-\theta_g)}{18\theta_g^2} \tag{60}$$

Combining Wen & Yu and Ergun equations (equations 58 – 60) results in the Gidaspow model and is given as:

$$D_p = \begin{matrix} D_{p,1} & \phi < 0.75\theta_{CP} \\ \{(D_{p,2} - D_{p,1})(\frac{\phi - 0.75\theta_{CP}}{0.85\theta_{CP} - 0.75\theta_{CP}}) + D_{p,1} & 0.75\theta_{CP} \leq \phi \leq 0.85\theta_{CP} \\ D_{p,2} & \phi > 0.85\theta_{CP} \end{matrix} \tag{61}$$

c. *Wen-Yu drag*

The third drag model, Wen-Yu drag model, was proposed as an early theoretical formulation relating drag forces to particle Reynolds number in fluid-particle systems. Although the Wen-Yu model tends to neglect interaction effects that become significant at high particle concentrations, one of the key advantages of the model is its simplicity and ease of implementation. The model uses a relatively straightforward mathematical expression that captures the essential physics of the gas-solid interaction through the θ_g term [427]. It is represented as:

$$D_p = C_d \theta_g^{-3.65} \quad (62)$$

$$C_d = \begin{cases} 1 + 0.15\mathrm{Re}^{0.687} & \mathrm{Re} \leq 1000 \\ 0.44\frac{\mathrm{Re}}{24} & \mathrm{Re} > 1000 \end{cases} \quad (63)$$

4.2.2 Kinetic models

In this study, two representative kinetic schemes were applied - steam methane reforming and carbonation. The steam methane reforming (SMR) model describes the reactions between methane and steam to produce hydrogen and CO_2. Carbonation refers to the reversible reaction where CO_2 reacts with calcium oxide-based sorbent (dolomite) to form calcium carbonate. Modelling this reaction accurately captures carbon capture using dolomite sorbents.

i. SMR kinetics

Several kinetic models have been proposed in the literature to simulate SMR processes. There are two widely used schemes developed by Numaguchi and Kikuchi (NK) [429] and Xu and Froment (XF) [430], due to their predictive capabilities. For this study, the NK kinetic model was selected for the following key reasons. First, it offers a simpler formulation compared to some alternatives, avoiding potential errors from numerous kinetic parameters. Additionally, a prior comparative study by Quirino et al. [431] found the NK approach demonstrated relatively high accuracy in modelling reforming reactions. It also exhibited lower numerical instability compared to other evaluated schemes. Stability is important for rigorous multiphase simulations. Given its validation in previous works and simplicity while still adequately representing chemical kinetics, the NK kinetic mechanism provided a suitable basis for the present study. Using its formulation, the steam reforming and water-gas shift (WGS) reactions occurring in SE-SR processes can be characterised as follows:

SMR: $CH_4 + H_2O \leftrightarrow 3H_2 + CO$ $\quad \Delta H^0_{298} = +206 kJ/mol$ (64)

WGS: $CO + H_2O \leftrightarrow H_2 + CO_2$ $\quad \Delta H^0_{298} = -41 kJ/mol$ (65)

A hybrid rate equation for the reactions is obtained by Numaguchi and Kikuchi [429] based on Langmuir-Hinshelwood and power rate law, and is expressed as:

$$r_{SMR} = \frac{k^0_{SMR} \cdot exp(-\frac{E_{SMR}}{RT})(p_{CH_4} p_{H_2O} - \frac{p_{CO} p^3_{H_2}}{K_{SMR}})}{p^{1.596}_{H_2O}} \ , \ [kmol/(kg_{cat}\ s)] \quad (66)$$

$$r_{WGS} = \frac{k^0_{WGS} \cdot exp(-\frac{E_{WGS}}{RT})(p_{CO} p_{H_2O} - \frac{p_{CO_2} p_{H_2}}{K_{WGS}})}{p_{H_2O}} \ , \ [kmol/(kg_{cat}\ s)] \quad (67)$$

Kinetic parameters k^0_{SMR}, k^0_{WGS}, E_{SMR}, E_{WGS}, K_{SMR} and K_{WGS} were obtained from Numaguchi and Kikuchi [429] and Hou and Hughes [432] and are presented in Table 4.1.

Table 4.1: Arrhenius parameters, activation energies and equilibrium constants for the reforming and shift reactions [429]

	k^0	E (kJ/mol)	K
SMR	2.634×10^{2}, $\left[\frac{kmol}{(kg_{cat}\ atm^{0.404}\ s)}\right]$	106.870	$1.167\times10^{13}\exp\left(-\frac{26830}{T}\right)$, $[atm^2]$
WGS	0.248, $\left[\frac{kmol}{(kg_{cat}\ atm\ s)}\right]$	54.531	$1.767\times10^{-2}\exp\left(\frac{4400}{T}\right)$

ii. Carbonation kinetics

The carbonation model proposed by Sun et al. [433] for dolomite and limestone sorbents was adopted for this study, as it has been successfully applied in similar research concerning SE-SR process [146]. The grain model used to describe the carbonation reaction considers how grain size distribution changes with the reaction. This level of detail is important, as the changes in grain size can influence product formation. Furthermore, the Sun et al. [433] model has demonstrated a remarkable capability in capturing the abrupt reduction in carbonation reaction rates that is often observed using CaO-based sorbent [434]. This phenomenon can have a profound impact on the overall performance of the sorbent material. The rate equation is given in terms of conversion and expressed below:

$$r_c = \frac{dx}{dt} = k_C\left(P_{co_2} - P_{co_{2,eq}}\right)^n S\ 1 - X_{CaO} \qquad 68$$

Where X_{CaO} is the conversion of CaO defined as:

$$X_{CaO} = \frac{reacted\ CaO\ moles}{total\ CaO\ moles} = \frac{[n_{CaO,0} - n_{CaO,t}]}{[n_{CaO,0}]} \qquad 69$$

S is the specific surface area of the sorbent. The surface area for the CaO part in the dolomite sorbent is calculated to be $3.1\times10^4 m^2/kg_{sorb}$ [433]. For the dolomite carbonation, a first-order reaction was ascertained for P_{CO_2} <10 kPa, whereas a zero-order reaction was reported for P_{CO_2} >10 kPa. Therefore, the carbonation rate constant, k_C under both conditions is presented in the equation below:

$$k_C = \begin{cases} 1.04\times10^{-10} exp\left(\frac{-24000}{RT}\right)\ kmol/(m^2 s Pa)\ \ at\ P_{CO_2} - P_{CO_2,eq} \le 10kPa\ ;\ n=1 \\ 1.04\times10^{-3} exp\left(\frac{-24000}{RT}\right)\ kmol/(m^2 s)\quad at\ \ P_{CO_2} - P_{CO_2,eq} \ge 10kPa\ ;\ n=0 \end{cases} \qquad 70$$

The equilibrium pressure, $P_{CO_{2,eq}}$, is a function of temperature [435], and is calculated according to the equation:

$$C_{\mathrm{CO_2,eq}} = (\tfrac{1.462\times10^{11}}{T})exp\ \tfrac{-19130}{T}\ ;\quad P_{\mathrm{CO_2,eq}} = C_{\mathrm{CO_2,eq}}RT\ [atm] \qquad 71$$

4.2.3 Numerical solutions and model settings

The Eulerian conservation equations for the gas phase are solved using the finite volume method, while the particle phase equations are solved using computational parcels, which follow typical routes in phase space with particle velocities, locations, and sizes as coordinates. Parcel attributes are interpolated onto the Eulerian grid and the implicit approximations to the particle-phase are solved. The local gas velocities, gas pressure gradients, and solids stress gradients are interpolated back to parcel coordinates, and employed in a final explicit update of parcel velocities once the grid equations are solved.

The interpolation of particle properties to and from the Eulerian grid is achieved using interpolation operators. For a rectangular grid where a particle is located at $\mathbf{x_p}$ and $\mathbf{x}_\mathrm{p} = (x_\mathrm{p}, y_\mathrm{p}, z_\mathrm{p})$, the interpolation operator, *S*, in the cell centre x-direction takes the form for all nodes, *i*:

$$S_\mathrm{i}^x(\boldsymbol{x}_\mathbf{p}) = \begin{cases} 0 & x_{\mathrm{i}-1} \geq x_\mathrm{p}, x_\mathrm{p} \geq x_{\mathrm{i}+1} \\ 1 & x_\mathrm{p} = x_\mathrm{i} \end{cases} \qquad 72$$

and

$$\textstyle\sum_i S_i^x\ x_P\ = 1 \qquad 73$$

The operators are defined in a similar way for face centre directional interpolation operators, with properties as:

$$S_{\mathrm{i}+1/2}^x(\boldsymbol{x}_\mathbf{p}) = \begin{cases} 0 & x_{\mathrm{i}-1/2} \geq x_\mathrm{p}, x_\mathrm{p} \geq x_{\mathrm{i}+3/2} \\ 1 & x_\mathrm{p} = x_{\mathrm{i}+1/2} \end{cases} \qquad 74$$

and

$$\textstyle\sum_\xi S_\xi^x\ x_P\ = 1 \qquad 75$$

for all face nodes, ξ.

In three dimensions, $\boldsymbol{x}_\mathrm{p}$ is interpolated to eight grid nodes. The y and z operators follow similar patterns and are all independent of their counterpart coordinates. The motion of particles in the

continuum fluid momentum equation is coupled through an implicit coupling approach, in the numerical scheme. This approach results in the product of the particle to grid interpolation operators.

On the other hand, the grid-to-particle interpolation operator is used to interpolate the grid quantities back to the individual particle positions. The gradient of the grid-to-particle interpolation operator is important for calculating the forces acting on the particles. These force calculations then allow for updating the particle properties, during the next timestep of the simulation. The grid-to-particle interpolation operator is presented in equation 76 while the gradient of the particle properties is given in equation 77.

$$Q_p = \sum_{\xi=1}^{N} S_\xi \; x_P \; Q_\xi \tag{76}$$

$$\nabla Q_p = \sum_{\xi=1}^{N} \nabla S_\xi \; x_P \; Q_\xi + \sum_{\xi=1}^{N} S_\xi \; x_P \; (\nabla Q)_\xi \tag{77}$$

Detailed explanation for the product and gradient of interpolation operators for three-dimensional calculations are provided by Snider [423].

The model settings used in the simulation are presented in Table 4.2. Maximum momentum redirection from collision refers to the largest possible change in momentum that can occur when two particles collide. Tangent-to-wall momentum retention refers to how much of a particle's tangential momentum is maintained after colliding with a wall boundary, while normal-to-wall momentum retention similarly describes the degree to which normal momentum is conserved upon particle-wall collisions [422]. The blended acceleration model (BAM) was also set for the simulation. The BAM in dense polydisperse granular flows accounts for inhibited relative motion between differently sized particles in sustained contact. BAM calculates particle acceleration as a blend of approaches - an averaged value in dense packed regions where particles adhere collectively, and independent motion in dilute areas [436]. This better represents inter-particle interactions across flow regimes, improving predictions of segregation behaviour during fluidisation simulations. In the absence of experimental data, the default values provided by the simulation software were employed for these contact and collision models, as well as for wall interaction models. The particles were modelled as 'hard particles' in the CPFD model.

Table 4.2: Model parameters and settings used in the CPFD software

Parameters	Values	Units
Maximum momentum redirection from collision	40	%
Normal-to-wall momentum retention	0.85	-
Tangent-to-wall momentum retention	0.85	-
Courant–Friedrichs–Lewy (CFL) range	0.8 – 1.5	-
Time step	0.001	s
Simulation time	100	s
Averaging start time	50	s

The Courant–Friedrichs–Lewy (CFL) condition is a fundamental stability criterion in CFD. The CFL criterion relates the time step size, grid cell size and propagation speed, stating the time step must be small enough such that information cannot propagate further than the size of one cell in a single iteration [437]. If the CFL number is too high, information moves faster than waves, causing numerical dispersion errors. But too low (<0.1) wastes computational resources without benefiting stability.

4.2.4 Process description

The developed model was applied to a lab-scale bubbling fluidised bed reactor from Johnsen [438]. The lab-scale reactor with a dense bed and expanded regions was designed in SOLIDWORKS. The dense bed region is a cylinder of inner diameter, 0.102 m, and height, 0.66 m, while the freeboard has a length and inner diameter of 0.154 m and 0.365 m, respectively. A concentric reducer of height 0.15m joins both regions. A schematic diagram of the reactor is shown in Figure 4.1.

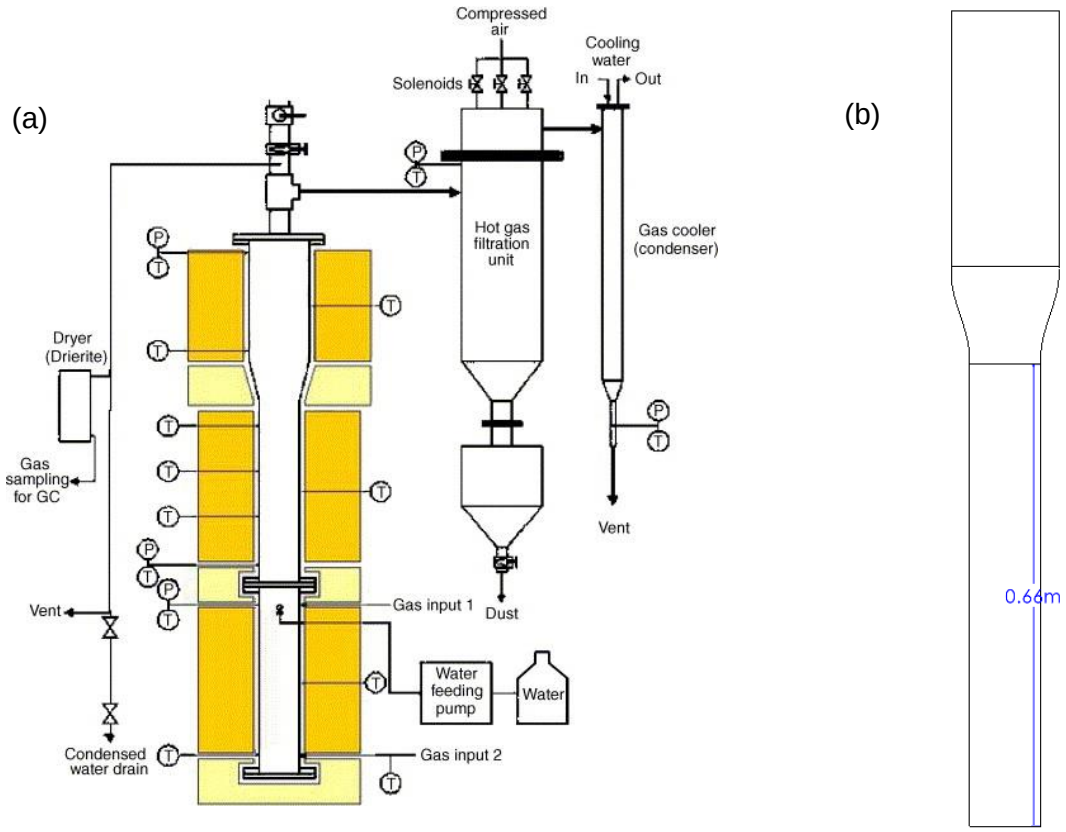

Figure 4.1: (a) Experimental reactor by [438] and (b) front view of the reactor's geometry simulated in this work.

The dimensions used and the mode of operation are the same as that of the experimental reactor. Steam and methane are introduced through the bottom of the reformer at a given velocity, with product gases leaving the reactor from the top. Similar to the experiment, the reformer was simulated as a batch setup without solids feeding lines to the reformer. The sorbent regenerator (calciner) was not considered in this study; therefore, the spent solids remain in the reactor.

4.2.5 Operating conditions and assumptions

The operating conditions in the simulation were selected to match those of the experimental study in literature. This was done to enable a fair and valid comparison of the simulation results to real-world data, allowing an evaluation of the model's ability to predict and replicate the behaviours observed experimentally. This rigorous matching of conditions therefore provided a sound basis for assessing and comparing the simulation results and empirical data. The pressure boundary condition was specified at the reactor outlet located at the top, where exit of gases from the reactor could be modelled. A velocity inlet boundary was defined at the bottom reactor entry point to introduce the

flowing gas phase. Specifying a uniform inlet velocity negated the need to explicitly model the gas distributor plate, simplifying the geometry while maintaining a representative flow profile. Isothermal operation was assumed in order to maintain approximately uniform temperature. Initial operating conditions for the process was taken from Johnsen et al. [438], to obtain consistent results during model validation and evaluation. Physical properties, operating and boundary conditions of the fluidising gas and particles are listed in Table 4.3.

Table 4.3: Initial operating conditions for the simulation of SE-SR of methane in a BFB reactor [438]

Parameters	**Value**	**Unit**
Reformer temperature	873	K
Reactor pressure	1	atm
Steam-to-carbon ratio	3	-
Superficial velocity	0.032	m/s
Total mass of solids in the system	3.1	kg
Catalyst-to-sorbent mass ratio	2.5	-
CaO/MgO	60/40	wt%
Sorbent particle size range	125 – 300	µm
Catalyst particle size range	150 – 250	µm
Catalyst density	2200	kg/m^3
Sorbent density	1540	kg/m^3
Close-pack volume fraction	0.6	-

4.2.6 Performance evaluation

The following indices were used to analyse the performance of SE-SR of methane in the BFB reactor: CH_4 conversion (X_{CH_4}), carbon capture efficiency (X_{CO_2}), and hydrogen purity. CH_4 conversion is an indication of the extent of methane consumption during the reforming process, and was determined as the percent of methane fed that was reformed or converted into product gas. CO_2 capture efficiency represented the percentage of CO_2 removed from the product gas via carbonation, calculated from the

molar flow rates of total carbon (CH_4) inlet and carbon (CO, CO_2 and CH_4) outlet. Hydrogen purity is the mole percent of hydrogen leaving the reactor and is calculated on a dry basis.

$$X_{CH_4} = \left(1 - \frac{n_{CH_4,out}}{n_{CH_4,in}}\right) \times 100\% \quad (78)$$

$$X_{CO_2} = \left(\frac{Flow_{CH_4,in} - Flow_{(CO_2+CH_4+CO),out}}{Flow_{CH_4,in}}\right) \times 100\% \quad (79)$$

$$H_2\ Purity = \left(\frac{n_{H_2,out}}{n_{(H_2+CO_2+CH_4+CO),out}}\right) \times 100\% \quad (80)$$

4.3 Results and discussion

Gridding is an important task in CFD simulations. The quality and structure of the grid can significantly impact the accuracy and efficiency of CFD simulations. When simulating the same scenario in both 2D and 3D, the 3D model has been shown to exhibit superior grid convergence characteristics – the effects of grid size on the solution were found to be smaller [439]. Regardless, a grid study was first conducted to ensure that model results are not dependent on the grid resolution. The grid size was refined twice from an initial size that was selected based on the smallest particle diameter in the system. The grid employed in the investigation is at least ten times the size of the smallest particles, a common practice for examining grid independence in fluidised bed simulations, and is deemed adequate for achieving a solution that is not reliant on grid size [440,441].

The computational domain was discretized using a three-dimensional, structured, hexahedral grid. The uniform grids were generated in Barracuda VR® with three different cells: 35,000 (coarse, Grid 1), 50,000 (fine, Grid 2) and 65,000 (very fine, Grid 3), to perform the grid independence study. Pressure profiles for the three grids after 100 s of simulation time are presented in Figure 4.2. The pressure outputs in the first 3 seconds of the simulation were excluded, due to the transient nature of the profile during simulation start-up, while the remaining were averaged at different heights of the reactor.

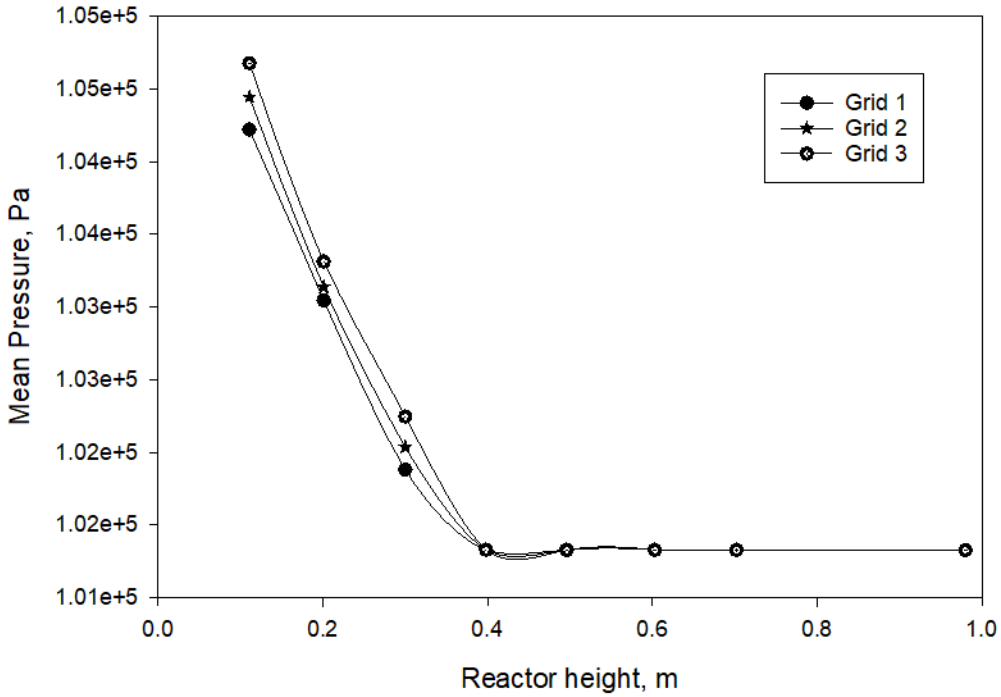

Figure 4.2: Mean pressure profiles for the different grid sizes in bubbling bed reactor.

The mean pressures for the three grids follow similar trend with a little deviation between 0.2 m and 0.4 m along the reactor height, which is tolerable for this study. Grid 2 was selected to reduce computational cost associated with simulating smaller grid sizes (Grid 3), while maintaining results independence on grid size. Moreover, a uniformity plot obtained for Grid 2 in Figure 4.3 shows that the cells lines are below severe and high aspect ratio. This means that the grids are very uniform.

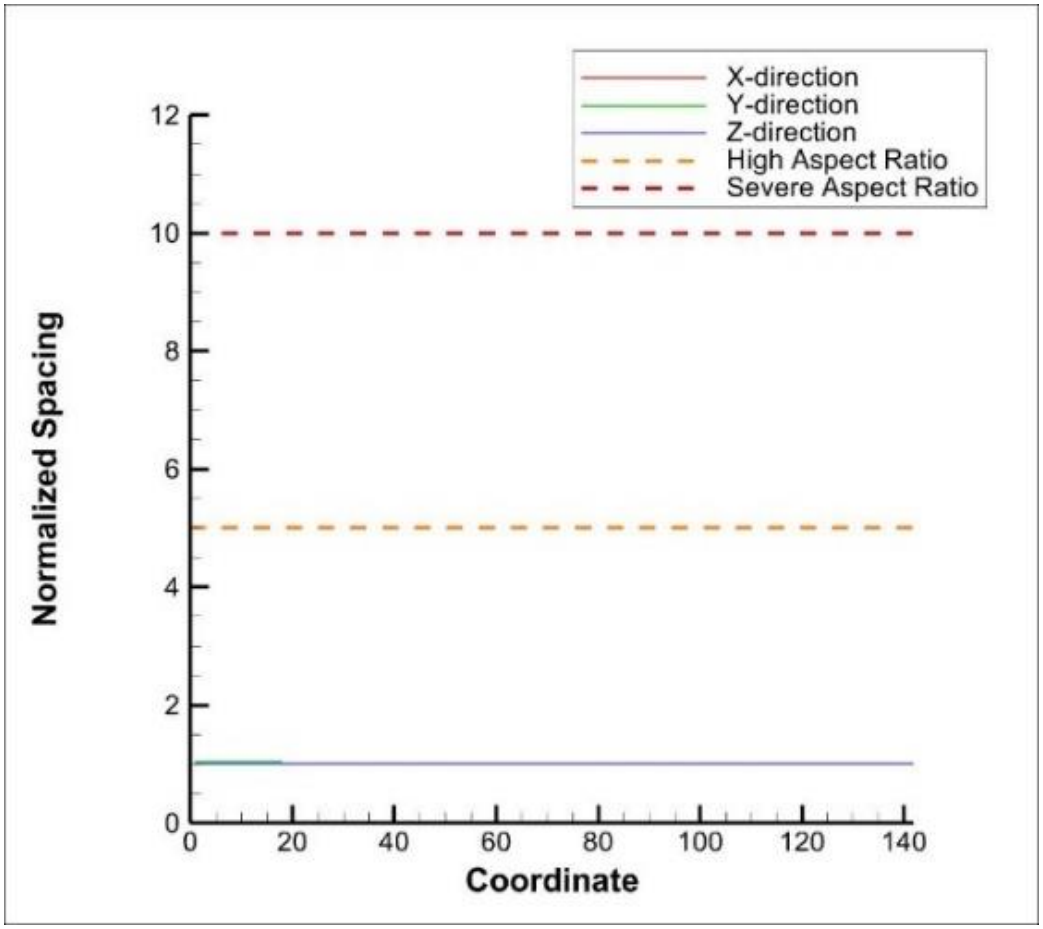

Figure 4.3: Uniformity plot for Grid 2 in bubbling bed reactor.

4.3.1 Model validation

CPFD models use complex constitutive relationships and assumptions that can introduce uncertainty, especially if the model is not calibrated. Therefore, it is important to validate CPFD models against experimental systems before using them extensively in parametric studies, to ensure confidence in the model results. Two model validations were carried out for the two sub-models employed within the CPFD model: one for the hydrodynamic sub-model and another for the SE-SR methane kinetics sub-model. In the case of the hydrodynamic sub-model, particle volume fraction served as the parameter for comparison with experimental data. For the kinetic sub-model, the composition of the product gas was the parameter used to assess the simulation results against the experimental data.

4.3.1.1 Hydrodynamic validation

The hydrodynamic model was first validated against the experimental work of Olivieri et al. [442], who assessed the fluidisation behaviour and segregation of binary particle mixtures comprising different particle sizes and densities. To directly compare simulation results with their experimental measurements, the key test conditions reported in the study such as reactor dimensions, particle

properties, and operating parameters were replicated identically in the CPFD model, as presented in Table 4.4. This rigorous matching of simulated and actual experimental setup allowed for a valid assessment of the model's ability to accurately track the volume fraction profiles of the heavier particles (jetsam) throughout the bed height, under fluidising conditions.

Table 4.4: Operating conditions used in the hydrodynamic validation of binary particles in fluidised bed reactor [442]

Parameters	**Values**	**Units**
Initial jetsam volume fraction (volume of jetsam/volume of solid particles, X_{j0})	0.2	-
Superficial gas velocity	0.064	m/s
Density of silica gel	600	kg/m^3
Density of silica sand	2600	kg/m^3
Particle size range of silica gel	350 – 400	µm
Particle size range of silica sand	100 – 150	µm
Bed weight	2.85	kg
Reactor inner diameter	0.12	m
Reactor height	1.5	m

Three drag models, EMMS-Yang, Gidaspow, and Wen-Yu, were evaluated to determine which one provides an accurate description of the hydrodynamic behaviour in the binary system used in the experiment. It is assumed that the drag model that performs best in accurately depicting the behaviour of the binary system used in the experiment, should also be suitable for describing the catalyst-sorbent system employed in this study. However, if such accuracy is not achieved, model fitting through optimisation may be necessary to recalculate the model constants.

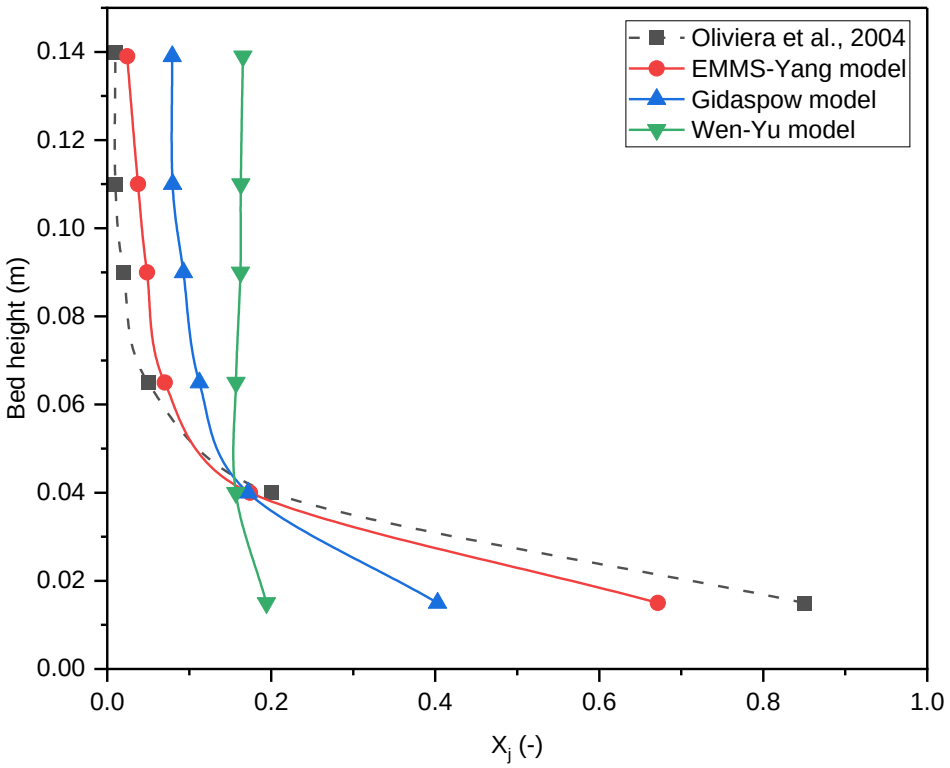

Figure 4.4: Solid concentration profiles comparing experimental data (dashed curve) with predicted results obtained for different drag models (solid curves).

The mean value of the time-averaged volume fractions on the XY data planes, at different Z- reactor heights was calculated at the end of the simulation. The jetsam volume fraction on a fluid-free basis was compared with the experimental data, as presented in Figure 4.4. The simulation result for the EMMS-Yang model showed better prediction of the experimental results compared with other two drag models. While the EMMS-Yang model was able to capture the noticeable segregation of the jetsam particles seen along the axial direction of the lower bed region, the Gidaspow and Wen-Yu models predicted a relatively uniform jetsam particle distribution along the bed height, thereby under-estimating segregation in the simulated reactor [443]. Therefore, the SE-SR simulation was conducted using the EMMS-Yang drag setup, given its close prediction of hydrodynamic interactions with the experiment.

4.3.1.2 Kinetic validation

Conversely, the SMR reaction kinetics, without carbonation reaction, was validated by initially simulating a unit cube geometry filled with 0.250 mm-diameter catalyst particles. The simple geometry

was operated in batch mode, with the aim of comparing steady-state composition of the product gases, with the SE-SR reactor model. The SMR simulation produced ~72% hydrogen concentration on a dry basis, which corresponds to the composition of steam reforming at equilibrium, reported in Johnsen et al. [444]. Concentrations of CH_4, CO_2 and CO were 8.4%, 12.2%, and ~8%, respectively, on a dry mole basis. Then, the SE-SR methane in BFB reactor was modelled using the operating conditions in Table 4.3, with the time-averaged dry gas composition for the species at the reactor outlet obtained after simulation. Comparison of the outlet gas composition is displayed in Figure 4.5. Hydrogen purity at the outlet reached ~97% on a dry basis, lower than that reported for the experiment at ~98%. Slight variation in the compositions of methane was also observed, with a deviation of ~1%, which is within an acceptable range.

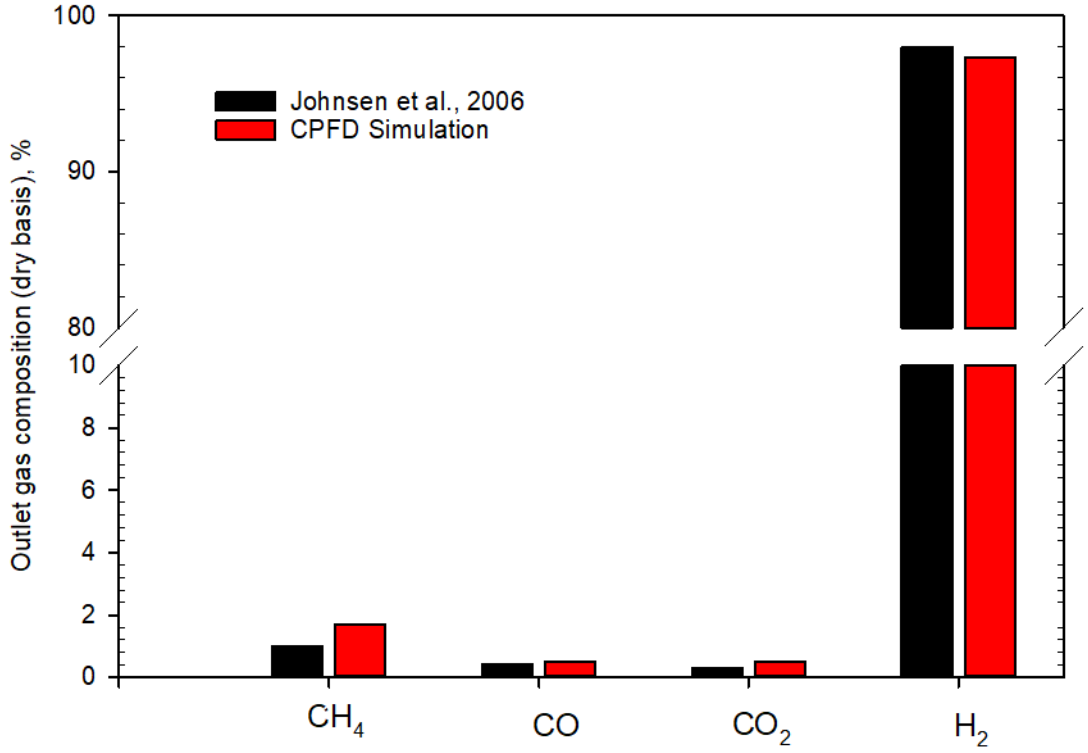

Figure 4.5: Comparison of outlet gas composition of the SE-SR of methane simulation results with experimental data (at velocity = 0.032 m/s, T = 873 K, P = 1 atm).

Following the hydrodynamic and kinetic validations, the CPFD model has been shown to be a suitable modelling tool for simulating SE-SR of methane in BFB reactor.

4.3.2 Hydrodynamic performance

Maintaining efficient contact between the gas and solid phases is essential in SE-SR of methane, in order to improve process performance metrics such as methane conversion and hydrogen production. This section describes the behaviour of particles in the reactor, highlighting on the particle volume

fraction and the velocities of the solid and gas phases. Following model validation with literature data, the base conditions for temperature, pressure and S/C ratio were maintained at: 873 K, 1 atm and 3, respectively, while the superficial gas velocity was increased to 0.1 m/s, which is still within the bubbling regime. Increasing the velocity above the minimum fluidisation reported in literature (0.021 m/s – 0.032 m/s) used for model validation [202], allows for a greater momentum to fluidise and suspend the particles. Before the simulation starts, particle positions were randomly initialised without any segregated structure within the simulated bed, and solid particles were uniformly distributed throughout the spatial domain.

Figure 4.6 shows the volume fraction of the solid particles in the reactor at different time stamps from 0s to 100s and the time-averaged volume fraction. At 0s, the bed is stationary at a static bed height of 0.3 m but begins to expand as gas is passed through it. This is primarily due to small bubbles formed at the bottom of the bed, which grows in size along the reactor height (as seen in 6s). As bubbles rise and coalesce, they push particles upward in their wake, causing an overall expansion of the bed [445]. The bubbles erupt near the surface, scattering the solids into the freeboard region at 20s. After 20 seconds, the bed height stays pretty much constant over time. This means the fluidised bed has reached a quasi-steady state where the hydrodynamics no longer change much. The bed expands to approximately 1.4 times its initial height based on the time-averaged data, agreeing well with literature values for bubbling fluidised beds of comparable particles [446,447]. From the time-averaged contour plot shown in the same figure, it is also observed that the particle volume fraction is higher at the top of the bed compared to the bottom, indicating an increased local voidage at the bottom. Since bubbles are formed at the bottom of the reactor, it makes sense for particle volume fraction to be lower at the bottom, as voids are introduced in that region.

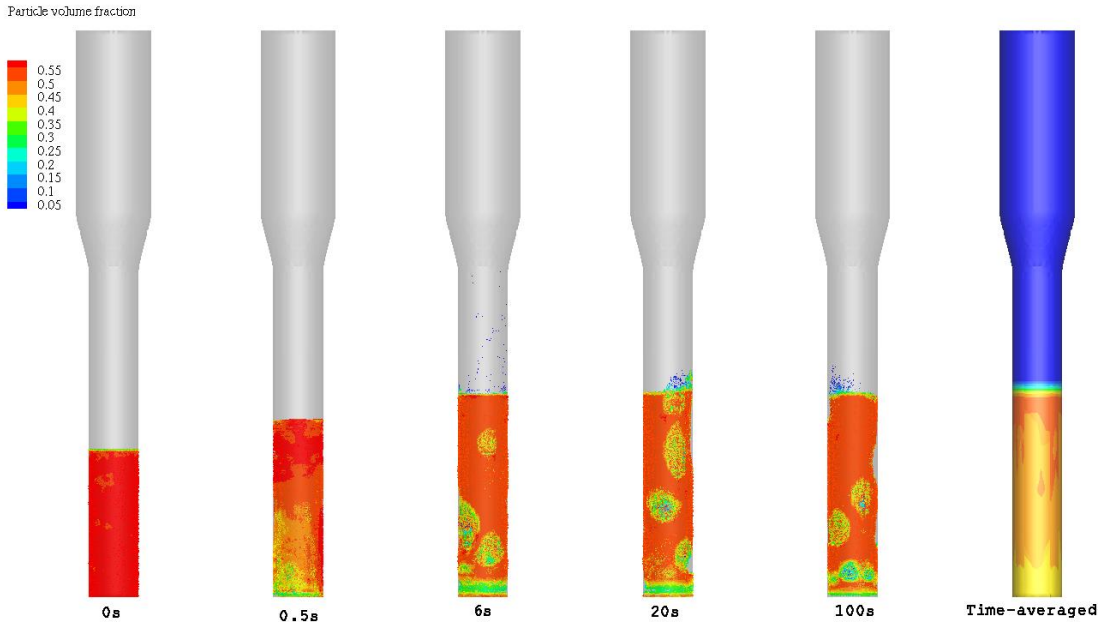

Figure 4.6: Instantaneous particle volume fraction for SE-SR of methane in BFB reactor.

Simultaneously, the fluid pressure is higher towards the bottom of the bed where particle volume fraction appears to be low. Figure 4.7 shows the time-averaged pressure in the reactor. The weight of the bed particles exerts a higher pressure on the lower bed region, creating a hydrostatic pressure profile, with the pressure decreasing linearly upward through the bed. This inverse relationship between particle distribution and pressure can also be explained by the underlying bubble formation and motion, as discussed previously.

In the fluid velocity contour illustrated in Figure 4.7, localised high velocity spots are seen within areas where bubbling occurs. These regions of fast-moving gas correspond to the locations of rising bubbles. Bubbles contain an excess of gas which moves rapidly due to buoyancy forces and low drag [448]. The contour also reveals two distinct flow regimes within the reactor bed: a more distributed flow in the areas outside of the high velocity bubble zones, and a flow that cuts through the fast-moving bubble regions. Therefore, the total gas flow seen in the reactor can be characterised by three main phases: dense flow in the regions of high solids concentration, where gas percolates slowly through narrow voids between particles; bubble flow in discrete pockets where bubbles rise and contain faster moving gas; and throughflow for gas that passes through the bubbles, moving rapidly like the bubble phase but through open areas of the bed outside the bubbles [449]. It is clear that some degree of non-uniformity in gas velocities is inevitable in a bubbling bed due to the discrete nature of the bubbles.

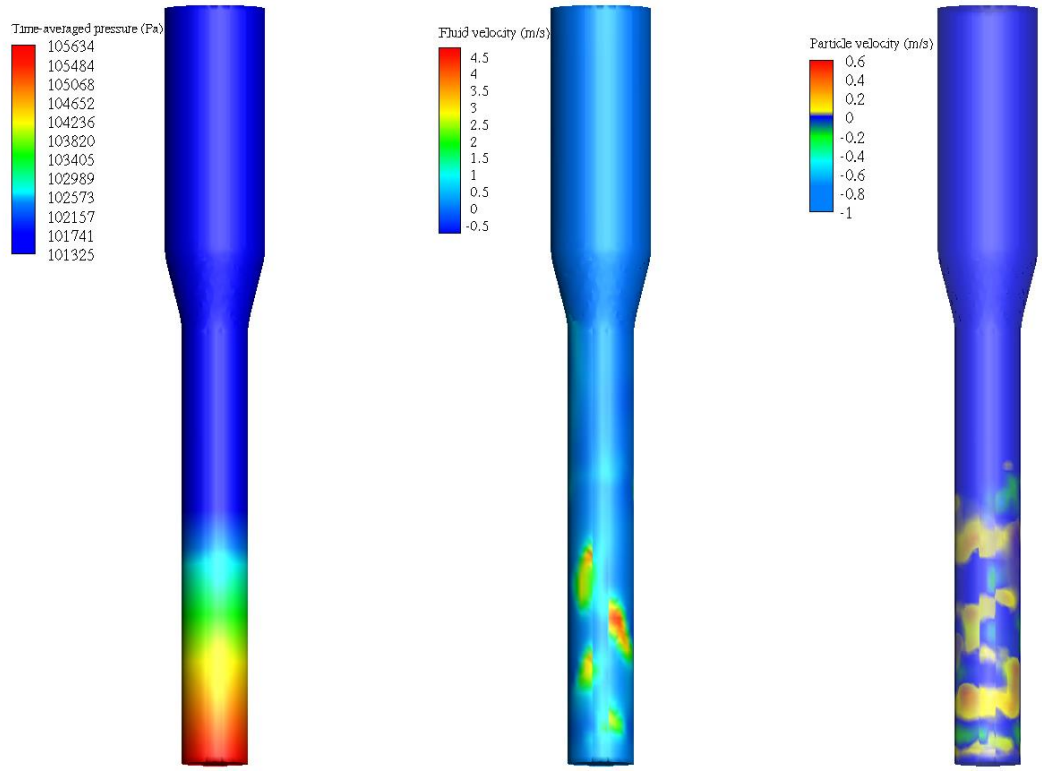

Figure 4.7: Contour plots of time-averaged pressure and gas and particle velocity in the Z-direction.

The contour plots of particle velocity reveal some regions exhibiting negative values, indicating downward solids motion opposite to the prevailing upward gas flow direction. This is likely due to wall effects and recirculation. Although, negative solid flows are also seen in the bubble region area at the bottom of the bed. As noted by Zenz [450], bubbles are displaced upward by steady particle influx from the surrounding emulsion phase. The shallow angle of repose of the fluidised solids precludes steep 90° walls around the rising bubbles. Instead, particles slide down into the wake region at the bottom. The wake mixes and recirculates particles. This circulation of particles is clearly seen in Figure 4.8.

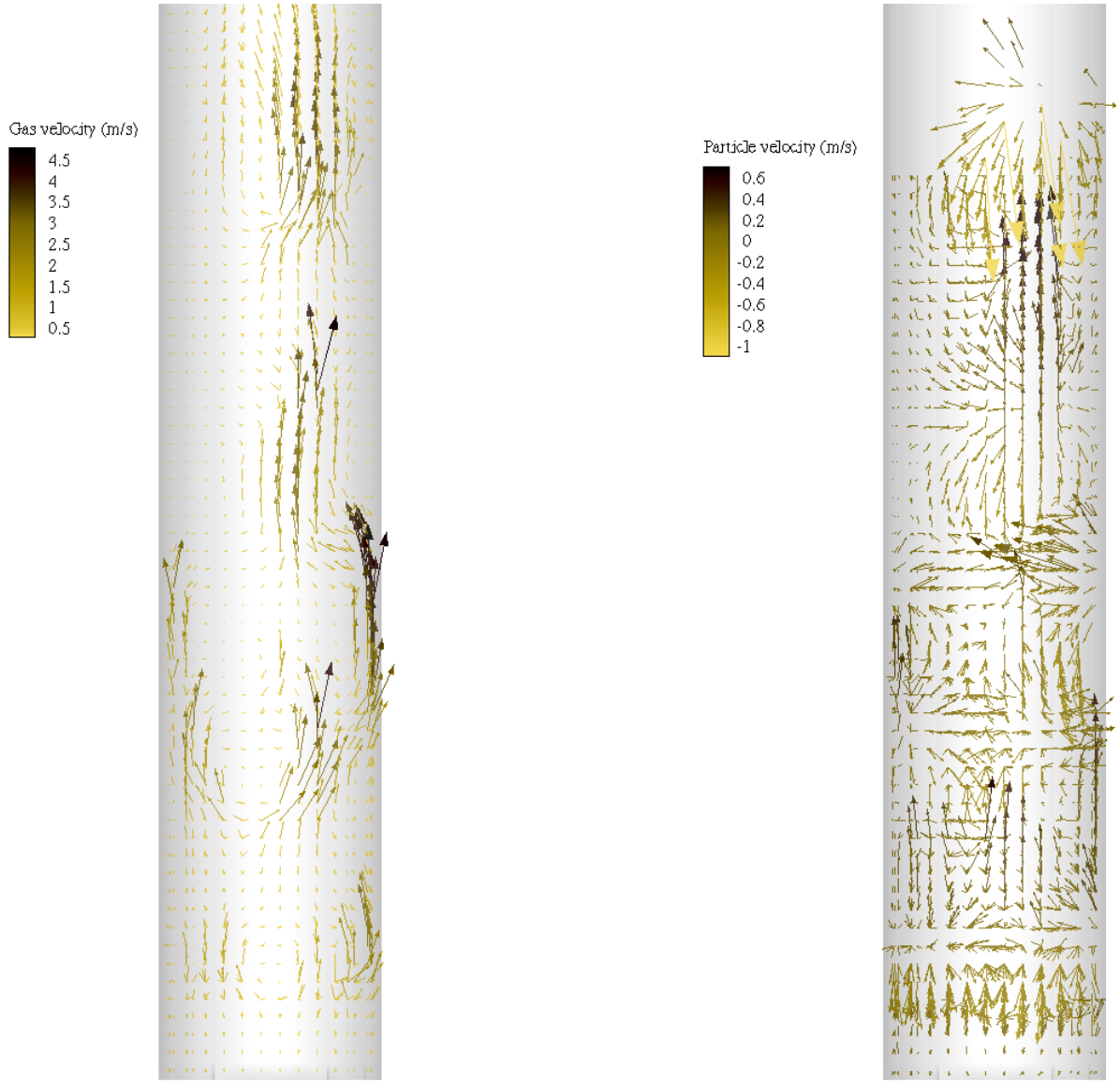

Figure 4.8: Gas and solid flow pattern coloured by gas and solid velocities, respectively.

The gas and particle flow patterns in the dense bed region are depicted in Figure 4.8. As discussed previously, locations of rising bubbles correspond to zones of high magnitude upward gas velocity seen in the gas flow contour (Figure 4.8a). Corresponding downward motion of solid particles is also evident in these areas from the particle flow pattern image (Figure 4.8b). Vortices appear near the top centre and sides of the reactor bed, indicative of mixing between the bubble and emulsion phases [451]. Intense particle motion is observed primarily in the downward direction at the bottom of the bed, likely due to recirculation effects. At the bed surface, erupting bubbles create scattered particle flow patterns.

The developed CPFD model was able to predict distinct hydrodynamic zones within the reactor bed, with bubbles generating localised regions of upward gas flow and downward recirculating particle

motion. The vortices and flow patterns highlight the key role of bubbles in inducing circulation and gas-solids contact.

4.3.3 Spatial distribution of solids and gas species

Characterising the spatial profiles of key gas and solid species can provide valuable insights into the chemical performance of a process. This sub-section examines the CPFD-simulated concentration fields of the gas and solid phase compounds within the modelled reactor.

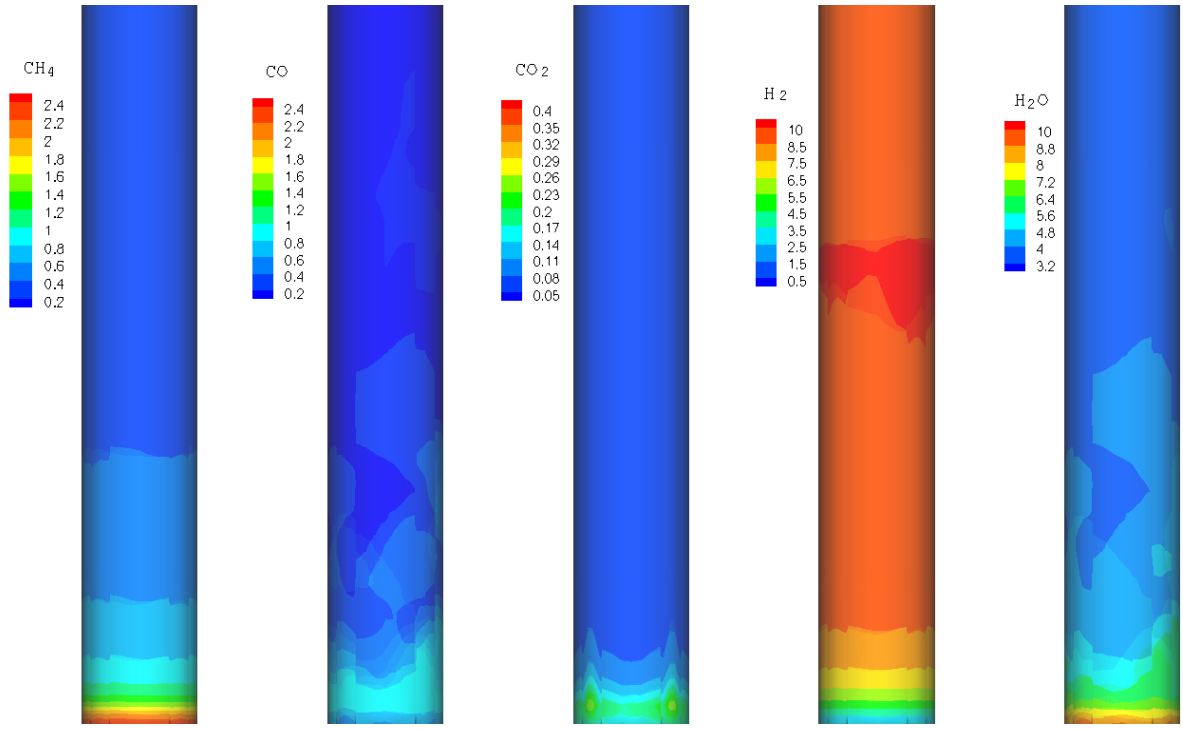

Figure 4.9: Gas species distribution coloured by mole concentration (mol/m^3) at S/C = 3, T = 873 K, P = 1 atm.

Figure 4.9 shows the contour mapping of the gas species concentration at steady-state condition. The simulated methane concentration exhibits a high value at the reactor bottom before progressively decreasing along the bed height. This decline in the main feed gas indicates consumption within the inlet region due to instantaneous steam reforming reactions. Correspondingly, CO levels drop sharply near the bottom as well, providing evidence for the occurrence of water-gas shift reaction in this lower region of the reactor. CO_2 concentrations also peak in this inlet section but are then reduced along the bed height. This attenuation arises from adsorption of CO_2 by the sorbent particles downstream of the inlet. As expected, based on the reaction chemistry, hydrogen is the predominant species in the upper reactor region. However, the hydrogen concentration contour reveals a region of increased hydrogen content in the middle section of the reactor, which is likely indicative of hydrogen backflow. Based on

Figure 4.9, the different reaction zones in SE-SR of methane in bubbling fluidised bed reactor can be summarised as:

i. **Inlet/lower bed region**:

- Methane concentration is highest but starts decreasing due to steam reforming reactions.
- CO levels also drop sharply due to steam reforming and water-gas shift reactions.
- CO_2 concentrations peak here from the reforming reactions.

ii. **Mid bed region**:

- CO_2 sorption by the sorbent particles causes CO_2 levels to reduce along the bed height downstream of the inlet.
- Water-gas shift reaction continues to consume CO and produce CO_2 and H_2.

iii. **Upper bed region**:

- Reforming and shift reactions have largely reached completion.
- Hydrogen concentration is highest and uniformly distributed as the primary product.
- CO and CO_2 levels are much lower due to conversion and adsorption reactions.

The catalyst and sorbent particles appear well-mixed initially and remain uniformly distributed even after reaching steady state, as shown in Figure 4.10. No visible particle segregation is evident, which helps maintain gas-sorbent contact and rapid adsorption following CO_2 generation. The spent sorbent particles represented by $CaCO_3$ remain dispersed among the catalyst across all bed regions under the simulated operating conditions. However, Figure 4.10 does illustrate higher $CaCO_3$ mass fractions concentrated near the reactor bottom. This aligns with the high inlet CO_2 levels generated from methane reforming in this lower section, which locally yields greater sorbent conversion and $CaCO_3$ production. But importantly, the sorbent inventory is not segregated or depleted in any areas despite the axial variation in CaO conversion. The sustained mixed state shows that sufficient sorbent is available to adsorb CO_2 wherever it is generated in the reactor.

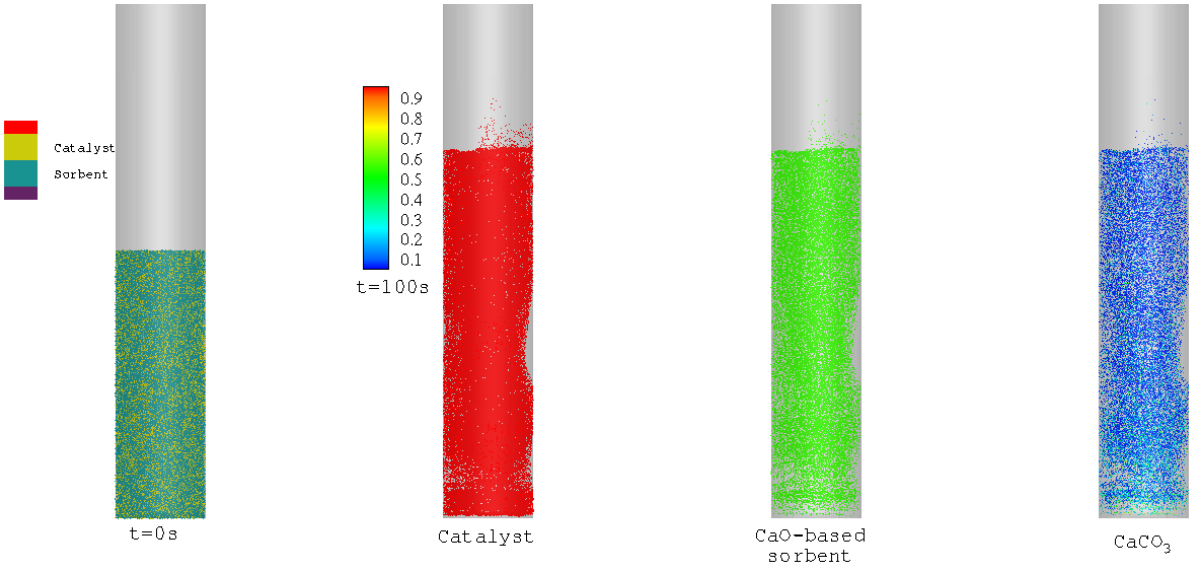

Figure 4.10: Distribution of solid materials coloured by particle species before the simulation (t=0s), and at t = 100 s for the catalyst, sorbent, and $CaCO_3$ coloured by mass fraction.

4.3.4 Effect of operating conditions

A parametric analysis was conducted to understand the CPFD model's prediction of selected performance parameters – product composition, hydrogen purity, CO_2 capture efficiency, and methane conversion. The process variables used are pressure, superficial gas velocity and steam-to-carbon ratio.

4.3.4.1 Effect of pressure

In an industrial scenario, hydrogen is usually produced at higher pressures, up to 25 atm, to reduce the cost associated with compressing hydrogen downstream. While keeping superficial gas velocity at 0.1 m/s, S/C ratio at 3, and temperature at 873 K, the performance of SE-SR of methane under different pressures of 5, 15 and 25 atm was investigated. Figure 4.11a and Figure 4.11b illustrate the impact of pressure on product composition and performance metrics, respectively. As pressure increases, the composition profiles in Figure 4.11a demonstrate decreasing CO_2 and H_2 mole fractions, while methane mole fraction rises. The low CO_2 concentrations at high pressure results from the higher CO_2 partial pressure, which provides a greater driving force for CO_2 to be adsorbed onto the solid sorbent sites [452]. CO_2 fraction decreased by 83% from 0.0051 while H_2 mole fraction decreased to ~0.72 from ~0.95, when pressure was increased from 1 atm to 25 atm.

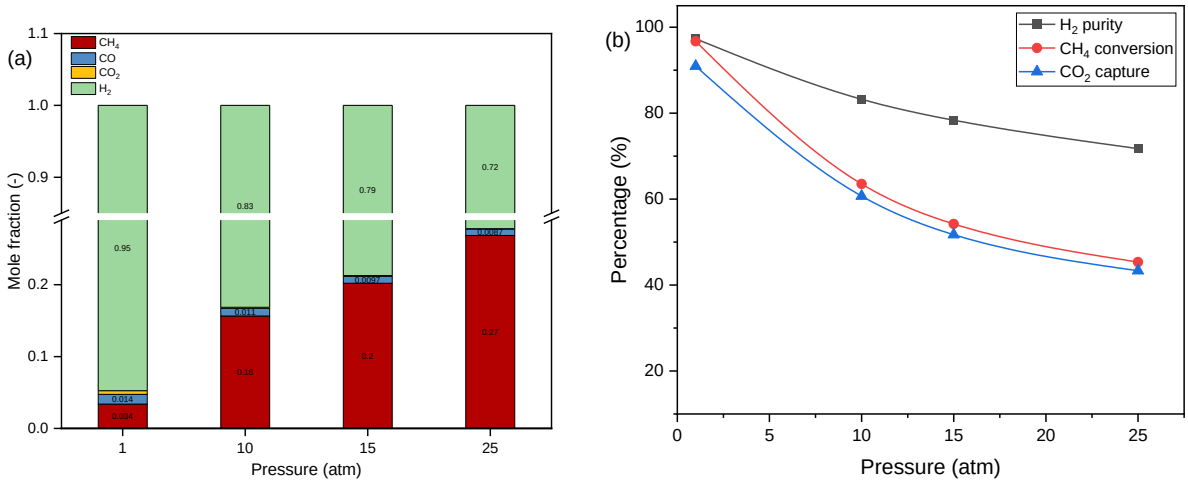

Figure 4.11: (a) product composition (dry basis) and (b) performance indicators under isothermal conditions, at varying pressures.

Correspondingly, the performance metrics in Figure 4.11b exhibit declining trends as pressure is elevated, including drops in hydrogen yield, methane conversion and invariably CO_2 capture efficiency. The steam reforming reaction produces more gaseous moles in the products than are present in the reactants, so an increase pressure shifts the equilibrium towards the side with fewer moles of gas, disfavouring methane conversion [453]. When operating pressure increased from atmospheric (1 atm) to 25 atm, methane conversion decreased significantly from an initial ~91% down to approximately 45%. This drop in methane conversion led to a corresponding reduction in CO_2 capture efficiency, which fell from around 90% to 43%. However, SE-SR of methane process demonstrates improvements in methane conversion and hydrogen composition relative to the conventional SMR process under high pressure conditions [454]. Wang et al. [250] found that for both SMR and SE-SR of methane processes, increasing the pressure raised the methane concentration while lowering the hydrogen concentration. However, the conventional SMR was more severely impacted by elevated pressures in terms of its reaction performance and product yields. When pressure was increased from 1 to 10 bar, hydrogen purity reduced by 3% for SE-SR and 16% for the conventional SMR process. The SE-SR enhanced tolerance to high pressures was attributed to the effect of CO_2 adsorption on the sorbent. The CO_2 capture countered the inhibiting impacts of pressure on the reforming reactions, allowing for greater methane conversion compared to SMR alone.

Primarily, the coupled composition and performance data clearly indicate pressure has an unfavourable effect, reducing hydrogen production and CO_2 capture while allowing more unreacted methane to breakthrough.

4.3.4.2 Effect of S/C ratio

As shown in Figure 4.12a, the mole fraction of hydrogen produced increased from approximately 0.95 to about 0.97 when the S/C ratio was raised from 3 to 5. This is accompanied by a decrease in the mole fractions of CH_4 and CO. This is due to the improved methane conversion that occurs at high S/C ratios, as illustrated in Figure 4.12b. Increasing the S/C ratio from 3 to 5 resulted in an increase in methane conversion from approximately 91% to 97%, and a corresponding rise in H_2 purity and CO_2 capture efficiency from ~95% to 97.3% and ~90% to 91%, respectively. However, CO_2 concentrations increased with higher steam-to-carbon feed ratios, despite the simultaneous CO_2 adsorption by sorbent material in the SE-SMR process. This somewhat counterintuitive result can be explained by two factors: The enhanced water-gas shift activity which produces more CO_2, and the increased steam partial pressure, which lowers CO_2 adsorption driving force.

The improved CH_4 conversion and increased CO_2 composition, with higher steam levels, can be attributed to the shift in the reforming equilibrium, which favours increased production of hydrogen and CO_2. In particular, the added steam drives the water-gas shift reaction ($CO + H_2O \leftrightarrow CO_2 + H_2$) further to the right, consuming more CO while generating additional H_2 and CO_2 [453]. Similar observation has been reported in the literature for increased S/C ratios. Abbas et al. [269] observed that a higher steam-to-carbon feed ratio in the SE-SMR process operated in a packed bed reactor improved hydrogen yields while also slowing the carbonation rate.

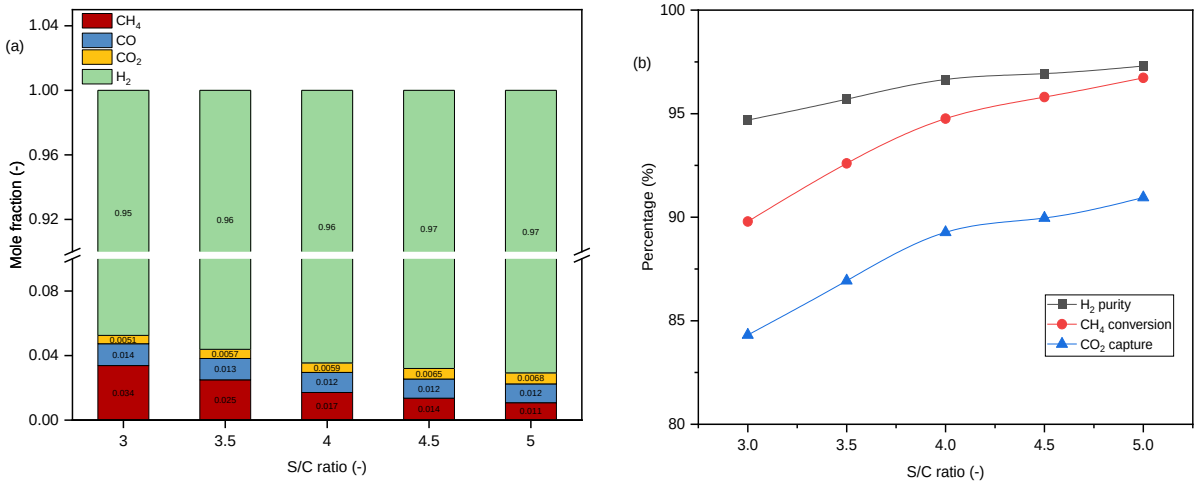

Figure 4.12: (a) Product composition and (b) performance metrics on dry basis under different S/C ratios.

Although a high S/C ratio improves methane conversion and hydrogen production, the concomitant increase in CO_2 levels highlights the limitations in the sorbent's ability to adsorb all of the CO_2 produced

under this condition. Therefore, optimising operating conditions could help achieve adequate CO_2 uptake rates at higher S/C ratios.

4.3.4.3 Effect of gas velocity

At higher gas velocities, such as increasing from 0.1 m/s to 0.4 m/s, the time available for the reforming reactions to occur is reduced, as reactants pass more quickly through the reactor bed. With less residence time, methane conversion can be expected to decrease significantly [455]. This is clearly seen in Figure 4.13, as methane conversion drops from approximately 90% to just 51% over this velocity range tested. Correspondingly, the outlet hydrogen purity also falls sharply, declining from around 95% purity down to 65% despite velocity ascent. Although the initial hydrogen production rate was observed to be enhanced at higher velocities during the first few seconds of the simulation, the reduced reactant gas contact time could not sustain this production rate, therefore hydrogen yields reduced accordingly.

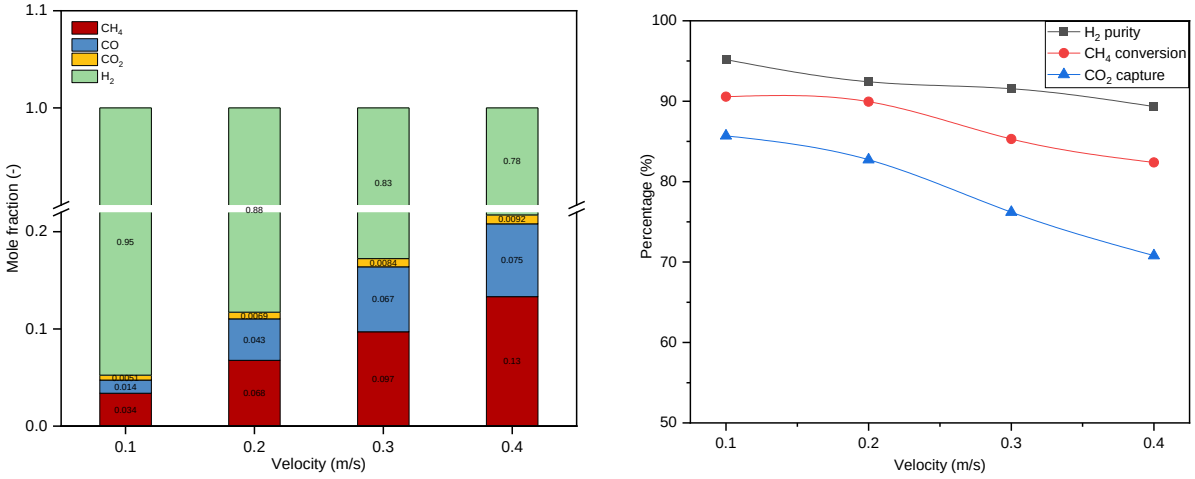

Figure 4.13: Effect of gas velocity on (a) product composition (b) H_2 purity, CH_4 conversion, CO_2 capture efficiency at 873 K and 1 atm.

In Figure 4.13a, CH_4, CO and CO_2 compositions rise markedly as the primary reforming, water-gas shift reactions and sorption are increasingly limited in extent by inadequate contact time. Higher gas velocities also lower average bed temperatures, in addition to reduced residence times, correlating to poorer methane reforming performance and CO_2 sorption [456].

4.4 Summary

This chapter was aimed at developing a reactor model to improve the description of reactor performance for SE-SR process. In this chapter, a three-dimensional CPFD model was developed for sorption-enhanced steam reforming of methane in a bubbling fluidised bed reactor, using Barracuda

VR® software. Validation of the model was carried out for both the hydrodynamic and kinetic sub-models by comparing simulation results of the particle volume fraction and product gas compositions, respectively, with experimental data available in literature. Three drag models tested revealed the EMMS-Yang drag model as closely matching the hydrodynamic behaviour of the experimental literature. The gas-solid flow characteristics, influence of pressure (1 – 25 atm), steam-to-carbon ratio (3 – 5), and velocity (1 – 4 m/s) were analysed. The results obtained from the simulation showed that the three-dimensional CPFD model was efficient in predicting the complex gas-solid characteristics, as well as the performance of SE-SR in bubbling fluidised bed reactor. The CPFD model developed in this chapter provides a foundation for further improvement for application to circulating fluidised bed reactors in the following chapter. It is also expected to be valid for scale-up studies conducted in Chapter 6 and Chapter 7.

5 Computational simulation of SE-SR of methane in a bench-scale dual circulating fluidised bed reactor

This chapter is based on the peer-reviewed publication:

- Udemu C, Font-Palma C. Computational simulation of SE-SR of methane in a bench-scale circulating fluidised bed reactor: Insights into the effects of bed geometry design and catalyst-sorbent ratios. Fuel 2024;377:132817. https://doi.org/10.1016/j.fuel.2024.132817.

5.1 Introduction

This chapter extends the CPFD model validated in Chapter 4 to include the calcination process, thereby simulating the full-loop (reforming/carbonation and calcination) SE-SR of methane system. Various reactor concepts have been proposed and reported for SE-SR of methane, including trickle bed, fixed bed and fluidised bed reactors. In trickle bed, the gaseous reactants are passed from the bottom through an immobilised bed of catalysts while the sorbents are introduced into the reactor from the top, which trickles down the bed and are then collected at the bottom [233,234]. Formation of hotspot within the catalysts and scaleup challenges due to its complex phenomena are setbacks associated with this reactor concept [235,236]. For fixed bed reactors, a fixed ratio of sorbents and catalyst is contained in a reactor with gaseous reactants passed over the bed of mixed solids to produce hydrogen [244,286]. Whilst fixed-bed reactors are simpler and are well-suited for high-pressure hydrogen production, they could face challenges with temperature control (to prevent the formation of hotspots) at large-scale operation [457]. Also, solids circulation between reforming/carbonation and calcination reactors can be complicated using this reactor concept. Thus, fluidised bed reactors were selected for this study due to their suitability for facilitating the continuous circulation of solids between reactors, a key requirement for the sorption-enhanced steam reforming process. This continuous circulation loop is integral to maintaining the sorbent circulation necessary for hydrogen production on an industrial scale.

Few configurations of fluidised bed reactors have been proposed for use in SE-SR of methane, such as the use of dual bubbling fluidised bed reactors for both the reformer and calciner units [245,279], the employment of fast fluidised bed (risers) and bubbling bed reactors for the calciner and reformer, respectively [247,419,458], and the use of fast fluidised for both reformer and calciner [459]. However, riser reformers have been shown to achieve lower hydrogen yields than bubbling bed reformers due to the shorter solids' residence time in the reactor. Jakobsen and Halmøy's [257] modelling study

provided a valuable comparison of performance between SE-SR using bubbling and riser fluidised beds reformers with lithium orthosilicate, sodium zirconate, and dolomite sorbents. In their study, using CaO as the sorbent in a riser reactor resulted in only a modest increase in hydrogen yield, due to slow sorption kinetics and insufficient solids residence time for CaO to achieve significant conversion. This meant that an exceptionally long riser would be needed to adequately enhance the reforming process via sorption. In contrast, bubbling bed simulations showed much higher hydrogen yields up to 99.9%. While a bubbling fluidised bed configuration is preferable to a riser for SE-SR of methane with CaO due to residence time considerations, the reactor geometry and design could impact process performance. Features like aspect ratio, inlet/outlet positioning and internals can influence solids mixing and segregation, respectively enhancing or hindering mass transfer between phases [460–463].

Previous studies have investigated the impacts of key operating variables like temperature, pressure and gas velocity on SE-SR of methane [146]; however, the influence of the catalyst-to-sorbent ratio and reactor design has been relatively underexplored. This chapter addresses this gap by modelling and analysing SE-SR performance under varying solids loadings, in addition to exploring two different dual bubbling bed reactor geometries. Simulations are conducted by intentionally using low catalyst loadings, to provide insights into process robustness when catalyst activity is diminished, analogous to real-world catalyst deactivation. Furthermore, testing low sorbent loadings will elucidate the impact of declining sorbent inventory on the SE-SR of methane performance, similar to sorbent degradation over repeated cycles. The CPFD model developed in Chapter 4 was extended to simulate the dual bubbling beds in circulating mode. Due to high computational requirements, only two reactor bed designs were considered. The outcome of this modelling work will provide a basis for the selection of reactor geometry and initial conditions for scale-up studies.

5.2 Methodology

In Chapter 4, a CPFD model was developed to simulate the performance of SE-SR of methane in a bubbling fluidised bed reactor. The simulation included the reformer/carbonator zone and incorporated EMMS-Yang drag sub-models and kinetic sub-models (for carbonation and SMR reactions). The EMMS-Yang drag model was adopted for hydrodynamic simulations based on its successful validation in Chapter 4. In the current chapter, the CPFD model has been extended to include a calcination kinetic sub-model for regenerating the spent sorbent in the calciner. The kinetic sub-model for calcination is described in this section. The overall reactor setup and operating conditions for the combined reformer/carbonator and calciner zones are also discussed here, as they differ from what was employed solely for the reformer/carbonator in Chapter 4. However, the

previously validated CPFD model for the reformer/carbonator is retained without modification in the current work.

5.2.1 Reactor setup

This study models the cyclic performance of SE-SR of methane based on a bench-scale setup similar to that developed at SINTEF [464]. Two reactor systems are evaluated in this study. The first design (Figure 5.1a) replicates the system used at SINTEF, and employs a bubbling fluidised bed reactor with an internal pipe for particle outlet from the bottom of the bed. The second design (Figure 5.1b) incorporates a side-exit particle outflow mechanism to let out solids from the bed. Both designs consist of interconnected bubbling fluidised bed reactors performing key roles - a reformer/carbonator for the endothermic reforming and exothermic sorption reactions, a calciner for the endothermic calcination reaction, and auxiliary components like loop seals and a riser facilitating continuous solids circulation. The internal dimensions of the reactor units are provided in Figure . For each CFB system – CFB1 and CFB2, the reformer/carbonator and calciner have the same dimensions. The bed height and volume are also considered to be constant for CFB1 and CFB2, at the bed volumes considered in this study (see Table 5.4).

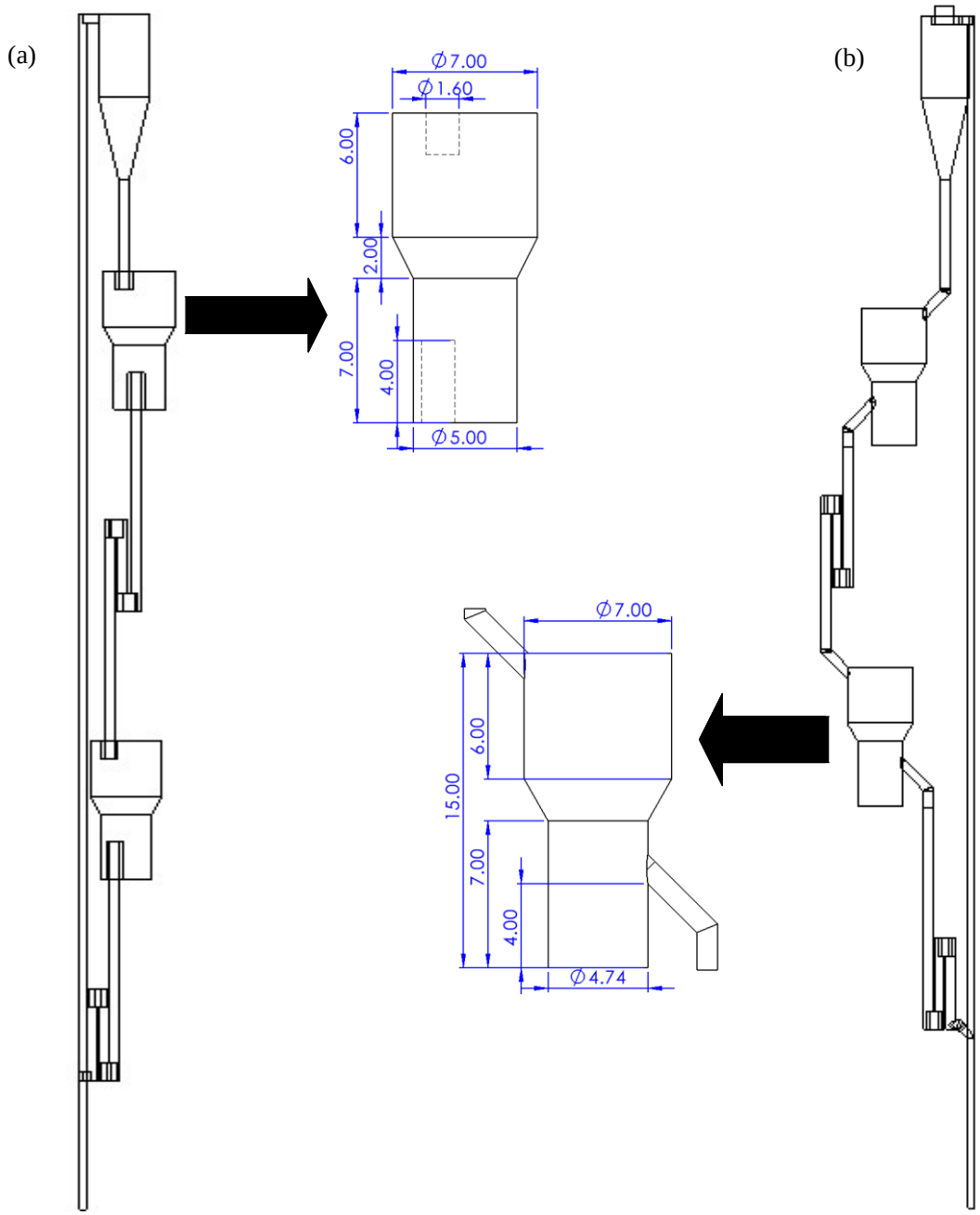

Figure 5.1: Design and dimensions of (a) reactor bed design with internal particle outflow (CFB1), and (b) reactor bed design with side particle outflow (CFB2) of the SE-SR reactors used in the simulation (all dimensions in cm).

During operation, fluidising gases are introduced to the bottom of the reformer (located just below the cyclone), where reforming and carbonation reactions occur. The product gases leave the reactor from the top while the spent solids leave the reactor through the overflow pipe located inside the reactor for CFB1, and the side exit for CFB2. The solids enter the first loop seal, as seen in Figure 5.1, then to the regenerator (second reactor at the bottom). The loop seal is aerated with a fluidising gas,

forcing the solids to overflow into the regenerator. The loop seal is attached to maintain the pressure levels, improve solids circulation rate and minimise gas leakages between the reactors. In the regenerator, the hot fluidising gas provides enough heat for decarbonation of the spent sorbent; and operates in similar bubbling manner as the reformer. The regenerated solids overflow to the bottom loop seal and are transported through the riser back to the reformer, using a fluidising gas. The cyclone in this system is only used to return solid particles to the reformer. Completely mixed sorbents and catalysts were introduced into the reactor, with an estimated sorbent-to-catalyst volume ratio of 4 in the reformer. The superficial velocities of the fluidising gases are presented in Table 5.1.

Table 5.1: Gas flows in the SE-SR system

Reactor units	**Fluidising gas**	**Superficial velocity (m/s)**
Reformer	Nitrogen, steam, and methane	0.062
Calciner	Nitrogen	0.056

5.2.2 Calcination model

As $CaCO_3$ particles decompose during calcination, their size decreases due to the diffusion of CO_2 from the interior to the surface. The changing grain size model considers how grain size distribution changes with the reaction, while incorporating the unreacted shrinking core model to provide a more accurate representation of diffusion control compared to simpler models [465]. Garcia-Labiano et al. [466] developed a changing grain size model based on the dolomite particles' granular texture, while accounting for internal diffusion limitations. They suggested using the well-known Langmuir–Hinshelwood model to explain the calcination mechanism. Their model took into consideration the diffusion and reaction of gases within a particle's differential volume and was represented using a two-step Langmuir–Hinshelwood mechanism. The first step involves decomposition of $CaCO_3$ to CaO and chemisorbed CO_2, whereas in the second step, CO_2 desorbs from the active site. Their model provided a good representation and fit to experimental data for dolomite across various operating conditions tested; therefore, it was adopted in this simulation. The calcination reaction is a function of CO_2 partial pressure and is given by

$$R_{calc} = k_c S_e \; 1-\theta \; \left(1 - \frac{P_{\mathrm{CO_2}}}{P_{co_{2,eq}}}\right) \; \left[\frac{\mathrm{mol}}{\mathrm{kgs}}\right] \tag{81}$$

The fraction of occupied active sites (θ) was found to align with the Freundlich isotherm, with the adsorption constant, c, represented via the Arrhenius expression. θ is the fraction of active sites

occupied by CO_2 and is a function of CO_2 partial pressure and adsorption constant, according to the Freundlich isotherm expression below:

$$\theta = c\sqrt{P_{CO_2}} \quad 82$$

The adsorption constant, c, and the kinetic rate constant, k_c $[molm^{-2}s^{-1}]$, are given by

$$c = c_0 e^{\frac{E_a}{RT}} \quad 83$$

$$k_c = k_0 e^{\frac{E_c}{RT}} \quad 84$$

Consistent with changing grain size models, the reaction surface area is determined by the particle radius, which changes as the reaction progresses. Therefore, the specific surface area of the sorbent, S_e, is based on equation 85, where r_0 and r_1 are the initial radius of $CaCO_3$ and the radius of its unreacted core, respectively.

$$S_e = S_0\left(\frac{r_1}{r_0}\right)^2 \quad 85$$

For simplicity, r_1 is assumed to be independent of the grain's radial position, so that a correlation between $\frac{r_1}{r_0}$ and the unconverted $CaCO_3$ (X_{CaCO_3}) can be determined [467]. Therefore, S_e is estimated in equation 86. Additionally, the S_0 is taken to be 9.57×10^3 m^2/kg [466].

$$S_e = S_0(X_{CaCO_3})^{\frac{2}{3}} \quad 86$$

The equilibrium pressure, $P_{co_{2,eq}}$, is a function of temperature as described by Barin [468], and for a high-temperature calcination process, is calculated according to the equation:

$$C_{\mathrm{CO_2,eq}} = \left(\frac{4.137\times10^{12}}{T}\right)exp\ \frac{-20474}{T}\ ;\quad P_{\mathrm{CO_2,eq}} = C_{\mathrm{CO_2,eq}}RT\ [atm] \quad 87$$

The kinetic parameters used in the calcination sub-model are provided in Table 5.2.

Table 5.2: Kinetic parameters for the calcination of dolomite [466]

Parameter	Value	Units
E_c	114	$kJmol^{-1}$
E_a	-90	$kJmol^{-1}$
c_0	3.5×10^{-7}	$Pa^{-0.5}$
k_0	29.5	$molm^{-2}s^{-1}$

5.2.3 Operating conditions and assumptions

5.2.3.1 Case descriptions

As seen in Table 5.3, three scenarios were considered to evaluate system performance under conditions simulating sorbent degradation and catalyst deactivation over time. A low catalyst loading scenario (volume ratio: 0.25) was used to mimic gradual catalyst deactivation by providing less active catalytic sites. This allows studying how conversion rates decline with lower catalytic activity and whether reforming and carbonation reactions can still sufficiently proceed. A high catalyst loading but low sorbent addition scenario (volume ratio: 4) was used to simulate the effects of sorbent degradation by providing less sorbent. This scenario can provide insights into how product selectivity shifts as sorbent capacity decreases. Whilst very few catalyst deactivation models for SMR still exist [469], a reduced loading approach provides insights without additional complexity. Further, no validated deactivation models currently consider the SE-SR condition. Further, no validated deactivation models currently consider the SE-SR condition. An intermediate, baseline scenario with equal catalyst and sorbent addition was also evaluated.

Also, the two computational geometries – CFB1 and CFB2 – were designed, where CFB1 and CFB2 have equal bed volumes. Each geometry was then modelled at three different scenarios of catalyst to sorbent volume ratios, as seen in Table 5.3. This resulted in six total cases to be simulated, each parameterised with a range of catalyst to sorbent ratios. These cases were configured to provide insight into how both structural modifications and material loading ratios could influence hydrodynamics and reaction kinetics within the dual CFB reactor system. Assessing the SE-SR performance across these varied conditions will help improve the understanding of the impacts of catalyst-to-sorbent ratios and invariably catalyst deactivation and sorbent degradation, in order to maximise the system's long-term operation and resilience against these expected modes of decline.

Table 5.3: Case description for the simulated reactors

Cases	Geometry	Catalyst-to-sorbent volumetric ratio (Reformer)	Catalyst-to-sorbent mass ratio (Reformer)
CFB1-0.25	1	0.25	0.3
CFB1-1	1	1	1.3
CFB1-4	1	4	3
CFB2-0.25	2	0.25	0.3
CFB2-1	2	1	1.3
CFB2-4	2	4	3

5.2.3.2 Operating conditions

The initial operating conditions for the system were taken from Arstad et al. [12], to obtain consistent results for model validation and evaluation. Pressure and velocity boundary conditions were used to model the flow in the reactor. The pressure boundary condition was specified at the outlet of the reactors, and the velocity boundary condition was specified at the inlet of the reactors and loopseals. The fluidised bed system was modelled under adiabatic condition, without the added complexity of heat losses in and out. Physical properties and operating conditions of the fluidising gas and particles are listed in Table 5.4.

Table 5.4: Operating conditions used for the simulation of SE-SR of methane in the CFB reactors [12]

Parameters	**Value**	**Unit**
Total volume of solids in the system	0.160	L
Bed voidage	0.55	-
Catalyst and sorbent particle size range	90 – 200	µm
Catalyst density	2200	kg/m^3
Sorbent density	1500	kg/m^3
CaO/MgO conc.	60/40	wt%
Sorbent thermal conductivity (at room temperature) [470,471]	15	W/(mK)
Catalyst thermal conductivity [472]	0.33	W/(mK)
Steam-to-carbon ratio	4	-
Reformer temperature	873	K
Calciner temperature	1173	K
Reactor pressure	1	atm

The model settings for particle-wall interactions, such as normal-to-wall and tangent-to-wall momentum retention coefficients, are the same as those reported in Table 4.2 and validated in Chapter 4. A summary of these kinetic parameters is provided in Table 5.5 for reference.

Table 5.5: Summary of model settings used for simulating the CFB systems

Parameters	Values	Units
Close-pack volume fraction	0.55	-
Maximum momentum redirection from collision	40	%
Normal-to-wall momentum retention	0.85	-
Tangent-to-wall momentum retention	0.85	-
Time step	0.001	s
Simulation time	200	s
Averaging start time	100	s

The fluidised bed system was modelled under adiabatic condition, without the added complexity of heat losses in and out. Radiative heat transfer was neglected for simplicity due to the small temperature difference between the particles and gas, and a small contribution from particle radiation to the total heat transfer compared to conduction and convection [473]. Heat transfer from fluid to particles and fluid to wall was calculated using fluid-to-particle and convective fluid-to-wall heat transfer models, respectively. The maximum number of iterations used for convergence of volume, pressure, velocity, and energy were 30, 2000, 50, and 100, respectively. The corresponding residual tolerances for convergence were 1×10^{-7}, 1×10^{-6}, 1×10^{-7}, and 1×10^{-6}, respectively. The heat transfer model equations are presented in Appendix A.

Following the completion of the simulation, product gas compositions from the exit stream were obtained on a dry basis, with methane conversions (X_{CH_4}) and hydrogen yields (Y_{H_2}) calculated from equations 88 and 89, respectively. The carbon capture efficiency (CCE) in equation 90 is based on carbon mass balance around the reformer, while equation 91 presents the reformer's process efficiency (PE).

$$X_{CH_4} = \left(1 - \frac{n_{CH_4,out}}{n_{CH_4,in}}\right) \times 100\% \quad (88)$$

$$Y_{H_2} = \frac{n_{H_2,out}}{4n_{CH_4,in}} \times 100\% \quad (89)$$

$$CCE = \left(\frac{x_{CH_4,in} - (x_{CO_2,out} + x_{CH_4,out} + x_{CO,out})}{x_{CH_4,in} - (x_{CH_4,out} + x_{CO,out})}\right)_{reformer} \times 100\% \quad (90)$$

$$PE = \left(\frac{m_{H_2} \times LHV_{H_2}}{(m_{CH_4,in} \times LHV_{CH_4})}\right) \times 100\% \quad (91)$$

5.3 Results and discussion

Simulation of the bench-scale dual CFB reactor in the CPFD program began with the random particle initialisation of mass in the domain, where the total mass of particles in the system was approximately 1.5 kg. This initial particle randomisation is important to properly set up the computational model before the dynamic simulation captures how the particles interact with the flowing gas streams. The simulation was run for 200 seconds for each of the cases defined for the dual CFB reactor system. This simulation time was sufficient to capture multiple cycles of particle flow and mixing within the two interconnected reactor vessels being modelled. The simulation results over the 200 second period were then analysed for each of the cases to evaluate system hydrodynamics and parameters of interest for the bench-scale SE-SR system. This section reports the results of the simulation, starting first with the grid independence study.

5.3.1 Grid independence study

A grid independence study was conducted to evaluate the effect of cell size on the accuracy of the reactor model. Three different mesh sizes were chosen - 1 million cells (coarse), 1.2 million cells (fine) and 1.5 million cells (very fine). Simulations were run using each mesh size, and pressure profiles along the vertical height of the connecting transport riser were examined and compared. This transport riser was chosen as the basis for comparison since it is common to both geometries. Figure 5.2 shows the results of the pressure profiles.

With 1 million cells, the pressure profile showed higher pressure at the bottom, which reduced along the height of the riser. When the mesh was refined to 1.2 million cells, the pressure profile appeared the same with fewer irregular variations. Increasing the mesh size further to 1.5 million cells did not lead to significant changes in the pressure profile. The profiles matched very closely, suggesting that further mesh refinement beyond 1.2 million cells was not providing additional insight into the flow behaviour. The percent difference in pressures between the coarse and fine cell meshes ranged from 0.01% – 0.06% at different points, showing a noticeable effect of mesh size. However, the difference was only 0.012% – 0.13% when comparing the fine and very fine cell meshes. This indicated that the solution was relatively independent of further mesh refinement and 1.2 million cells was providing an

appropriately well resolved solution. Based on the pressure profile comparisons, the fine grid was concluded to be a suitable mesh that balanced accuracy with computational cost. While the very fine mesh may have resulted in marginal increase in mean pressures, the minimal improvement did not justify the slow real-time simulation.

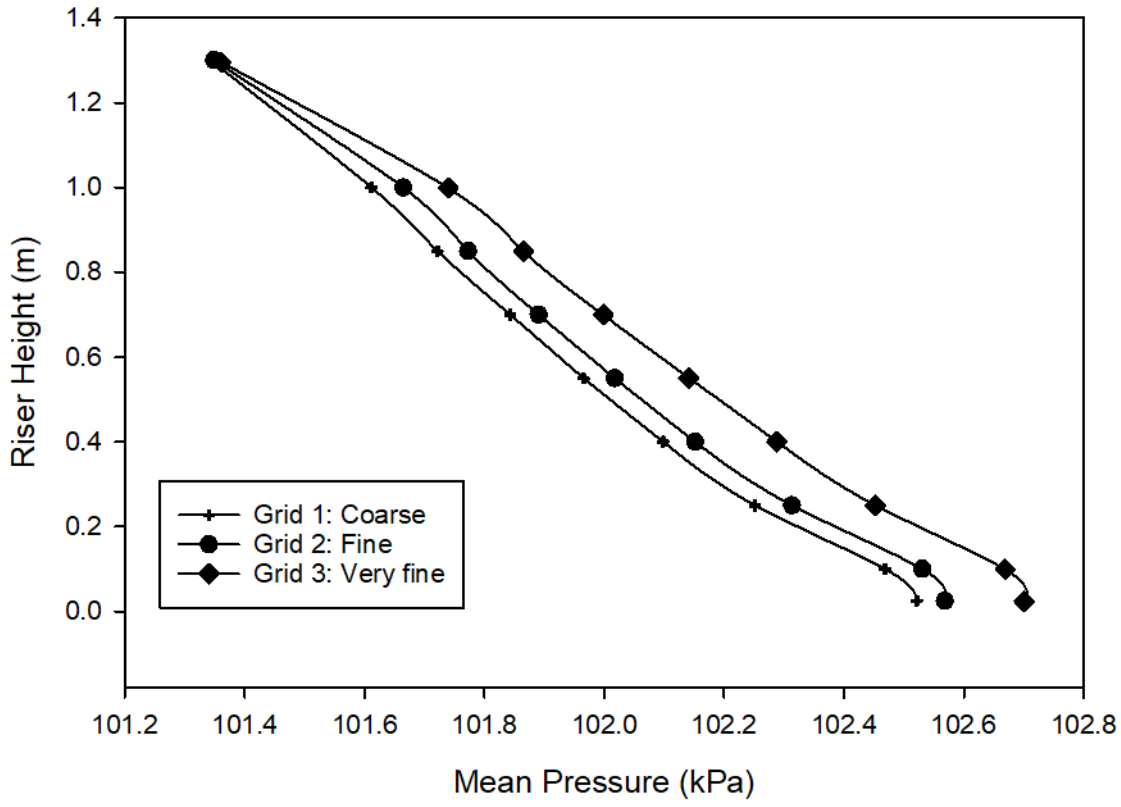

Figure 5.2: Comparison of the transport riser pressure profiles for the different grid cell sizes.

5.3.2 Model validation

The calcination kinetics was validated by simulating a unit cube geometry under operating conditions similar to that of the literature data. The unit cube geometry, as displayed in Figure 5.3, is a simplified model replicating the operating conditions (pressure, temperature, particle size and density) of the thermo-gravimetric analyser (TGA) experiment conducted by García-Labiano et al. [466]. This single-cell case was adopted to simplify the simulation setup, reduce the computational time, and make it easier to identify and troubleshoot any issues with the calcination reaction rates. The cube was filled with 0.4 – 0.6 mm diameter of half-calcined dolomite ($CaCO_3$·MgO) particles at atmospheric pressure, in a nitrogen environment and 0% CO_2 partial pressure. The reaction temperature was set at 1123 K and the simulation was run for 50 seconds for complete calcination.

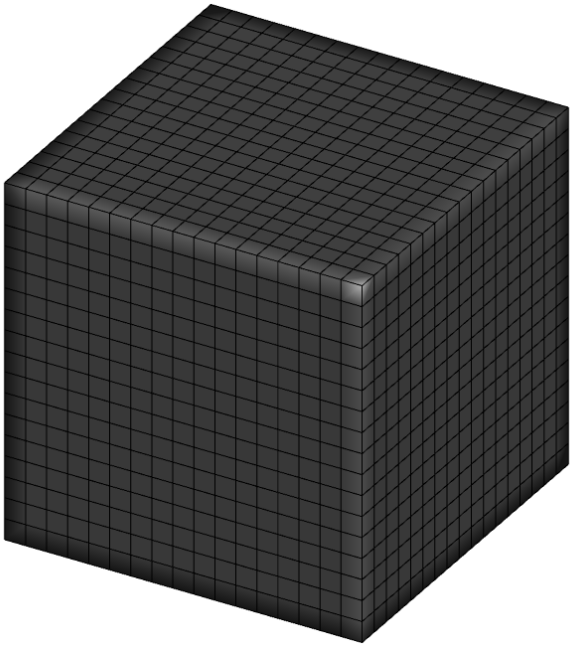

Figure 5.3: Gridded simple-cell geometry used to validate the calcination chemistry.

A conversion-time plot for the calcination process was generated from the simulation and compared with the experimental result from García-Labiano et al. [466], as shown in Figure 5.4. The plot shows that complete calcination of the carbonated dolomite particles was achieved after 20 seconds in the simulation, compared with ~22 seconds observed in the experiment. Since the simulation and experimental results are close, the kinetic model is considered to be suitable for further adoption in the CFB reactor modelling.

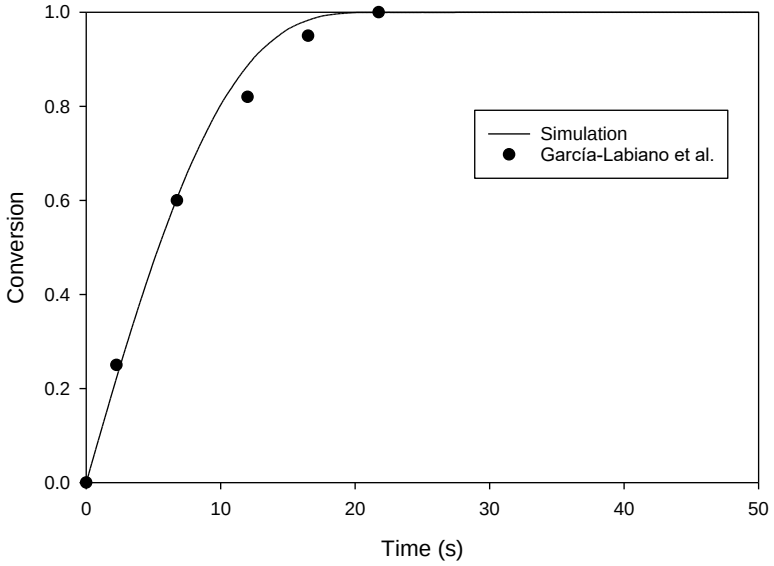

Figure 5.4: Comparison of calcination conversion level from the simulation case with literature data, both at 1 atm, 1123 K and 0% CO_2 [466].

Following the validation of the calcination reaction model, it was integrated into the CFB reactor model and the full-loop system was validated. To validate the accuracy of the SE-SR in dual CFB reactor simulation model, a comparison was made between the experimental data by Arstad et al. [12] and results from the simulation case – CFB1-1. This case was used because it had similar geometric parameters and operating conditions (including pressure, temperature, particle size and density) representing the actual bench-scale reactor. The simulated reformer/carbonator product composition for the last 10 seconds, after 200 seconds simulation time, was extracted and averaged from the CFB1-1 case data and compared with the experimental compositions on a dry volume (%) basis. If the simulated composition matches the experimental data, it indicates that the underlying reaction mechanisms and hydrodynamics modelled in the simulation are likely capturing the actual chemistry taking place.

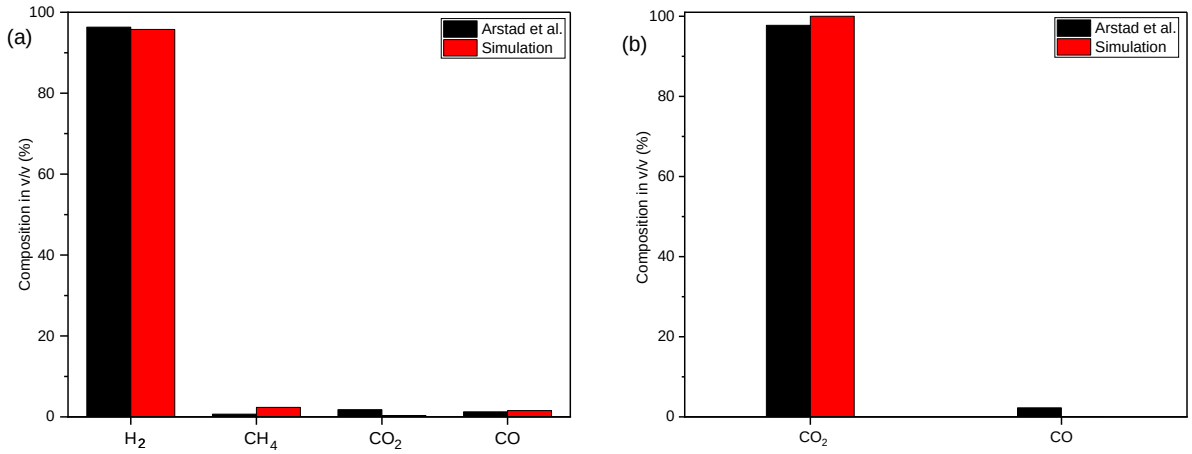

Figure 5.5: Comparison of the (a) reformer and (b) calciner product compositions from the simulation case with literature data [12].

Figure 5.5a shows the model generally captured the product compositions from the reformer/carbonator, with minor deviations. The simulation underpredicted the H_2 and CO_2 outlet compositions by 0.56% and 1.44% respectively, while overpredicting CH_4 and CO by 1.67% and 0.33%, respectively. Figure 5.5b illustrates the model also adequately predicted the calciner outlet compositions. The trends in all compositions agreed well between the simulation and experimental data for both reactors. While some compositions exhibited under or overpredictions of less than 2%, the modelling approach was still able to capture the overall product compositions leaving the reactors.

The slight differences in compositions between the simulation and literature data could be due to the kinetic model adopted in the simulation. Past studies on SMR kinetics developed and proposed

different reaction mechanisms for steam methane reforming [431]. Xu and Froment [430] proposed that CO_2 is formed by both water-gas shift and steam reforming reactions, and includes a third overall reaction producing CO_2 and H_2. In contrast, Numaguchi and Kikuchi's (NK) model [429] used in this study omitted this additional reaction pathway, which has recently been reported in another study [431] to predominate at the lower temperatures (< 850 K) that were considered. Nevertheless, the NK model has shown good prediction for SE-SR experimental studies [246,474,475]. Having successfully validated the model against experimental data, the calcination model was then used to conduct further studies.

5.3.3 Product distribution and performance at various solids loadings

Figure 5.6a shows that there is a significant impact of the selection of catalyst-to-sorbent ratio. Improving catalyst loading, and invariably catalyst-to-sorbent ratio, reduced the methane content in the outlet streams by promoting higher methane conversion. Figure 5.6a also demonstrates that lower catalyst mass led to higher methane levels in the product stream as a result of decreased methane conversion, approximating the effects of losing catalytic activity over time. Lowering the catalyst loading simulated the impact of gradual catalyst deactivation by reducing the number of active catalyst sites available for reforming reactions.

Although lower catalyst loading impacted methane levels, the relatively low outlet compositions of CO and CO_2 in Figure 5.6b and Figure 5.6c, respectively, indicate the presence of sorbent still benefitted the process. Prior to developing the SE-SMR model, batch simulations without sorbent produced higher residual methane as well as CO and CO_2. The SMR reaction without CaO sorbent was simulated in a reactor filled with catalyst particles for the three catalyst masses used in each of the C-S mass ratios. The composition of the product streams for the three cases, in the absence of CaO sorbent, are presented in Table 5.6. The data in Table 5.6 shows that increasing the catalyst mass improved activity, as evidenced by decreasing methane content and increasing hydrogen content in the product gas.

Table 5.6 also includes data of the equilibrium composition of the reaction from the CPFD model, validated in a thermodynamic software – Aspen Plus. Aspen Plus V14.1 was used to model the equilibrium composition by applying the Peng-Robinson equation of state to simulate the RGibbs reactor, which uses the Gibbs free energy minimization to determine the reactor outlet composition at chemical equilibrium [476]. At S/C ratio, temperature, and pressure of 4, 873 K, and 1 atm, respectively, the equilibrium compositions from the Aspen Plus and CPFD models are comparable, as seen in Table 5.6. Comparing the product gas compositions predicted at different catalyst loadings against the equilibrium compositions shows that increasing the catalyst mass from 0.02 kg to 0.05 kg

enabled closer approach towards equilibrium composition, which is consistent with faster reaction kinetics expected from more available active sites. However, increasing catalyst mass above 0.034 kg did not show any appreciable change in both CH_4 content in the outlet stream and methane conversion. In addition, the CPFD model still predicts some deviation from complete thermodynamic equilibrium even at 0.05 kg loading, due to their different calculation methods and thermodynamic databases. However, as Figure 5.6 demonstrates, combining the catalyst with sorbent significantly enhanced the product composition compared to catalyst alone, even under conditions of reduced catalytic activity.

Table 5.6: Composition of the product gas from the reformer for the various catalyst masses in the absence of sorbent (dry basis).

Catalyst mass (kg)	**CH_4 (%)**	**CO (%)**	**CO_2 (%)**	**H_2 (%)**	**CH_4 Conversion (%)**
0.014	8.44	4.49	14.72	72.35	84.43
0.034	4.91	5.55	14.58	74.96	90.15
0.054	4.37	5.76	14.52	75.36	91.23
Equilibrium (CPFD model)	0.18	7.74	13.75	78.32	99.00
Equilibrium (Aspen model)	0.38	7.00	14.32	78.30	98.34

While the CO_2 sorbent was able to enhance the product composition, Figure 5.6b shows relatively high composition of CO specifically under the low catalyst loading condition. For instance, in CFB1, the CO level initially decreased from 5.70% to 1.56% as the C-S ratio was increased from 0.3 to 1.3, but then increased again to 2.36% at a ratio of 3. A couple of reasons could explain this non-linear trend. At C-S mass ratio of 0.3, the high observed CO concentration can be attributed to the slow CO_2 sorption kinetics from the unfavourably low CO_2 driving force under the current operating conditions. Literature indicates that for rapid CO_2 sorption kinetics, the CO_2 partial pressure needs to be higher than the equilibrium value to provide adequate chemical potential for carbonation using CaO [433]. In this case, the low partial pressure was likely below the threshold needed for appreciable uptake rates. However, this still allowed some methane to be converted to CO via the steam reforming reactions while increasing the CO levels leaving the reactor. Another reason for the relatively high CO in the product stream could be the low water-gas shift activity resulting from the low catalyst loading. Since more methane is being converted following CO_2 sorption, the water-gas shift activity will go even lower, limiting CO conversion to CO_2, due to the low catalyst loading. The high level of CO observed for this

low C-S ratio is not peculiar to this study. Chanburanasiri et al. [477] investigated the effects of varying Ni catalyst loading in a Ni/CaO multifunctional particle at 873K, 1 atm, and a steam-to-carbon ratio of 3. They reported that increasing Ni loading to 12.5 wt% yielded 80% H_2, 6% CO, and 2% CO_2, though the CaO was reported to having only 45% of its pure component sorption capacity. Other reports have also highlighted the role of catalysts in driving water-gas shift reactions, even in enhanced conditions [478–480]. Thus, a certain level of catalytic activity is essential to promote the water-gas shift reaction and adequately convert CO to CO_2. Further, the CO levels observed at C-S mass ratios of 0.3, 1.3, and 3 provide insight into the relationship between CO levels and C-S ratios. At a C-S ratio of 0.3, representing a low catalyst loading, CO levels remained high, highlighting the need for sufficient catalyst sites to drive the water-gas shift reaction. A C-S ratio of 1.3, demonstrating a balanced loading of both catalyst and sorbent, produced lower CO levels, showing the synergistic benefits of the combined solids. Finally, a C-S ratio of 3, equivalent to a low sorbent loading, also resulted in slightly high CO, signifying the importance of adequate sorbent mass to promote equilibrium shifts through sorption.

SE-SR involves continuous cycles of carbonation and calcination, making it prone to sintering and reducing its sorption capacity over time. The reduced mass of CaO sorbent at C-S ratio of 3, in the reformer/carbonator, represents lower sorption capacity and activity as the sorbent degrades. Figure 5.6c illustrates how varying the sorbent loading relative to catalyst mass (C-S ratio) impacts the CO_2 concentration in the outlet stream. At low C-S ratios (of 0.3) where sorbent mass dominates, higher sorbent levels effectively lowered CO_2 levels through selective sorption. However, comparing the C-S ratios of 0.3 and 1.3, where the sorbent loading was reduced by approximately 39%, the CO_2 concentration significantly decreased from 3.59% to 0.34% and 2.74% to 0.35% for reactor CFB1 and CFB2, respectively, despite the lower absolute sorbent mass. This could be due to the improved sorption capability afforded by an increase in the partial pressure of CO_2, as a result of steam methane reforming driven by the presence of additional catalyst at C-S ratio of 1.3. As the sorbent mass reduces into the sintered region at C-S ratio of 3, the simulated reduced sorbent capacity results in less CO_2 being captured from the gas stream. This causes CO_2 concentrations to initially decrease then rise again, as shown in the figure. Although, in cases where SE-SR is operated at high pressures, the behaviour of the system under low catalyst loading (0.3) is likely to be different, as high pressures favour sorption of CO_2 [481].

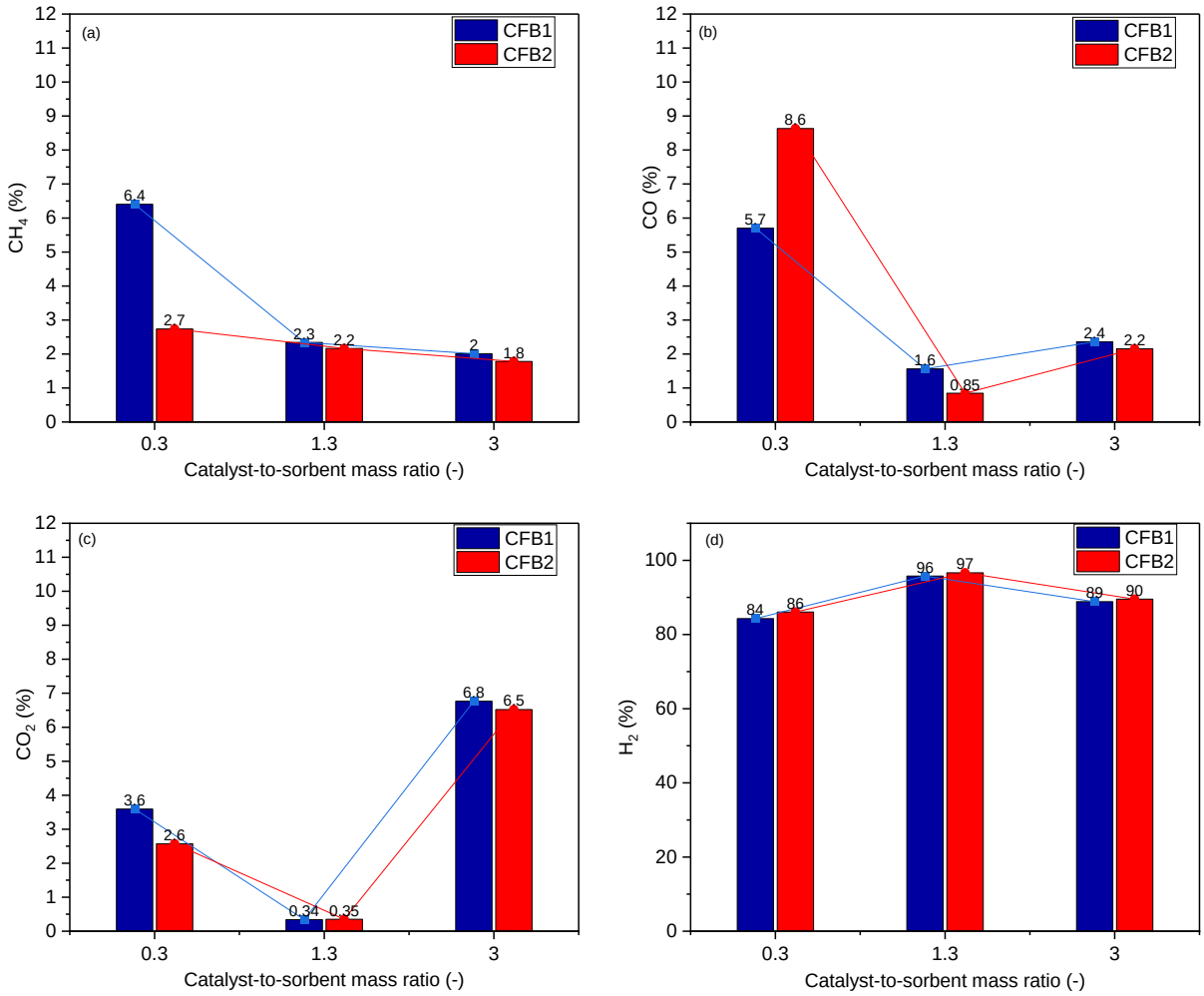

Figure 5.6: Product distribution of (a) CH_4 (b) CO (c) CO_2 and (d) H_2 at the reformer exit for designs 1 (Blue bar with blue trendlines) and 2 (Red bar with red trend lines) at catalyst-to-sorbent mass ratios of 0.3, 1.3 and 3.

The sorption of CO_2 serves to shift the equilibrium of the steam methane reforming reaction in favour of more hydrogen production. As seen in Figure 5.6d, despite the low activity observed at C-S of 0.3, there was still an improvement in hydrogen concentration, which increased from 78.32% at equilibrium, to 84.30% and 86.06% for geometries 1 and 2, respectively. This was increased further to 95.75 – 96.64% at C-S of 1.3, following more CO_2 sorption but reduced to 88.86 – 89.50% at C-S of 3, due to low sorbent amount. At the low C-S ratio of 0.3 with minimal catalyst, the relatively substantial sorbent in the system did not increase hydrogen concentrations beyond the level achieved at the lower sorbent loading of C-S = 3. Thus, during periods of poor catalyst activity, simply adding more sorbents does not necessarily enhance performance compared to optimising catalyst loading. The activity of the steam reforming catalyst imposes fundamental limits on hydrogen production that cannot be overcome through sorbent amounts alone when catalyst loading is insufficient. Additionally, Table 5.6

shows that above a catalyst loading of 0.034 kg (without sorbent), corresponding to 55 wt% (total solids) of catalyst interspersed with sorbent, there was minimal gains in hydrogen concentration. This suggests that in the presence of sufficient or optimum catalyst mass, a sorbent (CaO.MgO) loading between 45-76 wt% (27-45 wt% CaO content) was adequate for improving hydrogen yield. Literature suggests CaO content of around 30 wt% for stable CO_2 sorption performance [482–484], aligning with this work results.

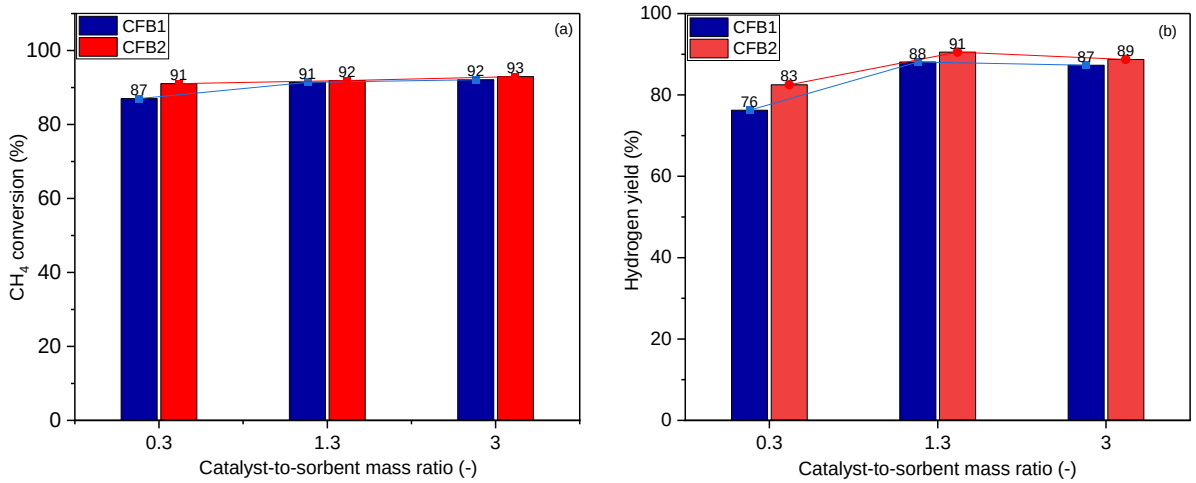

Figure 5.7: Methane conversion (a) and hydrogen yield (b) for designs 1 (Blue bar with blue trendlines) and 2 (Red bar with red trend lines) at catalyst-to-sorbent mass ratios of 0.3, 1.3 and 3.

Thus far, the impact of varying catalyst and sorbent loadings on component concentrations – CH_4, CO, CO_2 and H_2 in the product gas has been analysed. However, the primary value of SE-SR lies in its ability to produce high yield and high purity hydrogen. Adjusting parameters like C-S ratio not only affect equilibrium conditions through sorbent-mediation, but also influence hydrogen yields. Figure 5.7 builds upon the findings of Figure 5.6 by showing how the different loading schemes corresponding to various C-S ratios impacted the methane conversion and hydrogen yield. In Figure 5.7a, the lower methane conversion observed under the low catalyst loading condition aligns with literature showing reduced conversion at lower catalyst activities [485,486]. This is attributable to slower reaction kinetics with fewer active sites. Despite the poor catalyst activity, adding sorbent still improved methane conversion from ~84% (without sorbent) to 87-91%. Increasing the sorbent amount (C-S = 0.3) gave comparable improvements in methane conversion to those achieved by using relatively high catalyst loading – low sorbent loading (C-S = 3) to represent a high conversion scenario, especially for CFB2. For hydrogen yield in Figure 5.7b, low catalyst loading – high sorbent loading (C-S = 0.3) was most detrimental to hydrogen yield, with much higher yield attained with lower sorbent loading. This is

similar to the hydrogen concentration trend and indicates that while sorbent provides equilibrium benefits, sufficient catalyst activity is essential for maximising hydrogen production rate and yield.

Table 5.7: CO_2 capture and process efficiencies for the different cases

Cases	CCE (%)	PE (%)
CFB1-0.3	80.22	73.13
CFB1-1.3	98.53	87.54
CFB1-3	67.82	86.77
CFB2-0.3	85.98	80.85
CFB2-1.3	98.51	90.76
CFB2-3	69.38	88.29

The C-S ratio significantly impacts CO_2 capture efficiency (CCE) and process efficiency (PE) in both CFB1 and CFB2 reactors. Table 5.7 summarises these efficiencies for the various C-S ratios. In CFB1, reducing sorbent loading (C-S = 3) decreased CCE from 98.53% at the base ratio (C-S = 1.3) to 67.82%. Similarly, CFB2 showed a CCE reduction from 98.51% to 69.38% at C-S = 3. Conversely, reduced catalytic activity (C-S = 0.3) lowered CCE to 80.22% in CFB1 and 85.98% in CFB2, compared to their respective base ratios. For both reactor designs, the lowest CCE occurred at C-S = 3, corresponding to low sorbent loading. Process efficiency was lowest at C-S = 0.3, where catalyst activity was low. These results indicate that catalyst activity has a more pronounced effect on methane conversion efficiency, hydrogen yield, and process efficiency than on carbon capture efficiency. Within this study's parameters, low sorbent loading impacts carbon capture efficiency, with relatively less influence on methane conversion, process efficiency and hydrogen yield.

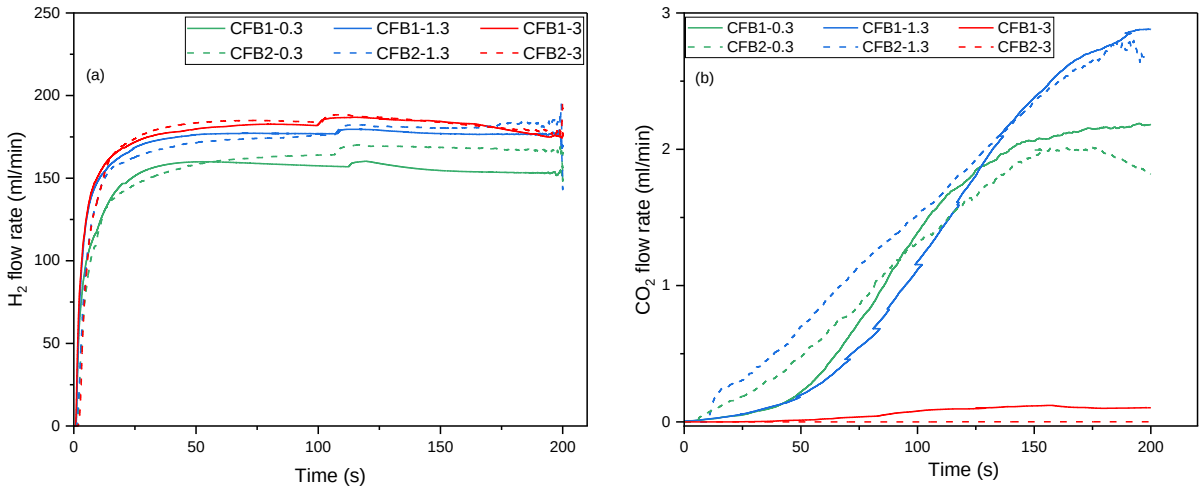

Figure 5.8: Flow rate of (a) hydrogen produced from the reformer/carbonator and (b) CO_2 released from the calciner.

The curves in Figure 5.8 illustrate the time-dependent production of hydrogen from the reformer/carbonator, and the concomitant CO_2 release from the calciner unit used to regenerate the sorbent. In Figure 5.8a, the hydrogen production rate profiles show comparable rates between the C-S ratios of 1.3 and 3 (low sorbent loading) initially. However, the C-S 3 (red curves) starts declining earlier versus C-S 1.3 (blue curves) as the cycle progressed, for both geometries. This is attributable to the insufficient sorbent in the reformer resulting in slower regeneration kinetics and leading to the eventual production decline. The corresponding CO_2 generation trends in Figure 5.8b reflect this, with C-S 3 showing delayed onset but later increase slightly in its calciner CO_2 release. This means more unused catalyst ends up in the calciner, which is inefficient. Using bifunctional catalysts with integrated sorbent could help mitigate this issue. The earlier CO_2 generation for C-S 0.3 (low catalyst/high sorbent loading) reflects the large sorbent inventory sending more material for regeneration early on. While the C-S = 1.3 (blue curves) case begins with a lower calciner CO_2 rate than 0.3, it soon surpasses it as more used sorbent accumulates for regeneration.

As this study also sought to evaluate how the CFB1 (internal outflow pipe) bed geometry design compares with CFB2 (side solids exit), simulations results compared key reactor performance metrics including thermal performance, solids distribution, and product composition between the original and modified geometries across a range of catalyst-to-sorbent (C-S) ratios. The bed volume in both geometries were kept the same for transparent comparison. Beyond simplifying bed geometry to facilitate scale-up studies, one objective of this comparison is to also understand how bed geometry design influence mixing and flow between the interconnected fluidised beds and overall system performance. Bed geometry can affect the hydrodynamics of a system, which in turn, impacts on the

heat and mass transfer and overall chemical performance [487]. From the results presented so far, it is clear that both geometries performed slightly similar except for the obvious disparity at C-S of 0.3. Perhaps, the presence of an obstruction (pipe) inside the reactor in CFB1, in addition to reduced catalyst surface area, influenced the methane flow behaviour such that it reaches more height (especially around the pipe area) into the bed before it is substantially converted.

Analyses of component distributions also show similar behaviour observed for CO_2 and CO distribution in CFB1 at C-S 1.3, as presented in Figure 5.9. Figure 5.9 shows the component distribution inside the reformers of both reactor geometries, cut in the axial direction, at C-S 1.3. For CFB2, there was a slight improvement in the reduction of CO_2, which can be attributed to increased usable sorbent surface area and reactants' better access to the sorbent, as they were not channelled away around the pipe area like CFB1.

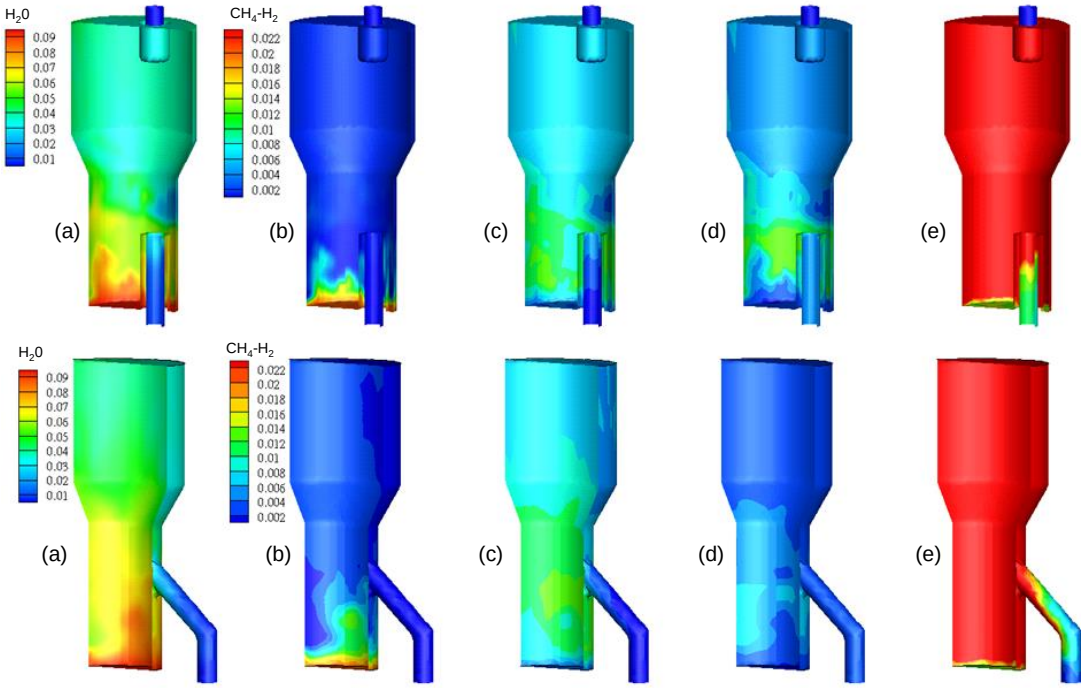

Figure 5.9: Contours of (a) H_2O, (b) CH_4, (c) CO, (d) CO_2, and (e) H_2 distributions (mol/m^3) in the reformer/carbonator of CFB1 (top) and CFB2 (bottom) bed geometries cut into half axially.

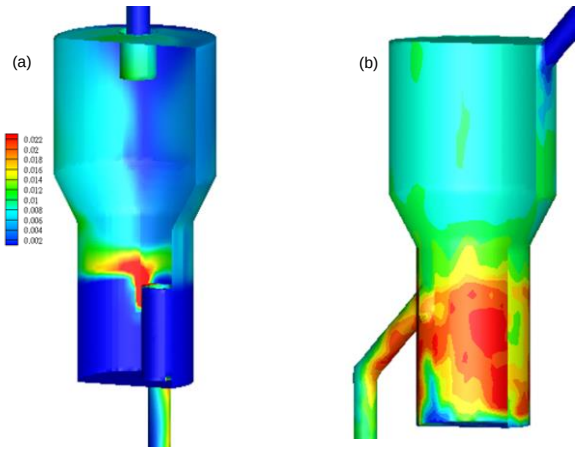

Figure 5.10: Contours of CO_2 distributions (mol/m^3) in the calciner of (a) CFB1 and (b) CFB2 bed geometries cut into half axially.

It is interesting to see how CO_2 is distributed within the calciners in Figure 5.10 for both bed geometries. CFB2 exhibited a higher CO_2 concentration centred along the reactor axis, indicating preferential gas flow through the core region. In contrast, CFB1 featured a more localised accumulation of CO_2 surrounding the top of the internal pipe perimeter. This localised distribution in CFB1 suggests the pipe

geometry imposed a degree of directiveness on the local fluidisation patterns, leading to a flow closer to the wall. Bubbles in CFB1 may have been steered toward the open radial slots between the pipe and wall surface.

5.3.4 Time evolution and spatial distribution of particle temperature

While operating with a large sorbent inventory helped improve CO_2 capture to an extent as well as increase CO_2 release in the calciner due to more spent sorbent circulation, it came at the cost of higher thermal energy requirements, especially in the calciner. Some studies use excess solid sorbent in the reformer to try to improve the system's thermal neutrality [252,253,488], but this only marginally helps the reforming process while imposing an energy penalty during sorbent regeneration, as illustrated in Figure 5.11. Furthermore, adding excess sorbent has minimal impact on improving CO_2 capture, as previously explained. The marginal gains in CO_2 release do not justify the significant energy penalty for regenerating the extra sorbent. Therefore, optimisation is required to find the sorbent circulation rate that balances adequate CO_2 capture with sustainable thermal management and energy usage, rather than increasing sorbent inventory.

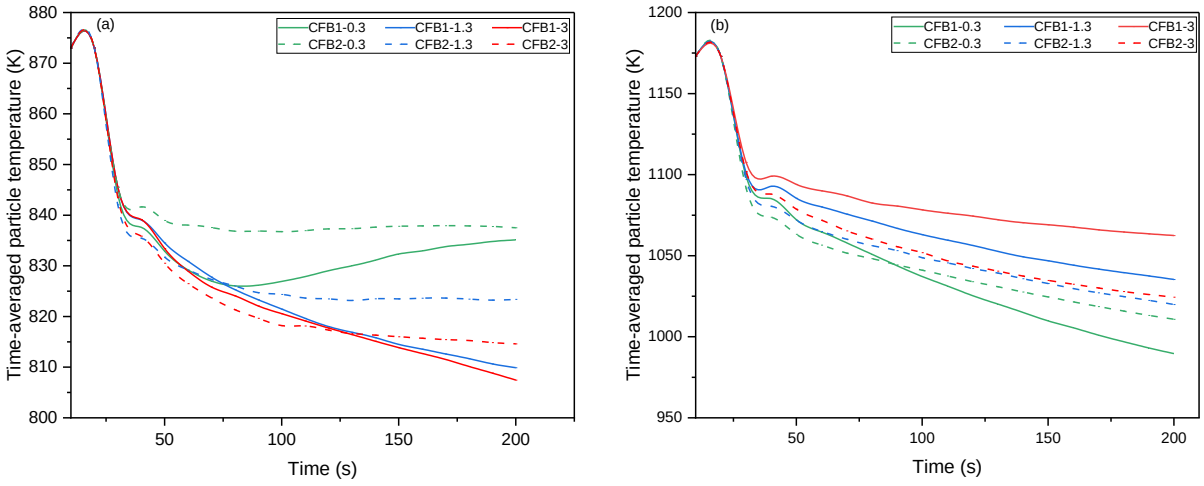

Figure 5.11: Time-averaged particle temperatures in the (a) reformer/carbonator and (b) calciner for CFB 1 and 2 at different catalyst-to-sorbent ratios.

The temperature drop trends across the reformer and calciner units shown in Figure 5.11 provide insight into how sorbent loading impacts heat transfer. In the reformer, cases with relatively large sorbent amounts (C-S = 0.3 and 1.3) demonstrated lower temperature drop with time, compared to the case having a lower sorbent loading (C-S = 3). The low temperature drop suggests that higher sorbent loadings aided in maintaining heat within the reformer/carbonator via exothermic carbonation reaction. Conversely, the temperature drop in the calciner followed the opposite pattern,

as seen in Figure 5.11b. The scenario with the highest sorbent loading (C-S = 0.3) exhibited the greatest temperature drop, followed by intermediate (C-S = 1.3) and then lowest (C-S = 3) sorbent conditions. This suggests a larger heat sink was imposed on the calciner by higher sorbent mass, making more heat to be absorbed via the solid phase. Additionally, the relatively low temperature drop observed in C-S = 3 (low sorbent loading) is also associated with the low spent sorbent being sent to the calciner. These results indicate that the bed temperature profiles in the calciner are sensitive to variations in sorbent loading. Therefore, careful thermal management, through improved heat integration to the calciner, will be necessary to maintain sufficient temperature for complete regeneration as loading increases.

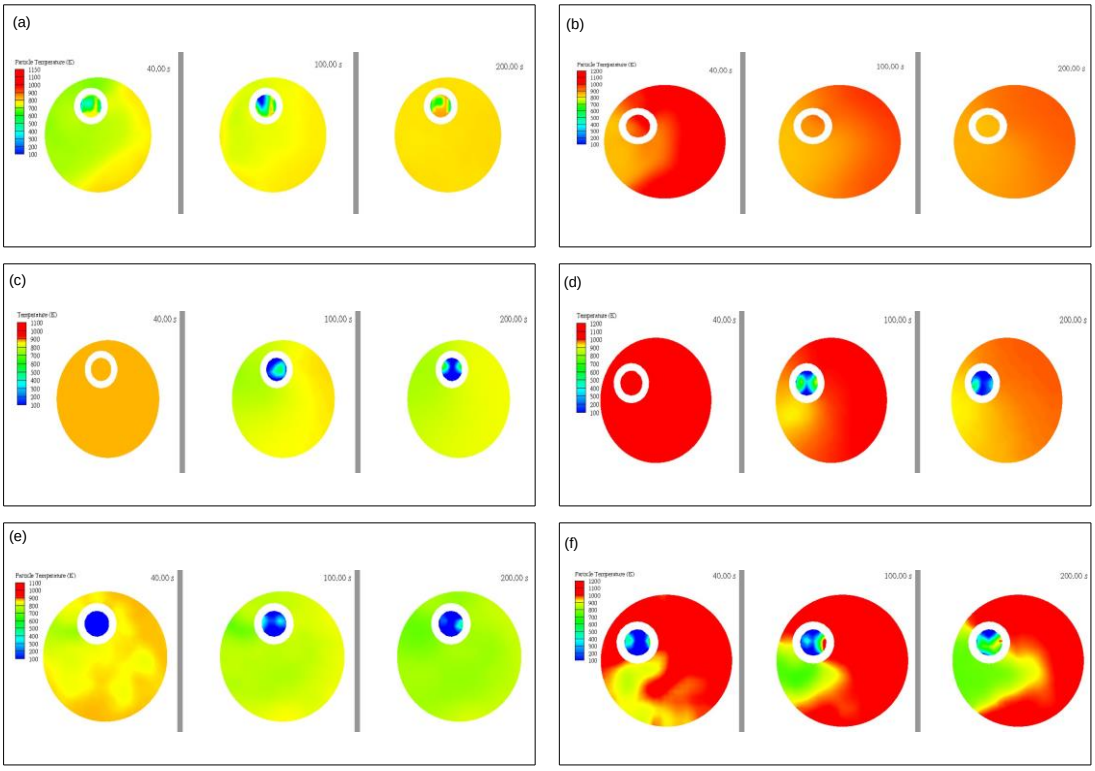

Figure 5.12: Contours of temperature distribution mid-bed CFB 1 for catalyst-to-sorbent ratios (a),(b) 0.3 (c),(d) 1.3 and (e),(f) 3 in the reformer/carbonator (a,c,e) and calciner (b,d,f).

To shed more light on the thermal behaviour of the reactor beds, it will be helpful to examine the temperature distribution profiles within the reactors. Figure 5.12 and Figure 5.13 show the contour plots of the modelled temperature distributions for CFB1 and CFB2, respectively, taken at the centre of the reformer and calciner reactor beds at different sorbent loadings and simulation times. In the reformer, the higher sorbent cases (C-S 0.3, 1.3) maintain a more uniform temperature contour with less radial variation compared to the lower sorbent case (C-S 3), particularly as the reaction and

circulation progresses. The lower sorbent case (C-S 3) takes more time to achieve uniformity especially in CFB 1. Similar observation is seen in the calciners where the higher sorbent cases (C-S 0.3, 1.3) achieve uniformity as time progresses but reducing in temperature, while C-S 3 takes more time to reach a uniform temperature distribution.

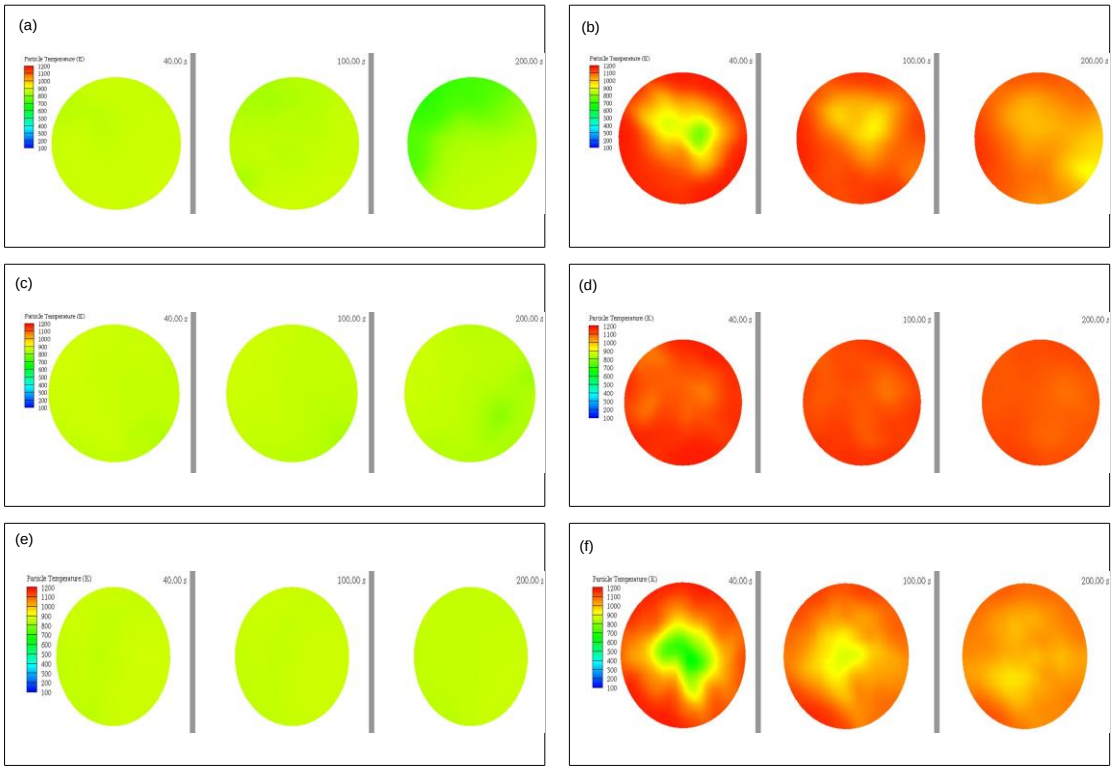

Figure 5.13: Contours of temperature distribution mid-bed CFB 2 for catalyst-to-sorbent ratios (a),(b) 0.3 (c),(d) 1.3 and (e),(f) 3 in the reformer/carbonator (a,c,e) and calciner (b,d,f).

5.3.5 Hydrodynamic behaviour within the reactors

Fluidisation hydrodynamics impact on reactor performance factors such as gas-solids contacting, mass and heat transfer, and reaction kinetics [489]. The hydrodynamic characteristics of the two bubbling fluidised bed reactors, CFB1 and CFB2, were evaluated at C-S (=1.3) and compared through analysis of pressure profiles, particle volume fraction and solids distribution. This section will discuss these hydrodynamics and examine how the geometrical configuration of each reactor influences flow characteristics.

5.3.5.1 Pressure profiles

Pressure distribution provides insights into solids holdup, mixing, and transport dynamics [490]. Figure 5.14 and Figure 5.15 display the full-loop pressure profile along the heights of the CFB systems, CFB1 and CFB2. Pressure data points (depicted as red dots in the figures) were placed at various heights along the centreline of the reformer/carbonators, calciners, top and bottom loopseals and the transport risers. Results were obtained by averaging the last 10 seconds of data from the simulation.

For both designs, there is a gradual decrease in pressure along the length of the transport riser section as solids are transported upward. The pressure drop remains relatively small across the connections feeding into the cyclone units. Within the cyclones and upper sections of the reformer/carbonator reactors, the pressure levels off at a near-constant value. However, a slight increase is observed lower down in the reactors where the solids holdup begins to build up again. A similar minor increase in pressure also occurs at the top loopseal as solids transfer to the calciner. This was followed by a constant reduction and then slight increase again at the calciner inlet and outlet, respectively. Finally, a sharp spike in pressure is noted within the base of the bottom loopseal, indicating high level of solids accumulation. The high pressure profile in the loopseal region is especially important for maintaining proper solids circulation in such a dual circulating fluidised bed system [491,492].

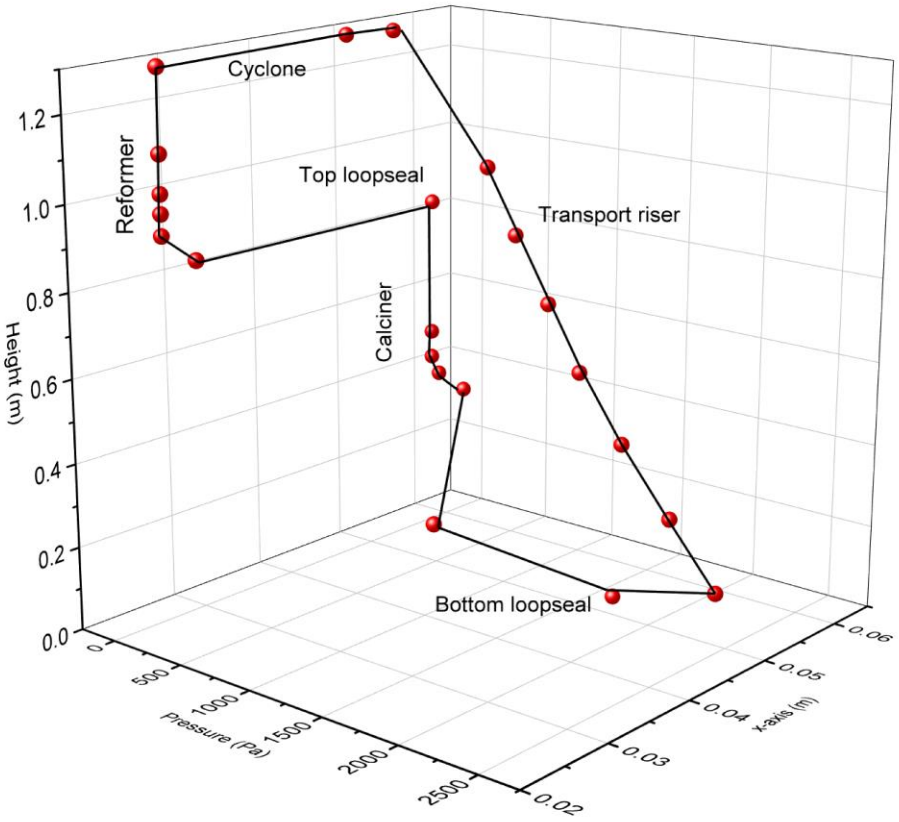

Figure 5.14: Time-averaged pressure distribution profile along the heights of the reformer/carbonator, top loopseal, calciner, bottom loopseal, transport riser and cyclone for CFB1. x-axis represents the distance between the centres of the reactors, loopseals, and the riser.

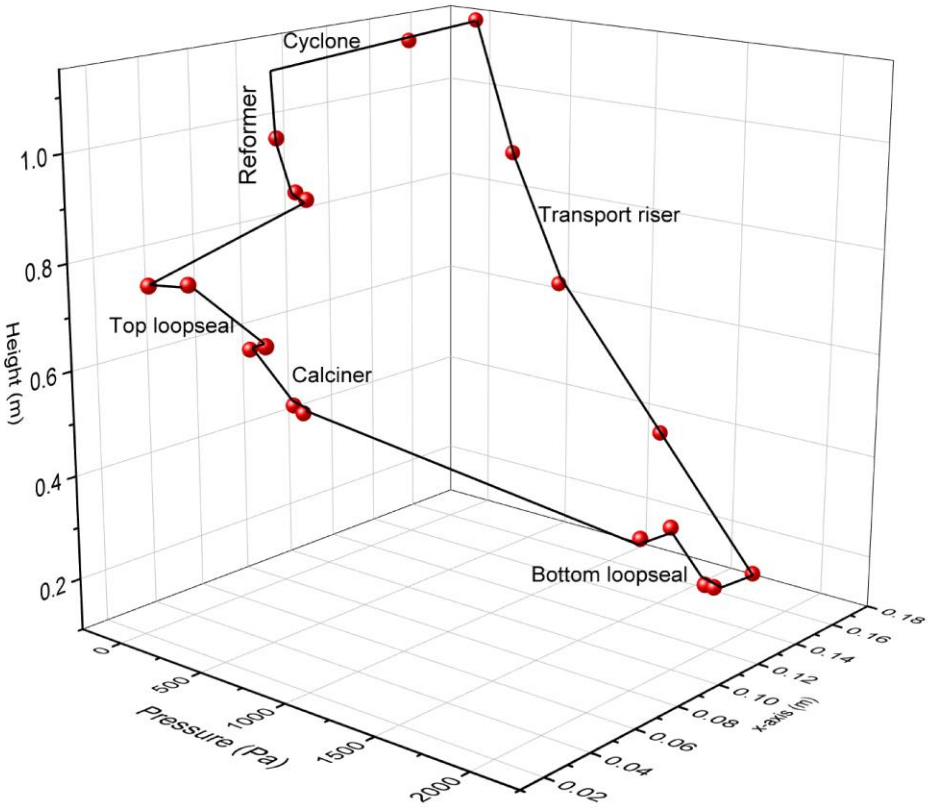

Figure 5.15: Time-averaged pressure distribution profile along the heights of the reformer/carbonator, top loopseal, calciner, bottom loopseal, transport riser and cyclone for CFB2. x-axis represents the distance between the centres of the reactors, loopseals, and the riser.

The maximum simulated pressure drops across key components of the dual fluidised bed systems (the reactors, loopseals and transport riser) are summarised in Table 5.8. These maximum values were extracted from the CPFD-generated pressure profiles at the bottom region of each reactor, loop seal, and riser where the highest pressures occurred. Generally, the pressure drops across the reformer and top loopseals connecting to the calciner tend to be lower in magnitude compared to those in the calciner reactor and associated bottom loopseals, with the highest simulated pressure in the system occurring in the bottom loopseal. This is due to large solid holdup and high resistance to solids flowrate in the opening between the supply pipe (connected to the calciner) and the recycle pipe (connected to the riser) [493]. Meanwhile, the high pressure drops occurring within the transport riser zones is consistent with the high velocities and circulation rates required to transport particles over long characteristic paths [494].

Table 5.8: Maximum pressure drops across the key components of the system for CFB1 and CFB2

Maximum pressure drop	CFB1 (Pa)	CFB2 (Pa)
Reformer/carbonator	251.52	245.89
Top loopseal	780.06	658.02
Calciner	300.67	326.56
Bottom loopseal	2175	1982.12
Transport riser	2135.60	1942.80

CFB1 exhibited a notably higher overall pressure drop compared to CFB2 under similar operating conditions. The percent difference in simulated total pressure drop between the two systems ranged from 2.20% to 15.60%. The largest deviation was observed in the top loopseal, where the total pressure drop for CFB1 was 15.60% higher than CFB2. The relatively high simulated pressure drops in CFB1 signify greater flow resistance compared to CFB2.

5.3.5.2 Particle volume fraction

Figure 5.16 displays the radially distributed, time-averaged particle volume fraction profiles extracted from the simulations at the central bed height ($1.87<H_B<2$ cm) of both reactors – CFB1 and CFB2. The profiles tend to be slightly higher near the wall than at the centre, especially for CFB2. The gradual drop and peaks near the walls for each bed indicate high concentrations of solids at the walls as bubbles travel upwards through the central region. As gas bubbles rise through the centre of the bed, they exert forces on surrounding particles and push solids nearby in the radial direction toward the wall, while propelling particles ahead in the axial flow direction [495]. However, the particle fraction distribution in the reformer shows a slightly different trend near the walls, particularly for CFB1. Since they both have the same fluidising gas, this difference in profiles between CFB1 and CFB2 reformers is likely caused by geometric factors. In CFB1, a lower particle volume fraction is observed near the wall compared to the central region, as shown in Figure 5.16, for normalised diameters under 0.3. This reversed wall effect indicates bubbles are concentrating more towards the reactor periphery rather than the core. This altered bubble flow is likely caused by the internal overflow pipe in CFB1's reformer being positioned close to the wall. The pipe obstruction may block lateral movement of bubbles, forcing them to travel upwards closer to the wall and displacing more particles inward. Nevertheless, the profiles appear fairly uniform across the radius for both systems, indicative of effective radial mixing by bed bubbles.

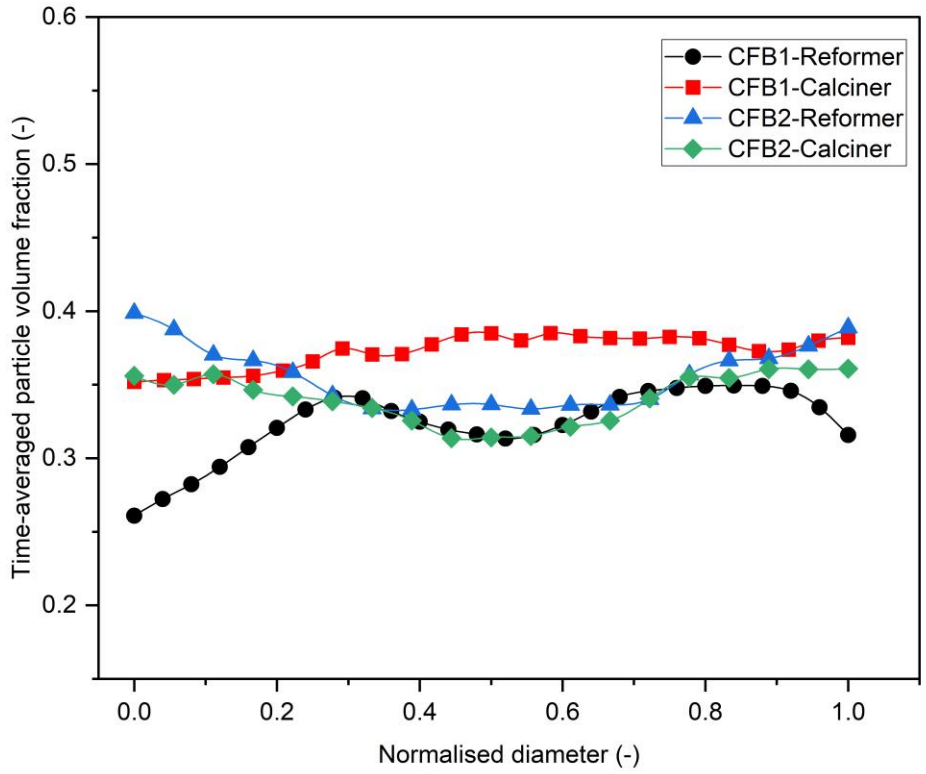

Figure 5.16: Radial distribution of time-averaged particle volume fraction at the central bed heights of the reformer and calciner for CFB1 and CFB2.

5.3.5.3 Solids distribution

The fluidised bed reactors contain a mixture of CaO sorbent, catalytic particles, and $CaCO_3$ product. Analysing the distinct concentration profiles for these solids can reveal segregation patterns and mixing behaviour. Therefore, the distribution of the solids' species are presented in Figure 5.17 and Figure 5.18, to give further perspectives on the distribution of the sorbent, catalyst, and $CaCO_3$ product particles in the full-loop system. It is important to note that the catalyst mass fraction is normalised based on its pure fraction in the total reactor inventory, and hence remains around a value of 1 throughout. Meanwhile, the CaO sorbent mass fraction is normalised by the total sorbent (CaO.MgO) concentration circulated in the system. The $CaCO_3$ product fraction depends directly on the local availability of CaO particles and is also normalised based on the total sorbent. Examining the contours after 200 seconds of simulated operation first reveals the expected result that CaO mass fraction is lower in the reformers versus calciners for both CFB1 and CFB2. However, CFB2 demonstrates notably higher $CaCO_3$ levels in the reformer and slightly in the calciner, suggesting improved sorbent utilisation.

This corresponds to the reduced concentration of CO_2 observed in the CFB2 reactor, as indicated by the composition contour in Figure 5.9. This reduced CO_2 concentration was attributed to an increase in usable sorbent surface area and the reactant's (CO_2) better access to the sorbent. Conversely, no apparent segregation of solids was observed for CFB1 and CFB2 upon further analysis of solids distribution, and solids were uniformly distributed as shown in Figure 5.17 and Figure 5.18.

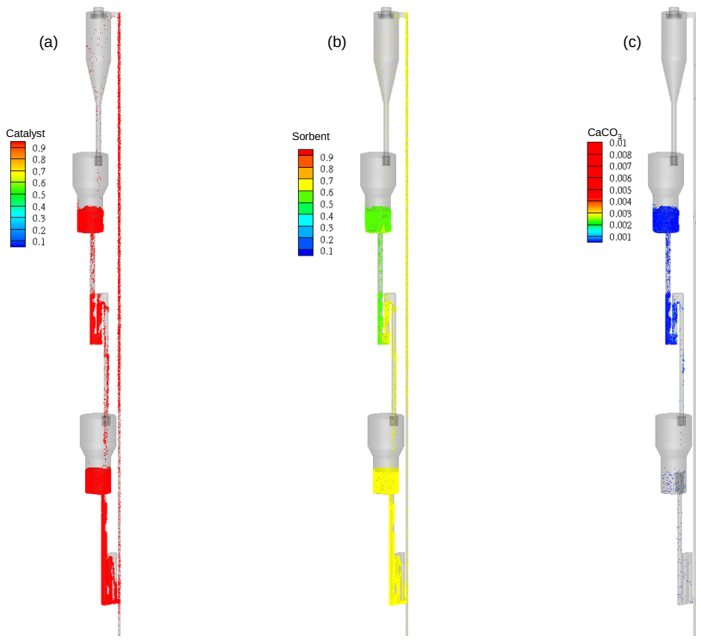

Figure 5.17: Distribution of (a) catalyst, (b) sorbent and (c) $CaCO_3$ within the full-loop system for CFB1 coloured by mass fraction.

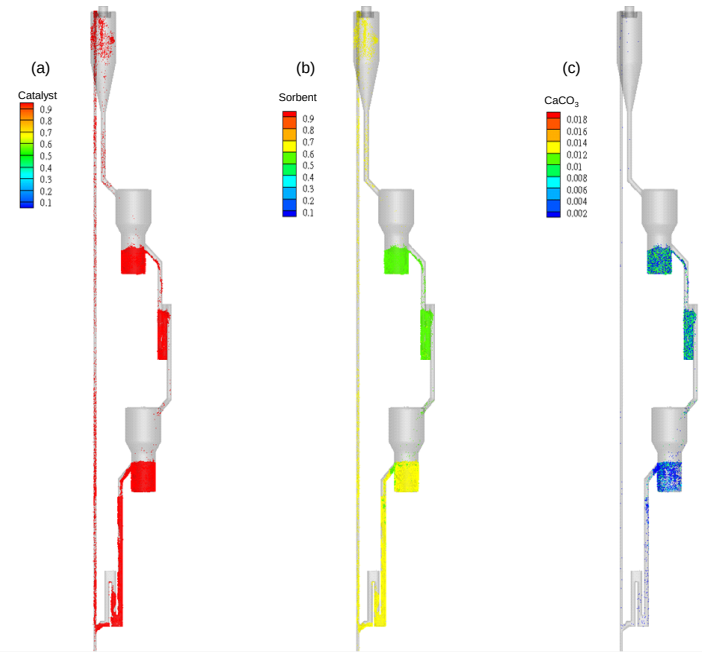

Figure 5.18: Distribution of (a) catalyst, (b) sorbent and (c) $CaCO_3$ within the full-loop system for CFB2 coloured by mass fraction.

5.4 Summary

This chapter develops a full-loop CPFD reactor model to analyse the impact of catalyst and sorbent ratios on cyclic SE-SR performance. These simulations introduce potential operational complexities by modelling reduced catalyst activity and sorbent inventory scenarios to gain insights for continuous run times. The impacts of two bed geometry designs are also examined. Results indicate that varying solids ratios influenced reaction progress, with optimal methane conversion and CO_2 capture observed at nearly equal volume ratios of catalyst and sorbent. Higher sorbent loadings enhanced thermal neutrality but risked increased calciner energy penalties. Bed geometry also influenced localised hydrodynamics. Detailed solids and gas concentration contours provided insights into transient mixing and spatial product distribution in the two designs. Furthermore, comparison of pressure profiles clarified effects on heat distribution and mass transfer driving forces.

Conversely, the performance of the modified CFB reactor design, CFB2, was comparable to the original design, CFB1, without any degradation. For the purposes of scale-up in the subsequent chapter, CFB2 offers some advantages in simplicity over CFB1 that help avoid potential complications during the geometric design process for a larger system. Its performance being slightly equivalent to CFB1, but with a more straightforward scale-up path, makes CFB2 the preferred choice to carry forward for further scale-up evaluations. The selection of CFB2 aims to facilitate scale-up studies presented in the

next chapter, while maintaining the desired reactor operation and performance demonstrated at the bench-scale.

6 Scale-up strategy for SE-SR of methane in bubbling fluidised bed reactors

6.1 Introduction

In Chapter 5, the modified CFB reactor design, CFB2, was selected over the original CFB1 for scale-up efforts, based on its comparable performance with a less complex design. The objective of the current chapter is to develop and validate a scale-up strategy to replicate the reactive process demonstrated at the small scale in CFB2 at a larger scale. Successfully scaling fluidised bed processes requires maintaining similarities in important hydrodynamics, chemical reaction, and heat transfer parameters between scales to preserve desired process performance as the system size increases. This chapter aims to establish a scale-up methodology that satisfies these scale-invariance principles, allowing the scale of operation to be increased while retaining key operational characteristics demonstrated originally in CFB2.

The key scaling criteria for fluidised beds focus on matching dimensionless groups that characterise the gas-solid hydrodynamics and reactive or heat and mass transfer [496]. These criteria aim to keep the flow patterns and mixing characteristics similar between the lab/pilot reactor and industrial scale. The dimensionless groups usually include the velocity and gas-solid density ratios, Froude (Fr), Reynolds (Re), Archimedes (Ar), Damköhler, and Nusselt (Nu) numbers. Archimedes number represents the balance between gravitational forces and viscous forces while Reynold's number indicates the flow regime, whether laminar or turbulent. Froude and Nusselt numbers characterise fluid flow under gravity and heat transfer relation between the fluid and solids, respectively [497]. In addition to matching dimensionless groups, geometric similarity is also important [498]. Key aspects that should be geometrically similar include the reactor height to diameter ratio and cross-sectional shape.

Over the years, various scaling laws for bubbling bed reactors have been developed and applied to ensure that the reactor's behaviour and performance are consistent across different scales [499–503]. Early research focused on developing dimensionless groups to characterise hydrodynamics, with seminal work by Glicksman [504] deriving scaling relationships based on the non-dimensionalisation of the governing equations of fluid dynamics and their boundary conditions. Dimensionless groups like the Froude number, Reynolds number, gas to solid density ratio, particle to bed diameter ratio, sphericity and particle size distribution were proposed and referred to as the full set scaling criteria. However, these full criteria require geometric similarity to be matched with multiple dimensionless

groups, making scaling more complex and constraining. To resolve this, a simplified set of dimensionless groups which replaced Reynolds number with the velocity ratio and eliminated particle to bed diameter ratio was proposed [505]. This set was also made to simplify scale up in cases where viscous forces dominate at low Reynolds numbers or inertial forces dominate at high Reynolds numbers. In their study on the scale-up of gas-solid conical fluidised beds, Kalo et al. [506] performed detailed experiments using the radioactive particle tracking (RPT) technique to examine the applicability of Glicksman's scaling laws. They investigated two different scaling approaches – the inertial limit set (Re_p > 1000) and the simplified set – by comparing the fluid dynamic parameters between a smaller column (0.05 m bottom diameter) and a larger column (0.1 m bottom diameter). The authors found that for the inertial limit scaling, the mean axial and radial velocities, axial root-mean-square (rms) velocities, and granular temperature matched quantitatively between the two scales. This indicated that this scaling approach was able to capture key flow physics accurately during scale-up. In contrast, the simplified scaling approach showed qualitative agreement but quantitative differences in these parameters, which the authors attributed to the change in the column diameter to particle diameter (D_c/d_p) ratio between the scales. Nevertheless, further analysis of the RPT data revealed that both scaling laws were able to predict the global behaviour of the system.

Similarly, Horio et al. [503] put forth a scaling rule for fluidised beds focused on preserving bubble behaviour when viscous forces are dominant, by satisfying similarities in bubble coalescence, and interstitial flow pattern and bubble splitting. Roy and Davidson [507] experimentally validated the scaling rules proposed by Horio et al. [503], for bubbling fluidised beds with different bed geometries and particle systems. They tested Horio's set of dimensionless numbers, at m = 0.417 and m = 0.171 using cold flow models, where ‘m’ is the magnification of length scale. The authors found that Horio's scaling rules, with m = 0.417, worked particularly well for scaling the hydrodynamic behaviour of BFBs with Geldart B particles, even at moderate particle Reynolds numbers (Rep < 33). Good agreement was observed in scaling bubble properties, such as bubble size, bubble rise velocity, and bed expansion, when using Horio's scaling rules with m = 0.417. Also, Stein et al. [502] experimentally verified dimensionless groups equivalent to that of Horio’s scaling rules by operating three geometrically similar columns. The experimental results were not affected much by the gas-to-particle density ratio, but changing the particle-to-bed diameter ratio had a small effect.

Many of these early fluidised bed scaling laws focused on hydrodynamic similarity without accounting for reaction kinetics and heat transfer influences. Ignoring these effects assumes that if hydrodynamic similarity is achieved between a large and small bed, then the reaction and heat transfer behaviour will automatically also be similar. However, some differences in intrinsic reaction kinetics or heat transfer rates at different scales may still exist that are unaccounted for. Incorporating dimensionless

groups that consider reaction effect in reactive fluidised beds can improve scaling accuracy, but also increase complexity. Therefore, Kelkar and Ng [501] developed a dimensionless two-phase model for first-order reactions, and produced two dimensionless parameters – reaction and mass transfer numbers – to explore the effects of scale-up on reactive fluidised bed reactor performance. This dimensionless parameter is similar to the Damköhler number, which is especially relevant in chemical reaction kinetics as it relates the timescale of the chemical reaction to the timescale of the transport process [508].

In addition to conventional scale-up approaches combining dimensionless numbers and pilot testing, CFD simulations have emerged as a powerful tool to guide fluidised bed scale-up and design. CFD can be used to test a range of dimensionless groups and scaling variables to determine which parameters most significantly influence performance and hydrodynamics between scales. This activity could be more time-consuming, if experiments were employed instead. Van Ommen et al. [509] computationally investigated the validity of different scaling rules for fluidised beds using CFD simulations, where two geometrically similar 2D fluidised beds were modelled using Eulerian-Eulerian approach based on the kinetic theory of granular flows. Three sets of scaling rules were tested: the simplified set (matching bed geometry, gas velocity ratio, density ratio, Froude's number, particle size distribution), the full set (additionally matching particle size ratio and Reynolds numbers), and the full set extended by adding the dimensionless pressure group. Matching geometry and one or two key dimensionless groups gave better results than satisfying the full set. But even the best case did not yield full similarity, highlighting needs for improved scale-up methodologies. Similarly, Wang et al. [510] investigated the capability of a modified scaling rule for jetting fluidised beds (JFB) using CFD simulations based on the two-fluid model. The results showed promise for guiding jetting bed scale-up design and achieving equivalent performance across scales.

Very few demonstration plants have been established for SE-SR process and there have not been extensive studies done at commercial scales [146]. Therefore, this chapter aims to advance the commercialisation of this promising SE-SR process for hydrogen production by identifying the appropriate scaling relationships, and applying the already validated CPFD model to perform the scale-up simulations. To the best of my knowledge, this study represents the first attempt to scale-up SE-SR of methane using the scaling approach described here. Carefully selecting and applying scaling rules can provide guidance and help inform scale-up decisions and enable a scale-appropriate design for large-scale SE-SR production plant.

6.2 Methodology

In this section, the computational modelling approach and scaling framework are described. Operating parameters and boundary conditions applied across scales are also covered.

6.2.1 Model development and description

Consistent with the approach described in Section 4.2 of Chapter 4, the same modelling methodology was applied here, including the hydrodynamic model, kinetic models, and numerical solution technique. To provide relevant context when deriving the scaling methodology in the subsequent section, a summary of the key governing equations is presented in Table 6.1. These equations are identical to those outlined previously in Chapter 4, upon which the current scale-up study is based.

Table 6.1: Summary of governing and constitutive equations for the hydrodynamic and kinetic models

Description	Expressions	Equations
Continuity equation (gas)	$\frac{\partial(\theta_g \rho_g)}{\partial t} + \nabla \cdot (\theta_g \rho_g \boldsymbol{u}_g) = \mathrm{S}m_g$	92
Momentum equation (gas)	$\frac{\partial(\theta_g \rho_g \boldsymbol{u}_g)}{\partial t} + \nabla \cdot (\theta_g \rho_g \boldsymbol{u}_g \boldsymbol{u}_g) = -\nabla P + \boldsymbol{F} + \theta_g \rho_g \boldsymbol{g} + \nabla \cdot (\theta_g \tau_g)$	93
Particle transport	$\frac{\partial \phi}{\partial t} + \nabla \cdot (\phi \boldsymbol{u}_p) + \nabla_{\boldsymbol{u}_p} \cdot (\phi \boldsymbol{a}_p) = 0$	94
Particle acceleration	$\boldsymbol{a}_p = D_p(\boldsymbol{u}_g - \boldsymbol{u}_p) - \frac{1}{\rho_p}\nabla P + \boldsymbol{g} - \frac{1}{\theta_p \rho_p}\nabla \tau_p$	95

6.2.2 Scaling criteria

The scaling approach adopted combines dimensionless parameters that were developed by non-dimensionalising the governing equations based on relevant physical properties and design specifications such as reactor dimensions, and production capacity. Two specific scaling methodologies – Glicksman's (Model G) and Horio et al.'s (Model H) scaling relationships – were formulated and tested, based on matching different sets of relevant dimensionless groups between the baseline and scaled reactors. This testing and validation only consider the reformer/carbonator used for SE-SR of methane and was conducted under isothermal condition.

The baseline model is the lab-scale fluidised bed reactor (CFB2) that was previously designed and characterised in Chapter 5. To streamline the present modelling scope and focus exclusively on examining hydrodynamic and reactive scaling effects, some modifications were made to the baseline geometry. Precisely, the full solids recirculation loop was excluded from the current model. This simplification removed added complexities associated with particle recirculation dynamics that could

obscure analysis of the core bubbling bed characteristics targeted for similarity evaluation. Therefore, the baseline model domain focused solely on the bubbling bed section where reforming and carbonation reactions occurs. Furthermore, the scaled model is based on a 1 $MWth_{(LHV)}$ hydrogen production capacity plant.

For the purpose of non-dimensionalising the model, the characteristic length and velocity were made dimensionless using the bed diameter, D, and the superficial gas velocity, u_o, respectively, as reference values [498]. Then, all variables are non-dimensionalised as:

$$u_g' = \frac{u_g}{u_0};\ u_p' = \frac{u_p}{u_0};\ \ x' = \frac{x}{D};\ y' = \frac{y}{D};\ t' = \frac{u_0}{D}t;\ \ \nabla' = \nabla D$$

These are applied to the governing equations summarised in Table 6.1 and rearranged in terms of non-dimensional groups as described below.

6.2.2.1 Model G

The dimensionless form of the continuity expression in Table 6.1, for the gas phase is given as [511]:

$$\frac{\rho_g}{\rho_p}\left[\frac{\partial \theta_g}{\partial t'} + \nabla' \cdot (\theta_g u_g')\right] = \frac{u_0}{\rho_p D}\left[Sm_g\right] \qquad 96$$

In the momentum equation (Equation 93), the interphase force term, **F**, is nondimensionalised as:

$$\frac{\mathrm{D}\boldsymbol{F}}{\rho_g u_o^2} = \frac{\mathrm{D}D_p}{\rho_g u_0}(u_g' - u_p') \qquad 97$$

To simplify the analysis, the stress tensor was ignored, and pressure terms were combined. Therefore, combining equations 93 and 97, the momentum balance equation for the gas phase is written in dimensionless parameters as:

$$\frac{\rho_g}{\rho_p}\left[\frac{\partial(\theta_g u_g')}{\partial t'} + \nabla' \cdot (\theta_g u_g' u_g')\right] = -\nabla'\left(\frac{P}{\rho_g u_o^2}\right) + \theta_g \frac{\rho_g}{\rho_p}\frac{\mathrm{gD}}{u_o^2} - \frac{\mathrm{D}D_p}{\rho_g u_0}(u_g' - u_p') \qquad 98$$

In the MP-PIC approach, the solid phase is represented by computational particles that have the properties: position, mass, velocity, whose distribution in phase space is defined by the particle distribution function, ϕ (x, m, u_p, t). Then, the dimensionless distribution function is defined as $\phi'(\mathrm{x}', \mathrm{m}', u_p{}', \mathrm{t}') = Du_0\phi\ (\mathrm{x}, \mathrm{m}, u_p, \mathrm{t})$.

Therefore, the dimensionless form of the transport equation (Equation 94) for the solid phase is

$$\frac{\partial \phi'}{\partial t'} + \nabla' \cdot (\phi' u_p') + \nabla' \cdot \left(\phi' \frac{\mathrm{D}D_p}{\rho_g u_0}(u_g' - u_p') - \frac{\rho_g}{\rho_p} \cdot \frac{P}{\rho_g u_o^2} + \frac{\mathrm{gD}}{u_o^2}\right) = 0 \qquad 99$$

Where the particle stress tensor is omitted to minimise complexity, and the particle acceleration, $\boldsymbol{a}_p$ is written in dimensionless form and replaced by

$$\boldsymbol{a}_p' = \frac{\mathrm{D}D_p}{\rho_g u_0}(u_g' - u_p') - \frac{\rho_g}{\rho_p}.\frac{P}{\rho_g u_o^2} + \frac{\mathrm{gD}}{u_o^2} \quad 100$$

$\frac{\mathrm{D}D_p}{\rho_g u_0}$ is the dimensionless drag function where the drag function, D_p, is dependent on the drag model being applied. D_p is a function of particle density, ρ_p, particle size, d_p and a drag coefficient that depends on Reynolds number, Re, and is expressed mathematically in non-dimensionless groups as;

$$\frac{\mathrm{D}D_p}{\rho_g u_0} = f\left[\frac{\rho_p d_p^2 u_o}{\mu D}, \frac{\rho_g d_p u_o}{\mu}\ \frac{\rho_p}{\rho_g}, \frac{d_p}{D}\right] \quad 101$$

To enhance flexibility during scaleup, the scaling relationships is streamlined by reducing the parameters required to be maintained. At low particle Reynolds numbers for bubbling beds, Glicksman [511] posited that maintaining $\frac{u_o}{u_{mf}}, \frac{\mathrm{gD}}{u_o^2}$ and ε_{mf} between scales ensures that $\frac{\mathrm{D}D_p}{\rho_g u_0}$ is also maintained. Since isothermal condition was assumed, thermal scaling was not considered as part of this study. The focus was instead on simulating flow behaviour and particle dynamics across scales without modelling additional heat/mass transfer effects.

Boundary conditions:

The reactor is modelled as a three-dimensional cylindrical volume, with the x, y cartesian coordinates defining locations on the circular base, and the z coordinate measuring the vertical dimension representing the reactor's height. The side walls are located at x=0 and x=D, where D is the diameter of the reactor. At these boundaries, no particles can enter or exit the reactor. Therefore, the normal component of the particle velocity, $u_{p_{normal}}$, must be zero.

Mathematically, this can be expressed as:

$$at\ \ x = 0, D;\ \ u_{p_{normal}} = 0 \quad 102$$

Similarly, at the bottom where z = 0, the normal solids velocity;

$$u_{p_{normal}} = 0 \quad 103$$

For the gaseous phase velocity, a no-slip condition applies at the reactor walls and at the bottom, a uniform velocity is assumed. The boundary is expressed as

$$at\ \ x = 0, D;\ \ u_g = 0 \quad 104$$

Therefore, the dimensionless boundary conditions for the gas and solid phases are

$$at \;\; x' = 0, \frac{D}{H}; \;\; u_{p_{normal}} = 0 \tag{105}$$

$$at \;\; z' = 0; \;\; u_{p_{normal}} = 0 \tag{106}$$

$$at \;\; x' = 0, \frac{D}{H}; \;\; u'_g = 0 \tag{107}$$

Therefore, combining equations 96 to 107, the set of Glicksman's dimensionless parameters can be written as:

$$\frac{\rho_g d_p u_o}{\mu}, \; \frac{\rho_p}{\rho_g}, \; \frac{D}{d_p}, \; \frac{u_o^2}{\mathrm{gD}}, \; \frac{u_o}{u_{mf}}, \; \frac{D}{H}, \varphi_p, \; bed \; geometry \; and \; particle \; size \; distribution$$

6.2.2.2 Model H

Horio et al. [503] introduced a set of scaling principles in which various structural parameters such as bed diameter (D), bed height (H), distributor orifice diameter (do), among others, are changed proportionally based on a common scaling parameter, m:

$$m = \frac{(D)_s}{(D)_b} = \frac{(H)_s}{(H)_b} = \frac{(do)_s}{(do)_b} \tag{108}$$

The superscripts, s and b, represent scaled and bench-scale models, respectively.

Bubbling fluidised bed hydrodynamics is largely influenced by bubble characteristics. Achieving proportional geometric similarity in fluidisation conditions between two different bed scales results in proportional geometric similarity of their bubbling behaviours. To realise geometric similarity of fluidisation between beds of differing scales, this scaling law stipulates that both the fluidising gas velocity and minimum fluidisation velocity must be adjusted as

$$\frac{(u_o - u_{mf})_s}{\sqrt{gD_s}} = \frac{(u_o - u_{mf})_b}{\sqrt{gD_b}} \tag{109}$$

$$\frac{(u_{mf})_s}{\sqrt{gD_s}} = \frac{(u_{mf})_b}{\sqrt{gD_b}} \tag{110}$$

D, the bed diameter, is adopted as the characteristic length, as the model excludes the explicit influence of both bed surface height and particle size.

Rearranging equations 109 and 110 results in the final expressions, which are in direct proportion to the square root of the scale ratio, m:

$$(u_o - u_{mf})_s = \sqrt{m}(u_o - u_{mf})_b \quad (111)$$

$$(u_{mf})_s = \sqrt{m}(u_{mf})_b \quad (112)$$

Equations 111 and 112 describes the criteria for similar bubble coalescence and for uniform flow field surrounding a bubble and bubble splitting, respectively. Furthermore, Horio's model was expanded to incorporate chemical similarity criteria, related to reaction kinetics and mass transfer, in order to ensure similar chemical conversion rates across the different scales. This is achieved by introducing a dimensionless parameter to represent the relative rate of the chemical reaction in comparison to fluid flow [503]. This parameter, N_r, is defined as the ratio of the characteristic chemical reaction time scale to the gas residence time scale, and is expressed mathematically as

$$N_r \equiv \frac{k_r H_b}{u_o} \quad (113)$$

Assuming the same pressure, temperature and rate constant between the bench-scale (b) and scaled (s) models, and according to the scaling rule, N_r then scales as

$$N_{r_s} = \sqrt{m} N_{r_b} \quad (114)$$

H_b is the initial bed height, while k_r is the reaction rate constant and is based on a first-order reaction. However, for steam methane reforming reaction, the rate expression is more complex than first-order kinetics since it also depends on the mass of catalyst present. Therefore, k_r is calculated using the SMR rate constant (k_{SMR}) and assuming constant gas residence time across scales. The Damköhler number, Da, which represents the ratio of chemical reaction to fluid transport rates, is then used to determine the required catalyst loading in the scaled-up reactor, based on maintaining similarity between space time and reaction kinetics demonstrated at the original scale. This is defined by

$$Da = \frac{P^{0.404} k_{SMR} V_{cat} \rho_{cat}}{F_{CH_4 - in}} \quad (115)$$

Where pressure and rate constant are the same between scales, as previously mentioned, F_{CH_4-in} is the methane flowrate (mol/s) into the reactor and $k_{SMR} = 2.634 \times 10^2 exp\frac{12854.2}{\mathrm{T}}, \quad \left[\frac{kmol}{(\mathrm{kg_{cat}}\ atm^{0.404}\ s)}\right]$.

Therefore, Horio's dimensionless parameters is summarised as:

$$\frac{D_s}{D_b}, \quad \frac{H_s}{H_b}, \frac{u_o - u_{mf}}{\sqrt{gD}}, \frac{u_{mf}}{\sqrt{gD}}, N_r, bed\ geometry$$

6.2.3 Reactor description

A single reactor unit (reformer/carbonator) was used to model SE-SR of methane at different scales - a bench-scale unit and a scaled-up unit. Maintaining geometric similarity between the reactors was important to enable direct scaling of results. Therefore, the bench-scale geometry shown in Figure 6.1 was replicated for the scaled Model G and Model H.

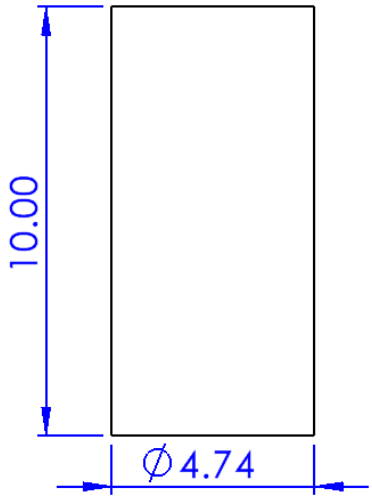

Figure 6.1: Geometry and dimension (cm) of the reformer/carbonator unit for the bench-scale model.

6.2.4 Bed dimensions and operating conditions

In this section, the operating conditions and physical parameters for Model G and Model H are described. The operating parameters, shown in Table 6.2, for the largescale reactors were calculated in order to fulfil Glicksman's and Horio et al.'s scaling criteria for similarity. To scale the bench-scale (5 – 10 kWth) to a production capacity of 1 MWth using Model H, the bench-scale is required to scale by a factor of approximately $m = 33.5$. The sorbent mass for the new scale was determined from a catalyst-to-sorbent mass ratio of 1.3, similar to the bench-scale, while the steam-to-carbon ratio was maintained at 4 for both scales.

Table 6.2: Operating conditions and bed dimensions for the bench-scale and scaled Model G and H

Description	u_{mf} $\left(\frac{m}{s}\right)$	$d_{p(avg)}$ (m)	$(\mu)_{avg}$ (kg. $m^{-1}s^{-1}$)	$(\rho_p)_{vg}$ (kg/m^3)	u_o $\left(\frac{m}{s}\right)$	H_i (m)	D (m)	$(\rho_g)_{avg}$ (kg/m^3)	m_{sorb} (kg)	m_{cat} (g)
Case A (Reduced velocity)										
Bench-scale	0.008	1.45×10^{-4}	3.65×10^{-5}	1864.80	0.05	0.037	0.047	0.38	0.027	0.034
1MWth (Model G)	0.050	5×10^{-4}	3.11×10^{-5}	1864.80	0.32	1.41	1.79	0.25	1472.01	1844.44
1MWth (Model H)	0.046	5×10^{-4}	3.11×10^{-5}	1864.80	0.29	1.26	1.59	0.25	1029.62	1290.12
Case B (Baseline velocity)										
Bench-scale	0.008	1.45×10^{-4}	3.65×10^{-5}	1864.80	0.06	0.037	0.047	0.38	0.027	0.034
1MWth (Model G)	0.050	5×10^{-4}	3.11×10^{-5}	1864.80	0.36	1.41	1.79	0.25	1472.01	1844.44
1MWth (Model H)	0.046	5×10^{-4}	3.11×10^{-5}	1864.80	0.34	1.26	1.59	0.25	1029.62	1290.12
Case C (High velocity)										
Bench-scale	0.008	1.45×10^{-4}	3.65×10^{-5}	1864.80	0.075	0.037	0.047	0.38	0.027	0.034
1MWth (Model G)	0.050	5×10^{-4}	3.11×10^{-5}	1864.80	0.46	1.41	1.79	0.25	1472.01	1844.44
1MWth (Model H)	0.046	5×10^{-4}	3.11×10^{-5}	1864.80	0.43	1.26	1.59	0.25	1029.62	1290.12
Case D (Constant particle size)										
Bench-scale	0.008	2.00×10^{-4}	3.65×10^{-5}	1864.80	0.06	0.037	0.047	0.38	0.027	0.034
1MWth (Model G)	0.0094	2.00×10^{-4}	3.11×10^{-5}	1864.80	0.36	1.41	1.79	0.25	1472.01	1844.44
1MWth (Model H)	0.0094	2.00×10^{-4}	3.11×10^{-5}	1864.80	0.34	1.26	1.59	0.25	1029.62	1290.12

The inlet gas composition for the bench-scale model was designed to mimic conditions reported in literature and described in Chapter 4, including the use of nitrogen to facilitate fluidisation. However, when scaling the SE-SR of methane process to an industrially relevant scale, the addition of nitrogen may not be necessary. While nitrogen improved fluidisation handling at the small experimental scale, its inclusion would unnecessarily increase costs and complexity at larger scale. Therefore, small differences exist between the gas viscosity and density values reported for the bench and scaled systems in Table 6.2. Nonetheless, similarity was maintained where possible - the particle density, an important solid property, was kept proportionally constant between scales. The particle size, d_p, for the scaled model was adjusted to match the minimum fluidisation velocity, u_{mf}, resulting in an initial size of approximately 0.46 mm and 0.45 mm for Models G and H, respectively. This was rounded-off to 0.5 mm for both scaled models to maintain consistency in Cases A, B and C; whereas an average particle size of 0.2 mm, similar to the bench scale model was maintained in Case D. The particle sizes used for the scaled-model are still within the same Geldart B particle group as that used for the bench-scale [512]. The Geldart B particle type has been described as exhibiting bubbly fluidisation behaviour and consists of particle diameter and density in the range of 40 µm – 500 µm and 1.4 g/cm^3 – 4 g/cm^3, respectively. Pressure and temperature were kept constant throughout at 1 atm and 873 K, respectively. While literal replication of all experimental parameters is infeasible when scaling up, the design prioritised retaining geometrically similar transport and reaction behaviours through proportional matching of influential physicochemical properties. To quantify the degree of similarity achieved between the scales, the dimensionless parameters for the bench-scale, Model G and Model H are presented in Table 6.3.

Table 6.3: Values of dimensionless parameters for the bench-scale, Model G and Model H units

	$\frac{u_o-u_{mf}}{\sqrt{gD}}$	$\frac{u_{mf}}{\sqrt{gD}}$	N_r	$\frac{\rho_g d_p u_o}{\mu}$	$\frac{\rho_p}{\rho_g}$	$\frac{d_p}{D}$	$\frac{u_o^2}{gD}$	$\frac{u_o}{u_{mf}}$	$\left(\frac{D}{H}\right)_{bed}$
Case A									
Bench-scale	0.062	0.012	7.95×10^{-5}	0.10	4936.72	4.23×10^{-3}	0.0054	6.23	1.26
1MWth (Model G)	-	-	-	1.08	7579.03	2.8×10^{-4}	0.0054	6.23	1.26
1MWth (Model H)	0.062	0.012	4.60×10^{-4}	1.02	7579.03	3.15×10^{-4}	-	-	1.26
Case B									
Bench-scale	0.075	0.012	6.74×10^{-5}	0.12	4936.72	4.23×10^{-3}	0.0075	7.36	1.26
1MWth (Model G)	-	-	-	1.30	7579.03	2.8×10^{-4}	0.0075	7.36	1.26
1MWth (Model H)	0.075	0.012	3.9×10^{-4}	1.23	7579.03	3.15×10^{-4}	-	-	1.26
Case C									
Bench-scale	0.098	0.012	5.30×10^{-5}	0.16	4936.72	4.23×10^{-3}	0.012	9.35	1.26
1MWth (Model G)	-	-	-	1.63	7579.03	2.8×10^{-4}	0.012	9.35	1.26
1MWth (Model H)	0.098	0.012	3.07×10^{-4}	1.53	7579.03	3.15×10^{-4}	-	-	1.26
Case D									
1MWth (Model G)	-	-	-	0.73	7579.03	1.12×10^{-4}	0.0075	38.52	1.26
1MWth (Model H)	0.084	0.0024	3.9×10^{-4}	0.55	7579.03	1.26×10^{-4}	-	-	1.26

6.3 Results and discussion

In this section, the effectiveness of Glicksman and Horio's models are assessed by comparing bubble sizes, voidage, methane conversion, and hydrogen purity results with that of the bench-scale unit. Bubble size and voidage were analysed to compare hydrodynamic similarities while methane conversion and hydrogen purity were analysed between scale to compare chemical similarities.

6.3.1 Bubble size and bubble size distribution

When gas is introduced into a bubbling fluidised bed reactor at a rate exceeding minimum fluidisation velocity, pockets of gas form within the bed of particulate solids and rise in the form of discreet bubbles that grow in size through coalescence, as they travel upward through the bed [513]. This bubbling action drives heat and mass transfer, overall hydrodynamics, and voidage profiles.

For the bubble analysis, computational cells having particle void fraction of 0.2-0.35 were classified as bubbles. Some studies have commonly used particle void fraction thresholds to identify bubble boundaries during bubble characterisation [514–516]. The void fraction range used in this work was found to be adequate in capturing the bubble outline. A Python script was then used to process the simulation results and extract key bubble attributes. Bubble size was estimated by approximating each bubble as a sphere, allowing for the calculation of an equivalent diameter based on the cell volume. This automated approach leveraged the existing reactor simulation data to characterise bubble formation and hydrodynamics across various scales.

Figure 6.2 shows the distribution of bubbles along the normalised expanded bed heights (up to the surface where bubbles burst), for each of the simulated scales. The bubble size, d_b, was normalised with bed diameter, D, to provide a fair basis for comparison, since bubbles tend to grow with reactor size. The non-dimensionalised distribution in the figure shows high concentrations of small bubbles at the bottom of the bed, which then grows in size along the reactor bed height. The bench-scale unit shows relatively large d_b/D along the bed height, reaching 0.46 compared to Model G and Model H. Contrarily, the largest d_b/D observed for Model G and Model H were 0.245 and 0.257, respectively. However, the mean d_b/D calculated for bench-scale, Model G, and Model H were 0.07, 0.073, and 0.078, respectively, indicating a deviation of ~4.20% and 12.40% from bench-scale, for Model G and Model H, respectively. A small concentration of large bubbles (d_b/D=0.36 – 0.47) is also found at the bottom of the bench-scale reactor. This is probably due to the absence of distributor and assumption of uniform velocity at the reactor inlet, but also wall effects. Wall effects pose a challenge for fluidised

bed scale-up since process parameters can be highly sensitive to even small percentage changes in bed diameter [517].

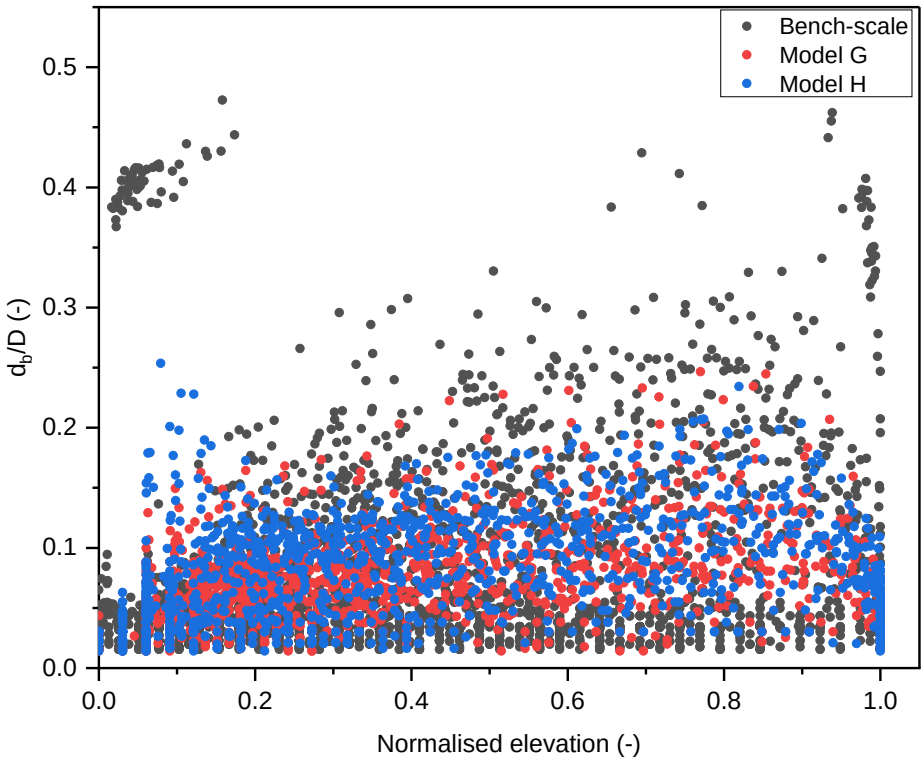

Figure 6.2: Distribution of dimensionless bubble size at normalised bed height for bench-scale (Grey dots) and scaled 1 MWth hydrogen production capacity based on Glicksman's (Red dots) and Horio's (Blue dots) models.

Although the mean bubble size $(d_b/D)_{mean}$ was scaled to almost a similar value for Model G and Model H, maintaining consistent bubble size distributions during scale-up of this bubbling bed bench-scale unit can be difficult, as observed from Figure 6.2. This is due to the influences of bed size, as highlighted previously, and also distributor design, which was not considered in this study. As the bed diameter expands, the relative influence of wall effects on bubble dynamics becomes more pronounced, potentially disrupting the bubble growth and coalescence patterns observed in the bench-scale unit. Thus, a meticulous design of gas distributors and reactor bed aspect ratios may be necessary to mitigate scale-up distortions and achieve similitude in bubble size characteristics between the bench-scale unit and the 1 MWth reactor.

Since the rate at which parameters change with respect to bed size eventually levels out to a near-constant value as diameter increases, Knowlton et al. [517] suggests collecting process data over this range of diameters to improve the prediction of these parameters when scaled up. Nonetheless, the dimensions used in this study were adjusted to maintain similitudes across all the dimensionless parameters considered.

6.3.2 Time-averaged lateral voidage (changing velocities)

Bubble dynamics influence voidage fluctuations measured locally within a fluidised bed. As such, comparing voidage profiles between different scales can improve understanding of hydrodynamic similarity between scales. Also, analysing voidage distribution throughout a bed cross-section helps identify flow regimes in fluidised bed systems [518]. This means that despite only capturing localised fluidisation properties, analysing voidage signal similarity still functions as a useful index for validating hydrodynamic scaling methodologies [509]. Therefore, time-averaged voidage results in the horizontal direction (lateral position), obtained from the simulations, were used to analyse hydrodynamic similarity between the bench-scale reactor and scaled Model G and Model H reactors. The voidage results over the final ten seconds of simulation time were averaged, with data points taken from wall-to-wall positions and at the centreline of each reactor. The three different bed heights (at the lower, middle and top regions) where the lateral time-averaged voidage were taken, were normalised with the initial bed heights of each reactor. Figure 6.3 to Figure 6.5 display the time-averaged voidage at different velocities. The voidage values plotted were averaged over the final 10 seconds of each simulation, once quasi-steady-state hydrodynamic conditions had been achieved.

The voidage profiles in Figure 6.3 for the bench-scale, Model G and Model H show two distinct zones within the bed: an outer annular region near the walls that displays a sharp gradient in the voidage profile, and a central core region that maintains a more uniform solid distribution. These two regions have been widely observed in the radial voidage profiles of the different fluidisation regimes, especially in CFBs [519,520]. This phenomenon arises due to the interaction between the gas flow and particle dynamics. As gas bubbles rise through the centre of the bed, sometimes carrying particles with them, they leave a more dilute core while pushing particles towards the walls. This behaviour creates a denser annular zone with lower voidage near the walls, disrupts the uniform packing of particles and lead to a higher voidage core region. At the bottom region of the bed ($h/H_b = 0.25$), a large disparity is noticed in the voidage distribution between the bench-scale and scaled models. The small scale exhibits a relative rise in voidage at its core region, suggesting large zones of more dilute solids and high particle movement. In this bottom region, the bench-scale is also observed to have the lowest cross-sectionally averaged voidage of 0.6 compared to 0.559 and 0.556 calculated for Model G and

Model H, respectively. Near the bed surface of the bench-scale model, at h/H_b=0.75, relatively higher voidage values (0.61) were observed compared to other heights (h/H_b). This indicates the possible presence of larger gas bubbles or more frequent bubble rupturing/coalescence events occurring closer to the freeboard region for the bench-scale unit, relative to the other scales. However, throughout the height of the reactor scales in Figure 6.3, hydrodynamic flow remained within the dense phase continuous bubbling regime, with no visible cluster regions usually seen in fast fluidised beds [521]. The parity plot in Figure 6.3d comparing some voidage values across the bed between the scaled-up models and bench-scale model, shows that the vast majority of data points fall within 10% confidence bounds. Some outliers exist, consisting predominantly of points from Model G that deviate below the defined limits. This close agreement suggests that a suitable level of consistency and dynamic similarity was achieved in scaling up the SE-SR process in bubbling bed reactor.

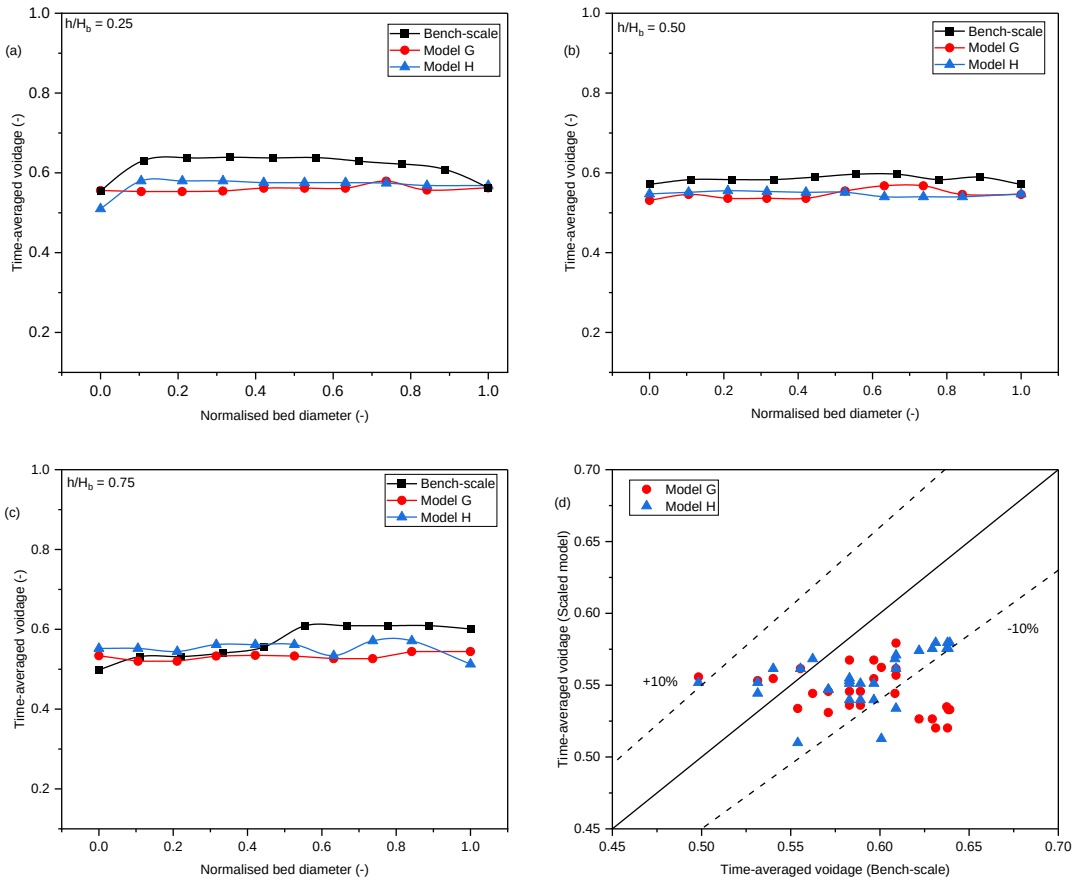

Figure 6.3: (a-c) Distribution of lateral time-averaged voidage at different dimensionless bed heights for Case A and (d) parity plots comparing the various lateral voidage of the scaled models with the bench-scale model.

Figure 6.4 presents the time-averaged voidage distribution profiles taken at the original gas velocity (0.06 m/s) used in scaling the bench-scale model. As with the reduced velocity results shown in Figure 6.3, an annular region of low voidage surrounding a higher voidage core region (dense annulus, lean core) is observed for both scaled models, especially Model H. However, towards the bottom (h/H_b=0.25) and mid-bed region (h/H_b=0.5), the bench-scale and Model G profile exhibit a diverging trend of increasing voidage near the side-walls, not seen in the Model H. This localised deviation may suggest enhanced bubble coalescence in the bench-scale model and Model G or altered hydrodynamics near the bed wall. The cross-sectional average voidage calculated for the bench-scale, Model G, and Model H were 0.61, 0.56, and 0.55, at h/H_b=0.25, while at h/H_b=0.5, average voidage values obtained were 0.58, 0.54 and 0.52, respectively. At h/H_b=0.75, the bench-scale, Model G and Model H reduced further to 0.56, 0.53 and 0.51, respectively. Across all models, the cross-sectional average voidage values decreased along the bed height, from h/H_b = 0.25 to 0.75. This progressive decline in voidage along the height of the bench-scale and scaled models (Models G and H) demonstrates that the mean gas holdup within the fluidised beds became gradually more reduced, moving from lower to upper section of the bed.

It is difficult to correlate these findings well with expected hydrodynamic behaviour, as less research has examined the cross-sectional average voidage behaviour along the bed height and within bubbling fluidised bed regimes of the type tested here for binary particles. However, in a more recent study, Yu et al. [522] investigated the voidage distribution in a 10 cm diameter bubbling fluidised bed, using glass beads with a particle size and a density of 246 µm and 2500 kg/m^3. They found that the void fraction distribution within the bubbling fluidised bed exhibited distinct trends based on the measuring probe's radial position and gas velocity. Closer to the wall (1-2 cm) and in the central region (5 cm), the average voidage lacked a clear vertical pattern, likely due to frictional effects near the wall and increased bubble collisions in the centre. At intermediate radial locations (3-4 cm), the average voidage increased with bed height, attributed to bubble coalescence. Furthermore, higher gas velocities corresponded to elevated average voidage values and more discrete voidage distributions along the bed height.

Figure 6.4d presents a parity plot comparing the lateral voidage for Model G and H with the bench-scale model. Although few data points deviate beyond the 10% confidence band, the majority of the points lie within the 10% band, exhibiting closer agreement with the bench-scale model.

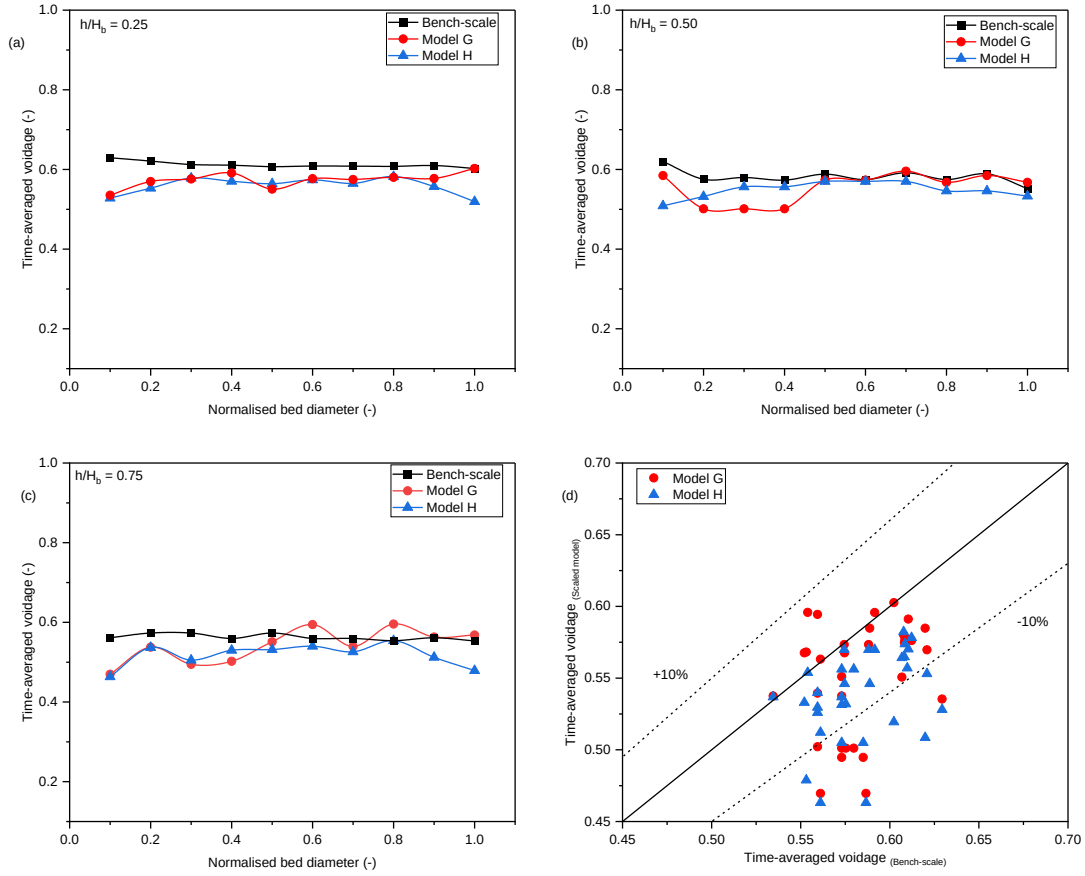

Figure 6.4: (a-c) Distribution of lateral time-averaged voidage at different dimensionless bed heights for Case B and (d) parity plots of the various lateral voidage.

Increasing the gas velocity at the original bench-scale by 25%, and proportionally scaling the velocity in the larger reactors, resulted in asymmetrical lateral voidage profiles developing. At these flow rates, the characteristic two-zone structure within the beds — an outer annular region and central core section — became imbalanced. The voidage profiles observed in the bench-scale model exhibited higher values near the wall region. This suggests non-uniform gas distribution may have been occurring, with a possibility of gas channelling preferentially along the wall boundaries. Such channelling could have displaced solid particles away from walls towards the centre, thereby creating locally high void spaces. Cross-sectional average voidage values were computed at the various bed heights (h/H_b), for the bench-scale and scaled-up models. Near the bottom of the bed (h/H_b=0.25), voidage of 0.63, 0.57, and 0.56 were observed for the bench-scale, Model G, and Model H, respectively. At the mid-height (h/H_b=0.5), these values decreased slightly to 0.61, 0.55, and 0.54, respectively. Closer to the bed surface (h/H_b=0.75), further reductions were seen to 0.6, 0.53, and 0.53, respectively.

The parity plot reveals that as velocity was increased, some data points diverge increasingly from the centreline and fall beyond the 10% confidence bounds, suggesting a loss of similarity. This implies factors such as voidage and bubble dynamics could behave in progressively more complex, nonlinear ways under stronger fluidisation, hindering hydrodynamic similarity.

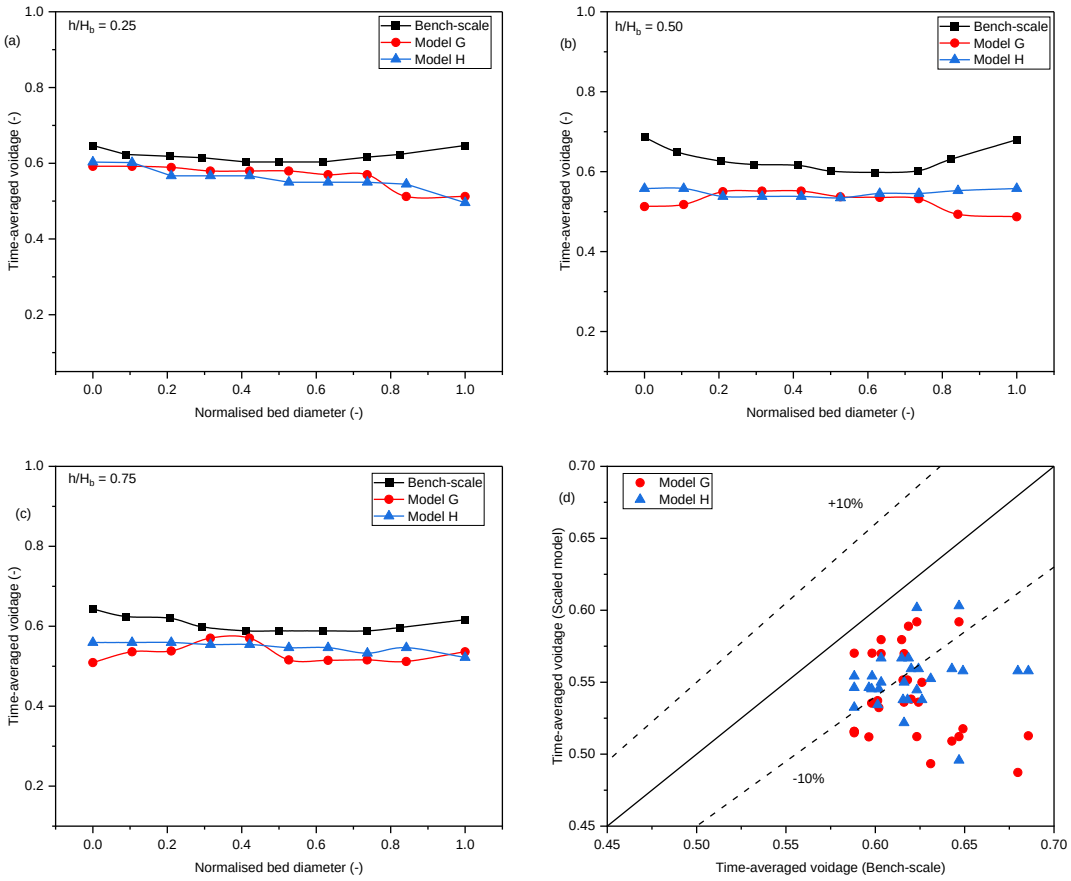

Figure 6.5: (a-c) Distribution of lateral time-averaged voidage at different dimensionless bed heights for Case C and (d) parity plots of the various lateral voidage.

The examination of lateral time-averaged voidage, under different velocities, revealed findings regarding the consistency of the scaled models with the bench-scale model. When fluid velocity was increased, there was a slight rise in the cross-sectional average voidage across the different scale models. However, a decrease in the average cross-sectional voidage was observed as one moved along the bed height, for the various velocities studied. This may be the result of solid recirculation or re-entry of solids into the bed at various heights, leading to localised increases in particle concentration and decreased voidage at those bed heights [523]. Furthermore, the analysis of parity plots indicated a departure from hydrodynamic similarity with increasing velocity, suggesting that higher fluid velocities may introduce scale-dependent behaviours in the system.

6.3.3 Methane conversion and hydrogen purity (changing velocities)

Further, comparing conversion and product concentration profiles across reactor units of varying size provides insight into the degree of consistency achieved in reaction during the scale-up process [501]. Thus, methane conversion and H_2 purity profiles, simulated under the different scaling criteria, were compared with the bench-scale model to check for chemical similarity between scales.

Figure 6.6, Figure 6.7, and Figure 6.8 show the lateral methane conversion profiles at different bed heights (h/H_b) within the bench-scale reactor and scaled models. Across all scales, a trend is observed where methane conversion increases from the bottom to the upper region, consistent with reaction progression through the bed. For Case A presented in Figure 6.6, the cross-sectional average methane conversion at h/H_b=0.25 for the bench-scale, Model G, and Model H is 88%, 86%, and 85%, respectively, which increased by 16%, 10%, and 10.5% at h/H_b=0.75. In Figure 6.7 (Case B), the lateral cross-sectional conversion is 83%, 82%, and 82%, for the bench-scale, Model G, and Model H, and is seen to increase along the bed height from h/H_b=0.25 to h/H_b=0.75 by 11.5%, 13.1%, and 13.3%, respectively. As the velocity increases in Case C, there was a corresponding drop in methane conversion as a result of low gas residence time. Methane conversion reduces across all the scales while increasing along the bed height (from h/H_b=0.25 to h/H_b=0.75) by 13.8%, 10.3, and 14% for the bench-scale, Model G, and Model H, from conversion points of 78.2%, 83.5%, and 79.3% at h/H_b=0.25, respectively.

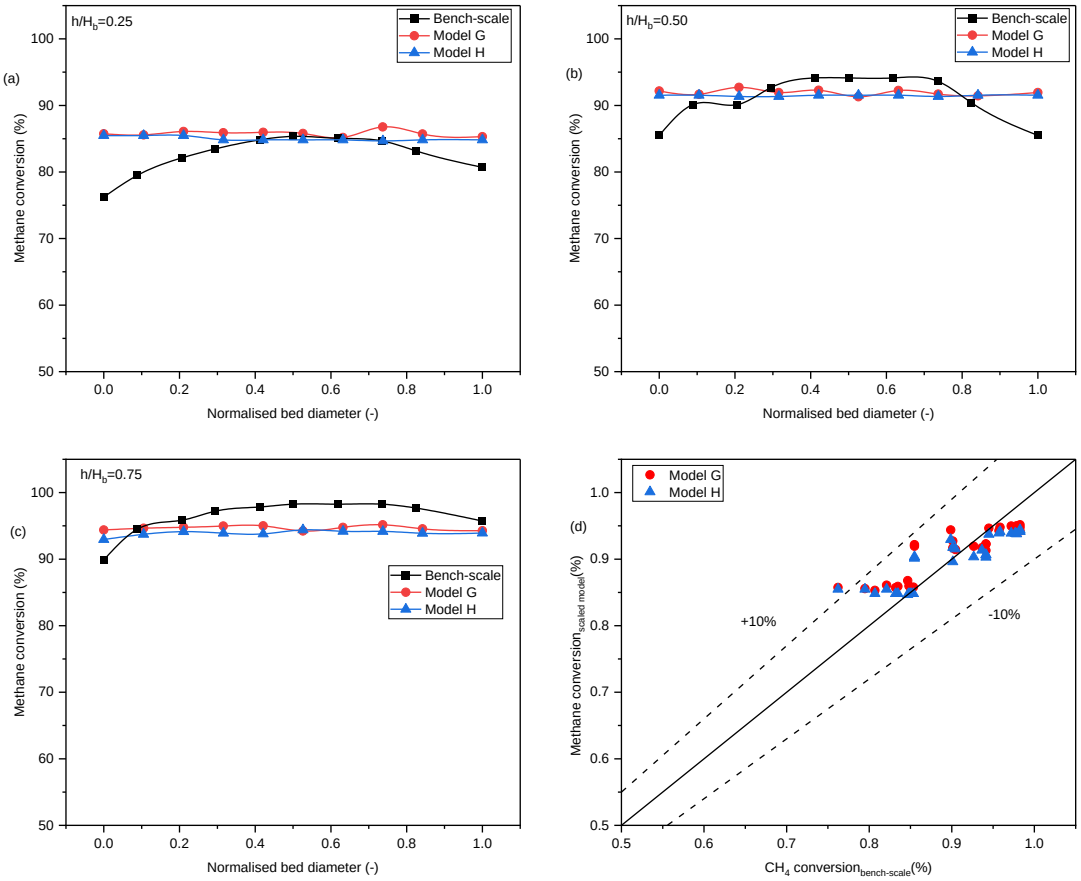

Figure 6.6: (a-c) Distribution of lateral time-averaged methane conversion at different dimensionless bed heights for Case A and (d) parity plots of the various lateral methane conversion.

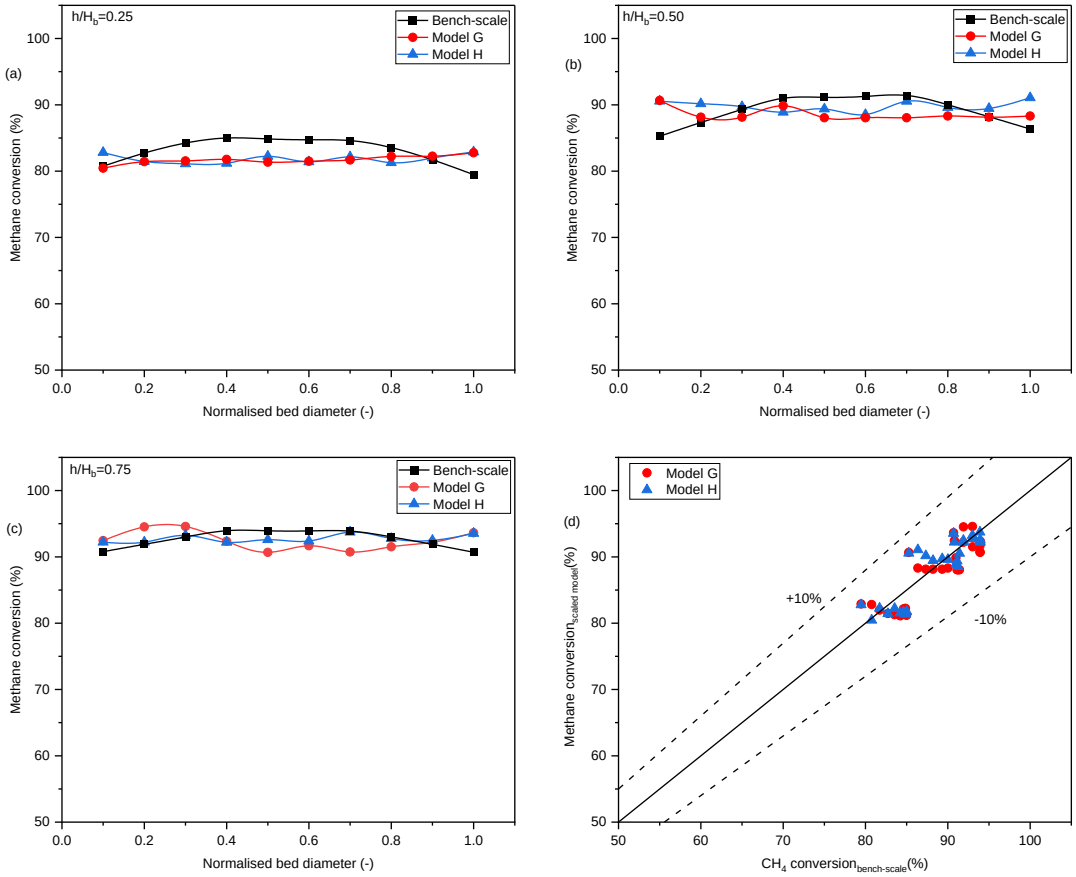

Figure 6.7: (a-c) Distribution of lateral time-averaged methane conversion at different dimensionless bed heights for Case B and (d) parity plots of the various lateral methane conversion.

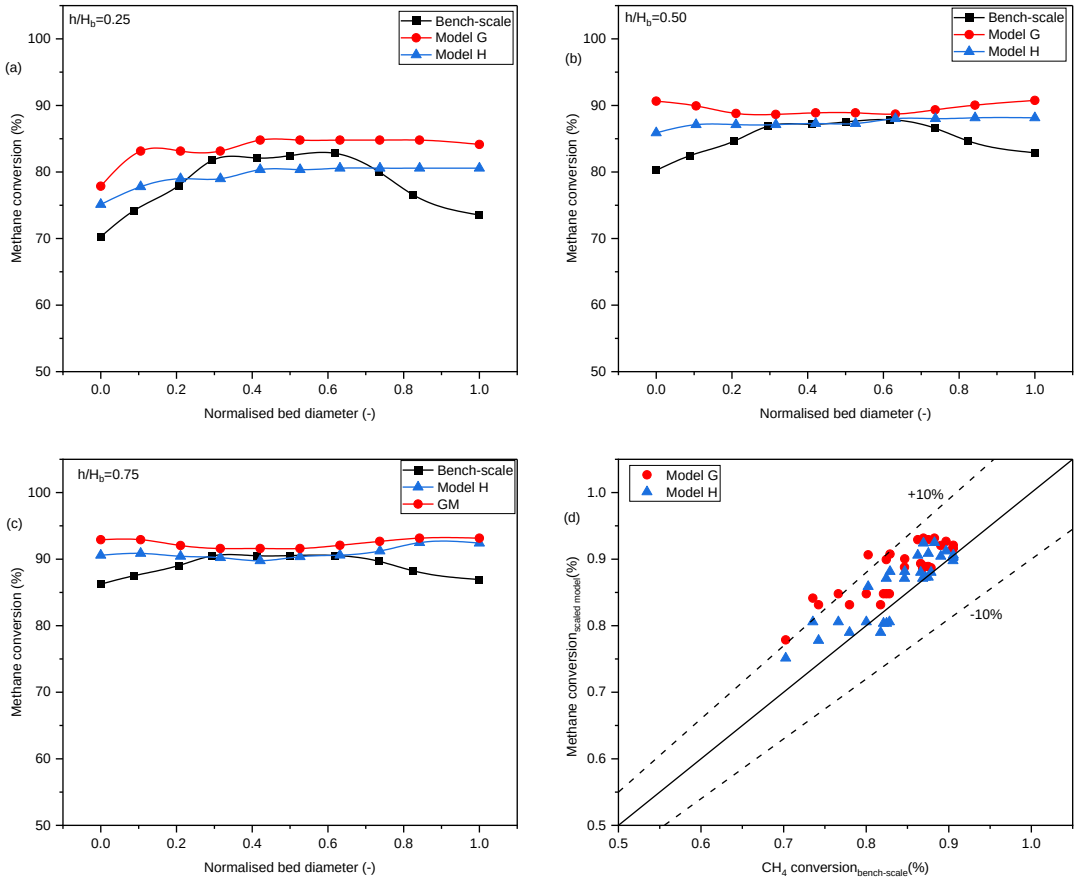

Figure 6.8: (a-c) Distribution of lateral time-averaged methane conversion at different dimensionless bed heights for Case C and (d) parity plots of the various lateral methane conversion.

In Figure 6.6, the scaled models demonstrate close similarity to each other as well as good agreement with the bench-scale values at h/H_b=0.25, especially towards the bed centreline. However, closer inspection reveals values in the wall region begin to diverge slightly, with the bench-scale model exhibiting a more substantial reduction in methane conversion compared to the scaled cases. Similar observation is seen for Figure 6.7 (Case B) and Figure 6.8 (Case C). It is expected that methane conversion at the walls be higher due to large particle concentrations and low voidage in these regions [524], especially for the low velocity case. However, this only happens for the scaled models. The noticeably low conversion at the wall regions in the bench-scale model suggests lower contact between methane and catalyst in that region, which could potentially stem from differences in the fluidising gas composition used for the bench-scale model. The inlet gas mixture contains steam, methane and nitrogen. This inert nitrogen could have preferentially diffused towards the wall regions, locally displacing methane from those areas and effectively reducing the methane partial pressure and concentration in the wall-adjacent zones, compared to the core of the reactor. Conversely, the drop in

conversion seen at the wall regions of the scaled models at h/H_b=0.25 for Case C, is due to the relatively high voidage experienced at the bottom as a result of increased velocity.

Examination of the parity plots indicates that for the cases tested, the data collapse closely around the centreline, with most points falling within the ±10% confidence bounds. This tight clustering can be seen especially for Case B, confirming strong similarity was achieved across scales under baseline operating parameters. When velocity was proportionally increased, the parity plots continue to demonstrate similarity on the whole, with the data still confined by the ±10% bounds. However, closer inspection reveals a small number of Model H data points now diverge slightly outside this tighter acceptance range.

Figure 6.9 shows the parity plots comparing the obtained hydrogen purity (calculated based on dry basis hydrogen fraction) between the bench-scale reactor and scaled models, at various locations along the bed heights. The results show that for the cases (A to C) tested, the vast majority of data points lie within ±10% of the parity line, demonstrating close agreement between scales. However, for case C operated at a higher velocity, some outliers above +10% were observed. That is, the scaled models (Model G and Model H) measured a hydrogen purity value that was slightly more than 10% higher than what was measured in the bench-scale unit. This overprediction occurred mostly at the lower bed region, suggesting that hydrodynamic effects influencing gas-solid contacting and reactant mixing may have scaled up less consistently between units at high velocity condition and closer to the gas inlet region.

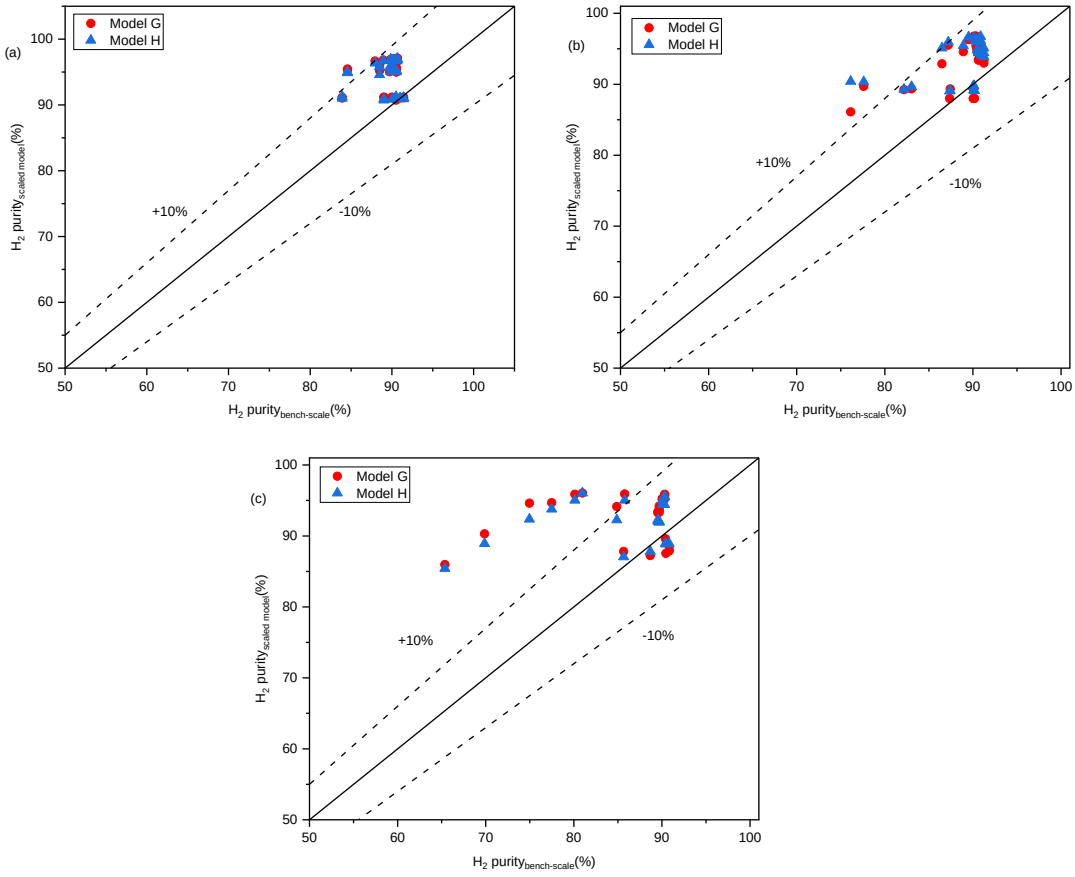

Figure 6.9: Parity plots of hydrogen purity for bench-scale model versus Model G and Model H for (a) Case A, (b) Case B and (c) Case C.

6.3.4 Time-averaged voidage and methane conversion (constant particle size)

Figure 6.10 presents a comparison of voidage distribution profiles and methane conversion across the bench-scale model and scaled Models G and H under two sets of conditions: 1) where particle size was kept constant between scales at 200 micron, and 2) where particle size in Models G and H was increased to 500 micron. This analysis allowed for checking the extent to which hydrodynamic and chemical similarity held when the particle phase property was modified in the scaled equipment.

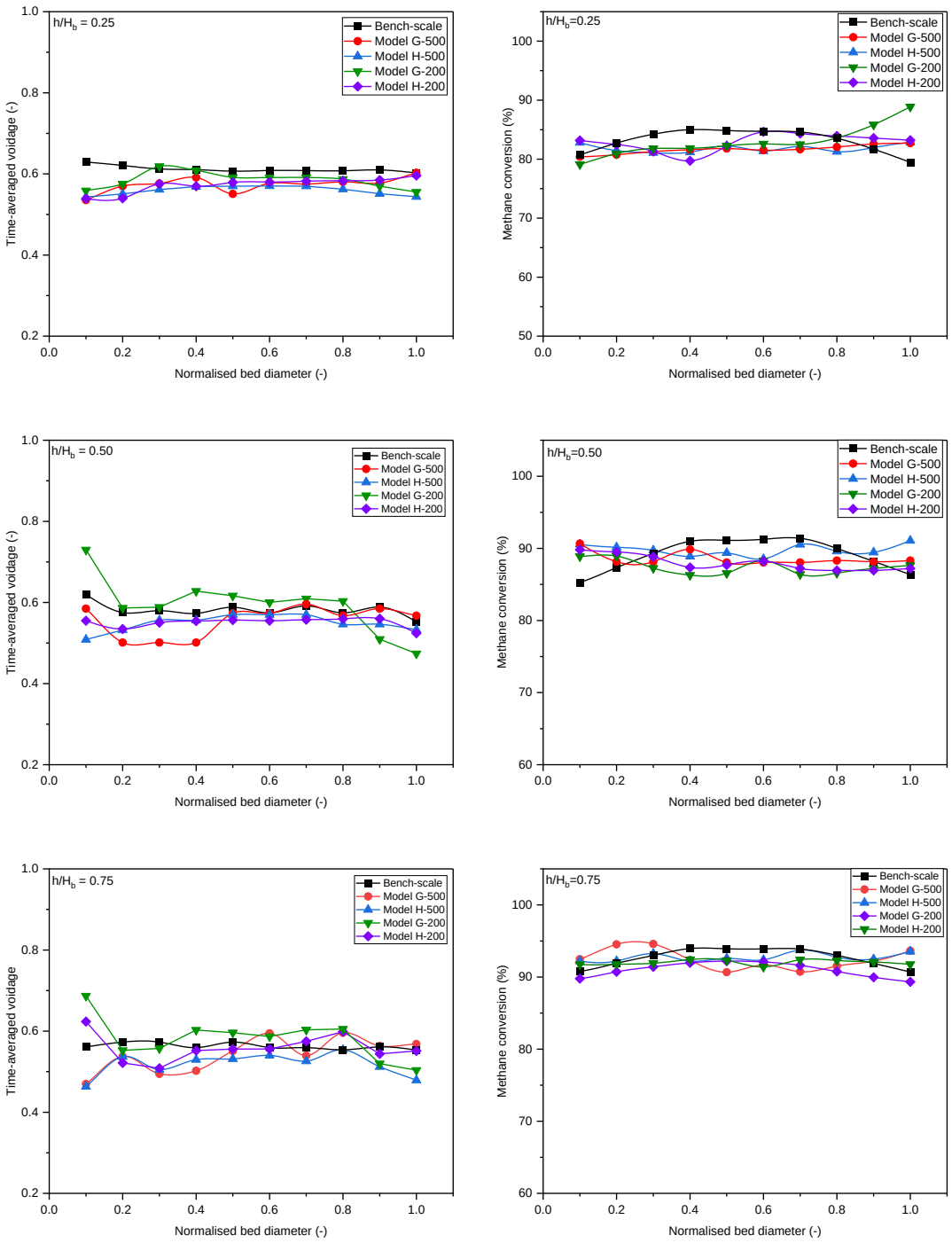

Figure 6.10: Distribution of lateral time-averaged voidage at different dimensionless bed heights for Case D (left-hand side plots) and the distribution of lateral time-averaged methane conversion at different bed heights for Case D (right-hand side plots).

When a smaller particle size of 200 micron was used, the voidage profiles of Models G and H showed relatively higher average voidage values compared to when the particle size was increased to 500 micron. This trend is consistent with findings reported by Abrahamsen and Geldart [525] in their study of dense phase bubbling fluidised beds, where it was noted that the voidage increased with decreasing mean particle size, higher fractions of fines, decreasing particle density, increasing gas density, and increasing gas viscosity. Although their study employed group A particle type, the observations still underscore the influence of particle properties and gas conditions on the characteristics of dense phase voidage within bubbling fluidised bed systems. This high voidage observed for both scaled models at 200 micron showed higher values at most of the wall regions, which correspondingly displayed low conversions. However, in general, the results showed higher disparity and less uniformity at 200 micron compared to the bench-scale model, than when the particle size was increased to 500 microns for Model G and H.

Figure 6.11 visually depicts this disparity through contour images of the particle volume fraction distributions. At 200 micron, both scaled models (G and H) exhibit a more chaotic and turbulent distribution, relative to the bench-scale and scaled models at 500 micron. The irregular patterns indicate lesser consistency in the fluid dynamic behaviour across these fluidised beds under the finer particle condition.

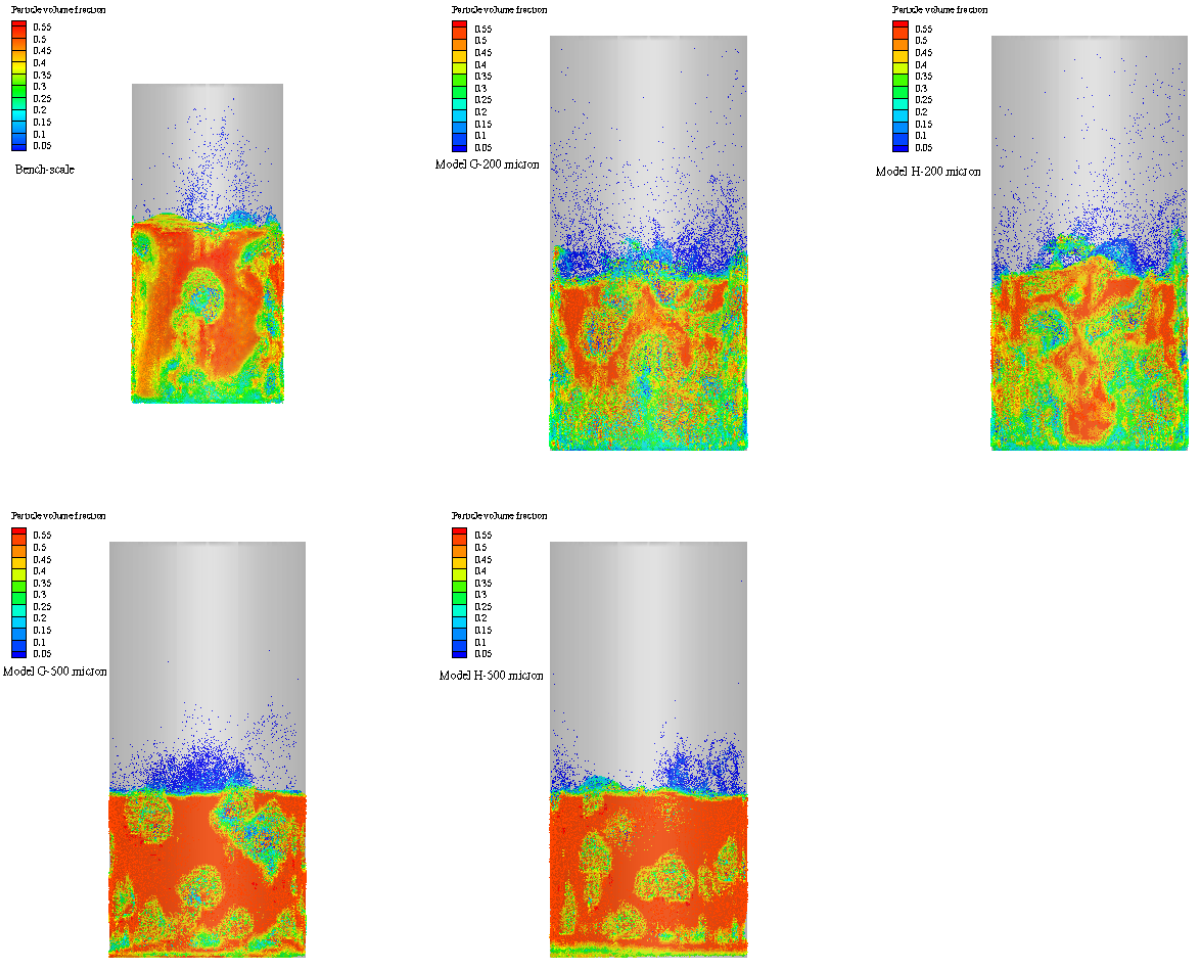

Figure 6.11: Contour of particle volume fraction for the bench-scale, Model G and Model H at 200 and 500 micron particle sizes.

6.4 Summary

Scaling fluidised bed reactors from lab to commercial scales poses hydrodynamic challenges due to complex multiphase flows. This work applied CPFD modelling and similarity principles to scale up an SE-SR hydrogen production process operating in the bubbling regime. Two scaling models by Glicksman and Horio et al., were validated for the first time for SE-SR of methane, by comparing conversion and voidage trends to a validated bench-scale model under varying conditions. Hydrodynamics and reaction performance across scales were evaluated at different gas velocities and particle sizes. Whilst similarity was generally demonstrated qualitatively, minor deviations beyond ±10% tolerance emerged under more vigorous bubbling and with finer particles. Nonetheless, over 90% of scaled model data agreed closely with bench-scale trends, validating the scaling methods. Model G and H simulations achieved near-identical results, though Model G required slightly larger dimensions and mass. As a result, Model H is selected for further scale-up studies in the next chapter.

7 Effect of scale on the performance of SE-SR of methane in bubbling fluidised bed reactors

7.1 Introduction

The previous chapter demonstrated the influence of scale-up criteria and strategy on the performance of SE-SR of methane in bubbling FBR. Two cases considering only hydrodynamic similarity (Model G) and hydrodynamic with chemical similarity (Model H) were compared. The study was conducted using the validated CPFD tool developed in Chapters 4 and 5. Model H was selected for further scale-up studies, as it offered equivalent results with likely less demanding physical/materials requirement (due to relatively reduced reactor dimensions), and invariably better economics.

Scaling up fluidised beds, particularly for reactive systems, presents numerous challenges due to inherent complexities and nonlinearities in fluidisation behaviour and reaction kinetics. A rule of thumb for geometrically scaling up a fluidised bed reactor while maintaining its performance is to maintain similarity in hydrodynamics, heat and mass transfer, and resulting reaction performance. Hydrodynamics in FBRs is governed by various mechanisms, such as bubbling, slugging, turbulent, and fast fluidisation, which are influenced by gas velocity, particle size, and particle density, among other factors [495]. These phenomena are inherently scale-dependent and can also influence reaction kinetics [526]. Moreover, the rate of chemical reactions could change significantly with reactor scale due to differences in temperature, pressure, and concentration profiles. Scaling up reactive FBRs can also affect rates of heat and mass transfer, which can vary between bench and industrial scales. Key factors like the heat transfer coefficient, axial and radial temperature gradients, intraparticle diffusion limitations, and wall heat losses in the larger reactors may deviate significantly from the bench scale performance [527].

The current knowledge on the behaviour and performance of binary reactive fluidised beds such as the SE-SR, at large scale is limited. Herce et al. [488] developed a 2D CFD model to simulate the SE-SR of methane in FBR with a diameter of 1 m, corresponding to the 500 kWth ZECOMIX reactor system. The model was implemented in ANSYS Fluent and incorporated sub-models for SMR kinetics, CO_2 capture kinetics, and a modified drag model for coarse grid simulations. It was first validated against experimental data from lab scale SE-SR studies, then applied to the retrofitted 500 kWth ZECOMIX reactor system, assuming uniform particle sizes and isothermal conditions. They highlighted that hydrogen production reached around 97% (dry basis) purity.

In this chapter, the effect of scale on the overall performance of SE-SR of methane is first analysed at 1 MWth scale, then scaled to 50 MWth and 150 MWth using the 3D CPFD model developed in Barracuda VR®. Previously validated kinetic and hydrodynamic sub-models in Chapters 4 and 5 were incorporated to perform the simulation.

7.2 Methodology

This study adopts the developed mathematical model and model settings, detailed in Chapters 4 and 5, to simulate the fluidised bed reactor hydrodynamics and reaction kinetics. The scaling criteria applied in upscaling the reactor design capacity to 50 MWth and 150 MWth draw upon insights obtained from Model H (see Chapter 6). Model H was chosen as the scaling prototype because its bed dimensions offered a prudent compromise between considerations of cost, process intensification needs and preservation of scale-relevant hydrodynamics.

7.2.1 Physical properties and operating conditions

The parameters obtained by scaling the model to Scale 2 (50 MWth) and Scale 3 (150 MWth) capacities are presented here, while the parameters for the Scale 1 (1 MWth) capacity presented in Chapter 6 for Model H remain unchanged. These properties and operating conditions also preserve the dimensionless parameters obtained for scales 2 and 3 using Model H. Temperature, pressure, steam-to-carbon ratio and catalyst-to-sorbent mass ratios also remain constant at 873 K, 1 atm, 4, and 1.3, respectively, for all the cases.

Table 7.1: Operating conditions and design parameters used for the scaled models (1 MWth, 50 MWth and 150 MWth)

Description	u_{mf} $\left(\frac{m}{s}\right)$	$d_{p(avg)}$ (m)	$(\mu)_{avg}$ (kg. $m^{-1}s^{-1}$)	$(\rho_p)_{avg}$ (kg/m^3)	u_o $\left(\frac{m}{s}\right)$	H_i (m)	D (m)	$(\rho_g)_{avg}$ (kg/m^3)	m_{sorb} (kg)	m_{cat} (kg)
Scale 1 (1 MWth)	0.046	5×10^{-4}	3.11×10^{-5}	1864.80	0.34	1.26	1.59	0.25	1029.62	1290.12
Scale 2 (50 MWth)	0.046	5×10^{-4}	3.11×10^{-5}	1864.80	0.66	4.61	5.83	0.25	51.11×10^{3}	64.05×10^{3}
Scale 3 (150 MWth)	0.046	5×10^{-4}	3.11×10^{-5}	1864.80	0.78	6.53	8.25	0.25	145.02×10^{3}	181.71×10^{3}

7.2.2 Design of Loopseal for the 1 MWth scale

A loopseal allows solids to take on fluid-like characteristics by utilising a controlled amount of air, while maintaining pressure equilibrium. When subjected to a differential static pressure, the loopseal gives solids the ability to flow freely. In this study, the loopseal is designed following the design considerations of Basu [528], by assuming that the pressure where solids exit the loopseal is the same as the pressure where solids enter the calciner or reformer. The schematic of the loopseal design used in this study is presented in Figure 7.1.

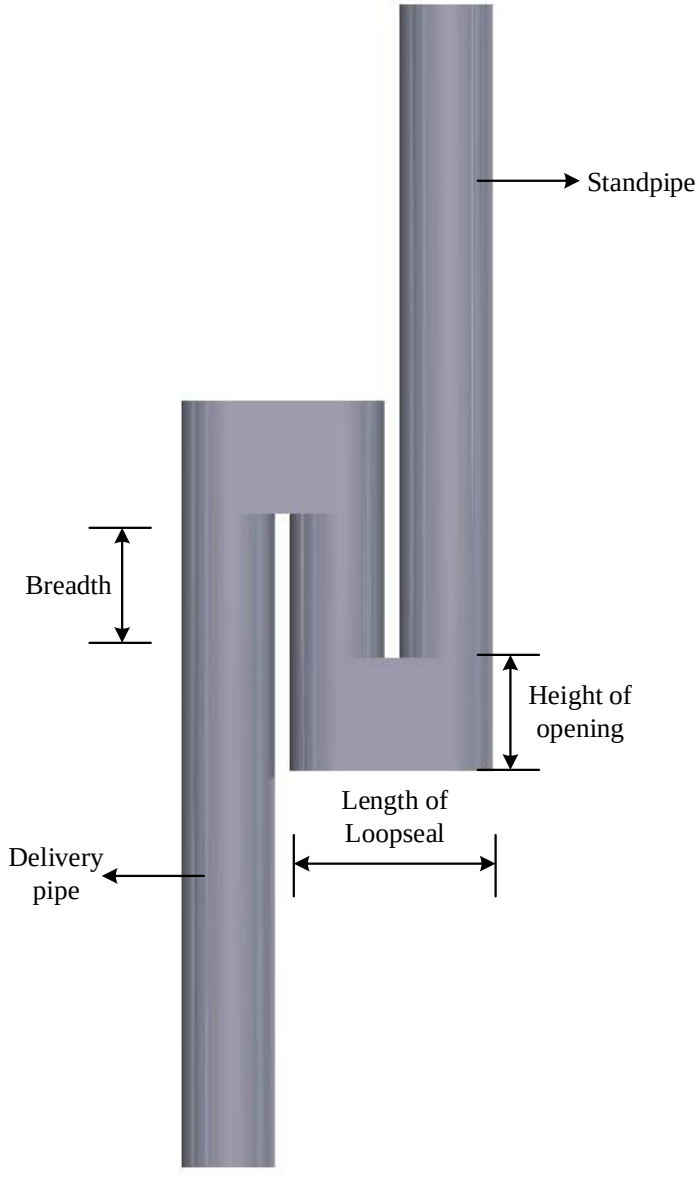

Figure 7.1: Schematic design of the loopseal showing the design parameters.

The diameter of the standpipe, d_s, is related to the velocity of solid in the standpipe, v_s, as:

$$d_s = \sqrt{\frac{4W_s}{\pi\ 1-\varepsilon_s\ \rho_P V_s}} \quad 116$$

where ε_s is the voidage of solids in the standpipe and taken as 0.5, and W_s is solid flow rate (kg/s) through the standpipe that is related to the circulation rate through the bed as:

$$W_s = G_s \times \text{ bed area} \quad 117$$

The solid flux, G_s, was calculated using the dimensionless parameter presented in equation 118. This value was first obtained from the bench-scale model and was then scaled to determine the new G_s for the 1 MWth scale. The new value for Scale-1 is calculated to be 6.833 kg/m^{2}s.

$$\frac{G_s}{\rho_s u_0} \quad 118$$

The conservative values of solid velocity in the standpipe, v_s, length of the loop seal, L_{ls}, and breadth of the loop seal, B_{ls}, are presented in Table 7.2. These values align with the guidelines provided by Basu [528]. The solid velocity was maintained at a reduced rate to guarantee a consistent movement of particles through the standpipe without risk of clogging. Guidelines suggest keeping the solid velocity under 1 m/s, or preferably 0.15 m/s, to facilitate this smooth flow.

Table 7.2: Key dimensions and mathematical relationships for the loopseal structure

Parameters	Values	Units
V_s	0.15	m/s
L_{ls}	$2.5d_s$	m
B_{ls}	$1.6d_s$	m

The height of opening for the loopseal can be calculated from equation 119. This is determined based on a horizontal solid speed, v_h, which should fall within a range of 0.25 to 0.05 m/s in order to ensure proper functioning [528].

$$Height\ of\ the\ opening = \frac{W_s}{1-\varepsilon_s\ \rho_P V_h B} \quad 119$$

The loopseal design parameter values were then determined through calculations and are presented in Table 7.3. The fluidising velocity of loopseal recommended is 2.5*U_{mf}. Therefore, the fluidising

velocity was calculated based on particle size of ~500 micron and minimum fluidisation velocity of 0.04645 m/s.

Table 7.3: Results of the calculated values of the loopseal design parameters used for the simulation of the 1 MWth reactor

Parameters	Values	Units
G_s	6.833	kg/m^{2}s
d_s	0.25	m
L_{ls}	0.625	m
B_{ls}	0.40	m
Height of the opening	0.311	m
Loopseal fluidising velocity	0.116	m/s

7.2.3 Reactor description and boundary conditions for the circulating mode

Scale 1 was first studied in a stand-alone bubbling fluidised bed reactor, then scaled to Scale 2 and 3, without the additional components like the loopseal and the calciner. The geometry used for the stand-alone cases was simple and the same as that described in Chapter 6. The reactor geometry used to analyse performance in circulating mode for the scaled-up SE-SR process was modelled for only the 1 MWth fluidised bed reactor, due to computational requirements.

The circulating mode comprises two loopseals and two bubbling fluidised bed reactors of similar dimensions for the reformer/carbonator and the calciner. The first loopseal (Loopseal 1) is used to transport solid from the reformer to the calciner, while the second loopseal (Loopseal 2) is attached to the calciner. A reduced model is adopted, where a 'boundary connector' was used to connect the solids exit from the Loopseal 2 to the reformer, eliminating the need for a transport riser, as seen in Figure 7.2. This option has been shown to be highly beneficial when modelling part of a complex system that involves a closed-loop solid flow, while reducing computational requirement [529]. The tops of the reactors are open to allow for the exit of gases. Pressure boundary was set at the reactor top while flow boundary was set at the reactor inlet. Adiabatic boundary conditions are applied to the exterior walls, implying no heat transfer to the surroundings. Gas is fed into the reactor at the given

temperature and atmospheric pressure. Mixture of catalysts and sorbents are continuously fed into the top of the reactors, from the loopseals, during circulation. The calciner was modelled to have the same solid inventory and solid properties as the reformer/carbonator, while other conditions, including the fluidising gas, were different and presented in Table 7.4.

Table 7.4: Operating conditions in the calciner for the 1 MWth production scale

Parameters	**Values**	**Units**
Fluidising gas	Nitrogen	-
Fluidising gas temperature	1173	K
Bed initial temperature	1173	K
Pressure	1	atm
Gas velocity	0.34	m/s

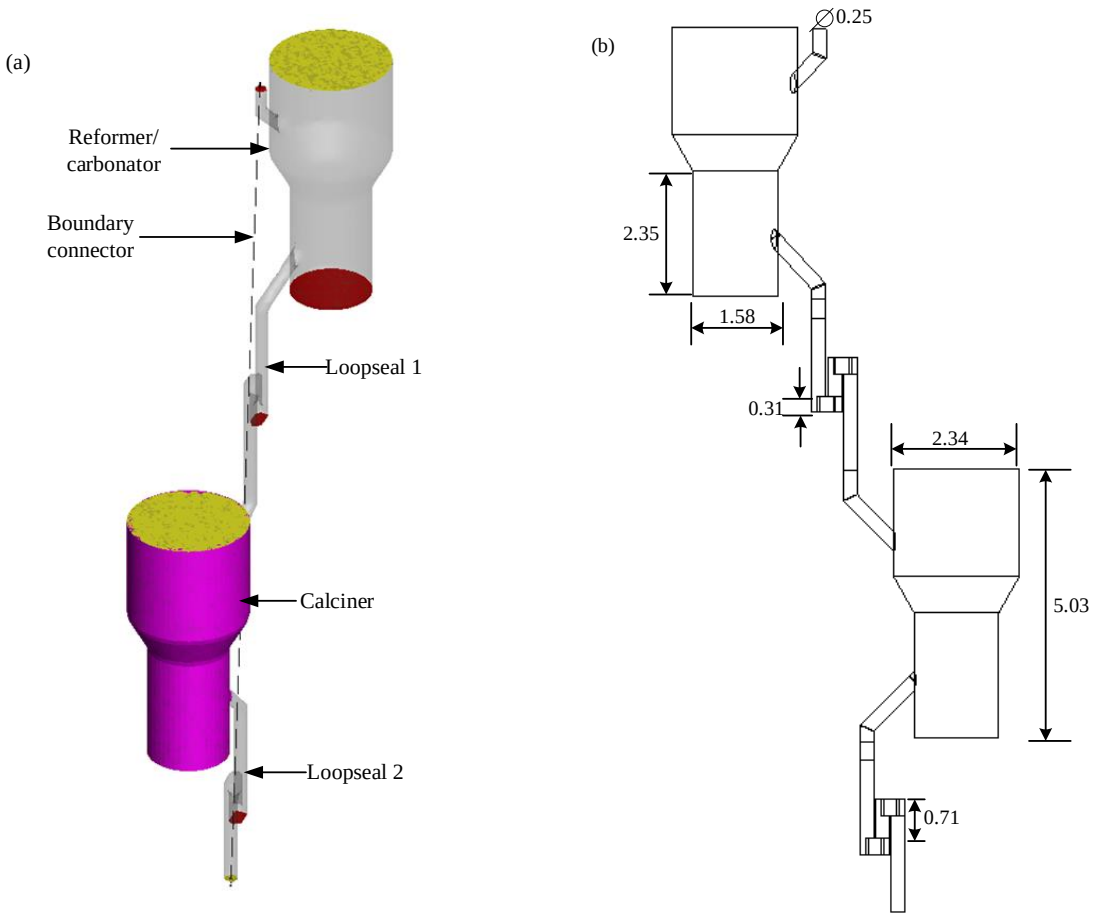

Figure 7.2: Boundary conditions (a) and Reactor dimensions (b) for the 1 MWth SE-SR in circulating mode (all dimensions in m).

7.3 Results and discussion

This section analyses the performance of SE-SR of methane for hydrogen production in a 1 MW_{th} bubbling fluidised bed reactor. The analysis begins by examining the influence of select operating parameters, including initial bed temperature, particle size and bed aspect ratio. Then, the product compositions resulting from the different conditions are compared. Next, a reduced model is used to analyse the 1 MW_{th} capacity system operating in circulating mode, which includes scaled loopseals and calciner.

The second part of this section focuses on evaluating the performance of industrial size SE-SR reactor, scaled up using Model H. Comparisons of product composition, particle volume fraction, bubble distribution, and pressure drop are made to analyse both hydrodynamic and chemical performance changes with scale. This provides insights into how process performance may be impacted at different capacity levels.

7.3.1 Performance analysis of 1 MWth reactor scale for SE-SR of methane in BFB reactor

7.3.1.1 Effect of initial bed temperatures

Bed temperature is a crucial parameter as it can directly influence the kinetics of chemical reactions, overall thermodynamic equilibrium as well as fluidisation hydrodynamics [530]. Temperature governs the rates of methane reforming, water-gas shift reaction, and carbonation/calcination cycles, which determine the extent of hydrogen production and CO_2 capture. The effect of bed temperature was evaluated by varying the initial bed temperature between 773 and 1023 K, while holding all other operating parameters including pressure and superficial gas velocity constant. The temperature and superficial velocity of the gas inlet were maintained at 873 K and 0.34 m/s, respectively, as presented in Table 6.2. Other parameters including S/C ratio and sorbent composition is same as that of the bench-scale listed in Table 5.4.

Figure 7.3 shows how the product distribution (dry basis) profile changes with increasing bed temperature. At lower bed temperature (773 K), the hydrogen composition is relatively low (70.5%), primarily due to the limited catalytic activity of the Ni-based catalyst at those temperatures. It has been reported that temperatures below a certain threshold (typically around 720 K) significantly affect hydrogen production due to the activation energy of the reaction and conditions [531,532]. As the bed temperature rises to 873 K, hydrogen composition increases to approximately 96%, owing to the enhanced kinetics of the methane steam reforming reaction and the simultaneous carbonation reaction. However, beyond a bed temperature of 873 K in this case, the hydrogen composition starts to decrease, reaching 77% at 1073 K. This reduction in hydrogen composition at very high temperatures is likely due to the reverse water-gas shift reaction becoming more prominent, consuming hydrogen to produce carbon monoxide and water.

The opposite trend is observed for CO and CO_2. It should be expected that since the water-gas shift reaction favours the conversion of CO to CO_2 at lower temperatures, increasing temperature should lead to a rise in CO composition. However, it is interesting to see that CO reduces from 3.72% observed at 773 K to ~1% at 873 K, before rising to 12.67% at 1073 K due to equilibrium shift towards the production of CO. This initial reduction in CO composition can be attributed to the improved catalytic activity and subsequent kinetics of the water-gas shift reaction at that temperature, coupled with the in-situ CO_2 removal, which overshadowed the equilibrium shift favouring CO production. Conversely, the CO_2 composition initially increases from 0.087% at 773 K to 0.61% at 873 K, but then further increases to 9.8% at 1073 K, primarily due to reduced carbonation, since carbonation reaction is exothermic. The methane composition continuously decreases from 25.6% to near zero as the bed

temperature increases, indicating higher methane conversion at elevated temperatures. This behaviour is expected, as the endothermic methane steam reforming reaction is favoured at higher temperatures.

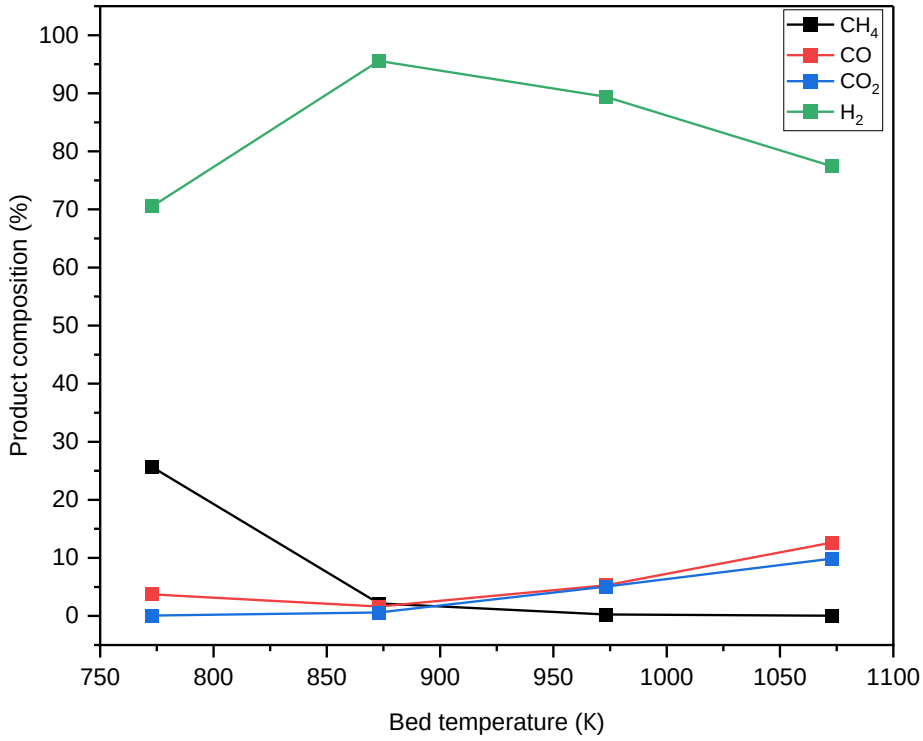

Figure 7.3: Distribution of CH_4, CO, CO_2 and H_2 compositions as a function of bed temperature.

It is also important to consider the transient temperature profiles of the particles and fluid phases during operation at different bed temperatures. Figure 7.4 illustrates the time evolution of both the particle and fluid temperatures in the reactor at different bed temperatures. Interestingly, at a bed temperature of 773 K, the temperature gradients between the particle and fluid phases are initially higher, indicating thermal limitations within the system. The fluid temperature exhibits an initial drop of 78.78 K, which continues to decrease before stabilising after approximately 70 seconds. The bed temperature drop was only 0.2 K after 100 seconds. However, as the bed temperature increases, the temperature gradients between the particles and the fluid phase are relatively smaller, while the bed temperature drops become relatively more pronounced. At a bed temperature of 873 K, the fluid temperature is the same as the bed's, with a bed temperature drop of 0.88 K after 100 seconds of simulation time. At 973 K, there is a temperature drop of 6.09 K in the particle phase, which stabilises after approximately 40 seconds. Similarly, at 1073 K, a temperature drop of 9.24 K is observed, with the bed reaching stabilisation after around 60 seconds.

These temperature drops can be attributed to the dominance of the SMR reaction during the initial stages of the process. The shorter stabilisation times observed at higher bed temperatures (40 seconds at 973 K and 60 seconds at 1073 K) compared to the lower temperature of 773 K (70 seconds), suggest improved heat transfer dynamics and faster thermal equilibrium at elevated temperatures. As the reaction progresses, the WGS reaction and the heat released from the carbonation of the sorbent material contribute to the heat balance within the reactor.

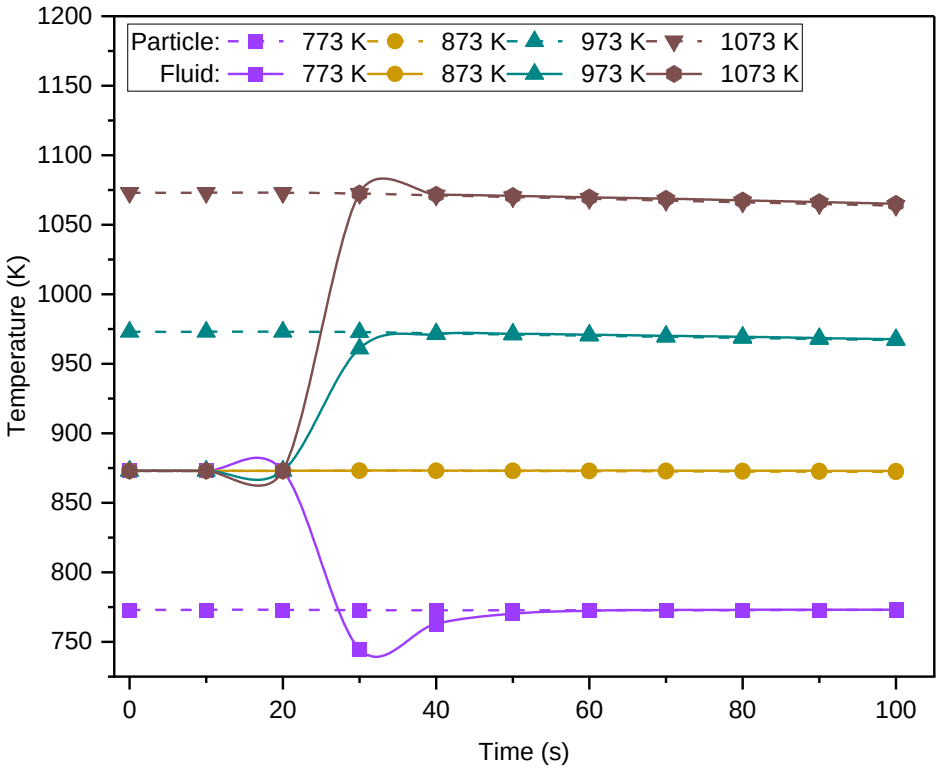

Figure 7.4: Time evolution of particle and fluid temperatures at different initial bed temperatures. Dashed lines represent average particle temperature and solid lines represent average fluid temperatures.

To further understand the heat transfer characteristics at various bed temperatures, Figure 7.5 shows the contours of temperature distribution within the reactor volume. At lower temperature of 773K, a clear temperature gradient can be seen at the bottom, with colder temperatures near the bottom that gradually increase up the reactor height. However, as the initial bed temperature rises to 873 K, 973K and 1073K, the contours become more uniformly spaced at the bottom, indicating more consistent heat transfer across the bed.

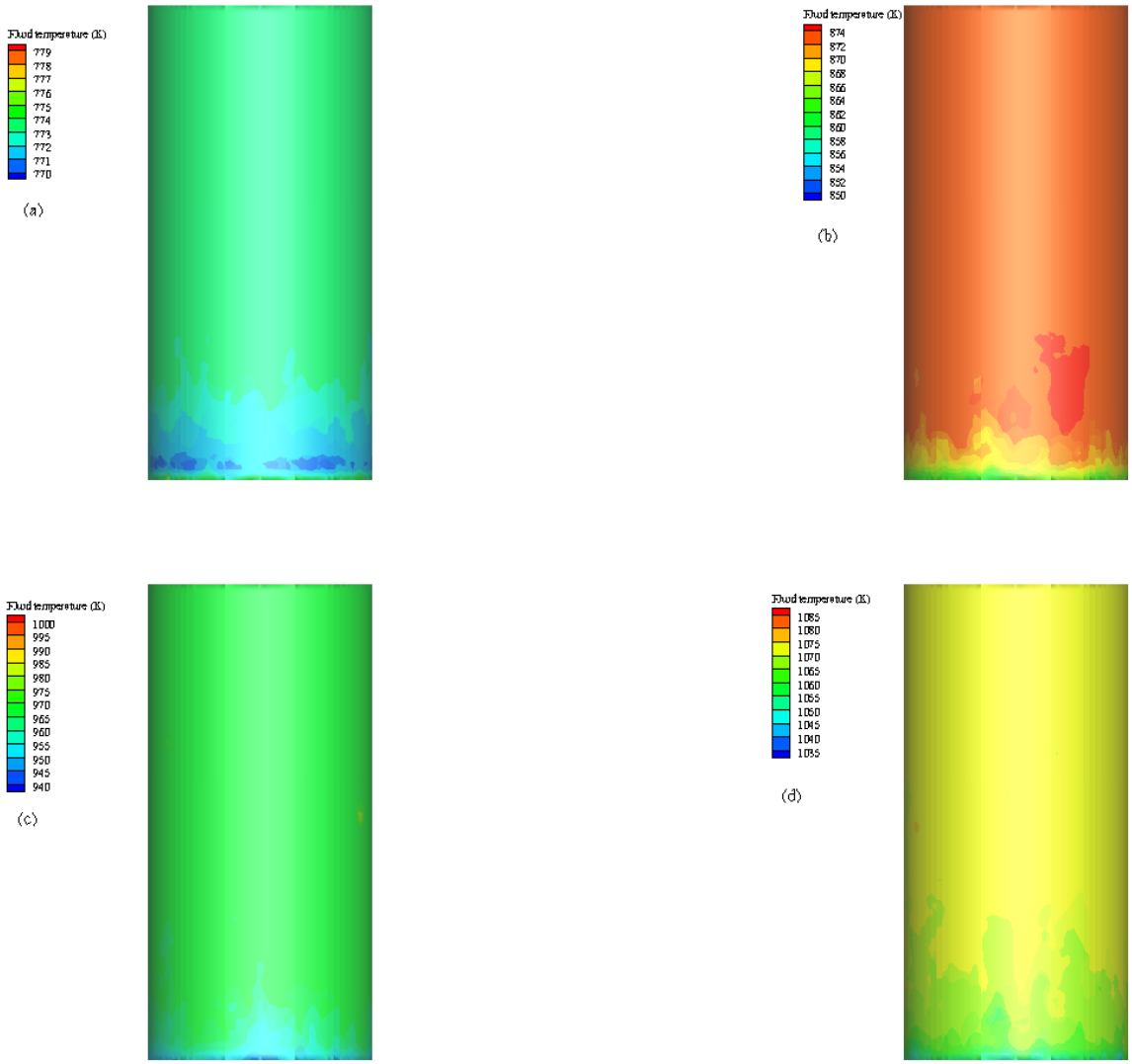

Figure 7.5: Contour of temperature distribution coloured by fluid temperature within the reactor at different initial bed temperatures of (a) 773 K, (b) 873 K, (c) 973 K and (d) 1073 K.

7.3.1.2 Effect of bed aspect ratios

The aspect ratio of a fluidised bed, defined as the ratio of its height to its diameter, can influence its hydrodynamics and performance [533]. This section explores how variations in bed aspect ratio impact factors like bubble size distribution, particle mixing, and product composition for the 1 MW_{th} hydrogen production scale. Bed aspect ratios of 0.4, 1.2, 1.6 and 2 were investigated, with superficial velocity maintained at 0.34 m/s. A low aspect ratio corresponds to a wider, shorter bed while a higher ratio indicates a narrower, taller configuration.

Figure 7.6 displays the variation in product gas composition as a function of the bed aspect ratio (H/D), revealing the influence of this parameter on SE-SR of methane. As the bed aspect ratio increases from 0.4 to 0.8, the hydrogen composition exhibits an increase from 92.4% to 96%. This increase can be

attributed to the improved gas-solid contact and enhanced mass transfer at the higher bed aspect ratio, promoting SMR and WGS reactions responsible for hydrogen production. Interestingly, as H/D is further increased from 0.8 to 2, the hydrogen composition remains relatively constant, with only a marginal increase of 1.5%. This observation suggests that beyond a certain bed aspect ratio, the benefits of improved gas-solid contact and mass transfer may reach a plateau, and other factors, such as heat transfer limitations, become more dominant in influencing the hydrogen production. In contrast to the behaviour of hydrogen, the compositions of methane, CO and CO_2 exhibit a decreasing trend with increasing bed aspect ratio. The methane composition decreases from 3.65% at H/D = 0.4 to approximately 1% at H/D = 2, indicating improved methane conversion at higher bed aspect ratios due to better gas-solid interactions and longer residence times. Similarly, the CO composition decreases from approximately 3% at H/D = 0.4 to 0.8% at H/D = 2, while the CO_2 composition reduces from 0.67% to approximately 0.6% over the same range. These reductions in CO and CO_2 compositions can be attributed to the enhanced WGS reaction and improved carbonation of the sorbent material at higher bed aspect ratios, facilitated by the improved gas-solid contact and longer gas residence time.

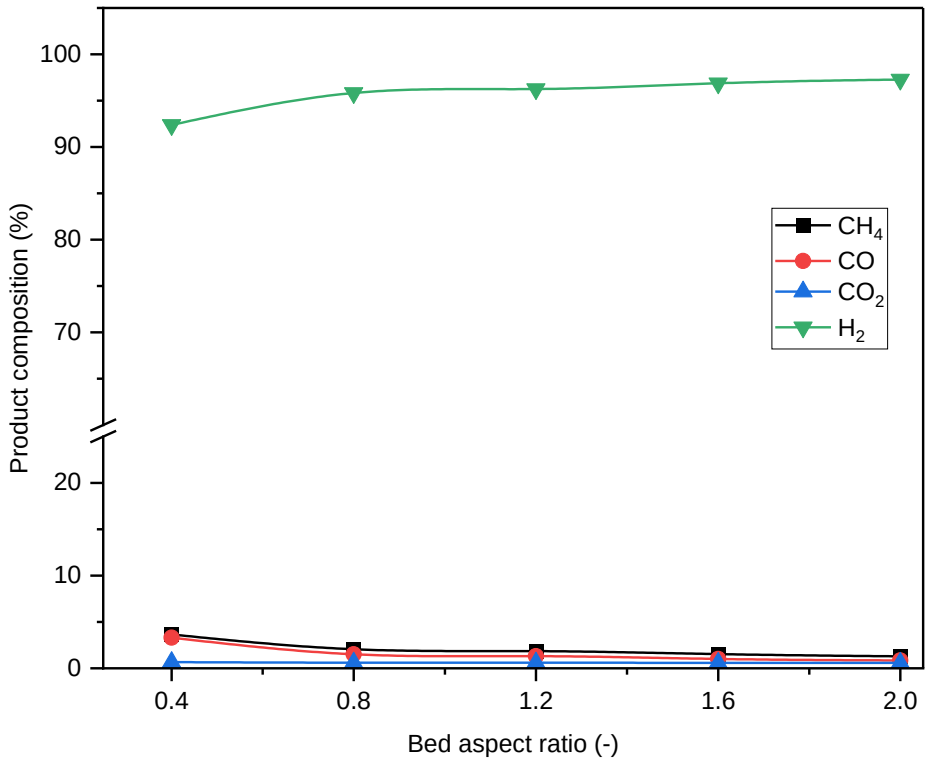

Figure 7.6: Distribution of CH_4, CO, CO_2 and H_2 compositions as a function of bed aspect ratios.

While higher bed aspect ratios generally favour improved gas-solid contact and hydrogen purity, Figure 7.7 reveals reduced gas flow rates for CH_4, CO, CO_2, and H_2 as the bed aspect ratio increases. This behaviour can be attributed to a couple of key reasons. Firstly, for higher bed aspect ratios, the

extended contact period between the gas and solid phases enhances mass transfer and reactive performance. This increased residence time allows for more efficient conversion of methane and subsequent production of hydrogen, CO, and CO_2. However, it also means that the gases spend relatively longer time traversing the length of the reactor before exiting, as evidenced by the delayed appearance of the exit gases in the graphs for H/D=2, where the gas is observed after 5 seconds.

Secondly, the low gas flow rates observed at higher bed aspect ratios could be a result of high bubble gas holdup. As reported by Werther [534], an increase in bed diameter causes a reduction in bubble gas holdup. Therefore, at higher bed aspect ratios, the relatively low bed diameter and subsequently high bubble gas holdup can contribute to higher gas residence time, effectively reducing the product gas flow rates at the reactor outlet. Although the longer contact time promotes better conversion and utilisation of the reactants, the increased bubble gas holdup counteracts this effect by retaining a portion of the gas within the reactor, resulting in lower gas flow rates at the outlet.

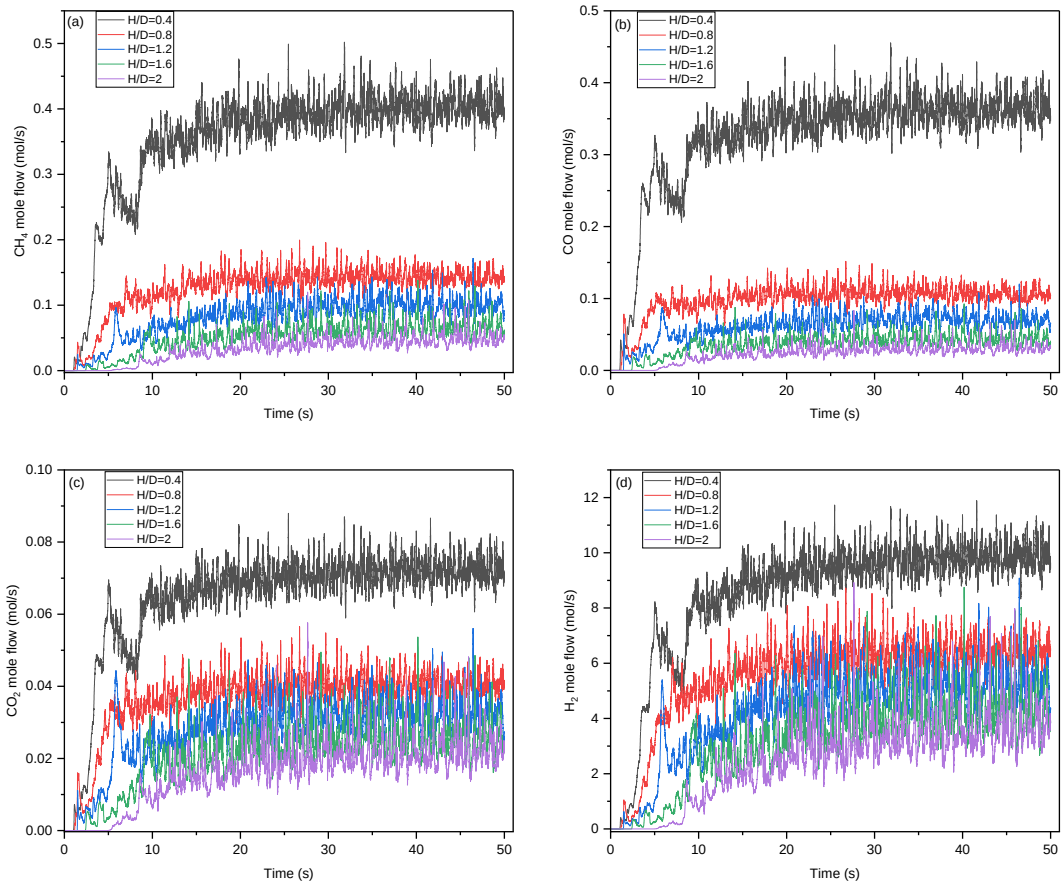

Figure 7.7: Instantaneous molar flow rates of (a) CH_4, (b) CO, (c) CO_2, and (d) H_2 over time.

In addition to influencing product composition and residence times, the bed aspect ratio also alters the gas bubble characteristics. Figure 7.8 shows the number of bubbles appearing for each H/D and their mean bubble sizes, obtained for the last 2 seconds. The number of bubbles exhibits an inverse relationship with the bed aspect ratio. At higher bed aspect ratios, a lower bubble count is observed, suggesting that fewer but larger bubbles are present within the reactor. Conversely, at lower bed aspect ratios, a higher number of smaller bubbles are observed. The total bubble count reduced from 856 at H/D = 0.4 to 610 observed at H/D = 2.

In contrast to bubble count behaviour, the mean bubble size increased from 0.058 to 0.104 as H/D increases from 0.4 to 2, respectively, which indicates the tendency for bubbles to coalesce and grow in size as they rise through the increased bed height. This phenomenon can be attributed to the increased residence time and the potential for bubble coalescence over the longer path length [535]. However, most of the bubble sizes lie between 0.05 and 0.15 m. This bubble behaviour is also visually depicted in the contour of volume fraction presented in Figure 7.9. More bubbles can be seen in the wider bed compared to the narrow bed (high H/D).

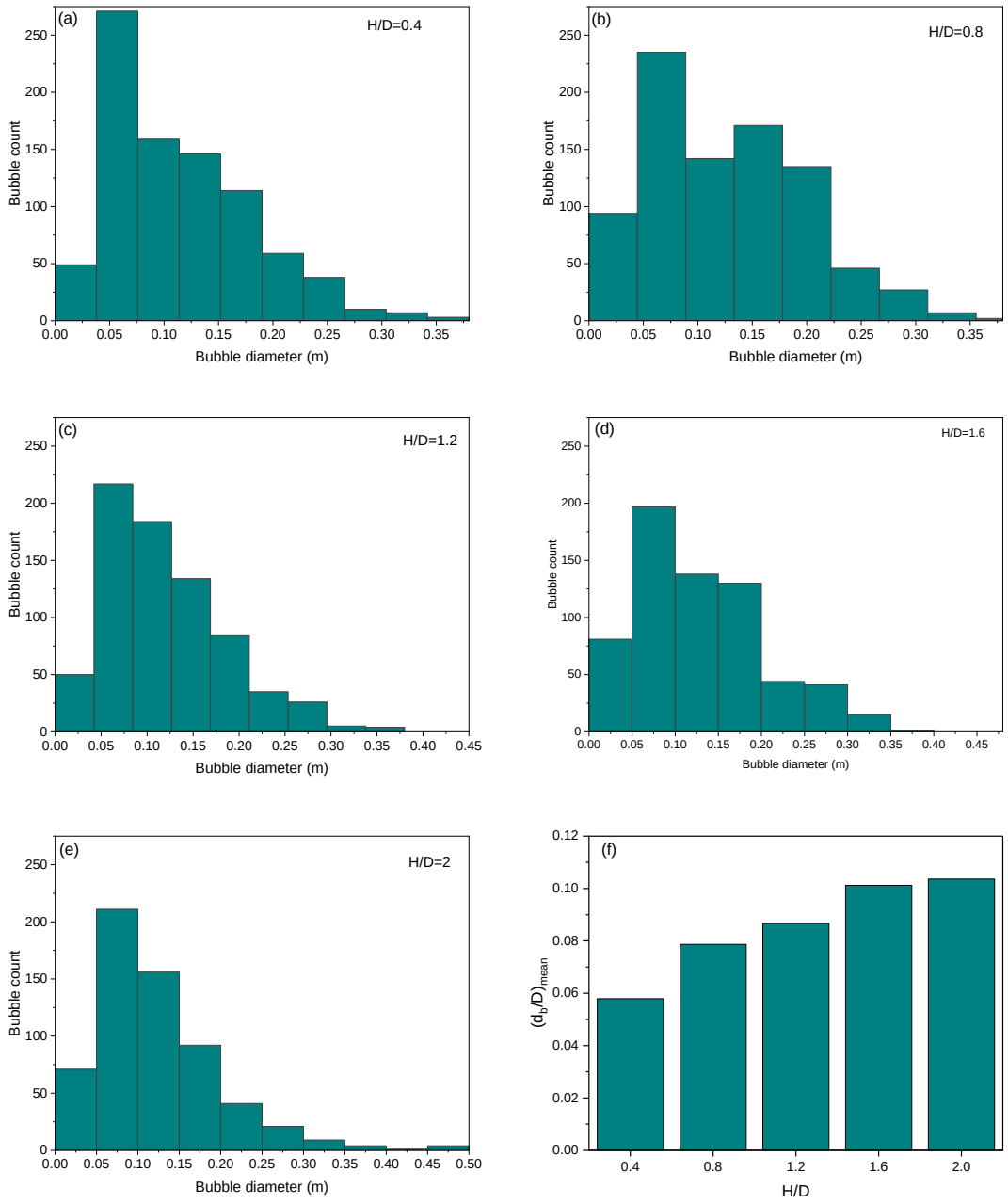

Figure 7.8: Bubble size distribution at various bed aspect ratios (a-e), and (f) mean bubble diameter for the different bed aspect ratios. d_b is the bubble size while D is the bed diameter for each aspect ratio.

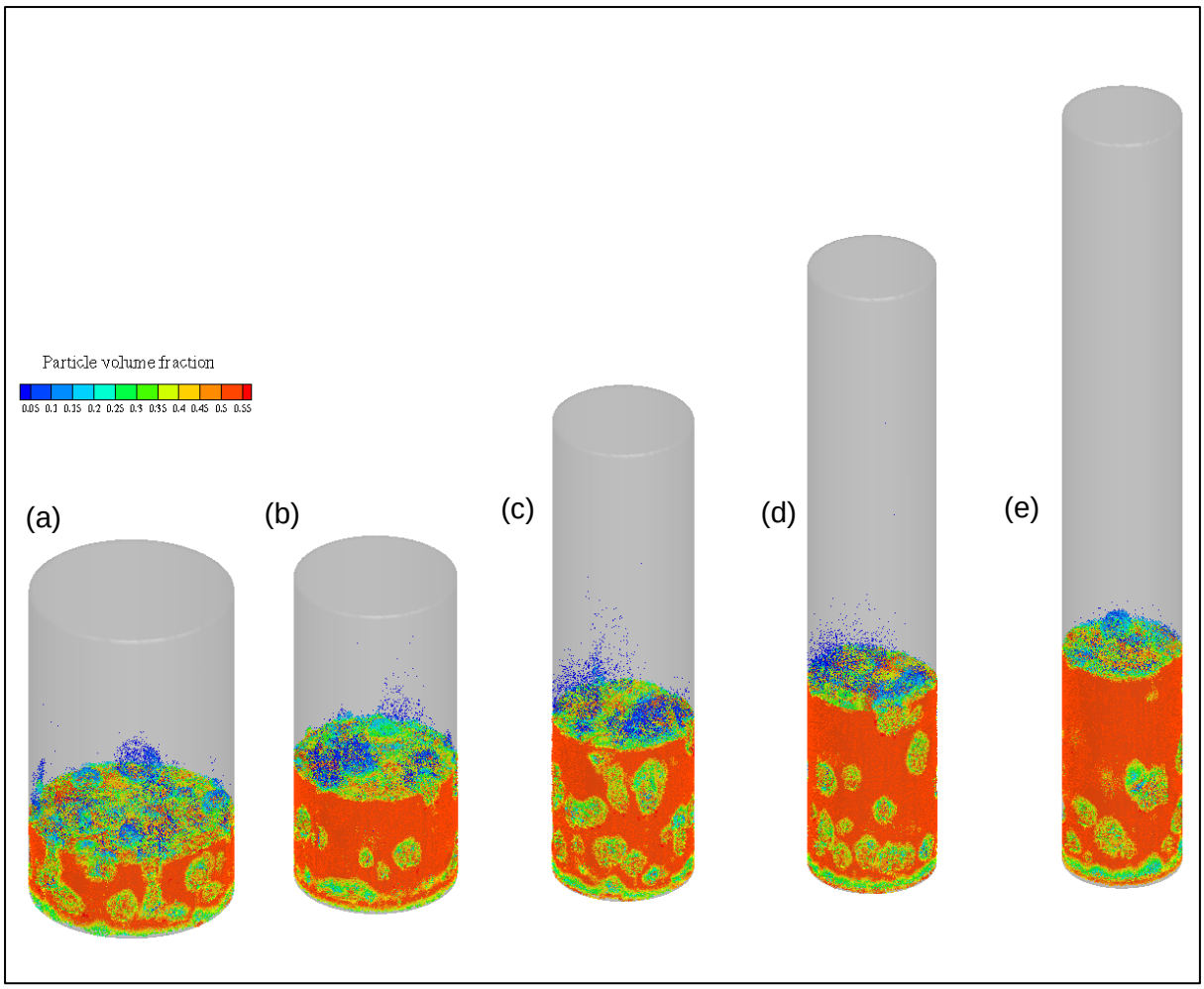

Figure 7.9: Contour of particle motion at different bed aspect ratio coloured by particle volume fraction, where (a), (b), (c), (d), and (e) represents H/D = 0.4, 0.8, 1.2, 1.6, and 2, respectively.

Figure 7.10 reveals the trend in pressure drop along the height of the reactor with respect to the bed aspect ratio. As the aspect ratio increases, reflecting a taller, narrower bed configuration, the pressure drop also increases. Conversely, reducing the aspect ratio leads to a decrease in pressure drop across the reactor. This behaviour can be explained by considering the combined effects of the bed weight, geometry, and superficial gas velocity. At higher aspect ratios, the increased bed height contributes to a larger static bed weight, resulting in a higher pressure drop. According to the study by Rao et al. [536], this then necessitates higher gas velocities to overcome the effects of greater pressure drop and bed weight associated with taller, narrower geometries. A study by Rao et al. [536] found through experiments that the minimum velocity needed for fluidisation increases when the diameter of the column becomes smaller or the height of the particulate bed rises. Their work attributed these observations to wall friction effects, which counter both the weight of the bed and the drag force exerted on particles during fluidisation.

This study's trend of declining gas flowrates with increasing aspect ratio (Figure 7.7) further supports the need for higher velocities at taller, narrower configurations to maintain the desired 1 MWth hydrogen output against stronger pressure drops. The gas velocity must increase to achieve the desired hydrogen flowrate, especially for reactors with a small cross-section like H/D=2.

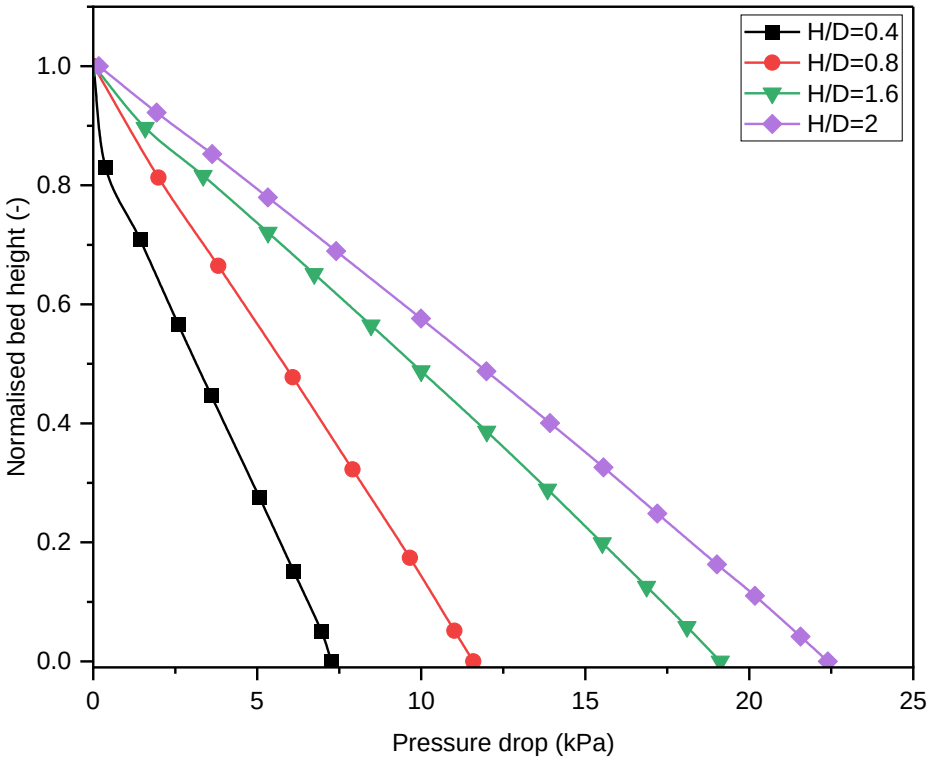

Figure 7.10: Pressure-height profiles for SE-SR of methane at different bed aspect ratios from 0.4 to 2.0.

7.3.1.3 Effect of particle size

In fluidised bed systems, particle size and particle size distribution play a pivotal role in determining the minimum fluidisation velocity, bubble dynamics, and pressure drop across the reactor [537–539]. Thus, it is worthwhile to investigate how varying the particle size of the sorbent and catalyst material may influence the 1 MWth SE-SR process. Therefore, a range of particle sizes (500 µm – 1200 µm) was modelled and tested to understand their effects on the product gas composition and pressure profiles at this 1 MWth pilot-scale level, while maintaining the superficial gas velocity, solid mass and initial bed heights provided in Table 7.1.

Figure 7.11 presents the product distribution at different particle sizes for SE-SR of methane. The trends indicate that increasing particle size did not significantly impact the overall composition, as hydrogen composition only increases slightly by ~1% as particle size rises from 500 to 1200 µm, while CH_4 and CO both reduce by 0.8% and 0.78%, respectively. Interestingly, the trend observed for CO_2 composition deviates from the other components. Initially, the CO_2 concentration drops by 0.035% as the particle size increases from 500 to 800 µm. However, as the particle size was further increased from 1000 to 1200 µm, the CO_2 concentration rose by 0.02%. This non-monotonic behaviour could be related to changes in heat transfer mechanics associated with larger particle sizes [537]. With the exothermic nature of the carbonation reaction, coupled with the larger particle sizes and the associated reduced heat transfer, the carbonation reaction may be hindered, thereby leading to a relatively higher CO_2 concentration in the product stream. From the combined results of Figure 7.11 and Figure 7.12, sizes between 500 µm and 600 µm seem to optimise hydrogen yield while minimising CO_2 production, without impacting on bubble dynamics.

In Figure 7.12, the contour of the volume fraction shows a decline in bubble numbers and size within the reactor as the particle size increases, indicating that the superficial gas velocity was no longer sufficiently above the minimum needed to sustain bubbling fluidisation. Based on calculation and the current u_{mf} used in this study, this observation suggests that the superficial gas velocity must be more than 3.4 times or at least 5.8 times the minimum fluidisation velocity ($5.8u_{mf}$ or $>3.4u_{mf}$), to maintain a bubbling fluidised state for larger particle sizes and avoid packed bed conditions.

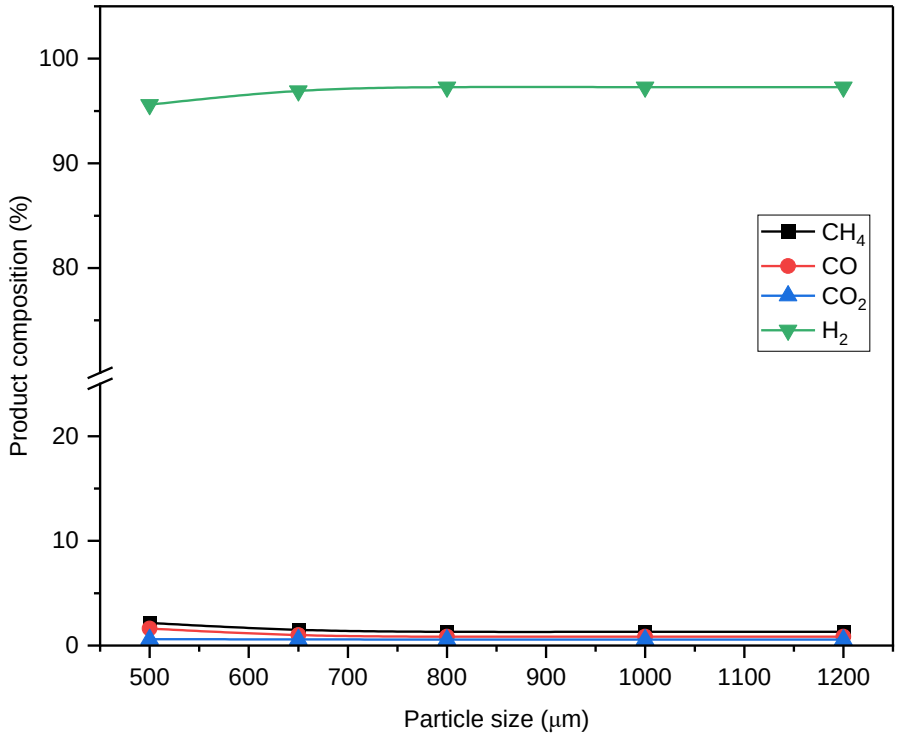

Figure 7.11: Influence of particle sizes on the product composition of SE-SR of methane at constant superficial gas velocity (0.34 m/s) for 1MWth case.

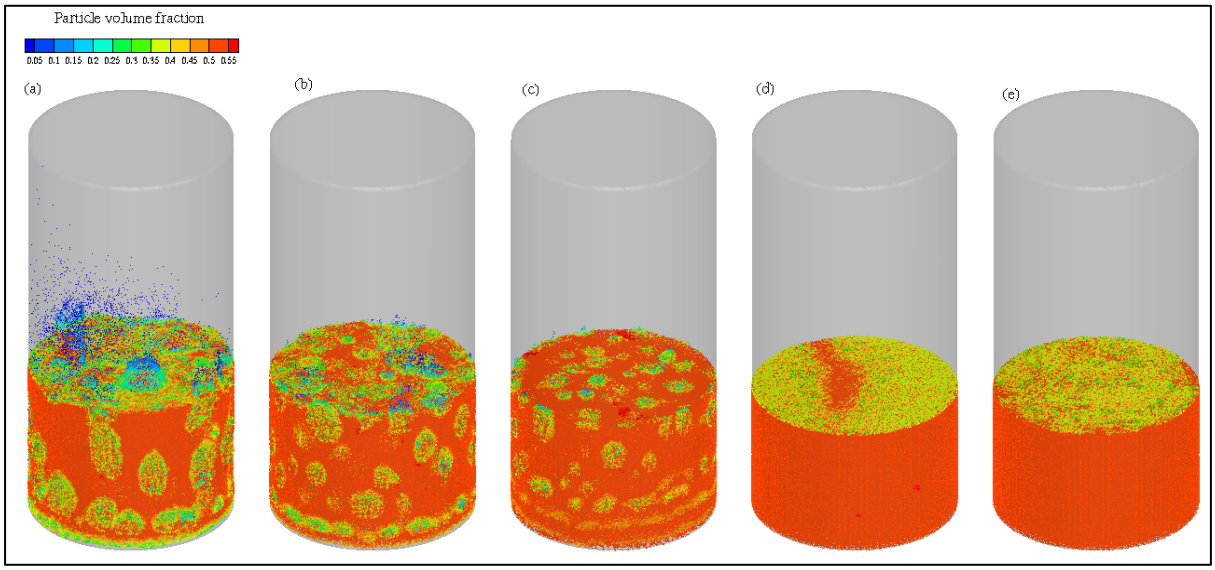

Figure 7.12: Contour of particle volume fraction at different particle sizes: (a) 500 μm, (b) 650 μm, (c) 800 μm, (d) 1000 μm and (e) 1200 μm.

The packed bed behaviour observed with increasing particle size is also reflected in the pressure drop profiles shown in Figure 7.13. Figure 7.13 presents the time-averaged pressure drop profiles for the different particle sizes at a constant gas velocity of 0.34 m/s. The graph depicts that as the particle size increases, the pressure drop across the bed decreases. This behaviour can be explained by the well-known Ergun equation, which relates the pressure drop across a fluid flow through a packed bed, to the particle size and other parameters like superficial gas velocity. The Ergun equation is given by [495]:

$$\frac{\Delta P}{L} = 150\frac{1-\varepsilon_m{}^2}{\varepsilon_m^3}\frac{\mu u_0}{\phi d_P{}^2} + 1.75\frac{1-\varepsilon_m}{\varepsilon_m^3}\frac{\rho_f u_0^2}{\phi d_p} \quad (120)$$

From the Ergun equation, it is clear that the pressure drop per unit length (ΔP/L) is inversely proportional to the particle diameter (d_p). This means that as the particle size increases, the pressure drop decreases under packed bed conditions, as observed for particle sizes between 650 and 1200 µm. The impact of this decreased pressure drop with larger particle sizes could lead to potential hot spot formation and thermal limitations, as evident from the increasing CO_2 concentration observed when the particle size was increased to 1200 µm. Moreover, it is well-established that the pressure drop in bubbling fluidised beds is generally higher than in fixed bed conditions [540].

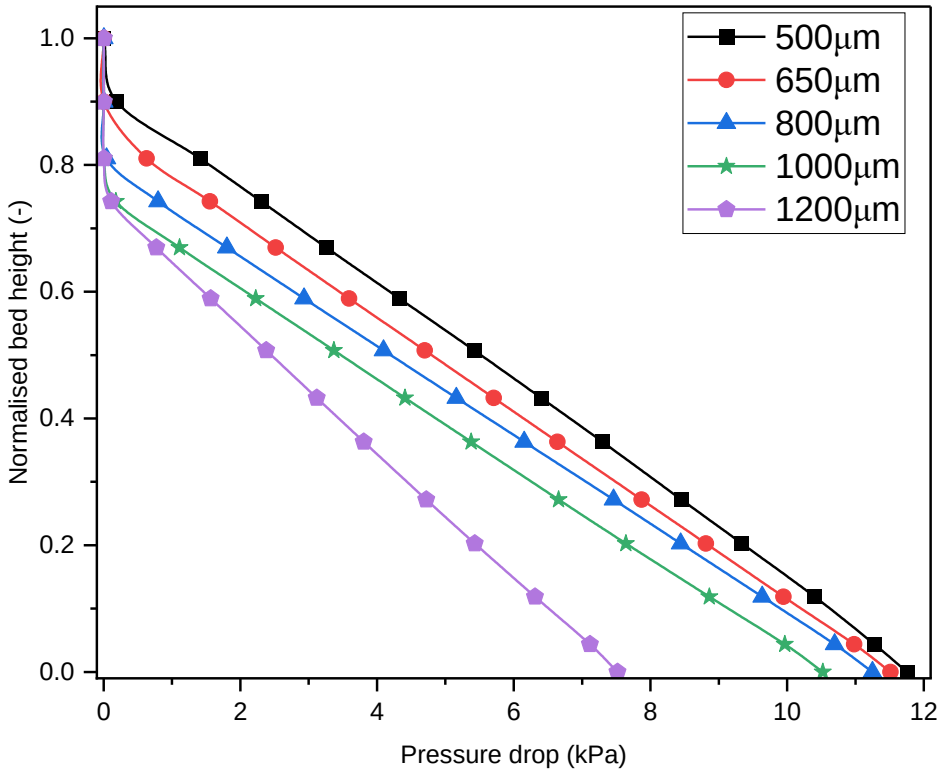

Figure 7.13: Time-averaged pressure profiles for SE-SR of methane at different particle sizes from 500 µm to 1200 µm along the normalised bed height.

While velocity was kept constant in this study, it would be interesting to investigate the behaviour of the process when the ratio of the superficial gas velocity to the minimum fluidisation velocity (u_o/u_{mf}) is kept constant. This approach would necessitate increasing the superficial gas velocities between 0.58 and ~2 m/s to maintain the bubbling fluidised state for particle sizes between 650 and 1200 µm, as the minimum fluidisation velocity is known to increase with increasing particle size.

7.3.2 Performance of 1MWth SE-SR capacity in circulating mode

The SE-SR process was further investigated in circulating mode to provide a more comprehensive understanding of the overall system performance, using a reduced model. In this modified design, the original bubbling bed reformer/carbonator was integrated with a bubbling bed calciner using loopseals, allowing the sorbent particles to internally circulate between the two reaction zones. The use of a reduced model in simulating the circulating mode allows for a computationally efficient approach while capturing the essential dynamics and interactions between the various process units.

Figure 7.14 presents the simulation results of the product gas composition, after 400 seconds simulation time, in the reformer and calciner when operating in circulating mode. In the reformer, the mole fractions of hydrogen and methane are seen to decrease by approximately 1%, while the CO and CO_2 compositions increased by a similar amount, relative to the product compositions of the standalone bubbling bed SE-SR reformer discussed in Section 7.3.1. This behaviour can be attributed to the circulation of hot solids between the reformer and calciner. The hot solids originating from the calciner, which operates at a much higher temperature than the reformer, increased the average bed temperature in the reformer above its initial temperature of 873 K. This higher temperature in the reformer has two noticeable impacts on the product gas composition. Firstly, the increased temperature favoured the SMR reaction, leading to enhanced methane conversion. This results in a decrease in the mole fraction of methane in the reformer's product gas, as more methane is converted to CO and hydrogen. Secondly, the higher temperatures in the reformer reduced the CO_2 sorption capacity of the sorbent material. This means that CO_2 capture from the product gas is slightly reduced, leading to an increase in the mole fraction of CO_2 in the reformer's output. The combined effect of increased methane conversion and reduced CO_2 sorption due to the elevated temperatures in the reformer explains the observed decrease in hydrogen and methane, and the increase in CO and CO_2 compositions in the product gas when operating in the circulating mode.

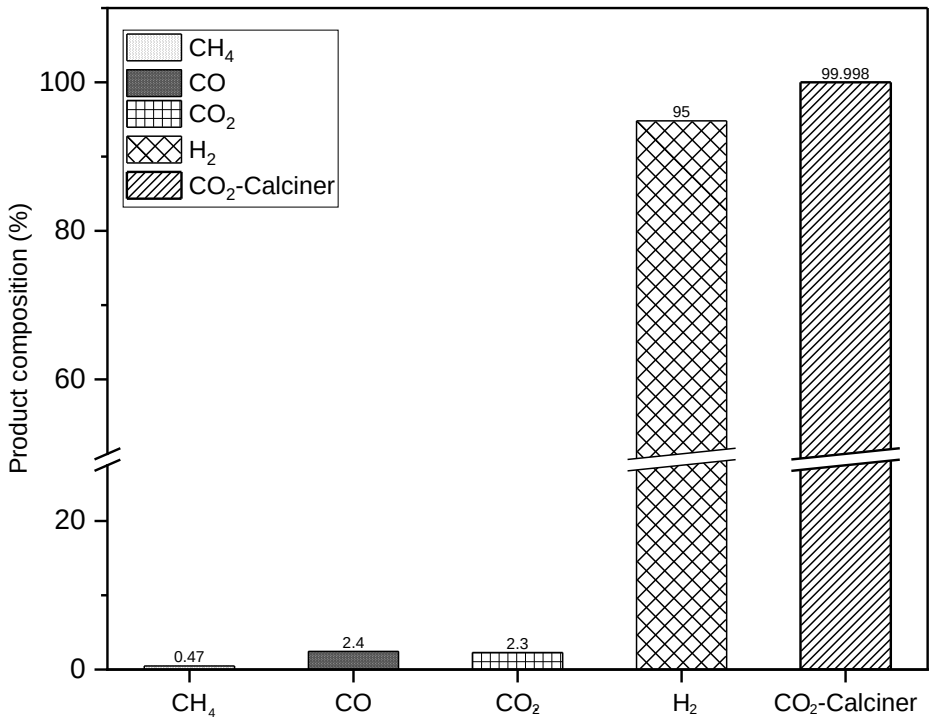

Figure 7.14: Distribution of product compositions in the reformer/carbonator and the calciner of the 1 MWth SE-SR of methane in CFB system.

Moreover, it has been earlier discussed that higher bed temperatures in the reformer adversely affects product composition through increased methane conversion and reduced CO_2 sorption. Meanwhile, the product gas in the calciner was mainly composed of CO_2, indicating an absence of unconverted feed gas or hydrogen slipping into the calciner from the reformer. This suggests effective separation and capture of the hydrogen-rich stream in the reformer.

As shown in Figure 7.15, the temperature profile within the reformer increases significantly for both the particle and fluid phases. The average particle temperature reaches 977.9 K, while the fluid temperature reaches 982.2 K, representing a substantial rise from the initial temperature of 873 K. Immediately after the reformer, in the first loopseal (Loopseal 1), the temperature remains slightly higher than that of the reformer, maintained around 983 K. This suggests that the hot solids flowing from the reformer are maintaining the elevated temperature in the loopseal. In contrast, the temperature drop observed in the calciner is much more pronounced, with a 144 K decrease for the particle temperature and a 122 K decrease for the fluidising gas temperature. The average temperature in the calciner is about 1040 K, representing a drop from an initial temperature of 1173 K. This larger

temperature difference indicates that the calciner is effectively removing a significant amount of heat from the system. The second loopseal returning solids from the calciner to the reformer (Loopseal 2) reaches a markedly higher average temperature of around 1039 K, compared to Loopseal 1. This temperature rise in the second loopseal is a direct consequence of the hot solids being introduced from the calciner, leading to a substantial increase in the local temperature prior to re-entering the reformer bed.

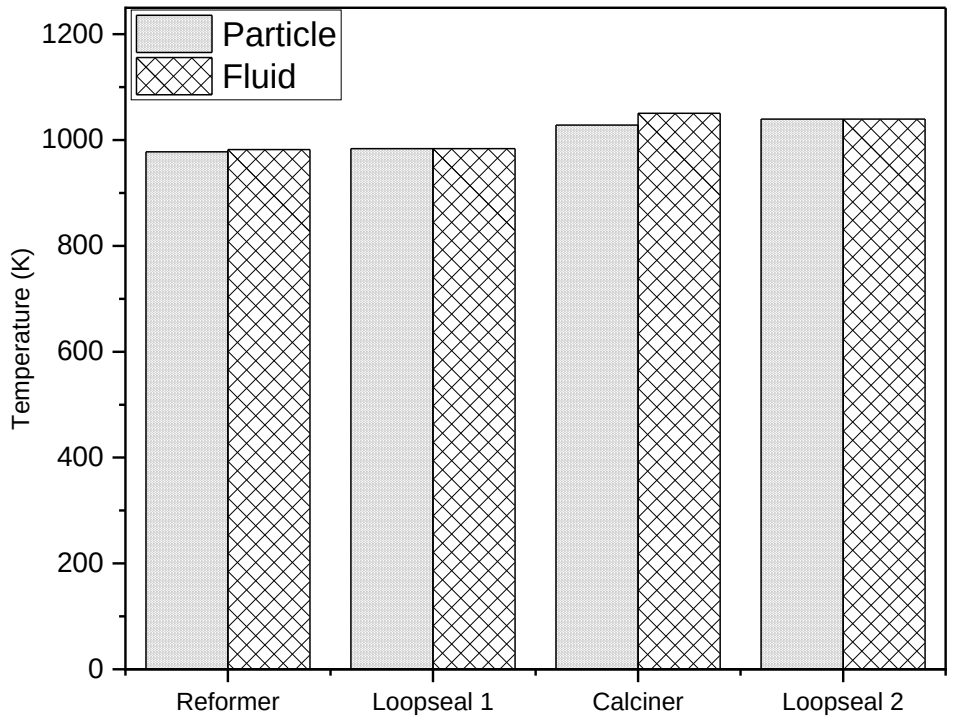

Figure 7.15: Particle and fluid temperature distribution in the CFB components – reformer/carbonator, loopseals and calciner after 400 seconds simulation time.

The contour plots of the time-averaged temperature distribution within the system, presented in Figure 7.16, provide further insights into the thermal behaviour and its spatial variation across the different unit components. Starting with the particle temperature, the contour plots reveal a relatively uniform distribution in the bottom sections of both the reformer and the calciner. This suggests that the solid particle phase maintains a consistent temperature in the lower regions of these reactors, which are dominated by the dense bed of solids. The uniform particle temperature in these areas indicates efficient heat transfer and mixing within the dense particle bed, ensuring a homogeneous thermal environment. However, the temperature distribution is less uniform in the section of the

loopseals connecting the reactors. These transition zones exhibit localised temperature variations, likely due to the complex flow patterns and mixing dynamics of the solid particles as they circulate between the reactors. The presence of these temperature gradients in the loopseals underscores the importance of carefully designing and managing these interconnected components to ensure the desired thermal conditions are maintained throughout the system.

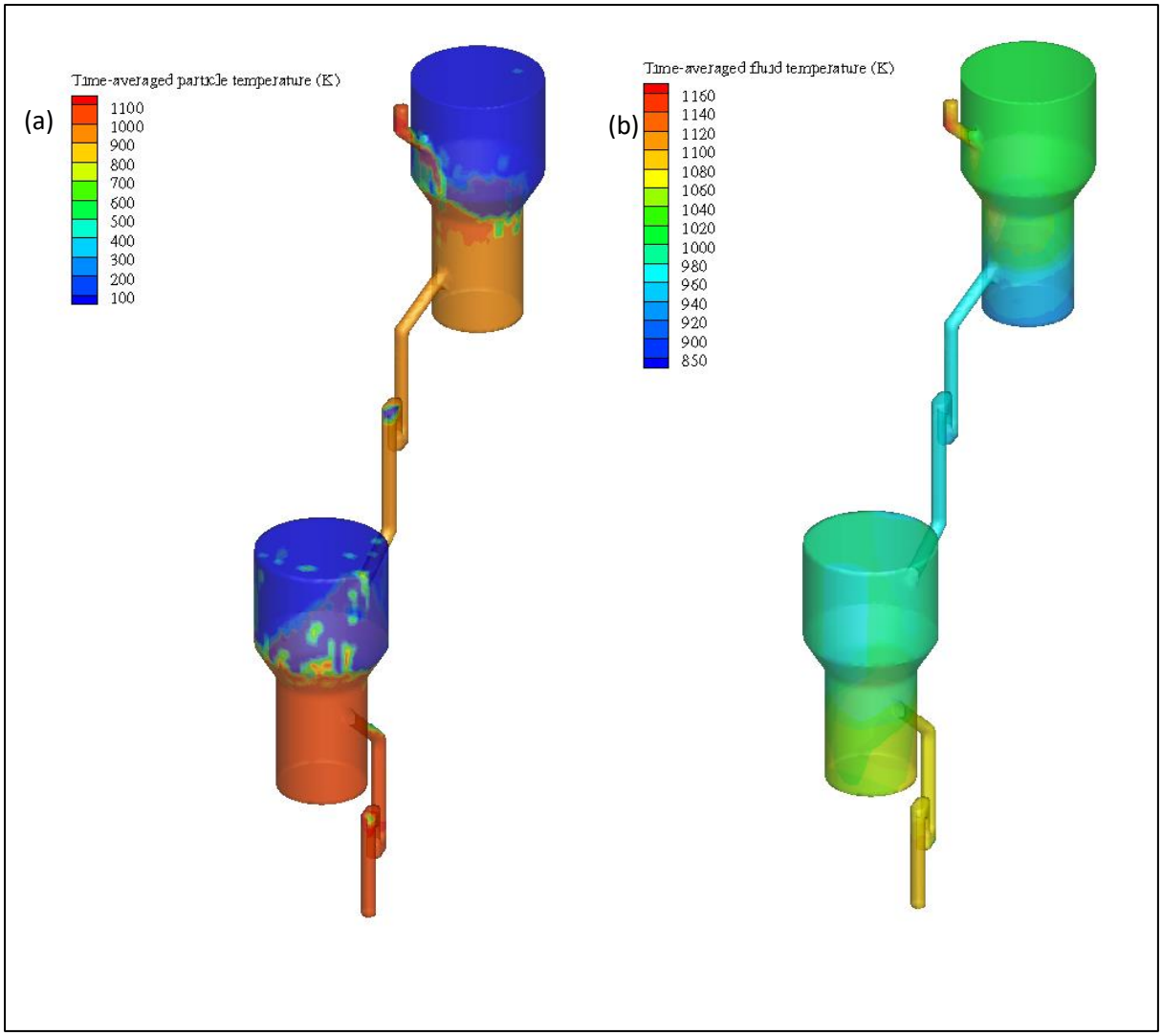

Figure 7.16: Contour plot of the time-averaged (a) particle and (b) fluid temperature distribution for the 1 MWth SE-SR of methane in CFB system.

Turning to the fluid temperature in Figure 7.16b, the contour plots show a more uniform distribution across the different reactor sections. In the reformer, the fluid temperature is observed to increase gradually from the bottom to the top, indicating that the hot solids entering the reformer from the calciner are effectively heating the gas phase as it flows upward. This temperature gradient in the reformer can influence the reaction kinetics and product composition, as discussed earlier. Conversely, in the calciner, the fluid temperature exhibits a slight axial reduction from the bottom to the top. This

suggests that the heat is being effectively extracted from the gas phase, through the endothermic decomposition of the sorbent material and the release of CO_2. Notably, at the solid inlet to the reformer, the fluid temperature is observed to be higher, a direct consequence of the hot solids coming from the high-temperature calciner.

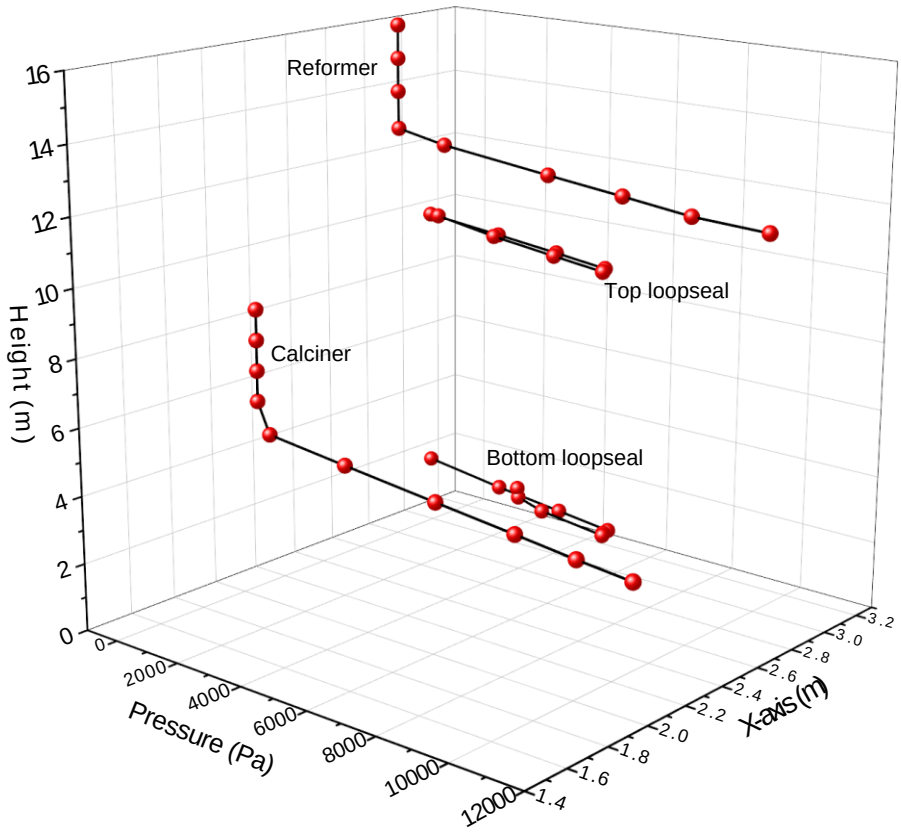

Figure 7.17: Pressure profile in the reactor components for the 1 MWth SE-SR of methane in CFB system.

The pressure profiles within the different components of the SE-SR CFB system, as depicted in Figure 7.17, provide insights into the fluid dynamics and flow resistance encountered throughout the system. There is a reducing pressure profile along the height of both the reformer and calciner beds due to the typical hydrodynamic behaviour of fluidised beds [541]. As the fluidising gas flows upward through the dense particle bed, the pressure drop tends to decrease along the bed height due to the decreasing solids inventory and the expansion of the gas volume.

Interestingly, when comparing the maximum pressure drop at similar locations (ΔP/H), the calciner was found to have a slightly higher pressure drop than the reformer, by approximately 1.62%. This small difference in pressure drop between the two reactors can be understood by considering the

differences in the operating conditions and the physicochemical processes occurring within each unit. Within the calciner, the endothermic sorbent regeneration reaction results in a substantial temperature decrease of over 100 K, as evidenced in Figure 7.15. This cooler temperature for the nitrogen gas leads to an increase in the density of the fluidising gas. Higher fluid density is known to correlate with increased flow resistance. In fluidised beds, pressure drop has been reported to decrease with increasing temperature due to the reduction in gas density at elevated temperatures [542].

Regarding the pressure drop in the loopseals, the results show that the top loopseal (Loopseal 1) experiences a higher pressure drop than the bottom loopseal (Loopseal 2). The maximum pressure drops were 6.11 kPa and 5.90 kPa for Loopseal 1 and Loopseal 2, respectively. This behaviour can be correlated to increased solids carryover and circulation momentum in loopseal connected to reactor exits versus inlets. Previous studies have established that bed inventory of solid particles in a CFB system has a significant influence on the pressure drop across various components [543]. Specifically, an increase in the bed inventory leads to a higher pressure drop. The denser particle bed in Loopseal 1 contributed to the observed higher pressure drop of 6.11 kPa in this component. In contrast, Loopseal 2 at the bottom of the system required a higher aeration rate to facilitate the efficient circulation of solids from the calciner to the reformer. A previous study has shown that, an increase in the aeration rate leads to a higher solid circulation rate, when fluidising gas velocity and bed inventory are kept constant [544]. The higher aeration rate maintained in Loopseal 2 kept the solid concentration relatively lower in this section, compared to Loopseal 1. This reduced solids concentration in Loopseal 2, then resulted in a lower pressure drop of 5.90 kPa, as observed in the results. The solid concentration within the system is visually depicted in Figure 7.18.

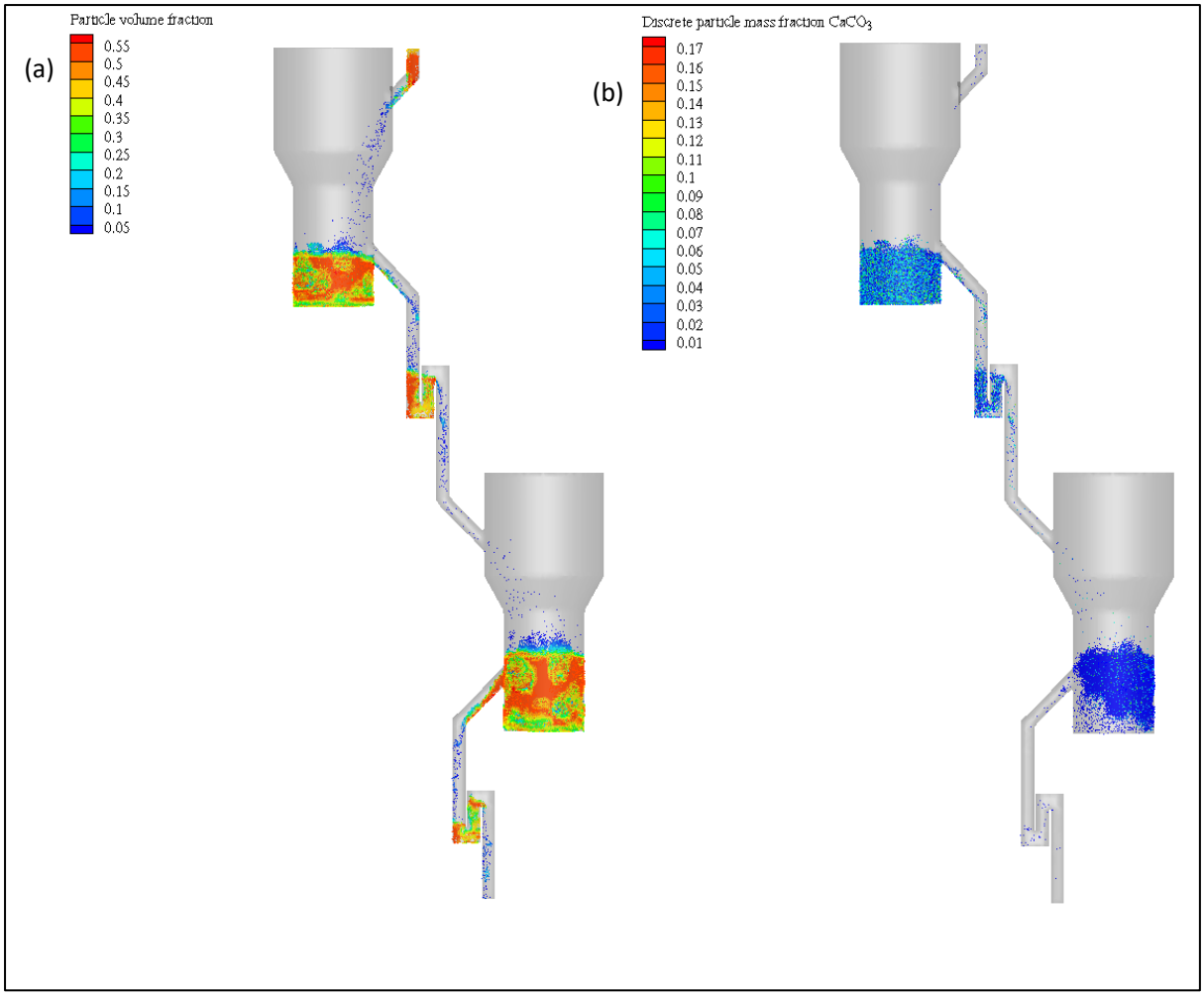

Figure 7.18: Contour plot of (a) particle volume fraction and (b) $CaCO_3$ mass fraction distribution for the 1 MWth SE-SR of methane in CFB system.

Figure 7.18a depicts the contour plot of the spatial distribution in the concentration of solid particles throughout the different components of the SE-SR CFB system. In the reformer, the contour plot shows a relatively high solid volume fraction, shown in red, and uniformly distributed bubbles in the bottom section, indicating a dense particle bed. This dense bed region is essential for efficient contact between the solid sorbent, the reactant gases, and the heat transfer required for the SMR reactions. At the top of the reformer bed, the concentration lessens into dilute dispersion, depicted in blues, where solids become less dense and bubbles erupt. This behaviour aligns with expected fluidisation hydrodynamics [545]. The loopseals connecting the reformer and the calciner also exhibited higher particle volume fractions. This observation suggests that the loopseals effectively captured and circulated the solid particles between the two reactors, maintaining a consistent solids inventory and flow throughout the system. Evidently, Loopseal 1 displays strongly dense regions, supporting its higher measured pressure drop, in comparison with Loopseal 2.

Complementing the solid volume fraction distribution, the $CaCO_3$ distribution contour plot provides insights into the spatial distribution of the sorbent material within the system. In the reformer, the $CaCO_3$ concentration is slightly higher in the bottom section, where the dense particle bed resides. This distribution aligns with the expected behaviour discussed in Chapter 4, as the sorbent material is primarily responsible for the CO_2 capture in the reformer. Nevertheless, across the reformer the sorbent material is evenly distributed, without noticeable particle segregation. The calciner exhibited a reverse trend, with strong $CaCO_3$ depletion at the bottom, indicating efficient desorption in this region.

7.3.3 Effect of scale

The previous section focused on a 1 MWth hydrogen production system, providing insights into the thermal dynamics, flow characteristics, and overall performance within the system. In this section, the effect of scale is investigated by expanding the analysis to 50 MWth and 150 MWth hydrogen production capacities to cover a range of small to medium industrial scale applications. This analysis will focus on the solid-gas flow patterns, pressure profiles, and product gas composition. Additionally, a quantitative equation was developed through non-linear regression analysis to describe the scale factor relationship based on methane conversion. The findings from this multi-scale analysis will contribute to the development of design guidelines and operational strategies for the successful implementation of SE-SR of methane at industrial scales.

7.3.3.1 Bubble distribution and particle volume fraction

The dimensionless bubble distribution plotted in Figure 7.19 showed some similarities across various scales, albeit with slight deviations worth further examination. It is observed that in Scale 1 (1MWth), the bubble at the bottom appears marginally larger than those in Scales 2 (50 MWth) and 3 (150 MWth). Conversely, at the top of the bed, scales 2 and 3 demonstrate comparatively larger bubble sizes than the 1 MWth scale. Interestingly, this observation parallels findings in Chapter 6 between bubble size distribution of the bench-scale and 1 MWth systems, where the bench-scale exhibited larger bubbles at the bottom. However, the disparity between Scales 2 and 3 diminishes, with bubble sizes displaying greater similarity, as depicted in Figure 7.19. Knowlton et al. [517] have observed that scaling parameters may change rapidly at small scales but level out to a near-constant value as size increases. This behaviour appears validated here by the diminished difference between the 50 and 150 MWth bubble profiles.

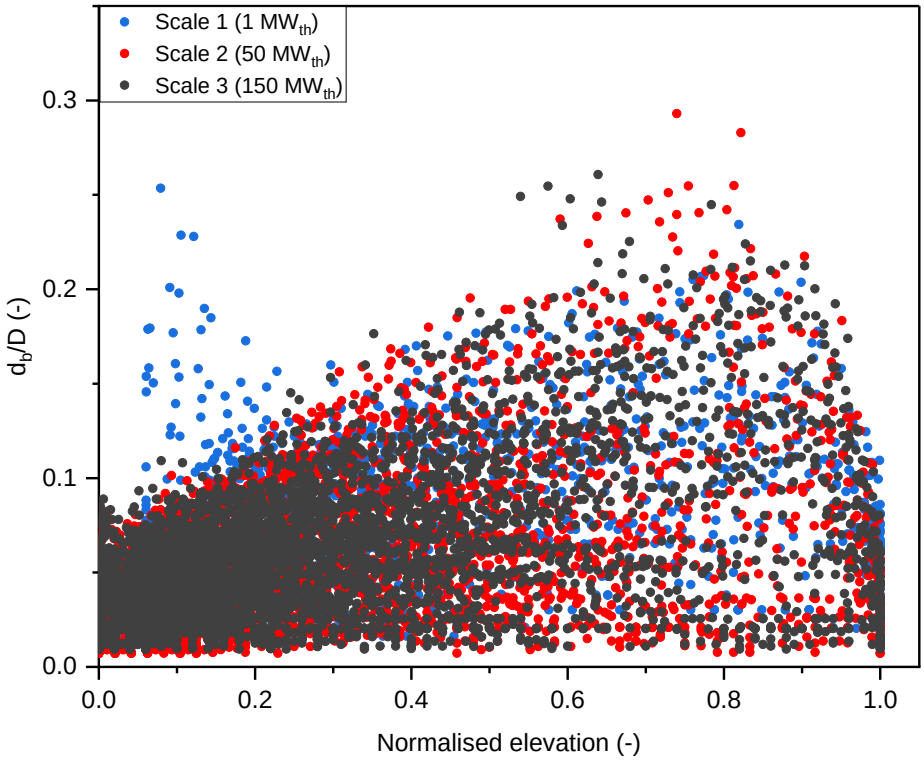

Figure 7.19: Scatter plot of normalised bubble size distribution at different scales – 1, 50 and 150 MW_{th}.

The contour of particle volume fraction in Figure 7.20 illustrates the solid-gas flow patterns and particle distribution across different scales within the fluidised bed reformer/carbonator. Across all scales modelled, the volume fraction contours exhibited lower solids concentrations in the bottom region, indicating the typical formation of initial bubbles where the gas enters. The contour map also shows bubbles preferentially populating the central areas. This behaviour is well-established, as the centre offers lower frictional resistance for bubble ascent early in the bed. Moreover, previous studies have also observed this phenomena of centre-dominant bubble accumulation in fluidised beds, attributed to weaker wall interference allowing coalescence into larger cylindrical bubbles [546,547].

Furthermore, at the 1 MWth scale, the contour in Figure 7.20 indicates a relatively lower volume fraction towards the freeboard region, suggesting less particle ejection compared to the larger scales. This observation could be attributed to the milder hydrodynamic conditions prevalent in smaller reactors. Lower gas velocities and shallower bed depths typically associated with small-scale reactors may result in reduced turbulence and less vigorous particle movement, thus limiting particle entrainment into the freeboard. Progressing to 50 and 150 MWth scales, the contour exhibits higher solid volume fractions extending into the freeboard region, indicating a greater propensity for particle ejection at larger scales. This ties directly to the increased bubble size and breakage propounded to explain the shifting of 50-150 MWth bubble size distributions seen in Figure 7.19.

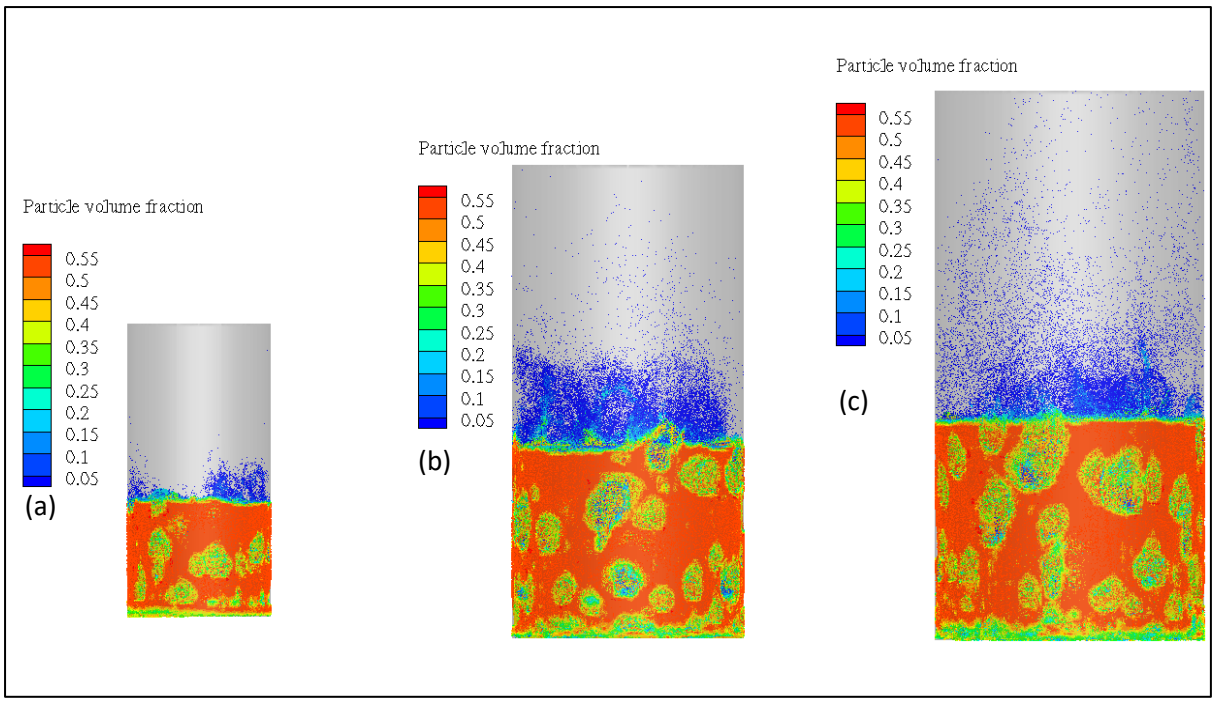

Figure 7.20: Contour of particle volume fraction for the reformer/carbonator at different scales: (a) 1 MW_{th}, (b) 50 MW_{th} and (c) 150 MW_{th}.

7.3.3.2 Product composition

The composition of product gas from the reformer/carbonator for each of the scales was determined by averaging results of the last 10 seconds of simulation time when simulation reached quasi-steady state, while maintaining constant particle sizes across scale and under isothermal conditions. Figure 7.21 shows very slightly scale-dependent trends for the compositions.

The hydrogen composition in the product gas showed a slight increase as the scale was increased. At the smaller Scale 1, the hydrogen composition was around 96%. This increased to 96.3% for Scale 2 and further to 96.8% for Scale 3. There are number of reason this could happen. Firstly, the high degree of turbulence achieved in the larger reactors, as discussed in Section 7.3.1, likely led to improved mixing between the reactants and the particles. This more effective mixing would enhance the steam reforming reaction kinetics and drive the reaction further towards production of hydrogen. This assumption of high level of turbulence corresponding to effective mixing, is often valid for large-scales, as the relationship between turbulence intensity and mixing efficiency can be more nuanced at smaller scales [548]. Secondly, the larger reactors, with their increased overall volume, could have provided more total active sites for the reforming and carbonation reactions to occur. This increase in active sites, particularly on the sorbent, could further enhance hydrogen production by favouring these reactions over competing side reactions. Thirdly, any heat transfer or mass transfer limitations within

the sorbent particles that may be present at the smaller scales could be lessened in the larger reactors. However, further experiments are still needed to definitively elucidate the cause of this behaviour.

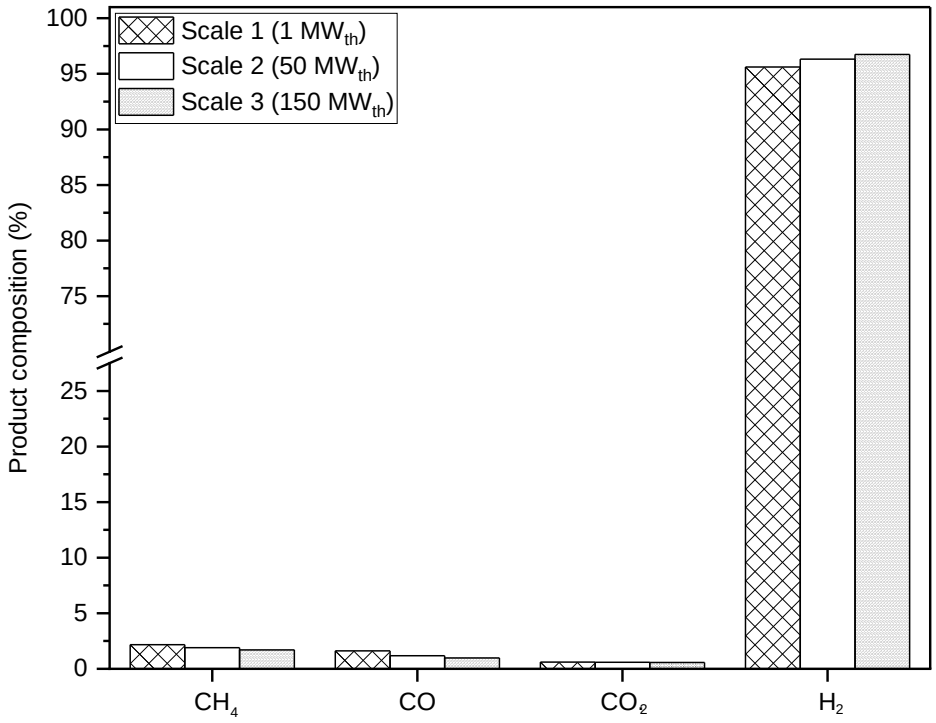

Figure 7.21: Composition of CH_4, CO, CO_2, and H_2 in the product gas of the reformer/carbonator at different scales.

Accordingly, the methane, CO and CO_2 contents all saw a decreasing trend with scale. The decreasing trends observed in the CO and CO_2 compositions, from 1.6% and 0.6% at the 1 MWth scale to around 0.98% and 0.58% at the 150 MWth scale, respectively, demonstrate improved CO conversion and CO_2 sorption. Conversely, the slight reduction in methane composition from around 2% at the 1 MWth scale to 1.7% at the 150 MWth scale indicates improved methane conversion.

In Figure 7.22, the species distribution contours depict the reaction progression within the reactors across scales. Near the bottom, high methane concentrations are observed for all cases. This is expected, as this is the region where the reactant gas (methane) is introduced and the initial steam reforming reactions take place. As the gas flow upwards through the reactor, the methane concentration gradually decreases along the reactor height, indicating the progressive conversion of methane to other products. Slightly above the methane-rich bottom region, another consistent feature

is the presence of a zone with higher CO concentration. This CO-rich region is due to the intermediate formation of CO as an early product of the methane steam reforming reaction. However, similar to the methane, the CO concentration also decreases along the reactor height, suggesting that water-gas shift reaction is converting the CO to hydrogen and CO_2. Notably, the height and uniformity of these stratified reaction profiles remain highly consistent between scales. Analogous to the CO distribution, the CO_2 concentration shows a similar trend, with higher values in the middle regions of the reactor and a decrease towards the top due to CO_2 sorption by the sorbent. Finally, at the top region of the reactor, the dominant species is observed to be hydrogen.

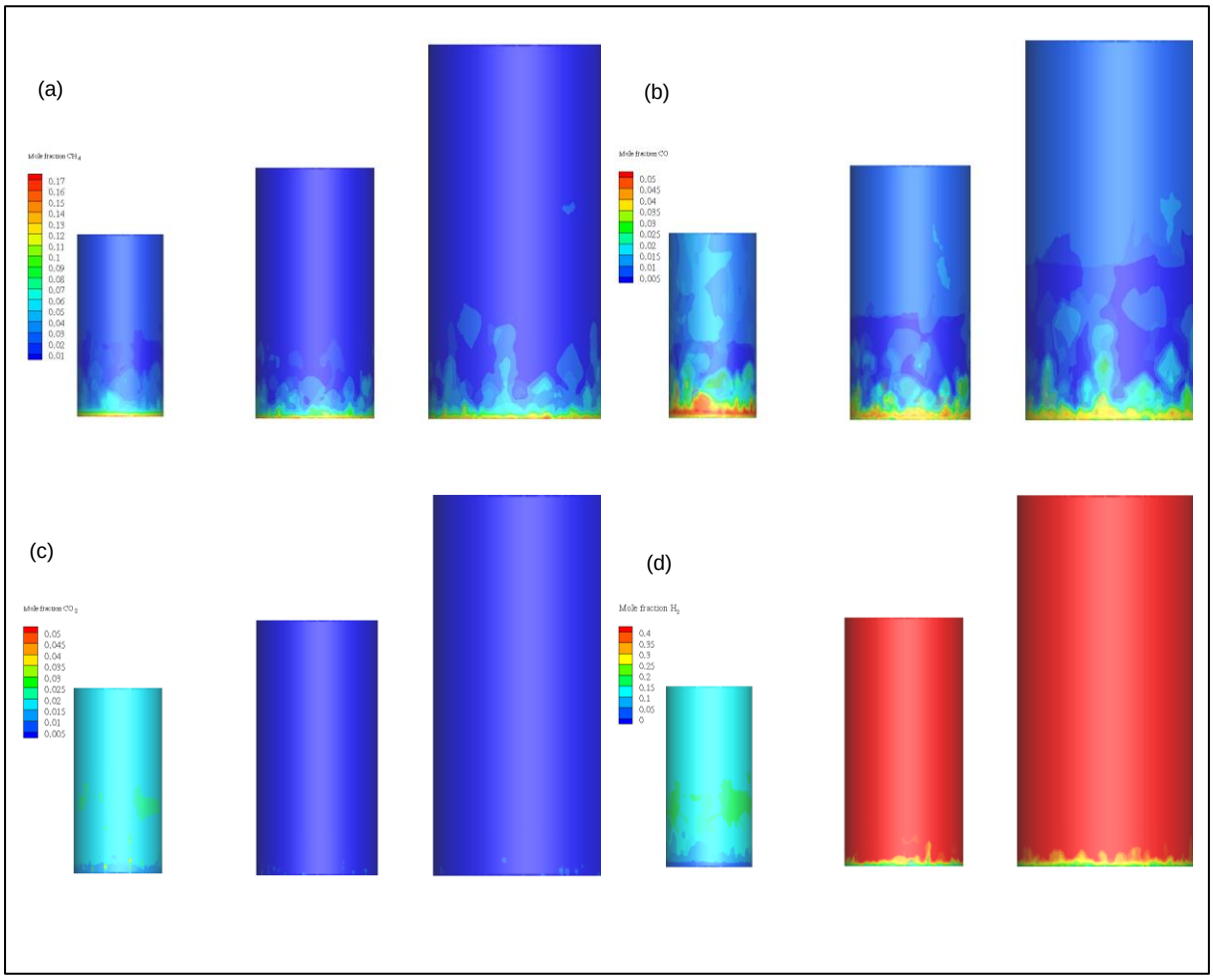

Figure 7.22: Contour of product distribution (a) CH_4, (b) CO, (c) CO_2, and (d) H_2 in the reformer/carbonator at different scales from 1 to 150 MWth, coloured by mole fraction (wet basis).

7.3.3.3 Pressure drop profile

The data in Figure 7.23 shows a significant rise in the maximum pressure drop, from 11.6 kPa at the 1 MWth scale to 39.8 kPa at the 50 MWth scale and further to 62.1 kPa at the 150 MWth scale. One of the primary reasons for the higher pressure drop in the larger-scale reactors is the increase in bed

height. As the reactor size is scaled up, the bed depth also increases to accommodate the larger volumetric throughput of the reactants. According to the Ergun equation, which describes the pressure drop in a packed bed, the pressure drop is directly proportional to the bed height [428]. Therefore, the taller beds in the 50 MWth and 150 MWth scales naturally result in higher overall pressure drops compared to the smaller 1 MWth scale. While it is true that the increase in pressure drop with scale is a common challenge in the scale-up of fluidised bed systems and is not unique to the SE-SR process, is important to note that the magnitude of the pressure drop can have significant implications for the operation of this SE-SR system at larger scales.

According to Knowlton et al. [517], scaling up enlarges the bed depth dimensions, creating a much greater pressure differential across the enlarged height that intensifies gas compression effects. Particularly, the high pressure at the bottom drives the gas to find the path of least resistance to efficiently reach the lower pressure at the top. This can eventually result in channelling flow rather than uniform fluidisation. However, operating at higher system pressures reduces this risk. That is because increasing the baseline system pressure decreases the relative impact of the same differential pressure across the bed height, on gas compression. Put another way, the gas is compressed over a smaller range relative to the operating pressure. Therefore, taller beds are less prone to bypassing behaviours at higher operating pressures. This mean that the higher pressure drops encountered in larger-scale SE-SR reactors may require the use of more powerful blowers or compressors to overcome the increased flow resistance, leading to higher energy consumption and operating costs [496].

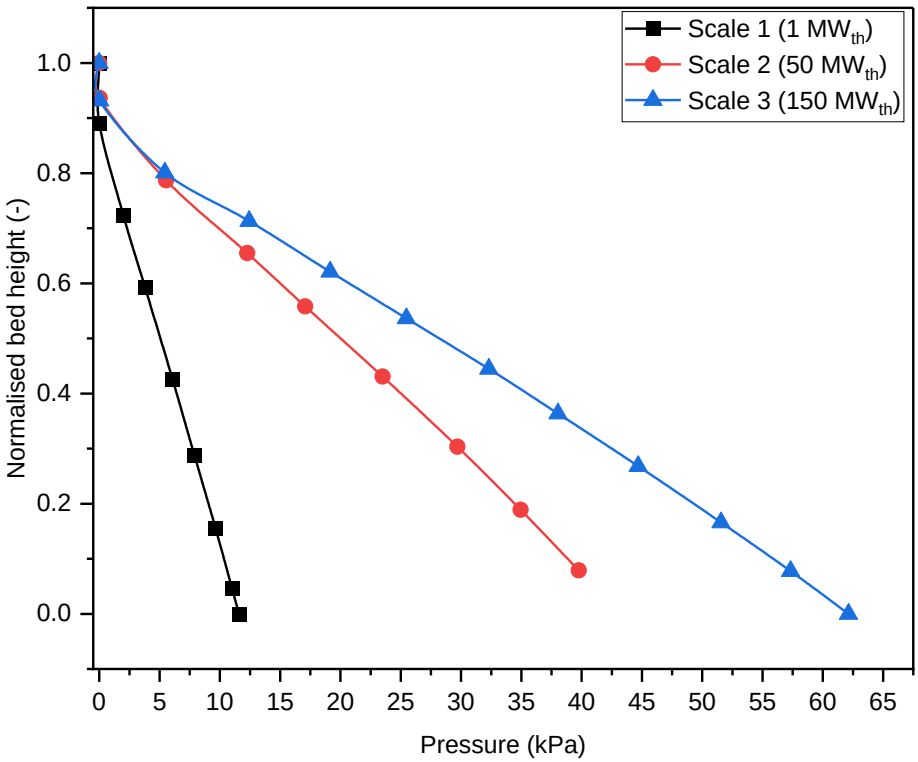

Figure 7.23: Pressure drop profiles along the normalised bed height of the reformer/carbonator at different scales.

7.4 Summary

This chapter has explored the performance of scaled-up SE-SR of methane, analysing the impact of various operating parameters and performance at much larger scales. The analysis began by examining the influence of bed temperature, particle size, and bed aspect ratio on the product composition in a bubbling fluidised bed reactor for 1 MWth hydrogen production.

Building upon the 1 MWth bubbling bed studies, the focus then shifted to evaluating the performance of the SE-SR process in a circulating mode, where the reformer/carbonator was integrated with the calciner and loopseals using a reduced model. This approach allowed for the examination of the complete process cycle, including sorbent regeneration and continuous operation. The product distribution in the reformer under circulating mode conditions revealed changes compared to the standalone bubbling bed, with reductions in hydrogen and methane compositions, and increases in CO and CO_2 concentrations, which were attributed to the impacts of sorbent regeneration and thermal changes.

Thereafter, the system with 1 MW hydrogen production capacity was scaled up to larger 50 MW and 150 MW scales to examine the effects and effectiveness. The analysis highlighted the observed differences in the bubble distribution and particle entrainment within the reformer at the different scales. Pressure drops considerations were discussed and a scaleup function model based on methane conversion was also proposed.

The CPFD analysis of SE-SR conducted in this chapter for 1 – 150 MWth has aided in understanding the micro-level details of the process, which are critical during the initial stages of technology development and scale-up. Now that the behaviour of this process at large scales has been established, the focus of the next chapter shifts to evaluating the economic viability and overall system performance at larger, industrially relevant scales.

8 Bench-marking large-scale SE-SR of methane against conventional technologies for low-carbon hydrogen generation

This chapter is based on the peer-reviewed publication:

- Udemu C, Font-Palma C. Potential cost savings of large-scale blue hydrogen production via sorption-enhanced steam reforming process. Energy Convers Manag 2024;302:118132. https://doi.org/10.1016/j.enconman.2024.118132.

8.1 Introduction

This chapter adopts a process simulation tool (Aspen Plus® software), incorporating more complete unit operations (including hydrogen compression unit), to benchmark SE-SR of methane against commercially competitive blue hydrogen technologies, including SMR and ATR-GHR with CCS. These technologies have been reviewed in Section 2.2.3 of Chapter 2. An advanced variation of the traditional SMR, known as gas heated reforming (GHR), can be integrated with an ATR, in a novel configuration. The heat required for steam reforming in the GHR is supplied by heat exchange from a high-temperature effluent gas leaving the ATR, as opposed to furnace used in conventional SMR process [549]. The combined system can serve the purpose of improved energy efficiency (for the SMR side), reduced oxygen consumption and improved H_2/CO ratio (for the ATR side). There are few studies concerning this combined ATR-GHR system available in the public domain [106,549]. In this study, a CCS unit will be integrated into the SMR and ATR-GHR technologies to capture emitted CO_2 from the plants.

Amine-based absorption is a widely researched and implemented approach for CO_2 capture from industrial flue gases [550,551] and have been retrofitted into existing reforming plants [552]. Monoethanolamine (MEA) is the most used solvent but its high energy consumption during the regeneration phase is a major concern. This has led to the development of tertiary amines such as methyldiethanolamine (MDEA) as alternative solvents. MDEA, when modified or activated with high CO_2-reactive compounds like piperazine (PZ), enhances CO_2 absorption and reduces energy requirements compared to other amines [553]. Oh et al. [554] evaluated the performance of activated (PZ) MDEA based CCS, integrated with hydrogen production plant, under different operating parameters such as solvent composition, CO_2 removal efficiency and CO_2 loading. Sensitivity analysis showed that CO_2 removal efficiency and solvent composition had great impacts on energy consumption. Optimal PZ and MDEA concentrations varied with CO_2 removal target. At high CO_2

removal efficiency of 95%, higher MDEA concentration reduced energy needs due to increased solvent flow rate. At 95% removal efficiency, the reboiler duty slightly decreased when PZ concentration increased from 10 to 15 wt%, whereas at 90% removal efficiency, the reboiler duty increased for PZ concentrations of 10% or higher. Similarly, Kum et al. [555] evaluated the role of activated MDEA solvent to significantly reduce thermal energy requirements and CO_2 capture costs in a medium-sized hydrogen production plant, with an output of approximately 5,126.5 kmol/h (equivalent to 340 $MW_{th\ (LHV)}$). Using process simulation and techno-economic optimisation, they found that at 90 and 99% CO_2 capture rates, the reboiler duty of the CCS plants was around 70% lower, compared to typical amine-based processes.

For a large-scale blue hydrogen production plant, an additional important consideration is hydrogen storage and transmission. Some economic analyses in the literature currently overlook the costs linked to hydrogen storage downstream of production, with initial techno-economic assessments often concentrating solely on the production process. This chapter lays important groundwork by considering hydrogen storage costs, since hydrogen storage can introduce further capital expenditures and energy penalties that can influence end-user pricing. Several hydrogen storage methods exist, including physical methods like compressed hydrogen, adsorption method, as well as chemical methods such as metal hydrides. However, among these, compressed hydrogen remains the most established storage method [556]. Hydrogen is usually produced at low pressures from these reforming plants; therefore, further compression is required to load the hydrogen into vessels or pipelines for storage and distribution. Centrifugal and reciprocating compressors are generally used for hydrogen compression, with key design factors including the discharge pressure, flow rate and compressor staging [557]. In this work, hydrogen compression to 200 bar is adopted to meet both storage and pipeline transport requirements [558].

SE-SR is a promising hydrogen production technology but remains in its early stages of development, with very few small-scale pilot plants in existence [146]. Because of its low TRL, SE-SR requires further evaluation to strengthen understanding of its real-world costs under scaled-up conditions. Therefore, the aim of this study is to benchmark SE-SR of methane against SMR and ATR-GHR with CCS for large-scale blue hydrogen production, whilst providing insights into the end-to-end potential cost reduction opportunities as the processes are scaled up. SE-SR technology and well-established SMR and ATR-GHR processes, integrated with piperazine/methyl diethanolamine (a-MDEA) CCS technology, were assessed based on a hydrogen production capacity of 600 $MWth_{(LHV)}$. Considering that some major energy companies have announced projects in the 500 – 1000 MWth range for commercial-scale blue hydrogen plants, these processes were also scaled up to 1000 $MWth_{(LHV)}$ to gain insights into their scalability. To enhance CO_2 removal from high-pressure process gas while reducing reboiler duty, an

improved a-MDEA CCS configuration was adopted, which involves splitting and recycling semi-regenerated solvent back into the absorber column. The SE-SR configuration adopted consists of an oxy-fuel combustion unit used to supply heat to the calciner. Cost sensitivity analysis was also conducted for these technologies with the impact of carbon pricing extensively studied. These plants were simulated using Aspen Plus® process simulation software, and the process models were validated against literature data.

8.2 Methods

This study conducts a comparative assessment of SE-SR technology and SMR and ATR-GHR (with CCS) technologies in the context of a newly constructed large-scale hydrogen production facility, including hydrogen compression, in the Humber region, UK. Using natural gas as the major feedstock, 600 MW hydrogen production capacity was evaluated, similar to the proposed capacity for the Hydrogen to Humber (H2H) Saltend project [559]. Methyldiethanolamine blended with an activator – piperazine – (a-MDEA) is used as the CO_2 capture solvent due to its high CO_2 removal rate [553]. SMR without CCS is used as the reference case for performing the cost assessment for the hydrogen plants, as described in Table 8.1.

Table 8.1: Summary of all the cases studied.

Production capacity	Cases	Description
600 MW	SMR-600	Reference hydrogen production by steam reforming without carbon capture.
	SMR-CCS-600	Hydrogen production by steam reforming with a-MDEA carbon capture.
	SE-600	Sorption-enhanced steam reforming plant
	AG-CCS-600	Autothermal and gas-heated reforming with a-MDEA carbon capture plant.

8.2.1 Process description and flow diagram

8.2.1.1 Steam methane reforming (SMR)

The process configuration and conditions for the SMR process studied, follows that of the industrial SMR plant described by Salem et al. [560]. High-pressure natural gas is supplied by the UK National Transmission System (NTS) and laminated to 30 bar. As shown in Figure 8.1, the fuel is pre-reformed

at 450°C over a nickel-based catalyst. The pre-reformer unit helps to breakdown the C2-C4 hydrocarbons present in the natural gas and improve hydrogen yield. Product stream from the pre-reformer is sent to the primary reformer to produce syngas. Due to the highly endothermic nature of steam reforming reaction, the primary reformer is operated at 870°C and steam-to-carbon ratio of 3, in the presence of a nickel-based catalyst. The generated syngas from the reformer is shifted under medium temperature to produce more hydrogen, which is then sent to the purification section. Using a medium temperature shift converter eliminates the need for two separate shift converters and is operated at a low temperature of 314°C, in the presence of $CuO/ZnO/Al_2O_3$ catalyst [561]. The process gas from the shift converter is then directed towards a four-bed pressure swing adsorber (PSA) unit, where 90% hydrogen is recovered at 99.99% purity, and the PSA off-gas directed to the furnace (with make-up natural gas) to produce heat for the plant [562]. Whilst the heat generated by the furnace is supplied to the reformer, the produced hydrogen is further compressed to a medium pressure of 200 bar to enable transport via pipelines or tube trailers. This SMR process is used as the base case and has no CO_2 capture unit integrated to it, whereas the SMR-CCS cases have CCS unit integrated at the exit of the reformer furnace. The CCS unit is described later in the section.

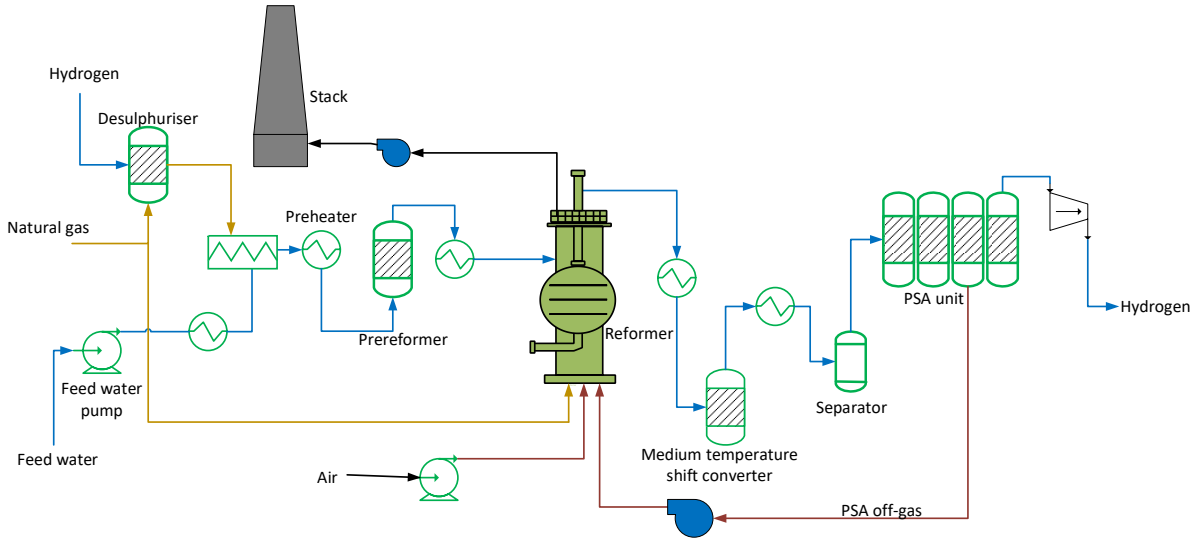

Figure 8.1: Process flow diagram for the conventional steam methane reforming process.

8.2.1.2 Sorption-enhanced steam reforming (SE-SR)

The SE-SR process, as shown in Figure 8.2, includes a dual bubbling fluidised reformer/carbonator and calciner, an oxyfuel combustor, pressure swing adsorption (PSA) columns, heat exchangers and other supporting and auxiliary units. Hydrogen production and CO_2 capture takes place in the same reactor – reformer/carbonator. In the fluidised bed reformer/carbonator, natural gas is reformed with steam at an S/C ratio of 5, in the presence of a nickel-based catalyst to produce mainly hydrogen and CO_2

[243]. The calcined dolomite sorbent material captures the CO_2 generated during the reforming process, thereby shifting the equilibrium of the reforming reactions towards higher hydrogen yields, according to Le Chatelier's principle. The spent sorbent is regenerated in the calciner at a high temperature of 900°C and recycled to the reformer/carbonator [563]. Hydrogen-rich stream from the reformer is sent to the PSA to purify hydrogen to 99.99% purity with 90% recovery, and thereafter compressed to 200 bar. The heat required for calcination is supplied by the oxyfuel combustion unit by reacting the PSA off-gas and make-up fuel with pure oxygen provided by the air separation unit (ASU) [564]. Exit stream from the oxyfuel combustion unit is rich in CO_2 and is combined with the CO_2 from the calciner for drying and compression. The CO_2 stream is then compressed to 110 bar for transport.

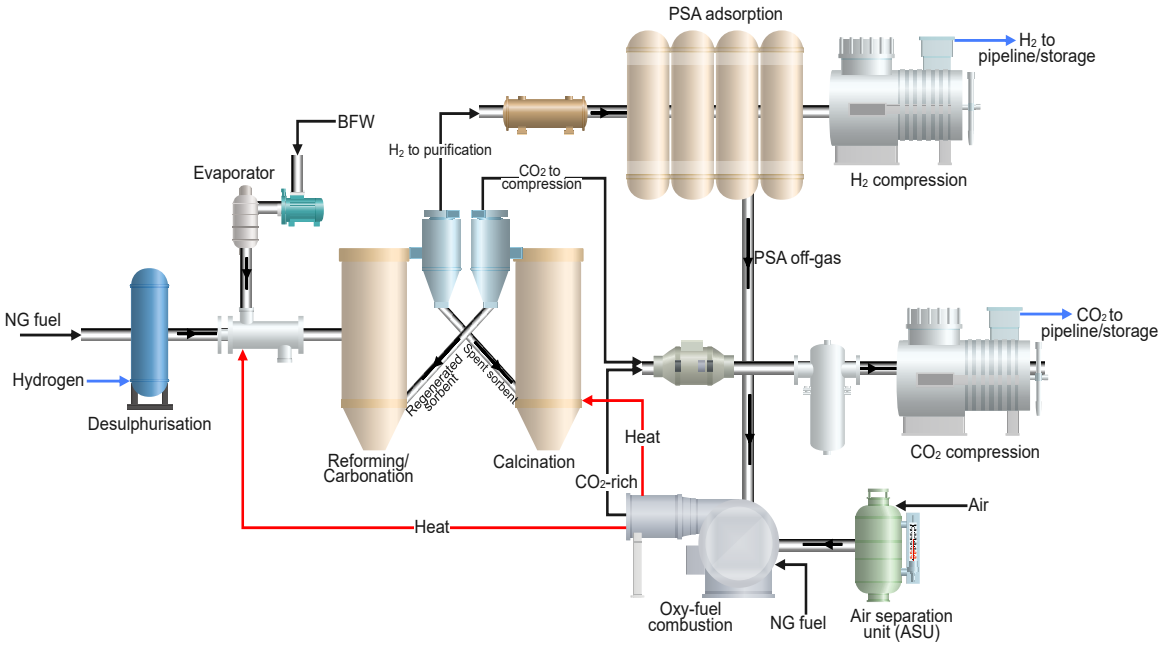

Figure 8.2: Process flow diagram for sorption-enhanced steam reforming process.

8.2.1.3 Autothermal gas-heated reformer with CCS

Figure 8.3 presents the hydrogen production process for an autothermal and gas heated reformer with CCS, similar to Johnson Matthey's low carbon hydrogen process [565]. It comprises an autothermal reformer, gas-heated reformer, hydrogen purification and compression unit, a separate carbon capture unit and CO_2 compression unit. Natural gas is first partially reformed in the gas-heated reformer (GHR) at S/C ratio of 1.5 and over nickel-based catalysts, to achieve 30% methane conversion [566]. The use of the GHR eliminates the need for an external heat source or furnace, as the heat is provided by the hot process gas leaving the ATR. The exit stream of the GHR contains hydrogen, CO_2, and methane at

778°C and 35.3 bar and is directed to the ATR unit. In the ATR, the feed stream is oxidised with pure oxygen stream from the ASU unit at an oxygen-to-carbon (O/C) ratio of about 1.2, and at high temperature of 1050°C, to achieve ~99% methane conversion. The syngas from the reformer is cooled and sent to a medium temperature shift converter or isothermal shift converter, where water-gas reaction occurs at medium temperature of about 270°C, in the presence of modified Cu-based catalyst, to yield a reformer gas containing mainly CO_2 and H_2. The CO_2 in reformer gas is removed in the carbon capture unit, while the H_2-rich stream from the absorber is sent to the PSA, where 90% hydrogen is recovered at 99% purity.

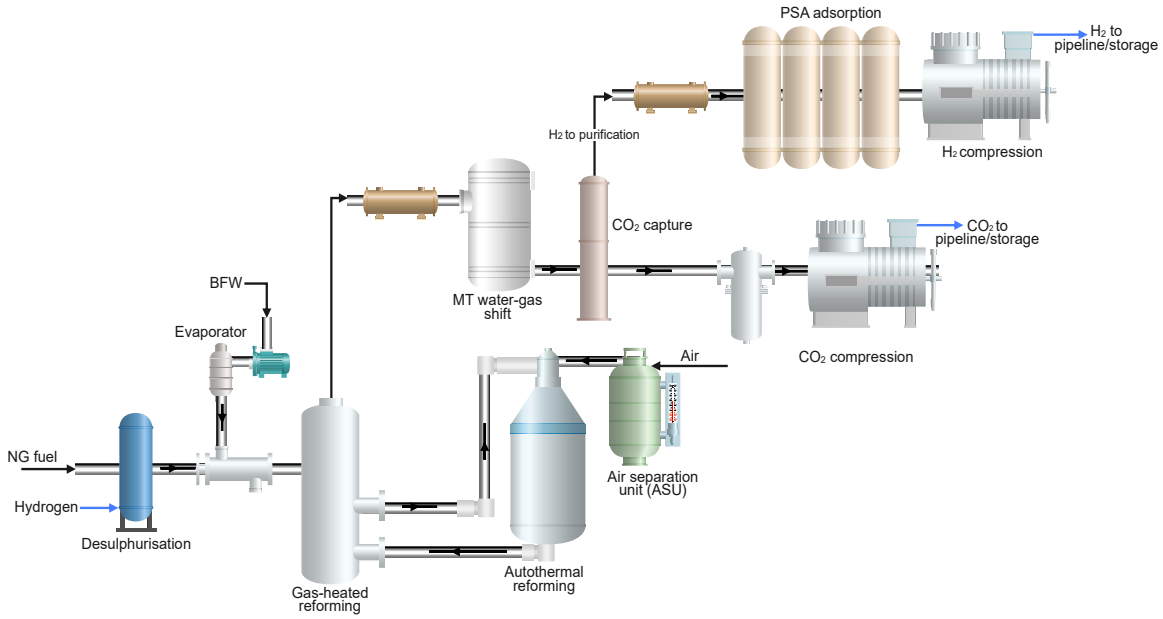

Figure 8.3: Process flow diagram for GHR-ATR process with CCS unit.

8.2.1.4 CO_2 capture Unit

The CO_2 capture unit uses amine-based solvent to remove CO_2 from the reformer gas. Amine-based solutions are a widely used class of solvents generally composed of organic compounds containing amine functional groups, which can form chemical complexes with CO_2 through absorption. There are several types of amines that are commonly used for carbon capture, including monoethanolamine (MEA), diethanolamine (DEA), and methyldiethanolamine (MDEA). MDEA is known for its low regeneration energy required to release the captured CO_2 [567]. Piperazine (PZ) is another commonly used amine for carbon capture. It is a secondary amine with two nitrogen atoms, which can form strong chemical bonds with CO_2 [553]. When MDEA and PZ are blended, they can offer improved performance for carbon capture. The PZ serves as an activator and can enhance the absorption capacity and selectivity of the MDEA, while the MDEA can improve the stability and regeneration properties of the PZ. This blended solvent, called a-MDEA, can also offer lower energy requirements compared to using

either solvent alone. In this work, the CO_2 capture unit configuration presented in Figure 8.4 is similar to that of BASF carbon capture process, described by Matteo et al. [568]. The CCS unit includes an absorber column, a stripper, low pressure and high-pressure flash drums, as shown in Figure 8.4. The equilibrium model adopted assumes instantaneous equilibrium without considering possible mass transfer resistances, which could yield less accurate results [569]. More information on the column specification and kinetic parameters are contained in Appendix C.

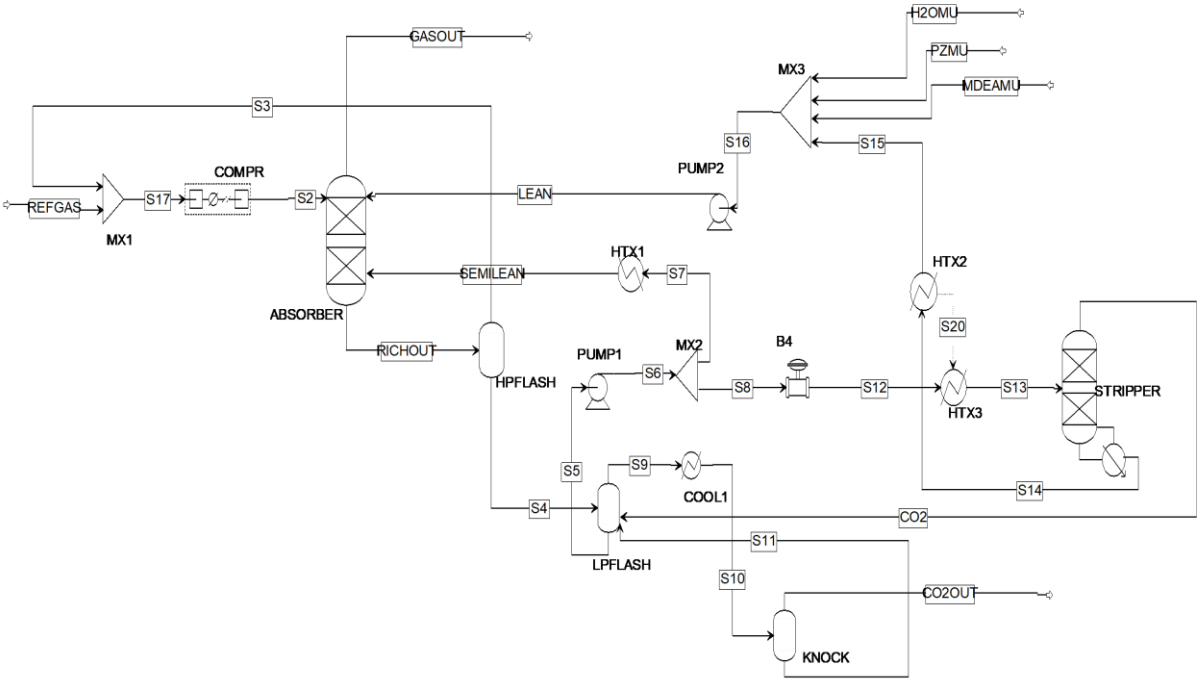

Figure 8.4: Process flow diagram of the a-MDEA carbon capture process (MU=make-up stream).

For the ATR-GHR plant, the a-MDEA solvent captures CO_2 from the reformer gas stream in the absorber, which is operated at a high pressure of 34 bar similar with the process gas. Operating the absorber at such pressure can improve the CO_2 capture rate. Past studies have been conducted employing high operating pressure for the absorber column [570–572]. The CO_2-rich solvent exiting the absorber first enters the high-pressure flash drum operating at 5 bar where some of the reformer gas is recovered, then to the low-pressure flash to regenerate some of the CO_2. Exit stream from the low-pressure flash is split into two; the semi-lean solution recycled back to the absorber, and the other stream directed to the stripper at 1.15 bar to completely regenerate the CO_2. The pure CO_2 leaving the CCS unit is compressed to 110 bar for transport. However, for the SMR plant, the CO_2 absorber is operated at a much lower pressure of 6 bar, due to the low pressure of the flue gas leaving the reformer furnace. The configuration of the CCS unit and other components' process conditions remains the same, as described in the previous paragraph. The kinetic parameters and specification of the columns are presented in Appendix C.

8.2.1.5 Hydrogen and CO_2 compression unit

Hydrogen exits the plant at a pressure of 200 bar and temperature of 25°C [558]. A multi-stage centrifugal compressor was employed to achieve four-stage compression, with intercoolers positioned between each stage, as shown in Figure 8.5. Flash drums are included to separate any liquids present and an equal pressure ratio is applied between each stage. The hydrogen feed from the hydrogen purification unit enters Compressor 1, where it is compressed. Upon exiting, the hot compressed gas flows through an intercooler where cooling water lowers its temperature to 30°C. Then at an elevated pressure, it enters Compressor 2 for further compression. Again, intercooling cools the gas before the Compressor 3 further pressurises it. A final intercooler prepares the gas for the fourth stage compressor. From here, the hydrogen gas passes through a final cooler to reduce the temperature to 25°C. More information on the operating conditions and parameters is presented in Table 8.3.

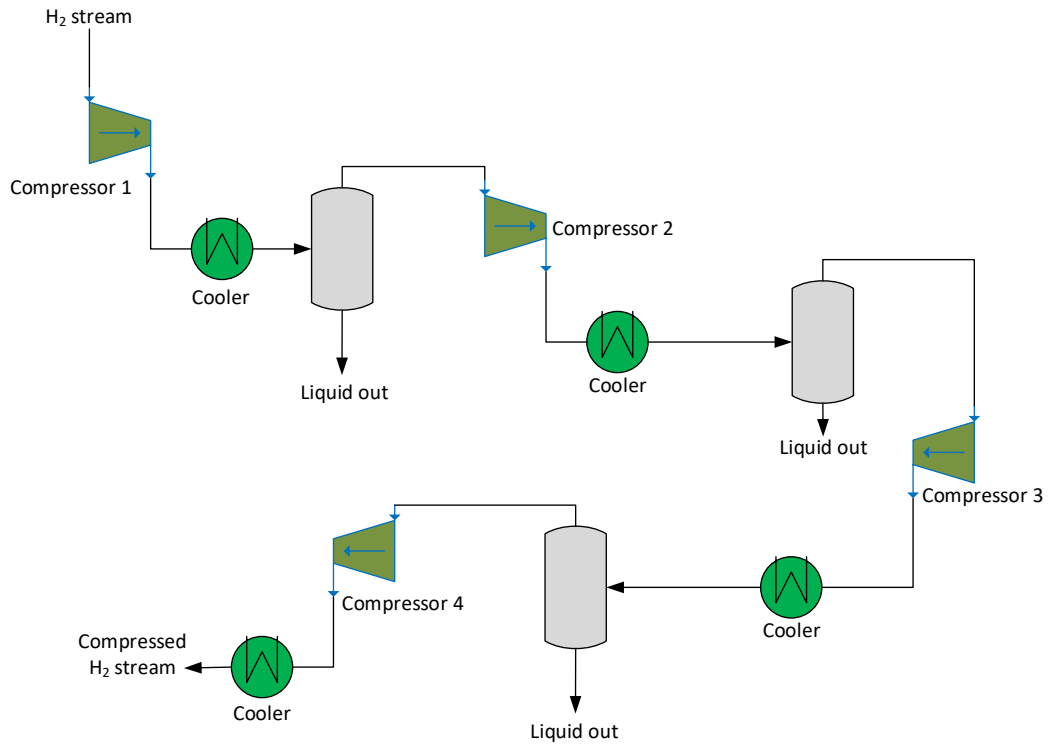

Figure 8.5: Process flow diagram of the hydrogen compression system.

8.2.2 Process simulation

A commercial simulation tool, Aspen Plus®, was used to evaluate the mass and energy for the processes studied. Peng-Robinson-Boston-Mathias (PR-BM) and Steam-National Bureau of Standards (Steam-NBS) equation of state (EOS) were used for SMR, SE-SR and ATR-GHR hydrogen production section of the plant, while the Electrolyte NRTL model was used for the a-MDEA CO_2 capture process. The PR-BM EOS is suitable for modelling hydrocarbon systems, including natural gas and hydrogen, at high

pressures [476]. Steady-state conditions were assumed for all the processes, with uniform temperatures and pressures in the reforming reactors. The reactions used to model the processes, including the CO_2-PZ-MDEA system are presented in the Appendix C. The main model inputs and operating conditions are presented in Table 8.2 and Table 8.3. All the process flowsheets developed in Aspen Plus are shown in the Appendix C.

Table 8.2: Natural gas composition [573]

Components	**Values (%mol)**
CO_2	0.780
CH_4	92.420
N_2	2.880
Ethane	0.302
Propane	0.590
C_4+	0.310

Table 8.3: Operating conditions and key units used in the model

Process units	Aspen unit model	Parameter	Value	Unit	Ref
Reformer/ carbonator	RGibbs	Temperature	600	°C	[574]
Calciner	RGibbs	Temperature	900	°C	[574]
		Pressure	1	Bar	[574]
ATR	RGibbs	Temperature	1050	°C	[575]
Medium temperature shift converter	RStoic	Temperature	270 - 313	°C	[560]
Pumps	Pump	Mechanical Efficiency	85	%	[288]
Oxy-fuel combustor	RStoic	Pressure	5	Bar	[576]
		Oxygen purity	99	%	[577]
H_2 compressor	MCompr	Isentropic efficiency	60	%	[578]
		Mechanical efficiency	92	%	[578]
		Intercooling temperature	30	°C	[579]
		Final stage H_2 cooler temperature	25	°C	[579]
CO_2 compressor	MCompr	Isentropic efficiency	80	%	[580]
		Mechanical efficiency	97	%	[580]
		Number of compression stages	4	-	[580]
		Intercooling temperature	30	°C	[581]
		Final stage CO_2 cooler temperature	30	°C	[581]

8.2.3 Process performance indicators

The performance of each of the processes were analysed using some key performance indicators including net process efficiency, cold gas efficiency, carbon capture efficiency, specific CO_2 emissions and specific CO_2 captured. The equations for calculating these parameters are presented in Table 8.4. Natural gas to electrical conversion efficiency, $\eta_{e,eff}$ of 49% was used, which corresponds to the average thermal efficiency of combined cycle gas power stations in the UK [582].

Table 8.4: Technical performance indicators for the processes

Parameters	Expressions	Equation
Methane conversion (%)	$\left(1-\frac{n_{CH_4,out}}{n_{CH_4,in}}\right)\times 100\%$	121
Cold Gas Efficiency (%)	$\frac{m_{H_2}\times LHV_{H_2}}{m_{NG,total}\times LHV_{NG}}$	122
Net Process Efficiency (%)	$\left(\frac{m_{H_2}\times LHV_{H_2}}{(m_{NG,total}\times LHV_{NG})+\frac{P_e}{\eta_{e,eff}}}\right)\times 100\%$	123
Overall Carbon Capture efficiency (%)	$\left(\frac{n_{CO_2,compressor}}{n_{C_{in},total}}\right)\times 100\%$	124
Specific CO_2 Emissions (kg_{CO_2}/kg_{H_2})	$\frac{m_{CO_2}}{m_{H_2}\times LHV_{H_2}}$	125

8.2.4 Economic assessment

The IEAGHG cost method and criteria for CCS plants and plants with low CO_2 emissions was used to estimate elements of the capital and operating costs for each of the hydrogen plants and is presented in Table 8.5 [583,584]. Total Direct Cost (TDC) includes the direct costs of all equipment required for the plant, as well as direct project costs like installation. The total plant cost (TPC) was calculated from the sum of all the costs captured in TDC, Engineering, procurement and construction (EPC) services, and contingencies; and upon addition of owner's cost, results in the total capital requirement (TCR) for the various blue hydrogen plants. Conversely, the operating and maintenance labour, overheads, property taxes, insurance, fuel, electricity and other consumables were considered in the estimation of the operating cost, with all the cost projections' level of accuracy categorised under the AACE Class 4. The Association for the Advancement of Cost Engineering (AACE) classification system provides a structured framework for establishing cost estimate accuracy levels based on the stage of project definition and design. Class 4 is a study or feasibility estimate created early in project concept

development. Accuracy range is -15% to -30% on the low side, and +20% to +50% on the high side [585]. A contingency of 40% was applied to the SE-SR plant due to its low maturity level. A comprehensive equipment cost scaling approach, based on the correlation by Peters et al. [586], was employed for the main reactors including the ATR, GHR, reformer/carbonator, calciner, considering the Chemical Engineering Plant Cost Index (CEPCI) and accounting for the impact of inflation over time. Details of the parameters used in estimating the equipment cost is reported in Appendix C. The January 2023 CEPCI was used for the calculations, while the March 2023 Oanda exchange rate was used to convert Euros and USD to Pound sterling, £ [587]. The costs were first converted using the exchange rate, then updated using CEPCI to 2023. Installed costs of the remaining plant components were obtained from Aspen Process Economic Analyser® (APEA), using the 2019 UK currency basis. The levelised cost of hydrogen (LCOH) was evaluated by dividing the net present value of the total hydrogen production cost by the net present value (NPV) of hydrogen produced over the plant's lifetime, as published by the Department for Energy Security and Net Zero, DESNZ (formerly Department for Business, Energy & Industrial Strategy, BEIS) [588].

$$NPV\ of\ Total\ costs = \sum_n \frac{Total\ CAPEX\ and\ OPEX_n}{(1+discount\ rate)^n} \quad (126)$$

$$NPV\ of\ hydrogen\ production = \sum_n \frac{Hydrogen\ production_n}{(1+discount\ rate)^n} \quad (127)$$

$$Levelised\ Cost\ of\ Hydrogen = \frac{NPV\ of\ total\ costs}{NPV\ of\ hydrogen\ production} \quad (128)$$

Where *n* is the period. The cost of CO_2 avoidance is calculated from equation 129.

$$Cost\ of\ CO_2\ avoided\ \ CCA\ = \frac{LCOH_{CCS} - LCOH_{REF}}{CO_2 Emissions_{REF} - CO_2 Emissions_{CCS}} \quad (129)$$

Table 8.5: Economic criteria applied to each of the plants (TDC=Total direct cost; TPC=Total plant cost) [583,584].

Parameters	**Values**
Plant life	25 Years
Capacity factor: Year 1, Year 2 – 25	70%, 95%
EPC	30% TDC
Construction	20% TDC
Other costs	0.5% TDC
Contingency	20%TPC (40% for SE-SR)
Working capital	Inventories for chemicals and materials for extra one month
Spare parts cost	0.5% TPC
Owner's costs	7% TPC
Annual operating and maintenance cost	2.1% TPC
Administrative and general overhead cost	30% of direct and maintenance labour cost
Indicative costs	2.5% TPC
Insurance	0.5% TPC
Local taxes and fees	0.5% TPC
Construction period	3 Years
Capital Expenditure Curve	
Year 1	25%
Year 2	45%
Year 3	30%
Discount rate (Initial)	8%
Variable costs	**Refs.**

Electricity, (£/GJ)	37.60	[589,590]
Natural gas, (£/GJ)	12.75	[590,591]
Water, (£/m^3)	0.8517	[592]
Catalysts, (£/ton)	11,704	[593]
MDEA, (£/ton)	2,400	[594]
Piperazine, (£/ton)	22,399	[595]
Dolomite, (£/ton)	80	[596]
CO_2 transport & storage (offshore), £/tCO_2 stored	10	[597]
Carbon price, (£/tCO_2e)	83.03	[598]

8.2.4.1 Estimation of CO_2 emissions cost

Carbon pricing mechanisms are implemented to quantify the cost of CO_2 emissions, making it a crucial factor in evaluating the economic viability of hydrogen production from fossil fuels. In recent years, the UK has focused on two primary carbon pricing mechanisms to reduce emissions – the EU Emissions Trading System (EU ETS) and the UK Carbon Price Support (CPS) mechanism [599]. However, following Brexit, the UK replaced the EU ETS with its independent Emissions Trading Scheme (UK ETS), which continues to operate on the same cap-and-trade principles but with a separate market for allowances.

Given the uncertain long-term prospects of the CPS policy and its focus on the use of fossil fuels for power generation, the carbon price used in this study is based on only the UK ETS pricing, to ensure a consistent carbon price signal throughout the hydrogen plant's lifetime. Therefore, a carbon price of £83.03/tCO_2e set by the UK ETS for January 1, 2023, is applied in this study [598].

8.2.4.2 Estimation of hydrogen compressor cost

Hydrogen compression would be required for most production technologies, if the hydrogen needs to be stored or transported via pipelines to end-users [588]. Therefore, this analysis assumed that hydrogen will be compressed to 200 bar to accommodate both storage and pipeline transportation [600,601]. The installed cost of hydrogen compressor was calculated based on the correlations by Khan et al. [602], which depends on the power requirements of the compressor motor.

$$Total\ installed\ cost,\ CAD\$ = 2 \times (3083.3 * kW^{SF}) \quad (130)$$

Where Scale factor, SF = 0.8335 and kW is the compressor power. The installed cost is escalated from 2019 to 2023 rate using the Chemical Engineering Plant Cost Index (CEPCI) and converted to £.

8.2.4.3 Sensitivity analysis

Sensitivity analysis was conducted to determine the impact of -25%/+50% variations in key parameters such as natural gas prices, electricity prices, CO_2 emissions costs and discount rate on the LCOH and CCA. Using the operating cost assumptions in Table 8.5 as the baseline values, the sensitivity ranges are presented in Table 8.6.

Table 8.6: Sensitivity ranges used for the cases.

Sensitivity variables	Units	Lower bound	Baseline	Upper bound
Feedstock and fuel price	£/GJ (LHV)	9.38	12.75	19.13
Electricity price	£/MWh	101.7	135.60	203.4
Discount rate	%	6	8	12
CO_2 transport & storage (offshore)	£/tCO_2 stored	7.5	10	15
CO_2 emission costs	£/tCO_2e	62.25	83	124.5

8.3 Results and discussion

In this section, the key findings from the process simulation and economic evaluation of the selected hydrogen production processes are presented. The simulation was carried out using Aspen Plus software to model material and energy balances across the system. Detailed material and stream tables for the flowsheet are provided in Appendix C.

8.3.1 Model validation

In this section, the validation results of the simulated plants in Aspen Plus and the comparison with experimental data obtained from relevant literature are presented. Model validation was conducted and relative errors, although small, are reported with the understanding that the subsequent results may have a small error. To validate the simulation results, the operating conditions from the literature were replicated in the simulations. Subsequently, the simulation outcomes were compared to the

experimental findings. For the SMR and SE-SR processes, the comparison was conducted based on the composition of the product streams from the main reactors in the processes. In the ATR-GHR plant, the comparison was based on the energy input required for the overall process.

The simulated SE-SR plant was validated with the experimental data from Martínez et al. [574]. By comparing the reformer outlet compositions obtained from the SE-SR process model with experimental data, a good agreement was observed at the outlet composition, as shown in Figure 8.6, except for Figure 8.6 which showed a slight deviation for methane composition at temperatures between 600 and 700 °C. In addition, the model slightly overestimated CH_4 conversion and H_2 yield, as presented in the Appendix C. However, the absolute errors between the simulation and literature data were calculated to be less than 14% and 2% for H_2 yield and CH_4 conversion, respectively. This deviation is caused by the difficulty in balancing the temperature approaches for the steam reforming reaction and carbonation reaction. Nevertheless, the range of relative error indicates an acceptable level of accuracy for the developed model [603,604].

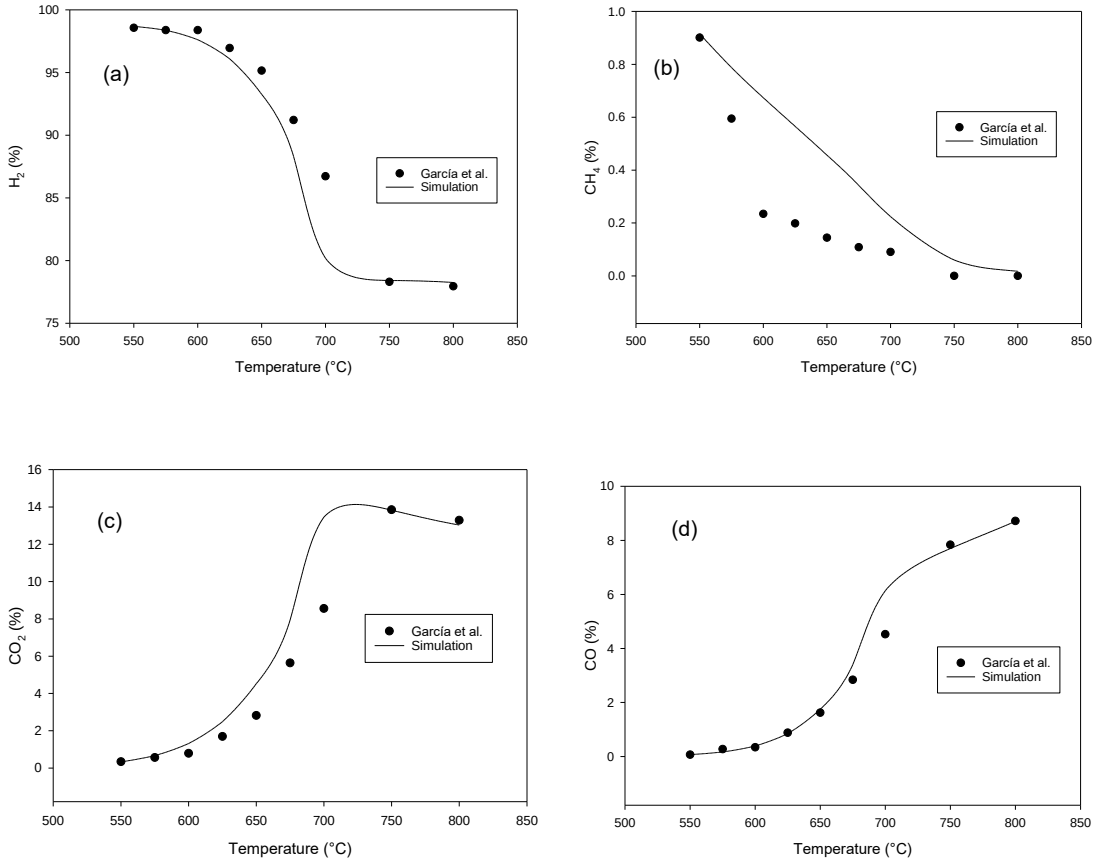

Figure 8.6: Comparison of gas compositions (on dry basis) between experimental [574] and simulated data for SE-SR of methane at different reactor temperatures.

The validation of the simulated SMR plant utilised data from a ~60MWth$_{(LHV)}$ SMR plant reported by Salem et al. [560]. The results for the SMR process were consistent with the reported values, as seen in Figure 8.7. The ATR-GHR plant relied on output data reported by Johnson Matthey for a 322 MWth$_{(LHV)}$ hydrogen production capacity [565]. For an ATR-GHR-CCS plant with hydrogen production capacity of 107.4 kNm^3/hr, the required natural gas feed from literature is 38.31 kNm^3/hr [565], compared to the simulated plant requiring 39.108 kNm^3/hr. The relative error between literature data and the simulated is 2%, which is acceptable for this study's objectives and the level of accuracy typically achievable in process simulations [560]. Therefore, the model was used for further simulations.

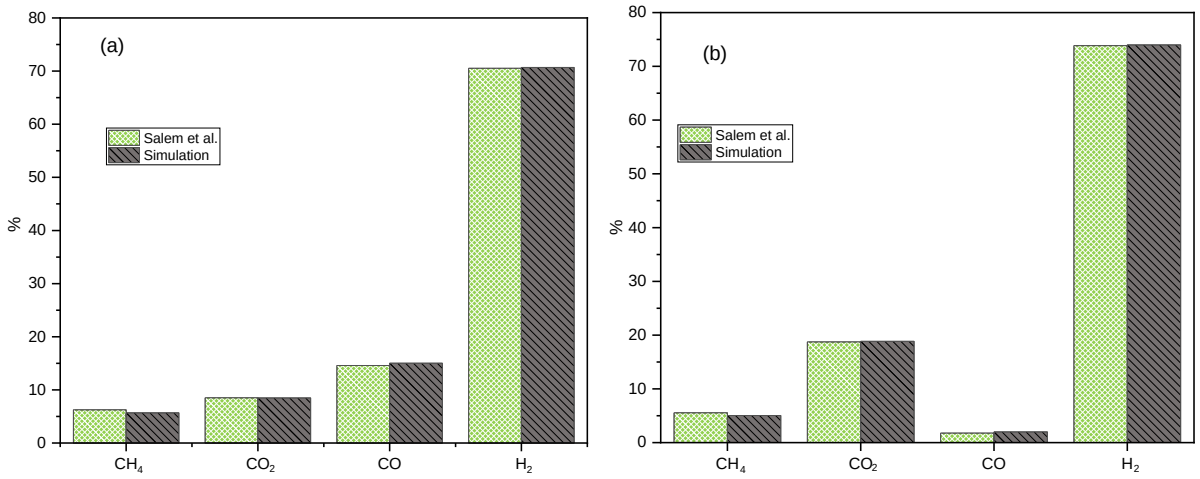

Figure 8.7: Outlet compositions from (a) the reformer and (b) the shift converter, contrasting plant data [560] with simulation results for the 60MWth$_{(LHV)}$ SMR process.

It should be acknowledged that while the validation studies in this work have provided favourable results, availability of data beyond bench-scale conditions could further enhance the robustness and applicability of the developed model, especially for the SE-SR plant.

8.3.2 Energy requirements

In modelling the hydrogen production plants, a power island was included to account for the on-site electricity demand. The power island consists of a steam turbine, sized to meet the average steam flow supplied by the heat recovery steam generator (HRSG). Waste heat from each of the hydrogen production processes is used to generate high-pressure steam in the HRSG.

The main source of energy in the plants is natural gas, which is also used as the feedstock. The total natural gas required for each of the plants is presented in Figure 8.8. A relatively high fuel input is seen in the SMR-CCS-600 plant, where it consumes 0.4% – 16% more natural gas than the other plants, due

to the extra fuel used to provide energy for auxiliary components like compressors and generating steam for the CCS plant. The integration of an a-MDEA CCS unit into the SMR plant, for blue hydrogen production, resulted in an 18% increase in overall fuel consumption. This increase is relatively lower compared to the findings of Oni et al. [605], who reported a higher fuel consumption penalty (39%) for an SMR plant, integrated with a MEA CCS system and for a slightly higher hydrogen production capacity (about 760 $MWth_{(LHV)}$). Despite having a slightly higher hydrogen production capacity than the SMR-CCS-600 system, the scaled-up 1000 MWth plant still exhibited a 16% increase in fuel consumption compared to the baseline SMR plant, for a similar CO_2 capture efficiency. Studies have indicated that employing a-MDEA solvent leads to a reduction in overall CCS energy consumption, largely attributed to a decline in reboiler energy requirements, compared to other amine solvents [572,606].

The fuel consumption of AG-CCS-600 is slightly lower than that of SMR-CCS-600 by 0.4%, which could be attributed to different reasons: the gas heated reformer design in AG-CCS-600 allows for effective heat recovery, which maximises energy recycling and drives the endothermic reforming reactions with less external fuel input. Fuel consumption in SE-600 is observed to be the lowest, at 13% - 27% lower than the rest of the hydrogen plants. Apart from having fewer process units which means the carbon capture system imposes a smaller energy penalty on the plant, the thermally neutral nature of the process must have played a role. In SE-SR, the heat energy required for steam reforming reaction is provided by the exothermic carbonation reaction, resulting in less heat input [146]. Figure 8.8a compares the energy requirements of the various hydrogen production technologies. It shows the amount of natural gas (NG) input required to produce one kilogram of hydrogen for each method. SE-600 has the lowest total NG requirement at around 0.156 GJ/kgH_2, whereas AG-CCS-600 requires more energy input at around 0.18 GJ/kgH_2. SMR-CCS-600 has the highest NG demand, necessitating about 0.21 GJ of input to generate 1 kg of hydrogen.

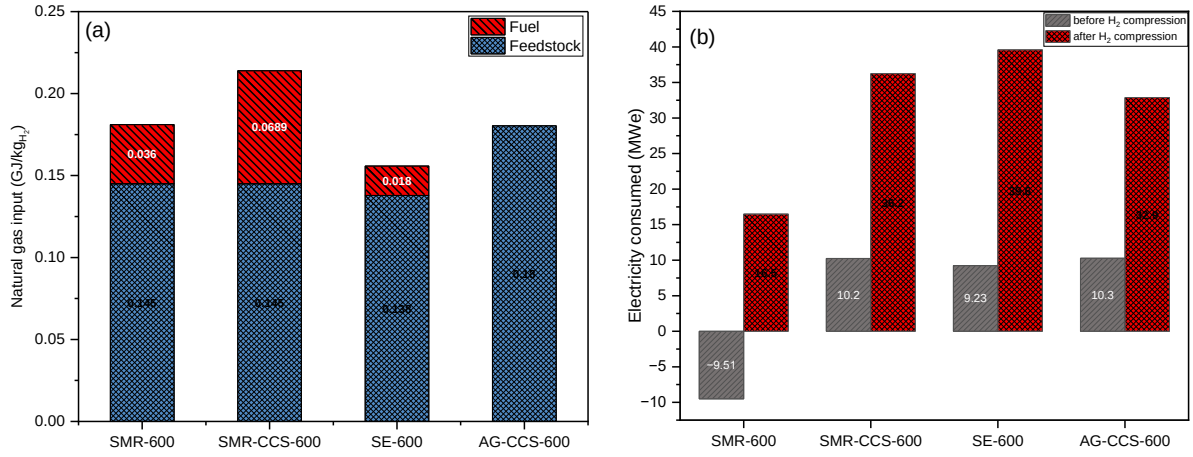

Figure 8.8: (a) Natural gas and (b) Electrical requirement for the hydrogen production plants.

Electricity produced was insufficient to fully meet the plant's electrical needs. Therefore, the final integrated process-power system model also included the ability to import additional electricity from the local grid network. Figure 8.8b reveals the electricity consumption of the various hydrogen production technologies and how much additional power is needed to compress the produced hydrogen gas for storage and transport.

Before hydrogen compression, AG-CCS-600 required the most power at around 10 MWe, followed by SMR-CCS-600 at about 10.2 MWe and SE-600 at 9.2 MWe. SMR-600 plant has an electricity excess of 9.5 MWe, which can be exported. The substantial electricity consumption of SMR-CCS-600 stems from the operation of air and PSA off-gas compressors (with large flowrates of air and off-gas), which are essential for the reformer furnace to provide thermal energy for the process. In the process design, reformer gas from the shift converter was purified, and PSA off-gas was routed back to the reformer furnace below 1 bar, thereby requiring compression for use as fuel. This configuration was adopted to capture CO_2 from the reforming furnace flue gas. CO_2 capture from furnace flue gas is recognised as the most efficient approach, as it yields the most concentrated CO_2 stream from steam reforming plant [607]. Additionally, the high natural gas input meant increased volume of CO_2 generated, consequently requiring more compression power downstream.

When hydrogen compression is included, the relative differences change significantly. This is due to differences in the initial hydrogen pressure before compression between technologies. SE-600 tops the list, requiring an additional electricity import of 30.6 MWe. SE-600 operates at relatively low pressure compared to SMR-CCS-600 and AG-CCS-600, so high compression ratio is required to compress H_2 to 200 bar. Despite the equilibrium benefits offered by the sorbent, lower pressure conditions continue to favour the thermodynamics of the underlying steam reforming reaction [608]. SMR-CCS-600 also

saw a sharp rise by 26 MWe due to its compression load. In contrast, AG-CCS-600 experienced a relatively low increase by 22.6 MWe.

Hydrogen compression is a significant contributor to the power demand of SMR-CCS-600, SE-600, and AG-CCS-600 plants. It accounts for 71.74%, 76.70%, and 68.76% of the total power demand in these plants, respectively. This high demand for power entails additional electricity imports, which increase by 254%, 329%, and 220%, respectively, for these plants.

8.3.3 Net process efficiency

A key performance metric for any production process is its overall energetic efficiency. Figure 8.9a illustrates the cold gas efficiencies achieved by the different hydrogen plants. SE-600 performed best with a cold gas efficiency of 82.8%, attributed to the thermally neutral characteristics of the process. SMR-600, SMR-CCS-600 and AG-CCS-600 realised cold gas efficiencies around 71.3%, 60.3% and 72%, respectively.

Figure 8.9b displays the process efficiencies achieved through simulations of different blue hydrogen production pathways. In this study, the power requirement for the auxiliary components, including the ASU, compressors and PSA, was considered in the calculation of the net process efficiency. Before H_2 compression, SE-600 achieved the highest net efficiency of around 79.6%, followed closely by AG-CCS-600 at 70.14%, then SMR-CCS-600 at a lower net efficiency of 60% due to its demand for external fuel. Its lower net efficiency, compared with SMR-600 also indicates greater energy penalty associated with downstream CO_2 capture and compression. Conversely, the AG-CCS-600 improved process efficiency, compared to SMR-CCS-600, was primarily due to the reduced energy inputs and power needs in the AG-CCS design, which lessened the efficiency penalties associated with the CCS unit. Integrating hydrogen compression to each of the plants saw a reduction in the net process efficiency of all the plants. SE-600 maintained the highest net process efficiency, while AG-CCS-600 achieved a higher net process efficiency of around 66.6% than SMR-600 at 56.1%. SMR-CCS, SE-600 and AG-CCS net efficiencies still decreased by 3-5 percentage points when hydrogen compression was added versus their non-H_2 compression baselines.

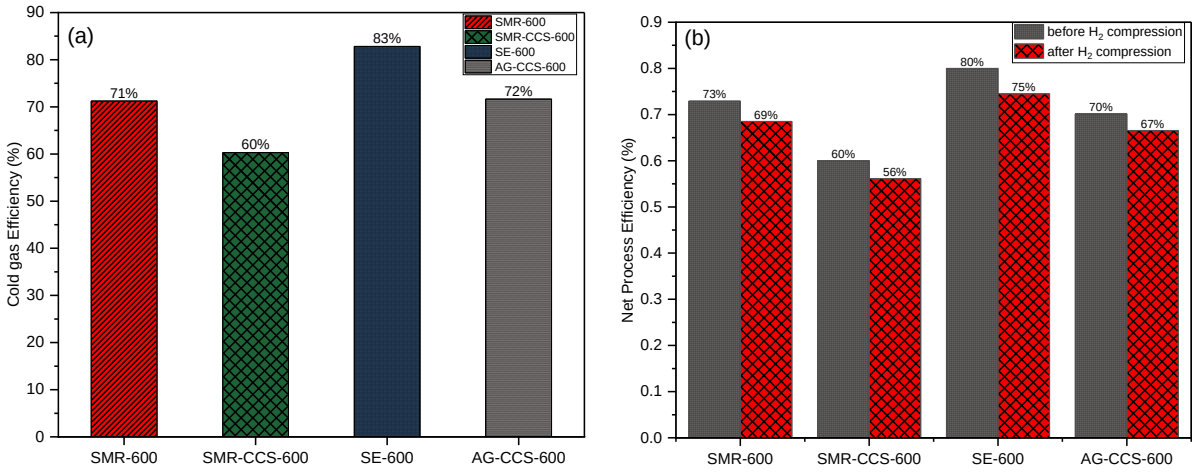

Figure 8.9: (a) Cold gas efficiencies and (b) Net process efficiencies of the hydrogen production plants.

Furthermore, this difference in net efficiency between these technologies stems partly from their distinct NG conversions. AG-CCS-600 achieved the highest fuel (NG) conversion of all the cases. The high fuel conversion results from the two-step reforming configuration in which 30% conversion was seen in the GHR, while ATR completely converts the NG to ca. 99.2%. It is important to acknowledge that in practice, achieving such high methane conversion could be challenging due to factors such as catalyst deactivation and heat and mass transfer limitations, which was not considered in this study. Fuel conversion from SE-600 reformer was observed to be lower than the AG-CCS-600, but higher than their counterpart SMR plants at 81.7%.

8.3.4 Carbon capture efficiency and On-site CO_2 emissions

Table 8.7 shows the carbon capture efficiency and on-site CO_2 emissions intensities for the different hydrogen production facilities. Methane conversion in the SE-SR unit fell below 82%, leaving some unconverted methane in the PSA off-gas, which can impact on the overall carbon capture efficiency in the plant. One drawback of SE-SR technology is the negative effects that higher operating pressures have on methane conversion and carbon capture efficiency, despite its in-situ CO_2 capture characteristics.

As the operating pressure increases, it influences the equilibrium of the endothermic reforming reaction in a way that makes it more difficult to fully convert the methane feedstock. With lower rates of reforming, more unreacted methane passes through to downstream units rather than being transformed into CO_2 and H_2. This low conversion reduces the amount of CO_2 available for capture, thereby weakening the process' overall carbon capture efficiency. A study by Abbas et al. [269] found that increasing the operating pressure of SE-SR of methane from 20 to 35 bar resulted in methane conversion dropping from 73.5% to 64.8%, and CO_2 capture decreasing from 64.5% to 58.8%. Design

modifications could help address such deterioration [266], but could drive up capital and operating costs. In this study's design, the lower methane conversion in the SE-SR unit is offset by the integrated oxy-fuel combustion unit. Since the oxy-fuel combustion uses pure oxygen (99% purity) to burn the extra fuel and PSA off-gas stream, highly concentrated CO_2 stream is generated, leading to an improved overall carbon capture efficiency for the entire plant. Thus, CO_2 emissions from SE-600 plant was significantly reduced.

For SMR-CCS-600, the high natural gas consumption for extra energy demand generated large volume of CO_2, which impacted on the overall carbon capture efficiency. It is important to note that SMR-CCS-600 was not optimised to achieve higher CO_2 capture rates. AG-CCS-600 sits between the two with an overall capture efficiency of about 94.5%, in line with the findings of Cotton [609].

Table 8.7: Carbon capture performance of the examined hydrogen production technologies

	Units	SMR-600	SMR-CCS-600	SE-600	AG-CCS-600
Overall Carbon Capture efficiency	%	-	85.2	98.99	94.54
Specific CO_2 Emissions	kg/kg H_2	9.86	2.44	0.08	0.53
CO_2 captured annually	kt/yr	-	1,634.03	1,274.41	1,463.34
CO_2 emissions annually	kt/yr	1,555.31	385.68	12.95	84.245

Inefficiencies in the CO_2 capture process can result in residual CO_2 emissions. Among the simulated blue hydrogen production plants, SE-600 had the lowest on-site CO_2 emissions at 0.08 kg CO_2/kg H_2, due to its high carbon capture efficiency. SMR-CCS-600 resulted in CO_2 emissions of 2.44 kg CO_2/kg H_2 owing to its relatively low carbon capture rate, while AG-CCS-600 maintained an intermediate emissions level of 0.53 kg CO_2/kg H_2. In comparison, SMR-600 yielded the highest emissions of all the hydrogen plants at 9.86 kg CO_2/kg H_2, as it lacks the carbon capture step.

8.3.5 Economic performance

This section evaluates the relative economic competitiveness of each technology, by comparing the capital and operating costs associated with each production pathway. It also examines how the resulting production costs are influenced by hydrogen compression and carbon prices. Given the large capital investments required for carbon capture infrastructure, the levelised cost of hydrogen (LCOH) production and cost of CO_2 avoided (CCA) are important metrics for assessing the long-term economic

competitiveness of blue hydrogen technologies. Therefore, this analysis focused on comparing these two indicators, alongside capital costs and operational costs. Table 8.8 presents a summary of the cost breakdown for all the hydrogen plants. 40% contingency was added to SE-600 cost estimates to account for uncertainties associated with low TRL technologies, while 20% was used for the other technologies.

Table 8.8: Cost breakdown including capital and operating costs for all the cases studied.

(M£)	**SMR-600**	**SMR-CCS-600**	**SE-600**	**AG-CCS-600**
Steam reformer and components	118.91	118.91	-	-
Fluidised bed reformer with Calciner and solid handling	-	-	107.76	-
PSA	-	-	63.88	33.55
H_2 Compressor	34.27	34.27	50.74	23.44
Combustor	-	-	29.56	-
ATR	-	-	-	238.82
GHR	-	-	-	14.88
CCS Unit	-	158.88	-	98.44
Steam turbine	19.81	26.28	11.80	18.92
ASU and oxygen compressor	-	-	77.14	108.31
Shift converter	-	-	-	10.18
Auxiliary components and CO_2 compressor	76.59	114.77	107.54	118.74
Total plant cost (TPC)	**249.57**	**453.10**	**448.41**	**665.27**
Contingency	49.91	90.62	179.37	133.05
Owner's costs	17.47	31.72	31.39	46.57
Spare parts cost	1.25	2.27	2.24	3.33
Working capital	28.40	33.56	24.66	28.30
Start-up costs	13.97	20.54	18.15	24.71
Total capital requirement (TCR)	**360.58**	**631.80**	**704.22**	**901.24**
Fixed costs (M£)				
Direct labour cost	1.38	1.50	1.50	1.49
Annual operating and maintenance cost	5.24	9.52	9.42	13.97
Administrative and general overhead cost	0.86	1.27	1.26	1.64
Indicative costs	6.24	11.33	11.21	16.63
Insurance	1.25	2.27	2.24	3.33
Local taxes and fees	1.25	2.27	2.24	3.33
Variable costs (M£)				
Fuel (Natural gas)	338.72	400.32	291.50	337.51
Water (Feed and Make up)	1.39	1.55	3.69	0.94
Catalysts	0.54	0.54	0.49	1.00
Other chemicals	0.10	0.10	0.10	0.10
MDEA	-	0.07	-	0.03
Piperazine	-	0.14	-	0.07
CaO	-	-	0.15	-
Electricity (with H_2 compression)	18.61	40.9	44.68	37.09
CO_2 transport & storage cost	0.00	16.34	12.75	14.63
Total OPEX (M£)	**375.59**	**471.76**	**381.32**	**431.76**
LCOH at zero carbon price (£/kg H_2)	**2.60**	**3.48**	**2.84**	**3.22**
CCA at zero carbon price (£/ton CO_2)	-	118.42	25.10	66.55
LCOH at carbon price of £83 (£/kg H_2)	**3.42**	**3.68**	**2.85**	**3.26**
CCA at carbon price of £83 (£/ton CO_2)	-	35.43	-57.89	-16.75

The total plant cost for each of the technologies account for at least 60% of the total capital investment, with AG-CCS-600 requiring the largest capital investment. The breakdown of the plant cost by components, for the hydrogen production technologies examined, is displayed in Figure 8.10.

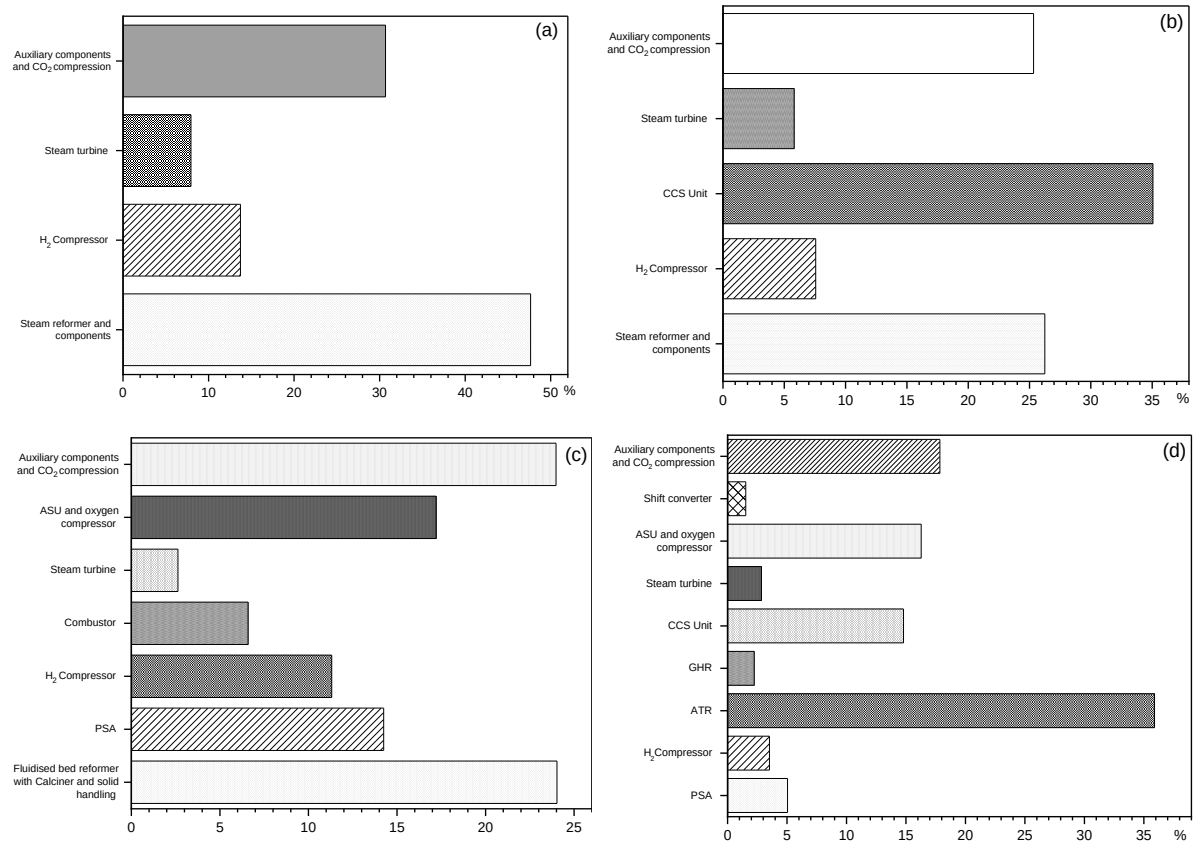

Figure 8.10: Percentage distribution of total plant cost across (a) SMR-600, (b) SMR-CCS-600 (c) SE-600 and (d) AG-CCS-600.

The ATR equipment has the biggest share of the plant cost at approximately 36%, in AG-CCS-600. It plays a key role in the generation of syngas and improving the overall fuel conversion of the process. Following closely is the ASU unit, which represents 16% of the total plant cost. The CCS unit accounts for 15% of the total plant cost, while the remaining 33% is divided among the hydrogen compressor, GHR, and auxiliary components. For SE-600, the SE-SR equipment has the largest cost contribution, accounting for approximately 24% of the total plant cost. This is followed by the ASU unit, which constitutes around 17% of the total plant cost, while H_2 compressors and oxy-fuel combustion unit make up 11.32% and 7.56% of the total plant cost, respectively. The a-MDEA CCS unit is the primary cost driver in the SMR-CCS-600, accounting for roughly 35% of the total plant cost. Additionally, the CO_2 compression unit accounts for 8% of the total plant cost, which exceeds the 7.6% contributed by the hydrogen compression unit. The large volume of flue gas generated due to the plant's high natural

gas requirements directly impacts the size and, inevitably, the cost of the CO_2 process equipment. Hydrogen compressors for SMR-600, SMR-CCS-600, SE-600 and AG-CCS-600 make up 13.73%, 7.56%, 11.32% and 3.52% of the total plant cost, respectively.

Moving beyond plant cost and total capital requirement, it is also important to consider the operating cost of the plant. These costs encompass labour, maintenance, energy consumption, and raw material expenditures. The running cost for SMR-600 plant exceeds its initial capital investments by 8.4%, with natural gas accounting for more than 80% of the operating cost. For SMR-CCS-600, the total OPEX is about 75% of its TCR per annum. This means that for every £1 invested, the SMR-CCS plant will require £0.75 to operate a 600 MW hydrogen plant each year. Total OPEX for SE-600 is 53% of its TCR, while AG-CCS-600 will require 44% of its initial capital investment to operate annually. Although some economic studies on conventional SMR have reported lower operating cost to capital costs ratio [605,610,611], the significant spike in the price of natural gas in the UK contributed to this increase in total OPEX reported in this study, as natural gas price has consistently increased by over 120% between 2020 and January 2023 [591]. When fuel costs are excluded, the variable operating costs including electricity and water consumption, contributed most significantly to SE-600 operating costs. SE-600 has the highest estimated non-fuel variable costs among the technologies.

The LCOH was estimated for each hydrogen technology pathway, based on their resulting capital and operating costs over a 25-year lifetime. At zero carbon price, SMR-600 had the lowest LCOH of £2.60/kg H_2, since carbon capture was not considered. Among the blue hydrogen technologies, SE-600 was found to have the lowest levelised cost of £2.84/kg H_2. This can be attributed to SE-SR's simpler design with fewer processing units, lowering both capital and operating expenses, compared to the other technologies. AG-CCS-600 resulted in an intermediate levelised cost of £3.22/kg H_2 due to its high capital cost, while SMR-CCS-600 had the highest levelised cost at £3.48/kg H_2. It is challenging to directly compare the LCOH estimated in this study against literature values, due to natural variations in the modelling, plant configuration and capacity, costing methodologies, and underlying assumptions applied such as carbon pricing, discount rates, and natural gas prices.

However, the general trend of SE-600 and AG-CCS-600 having lower costs than SMR-CCS-600 aligns with previously reported trends for autothermal and SE-SR processes in literature [612–614]. For a ~60 MWth SE-SMR capacity, the findings of Dat Vo et al. [613] revealed that the SE-SMR system achieved an energy efficiency of 82.2% based on lower heating value calculations. Moreover, they estimated SE-SMR production cost of £1.59/kgH_2 (after adjusting for inflation and currency conversion), representing a 12% reduction in production cost compared to the conventional SMR with CCS alternative. Similarly, Diglio et al. [612] reported a hydrogen production cost of £1.8/kgH_2 for an SE-SMR system integrated

with fuel cell, which was lower than SMR with MEA CO_2 capture system by ~33%. For a 1000 MWth autothermal and gas-heated reforming with CCS plant, Argyris et al. [106] reported LCOH range of £1.85 – £1.88/ kgH_2, lower than its counterpart SMR with CCS plant. The minor discrepancies in the numerical LCOH estimates between the current analysis and other sources do not necessarily indicate disagreement, as this analysis incorporated hydrogen compression costs and a different carbon pricing.

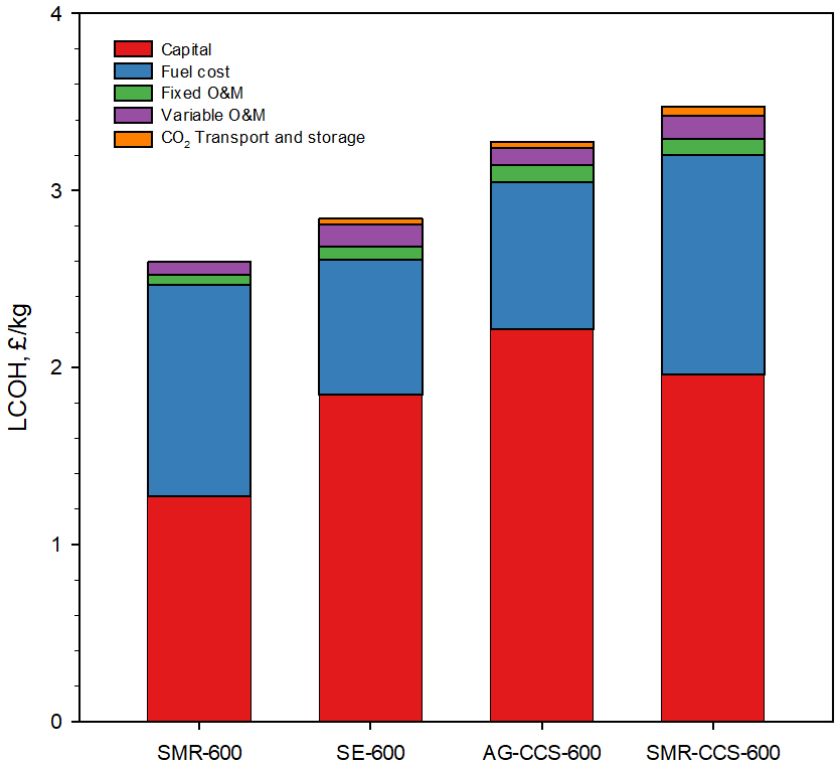

Figure 8.11: Distribution of levelised cost of hydrogen (LCOH) for all the technologies studied at 600 $MWth_{(LHV)}$ hydrogen production scale.

Figure 8.11 shows the breakdown of the levelised cost of hydrogen (LCOH) for the four different technologies based on capital costs, fuel costs, fixed and variable operating expenses (OPEX), and costs associated with CO_2 transport and storage via offshore. Total capital costs are the largest component of the LCOH for the SE-SR and ATR-GHR technologies, except for the SMR and SMR-CCS-cases, where fuel cost make up the largest share of their LCOH. This is closely followed by the fuel cost for the SE-SR and ATR-GHR, capital costs for the SMR and SMR-CCS-cases, then the variable and the fixed O&M for all the cases. The CO_2 transport and storage costs are the smallest component of the LCOH for the blue hydrogen technologies. However, these costs are larger for the AG-CSS-600 and SMR-CCS-600 compared to SE-600, due to the volume of natural gas processed in these plants.

The cost of avoided CO_2 (CCA) emissions is also an important economic metric when evaluating low-carbon technologies. It is important to note that the method used in this study to calculate CCA

depends on the extent of CO_2 reduction, and the change in LCOH between the reference SMR plant (without CCS) and the blue hydrogen plant (see equation 129). Simbeck and Beecy [615] highlighted three scenarios, using coal power plant as reference, to show how the CO_2 avoidance cost fluctuates depending on the reference and CCS plant. In this case, when there are small incremental increases in LCOH and significant reduction in CO_2 emissions, the CCA is low, whereas CCA is high when there are large increases in LCOH with small CO_2 reduction. In this study, the specific CO_2 emissions for SE-600 is 0.08 kg/kgH_2, which is a significant reduction from 9.64 kg/kgH_2 seen in the SMR-CCS-600. There was also a slight increase in LCOH from 2.60 £/kgH_2 (observed in the SMR plant) to 2.84 £/kgH_2 for SE-600, at zero carbon price. This results in lower CCA, when compared with AG-CCS-600 (specific CO_2 emission of 0.53 kg/kgH_2) and SMR-CCS-600 (specific CO_2 emission of 2.44 kg/kgH_2). The high CCA observed in SMR-CCS-600 is attributed to factors such as high fuel consumption and cost, and low net process efficiency. At zero carbon price, the cost of CO_2 avoided for the blue hydrogen technologies was estimated at £25.10–£118.42/tonne CO_2. SE-600 has the lowest avoidance cost of £25.10/tonne CO_2 due to its low hydrogen production costs. AG-CCS-600 had a CCA of £66.55/tonne CO_2, while SMR-CCS-600 had the highest CCA of £118.42/tonne CO_2.

As carbon price increases, the annual operating cost for the reference SMR plant also increases due to the rising cost of CO_2 emissions. Consequently, this leads to a higher LCOH for the reference plant and low LCOH for the blue hydrogen plants. This change in LCOH, in turn, affects the calculated CCA for the blue hydrogen plants. The influence of carbon price on these costs will be elaborated upon in the remainder of this chapter.

8.3.6 Impact of blue hydrogen production scale on cost

This section evaluates how the costs of SE-SR, ATR-GHR, and SMR with carbon capture may be impacted at larger production scales more relevant for emerging commercial markets. Hydrogen production scale was increased from 600 MW to 1000 MWth (LHV). As production scale increased from 600 to 1000 MW, the capital requirement went up across all the examined technologies, as shown in Figure 8.12. Capital costs surged by a minimum of 30% for each facility. SE-SR plant had the highest rise at 56% but remained lower than the ATR-GHR plants, which have the highest TCR amongst the hydrogen technologies studied.

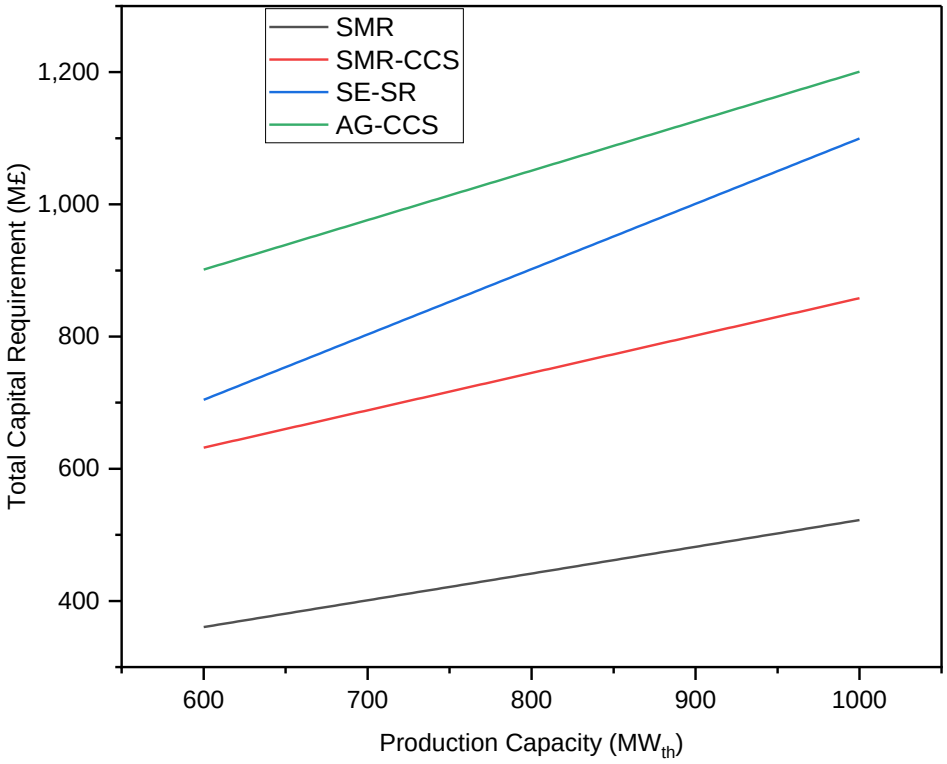

Figure 8.12: (a) Total capital requirement of the various technologies when upscaled, and (b) the distribution of LCOH at 1000 MWth hydrogen production capacity.

Figure 8.13a shows that the LCOH for all the hydrogen plants decreases as the production scale increases from 600 to 1000 MW. This is primarily due to economies of scale, where the larger plants benefit from cost efficiencies and higher production volumes, resulting in lower costs per unit of hydrogen produced. At zero carbon price scenario, the calculated LCOH for the SE-600 plant is £2.84/kg, which reduces to £2.79/kg at 1000 $MWth_{(LHV)}$. This is a decrease of ~2%. When the current average carbon price of 83 £/ton CO_2 is considered, similar reduction is observed. The LCOH of the AG-CCS-600 decreased by ~5.5% from 3.22 to 3.10 £/kgH_2, as the production scale increased to 1000 $MWth_{(LHV)}$. The SMR-CCS-case, which has the largest LCOH of the blue hydrogen plants, has its LCOH decrease by ~2.6%, as the hydrogen production scale increases from 600 to 1000 $MWth_{(LHV)}$.

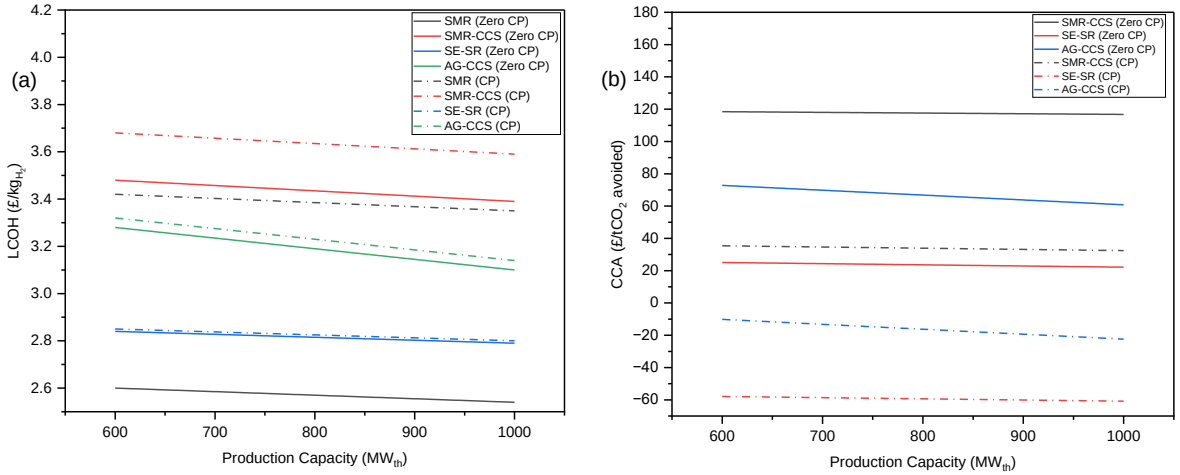

Figure 8.13: (a) LCOH and (b) CCA of the various upscaled technologies at zero carbon price (CP) and carbon price - £83/tCO$_2$.

The CCA also exhibits a similar pattern, as hydrogen production scales up. For the SE-600 case, the CCA fell by 11.55%, from 25.10 to 22.20 £/ton CO$_2$, when no carbon price was considered. Similar reductions were observed in the AG-CCS and SMR-CCS cases, with CCA decreasing by 8% (from 66.55 to 60.83 £/ton CO$_2$) and 1.42% (from 118.42 to 116.74 £/ton CO$_2$), respectively, at zero carbon price. With the introduction of a carbon price, there was still an overall reduction in the CCA for the blue hydrogen technologies.

8.3.7 Sensitivity analysis

Sensitivity analysis was conducted to evaluate the impact of select input variables on the LCOH and CCA for the hydrogen technologies. The analysis varied total plant costs, natural gas prices, electricity prices, CO$_2$ transport and storage costs via offshore, CO$_2$ emissions costs, discount rates, and plant lifetime by -25%/+50% from the baseline values used in the primary economic assessment, with a carbon price of 83 £/tCO$_2$. This wide input range was selected to capture potential changes and uncertainties in cost assumptions.

8.3.7.1 Natural gas price

As seen in Figure 8.14, variations in natural gas price have the highest impact on the LCOH across all cases. For AG-CCS-600, the LCOH reduced to 2.71 £/kgH$_2$ at the lower sensitivity bound, and increased to around 4.48 £/kgH$_2$ at the upper sensitivity bound. Similarly, the LCOH for SE-600 ranged from approximately 2.37 to 3.9 £/kgH$_2$, for the upper and lower sensitivity bounds, respectively. The LCOH values for SMR-CCS-600 were 3.03 and 5.13 £/kgH$_2$ for the upper and lower sensitivity bounds, respectively.

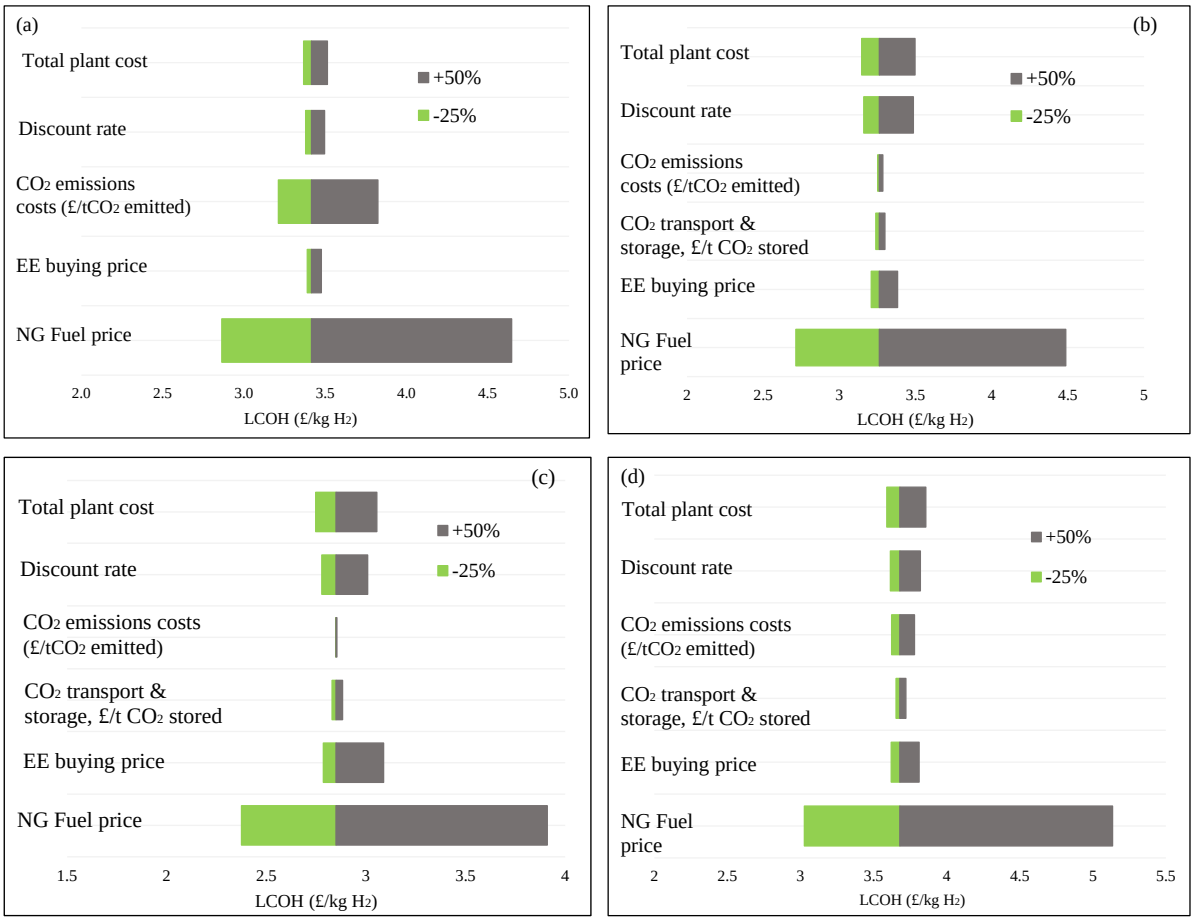

Figure 8.14: Sensitivity of select variables on LCOH for (a) SMR (b) AG-CCS-600 (c) SE-600 and (d) SMR-CCS-600. (NG: natural gas; EE: electricity).

In Figure 8.15, CCA for SMR-CCS-600 is most affected by changes in natural gas prices. As natural gas prices rise, the CCA for SMR-CCS-600 reaches as high as 65.65 £/tCO_2. This is due to the relatively large volume of natural gas utilised in the SMR-CCS plants, invariably causing large increases in their LCOH. On the other hand, changes in CCA for SE-600 and AG-CCS-600 plants were relatively minimal with changes in natural gas price. The CCA for SE-600 ranged from (-50) £/tCO_2 to (-75.45) £/tCO_2, while that of AG-CCS-600 ranged from (-16.08) £/tCO_2 to (-17.30) £/tCO_2, as natural gas price increases.

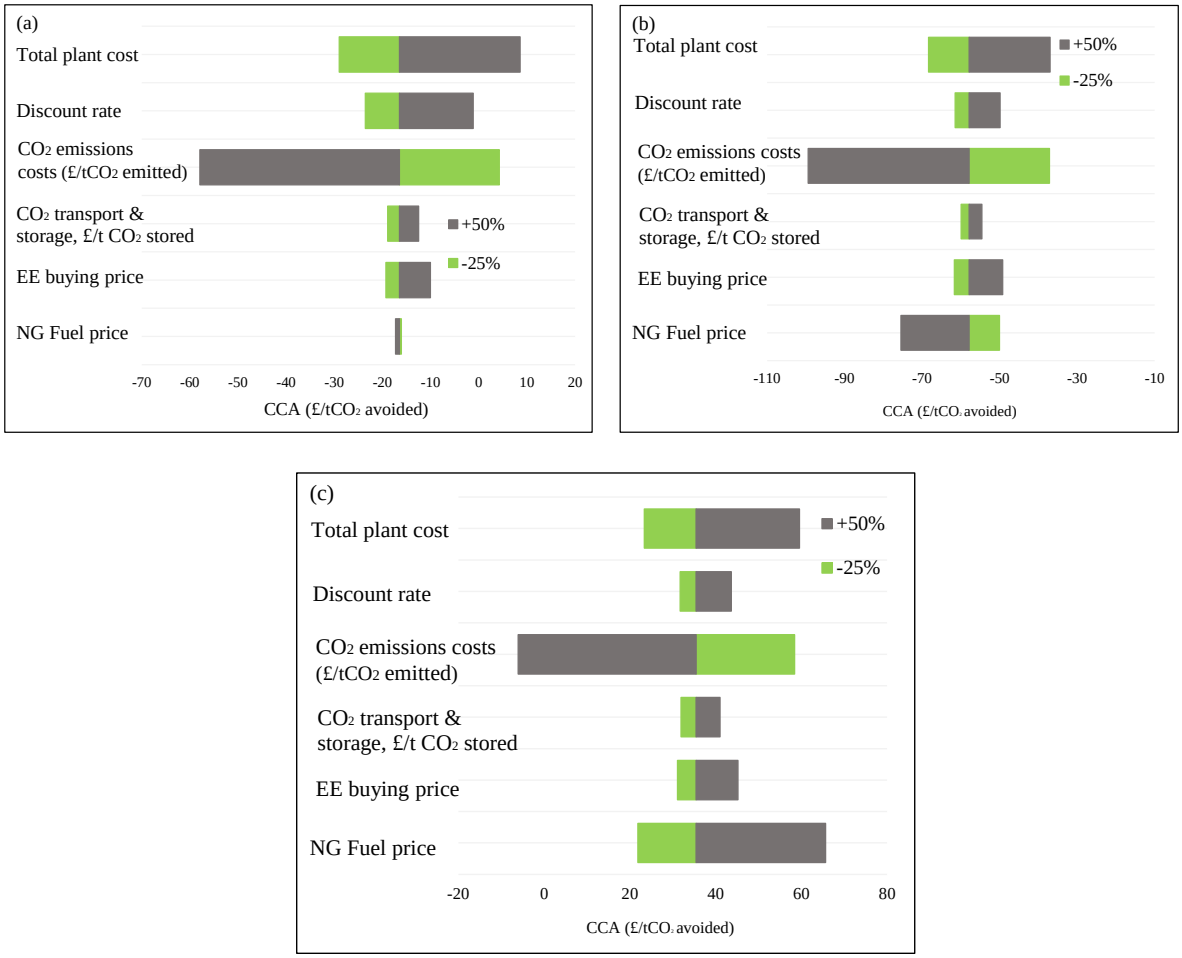

Figure 8.15: Sensitivity of select variables on CCA for (a) AG-CCS-600 (b) SE-600 and (c) SMR-CCS-600.

8.3.7.2 Electricity price

Among the various plants shown in Figure 8.14, SE-600 was the most affected by an increase in electricity prices, leading to an 8% increase in the LCOH, relative to the reference value of 2.85£/kgH_2. This plant relies significantly on electricity imports, making it particularly sensitive to changes in electricity prices. In contrast, the LCOH of AG-CCS-600 and SMR-CCS-600 increased by 3.68% and 3.60%, respectively, with increase in electricity prices. The CCA for the plants in Figure 8.15 are also seen to change slightly with variation in electricity prices.

8.3.7.3 CO_2 transport & storage

This study considered offshore scenario for CO_2 transport and storage, considering the geographical location of the plants. The strategic location of the Humber region offers potential for supporting offshore CO_2 storage, and there are roadmaps already in place to make this a reality [616]. As seen in Figure 8.14, the LCOH of SMR-CCS-600, AG-CCS-600, and SE-600 showed no significant increase, only dropping by ~0.7% and increasing ~1% at the lower and upper bounds, respectively. The cost of CO_2

transport and storage also had a slight impact on the CCA for these plants, ranging from 3% to 15% changes in CCA.

8.3.7.4 Carbon price

The monetary cost of CO_2 emissions was estimated from the carbon prices per tonne of CO_2 equivalent, based on the UK Emissions Trading Scheme. Figure 8.14 shows that carbon price affects SMR-600 the most, after natural gas price, with its LCOH changing by 5% to 12% with variation in carbon price. The LCOH of SE-600 and AG-CCS-600 both fluctuate between 0.06% and 0.6% over the carbon price range. The LCOH of SMR-CCS-600 was observed to change much higher (2% and 3% at the upper and lower ranges, respectively), due to relatively large CO_2 emissions from the plant.

Figure 8.15 revealed that among the input variables tested, carbon price had the strongest impact on the estimated CCA for the various blue hydrogen production facilities. A +50% change in the carbon price resulted in the largest swings in the CCA for each technology, with the CCA of SMR-CCS-600, SE-600, and AG-CCS-600 reducing by 117%, 71.6%, and 250% relative to the base CCA, respectively. Reducing carbon price by 25% resulted in 64.9%, 35.8% and 126% increase in the CCA of SMR-CCS-600, SE-600, and AG-CCS-600, respectively. The relatively high change in the CCA of AG-CCS-600 shows that this technology is the most impacted by carbon price. This is likely due to the distinct relationship between natural gas consumption, CO_2 emissions and carbon capture efficiency, where huge volume of the relatively large CO_2 generated was captured. So, a price on each tonne of CO_2 avoided translates into a disproportionately larger CCA.

To understand how carbon price can affect the economic competitiveness of these blue hydrogen technologies in the net-zero scenario, the carbon price sensitivity range was extended to consider the net-zero scenario (2050), which projects a central price of £200/tCO_2e with a potential to rise to £300/tCO_2e [617]. As seen in Figure 8.16, the LCOH of the blue hydrogen technologies slightly increases with increasing carbon price, while their CCA reduces with increasing carbon price. The negative values of CCA indicate cost savings associated with the use of these technologies. In this scenario, the use of these blue hydrogen technologies becomes desirable as the cost of avoiding CO_2 emissions is effectively offset and outweighed by benefits, such as the trading of carbon credits in carbon markets, to provide additional revenue streams. For SMR-600, there was a sharp increase in its LCOH as carbon price increases. The LCOH of SMR-600 can reach high values of £4.57/kgH_2, when carbon price is at 200 £/ton CO_2. At a carbon price of ~£40/ton CO_2 and £70/ton CO_2, the LCOH of SMR-600 increases to become equal to the LCOH of SE-600 and AG-CCS-600, respectively.

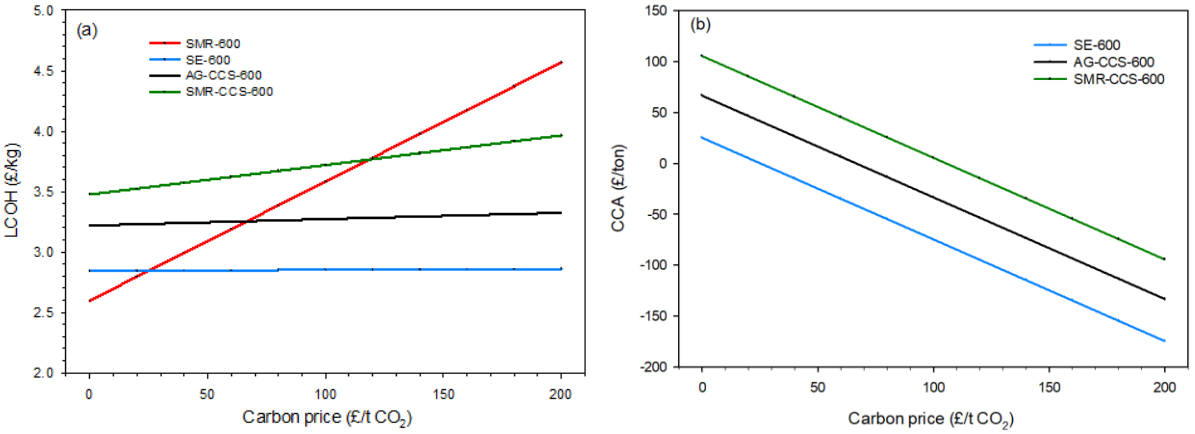

Figure 8.16: Sensitivity of (a) LCOH and (b) CCA to changes in carbon prices.

To compensate for the relatively high LCOH for SMR-CCS-600, the carbon price must be much higher at 117 £/tCO_2 to justify the use of SMR-CCS-600. At 117 £/tCO_2, the LCOH of SMR-CCS-600 becomes equal to SMR-600 and CCA turns negative, signifying cost savings from the use of CCS. However, following the UK's guidance on CCS achieving design capture rate of at least 95%, SMR-CCS-600 will need to demonstrate the achieved carbon capture efficiency [618]. At carbon prices above £40-£117/ tCO_2, producing hydrogen without CCS (SMR-600) becomes more expensive than blue hydrogen, depending on the blue hydrogen technology.

In the net-zero scenario, the LCOH of SE-600, AG-CCS-600, and SMR-CCS-600 plants show a slight increase to 2.89, 3.27 and 3.96 £/kgH_2, respectively compared to 2.84, 3.22, and 3.48 £/kgH_2, at zero carbon price. This represents a 1.55%, 1.76%, and 13.7% increase for SE-600, ATR-600 and SMR-CCS-600, respectively, which is insignificant compared to changes in their CCA. At a carbon price of 200£/ton CO_2, the CCA of the blue hydrogen technologies are all negative at -81.57£/tCO_2, -134.46£/tCO_2, and -174.88£/tCO_2 avoided for SMR-CCS-600, AG-CCS-600, and SE-600, indicating potential revenues.

8.3.7.5 Discount rate

As seen in Figure 8.14, the choice of discount rate has a noticeable impact on the LCOH of hydrogen. An upward trend in the LCOH was observed for all the plants as discount rate increases, with the SMR-CCS-600 plant displaying the highest value of £3.81/kgH_2 at 12% discount rate. Similarly, the cost of CO_2 avoidance followed a similar pattern, increasing as the discount rate increased.

8.3.7.6 Total plant cost

Figure 8.14 revealed that the different low-carbon hydrogen production technologies exhibited varying degrees of susceptibility to increases or decreases in projected total plant cost. Of the three blue

hydrogen technologies evaluated, SMR-CCS-600 demonstrated the lowest sensitivity to total plant cost. A +50% change in plant costs resulted in about 4.8% increase in LCOH for SMR-CCS-600, whereas ~7.1% increase in LCOH was observed for both AG-CCS-600 and SE-600 plants. Reducing plant cost by 25% resulted in 2.4% drop in the LCOH of SMR-CCS-600, and ~3.6% decrease in the LCOH of AG-CCS-600 and SE-600 plants.

When assessing the impact of total plant cost on CCA, the CCA estimate for AG-CCS showed the greatest sensitivity, reducing by 76% when plant cost is lowered by 25% and increasing by 152% at +50% plant cost range. SMR-CCS-600 showed intermediate sensitivity on CCA, fluctuating by roughly 34% and 68% at the lower and upper sensitivity bounds, respectively. Meanwhile, SE displayed the lowest sensitivity amongst the technologies, with its CCA changing by 18% and 36% at the lower and upper sensitivity bounds, respectively. Total plant cost has the second-greatest impact on the CCA of SE-600 and AG-CCS-600, after carbon price, and third-greatest impact on the CCA of SMR-CCS-600, after carbon price and natural gas price.

8.4 Summary

In this chapter, the potential cost of scaling up the emerging SE-SR technology was evaluated through a techno-economic assessment. With the goal of benchmarking the SE-SR technology, it was compared against SMR-CCS, ATR-GHR-aMDEA, and a base case conventional SMR at large-scale blue hydrogen production of 600 $MWth_{(LHV)}$ and scaled up to 1000 $MWth_{(LHV)}$. Aspen Plus® was used to develop the process model, which was validated using literature data. Cost sensitivity analyses were also performed on two key indicators: levelised cost of hydrogen and CO_2 avoidance cost by varying natural gas price, electricity price, CO_2 transport and storage cost, and carbon price. Results indicate that, at a carbon price of 83 £/tCO_2e, the LCOH for SE-SR of methane is the lowest at 2.85 £/kgH_2, which is 12.58% and 22.55% lower than that of ATR-GHR with CCS and SMR plant with CCS, respectively. The LCOH of ATR-GHR with CCS and SMR plant with CCS was estimated to be 3.26 and 3.68 £/kgH_2, respectively. The CO_2 avoidance cost was also observed to be lowest for SE-SR, followed by ATR-GHR with CCS, then SMR plant with CCS, and was observed to reduce as the plant scaled to 1000 $MWth_{(LHV)}$ for these technologies.

9 General discussion

CO_2 is a major greenhouse gas contributing to climate change due to its heat-trapping greenhouse gas properties and long lifespan in the atmosphere [14]. Lowering CO_2 emissions from fossil fuels and other sources is important for climate mitigation. Addressing this challenge demands diverse set of solutions, including the use of clean alternative fuels. Hydrogen is promising, if produced through low-carbon pathways like SE-SR. SE-SR and other innovative pathways assume greater importance as worldwide hydrogen demand is projected to continue growing to help decarbonise various sectors [16]. However, SE-SR remains at a low technology readiness level. Therefore, this PhD research investigated and applied a novel scaleup methodology and modelling tool to simulate the performance of SE-SR of methane at large capacity, in order to facilitate scale-up efforts that will improve SE-SR readiness.

CPFD modelling based on MP-PIC approach is an essential tool for simulating multiphase chemical processes, like SE-SR, that occur within fluidised bed reactors. The discrete nature of CPFD allows for detailed tracking of individual particles and gas bubbles, along with inter-particle collisions and particle-wall interactions. This provides insights into complex hydrodynamic behaviours that could be challenging to capture experimentally. CPFD was applied in this work to model the SE-SR process, first at lab-scale reformer/carbonator in Chapter 4, then at full-loop bench scale in Chapter 5, in order to establish the validity of the approach.

Three drag models were evaluated for their ability to simulate the hydrodynamic behaviour of a binary particulate system: the EMMS-Yang, Gidaspow, and Wen-Yu models. Each model was used to predict the fluidisation characteristics of a mixture containing two distinct particle size properties, based on validation data (jetsam volume fraction) from the literature. The EMMS-Yang and Gidaspow models were able to qualitatively capture the overall trends seen in the validation data, but their quantitative outputs diverged somewhat from measured values. The kinetic validation showed some level of agreement with the experimental data. In Chapter 4, the deviations for reforming/carbonation validation ranged from 0.09% to 0.71% for the different product compositions, on a dry basis. In Chapter 5, the full-loop model validation, including the reformer/carbonator and calciner, showed deviations ranging from 0.01% to 2% compared to experimental literature data. These slight deviations suggest a level of agreement between the model and experimental literature data. Moreover, some degree of error is expected in modelling efforts due to the simplifications and complexities involved.

CPFD modelling based on MP-PIC approach is a relatively recent development for simulating SE-SR processes. At the start of this PhD research, MP-PIC methods had never been applied to study SE-SR systems. This work proposed using an MP-PIC approach in Barracuda VR® software to model SE-SR of

methane process, at both lab and larger scales. However, since then, a few studies applying MP-PIC methods to SE-SR have been published. Wan et al. [418] applied the MP-PIC approach to model the SE-SR of methane in a lab-scale bubbling bed reactor. They validated their model against literature experimental data and achieved comparable results for hydrodynamic flow properties and predicted product yields. More recently, Di Nardo et al. [246] developed a CPFD model to simulate the lab-scale dual bubbling fluidised bed system, for SE-SR of methane over a bifunctional catalyst. Their model was validated using experimental measurements from a cylindrical apparatus measuring 8 cm in diameter, with a 20 cm static bed height. Di Nardo et al. [246] reported good agreement between their simulation outputs and the reference experimental dataset. These recent applications of CPFD modelling further establishes the validation of CPFD model as a useful tool for studying SE-SR processes, at lab and potentially larger scales.

Following validation, the developed CPFD model in this work was used to conduct a parametric analysis of the SE-SR process under varied conditions. First, the impact of operating pressure, gas velocity, and steam-to-carbon ratio were investigated for a stand-alone bubbling bed reactor configuration (Chapter 4). Hydrodynamic flow characteristics were also analysed. Next, the full dual bubbling fluidised bed loop system was simulated while limiting variations to catalyst-to-sorbent volume ratios and geometry design (Chapter 5). The model demonstrated good predictive capabilities in both scenarios. Varying the catalyst-to-sorbent ratio was found to influence reaction progress, with optimal methane conversion and CO_2 capture observed at nearly equal volume ratios of catalyst and sorbent. Higher sorbent loadings enhanced thermal neutrality but risked increasing energy demands for calciner regeneration. Minor influences of bed geometry on hydrodynamic behaviours were also seen. With the bench scale model validated, the CPFD model was then utilised to develop and test scaleup methodologies based on similarity principles.

As Matsen [619] stated, "fluidised bed scale-up is still not an exact science, but is rather that mix of physics, mathematics, witchcraft, history and common sense that we call engineering." The scale-up of multiphase reactors such as those required for commercialising SE-SR processes presents a significant challenge, due to the complex hydrodynamics involved. General principles and scaling methodologies can provide guidance but any new system will still require careful consideration of inherent uncertainties. Knowlton et al. [526] presented a multi-step method in scaling a new fluidised bed process, which involves the determination of reaction kinetics, selection of a mathematical model based on the fluidisation regime, construction of a pilot plant and large-scale cold flow model, followed by a commercial plant. When mathematical model is used for scaling, the methods could include process model and optimisation, reactor modelling, parametric analysis, and selection of reactor system [620]. However, there is no single strict procedure for scaling up fluidised bed reactors. For

scaling-up of CFB, Knowlton et al. [621] identified some hydrodynamic parameters to be determined to facilitate scaleup. These included: solids and gas velocity profiles within the riser, the radial gas dispersion coefficient, and the solids volume fraction or holdup, which is the most important parameter.

Two scaling laws proposed by Glicksman [511] and Horio et al. [503] were selected and evaluated using the CPFD model (Chapter 6). The scaling laws aim to establish dynamic similarity by selecting dimensionless parameters that remain constant between scales. The validated CPFD model was used to test scale-up from bench to a 1 MWth plant. Keeping all parameters constant proved challenging, given the differences in fluidising gas properties between scales. Nevertheless, an effort was made to keep several key parameters consistent, as summarised in Table 9.1.

Table 9.1: Summary of dimensionless parameters maintained for the different scaling laws.

Scaling laws	**Dimensionless parameters**
Glicksman (Model G) [511]	$\frac{u_o^2}{gD}$, $\frac{u_o}{u_{mf}}$, $\frac{D}{H}$, φ_p, bed geometry
Horio et al. (Model H) [503]	$\frac{D_s}{D_b}$, $\frac{H_s}{H_b}$, $\frac{u_o - u_{mf}}{\sqrt{gD}}$, $\frac{u_{mf}}{\sqrt{gD}}$, N_r, bed geometry

In general, the Glicksman and Horio et al. scaling laws were tested by:

i. Applying the scaling relationships derived from their dimensionless group analysis to geometrically scale the bench-scale model properties to the 1 MWth unit size.
ii. Using the validated CPFD model to simulate both scales under three different velocities and two particle sizes, while satisfying the scaling laws by maintaining matching values of parameters like Froude number ($\frac{u_o^2}{gD}$) and velocity ratios.
iii. Comparing the hydrodynamic behaviour predicted at each scale to validate that scaled dynamic similarity was achieved to the extent possible, given constraints like different gas properties.

While not all scale-up criteria could be strictly followed due to inherent scale differences, the validated CPFD model demonstrated that key dimensionless groups from established scaling laws could still be sufficiently matched to enable hydrodynamic and chemical similarity between scales, even if not identically replicated. The voidage and methane conversion profiles from scaling models G and H showed qualitatively similar behaviour to the bench-scale model, at low to moderate gas velocities. The profiles exhibited an annular-lean core pattern, where the outer annular region near the walls had a sharply decreasing voidage gradient and the central core maintained a more uniform, higher voidage.

However, at the highest velocity tested, a deviation was observed. The bench-scale voidage profile showed higher values near the wall, suggesting non-uniform gas distribution or preferential channelling along boundaries, but Models G and H retained the annular-lean core pattern. Quantitatively, the average lateral voidage and conversion from models G and H fell within the bench-scale model's 90% confidence interval, for low to moderate velocities. At the high velocity, the averages were below this threshold. This suggests the scaling models successfully matched the bench-scale behaviour across most operating ranges examined. However, at the highest gas velocity, hydrodynamic similarities began to diverge, potentially due to scale-dependent effects like poorer distribution not fully captured. Despite qualitative and quantitative similarities between the Model G and H, Model G would necessitate a larger physical reactor diameter and height to precisely satisfy its scale-up dimensional ratios, relative to the lab unit. This increases both capital and operating costs associated with purchases of raw materials, construction, and maintenance for essentially similar predicted performance to Model H. Therefore, Model H was selected for further scale-up studies.

The scale-up studies (Chapter 7) involved analysing the impact of design variable (bed aspect ratio – H/D) and bed conditions (initial bed temperature and particle sizes) on the performance of the standalone reformer/carbonator, at 1 MWth reactor scale. The bed aspect ratio and particle size had a lesser impact on the reactive performance but significantly influenced the hydrodynamics of the bed, as evidenced by the observed changes in bubble dynamics, pressure drop, and gas-solid contours. On the other hand, the initial bed temperature demonstrated the most substantial impact on the reactive performance of the reformer/carbonator, as reflected in the variations in product gas composition. At lower bed temperatures, the limited catalyst activity and slower reaction kinetics hindered the methane conversion and hydrogen production rates. However, as the bed temperature increased, the enhanced kinetics of the SMR reactions led to a significant increase in hydrogen composition, reaching a maximum of approximately 96% at 873 K. Beyond this temperature, carbonation reaction reduced, resulting in a decrease in hydrogen composition and an increase in CO_2 concentration. Although the bed aspect ratio and particle size did not drastically influence the product performance, their effects on the hydrodynamics were notable. Higher bed aspect ratios generally favoured improved gas-solid contact and mass transfer, leading to increased hydrogen production and reduced CH_4 and CO_2 compositions. However, high aspect ratios also resulted in increased pressure drop.

When the calciner was integrated and at constant solids circulation rate, the performance of the 1 MWth scale behaved differently. In the reformer, the mole fractions of hydrogen and methane are seen to decrease by approximately 1%, while the CO and CO_2 compositions increased by a similar amount, relative to the product compositions of the standalone bubbling bed SE-SR reformer. This behaviour was attributed to the introduction of hot solids originating from the calciner, which led to

an increase in the average particle temperature in the reformer/carbonator, from an initial value of 873 K to 978 K. The higher particle temperature in the reformer/carbonator influenced the equilibrium and kinetics of the reforming reactions, resulting in the observed changes in product gas composition. Despite maintaining a calciner wall temperature of 1173 K, the average particle temperature in the calciner continued to decrease, reaching around 1028 K at the end of the 400-second simulation time, from an initial value of 1173 K. This temperature drop in the calciner suggests the presence of heat transfer limitations and the need for higher wall temperatures or improved heat integration strategies, to maintain the desired particle temperature for efficient sorbent regeneration. The integration of the calciner and the introduction of hot solids from the regeneration process had an impact on the overall system behaviour at the 1 MWth scale. While the solids circulation facilitated continuous sorbent regeneration and CO_2 capture, the associated temperature changes affected the reaction equilibria and kinetics in the reformer/carbonator, leading to variations in the product gas composition. To address the observed temperature drop in the calciner and ensure efficient sorbent regeneration, further investigations into heat integration strategies and optimisation of the calciner operating conditions, such as wall temperature and solids residence time, may be necessary.

Across scales (1 MWth to 150 MWth), some similarities are observed for parameters like bubble distribution profiles and product distribution (Chapter 7). However, there are also deviations that warrant closer examination. The bubble size distributions show a shift where larger bubbles form at the bottom of the smaller 1 MWth scale, compared to the 50 and 150 MWth scales. However, at the top, the trend reverses with larger bubbles in the bigger scales. This could be attributed to differences in factors like turbulence intensity and particle dispersion impacting bubble behaviours locally within the beds. Interestingly, the 50 and 150 MWth scales more closely align in bubble sizes, validating the idea that scaling parameters can fluctuate more at small scales before levelling off [517]. This suggests bubble dynamics may become more consistent above a threshold scale.

Looking at particle distributions, the 1 MWth scale shows less loading in the freeboard compared with the other scales. The distinction in freeboard loading suggests entrainment is limited at smaller scale. This ties directly to the inferred greater turbulence driving bubble changes and breakage seen at larger scales. Product gas trends point to larger scales showing enhanced conversion, through higher turbulence and increased particle surface area (since particle size was kept constant across scales). The spatial product distribution profiles seen in the product composition contours are consistent at the different scales, given that the scale-up methodology also aimed to preserve chemical similarity. Apart from bed temperature which showed significant impact on product compositions when tested at 1 MWth, there is also pressure drop concerns that should be noted as scale increases.

Economically, SE-SR was found to be competitive. SE-SR was bench-marked against more established blue hydrogen production technologies like SMR and ATR-GHR integrated with CCS (Chapter 8). Its levelised cost of hydrogen production is estimated at £2.79-2.84/kgH_2, making it the lowest cost option modelled, even after including costs of hydrogen compression. SMR coupled with CCS has a clear cost disadvantage, with an LCOH over £3.40/kg due in part to high fuel usage. Capital costs are the main contributor to ATR-GHR's levelised cost of hydrogen, estimated at £3.10-3.22/kgH_2. Scaling the plants up to 1000 MW capacity provides some cost reductions across the board, as a result of economies of scale. However, SE-SR still maintains its cost advantage against the other blue hydrogen options. Sensitivity analysis reveals that natural gas prices have the biggest influence on LCOH, while carbon prices are most impactful on the cost of avoided CO_2 emissions.

10 Conclusion and recommendations

In this PhD research, a model-based scale-up studies was conducted to analyse behaviours and assess performance of SE-SR of methane in bubbling fluidised bed reactors. This was achieved through the following objectives:

1. Conducting a general literature review to examine the current state of research and development in the wider field of low-carbon hydrogen production, with a particular focus on SE-SR technology, as in Chapter 2.
2. Conducting a comprehensive review to understand the state-of-the-art in simulation and modelling approaches for SE-SR of methane in FBR, as in Chapter 3.
3. Developing and validating a CPFD model to simulate lab-scale SE-SR, benchmarked against published experimental data, as in Chapter 4.
4. Extending the CPFD model to simulate a full-loop bench-scale SE-SR system and validating model predictions, as in Chapter 5.
5. Developing and validating a scale-up methodology for SE-SR in bubbling fluidised bed reactors using the validated CPFD model, as in Chapter 6.
6. Evaluating the performance of a 1 MWth SE-SR of methane system at varying operating conditions and extrapolating the model to assess behaviour at larger scales of 1, 50, and 150 MWth, as in Chapter 7.
7. Conducting a techno-economic analysis of SE-SR for methane production at commercial scales to benchmark against established blue hydrogen technologies, using validated process simulation models, as in Chapter 8.

Concisely, a CPFD reactor model was developed and simulated in Barracuda VR® and validated against literature data. Initially, a 3D CPFD model was developed for a lab-scale reformer/carbonator only, with hydrodynamic and kinetic behaviour validated with literature data. Then, this model was extended to include the calciner, where the full-loop system including the loopseals were modelled and validated. Two scale-up methodologies, based on similarity principles, were developed and their performance validated using the CPFD model. One scale-up method was subsequently selected for use with the CPFD model, to conduct scale-up studies of SE-SR in bubbling fluidised bed reactors at larger scales. Finally, the performance of SE-SR was benchmarked against more established blue hydrogen production technologies at much larger scales, using process models developed in Aspen Plus V12.1 software. The main conclusions and recommendations from this research are presented in the following sections:

10.1 Conclusions

10.1.1 A three-dimensional computational particle fluid dynamic model for sorption-enhanced steam reforming of methane

In Chapter 4, a CPFD model was developed for a lab-scale SE-SR of methane in bubbling fluidised bed reactor and validated with experimental data available from literature. Parametric studies aimed at understanding the predictive capabilities of the CPFD model, as well as analysing characteristics of SE-SR in bubbling fluidised bed reactors that have yet to be examined in previous research, was conducted. The gas-solid flow characteristics, influence of pressure (1 – 25 atm), steam-to-carbon ratio (3 – 5), and velocity (1 – 4 m/s) were investigated. Validation of the model was carried out for both the hydrodynamic and kinetic sub-models, by comparing simulation results of volume fraction and compositions with available experimental data. In the hydrodynamics validation, three drag models – EMMS-Yang, Gidaspow, and Wen-Yu – were tested. Among these, only the EMMS-Yang model exhibited a similar trend to the experimental data, with a slight deviation attributable to the omission of modelling the high-pressure drop distributor. The kinetic model was also validated successfully, as the product composition results matched and agreed well with the experimental data.

The behaviour of particles in the reactor was also analysed, with a focus on particle volume fraction and the velocities of gas and solid phases. Time-averaged data showed the bed expanding approximately 1.4 times its initial height due to bubble formation and particle redistribution. Simultaneously, fluid pressure was higher at the bottom due to the weight of bed particles. The fluid velocity contour revealed distinct flow regimes, including dense flow, bubble flow, and throughflow. Negative solid flows were attributed to particle recirculation. The CPFD model effectively captured these hydrodynamics zones within the reactor, highlighting the role of bubbles in inducing circulation and gas-solids contact SE-SR process.

Based on the spatial gas species distribution predicted by the model, three distinct profiles were revealed at the inlet, middle and upper bed regions. The inlet/lower bed region exhibited high methane and CO concentrations, with CO_2 levels peaking due to steam reforming reactions. Moving to the mid bed region, CO_2 sorption reduced CO_2 concentrations, while water-gas shift reactions continue. In the upper bed region, reforming and shift reactions were largely completed, resulting in high and uniformly distributed hydrogen levels. The particles remained well-mixed, although $CaCO_3$ is concentrated at the reactor bottom due to high CO_2 levels.

The modelled species concentration profiles under varying operating parameters generally align with anticipated trends. Increasing pressure adversely affects SE-SR of methane performance, as increased

pressure reduces methane conversion and in turn, leads to reduced CO_2 capture efficiency. High S/C ratios enhance methane conversion, hydrogen production, and CO_2 capture efficiency but presented challenges for sorbent CO_2 adsorption due to high steam and low CO_2 partial pressures. Higher gas velocities resulted in reduced residence time for reforming reactions, causing a notable decline in methane conversion. This, in turn, led to decreased hydrogen purity, despite increased hydrogen production rate. Given its demonstrated predictive accuracy, the validated reformer/carbonator CPFD model was considered well-suited for further analysing the SE-SR system.

10.1.2 Computational simulation of SE-SR of methane in a bench-scale dual circulating fluidised bed reactor

In Chapter 5, the CPFD model was expanded to include the calciner, and other full-loop system components including the loopseals and cyclone. The impact of various catalyst-to-sorbent ratios (C-S) and two bed geometry designs (CFB1 and CFB2) on the chemical performance of a dual circulating fluidised bed system for SE-SR of methane, was investigated. Key reactor properties including product composition, thermal performance and solids distribution, were compared between the two bed geometry designs. Three C-S mass ratios (0.3, 1.3 and 3) were explored to analyse their chemical behaviour and hydrodynamic characteristics. At a low C-S of 0.3, methane conversion was lowest, with a product gas relatively high in unconverted CH_4 and CO, and low in H_2, suggesting incomplete reforming and CO shift reactions due to insufficient catalyst contact time. As a result, CO_2 capture was negatively impacted due to reduced CO_2 partial pressures and driving force. A moderate C-S of 1.3 resulted in an improved methane conversion and reduced levels of CO and CO_2 in the product, with the highest H_2 yield. At low sorbent loading (C-S=3) representing a low sorption capacity, CO_2 removal by the sorbent decreased, resulting in higher CO_2 emissions. However, the negative effects of low catalytic activity exceeded those of low sorbent activity on the overall process performance.

Varying the sorbent ratio also influenced heat management in the system. While higher sorbent loading enhanced heat retention in the reformer, it risked a steeper temperature drop in the calciner, increasing regeneration penalties. For optimal process efficiency, adjusting solid circulation rates, together with sorbent inventory, can help alleviate energy penalties associated with calcination temperature drop. The use of bifunctional catalysts may also enhance sorption kinetics at lower mass loadings, reducing heat requirements in the calciner. The instantaneous temperature contours revealed that achieving quick temperature homogenisation proved challenging at very low catalyst or sorbent levels.

The solids volume fraction profiles provided insights into bubble flow patterns within the two bed designs. In CFB1, bubbles appeared to preferentially migrate towards the wall perimeter, as indicated by the downward trend in particle concentration moving radially outward. Meanwhile, CFB2 exhibited a more gently downward sloped profile at the centre, suggesting a tendency for bubbles to accumulate more towards the central axis rather than the perimeter. Solids concentration contours revealed the expected reduced CaO fraction in reformers versus calciners, validating the cyclic carbonation-calcination process. A uniform $CaCO_3$ distribution were seen in the reformers, indicating adequate contact between phases without noticeable particle segregation.

The result from this chapter provided insights into the potential impact of catalyst deactivation and sorbent loading, emphasising the need to also match them with appropriate circulation rates, while considering the calciner's thermal requirements.

10.1.3 Scale-up strategy for SE-SR of methane in bubbling fluidised bed reactors

The study in Chapter 6 applied the principle of similarity and CPFD model to scale up SE-SR process for hydrogen production, operating in the bubbling fluidisation regime. The objective was to validate if the scaled models adopted – Glicksman's (Model G) and Horio's (Model H) models – can reliably replicate key performance metrics like conversion and reactor trends observed at bench scale. Hydrodynamic characteristics and reaction performance across scales were evaluated under varying operating conditions. Time-averaged voidage profiles and methane conversion were compared between the bench-scale model and scaled Models G and H under different gas velocities, and two discrete particle sizes.

While similarity was demonstrated on average across most conditions studied, some scale-dependent divergences emerged under more intense fluidisation. At higher superficial gas velocities corresponding to more vigorous bubbling, minor deviations beyond ±10% parity tolerance were observed for a few data points between units. Similarly, when replicating the bench-scale 200 µm particle size, voidage profiles for Models G and H became relatively non-uniform, compared to uniform trends observed at 500 µm.

However, scaled Models G and H generally exhibited close agreement with trends observed at bench-scale, with most data points falling within the ±10% parity band. Comparison of Model G to Model H showed the two scaled units achieved near-identical simulation of the bench reactor across all test cases, validating the reliability of the scaling methodologies. Although their performance aligned closely, Model G would require a slightly larger physical dimensions and particle inventory mass to geometrically match scale-up ratios.

10.1.4 Effect of scale on the performance of SE-SR of methane in a bubbling fluidised bed reactors

One novelty in this thesis includes the way CPFD model with scaling laws were employed in scaling-up SE-SR of methane in bubbling bed reactor. The developed models and findings provide guidelines for design and scale-up of future industrial SE-SR of methane system. In Chapter 7, the performance of 1MWth SE-SR was first analysed in a stand-alone bubbling bed, then in circulating mode using the CPFD model. This was shifted to a multi-scale analysis, spanning 1 MWth to 150 MWth capacities, to provide understanding into the scale-up performance and challenges.

For the 1 MWth SE-SR reactor, the effects of operating parameters including initial bed temperature, bed aspect ratio, and particle size were evaluated. Initial bed temperature was found to strongly influence product gas composition, with temperature around 873K producing the highest hydrogen yield of 96%. Temperatures above this led to decreasing hydrogen due to reduced carbonation reaction, while below resulted in lower methane conversion due to low reforming kinetics. Transient temperature profiles showed larger gradients at lower bed temperatures, indicating improved heat transfer at higher bed temperatures. Increasing bed aspect ratio from 0.4 to 0.8 enhanced gas-solid contact, improving hydrogen composition up to 96%. Above an aspect ratio of 0.8, little benefit was observed. Particle size had a minor impact on composition but strongly affected hydrodynamics, with larger sizes (>800 μm) exhibiting packed bed behaviour.

In the investigation of the SE-SR process in circulating mode, the integration of a bubbling bed calciner with the reformer/carbonator using loopseals enabled the internal circulation of sorbent particles between the reaction zones. This configuration led to changes in product gas composition, with slight decreases in hydrogen and methane mole fractions, accompanied by increases in CO and CO_2 compositions. These shifts were attributed to the circulation of hot solids from the calciner to the reformer, resulting in increased temperatures in the reformer and subsequent impacts on reaction kinetics and sorbent behaviour. Temperature profiles within the system revealed substantial increases in both particle and fluid temperatures, particularly in the reformer, highlighting the influence of hot solids circulation on thermal dynamics. In addition, pressure profiles indicated decreasing pressure gradients along the height of the reactors, with slightly higher pressure drops observed in the calciner compared to the reformer.

Furthermore, the investigation into the effect of scale on the SE-SR process elucidated negligible trends in product gas composition, pressure drop profiles, and methane conversion rates between scales. Scaling up the system revealed slight increases (<1%) in hydrogen composition alongside reductions in methane, CO, and CO_2 compositions, indicating improved methane conversion and sorbent

performance at larger scales. Though chemical similarity was well-maintained across scales. The larger reactors exhibited increased pressure drops, necessitating more powerful compression systems. Bubble size distribution and particle distributions were similar across scales, though larger reactors exhibited more particle carryover. Simulating larger scales up to 150 MWth revealed only minor deviations in trends like bubble size distribution and product compositions with scale. This validates the suitability of the proposed scaleup methodology for industrial-scale hydrogen production. The developed nonlinear regression model quantitatively describes the observed increase in methane conversion with scale, offering guidance for reactor design and scale-up.

10.1.5 Bench-marking large-scale SE-SR of methane against conventional technologies for low-carbon hydrogen generation

Chapter 8 concerns the benchmarking of SE-SR technology against SMR-CCS, ATR-GHR-aMDEA, and a base case conventional SMR at large-scale blue hydrogen production of 600 $MWth_{(LHV)}$ and scaled up to 1000 $MWth_{(LHV)}$. Sensitivity of natural gas price, electricity price, CO_2 transport and storage cost, carbon price, total plant cost, and discount rate on two key indicators – LCOH and CCA – was also conducted for all the cases examined.

The SMR-CCS plant has the lowest technical performance, of all the cases considered in this study. The net process efficiency dropped from ~69% to ~56%, when CCS unit was integrated into the process. In addition, its overall carbon capture efficiency was below 90%. Whilst AG-CCS-600 exhibited the highest high fuel conversion of ~99%, its net process efficiencies was low, reaching ca. 66%. This is because of the energy intensive ASU, H_2 compressor and CCS plant, which will require electricity imports of, at least, 30 MWe to operate. Conversely, SE-600 plant had the highest net process efficiency of ~74%, with the overall carbon capture efficiency reaching 98%. The specific CO_2 emissions for SMR, SMR-CCS, SE-SR, and ATR-GHR-aMDEA plants were found to be around 9.86, 2.44, 0.08, and 0.53 $kgCO_2/kgH_2$, respectively.

Upon scaling the plants from 600 to 1000 MW capacity, the LCOH and CCA reduced for all the technologies. At a carbon price of 83£/tCO_2e, the LCOH of SMR-CCS-600 is the highest at 3.68£/kgH_2, mainly attributed to the large volume of natural gas required to operate the process. The SMR plant had relatively higher LCOH at 3.42 £/kgH_2, due to its high emissions costs which are a result of the significant volume of CO_2 generated and emitted from the plants. LCOH for AG-CCS-600 was at 3.26 £/kgH_2, with capital costs as the major cost contributor, primarily due to the high cost of components such as autothermal reformers and the a-MDEA CCS plants. For SE-600, the LCOH was estimated to be 2.85 £/kgH_2, due to its compact nature and low natural gas consumption. Factors such as natural gas

prices, electricity prices, carbon price and total plant costs exerted noticeable impact on the LCOH and CCA for the hydrogen technologies. Natural gas price has the greatest impact on the LCOH for the technologies, while carbon price impacts the CCA mostly.

10.2 Recommendations for future study

Based on the findings of this thesis, a number of recommendations can be made to further advance the development and scale-up of SE-SR process. The following recommendations also address some of the most important challenges identified through this work:

i. It is important to note that the CPFD model was developed specifically for methane feedstock; therefore, its applicability and accuracy may be limited when using feedstocks with different compositions, properties, and reaction pathways. The kinetic mechanisms and transport properties incorporated into the model were tailored for and validated under conditions representing methane feedstock. Switching to alternate carbon sources would require recalibration of relevant model parameters against different experimental datasets. Additionally, impurities present in some fuels but not pure methane could introduce compounding complexities not captured here. The hydrodynamic scaling principles derived should transfer well, but achievability of performance objectives may differ without modifying chemical reaction schemes.

ii. One of the main limitations in this research was the use of kinetic parameters from small-scale laboratory studies without validation at larger pilot or industrial scales. Reaction kinetics can change with scale. Therefore, more work is needed to characterise how kinetics evolve with scale. This would allow developing scale-dependent rates for more accurate modelling of large industrial processes.

iii. In developing the scale-up methodology, isothermal conditions were assumed, which simplified the scale-up models but does not completely capture thermal similarity between scales. Temperature gradients drive many aspects of SE-SR performance like methane conversion and hydrogen purity. Developing and incorporating a full heat transfer model, and identifying dimensionless parameters would be mathematically and computationally intensive but important to do.

iv. Although the CPFD modelling provided useful insights into process performance at lab and much larger scales, additional experimentation work is still needed to verify the observed behaviours at large scale. In order words, the CPFD model would need to be validated with data from larger pilot plants.

v. The circulating hot solids from the calciner increased the average bed temperature in the reformer/carbonator and adversely impacted performance, while relatively large temperature drop was observed in the calciner. Therefore, thermal management strategies to further control solids temperatures between reactors should be explored. Optimising the solids circulation rate between the calciner and reformer/carbonator is one approach to addressing the temperature issue.

Appendix

Appendix A: Heat transfer model equations

Heat transfer from fluid to particles and wall was calculated using fluid-to-particle and convective fluid-to-wall heat transfer models, respectively. For the fluid-to-wall heat transfer, the local time-averaged heat transfer coefficient, h_{fw} is calculated by weighting the relative contributions of the lean gas and dense particle phases' heat transfer coefficients. The general equations for the lean gas (l) and dense particle (d) phases' heat transfer coefficients are presented in equations 132 and 133, respectively. The values of c_0, c_1 and c_2 in both equations were obtained from [527]. On the other hand, the fluid-to-particle heat transfer is modelled based on correlation in equation 134, with coefficient values taken from [622]. Summary of the heat transfer model equations are presented in Table A.1.

Table A.1: Summary of heat transfer model equations.

Parameters	Expressions	Equation
Heat transfer coefficient	$h_{fw} = h_l + f_d h_d$ $f_d = 1 - e^{-10(\theta_p/\theta_{cp})}$	131
Lean gas phase heat transfer coefficients	$h_l = \left(c_0 \mathrm{Re}_L^{n_1} \mathrm{Pr}^{n_2} + c_1 \frac{k_g}{L} + c_2 \right) \frac{\mathrm{W}}{\mathrm{m}^2 \cdot \mathrm{K}}$	132
Dense particle phase heat transfer coefficients	$h_d = \left(c_0 \mathrm{Re}_p^{n_1} \frac{k_f}{d_p} \right) \frac{\mathrm{W}}{\mathrm{m}^2 \cdot \mathrm{K}}$	133
Fluid-to-particle heat transfer	$h_p = \left((c_0 \mathrm{Re}_p^{n_1} \mathrm{Pr}^{0.33} + c_1) \frac{k_g}{d_p} + c_2 \right) \frac{\mathrm{W}}{\mathrm{m}^2 \cdot \mathrm{K}}$	134

Appendix B: Project file for the scaled-up SE-SR in bubbling fluidised bed

B1: Summary of material properties settings and codes

```
# This file was generated by Barracuda Virtual Reactor. It will be re-written
# the next time Barracuda Virtual Reactor is run. If you modify this file,
# expect your changes to be lost.
#
version 2210
# This file was generated by GUI version 22.1.2.i005.
projectUniqueIdStart

projectUniqueIdEnd
storeProjectFileAsUniqueId      1
projectCommentStart




projectCommentEnd
#
# ========== grid
grid
admesh 0
gridLastUsedTotalNumberCells 150000
rm_small_cells 3
rm_small_vol_I 0.040000
rm_small_vol_E 0.040000
max_aspect_ratio_I 30.000000
max_aspect_ratio_E 15.000000
open_closed_faces 1
rm_small_max_pass_combine 150
poly_col 0
draw_poly_faces 0
eps_scale -1.000000
stl 1
# x-Min and x-Max all stl files
 0.000000e+00  1.586186e+00
# y-Min and y-Max all stl files
 0.000000e+00  1.586186e+00
# z-Min and z-Max all stl files
 0.000000e+00  3.353459e+00
#
# ========== start stl file properties
New_Chem_Scale_1_reactor.stl
# header
header "solid  (null)"
# number facets
2880
# x-Min and x-Max
 0.000000e+00  1.586186e+00
# y-Min and y-Max
 0.000000e+00  1.586186e+00
# z-Min and z-Max
 0.000000e+00  3.353459e+00
# ========== end stl file properties
```

```
x0  0.000000e+00
y0  0.000000e+00
z0  0.000000e+00
xdist 1
41  1.586186e+00   0.0000
ydist 1
41  1.586186e+00   0.0000
zdist 1
87  3.353459e+00   0.0000
units m
endgrid
# ========== endgrid

# Variable units for solver output
InputOutputUnits
  time                    "s"
  length                  "m"
  mass                    "kg"
  temperature             "K"
  mole                    "mol"
  pressure                "Pa"
  pressureGradient        "Pa/m"
  velocity                "m/s"
  massFlux                "kg/(s*m^2)"
  density                 "kg/m^3"
  heatTransferCoef        "J/(s*m^2*K)"
  heatTransferFlux        "J/(s*m^2)"
  heatTransferRate        "J/s"
  chemReactionRate        "kmol/(s*m^3)"
  particleSize            "micron-diameter"
  massFlowRate            "kg/s"
  volumeFlowRate          "m^3/s"
  massConcentration       "kg/m^3"
  moleConcentration       "mol/m^3"
  viscosity               "Pa*s"
  kinematicViscosity      "m^2/s"
  thermalConductivity     "J/(s*m*K)"
  specificHeat            "J/(kg*K)"
  specificEnthalpy        "J/kg"
  molecularWeight         "g/mol"
  area                    "m^2"
  volume                  "m^3"
  energy                  "J"
  wear                    "kg^a*m^b/(s^b*m^2*yr)"
  attrition               "kg^a*m^b/s^b"
  cpuTime                 "hr"
  simSpeed                "s/day"
endInputOutputUnits

# Post-processor graphics mesh viewer to use for project
outputGmv 0
```

```
outputGmv 0
outputTecplot 1

# Thermal energy
isothermal      0
toggleThermal   off
radiationOn     0
isothermalT     8.730000e+02
presTermThermal 0
outputMinMaxTemp 1

toggleChem  on   0.000000e+00   0.000000e+00

# Put the number of fluids near start of input
numFluids  2

implicitParticleBuoyCalc on

# Put the use particles flag near start of input
useParticles 1

# Put the noParticleMomentum flag after useParticles
noParticleMomentum 0
allowPartialClouds on
virtualMassForce off
liftForce off

# Min and max temperature limit
minTempLimit  1.000000e+02
maxTempLimit  6.000000e+03

#Advanced GPU Options
decompSliceNormal automatic
tagParticlesByDecomposition OFF

# Put the name of grid file near start of input but after numFluids
gridFileName 00grid.grd

# minAreaBc used for minimum area percentage on flow/pres BC
minAreaBc    0.040000

# automatically take small time steps at start, 0 or 1
startSmallDt  1

# Time step control
time 1
#         dt       end time
#  ------------ ------------
    1.000000e-03  2.500000e+01
end_timeControl

# write the ray trace flag
```

```
rayTrace 1

# Iterations and convergance
maxErrPres     1.000000e-06
maxErrVel      1.000000e-07
maxErrVol      1.000000e-07
maxErrEnergy   1.000000e-06
maxErrRadiate  1.000000e-09
maxIterPres    2000
maxIterPres0   2000
maxIterVel     50
maxIterVol     30
maxIterEnergy  100
maxIterRadiate 1500
maxIterLoop    1

# Print, plot and restart frequency
printFreq         1.000000e-05
plotFreq          1.000000e-01
restartFreq       1.000000e+01
restartClockFreq  1.200000e+02

# Time interval adjustment flags
adjDtHighVolFrac 1
adjDtHighCFL     1
adjDtHighQ       0
adjDtHighPAcc    0
adjDtHighVolErr  0

# Min and max CFL
minCfl  8.000000e-01
maxCfl  1.500000e+00

# Min and max energy transfer rate
minQfl  1.000000e+01
maxQfl  7.000000e+01

# Min and max energy-driven acceleration
minPfl  8.000000e+00
maxPfl  1.500000e+01

# Turn on/off pressure work & drag work in energy equation - 1=on, 0=off
presWork 0

# Material phases (and properties), must be before init. gasMixturePropAve: 0=mass-based, 1=mole-based
MaterialPhases 10
  nMaterials        10
  gasMixturePropAve 1
  equState          1
  compressible      1
  plotDeltaT        1.000000e+00
  plotTMin          2.980000e+02
```

```
plotTMax          3.200000e+03
evalT             3.000000e+02
material
  chem_formula           "CH4_1"
  formula_description    "CH4 METHANE. CALCULATED USING THE RRHO METHOD"
  state                  G
  molecular_weight       1.604230e+01
  absorption_model OFF
  density                 0.000000e+00
  expression viscosity
    polynomial -3.844000e-07  4.011200e-08 -1.430300e-11  0.000000e+00  0.000000e+00
    value_units "Pa*s"
    temperature_units "K"
    temp_limits 1 9.100000e+01 1.402000e+03
    value_limits 0 1.000000e-07 1.000000e-03
  end_expression
  delta_hf(298)          -4.650434e+06
  expression heat_capacity
    double_polynomial
      lowerCoefs  2.668404e+03 -7.101000e+00  2.559163e-02 -2.549848e-05  8.816348e-09
      upperCoefs  9.909017e+02  4.977184e+00 -1.753905e-03  2.792651e-07 -1.655006e-11
      breakTemperature 1.000000e+03
    end_double_polynomial
    value_units "J/kg/K"
    temperature_units "K"
    temp_limits 1 2.000000e+02 6.000000e+03
    value_limits 0 0.000000e+00 1.000000e+00
  end_expression
  expression thermal_conductivity
    polynomial -9.350000e-03  1.402800e-04  3.318000e-08  0.000000e+00  0.000000e+00
    value_units "W/m/K"
    temperature_units "K"
    temp_limits 1 2.000000e+02 6.000000e+03
    value_limits 0 1.000000e-04 1.000000e+00
  end_expression
  absorption_coef         1.000000e-05
  scattering_coef         0.000000e+00
  refractive_index        1.000000e+00
  expression mass_diffusivity
    polynomial  0.000000e+00  0.000000e+00  0.000000e+00  0.000000e+00  0.000000e+00
    value_units "m^2/s"
    temperature_units "K"
    temp_limits 1 2.000000e+02 6.000000e+03
    value_limits 0 1.000000e-06 1.000000e-04
  end_expression
  molarVolume 0.000000e+00 # [m3/kmol]
  henrysLaw 0.000000e+00
end_material
material
  chem_formula           "CO"
  formula_description    "CO CARBON MONOXIDE"
```

```
  state                   G
  molecular_weight        2.801010e+01
  absorption_model OFF
  density                  0.000000e+00
  expression viscosity
    polynomial  3.228000e-06  4.747000e-08 -9.648000e-12  0.000000e+00  0.000000e+00
    value_units "Pa*s"
    temperature_units "K"
    temp_limits 1 6.800000e+01 2.460000e+03
    value_limits 0 1.000000e-07 1.000000e-03
  end_expression
  delta_hf(298)           -3.946267e+06
  expression heat_capacity
    double_polynomial
      lowerCoefs  1.062599e+03 -1.811859e-01  3.018454e-04  2.692483e-07 -2.684821e-10
      upperCoefs  9.049553e+02  4.012659e-01 -1.442099e-04  2.340802e-08 -1.394642e-12
      breakTemperature 1.000000e+03
    end_double_polynomial
    value_units "J/kg/K"
    temperature_units "K"
    temp_limits 1 2.000000e+02 6.000000e+03
    value_limits 0 0.000000e+00 1.000000e+00
  end_expression
  expression thermal_conductivity
    polynomial  5.066300e-04  9.123500e-05 -3.523800e-08  8.198200e-12  0.000000e+00
    value_units "W/m/K"
    temperature_units "K"
    temp_limits 1 2.000000e+02 6.000000e+03
    value_limits 0 1.000000e-04 1.000000e+00
  end_expression
  absorption_coef          1.000000e-05
  scattering_coef          0.000000e+00
  refractive_index         1.000000e+00
  expression mass_diffusivity
    polynomial  0.000000e+00  0.000000e+00  0.000000e+00  0.000000e+00  0.000000e+00
    value_units "m^2/s"
    temperature_units "K"
    temp_limits 1 2.000000e+02 6.000000e+03
    value_limits 0 1.000000e-06 1.000000e-04
  end_expression
  molarVolume 0.000000e+00 # [m3/kmol]
  henrysLaw 0.000000e+00
end_material
material
  chem_formula            "CO2"
  formula_description     "CO2 CARBON DIOXIDE"
  state                   G
  molecular_weight        4.400950e+01
  absorption_model OFF
  density                  0.000000e+00
  expression viscosity
```

```
    polynomial  2.545000e-06  4.549000e-08 -8.649000e-12  0.000000e+00  0.000000e+00
    value_units "Pa*s"
    temperature_units "K"
    temp_limits 1 1.950000e+02 2.629784e+03
    value_limits 0 1.000000e-07 1.000000e-03
  end_expression
  delta_hf(298)          -8.941945e+06
  expression heat_capacity
    double_polynomial
      lowerCoefs  4.452849e+02  1.697418e+00 -1.345608e-03  4.642706e-07 -2.699610e-11
      upperCoefs  8.760001e+02  5.179577e-01 -1.881601e-04  3.030268e-08 -1.731022e-12
      breakTemperature 1.000000e+03
    end_double_polynomial
    value_units "J/kg/K"
    temperature_units "K"
    temp_limits 1 2.000000e+02 6.000000e+03
    value_limits 0 0.000000e+00 1.000000e+00
  end_expression
  expression thermal_conductivity
    polynomial -1.200000e-02  1.020800e-04 -2.240300e-08  0.000000e+00  0.000000e+00
    value_units "W/m/K"
    temperature_units "K"
    temp_limits 1 1.950000e+02 2.278000e+03
    value_limits 0 1.000000e-04 1.000000e+00
  end_expression
  absorption_coef         1.000000e-05
  scattering_coef         0.000000e+00
  refractive_index        1.000000e+00
  expression mass_diffusivity
    polynomial  0.000000e+00  0.000000e+00  0.000000e+00  0.000000e+00  0.000000e+00
    value_units "m^2/s"
    temperature_units "K"
    temp_limits 1 2.000000e+02 6.000000e+03
    value_limits 0 1.000000e-06 1.000000e-04
  end_expression
  molarVolume 0.000000e+00 # [m3/kmol]
  henrysLaw 0.000000e+00
end_material
material
  chem_formula           "CaCO3"
  formula_description    "Calcium Carbonate"
  state                  S
  molecular_weight       1.000835e+02
  density                 2.416000e+03
  delta_hf(298)          -1.205913e+07
  expression heat_capacity
    polynomial  8.370000e+02  0.000000e+00  0.000000e+00  0.000000e+00  0.000000e+00
    value_units "J/kg/K"
    temperature_units "K"
    temp_limits 0 0.000000e+00 6.000000e+03
    value_limits 0 1.000000e+01 1.000000e+05
```

```
  end_expression
  expression thermal_conductivity
    polynomial  2.259000e+00  0.000000e+00  0.000000e+00  0.000000e+00  0.000000e+00
    value_units "W/m/K"
    temperature_units "K"
    temp_limits 0 0.000000e+00 6.000000e+03
    value_limits 0 1.000000e-04 1.000000e+00
  end_expression
end_material
material
  chem_formula           "CaO"
  formula_description    "Sorbent"
  state                  S
  molecular_weight       5.607400e+01
  density                 1.700000e+03
  delta_hf(298)          -1.134000e+07
  expression heat_capacity
    file "CaO_Heat_capacity.sff"
    value_units "J/kg/K"
    temperature_units "K"
    temp_limits 0 2.980000e+02 3.200000e+03
    value_limits 0 1.000000e+01 1.000000e+05
  end_expression
  expression thermal_conductivity
    file "CaO_Thermal_conductivity.sff"
    value_units "W/m/K"
    temperature_units "K"
    temp_limits 0 0.000000e+00 6.000000e+03
    value_limits 0 1.000000e-04 1.000000e+00
  end_expression
end_material
material
  chem_formula           "H2"
  formula_description    "H2 HYDROGEN. REF ELEMENT"
  state                  G
  molecular_weight       2.015800e+00
  absorption_model OFF
  density                 0.000000e+00
  expression viscosity
    polynomial  2.775840e-06  2.119300e-08 -3.284000e-12  0.000000e+00  0.000000e+00
    value_units "Pa*s"
    temperature_units "K"
    temp_limits 1 1.500000e+02 3.231000e+03
    value_limits 0 1.000000e-07 1.000000e-03
  end_expression
  delta_hf(298)           0.000000e+00
  expression heat_capacity
    double_polynomial
      lowerCoefs  9.669662e+03  3.291725e+01 -8.034153e-02  8.314244e-05 -3.042427e-08
      upperCoefs  1.209719e+04  3.409510e+00 -6.038657e-04  6.356178e-08 -2.841112e-12
      breakTemperature 1.000000e+03
```

```
    end_double_polynomial
    value_units "J/kg/K"
    temperature_units "K"
    temp_limits 1 2.000000e+02 6.000000e+03
    value_limits 0 0.000000e+00 1.000000e+00
  end_expression
  expression thermal_conductivity
    polynomial  3.951000e-02  4.591800e-04 -6.493300e-08  0.000000e+00  0.000000e+00
    value_units "W/m/K"
    temperature_units "K"
    temp_limits 1 1.500000e+02 5.000000e+03
    value_limits 0 1.000000e-04 1.000000e+00
  end_expression
  absorption_coef         1.000000e-05
  scattering_coef         0.000000e+00
  refractive_index        1.000000e+00
  expression mass_diffusivity
    polynomial  0.000000e+00  0.000000e+00  0.000000e+00  0.000000e+00  0.000000e+00
    value_units "m^2/s"
    temperature_units "K"
    temp_limits 1 2.000000e+02 6.000000e+03
    value_limits 0 1.000000e-06 1.000000e-04
  end_expression
  molarVolume 0.000000e+00 # [m3/kmol]
  henrysLaw 0.000000e+00
end_material
material
  chem_formula           "H2O"
  formula_description    "H2O STEAM"
  state                  G
  molecular_weight       1.801520e+01
  absorption_model OFF
  density                 0.000000e+00
  expression viscosity
    polynomial -3.682550e-06  4.291600e-08 -1.624000e-12  0.000000e+00  0.000000e+00
    value_units "Pa*s"
    temperature_units "K"
    temp_limits 1 2.500000e+02 3.219000e+03
    value_limits 0 1.000000e-07 1.000000e-03
  end_expression
  delta_hf(298)          -1.342417e+07
  expression heat_capacity
    double_polynomial
      lowerCoefs  1.937891e+03 -9.399066e-01  3.009481e-03 -2.532967e-06  8.178565e-10
      upperCoefs  1.235594e+03  1.372280e+00 -3.571351e-04  4.358604e-08 -1.970368e-12
      breakTemperature 1.000000e+03
    end_double_polynomial
    value_units "J/kg/K"
    temperature_units "K"
    temp_limits 1 2.000000e+02 6.000000e+03
```

```
    value_limits 0 0.000000e+00 1.000000e+00
  end_expression
  expression thermal_conductivity
    polynomial  5.300000e-04  4.709300e-05  4.955100e-08  0.000000e+00  0.000000e+00
    value_units "W/m/K"
    temperature_units "K"
    temp_limits 1 2.000000e+02 4.000000e+03
    value_limits 0 1.000000e-04 1.000000e+00
  end_expression
  absorption_coef         1.000000e-05
  scattering_coef         0.000000e+00
  refractive_index        1.000000e+00
  expression mass_diffusivity
    polynomial  0.000000e+00  0.000000e+00  0.000000e+00  0.000000e+00  0.000000e+00
    value_units "m^2/s"
    temperature_units "K"
    temp_limits 1 2.000000e+02 6.000000e+03
    value_limits 0 1.000000e-06 1.000000e-04
  end_expression
  molarVolume 0.000000e+00 # [m3/kmol]
  henrysLaw 0.000000e+00
end_material
material
  chem_formula           "MgO"
  formula_description    "MgO MAGNESIUM OXIDE (S)"
  state                  S
  molecular_weight       4.030440e+01
  density                 1.816000e+03
  delta_hf(298)          -1.491872e+07
  expression heat_capacity
    double_polynomial
      lowerCoefs -9.367063e+01  5.750395e+00 -1.012179e-02  8.350020e-06 -2.613956e-09
      upperCoefs  1.040782e+03  3.486184e-01 -1.560031e-04  4.185288e-08 -4.248083e-12
      breakTemperature 1.000000e+03
    end_double_polynomial
    value_units "J/kg/K"
    temperature_units "K"
    temp_limits 1 3.000000e+02 1.200000e+03
    value_limits 0 0.000000e+00 1.000000e+00
  end_expression
  expression thermal_conductivity
    polynomial  9.017250e+01 -1.601400e-01  7.716100e-05  0.000000e+00  0.000000e+00
    value_units "W/m/K"
    temperature_units "K"
    temp_limits 1 3.000000e+02 1.200000e+03
    value_limits 0 1.000000e-04 1.000000e+00
  end_expression
end_material
material
  chem_formula           "N2"
  formula_description    "N2 NITROGEN. REF ELEMENT"
```

```
  state                 G
  molecular_weight      2.801340e+01
  absorption_model OFF
  density                0.000000e+00
  expression viscosity
    polynomial  4.260640e-06  4.752500e-08 -9.882600e-12  0.000000e+00  0.000000e+00
    value_units "Pa*s"
    temperature_units "K"
    temp_limits 1 1.500000e+02 2.403000e+03
    value_limits 0 1.000000e-07 1.000000e-03
  end_expression
  delta_hf(298)          0.000000e+00
  expression heat_capacity
    double_polynomial
      lowerCoefs  1.048081e+03 -3.670533e-02 -1.493014e-04  7.228530e-07 -4.181668e-10
      upperCoefs  8.763903e+02  4.146311e-01 -1.462240e-04  2.333053e-08 -1.367624e-12
      breakTemperature 1.000000e+03
    end_double_polynomial
    value_units "J/kg/K"
    temperature_units "K"
    temp_limits 1 2.000000e+02 6.000000e+03
    value_limits 0 0.000000e+00 1.000000e+00
  end_expression
  expression thermal_conductivity
    polynomial  3.918600e-04  9.814300e-05 -5.066300e-08  1.503600e-11  0.000000e+00
    value_units "W/m/K"
    temperature_units "K"
    temp_limits 1 2.000000e+02 6.000000e+03
    value_limits 0 1.000000e-04 1.000000e+00
  end_expression
  absorption_coef        1.000000e-05
  scattering_coef        0.000000e+00
  refractive_index       1.000000e+00
  expression mass_diffusivity
    polynomial  0.000000e+00  0.000000e+00  0.000000e+00  0.000000e+00  0.000000e+00
    value_units "m^2/s"
    temperature_units "K"
    temp_limits 1 2.000000e+02 6.000000e+03
    value_limits 0 1.000000e-06 1.000000e-04
  end_expression
  molarVolume 0.000000e+00 # [m3/kmol]
  henrysLaw 0.000000e+00
end_material
material
  chem_formula          "NiMgAl2O3"
  formula_description   "Reforming Catalyst"
  state                 S
  molecular_weight      1.766540e+02
  density                2.200000e+03
  delta_hf(298)          0.000000e+00
  expression heat_capacity
```

```
      polynomial  1.045000e+03  0.000000e+00  0.000000e+00  0.000000e+00  0.000000e+00
      value_units "J/kg/K"
      temperature_units "K"
      temp_limits 0 0.000000e+00 6.000000e+03
      value_limits 0 1.000000e+01 1.000000e+05
    end_expression
    expression thermal_conductivity
      polynomial  3.290000e-01  0.000000e+00  0.000000e+00  0.000000e+00  0.000000e+00
      value_units "W/m/K"
      temperature_units "K"
      temp_limits 0 0.000000e+00 6.000000e+03
      value_limits 0 1.000000e-04 1.000000e+00
    end_expression
  end_material
endMaterialPhases


# Particles
Particles  3
  particleDescription
    particleSpcId   1
    massPerVol      0.000000e+00
    solidMaterial
      materialName  "NiMgAl2O3"
      massFraction  1.000000e+00
      ageFactor     1.000000e+00
    endSolidMaterial
    type            value
    fileName        ""
    radius1         5.00000e+02
    radius2         5.00000e+02
    units micron-diameter
    dragModel
      dragName              "EMMS-Yang-2004"
      multiplierFlag        CONSTANT
      multiplier            1.00000e+00
      multiplierFilePredef  ""
      multiplierFileUser    ""
      agglomeration
        onOff       off
        type        1
        radCut       1.80000e-05
        radBlend     5.00000e-06
        radBlendVar  2.00000e-01
        radFile      ""
        units micron-diameter
      endAgglomeration
    endDragModel
    sphericity      1.00000e+00
    emissivity      1.00000e+00
    scatterFactor   0.00000e+00
```

```
  comment          "Catalyst"
end
particleDescription
  particleSpcId    3
  massPerVol       0.000000e+00
  solidMaterial
    materialName   "CaO"
    massFraction   6.000000e-01
    ageFactor      1.000000e+00
  endSolidMaterial
  solidMaterial
    materialName   "MgO"
    massFraction   4.000000e-01
    ageFactor      1.000000e+00
  endSolidMaterial
  type             value
  fileName         ""
  radius1          5.00000e+02
  radius2          5.00000e+02
  units micron-diameter
  dragModel
    dragName               "EMMS-Yang-2004"
    multiplierFlag         CONSTANT
    multiplier             1.00000e+00
    multiplierFilePredef   ""
    multiplierFileUser     ""
    agglomeration
      onOff        off
      type         1
      radCut        1.80000e-05
      radBlend      5.00000e-06
      radBlendVar   2.00000e-01
      radFile       ""
      units micron-diameter
    endAgglomeration
  endDragModel
  sphericity       1.00000e+00
  emissivity       1.00000e+00
  scatterFactor    0.00000e+00
  comment          "Calcined_sorbent"
end
particleDescription
  particleSpcId    4
  massPerVol       0.000000e+00
  solidMaterial
    materialName   "MgO"
    massFraction   3.600000e-01
    ageFactor      1.000000e+00
  endSolidMaterial
  solidMaterial
    materialName   "CaCO3"
```

```
    massFraction  6.400000e-01
    ageFactor     1.000000e+00
  endSolidMaterial
  type            value
  fileName        ""
  radius1         5.00000e+02
  radius2         5.00000e+02
  units micron-diameter
  dragModel
    dragName              "EMMS-Yang-2004"
    multiplierFlag        CONSTANT
    multiplier            1.00000e+00
    multiplierFilePredef  ""
    multiplierFileUser    ""
    agglomeration
      onOff       off
      type        1
      radCut       1.80000e-05
      radBlend     5.00000e-06
      radBlendVar  2.00000e-01
      radFile      ""
      units micron-diameter
    endAgglomeration
  endDragModel
  sphericity      1.00000e+00
  emissivity      1.00000e+00
  scatterFactor   0.00000e+00
  comment         "Carbonated"
 end
endParticles


# Particle close pack vol frac.
voidCP 0.550000

# Local close pack vol frac. Vol frac are fraction of voidCP
#        on/off ResetVolFrac MinVolFrac  MaxVolFrac      C1        MinImpact
localVoidCP  0   0.8000000   1.0000000   1.1000000  1.000000e+03  -1.000000e+00

# Gravity (body force)
xGrav  0.000000e+00
yGrav  0.000000e+00
zGrav -9.800000e+00
rotationAxis NONE
rotationVel  0.000000e+00

# Particle-to-wall bounce
wallReflNRetain    0.850000
wallReflTRetain    0.850000
wallReflSpecular   5
wallAngleImpact 0.000000 0.710000 1.000000 0.970000 0.900000 0.800000 0.720000 0.610000 0.520000 0.380000 0.300000
```

B2: Summary of numerical solution settings and codes

```
# Collision model
collisionRestitCoef       9.800000e-01
collisionRelaxEquil       off
collisionRelaxIsotropy    off
collisionLiqMassTransfer  on
liquidCollisionParams
    kus 1.000000e-02
    kul 1.000000e-01
    R 1.000000e+00
endLiquidCollisionParams
#Collision Blend Acceleration model
collisionBlendAccel on  1.000000e-01  6.000000e-01

# Turbulence model
turbulence
  turbModel           2
  SmagorinskyConst    1.000000e-02
  keProductionConst   9.000000e-02
  keDissipationConst  0.000000e+00
  thermalModel        0
  particleInTurbEddy  off
endTurbulence

# Blend 1st and 2nd order advection
advection
  type       QSOU
  alphaQSOU  0.300000
  betaQSOU   1.000000
  blendDSOU  0.000000
  userWarned
end

# Blend explicit/implicit advection, diffusion and lumped resistance. 50=Crank-Nicolson
implicitWt 100

# Blend explicit/implicit Up in continuum drag
# (Note:  Not currently used)
implicitWtUp 100

# k-factor adjustment
kFactAdjust 0.000000

# Limit number of particles per cell based on ave  or max
pNumVolSize 1

# Method for adjusting initial volume fractions beyond close pack
adjMethodToClosePack 1

# Close pack limit coefficient for adjusting initial volume fractions
volFracCoefToClosePack 1.020000

# Set initial seed with or without random variation
randLoc 0

# damp particle normal stress induced velocity
wacker 1

# Scalar - Order is important.  Must be after fluid prop and after drag model.
scalarBC 0
```

B3: Energy equation parameters and the CPFD code

```
# ------------ Energy equation parameters ------------
thermal

  # cap total particle projected area in cells for radiation P1 model
  capParticleAreaRadiateP1    on

  interpParticleAreaRadiateP1    on


  # Thermal wall BCs
  thermalWallBc  0

  endThermalWallBc


  # Heat transfer coefficient constants

  # Fluid-to-wall heat transfer coefficient: c0 c1 c2 n1 n2
  htc_f2w_c0 4.600000e-01
  htc_f2w_c1 3.660000e+00
  htc_f2w_c2 0.000000e+00
  htc_f2w_n1 5.000000e-01
  htc_f2w_n2 3.300000e-01

  # Dense phase heat transfer coefficient: c0 n1
  htc_f2w_dense_c0  5.250000e-01
  htc_f2w_dense_n1  7.500000e-01

  # Fluid-to-particle heat transfer coefficient: c0 c1 c2 n1
  htc_f2p_c0 3.700000e-01
  htc_f2p_c1 1.000000e-01
  htc_f2p_c2 0.000000e+00
  htc_f2p_n1 6.000000e-01

endthermal
# ---------- End energy equation parameters ----------
```

B4: Summary of Python script used for bubble analysis

```
import tecplot as tp
from tecplot.exception import *
from tecplot.constant import *
import time
import math
import argparse
parser = argparse.ArgumentParser(description="Bubble analyzer script for CPFD")
parser.add_argument("layout_file", help="Path to the input layout file")
parser.add_argument("output_file", help="File name of a PLT file to save the results")
parser.add_argument("--connected", action='store_true', help="Run in connected mode.")
args = parser.parse_args()

def cfda_integrate_volume(zone):
    zone_index = zone.index+1
    tp.macro.execute_extended_command(command_processor_id='CFDAnalyzer4',
    volume = float(tp.active_frame().aux_data['CFDA.INTEGRATION_TOTAL'])
    return volume

def cfda_integrate_average(zone, variable):
    zone_index = zone.index+1
    variable_index = variable.index+1
    tp.macro.execute_extended_command(command_processor_id='CFDAnalyzer4',
    average = float(tp.active_frame().aux_data['CFDA.INTEGRATION_TOTAL'])
    return average

if args.connected:
    tp.session.connect()

start = time.time()
tp.new_layout()
tp.load_layout(args.layout_file)
frame = tp.active_frame()
dataset = frame.dataset
source_zones = list(dataset.zones("Cells"))
max_strand = max([z.strand for z in dataset.zones()])

# File to record text-based record of comprehensive bubble information for plotting
bubbleInfoFile = "bubble_information_comprehensive.sff"
f = open(bubbleInfoFile, 'w')
f.write("# Bubble information extracted via PyTecplot script\n")
f.write("#\n")
f.write("#@  1 \"Solution time\"            \"s\"\n")
f.write("#@  2 \"Bubble number\"            \"\"\n")
f.write("#@  3 \"Bubble x-center\"          \"m\"\n")
f.write("#@  4 \"Bubble y-center\"          \"m\"\n")
f.write("#@  5 \"Bubble z-center\"          \"m\"\n")
f.write("#@  6 \"Bubble volume\"            \"m^3\"\n")
f.write("#@  7 \"Bubble diameter\"          \"m\"\n")
f.write("#@  8 \"Bubble rise velocity\"     \"m/s\"\n")
f.write("#@  9 \"Bubble fluid u-velocity\"  \"m/s\"\n")
f.write("#@ 10 \"Bubble fluid v-velocity\"  \"m/s\"\n")
f.write("#@ 11 \"Bubble fluid w-velocity\"  \"m/s\"\n")
f.close()
```

```
with tp.session.suspend():
    print("Extracting blanked zones")
    zones_to_separate = tp.data.extract.extract_blanked_zones(source_zones)

    zones_to_save = []
    for source_zone in zones_to_separate:
        # Assign a strand as a follow up from the previous step so
        # that all "extract blanked zones" are grouped together
        source_zone.strand = max_strand+1

        solution_time = source_zone.solution_time
        print("Extracting connected regions at solution time:", "{:08.2f}".format(solution_time))
        extracted_regions = tp.data.extract.extract_connected_regions(source_zone)

        f = open(bubbleInfoFile, 'a')

        for i, zone in enumerate(extracted_regions):
            # Assign a strand and solution time as a follow up from the
            # previous step so that all "separated zones" are grouped together
            # and will animate through time
            zone.solution_time = source_zone.solution_time
            zone.strand = max_strand+2
            volume = cfda_integrate_volume(zone)
            avg_x = cfda_integrate_average(zone, dataset.variable("x"))
            avg_y = cfda_integrate_average(zone, dataset.variable("y"))
            avg_z = cfda_integrate_average(zone, dataset.variable("z"))
            avg_vel_mag = cfda_integrate_average(zone, dataset.variable("Fluid velocity magnitude"))
            avg_fluid_u = cfda_integrate_average(zone, dataset.variable("Fluid velocity u"))
            avg_fluid_v = cfda_integrate_average(zone, dataset.variable("Fluid velocity v"))
            avg_fluid_w = cfda_integrate_average(zone, dataset.variable("Fluid velocity w"))

            area = volume / thickness  # m^2
            radius = math.pow((3 * volume / 4 / math.pi), 1/3)  # m
            diameter = radius * 2  # m
```

```
            # Apply the values to the zone
            eqn = '{{bubble_number}} = {}\n'.format(i+1)
            eqn += '{{bubble_x}} = {}\n'.format(avg_x)
            eqn += '{{bubble_y}} = {}\n'.format(avg_y)
            eqn += '{{bubble_z}} = {}\n'.format(avg_z)
            eqn += '{{bubble_volume}} = {}\n'.format(volume)
            eqn += '{{bubble_diameter}} = {}\n'.format(diameter)
            eqn += '{{bubble_rise_velocity}} = {}\n'.format(avg_vel_mag)
            eqn += '{{bubble_avg_fluid_u}} = {}\n'.format(avg_fluid_u)
            eqn += '{{bubble_avg_fluid_v}} = {}\n'.format(avg_fluid_v)
            eqn += '{{bubble_avg_fluid_w}} = {}\n'.format(avg_fluid_w)
            #print(eqn)
            tp.data.operate.execute_equation(eqn, zones=[zone])

            # Write data to text-based files for plotting bubble statistics
            f.write("{0:8.5e}".format(solution_time))
            f.write("{0:6d}".format(i+1))
            f.write("{0:13.5e}".format(avg_x))
            f.write("{0:13.5e}".format(avg_y))
            f.write("{0:13.5e}".format(avg_z))
            f.write("{0:13.5e}".format(volume))
            f.write("{0:13.5e}".format(diameter))
            f.write("{0:13.5e}".format(avg_vel_mag))
            f.write("{0:13.5e}".format(avg_fluid_u))
            f.write("{0:13.5e}".format(avg_fluid_v))
            f.write("{0:13.5e}".format(avg_fluid_w) + "\n")

            zones_to_save.append(zone)

        f.close()

        f = open(bubblesVsTime, 'a')
        f.write("{0:.6e}".format(solution_time))
        f.write("{0:6d}".format(i+1) + "\n")
        f.close()

    tp.data.save_tecplot_plt(args.output_file, zones=zones_to_save)

print("Elapsed Time: ", time.time() - start)
```

Appendix C: Process model parameters and results used for benchmarking of SE-SR with other conventional blue hydrogen technologies

C1: Chemical reactions

This section describes the chemical reactions used to develop the models for each of the processes, including the H_2O-PZ-MDEA system for CO_2 capture.

1. Steam methane reforming

The main steam methane reforming reaction is given in equation 135. Considering the water-gas shift reaction expressed in equation 136, the overall chemical equation for steam reforming of methane is presented in equation 137.

$$CH_4+H_2O \rightleftharpoons CO+3H_2 \quad (135)$$

$$CO+H_2O \rightleftharpoons CO_2+H_2 \quad (136)$$

$$CH_4+2H_2O \rightleftharpoons CO_2+4H_2 \quad (137)$$

2. Autothermal and gas-heated reforming reactions

The first reaction occurs in the gas-heated reformer, where 30% methane conversion is achieved via SMR reaction, presented in the previous section, before proceeding to the ATR. The gas-heated reforming eliminates the need for external combustion for heat provision as the required heat is supplied by the high-temperature product stream from the ATR. In the ATR, partial oxidation reactions presented in equations 138-140 and steam reforming reaction described in equation 137 occurs.

$$CH_4+\tfrac{1}{2}O_2 \rightarrow CO+2H_2 \quad (138)$$

$$H_2+\tfrac{1}{2}O_2 \rightarrow H_2O \quad (139)$$

$$CO+\tfrac{1}{2}O_2 \rightarrow CO_2 \quad (140)$$

3. Sorption-enhanced steam reforming of methane reactions

SE-SMR reaction combines the SMR reaction described in equations 135-137, with the carbonation of CaO in the reformer given in equation 141. In the calciner the backward reaction of equation takes place to regenerate the CaO.

$$CaO + CO_2 \rightleftharpoons CaCO_3 \quad (141)$$

4. CO_2 capture plant

The CO_2 capture plant model was developed in Aspen Plus using the Electrolyte Non-Random Two-Liquid activity coefficient model (ELECNRTL). The reactions and parameters for the equilibrium and kinetic models were obtained from literature data [553,555,606] and presented in Table C.1. Equations 142-146 are equilibrium reactions while equations 147-154 are kinetic reactions.

Table C.1: Kinetic parameters for the CO_2-PZ-MDEA-H_2O system

Reactions	Parameters			No
Equilibrium reactions	A	B	C	
$H_2O+H^+PZCOO^- \rightleftharpoons H_3O^+ + PZCOO^-$	−14.0420	−3443.10	0	142
$2H_2O \rightleftharpoons OH^- + H_3O^+$	132.8990	-13445.90	-22.4773	143
$MDEAH + H_2O \rightleftharpoons MDEA + H_3O^+$	−9.4165	−4234.98	0	144
$HCO_3^- + H_2O \rightleftharpoons H_3O^+ + CO_3^{2-}$	216.049	-12431.70	-35.419	145
$PZH^+ + H_2O \rightleftharpoons PZ + H_3O^+$	−4.0762	−7773.20	0	146
Kinetic reactions	**Pre-exponential factor (kmol/(m³·s))**	**Activation energy (J/mol)**		
$MDEAH^+ + HCO_3^- \rightarrow MDEA + CO_2 + H_2O$	1.06×10^{16}	106323.168		147
$PZ(COO)_2^{2-} + H_3O^+ \rightarrow PZCOO^- + CO_2 + H_2O$	5.56×10^{25}	76831.704		148
$PZCOO^- + H_3O^+ \rightarrow PZ + CO_2 + H_2O$	7.94×10^{21}	65899.956		149
$HCO_3^- \rightarrow CO_2 + OH^-$	2.38×10^{17}	123164.082		150
$CO_2 + OH^- \rightarrow HCO_3^-$	4.32×10^{13}	55407.318		151
$PZ + CO_2 + H_2O \rightarrow PZCOO^- + H_3O^+$	4.14×10^{10}	33616.1706		152
$PZCOO^- + CO_2 + H_2O \rightarrow PZ(COO)_2^{2-} + H_3O^+$	3.62×10^{10}	33616.1706		153
$MDEA + CO_2 + H_2O \rightarrow MDEAH^+ + HCO_3^-$	1.06×10^{16}	106323.168		154

The dimensions and properties of the absorber column and stripper used for the simulation is also presented in Table C.2.

Table C.2: Specifications of the absorber and stripper

Properties	**Absorber**	**Stripper**
Column diameter (m)	5	8
Number of equilibrium stages	20	20
Packed height (m)	24	30
Type of packing	MELLAPAK 250Y	MELLAPAK 250Y

C2: Results from the validation of SE-SR of methane

To adjust the results of the SE-SR reactor in the simulation so that it matches the experimental data, the temperature approaches for the water-gas shift reactions and carbonation reaction were set to 30 °and 19 °C, respectively. Results of the simulation validated against experimental data [574] is presented in Table C.3.

Table C.3: Comparison of simulation results with experimental data from literature for SE-SR

	Experiment [574]		**Simulation**		**Simulation Errors**	
Reforming temperature (°C)	H_2 Yield (%)	CH_4 Conversion (%)	H_2 Yield (%)	CH_4 Conversion (%)	H_2 Yield (%)	CH_4 Conversion (%)
550	86.23	96.76	96.36	96.42	11.75	0.35
575	87.55	97.65	96.73	96.90	10.50	0.76
600	89.45	98.82	96.94	97.32	8.37	1.52
625	91.94	98.82	96.86	97.72	5.35	1.12
650	93.11	99.41	96.30	98.11	3.42	1.31
675	85.49	99.71	94.87	98.53	10.97	1.18
700	83.44	99.41	91.93	98.97	10.18	0.44
750	79.78	99.85	90.81	99.72	13.82	0.13
800	79.78	100.00	89.92	99.92	12.71	0.08

C3: Flowsheets of all the processes studied.

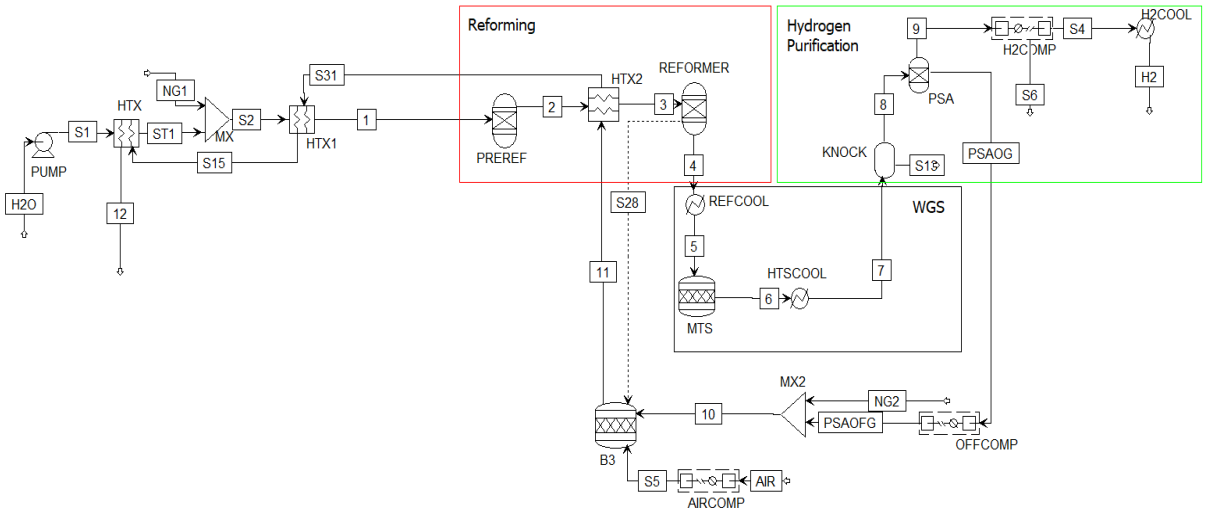

Figure C.1: Process flowsheet for steam methane reforming.

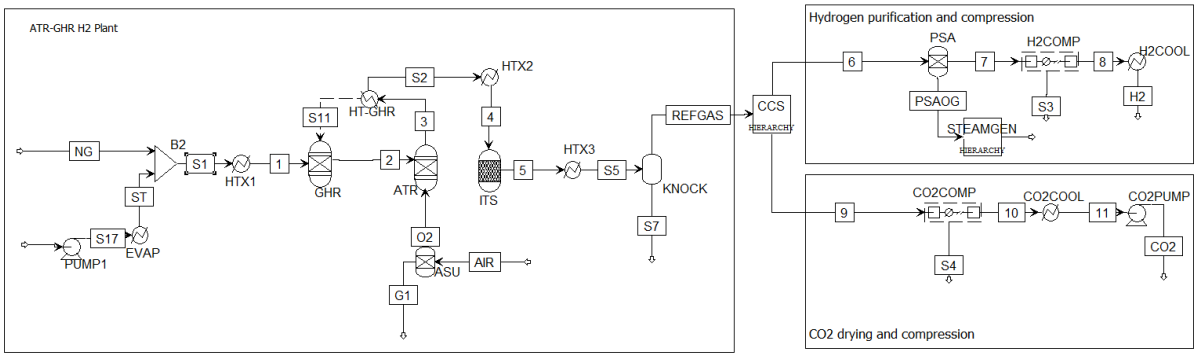

Figure C.2: Process flowsheet for autothermal with gas-heated reforming process.

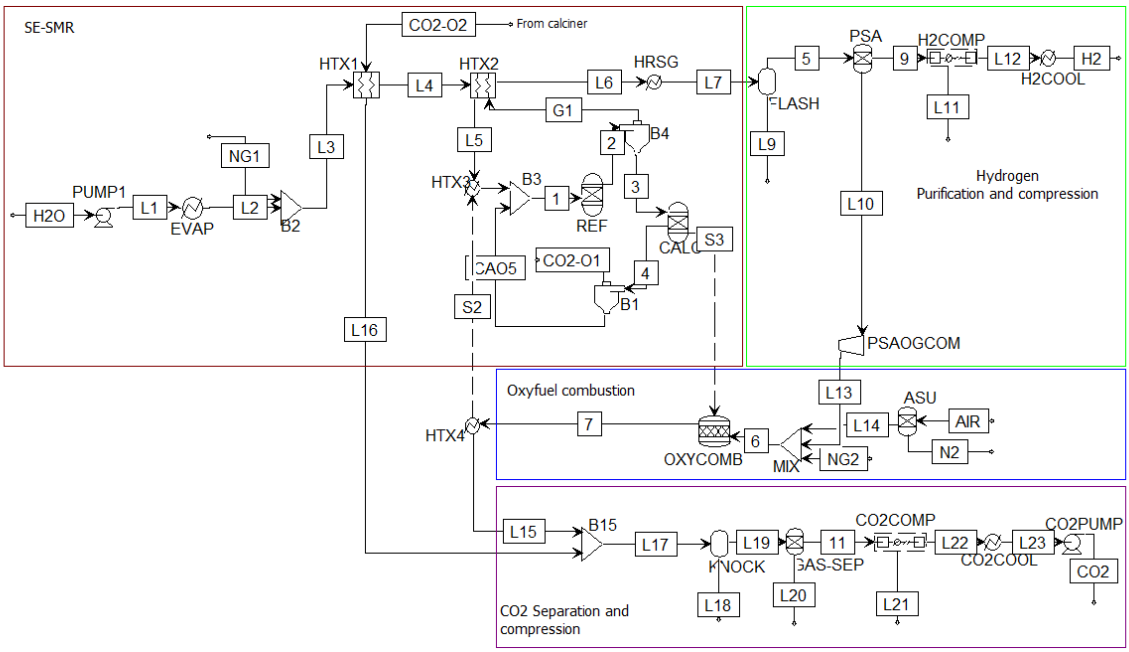

Figure C.3: Process flowsheet for sorption-enhanced steam reforming.

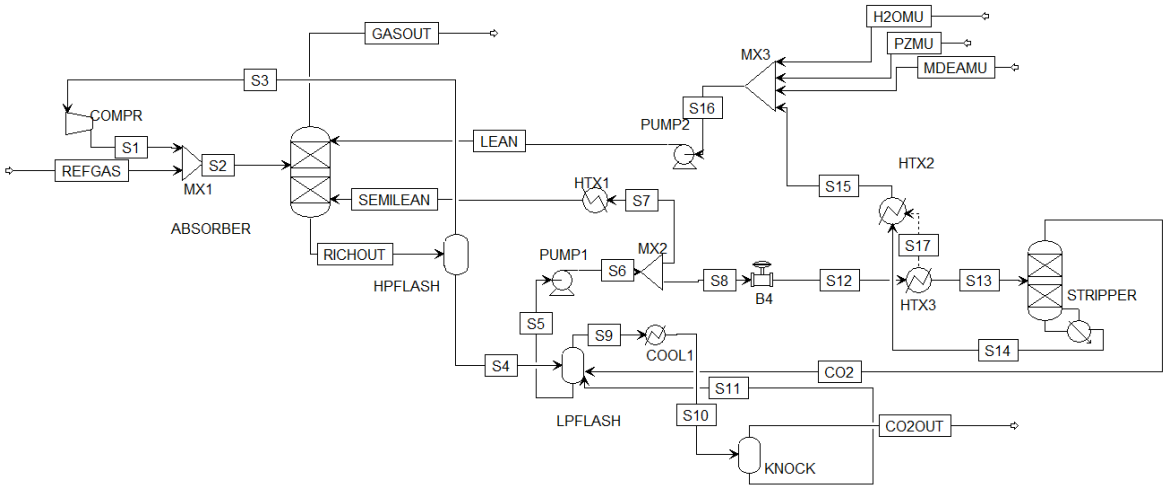

Figure C.4: Process flowsheet for the CO_2 capture unit.

C4: Stream properties

In this section, the summary of stream results is presented for all the cases studied at 600 MW hydrogen production scale.

Table C.4: Steam reforming of methane

Streams		**1**	**2**	**3**	**4**	**5**	**6**	**8**	**PSAOG**	**H_2**	**11**
Description		Pre-reformer In	Pre-reformer Out	Reformer In	Reformer Out	MTS In	MTS out	PSA in	PSAOG to Furnace	H_2 to pipeline	Furnace Out
Pressure	Bar	30.00	29.60	28.72	26.86	26.86	26.08	26.08	1.30	200.00	4.80
Temperature	℃	482.00	450.00	600.00	870.00	220.00	314.00	35.00	35.00	25.00	1034.20
Molar Flow	kmol/h	11,543.36	11,990.07	11,990.07	16,670.13	16,670.13	16,670.13	13,188.13	4,258.99	8,929.13	20,971.14
Mass Flow	kg/h	204,679.20	204,679.20	204,679.20	204,679.20	204,679.20	204,679.20	141,923.72	123,922.50	18,001.18	613,150.88
Composition											
CO_2	mol/mol	0.00	0.02	0.02	0.05	0.05	0.14	0.18	0.56	0.00	0.19
CO	mol/mol	0.00	0.00	0.00	0.10	0.10	0.01	0.01	0.04	0.00	0.00
Methane	mol/mol	0.25	0.25	0.25	0.04	0.04	0.04	0.05	0.15	0.00	0.00
Ethane	mol/mol	0.01	0.00	0.00	0.00	0.00	0.00	0.00	0.00	0.00	0.00
H_2O	mol/mol	0.73	0.67	0.67	0.30	0.30	0.21	0.00	0.01	0.00	0.19
n-butane	mol/mol	0.00	0.00	0.00	0.00	0.00	0.00	0.00	0.00	0.00	0.00
Nitrogen	mol/mol	0.00	0.00	0.00	0.00	0.00	0.00	0.00	0.00	0.00	0.62
Oxygen	mol/mol	0.00	0.00	0.00	0.00	0.00	0.00	0.00	0.00	0.00	0.00
Propane	mol/mol	0.00	0.00	0.00	0.00	0.00	0.00	0.00	0.00	0.00	0.00
Hydrogen	mol/mol	0.00	0.06	0.06	0.50	0.50	0.60	0.75	0.23	1.00	0.00
H_2S	mol/mol	0.00	0.00	0.00	0.00	0.00	0.00	0.00	0.00	0.00	0.00
NO_x	mol/mol	0.00	0.00	0.00	0.00	0.00	0.00	0.00	0.00	0.00	0.00

Table C.5: Autothermal gas-heated reforming with CCS

Streams		**1**	**2**	**2**	**3**	**4**	**5**	**6**	**7**	**H_2**	**9**	**CO_2**
		GHR In	GHR Out	ATR In	ATR Out	ITS In	ITS Out	PSA In	H_2 to compressor	H_2 to pipeline	CO_2 to compressor	CO_2 to pipeline
Pressure	Bar	35.50	35.30	35.30	34.80	34.80	34.50	34.00	34.00	200.00	1.15	110.00
Temperature	℃	500.00	777.87	777.87	1050.00	270.00	270.00	41.80	41.80	25.00	40.00	24.98
Molar Flow	kmol/h	9,574.23	12,634.08	12,634.08	17,926.00	17,926.00	17,926.00	10,346.53	8,946.09	8,946.09	4,079.15	3,830.08
Mass Flow	kg/h	168,258.13	168,258.13	168,258.13	272,014.79	272,014.79	272,014.79	37,521.88	18,000.00	18,000.00	171,420.71	166,933.38
Composition												
CO_2	mol/mol	0.00	0.05	0.05	0.08	0.08	0.22	0.02	0.00	0.00	0.93	0.99
CO	mol/mol	0.00	0.07	0.07	0.16	0.16	0.01	0.01	0.00	0.00	0.00	0.00
Methane	mol/mol	0.39	0.21	0.21	0.00	0.00	0.00	0.00	0.00	0.00	0.01	0.01
Ethane	mol/mol	0.02	0.00	0.00	0.00	0.00	0.00	0.00	0.00	0.00	0.00	0.00
H_2O	mol/mol	0.59	0.27	0.27	0.36	0.36	0.21	0.00	0.00	0.00	0.06	0.00
n-butane	mol/mol	0.00	0.00	0.00	0.00	0.00	0.00	0.00	0.00	0.00	0.00	0.00
Nitrogen	mol/mol	0.00	0.00	0.00	0.01	0.01	0.01	0.01	0.00	0.00	0.00	0.00
Oxygen	mol/mol	0.00	0.00	0.00	0.00	0.00	0.00	0.00	0.00	0.00	0.00	0.00
Propane	mol/mol	0.00	0.00	0.00	0.00	0.00	0.00	0.00	0.00	0.00	0.00	0.00
Hydrogen	mol/mol	0.00	0.40	0.40	0.40	0.40	0.55	0.95	1.00	1.00	0.00	0.00
H_2S	mol/mol	0.00	0.00	0.00	0.00	0.00	0.00	0.00	0.00	0.00	0.00	0.00
NOx	mol/mol	0.00	0.00	0.00	0.00	0.00	0.00	0.00	0.00	0.00	0.00	0.00
PZ	mol/mol	0.00	0.00	0.00	0.00	0.00	0.00	0.00	0.00	0.00	0.00	0.00
MDEA	mol/mol	0.00	0.00	0.00	0.00	0.00	0.00	0.00	0.00	0.00	0.00	0.00

Table C.6: Sorption-enhanced steam reforming of methane

Streams		**1**	2	3	4	5	6	7	H_2	CO_2
Description		Reformer/ Carb In	Reformer/ Carb Out	Calciner In	Calciner out	PSA in	Oxycomb In (+PSAOG)	Oxycomb Out	H_2 to pipeline	CO_2 to pipeline
Pressure	Bar	25.50	25.00	23.90	1.00	23.70	1.1	1.0	200.0	110.0
Temperature	℃	741.1	700.0	699.9	900.00	40.0	18.2	29.5	25.0	20.0
Molar Flow	kmol/h	24,282.55	26,889.75	2,936.47	5,380.66	10,591.08	2,033.70	4,011.47	8,929.10	3,424.80
Mass Flow	kg/h	546,110.07	546,110.07	272,237.80	272,237.80	33,149.66	21,451.92	100,361.64	18,000.00	150,724.59
Compositions										
CaO	mol/mol	0.12	0.02	0.17	0.55	0.00	0.00	0.00	0.00	0.00
$CaCO_3$	mol/mol	0.00	0.09	0.83	0.00	0.00	0.00	0.00	0.00	0.00
CO_2	mol/mol	0.00	0.00	0.00	0.45	0.01	0.04	0.03	0.00	0.00
CO	mol/mol	0.00	0.00	0.00	0.00	0.00	0.02	0.01	0.00	0.00
Methane	mol/mol	0.11	0.02	0.00	0.00	0.05	0.32	0.43	0.00	0.00
Ethane	mol/mol	0.01	0.00	0.00	0.00	0.00	0.00	0.01	0.00	0.00
H_2O	mol/mol	0.76	0.49	0.00	0.00	0.00	0.02	0.02	0.00	0.00
n-butane	mol/mol	0.00	0.00	0.00	0.00	0.00	0.00	0.00	0.00	0.00
Nitrogen	mol/mol	0.00	0.00	0.00	0.00	0.00	0.01	0.01	0.00	0.00
Oxygen	mol/mol	0.00	0.00	0.00	0.00	0.00	0.00	0.53	0.00	0.00
Propane	mol/mol	0.00	0.00	0.00	0.00	0.00	0.00	0.00	0.00	0.00
Hydrogen	mol/mol	0.00	0.37	0.00	0.00	0.94	0.60	0.49	1.00	1.00
H_2S	mol/mol	0.00	0.00	0.00	0.00	0.00	0.00	0.00	0.00	0.00
NO_x	mol/mol	0.00	0.00	0.00	0.00	0.00	0.00	0.00	0.00	0.00

C5: Cost of Equipment

The reference presented in Table C.7 was used to calculate the cost of the major reactors for each of the processes. Hydrogen compressor cost was estimated using equation 130 and escalating the cost from 2019 to 2023 rate [623].

$$Total\ installed\ cost, \qquad CAD\$ = 2 \times (3083.3 * kW^{SF}) \qquad 155$$

Where Scale factor, SF = 2

Table C.7: Parameters used to estimate the costs of equipment.

Process unit	Scaling parameter	Unit	Capacity	Currency	Cost ('000)	Cost type	Year	Scaling exponent	Ref.
Steam reformer	H_2 flowrate	kg/h	8994	€	40,677	Installed	2014	0.65	[624]
Autothermal reactor	Reformer exit	kg/h	633,660	$	329,244	Installed	2007	0.6	[625]
Gas-heated reactor	NG input	MW_{LHV}	1,800	€	12,770	Installed	2006	0.75	[626]
Shift converter	Syngas flowrate	kg/h	587,349	$	17,442	TPC	2020	0.8	[627]
SE-SR unit (including solids handling)	H_2 flowrate	Nm^3/h	100,000	$	28,030	Installed	2014	0.65	[628]
Oxy-fuel combustor	Power output	kW	622,000	$	92,021	TPC	2007	0.85	[629]
Steam turbine	Power output	kW	194,900	$	46,715	TPC	2007	0.7	[630]
Air separation unit with oxygen compressor	Oxygen flowrate	kg/h	250,000	$	193,147	TPC	2007	0.89	[631]
Pressure swing adsorber	Inlet flowrate	m^3/s	4.63	€	36,560	Installed	2017	1	[632]

References

[1] Mimura N. Sea-level rise caused by climate change and its implications for society. Proceedings of the Japan Academy, Series B 2013;89:281–301. https://doi.org/10.2183/pjab.89.281.

[2] Pörtner H-O, Roberts DC, Masson-Delmotte V, Zhai P, Tignor M, Poloczanska E, et al. The ocean and cryosphere in a changing climate. IPCC Special Report on the Ocean and Cryosphere in a Changing Climate 2019;1155.

[3] Bindoff NL, Cheung WWL, Kairo JG, Arístegui J, Guinder VA, Hallberg R, et al. Changing ocean, marine ecosystems, and dependent communities. IPCC Special Report on the Ocean and Cryosphere in a Changing Climate 2019:477–587.

[4] Seneviratne SI, Zhang X, Adnan M, Badi W, Dereczynski C, Di Luca A, et al. Weather and climate extreme events in a changing climate (Chapter 11) 2021.

[5] Eyring V, Gillett NP, Achuta Rao KM, Barimalala R, Barreiro Parrillo M, Bellouin N, et al. Human Influence on the Climate System. In: Masson-Delmotte V, Zhai P, Pirani A, Connors SL, Péan C, Berger S, et al., editors. Climate Change 2021 – The Physical Science Basis, Cambridge University Press; 2023, p. 423–552. https://doi.org/10.1017/9781009157896.005.

[6] Dhakal S, Minx JC, Toth F, Abdel-Aziz A, Figueroa Meza MJ, Hubacek K, et al. Emissions Trends and Drivers (Chapter 2) 2022.

[7] IEA. The Future of Hydrogen. IEA, Paris 2019. https://bit.ly/3YK5xiY (accessed April 9, 2023).

[8] IEA. Global Hydrogen Review 2024. IEA, Paris 2024. https://bit.ly/40pVn87 (accessed September 8, 2023).

[9] IEA. Global hydrogen demand in the Net Zero Scenario, 2022-2050. IEA, Paris 2023. https://bit.ly/3UwTKBT (accessed April 9, 2023).

[10] Navas-Anguita Z, García-Gusano D, Dufour J, Iribarren D. Revisiting the role of steam methane reforming with CO2 capture and storage for long-term hydrogen production. Science of The Total Environment 2021;771:145432. https://doi.org/10.1016/J.SCITOTENV.2021.145432.

[11] Voldsund M, Jordal K, Anantharaman R. Hydrogen production with CO2 capture. Int J Hydrogen Energy 2016;41:4969–92. https://doi.org/10.1016/J.IJHYDENE.2016.01.009.

[12] Arstad B, Prostak J, Blom R. Continuous hydrogen production by sorption enhanced steam methane reforming (SE-SMR) in a circulating fluidized bed reactor: Sorbent to catalyst ratio dependencies. Chemical Engineering Journal 2012;189–190:413–21.

[13] Johnsen K, Ryu HJ, Grace JR, Lim CJ. Sorption-enhanced steam reforming of methane in a fluidized bed reactor with dolomite as CO2-acceptor. Chem Eng Sci 2006;61:1195–202. https://doi.org/10.1016/j.ces.2005.08.022.

[14] Mitchell JFB. The “Greenhouse” effect and climate change. Reviews of Geophysics 1989;27:115–39. https://doi.org/10.1029/RG027i001p00115.

[15] Calvin K, Dasgupta D, Krinner G, Mukherji A, Thorne PW, Trisos C, et al. IPCC, 2023: Climate Change 2023: Synthesis Report. Contribution of Working Groups I, II and III to the Sixth

Assessment Report of the Intergovernmental Panel on Climate Change [Core Writing Team, H. Lee and J. Romero (eds.)]. IPCC, Geneva, Switzerland. 2023. https://doi.org/10.59327/IPCC/AR6-9789291691647.

[16] IEA. CO2 Emissions in 2023. IEA, Paris 2024. https://bit.ly/3USUP7x (accessed April 1, 2023).

[17] Lan X, Keeling R. Monthly Average Mauna Loa CO2. 2024.

[18] NOAA National Centers for Environmental Information. Monthly Global Climate Report for Annual 2023. 2024.

[19] UNFCC. Adoption of the Paris Agreement. 2015.

[20] Rogelj J, Shindell D, Fifita S, Forster P, Ginzburg V, Handa C, et al. Mitigation Pathways Compatible with 1.5°C in the Context of Sustainable Development. In: Masson-Delmotte V, Zhai P, Pörtner H-O, Roberts D, Skea J, Shukla PR, et al., editors. Global Warming of 1.5°C, Cambridge University Press; 2022, p. 93–174. https://doi.org/10.1017/9781009157940.004.

[21] HM Government. The Ten Point Plan for a Green Industrial Revolution. 2020.

[22] Department for Energy Security and Net Zero. Hydrogen Production Delivery Roadmap. 2023.

[23] Committee on Climate Change (CCC). The Sixth Carbon Budget: The UK's path to Net Zero. 2020.

[24] Sauser B, Verma D, Ramirez-Marquez J, Gove R. From TRL to SRL: The concept of systems readiness levels. Conference on Systems Engineering Research, vol. 5, Citeseer; 2006, p. 5–7.

[25] Srinivasan S, Bommaraju T. ELECTROCHEMICAL TECHNOLOGIES AND APPLICATIONS. Fuel Cells, Springer US; 2006, p. 93–186. https://doi.org/10.1007/0-387-35402-6_3.

[26] Shiva Kumar S, Himabindu V. Hydrogen production by PEM water electrolysis – A review. Mater Sci Energy Technol 2019;2:442–54. https://doi.org/10.1016/j.mset.2019.03.002.

[27] Badwal SPS, Giddey S, Munnings C. Hydrogen production via solid electrolytic routes. Wiley Interdiscip Rev Energy Environ 2013;2:473–87. https://doi.org/10.1002/wene.50.

[28] Schnuelle C, Wassermann T, Fuhrlaender D, Zondervan E. Dynamic hydrogen production from PV & wind direct electricity supply – Modeling and techno-economic assessment. Int J Hydrogen Energy 2020;45:29938–52. https://doi.org/10.1016/j.ijhydene.2020.08.044.

[29] Grimm A, de Jong WA, Kramer GJ. Renewable hydrogen production: A techno-economic comparison of photoelectrochemical cells and photovoltaic-electrolysis. Int J Hydrogen Energy 2020;45:22545–55. https://doi.org/10.1016/j.ijhydene.2020.06.092.

[30] Shiva Kumar S, Lim H. An overview of water electrolysis technologies for green hydrogen production. Energy Reports 2022;8:13793–813. https://doi.org/10.1016/j.egyr.2022.10.127.

[31] Sharshir SW, Joseph A, Elsayad MM, Tareemi AA, Kandeal AW, Elkadeem MR. A review of recent advances in alkaline electrolyzer for green hydrogen production: Performance improvement and applications. Int J Hydrogen Energy 2024;49:458–88. https://doi.org/10.1016/j.ijhydene.2023.08.107.

[32] Varela C, Mostafa M, Zondervan E. Modeling alkaline water electrolysis for power-to-x applications: A scheduling approach. Int J Hydrogen Energy 2021;46:9303–13. https://doi.org/10.1016/j.ijhydene.2020.12.111.

[33] Millet P, Grigoriev S. Water Electrolysis Technologies. Renewable Hydrogen Technologies, Elsevier; 2013, p. 19–41. https://doi.org/10.1016/B978-0-444-56352-1.00002-7.

[34] Brauns J, Turek T. Alkaline Water Electrolysis Powered by Renewable Energy: A Review. Processes 2020;8:248. https://doi.org/10.3390/pr8020248.

[35] Le Bideau D, Chocron O, Mandin P, Kiener P, Benbouzid M, Sellier M, et al. Evolutionary Design Optimization of an Alkaline Water Electrolysis Cell for Hydrogen Production. Applied Sciences 2020;10:8425. https://doi.org/10.3390/app10238425.

[36] Acevedo Y, Prosser J, Huya-Kouadio J, McNamara K, James B. Hydrogen Production Cost with Alkaline Electrolysis. Golden, CO (United States): 2023. https://doi.org/10.2172/2203367.

[37] Hill SJP, Bamisile O, Hatton L, Staffell I, Jansen M. The cost of clean hydrogen from offshore wind and electrolysis. J Clean Prod 2024;445:141162. https://doi.org/10.1016/j.jclepro.2024.141162.

[38] Ahmed KW, Jang MJ, Park MG, Chen Z, Fowler M. Effect of Components and Operating Conditions on the Performance of PEM Electrolyzers: A Review. Electrochem 2022;3:581–612. https://doi.org/10.3390/electrochem3040040.

[39] Wang T, Cao X, Jiao L. PEM water electrolysis for hydrogen production: fundamentals, advances, and prospects. Carbon Neutrality 2022;1:21. https://doi.org/10.1007/s43979-022-00022-8.

[40] Villagra A, Millet P. An analysis of PEM water electrolysis cells operating at elevated current densities. Int J Hydrogen Energy 2019;44:9708–17. https://doi.org/10.1016/j.ijhydene.2018.11.179.

[41] El-Emam RS, Özcan H. Comprehensive review on the techno-economics of sustainable large-scale clean hydrogen production. J Clean Prod 2019;220:593–609. https://doi.org/10.1016/j.jclepro.2019.01.309.

[42] Hauch A, Küngas R, Blennow P, Hansen AB, Hansen JB, Mathiesen B V., et al. Recent advances in solid oxide cell technology for electrolysis. Science (1979) 2020;370. https://doi.org/10.1126/science.aba6118.

[43] Min G, Choi S, Hong J. A review of solid oxide steam-electrolysis cell systems: Thermodynamics and thermal integration. Appl Energy 2022;328:120145. https://doi.org/10.1016/j.apenergy.2022.120145.

[44] Xu Y, Cai S, Chi B, Tu Z. Technological limitations and recent developments in a solid oxide electrolyzer cell: A review. Int J Hydrogen Energy 2024;50:548–91. https://doi.org/10.1016/j.ijhydene.2023.08.314.

[45] Nasser M, Megahed TF, Ookawara S, Hassan H. A review of water electrolysis–based systems for hydrogen production using hybrid/solar/wind energy systems. Environmental Science and Pollution Research 2022;29:86994–7018. https://doi.org/10.1007/s11356-022-23323-y.

[46] Wong YM, Wu TY, Juan JC. A review of sustainable hydrogen production using seed sludge via dark fermentation. Renewable and Sustainable Energy Reviews 2014;34:471–82. https://doi.org/10.1016/j.rser.2014.03.008.

[47] Turhal S, Turanbaev M, Argun H. Hydrogen production from melon and watermelon mixture by dark fermentation. Int J Hydrogen Energy 2019;44:18811–7. https://doi.org/10.1016/j.ijhydene.2018.10.011.

[48] Cavalcante de Amorim EL, Barros A, Rissato Zamariolli Damianovic M, Silva EL. Anaerobic fluidized bed reactor with expanded clay as support for hydrogen production through dark fermentation of glucose. Int J Hydrogen Energy 2009;34:783–90. https://doi.org/10.1016/j.ijhydene.2008.11.007.

[49] Megía PJ, Vizcaíno AJ, Calles JA, Carrero A. Hydrogen Production Technologies: From Fossil Fuels toward Renewable Sources. A Mini Review. Energy & Fuels 2021;35:16403–15. https://doi.org/10.1021/acs.energyfuels.1c02501.

[50] Li Y, Lin R, O'Shea R, Thaore V, Wall D, Murphy JD. A perspective on three sustainable hydrogen production technologies with a focus on technology readiness level, cost of production and life cycle environmental impacts. Heliyon 2024;10:e26637. https://doi.org/10.1016/j.heliyon.2024.e26637.

[51] Zhang Q, Wang Y, Zhang Z, Lee D-J, Zhou X, Jing Y, et al. Photo-fermentative hydrogen production from crop residue: A mini review. Bioresour Technol 2017;229:222–30. https://doi.org/10.1016/j.biortech.2017.01.008.

[52] Łukajtis R, Hołowacz I, Kucharska K, Glinka M, Rybarczyk P, Przyjazny A, et al. Hydrogen production from biomass using dark fermentation. Renewable and Sustainable Energy Reviews 2018;91:665–94. https://doi.org/10.1016/j.rser.2018.04.043.

[53] Keskin T, Abo-Hashesh M, Hallenbeck PC. Photofermentative hydrogen production from wastes. Bioresour Technol 2011;102:8557–68. https://doi.org/10.1016/j.biortech.2011.04.004.

[54] Mishra P, Krishnan S, Rana S, Singh L, Sakinah M, Ab Wahid Z. Outlook of fermentative hydrogen production techniques: An overview of dark, photo and integrated dark-photo fermentative approach to biomass. Energy Strategy Reviews 2019;24:27–37. https://doi.org/10.1016/j.esr.2019.01.001.

[55] Akhlaghi N, Najafpour-Darzi G. A comprehensive review on biological hydrogen production. Int J Hydrogen Energy 2020;45:22492–512. https://doi.org/10.1016/j.ijhydene.2020.06.182.

[56] Tamburic B, Dechatiwongse P, Zemichael FW, Maitland GC, Hellgardt K. Process and reactor design for biophotolytic hydrogen production. Physical Chemistry Chemical Physics 2013;15:10783–94. https://doi.org/10.1039/c3cp51866c.

[57] Yu J, Yu J, Takahashi P. Biophotolysis-based Hydrogen Production by Cyanobacteria and Green Microalgae. 2007.

[58] Rupprecht J, Hankamer B, Mussgnug JH, Ananyev G, Dismukes C, Kruse O. Perspectives and advances of biological H2 production in microorganisms. Appl Microbiol Biotechnol 2006;72:442–9. https://doi.org/10.1007/s00253-006-0528-x.

[59] Nikolaidis P, Poullikkas A. A comparative overview of hydrogen production processes. Renewable and Sustainable Energy Reviews 2017;67:597–611. https://doi.org/10.1016/j.rser.2016.09.044.

[60] Acar C, Dincer I. 3.1 Hydrogen Production. Comprehensive Energy Systems, Elsevier; 2018, p. 1–40. https://doi.org/10.1016/B978-0-12-809597-3.00304-7.

[61] El-Emam RS, Ozcan H, Zamfirescu C. Updates on promising thermochemical cycles for clean hydrogen production using nuclear energy. J Clean Prod 2020;262:121424. https://doi.org/10.1016/j.jclepro.2020.121424.

[62] Levêque G, Bader R, Lipiński W, Haussener S. High-flux optical systems for solar thermochemistry. Solar Energy 2017;156:133–48. https://doi.org/10.1016/j.solener.2017.07.046.

[63] Boretti A. Technology Readiness Level of Solar Thermochemical Splitting Cycles. ACS Energy Lett 2021:1170–4. https://doi.org/10.1021/acsenergylett.1c00181.

[64] Vitart X, Carles P, Anzieu P. A general survey of the potential and the main issues associated with the sulfur–iodine thermochemical cycle for hydrogen production using nuclear heat. Progress in Nuclear Energy 2008;50:402–10. https://doi.org/10.1016/j.pnucene.2007.11.023.

[65] Farsi A, Dincer I, Naterer GF. Review and evaluation of clean hydrogen production by the copper–chlorine thermochemical cycle. J Clean Prod 2020;276:123833. https://doi.org/10.1016/j.jclepro.2020.123833.

[66] Rosen MA. Advances in hydrogen production by thermochemical water decomposition: A review. Energy 2010;35:1068–76. https://doi.org/10.1016/j.energy.2009.06.018.

[67] Mehrpooya M, Habibi R. A review on hydrogen production thermochemical water-splitting cycles. J Clean Prod 2020;275:123836. https://doi.org/10.1016/j.jclepro.2020.123836.

[68] Oruc O, Dincer I. Assessing the potential of thermochemical water splitting cycles: A bridge towards for clean and sustainable hydrogen generation. Fuel 2021;286. https://doi.org/10.1016/j.fuel.2020.119325.

[69] Dou B, Zhang H, Song Y, Zhao L, Jiang B, He M, et al. Hydrogen production from the thermochemical conversion of biomass: Issues and challenges. Sustain Energy Fuels 2019;3:314–42. https://doi.org/10.1039/c8se00535d.

[70] Speight JG. Gasification processes for syngas and hydrogen production. Gasification for Synthetic Fuel Production: Fundamentals, Processes and Applications, Elsevier Ltd; 2015, p. 119–46. https://doi.org/10.1016/B978-0-85709-802-3.00006-0.

[71] Liu K, Deluga GD, Bitsch-Larsen A, Schmidt LD, Zhang L. Catalytic Partial Oxidation and Autothermal Reforming. Hydrogen and Syngas Production and Purification Technologies, Hoboken, NJ, USA: John Wiley & Sons, Inc.; 2009, p. 127–55. https://doi.org/10.1002/9780470561256.ch3.

[72] Vozniuk O, Tanchoux N, Millet JM, Albonetti S, Di Renzo F, Cavani F. Spinel Mixed Oxides for Chemical-Loop Reforming: From Solid State to Potential Application. Stud Surf Sci Catal, vol. 178, Elsevier Inc.; 2019, p. 281–302. https://doi.org/10.1016/B978-0-444-64127-4.00014-8.

[73] Al-Hamamre Z, Voß S, Trimis D. Hydrogen production by thermal partial oxidation of hydrocarbon fuels in porous media based reformer. Int J Hydrogen Energy 2009;34:827–32. https://doi.org/10.1016/j.ijhydene.2008.10.085.

[74] Kumar S, Kumar S, Prajapati JK. Hydrogen production by partial oxidation of methane: Modeling and simulation. Int J Hydrogen Energy 2009;34:6655–68. https://doi.org/10.1016/j.ijhydene.2009.06.043.

[75] Chen WH, Lin MR, Lu JJ, Chao Y, Leu TS. Thermodynamic analysis of hydrogen production from methane via autothermal reforming and partial oxidation followed by water gas shift reaction. Int J Hydrogen Energy 2010;35:11787–97. https://doi.org/10.1016/j.ijhydene.2010.08.126.

[76] Sengodan S, Lan R, Humphreys J, Du D, Xu W, Wang H, et al. Advances in reforming and partial oxidation of hydrocarbons for hydrogen production and fuel cell applications. Renewable and Sustainable Energy Reviews 2018;82:761–80. https://doi.org/10.1016/j.rser.2017.09.071.

[77] Lutz AE, Bradshaw RW, Bromberg L, Rabinovich A. Thermodynamic analysis of hydrogen production by partial oxidation reforming. Int J Hydrogen Energy 2004;29:809–16. https://doi.org/10.1016/j.ijhydene.2003.09.015.

[78] Kalamaras CM, Efstathiou AM, Al-Assaf Y, Poullikkas A. Conference Paper Hydrogen Production Technologies: Current State and Future Developments. Conference Papers in Energy 2013;2013. https://doi.org/10.1155/2013/690627.

[79] Sherif SA, Barbir F, Veziroglu TN. Hydrogen Energy Systems. Wiley Encyclopedia of Electrical and Electronics Engineering, Wiley; 1999. https://doi.org/10.1002/047134608X.W3025.

[80] Nahar G, Dupont V. Recent Advances in Hydrogen Production Via Autothermal Reforming Process (ATR): A Review of Patents and Research Articles. Recent Patents on Chemical Engineering 2013;6:8–42. https://doi.org/10.2174/2211334711306010003.

[81] Collidi G. IEAGHG Technical Review Reference data and Supporting Literature Reviews for SMR Based Hydrogen Production with CCS. 2017.

[82] Yan Y, Manovic V, Anthony EJ, Clough PT. Techno-economic analysis of low-carbon hydrogen production by sorption enhanced steam methane reforming (SE-SMR) processes. Energy Convers Manag 2020;226:113530. https://doi.org/10.1016/j.enconman.2020.113530.

[83] Udemu C, Font-Palma C. Potential cost savings of large-scale blue hydrogen production via sorption-enhanced steam reforming process. Energy Convers Manag 2024;302:118132. https://doi.org/10.1016/j.enconman.2024.118132.

[84] Stenberg V, Rydén M, Mattisson T, Lyngfelt A. Exploring novel hydrogen production processes by integration of steam methane reforming with chemical-looping combustion (CLC-SMR) and oxygen carrier aided combustion (OCAC-SMR). International Journal of Greenhouse Gas Control 2018;74:28–39. https://doi.org/10.1016/j.ijggc.2018.01.008.

[85] Hrabovsky M, Hlina M, Kopecky V, Maslani A, Krenek P, Serov A, et al. Steam Plasma Methane Reforming for Hydrogen Production. Plasma Chemistry and Plasma Processing 2018;38:743–58. https://doi.org/10.1007/s11090-018-9891-5.

[86] Franchi G, Capocelli M, De Falco M, Piemonte V, Barba D. Hydrogen Production via Steam Reforming: A Critical Analysis of MR and RMM Technologies. Membranes (Basel) 2020;10:10. https://doi.org/10.3390/membranes10010010.

[87] Shafiee A, Arab M, Lai Z, Liu Z, Abbas A. Modelling and sequential simulation of multi-tubular metallic membrane and techno-economics of a hydrogen production process employing thin-layer membrane reactor. Int J Hydrogen Energy 2016;41:19081–97. https://doi.org/10.1016/j.ijhydene.2016.08.172.

[88] Andrés MB, Boyd T, Grace JR, Jim Lim C, Gulamhusein A, Wan B, et al. In-situ CO2 capture in a pilot-scale fluidized-bed membrane reformer for ultra-pure hydrogen production. Int J Hydrogen Energy 2011;36:4038–55. https://doi.org/10.1016/j.ijhydene.2010.09.091.

[89] Chen Y, Mahecha-Botero A, Lim CJ, Grace JR, Zhang J, Zhao Y, et al. Hydrogen production in a sorption-enhanced fluidized-bed membrane reactor: Operating parameter investigation. Ind Eng Chem Res 2014;53:6230–42. https://doi.org/10.1021/ie500294k.

[90] IEAGHG. Reference data and Supporting Literature Reviews for SMR Based Hydrogen Production with CCS. 2017.

[91] Voitic G, Pichler B, Basile A, Iulianelli A, Malli K, Bock S, et al. Hydrogen production. Fuel Cells and Hydrogen: From Fundamentals to Applied Research, Elsevier; 2018, p. 215–41. https://doi.org/10.1016/B978-0-12-811459-9.00010-4.

[92] Lamb JJ, Hillestad M, Rytter E, Bock R, Nordgård ASR, Lien KM, et al. Traditional Routes for Hydrogen Production and Carbon Conversion. Hydrogen, Biomass and Bioenergy, Elsevier; 2020, p. 21–53. https://doi.org/10.1016/B978-0-08-102629-8.00003-7.

[93] de Souza TL, Rossi C de CR da S, Alonso CG, Guirardello R, Cabral VF, Fernandes-Machado NRC, et al. Thermodynamic analysis of autothermal reforming of methane via entropy maximization: Hydrogen production. Int J Hydrogen Energy 2014;39:8257–70. https://doi.org/10.1016/j.ijhydene.2014.03.078.

[94] Semelsberger TA. Fuels - Hydrogen Storage | Chemical Carriers. Encyclopedia of Electrochemical Power Sources, Elsevier; 2009, p. 504–18. https://doi.org/10.1016/B978-044452745-5.00331-2.

[95] Assabumrungrat S, Laosiripojana N. Fuels - Hydrogen Production | Autothermal Reforming. Encyclopedia of Electrochemical Power Sources, Elsevier; 2009, p. 238–48. https://doi.org/10.1016/B978-044452745-5.00296-3.

[96] Ortiz M, Abad A, De Diego LF, García-Labiano F, Gayán P, Adánez J. Optimization of hydrogen production by Chemical-Looping auto-thermal Reforming working with Ni-based oxygen-carriers. Int J Hydrogen Energy 2011;36:9663–72. https://doi.org/10.1016/j.ijhydene.2011.05.025.

[97] Cloete S, Khan MN, Amini S. Economic assessment of membrane-assisted autothermal reforming for cost effective hydrogen production with CO2 capture. Int J Hydrogen Energy 2019;44:3492–510. https://doi.org/10.1016/j.ijhydene.2018.12.110.

[98] Francisco Morgado J, Cloete S, Morud J, Gurker T, Amini S. Modelling study of two chemical looping reforming reactor configurations: looping vs. switching. Powder Technol 2017;316:599–613. https://doi.org/10.1016/j.powtec.2016.11.059.

[99] Holladay JD, Hu J, King DL, Wang Y. An overview of hydrogen production technologies. Catal Today 2009;139:244–60. https://doi.org/10.1016/j.cattod.2008.08.039.

[100] Carapellucci R, Giordano L. Steam, dry and autothermal methane reforming for hydrogen production: A thermodynamic equilibrium analysis. J Power Sources 2020;469:228391. https://doi.org/10.1016/j.jpowsour.2020.228391.

[101] Cloete S, Khan MN, Amini S. Economic assessment of membrane-assisted autothermal reforming for cost effective hydrogen production with CO2 capture. Int J Hydrogen Energy 2019;44:3492–510. https://doi.org/10.1016/j.ijhydene.2018.12.110.

[102] Arku P, Regmi B, Dutta A. A review of catalytic partial oxidation of fossil fuels and biofuels: Recent advances in catalyst development and kinetic modelling. Chemical Engineering Research and Design 2018;136:385–402. https://doi.org/10.1016/j.cherd.2018.05.044.

[103] Matus E V., Ismagilov IZ, Yashnik SA, Ushakov VA, Prosvirin IP, Kerzhentsev MA, et al. Hydrogen production through autothermal reforming of CH4: Efficiency and action mode of noble (M = Pt, Pd) and non-noble (M = Re, Mo, Sn) metal additives in the composition of Ni-M/Ce0.5Zr0.5O2/Al2O3 catalysts. Int J Hydrogen Energy 2020;45:33352–69. https://doi.org/10.1016/j.ijhydene.2020.09.011.

[104] Chen L, Qi Z, Zhang S, Su J, Somorjai GA. Catalytic hydrogen production from methane: A review on recent progress and prospect. Catalysts 2020;10:858. https://doi.org/10.3390/catal10080858.

[105] IEA. Hydrogen Projects Database. IEA, Paris 2021. https://bit.ly/3C4UkQZ (accessed September 14, 2021).

[106] Argyris PA, Wong J, Wright A, Pereira LMC, Spallina V. Reducing the cost of low-carbon hydrogen production via emerging chemical looping process. Energy Convers Manag 2023;277:116581. https://doi.org/10.1016/j.enconman.2022.116581.

[107] Rydén M, Lyngfelt A, Mattisson T. Synthesis gas generation by chemical-looping reforming in a continuously operating laboratory reactor. Fuel 2006;85:1631–41. https://doi.org/10.1016/J.FUEL.2006.02.004.

[108] Bhavsar S, ¨ Otz Veser G. Chemical looping beyond combustion: production of synthesis gas via chemical looping partial oxidation of methane 2014. https://doi.org/10.1039/c4ra06437b.

[109] García-Labiano F, De Diego LF, García-Díez E, Serrano A, Abad A, Gayán P, et al. Combustion and Reforming of Liquid Fossil Fuels through Chemical Looping Processes: Integration of Chemical Looping Processes in a Refinery. Energy Procedia 2017;114:325–33. https://doi.org/10.1016/J.EGYPRO.2017.03.1174.

[110] Nazir SM, Bolland O, Amini S. Analysis of Combined Cycle Power Plants with Chemical Looping Reforming of Natural Gas and Pre-Combustion CO2 Capture. Energies 2018, Vol 11, Page 147 2018;11:147. https://doi.org/10.3390/EN11010147.

[111] Beavis R. The EU FP6 CACHET project - Final results. Energy Procedia 2011;4:1074–81. https://doi.org/10.1016/J.EGYPRO.2011.01.157.

[112] Al-Haj Ibrahim H. Introductory Chapter: Pyrolysis. Recent Advances in Pyrolysis, IntechOpen; 2020. https://doi.org/10.5772/intechopen.90366.

[113] Muradov NZ. CO2-free production of hydrogen by catalytic pyrolysis of hydrocarbon fuel. Energy and Fuels 1998;12:41–8. https://doi.org/10.1021/ef9701145.

[114] Palmer C, Bunyan E, Gelinas J, Gordon MJ, Metiu H, McFarland EW. CO2-free hydrogen production by catalytic pyrolysis of hydrocarbon feedstocks in molten Ni-Bi. Energy and Fuels 2020;34:16073–80. https://doi.org/10.1021/acs.energyfuels.0c03080.

[115] Balat M. Hydrogen-rich gas production from biomass via pyrolysis and gasification processes and effects of catalyst on hydrogen yield. Energy Sources, Part A: Recovery, Utilization and Environmental Effects 2008;30:552–64. https://doi.org/10.1080/15567030600817191.

[116] Arregi A, Lopez G, Amutio M, Barbarias I, Bilbao J, Olazar M. Hydrogen production from biomass by continuous fast pyrolysis and in-line steam reforming. RSC Adv 2016;6:25975–85. https://doi.org/10.1039/c6ra01657j.

[117] Sánchez-Bastardo N, Schlögl R, Ruland H. Methane Pyrolysis for CO2 -Free H2 Production: A Green Process to Overcome Renewable Energies Unsteadiness. Chemie Ingenieur Technik 2020;92:1596–609. https://doi.org/10.1002/cite.202000029.

[118] Schneider S, Bajohr S, Graf F, Kolb T. State of the Art of Hydrogen Production via Pyrolysis of Natural Gas. ChemBioEng Reviews 2020;7:150–8. https://doi.org/10.1002/cben.202000014.

[119] Bridgwater A V. Principles and practice of biomass fast pyrolysis processes for liquids. J Anal Appl Pyrolysis 1999;51:3–22. https://doi.org/10.1016/S0165-2370(99)00005-4.

[120] Qinglan H, Chang W, Dingqiang L, Yao W, Dan L, Guiju L. Production of hydrogen-rich gas from plant biomass by catalytic pyrolysis at low temperature. Int J Hydrogen Energy 2010;35:8884–90. https://doi.org/10.1016/j.ijhydene.2010.06.039.

[121] Bakhtyari A, Makarem MA, Rahimpour MR. Hydrogen Production Through Pyrolysis. Encyclopedia of Sustainability Science and Technology, New York, NY: Springer New York; 2018, p. 1–28. https://doi.org/10.1007/978-1-4939-2493-6_956-1.

[122] Kang D, Rahimi N, Gordon MJ, Metiu H, McFarland EW. Catalytic methane pyrolysis in molten MnCl2-KCl. Appl Catal B 2019;254:659–66. https://doi.org/10.1016/j.apcatb.2019.05.026.

[123] Palmer C, Tarazkar M, Kristoffersen HH, Gelinas J, Gordon MJ, McFarland EW, et al. Methane Pyrolysis with a Molten Cu-Bi Alloy Catalyst. ACS Catal 2019;9:8337–45. https://doi.org/10.1021/acscatal.9b01833.

[124] Yang S, Zhang X, Chen L, Sun L, Xie X, Zhao B. Production of syngas from pyrolysis of biomass using Fe/CaO catalysts: Effect of operating conditions on the process. J Anal Appl Pyrolysis 2017;125:1–8. https://doi.org/10.1016/j.jaap.2017.05.007.

[125] Ren S, Lei H, Wang L, Bu Q, Chen S, Wu J. Hydrocarbon and hydrogen-rich syngas production by biomass catalytic pyrolysis and bio-oil upgrading over biochar catalysts. RSC Adv 2014;4:10731–7. https://doi.org/10.1039/c4ra00122b.

[126] Lestinsky P, Grycova B, Pryszcz A, Martaus A, Matejova L. Hydrogen production from microwave catalytic pyrolysis of spruce sawdust. J Anal Appl Pyrolysis 2017;124:175–9. https://doi.org/10.1016/j.jaap.2017.02.008.

[127] Lim TC, Cuellar A, Langseth K, Waldon JL. Technoeconomic Analysis of Negative Emissions Bioenergy with Carbon Capture and Storage through Pyrolysis and Bioenergy District Heating Infrastructure. Environ Sci Technol 2022;56:1875–84. https://doi.org/10.1021/acs.est.1c03478.

[128] Full J, Merseburg S, Miehe R, Sauer A. A New Perspective for Climate Change Mitigation—Introducing Carbon-Negative Hydrogen Production from Biomass with Carbon Capture and Storage (HyBECCS). Sustainability 2021;13:4026. https://doi.org/10.3390/su13074026.

[129] Full J, Geller M, Ziehn S, Schließ T, Miehe R, Sauer A. Carbon-negative hydrogen production (HyBECCS): An exemplary techno-economic and environmental assessment. Int J Hydrogen Energy 2024;52:594–609. https://doi.org/10.1016/j.ijhydene.2023.09.252.

[130] Shafizadeh F. Introduction to pyrolysis of biomass. J Anal Appl Pyrolysis 1982;3:283–305. https://doi.org/10.1016/0165-2370(82)80017-X.

[131] Huang C, Mohamed BA, Li LY. Comparative life-cycle energy and environmental analysis of sewage sludge and biomass co-pyrolysis for biofuel and biochar production. Chemical Engineering Journal 2023;457:141284. https://doi.org/10.1016/j.cej.2023.141284.

[132] Nikolaidis P, Poullikkas A. A comparative overview of hydrogen production processes. Renewable and Sustainable Energy Reviews 2017;67:597–611. https://doi.org/10.1016/j.rser.2016.09.044.

[133] Shahbaz M, Al-Ansari T, Inayat A, Inayat M. Technical readiness level of biohydrogen production process and its value chain. Value-Chain of Biofuels, Elsevier; 2022, p. 335–55. https://doi.org/10.1016/B978-0-12-824388-6.00017-8.

[134] Lettieri P, Al-Salem SM. Thermochemical Treatment of Plastic Solid Waste. Waste, Elsevier Inc.; 2011, p. 233–42. https://doi.org/10.1016/B978-0-12-381475-3.10017-8.

[135] Higman C. Gasification. Combustion Engineering Issues for Solid Fuel Systems, Elsevier Inc.; 2008, p. 423–68. https://doi.org/10.1016/B978-0-12-373611-6.00011-2.

[136] Belgiorno V, De Feo G, Della Rocca C, Napoli RMA. Energy from gasification of solid wastes. Waste Management 2003;23:1–15. https://doi.org/10.1016/S0956-053X(02)00149-6.

[137] Fan L-S, Zeng L, Wang W, Luo S. Chemical looping processes for CO2 capture and carbonaceous fuel conversion – prospect and opportunity. Energy Environ Sci 2012;5:7254–80. https://doi.org/10.1039/C2EE03198A.

[138] Chen J, Wang Q, Xu Z, E J, Leng E, Zhang F, et al. Process in supercritical water gasification of coal: A review of fundamentals, mechanisms, catalysts and element transformation. Energy Convers Manag 2021;237:114122. https://doi.org/10.1016/J.ENCONMAN.2021.114122.

[139] Sedghkerdar MH, Mostafavi E, Mahinpey N. Sorbent enhanced hydrogen production from steam gasification of coal integrated with CO2 capture. Int J Hydrogen Energy 2014;39:17001–8. https://doi.org/10.1016/J.IJHYDENE.2014.08.062.

[140] Couto N, Rouboa A, Silva V, Monteiro E, Bouziane K. TerraGreen13 International Conference Influence of the biomass gasification processes on the final composition of syngas. Energy Procedia 2013;36:596–606. https://doi.org/10.1016/j.egypro.2013.07.068.

[141] Ciferno JP, Marano JJ. Benchmarking Biomass Gasification Technologies for Fuels, Chemicals and Hydrogen Production. 2002.

[142] Pfeifer C. Sorption-enhanced gasification. Fluidized Bed Technologies for Near-Zero Emission Combustion and Gasification 2013:971–1001. https://doi.org/10.1533/9780857098801.4.971.

[143] Parvez AM, Hafner S, Hornberger M, Schmid M, Scheffknecht G. Sorption enhanced gasification (SEG) of biomass for tailored syngas production with in-situ CO2 capture: Current status, process scale-up experiences and outlook. Renewable and Sustainable Energy Reviews 2021;141:110756.

[144] Liu H, Consoli C, Zapantis A. Overview of Carbon Capture and Storage (CCS) Facilities Globally. SSRN Electronic Journal 2018. https://doi.org/10.2139/ssrn.3366353.

[145] Rosa L, Mazzotti M. Potential for hydrogen production from sustainable biomass with carbon capture and storage. Renewable and Sustainable Energy Reviews 2022;157:112123. https://doi.org/10.1016/j.rser.2022.112123.

[146] Udemu C, Font-Palma C. Modelling of sorption-enhanced steam reforming (SE-SR) process in fluidised bed reactors for low-carbon hydrogen production: A review. Fuel 2023;340:127588. https://doi.org/10.1016/J.FUEL.2023.127588.

[147] Chao C, Deng Y, Dewil R, Baeyens J, Fan X. Post-combustion carbon capture. Renewable and Sustainable Energy Reviews 2021;138:110490. https://doi.org/10.1016/j.rser.2020.110490.

[148] Kenarsari SD, Yang D, Jiang G, Zhang S, Wang J, Russell AG, et al. Review of recent advances in carbon dioxide separation and capture. RSC Adv 2013;3:22739. https://doi.org/10.1039/c3ra43965h.

[149] Kanniche M, Gros-Bonnivard R, Jaud P, Valle-Marcos J, Amann J-M, Bouallou C. Pre-combustion, post-combustion and oxy-combustion in thermal power plant for CO2 capture. Appl Therm Eng 2010;30:53–62. https://doi.org/10.1016/j.applthermaleng.2009.05.005.

[150] Han C, Zahid U, An J, Kim K, Kim C. CO2 transport: design considerations and project outlook. Curr Opin Chem Eng 2015;10:42–8. https://doi.org/10.1016/j.coche.2015.08.001.

[151] Metz B, Davidson O, De Coninck HC, Loos M, Meyer L. IPCC special report on carbon dioxide capture and storage. Cambridge: Cambridge University Press; 2005.

[152] Leung DYC, Caramanna G, Maroto-Valer MM. An overview of current status of carbon dioxide capture and storage technologies. Renewable and Sustainable Energy Reviews 2014;39:426–43. https://doi.org/10.1016/j.rser.2014.07.093.

[153] Cao C, Liu H, Hou Z, Mehmood F, Liao J, Feng W. A Review of CO2 Storage in View of Safety and Cost-Effectiveness. Energies (Basel) 2020;13:600. https://doi.org/10.3390/en13030600.

[154] Nemitallah MA, Habib MA, Badr HM, Said SA, Jamal A, Ben-Mansour R, et al. Oxy-fuel combustion technology: current status, applications, and trends. Int J Energy Res 2017;41:1670–708. https://doi.org/10.1002/er.3722.

[155] Ban ZH, Keong LK, Mohd Shariff A. Physical Absorption of CO2 Capture: A Review. Adv Mat Res 2014;917:134–43. https://doi.org/10.4028/www.scientific.net/AMR.917.134.

[156] Wang M, Lawal A, Stephenson P, Sidders J, Ramshaw C. Post-combustion CO2 capture with chemical absorption: A state-of-the-art review. Chemical Engineering Research and Design 2011;89:1609–24. https://doi.org/10.1016/j.cherd.2010.11.005.

[157] Ochedi FO, Yu J, Yu H, Liu Y, Hussain A. Carbon dioxide capture using liquid absorption methods: a review. Environ Chem Lett 2021;19:77–109. https://doi.org/10.1007/s10311-020-01093-8.

[158] Salvi BL, Jindal S. Recent developments and challenges ahead in carbon capture and sequestration technologies. SN Appl Sci 2019;1:885. https://doi.org/10.1007/s42452-019-0909-2.

[159] Dąbrowski A. Adsorption — from theory to practice. Adv Colloid Interface Sci 2001;93:135–224. https://doi.org/10.1016/S0001-8686(00)00082-8.

[160] Yu C-H, Huang C-H, Tan C-S. A Review of CO2 Capture by Absorption and Adsorption. Aerosol Air Qual Res 2012;12:745–69. https://doi.org/10.4209/aaqr.2012.05.0132.

[161] Webley PA, Danaci D. CO2 Capture by Adsorption Processes. Carbon Capture and Storage, The Royal Society of Chemistry; 2019, p. 106–67. https://doi.org/10.1039/9781788012744-00106.

[162] Lai JY, Ngu LH, Hashim SS. A review of CO2 adsorbents performance for different carbon capture technology processes conditions. Greenhouse Gases: Science and Technology 2021;11:1076–117. https://doi.org/10.1002/ghg.2112.

[163] Font-Palma C, Cann D, Udemu C, García O. Review of Cryogenic Carbon Capture Innovations and Their Potential Applications. C 2021, Vol 7, Page 58 2021;7:58. https://doi.org/10.3390/C7030058.

[164] Tuinier MJ, Hamers HP, van Sint Annaland M. Techno-economic evaluation of cryogenic CO2 capture—A comparison with absorption and membrane technology. International Journal of Greenhouse Gas Control 2011;5:1559–65. https://doi.org/10.1016/j.ijggc.2011.08.013.

[165] Shen M, Tong L, Yin S, Liu C, Wang L, Feng W, et al. Cryogenic technology progress for CO2 capture under carbon neutrality goals: A review. Sep Purif Technol 2022;299:121734. https://doi.org/10.1016/j.seppur.2022.121734.

[166] Norahim N, Yaisanga P, Faungnawakij K, Charinpanitkul T, Klaysom C. Recent Membrane Developments for CO2 Separation and Capture. Chem Eng Technol 2018;41:211–23. https://doi.org/10.1002/ceat.201700406.

[167] Luis P, Van Gerven T, Van der Bruggen B. Recent developments in membrane-based technologies for CO2 capture. Prog Energy Combust Sci 2012;38:419–48. https://doi.org/10.1016/j.pecs.2012.01.004.

[168] Sitter S, Chen Q, Grossmann IE. An overview of process intensification methods. Curr Opin Chem Eng 2019;25:87–94. https://doi.org/10.1016/j.coche.2018.12.006.

[169] García R, Gil M V., Rubiera F, Chen D, Pevida C. Renewable hydrogen production from biogas by sorption enhanced steam reforming (SESR): A parametric study. Energy 2021;218:119491. https://doi.org/10.1016/J.ENERGY.2020.119491.

[170] Xie H, Yu Q, Zuo Z, Han Z, Yao X, Qin Q. Hydrogen production via sorption-enhanced catalytic steam reforming of bio-oil. Int J Hydrogen Energy 2016;41:2345–53. https://doi.org/10.1016/J.IJHYDENE.2015.12.156.

[171] Chen H, Zhang T, Dou B, Dupont V, Williams P, Ghadiri M, et al. Thermodynamic analyses of adsorption-enhanced steam reforming of glycerol for hydrogen production. Int J Hydrogen Energy 2009;34:7208–22. https://doi.org/10.1016/j.ijhydene.2009.06.070.

[172] He L, Parra JMS, Blekkan EA, Chen D. Towards efficient hydrogen production from glycerol by sorption enhanced steam reforming. Energy Environ Sci 2010;3:1046–56. https://doi.org/10.1039/B922355J.

[173] Wang W, Cao Y. Hydrogen production via sorption enhanced steam reforming of butanol: Thermodynamic analysis. Int J Hydrogen Energy 2011;36:2887–95. https://doi.org/10.1016/J.IJHYDENE.2010.11.110.

[174] Dewoolkar KD, Vaidya PD. New Hybrid Materials for Improved Hydrogen Production by the Sorption-Enhanced Steam Reforming of Butanol. Energy Technology 2017;5:1300–10. https://doi.org/10.1002/ENTE.201600645.

[175] Lima Da Silva A, Müller IL. Hydrogen production by sorption enhanced steam reforming of oxygenated hydrocarbons (ethanol, glycerol, n-butanol and methanol): Thermodynamic modelling. Int J Hydrogen Energy 2011;36:2057–75. https://doi.org/10.1016/J.IJHYDENE.2010.11.051.

[176] Wu X, Wu S. Production of high-purity hydrogen by sorption-enhanced steam reforming process of methanol. Journal of Energy Chemistry 2015;24:315–21. https://doi.org/10.1016/S2095-4956(15)60317-5.

[177] Dewoolkar KD, Vaidya PD. Tailored hydrotalcite-based hybrid materials for hydrogen production via sorption-enhanced steam reforming of ethanol. Int J Hydrogen Energy 2016;41:6094–106. https://doi.org/10.1016/J.IJHYDENE.2015.10.034.

[178] Ghungrud SA, Vaidya PD. Improved Hydrogen Production from Sorption-Enhanced Steam Reforming of Ethanol (SESRE) Using Multifunctional Materials of Cobalt Catalyst and Mg-, Ce-, and Zr-Modified CaO Sorbents. Ind Eng Chem Res 2020;59:693–703. https://doi.org/10.1021/acs.iecr.9b05472.

[179] Han SJ, Song JH, Yoo J, Park S, Kang KH, Song IK. Sorption-enhanced hydrogen production by steam reforming of ethanol over mesoporous Co/CaOAl2O3 xerogel catalysts: Effect of Ca/Al molar ratio. Int J Hydrogen Energy 2017;42:5886–98. https://doi.org/10.1016/J.IJHYDENE.2016.12.075.

[180] Menendez RB, Graschinsky C, Amadeo NE. Sorption-Enhanced Ethanol Steam Reforming Process in a Fixed-Bed Reactor. Ind Eng Chem Res 2018;57:11547–53. https://doi.org/10.1021/ACS.IECR.8B01657.

[181] Lysikov A, Derevschikov V, Okunev A. Sorption-enhanced reforming of bioethanol in dual fixed bed reactor for continuous hydrogen production. Int J Hydrogen Energy 2015;40:14436–44. https://doi.org/10.1016/J.IJHYDENE.2015.06.029.

[182] Xie H, Yu Q, Zhang Y, Zhang J, Liu J, Qin Q. New process for hydrogen production from raw coke oven gas via sorption-enhanced steam reforming: Thermodynamic analysis. Int J Hydrogen Energy 2017;42:2914–23. https://doi.org/10.1016/J.IJHYDENE.2016.12.046.

[183] Chen Y, Mahecha-Botero A, Lim CJ, Grace JR, Zhang J, Zhao Y, et al. Hydrogen production in a sorption-enhanced fluidized-bed membrane reactor: Operating parameter investigation. Ind Eng Chem Res 2014;53:6230–42. https://doi.org/10.1021/ie500294k.

[184] Wu R, Wu SF. The ReSER-COG process for hydrogen production on a Ni–CaO/Al2O3 complex catalyst. Int J Hydrogen Energy 2013;38:11818–25. https://doi.org/10.1016/J.IJHYDENE.2013.06.117.

[185] Dou B, Wang K, Jiang B, Song Y, Zhang C, Chen H, et al. Fluidized-bed gasification combined continuous sorption-enhanced steam reforming system to continuous hydrogen production from waste plastic. Int J Hydrogen Energy 2016;41:3803–10. https://doi.org/10.1016/J.IJHYDENE.2015.12.197.

[186] Li H, Wu S, Dang C, Yang G, Cao Y, Wang H, et al. Production of high-purity hydrogen from paper recycling black liquor via sorption enhanced steam reforming. Green Energy & Environment 2021;6:771–9. https://doi.org/10.1016/J.GEE.2020.07.002.

[187] Xie H, Yu Q, Lu H, Zhang Y, Zhang J, Qin Q. Thermodynamic study for hydrogen production from bio-oil via sorption-enhanced steam reforming: Comparison with conventional steam reforming. Int J Hydrogen Energy 2017;42:28718–31. https://doi.org/10.1016/J.IJHYDENE.2017.09.155.

[188] Gil M V., Fermoso J, Rubiera F, Chen D. H2 production by sorption enhanced steam reforming of biomass-derived bio-oil in a fluidized bed reactor: An assessment of the effect of operation variables using response surface methodology. Catal Today 2015;242:19–34. https://doi.org/10.1016/J.CATTOD.2014.04.018.

[189] Wang X, Wang N, Wang L. Hydrogen production by sorption enhanced steam reforming of propane: A thermodynamic investigation. Int J Hydrogen Energy 2011;36:466–72. https://doi.org/10.1016/J.IJHYDENE.2010.09.021.

[190] Lysikov AI, Trukhan SN, Okunev AG. Sorption enhanced hydrocarbons reforming for fuel cell powered generators. Int J Hydrogen Energy 2008;33:3061–6. https://doi.org/10.1016/J.IJHYDENE.2008.03.041.

[191] Dang C, Wu S, Yang G, Cao Y, Wang H, Peng F, et al. Hydrogen Production from Sorption-Enhanced Steam Reforming of Phenol over a Ni–Ca–Al–O Bifunctional Catalyst. ACS Sustain Chem Eng 2020;8:7111–20. https://doi.org/10.1021/ACSSUSCHEMENG.0C01267.

[192] Wang X, He Y, Xu T, Xiao B, Liu S, Hu Z, et al. CO2 sorption-enhanced steam reforming of phenol using Ni–M/CaO–Ca12Al14O33 (M = Cu, Co, and Ce) as catalytic sorbents. Chemical Engineering Journal 2020;393:124769. https://doi.org/10.1016/J.CEJ.2020.124769.

[193] Hu R, Li D, Xue H, Zhang N, Liu Z, Liu Z. Hydrogen production by sorption-enhanced steam reforming of acetic acid over Ni/CexZr1−xO2-CaO catalysts. Int J Hydrogen Energy 2017;42:7786–97. https://doi.org/10.1016/J.IJHYDENE.2017.01.167.

[194] Tian X, Wang S, Zhou J, Xiang Y, Zhang F, Lin B, et al. Simulation and exergetic evaluation of hydrogen production from sorption enhanced and conventional steam reforming of acetic acid. Int J Hydrogen Energy 2016;41:21099–108. https://doi.org/10.1016/J.IJHYDENE.2016.09.184.

[195] Fu P, Yi W, Li Z, Li Y, Wang J, Bai X. Comparative analysis on sorption enhanced steam reforming and conventional steam reforming of hydroxyacetone for hydrogen production: Thermodynamic modeling. Int J Hydrogen Energy 2013;38:11893–901. https://doi.org/10.1016/J.IJHYDENE.2013.07.005.

[196] Dang C, Li H, Yang G, Cao Y, Wang H, Peng F, et al. High-purity hydrogen production by sorption-enhanced steam reforming of iso-octane over a Pd-promoted Ni-Ca-Al-O bi-functional catalyst. Fuel 2021;293:120430. https://doi.org/10.1016/J.FUEL.2021.120430.

[197] He L, Chen D. Hydrogen Production from Glucose and Sorbitol by Sorption-Enhanced Steam Reforming: Challenges and Promises. ChemSusChem 2012;5:587–95. https://doi.org/10.1002/CSSC.201100566.

[198] Barelli L, Bidini G, Gallorini F, Servili S. Hydrogen production through sorption-enhanced steam methane reforming and membrane technology: A review. Energy 2008;33:554–70. https://doi.org/10.1016/j.energy.2007.10.018.

[199] Rackley SA. Adsorption capture systems. Carbon Capture and Storage, Elsevier; 2017, p. 151–85. https://doi.org/10.1016/b978-0-12-812041-5.00007-6.

[200] Rusten HK, Ochoa-Fernández E, Lindborg H, Chen D, Jakobsen HA. Hydrogen production by sorption-enhanced steam methane reforming using lithium oxides as CO2-acceptor. Ind Eng Chem Res 2007;46:8729–37. https://doi.org/10.1021/ie070770k.

[201] Grasa GS, Abanades JC. CO2 capture capacity of CaO in long series of carbonation/calcination cycles. Ind Eng Chem Res 2006;45:8846–51. https://doi.org/10.1021/ie0606946.

[202] Johnsen K. Sorption-Enhanced Steam Methane Reforming in Fluidized Bed Reactors. NTNU-trykk, 2006.

[203] Broda M, Kierzkowska AM, Baudouin D, Imtiaz Q, Copéret C, Müller CR. Sorbent-Enhanced Methane Reforming over a Ni–Ca-Based, Bifunctional Catalyst Sorbent. ACS Catal 2012;2:1635–46. https://doi.org/10.1021/CS300247G.

[204] Broda M, Manovic V, Imtiaz Q, Kierzkowska AM, Anthony EJ, Müller CR. High-purity hydrogen via the sorption-enhanced steam methane reforming reaction over a synthetic CaO-based sorbent and a Ni catalyst. Environ Sci Technol 2013;47:6007–14. https://doi.org/10.1021/es305113p.

[205] Johnsen K, Grace JR, Elnashaie SSEH, Kolbeinsen L, Eriksen D. Modeling of sorption-enhanced steam reforming in a dual fluidized bubbling bed reactor. Ind Eng Chem Res 2006;45:4133–44. https://doi.org/10.1021/ie0511736.

[206] Martavaltzi CS, Pampaka EP, Korkakaki ES, Lemonidou AA. Hydrogen production via steam reforming of methane with simultaneous CO2 capture over CaO-Ca12Al14O33. Energy and Fuels, vol. 24, American Chemical Society; 2010, p. 2589–95. https://doi.org/10.1021/ef9014058.

[207] Pecharaumporn P, Wongsakulphasatch S, Glinrun T, Maneedaeng A, Hassan Z, Assabumrungrat S. Synthetic CaO-based sorbent for high-temperature CO2 capture in sorption-enhanced hydrogen production. Int J Hydrogen Energy 2019;44:20663–77. https://doi.org/10.1016/j.ijhydene.2018.06.153.

[208] Abanades JC, Rubin ES, Anthony EJ. Sorbent cost and performance in CO2 capture systems. Ind Eng Chem Res 2004;43:3462–6. https://doi.org/10.1021/ie049962v.

[209] Dou B, Wang C, Song Y, Chen H, Jiang B, Yang M, et al. Solid sorbents for in-situ CO2 removal during sorption-enhanced steam reforming process: A review. Renewable and Sustainable Energy Reviews 2016;53:536–46. https://doi.org/10.1016/j.rser.2015.08.068.

[210] Wang Y, Memon MZ, Seelro MA, Fu W, Gao Y, Dong Y, et al. A review of CO2 sorbents for promoting hydrogen production in the sorption-enhanced steam reforming process. Int J Hydrogen Energy 2021. https://doi.org/10.1016/j.ijhydene.2021.01.206.

[211] Meloni E, Martino M, Palma V. A short review on ni based catalysts and related engineering issues for methane steam reforming. Catalysts 2020;10:352. https://doi.org/10.3390/catal10030352.

[212] He L, Berntsen H, Ochoa-Fernández E, Walmsley JC, Blekkan EA, Chen D. Co–Ni Catalysts Derived from Hydrotalcite-Like Materials for Hydrogen Production by Ethanol Steam Reforming. Topics in Catalysis 2009 52:3 2009;52:206–17. https://doi.org/10.1007/S11244-008-9157-1.

[213] Mei D, Glezakou VA, Lebarbier V, Kovarik L, Wan H, Albrecht KO, et al. Highly active and stable MgAl2O4-supported Rh and Ir catalysts for methane steam reforming: A combined experimental and theoretical study. J Catal 2014;316:11–23. https://doi.org/10.1016/j.jcat.2014.04.021.

[214] Boudjeloud M, Boulahouache A, Rabia C, Salhi N. La-doped supported Ni catalysts for steam reforming of methane. Int J Hydrogen Energy 2019;44:9906–13. https://doi.org/10.1016/j.ijhydene.2019.01.140.

[215] Xia L, Fang X, Xu X, Liu Q, Yang M, Xu J, et al. The promotional effects of plasma treating on Ni/Y2Ti2O7 for steam reforming of methane (SRM): Elucidating the NiO-support interaction and the states of the surface oxygen anions. Int J Hydrogen Energy 2020;45:4556–69. https://doi.org/10.1016/j.ijhydene.2019.12.119.

[216] Vahid Shahed G, Taherian Z, Khataee A, Meshkani F, Orooji Y. Samarium-impregnated nickel catalysts over SBA-15 in steam reforming of CH4 process. Journal of Industrial and Engineering Chemistry 2020;86:73–80. https://doi.org/10.1016/j.jiec.2020.02.012.

[217] Nazari M, Alavi SM. An investigation of the simultaneous presence of Cu and Zn in different Ni/Al2O3 catalyst loads using Taguchi design of experiment in steam reforming of methane. Int J Hydrogen Energy 2020;45:691–702. https://doi.org/10.1016/j.ijhydene.2019.10.224.

[218] Ou Z, Zhang Z, Qin C, Xia H, Deng T, Niu J, et al. Highly active and stable Ni/perovskite catalysts in steam methane reforming for hydrogen production. Sustain Energy Fuels 2021;5:1845–56. https://doi.org/10.1039/d1se00082a.

[219] Wu C, Xiao Z, Wang L, Li G, Zhang X, Wang L. Modulating oxidation state of Ni/CeO2catalyst for steam methane reforming: a theoretical prediction with experimental verification. Catal Sci Technol 2021;11:1965–73. https://doi.org/10.1039/d0cy02197k.

[220] Wang M, Tan X, Motuzas J, Li J, Liu S. Hydrogen production by methane steam reforming using metallic nickel hollow fiber membranes. J Memb Sci 2021;620:118909. https://doi.org/10.1016/j.memsci.2020.118909.

[221] Karemore AL, Sinha R, Chugh P, Vaidya PD. Mixed reforming of methane over Ni–K/CeO2–Al2O3: Study of catalyst performance and reaction kinetics. Int J Hydrogen Energy 2021;46:5223–33. https://doi.org/10.1016/j.ijhydene.2020.11.221.

[222] Chanburanasiri N, Ribeiro AM, Rodrigues AE, Arpornwichanop A, Laosiripojana N, Praserthdam P, et al. Hydrogen production via sorption enhanced steam methane reforming process using Ni/CaO multifunctional catalyst. Ind Eng Chem Res 2011;50:13662–71. https://doi.org/10.1021/ie201226j.

[223] Kim JN, Ko CH, Yi KB. Sorption enhanced hydrogen production using one-body CaO-Ca 12Al14O33-Ni composite as catalytic absorbent. Int J Hydrogen Energy, vol. 38, Pergamon; 2013, p. 6072–8. https://doi.org/10.1016/j.ijhydene.2012.12.022.

[224] Radfarnia HR, Iliuta MC. Hydrogen production by sorption-enhanced steam methane reforming process using CaO-Zr/Ni bifunctional sorbent-catalyst. Chemical Engineering and Processing: Process Intensification 2014;86:96–103. https://doi.org/10.1016/j.cep.2014.10.014.

[225] Xu P, Zhou ZM, Zhao C, Cheng Z. Ni/CaO-Al2O3 bifunctional catalysts for sorption-enhanced steam methane reforming. AIChE Journal 2014;60:3547–56. https://doi.org/10.1002/aic.14543.

[226] Di Felice L, Kazi SS, Sørby MH, Martinez I, Grasa G, Maury D, et al. Combined sorbent and catalyst material for sorption enhanced reforming of methane under cyclic regeneration in presence of H2O and CO2. Fuel Processing Technology 2019;183:35–47. https://doi.org/10.1016/j.fuproc.2018.10.012.

[227] Kim SM, Abdala PM, Hosseini D, Armutlulu A, Margossian T, Copéret C, et al. Bi-functional Ru/Ca3Al2O6-CaO catalyst-CO2 sorbent for the production of high purity hydrogen: Via sorption-enhanced steam methane reforming. Catal Sci Technol 2019;9:5745–56. https://doi.org/10.1039/c9cy01095e.

[228] Cesário MR, Barros BS, Courson C, Melo DMA, Kiennemann A. Catalytic performances of Ni-CaO-mayenite in CO2 sorption enhanced steam methane reforming. Fuel Processing Technology 2015;131:247–53. https://doi.org/10.1016/j.fuproc.2014.11.028.

[229] García-Lario AL, Grasa GS, Murillo R. Performance of a combined CaO-based sorbent and catalyst on H2 production, via sorption enhanced methane steam reforming. Chemical Engineering Journal 2015;264:697–705. https://doi.org/10.1016/j.cej.2014.11.116.

[230] Di Giuliano A, Gallucci K. Sorption enhanced steam methane reforming based on nickel and calcium looping: a review. Chemical Engineering and Processing - Process Intensification 2018;130:240–52. https://doi.org/10.1016/j.cep.2018.06.021.

[231] Zhao C, Zhou Z, Cheng Z, Fang X. Sol-gel-derived, CaZrO3-stabilized Ni/CaO-CaZrO3 bifunctional catalyst for sorption-enhanced steam methane reforming. Appl Catal B 2016;196:16–26. https://doi.org/10.1016/j.apcatb.2016.05.021.

[232] Di Giuliano A, Giancaterino F, Courson C, Foscolo PU, Gallucci K. Development of a Ni-CaO-mayenite combined sorbent-catalyst material for multicycle sorption enhanced steam methane reforming. Fuel 2018;234:687–99. https://doi.org/10.1016/j.fuel.2018.07.071.

[233] Cherbański R, Molga E. Sorption-enhanced steam-methane reforming with simultaneous sequestration of CO2 on fly ashes – Proof of concept and simulations for gas-solid-solid trickle flow reactor. Chemical Engineering and Processing: Process Intensification 2018;124:37–49. https://doi.org/10.1016/j.cep.2017.11.010.

[234] Obradović A, Levec J. High Purity Hydrogen with Sorption-Enhanced Steam Methane Reforming in a Gas-Solid Trickle Bed Reactor. Ind Eng Chem Res 2017;56:13301–9. https://doi.org/10.1021/acs.iecr.7b01832.

[235] Ramachandran PA, Duduković MP, Mills PL. Recent advances in the analysis and design of trickle-bed reactors. Sadhana 1987;10:269–98. https://doi.org/10.1007/BF02816209.

[236] Ranade V, Chaudhari R, Gunjal PR. Trickle Bed Reactors. Elsevier; 2011. https://doi.org/10.1016/C2009-0-16553-4.

[237] Wang X, Economides M. Advanced natural gas engineering. Gulf; 2013. https://doi.org/10.1016/C2013-0-15532-8.

[238] Levenspiel O. Chemical reaction engineering. John Wiley & Sons; 1999.

[239] Reijers HTJ, Boon J, Elzinga GD, Cobden PD, Haije WG, Van Den Brink RW. Modeling study of the sorption-enhanced reaction process for CO2 capture. I. Model development and validation. Ind Eng Chem Res 2009;48:6966–74. https://doi.org/10.1021/ie801319q.

[240] Lee DK, Baek IH, Yoon WL. Modeling and simulation for the methane steam reforming enhanced by in situ CO2 removal utilizing the CaO carbonation for H2 production. Chem Eng Sci 2004;59:931–42. https://doi.org/10.1016/j.ces.2003.12.011.

[241] Xiu G, Li P, E. Rodrigues A. Sorption-enhanced reaction process with reactive regeneration. Chem Eng Sci 2002;57:3893–908. https://doi.org/10.1016/S0009-2509(02)00245-2.

[242] Rawadieh S, Gomes VG. Steam reforming for hydrogen generation with in situ adsorptive separation. Int J Hydrogen Energy 2009;34:343–55. https://doi.org/10.1016/j.ijhydene.2008.10.038.

[243] Fernandez JR, Abanades JC, Murillo R. Modeling of sorption enhanced steam methane reforming in an adiabatic fixed bed reactor. Chem Eng Sci 2012;84:1–11. https://doi.org/10.1016/j.ces.2012.07.039.

[244] Li ZS, Cai NS. Modeling of multiple cycles for sorption-enhanced steam methane reforming and sorbent regeneration in fixed bed reactor. Energy and Fuels 2007;21:2909–18. https://doi.org/10.1021/ef070112c.

[245] Meyer J, Mastin J, Smeets R. Hydrogen Production from Biogas by Sorption-Enhanced Steam Methane Reforming (SE-SMR) Demonstration of the Novel Process at the HyNor Lillestrøm Hydrogen Station. 2011.

[246] Di Nardo A, Savuto E, Calchetti G, Stendardo S. Computational particle fluid dynamics 3D simulation of the sorption-enhanced steam methane reforming process in a dual fluidized bed of bifunctional sorbent-catalyst particles. Powder Technol 2023;424:118568. https://doi.org/10.1016/j.powtec.2023.118568.

[247] Wang J, Wang Y, Jakobsen HA. The modeling of circulating fluidized bed reactors for SE-SMR process and sorbent regeneration. Chem Eng Sci 2014;108:57–65. https://doi.org/10.1016/j.ces.2013.12.012.

[248] Sánchez RA, Chao Z, Solsvik J, Jakobsen HA. One Dimensional Two-Fluid Model Simulations of the SE-SMR Process Operated in a Circulating Fluidized Bed Reactor. Procedia Eng 2012;42:1282–91. https://doi.org/10.1016/J.PROENG.2012.07.520.

[249] Solsvik J, Chao Z, Jakobsen HA. Modeling and simulation of bubbling fluidized bed reactors using a dynamic one-dimensional two-fluid model: The sorption-enhanced steam-methane reforming process. Advances in Engineering Software 2015;80:156–73. https://doi.org/10.1016/j.advengsoft.2014.09.011.

[250] Wang Y, Chao Z, Jakobsen HA. 3D Simulation of bubbling fluidized bed reactors for sorption enhanced steam methane reforming processes. J Nat Gas Sci Eng 2010;2:105–13. https://doi.org/10.1016/j.jngse.2010.04.004.

[251] Solsvik J, Sánchez RA, Chao Z, Jakobsen HA. Simulations of Steam Methane Reforming/Sorption-Enhanced Steam Methane Reforming Bubbling Fluidized Bed Reactors by

a Dynamic One-Dimensional Two-Fluid Model: Implementation Issues and Model Validation. Ind Eng Chem Res 2013;52:4202–20. https://doi.org/10.1021/ie303348r.

[252] Herce C, Cortés C, Stendardo S. Numerical simulation of a bubbling fluidized bed reactor for sorption-enhanced steam methane reforming under industrially relevant conditions: Effect of sorbent (dolomite and CaO-Ca12Al14O33) and operational parameters. Fuel Processing Technology 2019;186:137–48. https://doi.org/10.1016/j.fuproc.2019.01.003.

[253] Carlo A Di, Bocci E, Zuccari F, Dell'era A. Numerical investigation of sorption enhanced steam methane reforming process using computational fluid dynamics Eulerian-Eulerian code. Ind Eng Chem Res 2010;49:1561–76. https://doi.org/10.1021/ie900748t.

[254] Chen Y, Zhao Y, Zheng C, Zhang J. Numerical study of hydrogen production via sorption-enhanced steam methane reforming in a fluidized bed reactor at relatively low temperature. Chem Eng Sci 2013;92:67–80. https://doi.org/10.1016/j.ces.2013.01.024.

[255] Phuakpunk K, Chalermsinsuwan B, Putivisutisak S, Assabumrungrat S. Parametric study of hydrogen production via sorption enhanced steam methane reforming in a circulating fluidized bed riser. Chem Eng Sci 2018;192:1041–57. https://doi.org/10.1016/j.ces.2018.08.042.

[256] Phuakpunk K, Chalermsinsuwan B, Putivisutisak S, Assabumrungrat S. Factorial design analysis of parameters for the sorption-enhanced steam reforming of ethanol in a circulating fluidized bed riser using CFD. RSC Adv 2018;8:24209–30. https://doi.org/10.1039/C8RA03901A.

[257] Jakobsen JP, Halmøy E. Reactor modeling of sorption enhanced steam methane reforming. Energy Procedia 2009;1:725–32. https://doi.org/10.1016/j.egypro.2009.01.096.

[258] Meyer J, Mastin J, Pinilla CS. Sustainable hydrogen production from biogas using sorption-enhanced reforming. Energy Procedia 2014;63:6800–14. https://doi.org/10.1016/j.egypro.2014.11.714.

[259] Roses L, Gallucci F, Manzolini G, van Sint Annaland M. Experimental study of steam methane reforming in a Pd-based fluidized bed membrane reactor. Chemical Engineering Journal 2013;222:307–20. https://doi.org/10.1016/j.cej.2013.02.069.

[260] Adris AM, Lim CJ, Grace JR. The fluidized bed membrane reactor system: a pilot scale experimental study. Chem Eng Sci 1994;49:5833–43. https://doi.org/10.1016/0009-2509(94)00324-6.

[261] Mahecha-Botero A, Boyd T, Gulamhusein A, Comyn N, Lim CJ, Grace JR, et al. Pure hydrogen generation in a fluidized-bed membrane reactor: Experimental findings. Chem Eng Sci 2008;63:2752–62. https://doi.org/10.1016/j.ces.2008.02.032.

[262] Andrés MB, Boyd T, Grace JR, Jim Lim C, Gulamhusein A, Wan B, et al. In-situ CO2 capture in a pilot-scale fluidized-bed membrane reformer for ultra-pure hydrogen production. Int J Hydrogen Energy 2011;36:4038–55. https://doi.org/10.1016/j.ijhydene.2010.09.091.

[263] Andrés MB, Boyd T, Grace JR, Jim Lim C, Gulamhusein A, Wan B, et al. In-situ CO2 capture in a pilot-scale fluidized-bed membrane reformer for ultra-pure hydrogen production. Int J Hydrogen Energy 2011;36:4038–55. https://doi.org/10.1016/j.ijhydene.2010.09.091.

[264] Chen Y, Mahecha-Botero A, Lim CJ, Grace JR, Zhang J, Zhao Y, et al. Hydrogen production in a sorption-enhanced fluidized-bed membrane reactor: Operating parameter investigation. Ind Eng Chem Res 2014;53:6230–42. https://doi.org/10.1021/ie500294k.

[265] Wu X, Wu C, Wu S. Dual-enhanced steam methane reforming by membrane separation of H2 and reactive sorption of CO2. Chemical Engineering Research and Design 2015;96:150–7. https://doi.org/10.1016/j.cherd.2015.02.010.

[266] Yan Y, Thanganadar D, Clough PT, Mukherjee S, Patchigolla K, Manovic V, et al. Process simulations of blue hydrogen production by upgraded sorption enhanced steam methane reforming (SE-SMR) processes. Energy Convers Manag 2020;222:113144. https://doi.org/10.1016/j.enconman.2020.113144.

[267] Stegehake C, Riese J, Grünewald M. Modeling and Validating Fixed-Bed Reactors: A State-of-the-Art Review. ChemBioEng Reviews 2019;6:28–44. https://doi.org/10.1002/cben.201900002.

[268] Faheem HH, Tanveer HU, Abbas SZ, Maqbool F. Comparative study of conventional steam-methane-reforming (SMR) and auto-thermal-reforming (ATR) with their hybrid sorption enhanced (SE-SMR & SE-ATR) and environmentally benign process models for the hydrogen production. Fuel 2021;297. https://doi.org/10.1016/j.fuel.2021.120769.

[269] Abbas SZ, Dupont V, Mahmud T. Modelling of H2 production in a packed bed reactor via sorption enhanced steam methane reforming process. Int J Hydrogen Energy 2017;42:18910–21. https://doi.org/10.1016/j.ijhydene.2017.05.222.

[270] Ochoa-Fernández E, Rusten HK, Jakobsen HA, Rønning M, Holmen A, Chen D. Sorption enhanced hydrogen production by steam methane reforming using Li2ZrO3 as sorbent: Sorption kinetics and reactor simulation. Catal Today 2005;106:41–6. https://doi.org/10.1016/J.CATTOD.2005.07.146.

[271] Iliuta I, Radfarnia HR, Iliuta MC. Hydrogen Production by Sorption-Enhanced Steam Glycerol Reforming: Sorption Kinetics and Reactor Simulation 2012. https://doi.org/10.1002/aic.13979.

[272] Arora A, Iyer SS, Hasan MMF. GRAMS: A general framework describing adsorption, reaction and sorption-enhanced reaction processes. Chem Eng Sci 2018;192:335–58. https://doi.org/10.1016/J.CES.2018.07.031.

[273] Yan W, Sui S. Combination of Sorption-Enhanced Steam Methane Reforming and Electricity Generation by MCFC: Concept and Numerical Simulation Analysis. Sep Sci Technol 2009;44:3013–44. https://doi.org/10.1080/01496390903182560.

[274] Shahid MM, Abbas SZ, Maqbool F, Ramirez-Solis S, Dupont V, Mahmud T. Modeling of sorption enhanced steam methane reforming in an adiabatic packed bed reactor using various CO2 sorbents. J Environ Chem Eng 2021;9:105863. https://doi.org/10.1016/J.JECE.2021.105863.

[275] Froment GF. Analysis and Design of Fixed Bed Catalytic Reactors 1974. https://doi.org/10.1021/ba-1972-0109.ch001.

[276] Rusten HK, Ochoa-Fernández E, Chen D, Jakobsen HA. Numerical Investigation of Sorption Enhanced Steam Methane Reforming Using Li 2 ZrO 3 as CO 2 -acceptor. Ind Eng Chem Res 2007;46:4435–43. https://doi.org/10.1021/ie061525o.

[277] Wu Y-J, Li P, Yu J-G, Cunha AF, Rodrigues AE. Sorption-enhanced steam reforming of ethanol for continuous high-purity hydrogen production: 2D adsorptive reactor dynamics and process design. Chem Eng Sci 2014;118:83–93. https://doi.org/10.1016/j.ces.2014.07.005.

[278] Li Z, Cai N. Modeling of Multiple Cycles for Sorption-Enhanced Steam Methane Reforming and Sorbent Regeneration in Fixed Bed Reactor. Energy & Fuels 2007;21:2909–18. https://doi.org/10.1021/ef070112c.

[279] Johnsen K, Grace JR, Elnashaie SSEH, Kolbeinsen L, Eriksen D. Modeling of sorption-enhanced steam reforming in a dual fluidized bubbling bed reactor. Ind Eng Chem Res 2006;45:4133–44. https://doi.org/10.1021/ie0511736.

[280] Gidaspow D. Multiphase flow and fluidization : continuum and kinetic theory descriptions 1994:467.

[281] Lettieri P, Mazzei L. Challenges and Issues on the CFD Modeling of Fluidized Beds: A Review. The Journal of Computational Multiphase Flows 2009;1:83–131. https://doi.org/10.1260/175748209789563937.

[282] Ortiz AL, Harrison DP. Hydrogen production using sorption-enhanced reaction. Ind Eng Chem Res, vol. 40, American Chemical Society; 2001, p. 5102–9. https://doi.org/10.1021/ie001009c.

[283] Ochoa-Fernández E, Haugen G, Zhao T, Rønning M, Aartun I, Børresen B, et al. Process design simulation of H2 production by sorption enhanced steam methane reforming: Evaluation of potential CO2 acceptors. Green Chemistry 2007;9:654–66. https://doi.org/10.1039/b614270b.

[284] Cobden PD, van Beurden P, Reijers HTJ, Elzinga GD, Kluiters SCA, Dijkstra JW, et al. Sorption-enhanced hydrogen production for pre-combustion CO2 capture: Thermodynamic analysis and experimental results. International Journal of Greenhouse Gas Control 2007;1:170–9. https://doi.org/10.1016/S1750-5836(07)00021-7.

[285] Zhang X, Zhu L, He Y, Lv L, Rao D, Li S. Quad-generation of combined cooling, heating, power, and hydrogen in a dual-loop chemical looping process: Process simulation and thermodynamic evaluation. AIP Adv 2020;10:85223. https://doi.org/10.1063/5.0010301.

[286] Diglio G, Hanak DP, Bareschino P, Pepe F, Montagnaro F, Manovic V. Modelling of sorption-enhanced steam methane reforming in a fixed bed reactor network integrated with fuel cell. Appl Energy 2018;210:1–15. https://doi.org/10.1016/j.apenergy.2017.10.101.

[287] Tzanetis KF, Martavaltzi CS, Lemonidou AA. Comparative exergy analysis of sorption enhanced and conventional methane steam reforming. Int J Hydrogen Energy 2012;37:16308–20. https://doi.org/10.1016/j.ijhydene.2012.02.191.

[288] Zhu L, Li L, Fan J. A modified process for overcoming the drawbacks of conventional steam methane reforming for hydrogen production: Thermodynamic investigation. Chemical Engineering Research and Design 2015;104:792–806. https://doi.org/10.1016/j.cherd.2015.10.022.

[289] Alam S, Kumar JP, Rani KY, Sumana C. Self-sustained process scheme for high purity hydrogen production using sorption enhanced steam methane reforming coupled with chemical looping combustion. J Clean Prod 2017;162:687–701. https://doi.org/10.1016/j.jclepro.2017.05.136.

[290] Harrison DP. Sorption-enhanced hydrogen production: A review. Ind Eng Chem Res, vol. 47, American Chemical Society; 2008, p. 6486–501. https://doi.org/10.1021/ie800298z.

[291] Voldsund M, Jordal K, Anantharaman R. Hydrogen production with CO2 capture. Int J Hydrogen Energy 2016;41:4969–92. https://doi.org/10.1016/J.IJHYDENE.2016.01.009.

[292] Hanak DP, Michalski S, Manovic V. From post-combustion carbon capture to sorption-enhanced hydrogen production: A state-of-the-art review of carbonate looping process feasibility. Energy Convers Manag 2018;177:428–52. https://doi.org/10.1016/J.ENCONMAN.2018.09.058.

[293] Wang J, Huang L, Yang R, Zhang Z, Wu J, Gao Y, et al. Recent advances in solid sorbents for CO_2 capture and new development trends. Energy Environ Sci 2014;7. https://doi.org/10.1039/C4EE01647E.

[294] Di Giuliano A, Gallucci K. Sorption enhanced steam methane reforming based on nickel and calcium looping: a review. Chemical Engineering and Processing - Process Intensification 2018;130:240–52. https://doi.org/10.1016/j.cep.2018.06.021.

[295] Barelli L, Bidini G, Gallorini F, Servili S. Hydrogen production through sorption-enhanced steam methane reforming and membrane technology: A review. Energy 2008;33:554–70. https://doi.org/10.1016/j.energy.2007.10.018.

[296] Wu Y-J, Li P, Yu J-G, Cunha AF, Rodrigues AE. Progress on sorption-enhanced reaction process for hydrogen production. Reviews in Chemical Engineering 2016;0. https://doi.org/10.1515/revce-2015-0043.

[297] Romano MC, Martínez I, Murillo R, Arstad B, Blom R, Ozcan DC, et al. Process simulation of Ca-looping processes: review and guidelines. Energy Procedia 2013;37:142–50. https://doi.org/10.1016/J.EGYPRO.2013.05.095.

[298] Masoudi Soltani S, Lahiri A, Bahzad H, Clough P, Gorbounov M, Yan Y. Sorption-enhanced Steam Methane Reforming for Combined CO2 Capture and Hydrogen Production: A State-of-the-Art Review. Carbon Capture Science & Technology 2021;1:100003. https://doi.org/10.1016/J.CCST.2021.100003.

[299] Sikarwar VS, Pfeifer C, Ronsse F, Pohořelý M, Meers E, Kaviti AK, et al. Progress in in-situ CO2-sorption for enhanced hydrogen production. Prog Energy Combust Sci 2022;91:101008. https://doi.org/10.1016/J.PECS.2022.101008.

[300] Wilhelm G, Keller K, Schonfelder R, Klempt W. Production of hydrogen. US1816523A, 1931.

[301] Hufton JR, Mayorga S, Sircar S. Sorption-enhanced reaction process for hydrogen production. AIChE Journal 1999;45:248–56. https://doi.org/10.1002/aic.690450205.

[302] Berger AH, Bhown AS. Optimizing solid sorbents for CO2 capture. Energy Procedia, vol. 37, Elsevier Ltd; 2013, p. 25–32. https://doi.org/10.1016/j.egypro.2013.05.081.

[303] Cherbański R, Molga E. Sorption-enhanced steam-methane reforming with simultaneous sequestration of CO2 on fly ashes – Proof of concept and simulations for gas-solid-solid trickle flow reactor. Chemical Engineering and Processing: Process Intensification 2018;124:37–49. https://doi.org/10.1016/j.cep.2017.11.010.

[304] Obradović A, Levec J. High Purity Hydrogen with Sorption-Enhanced Steam Methane Reforming in a Gas-Solid Trickle Bed Reactor. Ind Eng Chem Res 2017;56:13301–9. https://doi.org/10.1021/acs.iecr.7b01832.

[305] Kwang BY, Harrison DP. Low-pressure sorption-enhanced hydrogen production. Ind Eng Chem Res 2005;44:1665–9. https://doi.org/10.1021/ie048883g.

[306] Ortiz AL, Balasubramanian B, Harrison DP. Combining steam-methane reforming, water-gas shift, and CO{sub 2} removal in a single-step process for hydrogen production. Final report for period March 15, 1997 - December 14, 2000. Argonne, IL (United States): 2001. https://doi.org/10.2172/807748.

[307] García-Lario AL, Grasa GS, Murillo R. Performance of a combined CaO-based sorbent and catalyst on H2 production, via sorption enhanced methane steam reforming. Chemical Engineering Journal 2015;264:697–705. https://doi.org/10.1016/j.cej.2014.11.116.

[308] Xie M, Zhou Z, Qi Y, Cheng Z, Yuan W. Sorption-enhanced steam methane reforming by in situ CO 2 capture on a CaO-Ca 9Al 6O 18 sorbent. Chemical Engineering Journal 2012;207–208:142–50. https://doi.org/10.1016/j.cej.2012.06.032.

[309] Huang W-J, Yu C-T, Sheu W-J, Chen Y-C. The effect of non-uniform temperature on the sorption-enhanced steam methane reforming in a tubular fixed-bed reactor. Int J Hydrogen Energy 2021;46:16522–33. https://doi.org/10.1016/j.ijhydene.2020.07.182.

[310] Neni A, Benguerba Y, Balsamo M, Erto A, Ernst B, Benachour D. Numerical study of sorption-enhanced methane steam reforming over Ni/Al2O3 catalyst in a fixed-bed reactor. Int J Heat Mass Transf 2021;165:120635. https://doi.org/10.1016/j.ijheatmasstransfer.2020.120635.

[311] Chanburanasiri N, Ribeiro AM, Rodrigues AE, Arpornwichanop A, Laosiripojana N, Praserthdam P, et al. Hydrogen production via sorption enhanced steam methane reforming process using Ni/CaO multifunctional catalyst. Ind Eng Chem Res 2011;50:13662–71. https://doi.org/10.1021/ie201226j.

[312] Aloisi I, Di Giuliano A, Di Carlo A, Foscolo PU, Courson C, Gallucci K. Sorption enhanced catalytic Steam Methane Reforming: Experimental data and simulations describing the behaviour of bi-functional particles. Chemical Engineering Journal 2017;314:570–82. https://doi.org/10.1016/j.cej.2016.12.014.

[313] Martavaltzi CS, Pampaka EP, Korkakaki ES, Lemonidou AA. Hydrogen production via steam reforming of methane with simultaneous CO2 capture over CaO-Ca12Al14O33. Energy and Fuels, vol. 24, American Chemical Society; 2010, p. 2589–95. https://doi.org/10.1021/ef9014058.

[314] Di Giuliano A, Giancaterino F, Courson C, Foscolo PU, Gallucci K. Development of a Ni-CaO-mayenite combined sorbent-catalyst material for multicycle sorption enhanced steam methane reforming. Fuel 2018;234:687–99. https://doi.org/10.1016/j.fuel.2018.07.071.

[315] Chen H, Zhang T, Dou B, Dupont V, Williams P, Ghadiri M, et al. Thermodynamic analyses of adsorption-enhanced steam reforming of glycerol for hydrogen production. Int J Hydrogen Energy 2009;34:7208–22. https://doi.org/10.1016/j.ijhydene.2009.06.070.

[316] Di Felice L, Kazi SS, Sørby MH, Martinez I, Grasa G, Maury D, et al. Combined sorbent and catalyst material for sorption enhanced reforming of methane under cyclic regeneration in presence of H2O and CO2. Fuel Processing Technology 2019;183:35–47. https://doi.org/10.1016/j.fuproc.2018.10.012.

[317] Rackley SA. Adsorption capture systems. Carbon Capture and Storage, Elsevier; 2017, p. 151–85. https://doi.org/10.1016/b978-0-12-812041-5.00007-6.

[318] Wu X, Wu S. Production of high-purity hydrogen by sorption-enhanced steam reforming process of methanol. Journal of Energy Chemistry 2015;24:315–21. https://doi.org/10.1016/S2095-4956(15)60317-5.

[319] Chen Y, Grace JR, Zhao Y, Zhang J. Multi-fluid reactive modeling of sorption enhanced steam reforming of coke oven gas in fluidized bed. Fuel 2017;204:152–70. https://doi.org/10.1016/j.fuel.2017.05.031.

[320] Glier JC, Rubin ES. Energy Procedia 00 (2013) 000-000 Assessment of solid sorbents as a competitive post-combustion CO 2 capture technology Selection and/or peer-review under responsibility of GHGT. 2013.

[321] Meloni E, Martino M, Palma V. A short review on ni based catalysts and related engineering issues for methane steam reforming. Catalysts 2020;10:352. https://doi.org/10.3390/catal10030352.

[322] Zhao C, Zhou Z, Cheng Z, Fang X. Sol-gel-derived, CaZrO3-stabilized Ni/CaO-CaZrO3 bifunctional catalyst for sorption-enhanced steam methane reforming. Appl Catal B 2016;196:16–26. https://doi.org/10.1016/j.apcatb.2016.05.021.

[323] Balasubramanian B, Ortiz AL, Kaytakoglu S, Harrison DP. Hydrogen from methane in a single-step process. Chem Eng Sci 1999;54:3543–52. https://doi.org/10.1016/S0009-2509(98)00425-4.

[324] Abbas SZ, Dupont V, Mahmud T. Modelling of H2 production in a packed bed reactor via sorption enhanced steam methane reforming process. Int J Hydrogen Energy 2017;42:18910–21.

[325] Johnsen K, Ryu HJ, Grace JR, Lim CJ. Sorption-enhanced steam reforming of methane in a fluidized bed reactor with dolomite as CO2-acceptor. Chem Eng Sci 2006;61:1195–202. https://doi.org/10.1016/j.ces.2005.08.022.

[326] Hildenbrand N, Readman J, Dahl IM, Blom R. Sorbent enhanced steam reforming (SESR) of methane using dolomite as internal carbon dioxide absorbent: Limitations due to Ca(OH)2 formation. Appl Catal A Gen 2006;303:131–7. https://doi.org/10.1016/J.APCATA.2006.02.015.

[327] Martínez I, Grasa G, Meyer J, Di Felice L, Kazi S, Sanz C, et al. Performance and operating limits of a sorbent-catalyst system for sorption-enhanced reforming (SER) in a fluidized bed reactor. Chem Eng Sci 2019;205:94–105. https://doi.org/10.1016/J.CES.2019.04.029.

[328] García R, Gil M V., Rubiera F, Chen D, Pevida C. Renewable hydrogen production from biogas by sorption enhanced steam reforming (SESR): A parametric study. Energy 2021;218:119491. https://doi.org/10.1016/J.ENERGY.2020.119491.

[329] Cranfield University, Gas Technology Institute, The Babcock Doosan. Bulk Hydrogen Production by Sorbent Enhanced Steam Reforming (HyPER) Project. 2019.

[330] IFE Hynor Hydrogen Technology Center (IFE Hynor) - IFE n.d. https://ife.no/en/laboratory/ife-hynor-hydrogen-technology-center-ife-hynor/ (accessed September 25, 2021).

[331] Meyer J, Mastin J, Bjørnebøle TK, Ryberg T, Eldrup N. Techno-economical study of the Zero Emission Gas power concept. Energy Procedia 2011;4:1949–56. https://doi.org/10.1016/J.EGYPRO.2011.02.075.

[332] Mays J. One Step Hydrogen Generation Through Sorption Enhanced Reforming. Golden, CO (United States): 2017. https://doi.org/10.2172/1373949.

[333] Mays J, Stanis R. Techno-Economic Analysis for GTI's Compact Hydrogen Generator. . United States: 2020.

[334] Lesemann M. Hydrogen Production with Integrated CO 2 Capture. 2019.

[335] Akers WW, Camp DP. Kinetics of the methane-steam reaction. AIChE Journal 1955;1:471–5. https://doi.org/10.1002/aic.690010415.

[336] Allen DW, Gerhard ER, Likins MR. Kinetics of the Methane-Steam Reaction. Industrial and Engineering Chemistry Process Design and Development 1975;14:256–9. https://doi.org/10.1021/i260055a010.

[337] Numaguchi T, Kikuchi K. Intrinsic kinetics and design simulation in a complex reaction network; steam-methane reforming. Tenth International Symposium on Chemical Reaction Engineering 1988:2295–301. https://doi.org/10.1016/B978-0-08-036969-3.50086-5.

[338] Xu J, Froment GF. Methane steam reforming, methanation and water-gas shift: I. Intrinsic kinetics. AIChE Journal 1989;35:88–96. https://doi.org/10.1002/aic.690350109.

[339] Zeppieri M, Villa PL, Verdone N, Scarsella M, De Filippis P. Kinetic of methane steam reforming reaction over nickel- and rhodium-based catalysts. Appl Catal A Gen 2010;387:147–54. https://doi.org/10.1016/j.apcata.2010.08.017.

[340] Wu YJ, Santos JC, Li P, Yu JG, Cunha AF, Rodrigues AE. Simplified kinetic model for steam reforming of ethanol on a Ni/Al2O3 catalyst. Canadian Journal of Chemical Engineering 2014;92:116–30. https://doi.org/10.1002/CJCE.21773.

[341] Cheng CK, Foo SY, Adesina AA. Glycerol steam reforming over bimetallic Co-Ni/Al2O3. Ind Eng Chem Res 2010;49:10804–17. https://doi.org/10.1021/IE100462T/ASSET/IMAGES/IE-2010-00462T_M067.GIF.

[342] Soliman MA, Adris AM, Al-Ubaid AS, El-Nashaie SSEH. Intrinsic kinetics of nickel/calcium aluminate catalyst for methane steam reforming. Journal of Chemical Technology & Biotechnology 1992;55:131–8. https://doi.org/10.1002/jctb.280550206.

[343] Katheria S, Kunzru D, Deo G. Kinetics of steam reforming of methane on Rh–Ni/MgAl2O4 catalyst. Reaction Kinetics, Mechanisms and Catalysis 2020;130:91–101. https://doi.org/10.1007/s11144-020-01767-y.

[344] Sugihara S, Kawamura Y, Iwai H. Rate equation of steam-methane reforming reaction on Ni-YSZ cermet considering its porous microstructure. J Phys Conf Ser, vol. 745, Institute of Physics Publishing; 2016, p. 032147. https://doi.org/10.1088/1742-6596/745/3/032147.

[345] Hou K, Hughes R. The kinetics of methane steam reforming over a Ni/-Al 2 O catalyst. vol. 82. 2001.

[346] Mosayebi A, Nasabi M. Steam methane reforming on LaNiO3 perovskite-type oxide for syngas production, activity tests, and kinetic modeling. Int J Energy Res 2020;44:5500–15. https://doi.org/10.1002/er.5300.

[347] Mas V, Bergamini ML, Baronetti G, Amadeo N, Laborde M. A kinetic study of ethanol steam reforming using a nickel based catalyst. Top Catal 2008;51:39–48. https://doi.org/10.1007/S11244-008-9123-Y/TABLES/4.

[348] Wang Y, Memon MZ, Seelro MA, Fu W, Gao Y, Dong Y, et al. A review of CO2 sorbents for promoting hydrogen production in the sorption-enhanced steam reforming process. Int J Hydrogen Energy 2021. https://doi.org/10.1016/j.ijhydene.2021.01.206.

[349] Rusten HK, Ochoa-Fernández E, Lindborg H, Chen D, Jakobsen HA. Hydrogen production by sorption-enhanced steam methane reforming using lithium oxides as CO2-acceptor. Ind Eng Chem Res 2007;46:8729–37. https://doi.org/10.1021/ie070770k.

[350] Fedunik-Hofman L, Bayon A, Donne SW. Kinetics of Solid-Gas Reactions and Their Application to Carbonate Looping Systems. Energies (Basel) 2019;12. https://doi.org/10.3390/en12152981.

[351] Johnsen K, Grace JR, Elnashaie SSEH, Kolbeinsen L, Eriksen D. Modeling of sorption-enhanced steam reforming in a dual fluidized bubbling bed reactor. Ind Eng Chem Res 2006;45:4133–44. https://doi.org/10.1021/ie0511736.

[352] Stendardo S, Foscolo PU. Carbon dioxide capture with dolomite: A model for gas-solid reaction within the grains of a particulate sorbent. Chem Eng Sci 2009;64:2343–52. https://doi.org/10.1016/j.ces.2009.02.009.

[353] Sun P, Grace JR, Lim CJ, Anthony EJ. Determination of intrinsic rate constants of the CaO-CO2 reaction. Chem Eng Sci 2008;63:47–56. https://doi.org/10.1016/j.ces.2007.08.055.

[354] Aloisi I, Jand N, Stendardo S, Foscolo PU. Hydrogen by sorption enhanced methane reforming: A grain model to study the behavior of bi-functional sorbent-catalyst particles. Chem Eng Sci 2016;149:22–34. https://doi.org/10.1016/j.ces.2016.03.042.

[355] Bhatia SK, Perlmutter DD. A random pore model for fluid-solid reactions: I. Isothermal, kinetic control. AIChE Journal 1980;26. https://doi.org/10.1002/aic.690260308.

[356] Li ZS, Cai NS. Modeling of multiple cycles for sorption-enhanced steam methane reforming and sorbent regeneration in fixed bed reactor. Energy and Fuels 2007;21:2909–18. https://doi.org/10.1021/ef070112c.

[357] LEE D. An apparent kinetic model for the carbonation of calcium oxide by carbon dioxide. Chemical Engineering Journal 2004;100:71–7. https://doi.org/10.1016/j.cej.2003.12.003.

[358] Ding Y, Alpay E. Equilibria and kinetics of CO2 adsorption on hydrotalcite adsorbent. Chem Eng Sci 2000;55:3461–74. https://doi.org/10.1016/S0009-2509(99)00596-5.

[359] Iliuta I, Radfarnia HR, Iliuta MC. Hydrogen Production by Sorption-Enhanced Steam Glycerol Reforming: Sorption Kinetics and Reactor Simulation 2012. https://doi.org/10.1002/aic.13979.

[360] Reijers HTJ, Boon J, Elzinga GD, Cobden PD, Haije WG, Van Den Brink RW. Modeling study of the sorption-enhanced reaction process for CO2 capture. I. Model development and validation. Ind Eng Chem Res 2009;48:6966–74. https://doi.org/10.1021/ie801319q.

[361] Ochoa-Fernández E, Rusten HK, Jakobsen HA, Rønning M, Holmen A, Chen D. Sorption enhanced hydrogen production by steam methane reforming using Li2ZrO3 as sorbent: Sorption kinetics and reactor simulation. Catal Today 2005;106:41–6. https://doi.org/10.1016/J.CATTOD.2005.07.146.

[362] Okunev AG, Nesterenko SS, Lysikov AI. Decarbonation rates of cycled CaO absorbents. Energy and Fuels 2008;22:1911–6. https://doi.org/10.1021/ef800047b.

[363] Johnstone HF, Toomey RD. Gas fluidization of solid particles. Chem Eng Prog 1952;48:220.

[364] Kunii D, Levenspiel O, Brenner H. Fluidization Engineering. 2nd ed. Elsevier Science; 1991.

[365] Davidson JF, Harrison D. Fluidised Particles. Cambridge University Press; 1963.

[366] Lee A, Miller DC. A One-Dimensional (1-D) Three-Region Model for a Bubbling Fluidized-Bed Adsorber. Ind Eng Chem Res 2012;52:121219160808001. https://doi.org/10.1021/ie300840q.

[367] Wen CY, Yu YH. A generalized method for predicting the minimum fluidization velocity. AIChE Journal 1966;12:610–2. https://doi.org/10.1002/aic.690120343.

[368] Mori S, Wen CY. Estimation of bubble diameter in gaseous fluidized beds. AIChE Journal 1975;21:109–15. https://doi.org/10.1002/aic.690210114.

[369] Pugsley TS, Berruti F. A predictive hydrodynamic model for circulating fluidized bed risers. Powder Technol 1996;89:57–69. https://doi.org/10.1016/S0032-5910(96)03154-3.

[370] Johnsen K. Sorption-Enhanced Steam Methane Reforming in Fluidized Bed Reactors. NTNU-trykk; 2006.

[371] Gidaspow D. Hydrodynamics of fiuidizatlon and heat transfer: Supercomputer modeling. Appl Mech Rev 1986;39:1–23. https://doi.org/10.1115/1.3143702.

[372] Lettieri P, Mazzei L. Challenges and issues on the CFD modeling of fluidized beds: A review. Journal of Computational Multiphase Flows 2009;1:83–131. https://doi.org/10.1260/175748209789563937.

[373] Jain V, Kalo L, Kumar D, Pant HJ, Upadhyay RK. Experimental and numerical investigation of liquid–solid binary fluidized beds: Radioactive particle tracking technique and dense discrete phase model simulations. Particuology 2017;33:112–22. https://doi.org/10.1016/j.partic.2016.07.011.

[374] Lindborg Hå, Lysberg M, Jakobsen HA. Practical validation of the two-fluid model applied to dense gas-solid flows in fluidized beds. Chem Eng Sci 2007;62:5854–69. https://doi.org/10.1016/j.ces.2007.06.011.

[375] Jakobsen HA. Chemical reactor modeling: Multiphase reactive flows: Second edition. vol. 9783319050928. Springer International Publishing; 2014. https://doi.org/10.1007/978-3-319-05092-8.

[376] Adnan M, Sun J, Ahmad N, Wei JJ. Comparative CFD modeling of a bubbling bed using a Eulerian–Eulerian two-fluid model (TFM) and a Eulerian-Lagrangian dense discrete phase model (DDPM). Powder Technol 2021;383:418–42. https://doi.org/10.1016/J.POWTEC.2021.01.063.

[377] Lun CKK, Savage SB, Jeffrey DJ, Chepurniy N. Kinetic theories for granular flow: inelastic particles in Couette flow and slightly inelastic particles in a general flowfield. J Fluid Mech 1984;140:223–56. https://doi.org/10.1017/S0022112084000586.

[378] Wen CY, Yu YH. Mechanics of fluidization. Chem Eng Prog Symp Ser 1966;62:100–11.

[379] Gidaspow D. Multiphase flow and fluidization : continuum and kinetic theory descriptions 1994:467.

[380] Syamlal M, O'Brien TJ. Computer simulation of bubbles in a fluidized bed. AIChE Symp. Ser, vol. 85, Publ by AIChE; 1989, p. 22–31.

[381] Gibilaro LG, Di Felice R, Waldram SP, Foscolo PU. A predictive model for the equilibrium composition and inversion of binary-solid liquid fluidized beds. Chem Eng Sci 1986;41:379–87. https://doi.org/10.1016/0009-2509(86)87017-8.

[382] Chen Y, Zhao Y, Zheng C, Zhang J. Numerical study of hydrogen production via sorption-enhanced steam methane reforming in a fluidized bed reactor at relatively low temperature. Chem Eng Sci 2013;92:67–80. https://doi.org/10.1016/j.ces.2013.01.024.

[383] Phuakpunk K, Chalermsinsuwan B, Putivisutisak S, Assabumrungrat S. Parametric study of hydrogen production via sorption enhanced steam methane reforming in a circulating fluidized bed riser. Chem Eng Sci 2018;192:1041–57. https://doi.org/10.1016/j.ces.2018.08.042.

[384] Herce C, Cortés C, Stendardo S. Numerical simulation of a bubbling fluidized bed reactor for sorption-enhanced steam methane reforming under industrially relevant conditions: Effect of sorbent (dolomite and CaO-Ca12Al14O33) and operational parameters. Fuel Processing Technology 2019;186:137–48. https://doi.org/10.1016/j.fuproc.2019.01.003.

[385] Herce C, Cortés C, Stendardo S. Computationally efficient CFD model for scale-up of bubbling fluidized bed reactors applied to sorption-enhanced steam methane reforming. Fuel Processing Technology 2017;167:747–61. https://doi.org/10.1016/j.fuproc.2017.07.003.

[386] Solsvik J, Sánchez RA, Chao Z, Jakobsen HA. Simulations of Steam Methane Reforming/Sorption-Enhanced Steam Methane Reforming Bubbling Fluidized Bed Reactors by a Dynamic One-Dimensional Two-Fluid Model: Implementation Issues and Model Validation. Ind Eng Chem Res 2013;52:4202–20. https://doi.org/10.1021/ie303348r.

[387] Solsvik J, Chao Z, Jakobsen HA. Modeling and simulation of bubbling fluidized bed reactors using a dynamic one-dimensional two-fluid model: The sorption-enhanced steam-methane reforming process. Advances in Engineering Software 2015;80:156–73. https://doi.org/10.1016/j.advengsoft.2014.09.011.

[388] Sánchez RA, Chao Z, Solsvik J, Jakobsen HA. One Dimensional Two-Fluid Model Simulations of the SE-SMR Process Operated in a Circulating Fluidized Bed Reactor. Procedia Eng 2012;42:1282–91. https://doi.org/10.1016/J.PROENG.2012.07.520.

[389] Di Carlo A, Aloisi I, Jand N, Stendardo S, Foscolo PU. Sorption enhanced steam methane reforming on catalyst-sorbent bifunctional particles: A CFD fluidized bed reactor model. Chem Eng Sci 2017;173:428–42. https://doi.org/10.1016/j.ces.2017.08.014.

[390] Solsvik J, Chao Z, Sánchez RA, Jakobsen HA. Numerical investigation of steam methane reforming with CO2-capture in bubbling fluidized bed reactors. Fuel Processing Technology 2014;125:290–300. https://doi.org/10.1016/J.FUPROC.2014.03.039.

[391] Lindborg H, Jakobsen HA. Sorption enhanced steam methane reforming process performance and bubbling fluidized bed reactor design analysis by use of a two-fluid model. Ind Eng Chem Res 2009;48:1332–42. https://doi.org/10.1021/ie800522p.

[392] Phuakpunk K, Chalermsinsuwan B, Putivisutisak S, Assabumrungrat S. Factorial design analysis of parameters for the sorption-enhanced steam reforming of ethanol in a circulating fluidized bed riser using CFD. RSC Adv 2018;8:24209–30. https://doi.org/10.1039/C8RA03901A.

[393] Arstad B, Blom R, Bakken E, Dahl I, Jakobsen JP, Røkke P. Sorption-enhanced methane steam reforming in a circulating fluidized bed reactor system. Energy Procedia 2009;1:715–20. https://doi.org/10.1016/j.egypro.2009.01.094.

[394] Wang Y, Chao Z, Jakobsen HA. 3D Simulation of bubbling fluidized bed reactors for sorption enhanced steam methane reforming processes. J Nat Gas Sci Eng 2010;2:105–13. https://doi.org/10.1016/j.jngse.2010.04.004.

[395] Wang Y, Chao Z, Jakobsen HA. Effects of gas-solid hydrodynamic behavior on the reactions of the sorption enhanced steam methane reforming process in bubbling fluidized bed reactors. Ind Eng Chem Res 2011;50:8430–7. https://doi.org/10.1021/ie102330d.

[396] Wang S, Yang X, Xu S, Zhang K, Li B. Assessment of sorption-enhanced crude glycerol steam reforming process via CFD simulation. Int J Hydrogen Energy 2018;43:14996–5004. https://doi.org/10.1016/J.IJHYDENE.2018.06.053.

[397] Chao Z, Zhang Y, Wang Y, Jakobsen JP, Jakobsen HA. Modelling of binary fluidized bed reactors for the sorption-enhanced steam methane reforming process. Canadian Journal of Chemical Engineering 2017;95:157–69. https://doi.org/10.1002/cjce.22602.

[398] Wang S, Yang X, Xu S, Zhang K, Li B. Evaluation of sorption-enhanced reforming of biodiesel by-product in fluidized beds by means of CFD approach. Fuel 2018;214:115–22. https://doi.org/10.1016/J.FUEL.2017.10.128.

[399] Wang S, Xu S, Liu S, Hu B. Prediction of sorption-enhanced reforming process on hydrotalcite sorbent in a fluidized bed reactor. Energy Convers Manag 2019;180:924–30.

[400] Wan Z, Yang S, Bao G, Hu J, Wang H. Multiphase particle-in-cell simulation study of sorption enhanced steam methane reforming process in a bubbling fluidized bed reactor. Chemical Engineering Journal 2022;429:132461. https://doi.org/10.1016/J.CEJ.2021.132461.

[401] Orcutt JC, Davidson JF, Pigford RL. Reaction time distributions in fluidized catalytic reactors. Chemical engineering progress symposium series, vol. 58, 1962, p. 1–15.

[402] Sánchez RA, Chao Z, Solsvik J, Jakobsen HA. An investigation of the heat integration between the two riser units constituting a circulating fluidized bed reactor for the SE-SMR process. Energy Procedia, vol. 37, Elsevier Ltd; 2013, p. 1218–27. https://doi.org/10.1016/j.egypro.2013.05.220.

[403] Phuakpunk K, Chalermsinsuwan B, Putivisutisak S, Assabumrungrat S. Simulations of sorbent regeneration in a circulating fluidized bed system for sorption enhanced steam reforming with dolomite. Particuology 2020;50:156–72. https://doi.org/10.1016/j.partic.2019.08.005.

[404] Carlo A Di, Bocci E, Zuccari F, Dell'era A. Numerical investigation of sorption enhanced steam methane reforming process using computational fluid dynamics Eulerian-Eulerian code. Ind Eng Chem Res 2010;49:1561–76. https://doi.org/10.1021/ie900748t.

[405] Dat Vo N, Kang JH, Oh M, Lee CH. Dynamic model and performance of an integrated sorption-enhanced steam methane reforming process with separators for the simultaneous blue H2

production and CO2 capture. Chemical Engineering Journal 2021;423:130044. https://doi.org/10.1016/J.CEJ.2021.130044.

[406] Martínez I, Grasa G, Murillo R, Arias B, Abanades JC. Kinetics of Calcination of Partially Carbonated Particles in a Ca-Looping System for CO 2 Capture. Energy & Fuels 2012;26:1432–40. https://doi.org/10.1021/ef201525k.

[407] Yang X, Wang S, Li B, Liu H, He Y. Evaluation of sorption-enhanced reforming over catalyst-sorbent bi-functional particles in an internally circulating fluidized bed. Advanced Powder Technology 2020;31:2566–72. https://doi.org/10.1016/j.apt.2020.04.020.

[408] Wang Y, Chao Z, Chen D, Jakobsen HA. SE-SMR process performance in CFB reactors: Simulation of the CO2 adsorption/desorption processes with CaO based sorbents. International Journal of Greenhouse Gas Control 2011;5:489–97. https://doi.org/10.1016/j.ijggc.2010.09.001.

[409] Wang J, Wang Y, Jakobsen HA. The modeling of circulating fluidized bed reactors for SE-SMR process and sorbent regeneration. Chem Eng Sci 2014;108:57–65. https://doi.org/10.1016/j.ces.2013.12.012.

[410] Dou B, Dupont V, Rickett G, Blakeman N, Williams PT, Chen H, et al. Hydrogen production by sorption-enhanced steam reforming of glycerol. Bioresour Technol 2009;100:3540–7. https://doi.org/10.1016/j.biortech.2009.02.036.

[411] Abbas SZ, Dupont V, Mahmud T. Kinetics study and modelling of steam methane reforming process over a NiO/Al2O3 catalyst in an adiabatic packed bed reactor. Int J Hydrogen Energy 2017;42:2889–903. https://doi.org/10.1016/j.ijhydene.2016.11.093.

[412] Faheem HH, Tanveer HU, Abbas SZ, Maqbool F. Comparative study of conventional steam-methane-reforming (SMR) and auto-thermal-reforming (ATR) with their hybrid sorption enhanced (SE-SMR & SE-ATR) and environmentally benign process models for the hydrogen production. Fuel 2021;297:120769.

[413] Werther J, Hartge E-U. Modeling of Industrial Fluidized-Bed Reactors. Ind Eng Chem Res 2004;43:5593–604. https://doi.org/10.1021/ie030760t.

[414] Chiesa M, Mathiesen V, Melheim JA, Halvorsen B. Numerical simulation of particulate flow by the Eulerian–Lagrangian and the Eulerian–Eulerian approach with application to a fluidized bed. Comput Chem Eng 2005;29:291–304. https://doi.org/10.1016/j.compchemeng.2004.09.002.

[415] Andrews MJ, O'Rourke PJ. The multiphase particle-in-cell (MP-PIC) method for dense particulate flows. International Journal of Multiphase Flow 1996;22:379–402. https://doi.org/10.1016/0301-9322(95)00072-0.

[416] Snider DM, O`Rourke PJ, Andrews MJ. An incompressible two-dimensional multiphase particle-in-cell model for dense particle flows. Los Alamos, NM: 1997. https://doi.org/10.2172/510351.

[417] Snider DM. An Incompressible Three-Dimensional Multiphase Particle-in-Cell Model for Dense Particle Flows. J Comput Phys 2001;170:523–49. https://doi.org/10.1006/jcph.2001.6747.

[418] Wan Z, Yang S, Bao G, Hu J, Wang H. Multiphase particle-in-cell simulation study of sorption enhanced steam methane reforming process in a bubbling fluidized bed reactor. Chemical Engineering Journal 2022;429:132461. https://doi.org/10.1016/J.CEJ.2021.132461.

[419] Nardo A Di, Calchetti G, Carlo A Di, Stendardo S. Sorption enhanced steam methane reforming in a bubbling fluidized bed reactor: Simulation and analysis by the CPFD method. Comput Chem Eng 2023;169:108080. https://doi.org/10.1016/j.compchemeng.2022.108080.

[420] Loha C, Chattopadhyay H, Chatterjee PK. Three dimensional kinetic modeling of fluidized bed biomass gasification. Chem Eng Sci 2014;109:53–64. https://doi.org/10.1016/J.CES.2014.01.017.

[421] Kraft S, Kuba M, Kirnbauer F, Bosch K, Hofbauer H. Optimization of a 50 MW bubbling fluidized bed biomass combustion chamber by means of computational particle fluid dynamics. Biomass Bioenergy 2016;89:31–9. https://doi.org/10.1016/J.BIOMBIOE.2016.02.020.

[422] CPFD Software LLC. Barracuda Virtual Reactor® User Manual 2023.

[423] Snider DM. An Incompressible Three-Dimensional Multiphase Particle-in-Cell Model for Dense Particle Flows. J Comput Phys 2001;170:523–49. https://doi.org/10.1006/JCPH.2001.6747.

[424] Gao X, Li T, Sarkar A, Lu L, Rogers WA. Development and validation of an enhanced filtered drag model for simulating gas-solid fluidization of Geldart A particles in all flow regimes. Chem Eng Sci 2018;184:33–51. https://doi.org/10.1016/j.ces.2018.03.038.

[425] Yang N, Wang W, Ge W, Wang L, Li J. Simulation of Heterogeneous Structure in a Circulating Fluidized-Bed Riser by Combining the Two-Fluid Model with the EMMS Approach. Ind Eng Chem Res 2004;43:5548–61. https://doi.org/10.1021/ie049773c.

[426] Li J, Kwauk M. Particle-fluid Two-phase Flow: The Energy-minimization Multi-scale Method. Metallurgical Industry Press; 1994.

[427] Wen CY, Yu YH. Mechanics of fluidization. Chemical Engineering Progress Symposium Series 1966;62:100–11.

[428] Ergun S. Fluid flow through packed columns. Chem Eng Prog 1952;48:89–94.

[429] Numaguchi T, Kikuchi K. Intrinsic kinetics and design simulation in a complex reaction network; steam-methane reforming. Tenth International Symposium on Chemical Reaction Engineering 1988:2295–301. https://doi.org/10.1016/B978-0-08-036969-3.50086-5.

[430] Xu J, Froment GF. Methane steam reforming, methanation and water-gas shift: I. Intrinsic kinetics. AIChE Journal 1989;35:88–96. https://doi.org/10.1002/aic.690350109.

[431] Quirino PPS, Amaral A, Pontes K V., Rossi F, Manenti F. Impact of kinetic models in the prediction accuracy of an industrial steam methane reforming unit. Comput Chem Eng 2021;152:107379. https://doi.org/10.1016/J.COMPCHEMENG.2021.107379.

[432] Hou K, Hughes R. The kinetics of methane steam reforming over a Ni/α-Al2O catalyst. Chemical Engineering Journal 2001;82:311–28. https://doi.org/10.1016/S1385-8947(00)00367-3.

[433] Sun P, Grace JR, Lim CJ, Anthony EJ. Determination of intrinsic rate constants of the CaO-CO2 reaction. Chem Eng Sci 2008;63:47–56. https://doi.org/10.1016/j.ces.2007.08.055.

[434] Abanades JC, Alvarez D. Conversion Limits in the Reaction of CO2 with Lime. Energy & Fuels 2003;17:308–15. https://doi.org/10.1021/ef020152a.

[435] Abanades JC, Anthony EJ, Lu DY, Salvador C, Alvarez D. Capture of CO2 from combustion gases in a fluidized bed of CaO. AIChE Journal 2004;50:1614–22. https://doi.org/10.1002/AIC.10132.

[436] O'Rourke PJ, Snider DM. A new blended acceleration model for the particle contact forces induced by an interstitial fluid in dense particle/fluid flows. Powder Technol 2014;256:39–51. https://doi.org/10.1016/j.powtec.2014.01.084.

[437] LeVeque RJ. Finite volume methods for hyperbolic problems. vol. 31. Cambridge university press; 2002.

[438] Johnsen K, Ryu HJ, Grace JR, Lim CJ. Sorption-enhanced steam reforming of methane in a fluidized bed reactor with dolomite as CO2-acceptor. Chem Eng Sci 2006;61:1195–202. https://doi.org/10.1016/j.ces.2005.08.022.

[439] Li T, Gel A, Pannala S, Shahnam M, Syamlal M. CFD simulations of circulating fluidized bed risers, part I: Grid study. Powder Technol 2014;254:170–80. https://doi.org/10.1016/j.powtec.2014.01.021.

[440] Uddin MH, Coronella CJ. Effects of grid size on predictions of bed expansion in bubbling fluidized beds of Geldart B particles: A generalized rule for a grid-independent solution of TFM simulations. Particuology 2017;34:61–9. https://doi.org/10.1016/j.partic.2016.12.002.

[441] Andrews, Loezos PN, Sundaresan S. Coarse-Grid Simulation of Gas-Particle Flows in Vertical Risers. Ind Eng Chem Res 2005;44:6022–37. https://doi.org/10.1021/ie0492193.

[442] Olivieri G, Marzocchella A, Salatino P. Segregation of fluidized binary mixtures of granular solids. AIChE Journal 2004;50:3095–106. https://doi.org/10.1002/aic.10340.

[443] Zhang Y, Zhao Y, Lu L, Ge W, Wang J, Duan C. Assessment of polydisperse drag models for the size segregation in a bubbling fluidized bed using discrete particle method. Chem Eng Sci 2017;160:106–12. https://doi.org/10.1016/j.ces.2016.11.028.

[444] Johnsen K, Ryu HJ, Grace JR, Lim CJ. Sorption-enhanced steam reforming of methane in a fluidized bed reactor with dolomite as CO2-acceptor. Chem Eng Sci 2006;61:1195–202. https://doi.org/10.1016/J.CES.2005.08.022.

[445] Davidson JF, Harrison D. Fluidised Particles. Cambridge University Press; 1963.

[446] Ranganathan P, Gu S. Computational fluid dynamics modelling of biomass fast pyrolysis in fluidised bed reactors, focusing different kinetic schemes. Bioresour Technol 2016;213:333–41. https://doi.org/10.1016/j.biortech.2016.02.042.

[447] Al-Zahrani AA, Daous MA. Bed expansion and average bubble rise velocity in a gas-solid fluidized bed. Powder Technol 1996;87:255–7. https://doi.org/10.1016/0032-5910(96)03095-1.

[448] Kunii D, Levenspiel O, Brenner H. Fluidization Engineering. 2nd ed. Elsevier Science; 1991.

[449] Bakshi A, Altantzis C, Glicksman LR, Ghoniem AF. Gas-flow distribution in bubbling fluidized beds: CFD-based analysis and impact of operating conditions. Powder Technol 2017;316:500–11. https://doi.org/10.1016/j.powtec.2017.01.005.

[450] Zenz FA. The fluid mechanics of bubbling beds. Fibonacci Quarterly 1978;16:171–83.

[451] Salehi M-S, Askarishahi M, Radl S. Quantification of Solid Mixing in Bubbling Fluidized Beds via Two-Fluid Model Simulations. Ind Eng Chem Res 2020;59:10606–21. https://doi.org/10.1021/acs.iecr.9b06343.

[452] Wiheeb AD, Helwani Z, Kim J, Othman MR. Pressure Swing Adsorption Technologies for Carbon Dioxide Capture. Separation & Purification Reviews 2016;45:108–21. https://doi.org/10.1080/15422119.2015.1047958.

[453] Adris AM, Pruden BB, Lim CJ, Grace JR. On the reported attempts to radically improve the performance of the steam methane reforming reactor. Can J Chem Eng 1996;74:177–86. https://doi.org/10.1002/cjce.5450740202.

[454] Mokheimer EMA, Ibrar Hussain M, Ahmed S, Habib MA, Al-Qutub AA. On the Modeling of Steam Methane Reforming. J Energy Resour Technol 2015;137. https://doi.org/10.1115/1.4027962.

[455] Pashchenko D. Experimental investigation of reforming and flow characteristics of a steam methane reformer filled with nickel catalyst of various shapes. Energy Convers Manag 2019;185:465–72. https://doi.org/10.1016/j.enconman.2019.01.103.

[456] Huang W-J, Yu C-T, Sheu W-J, Chen Y-C. The effect of non-uniform temperature on the sorption-enhanced steam methane reforming in a tubular fixed-bed reactor. Int J Hydrogen Energy 2021;46:16522–33. https://doi.org/10.1016/j.ijhydene.2020.07.182.

[457] Fernández J, Abanades J. Overview of the Ca–Cu looping process for hydrogen production and/or power generation. Curr Opin Chem Eng 2017;17:1–8. https://doi.org/10.1016/j.coche.2017.04.010.

[458] Phuakpunk K, Chalermsinsuwan B, Putivisutisak S, Assabumrungrat S. Simulations of sorbent regeneration in a circulating fluidized bed system for sorption enhanced steam reforming with dolomite. Particuology 2020;50:156–72. https://doi.org/10.1016/j.partic.2019.08.005.

[459] Sánchez RA, Chao Z, Solsvik J, Jakobsen HA. An investigation of the heat integration between the two riser units constituting a circulating fluidized bed reactor for the SE-SMR process. Energy Procedia, vol. 37, Elsevier Ltd; 2013, p. 1218–27. https://doi.org/10.1016/j.egypro.2013.05.220.

[460] Bello MM, Abdul Raman AA, Purushothaman M. Applications of fluidized bed reactors in wastewater treatment – A review of the major design and operational parameters. J Clean Prod 2017;141:1492–514. https://doi.org/10.1016/j.jclepro.2016.09.148.

[461] Cheng Y, Wei F, Yang G, Jin Y. Inlet and outlet effects on flow patterns in gas-solid risers. Powder Technol 1998;98:151–6. https://doi.org/10.1016/S0032-5910(98)00030-8.

[462] Lopes GC, Rosa LM, Mori M, Nunhez JR, Martignoni WP. CFD Study of Industrial FCC Risers: The Effect of Outlet Configurations on Hydrodynamics and Reactions. International Journal of Chemical Engineering 2012;2012:1–16. https://doi.org/10.1155/2012/193639.

[463] Gómez-Velásquez N, López-Montoya T, Bustamante-Chaverra CA, Nieto-Londoño C. Parametric study of particles homogenization in cold-flow riser reactors. International Journal of Thermofluids 2021;9:100058. https://doi.org/10.1016/j.ijft.2020.100058.

[464] Arstad B, Blom R, Bakken E, Dahl I, Jakobsen JP, Røkke P. Sorption-enhanced methane steam reforming in a circulating fluidized bed reactor system. Energy Procedia 2009;1:715–20. https://doi.org/10.1016/j.egypro.2009.01.094.

[465] Fedunik-Hofman L, Bayon A, Donne SW. Kinetics of Solid-Gas Reactions and Their Application to Carbonate Looping Systems. Energies (Basel) 2019;12. https://doi.org/10.3390/en12152981.

[466] García-Labiano F, Abad A, de Diego LF, Gayán P, Adánez J. Calcination of calcium-based sorbents at pressure in a broad range of CO2 concentrations. Chem Eng Sci 2002;57:2381–93. https://doi.org/10.1016/S0009-2509(02)00137-9.

[467] Kanellis G, Zeneli M, Nikolopoulos N, Hofmann C, Ströhle J, Karellas S, et al. CFD modelling of an indirectly heated calciner reactor, utilized for CO2 capture, in an Eulerian framework. Fuel 2023;346:128251. https://doi.org/10.1016/j.fuel.2023.128251.

[468] Barin I. Thermochemical Data of Pure Substances. vol. 304. Wiley; 1995. https://doi.org/10.1002/9783527619825.

[469] Shakor ZM, Al-Shafei EN. The mathematical catalyst deactivation models: a mini review. RSC Adv 2023;13:22579–92. https://doi.org/10.1039/D3RA02912C.

[470] Khan KA, Khan SZ, Khan MA. Effective thermal conductivity of two-phase composites containing highly conductive inclusions. Journal of Reinforced Plastics and Composites 2016;35:1586–99. https://doi.org/10.1177/0731684416661044.

[471] Mortazavi B, Shojaei F, Rabczuk T, Zhuang X. High tensile strength and thermal conductivity in BeO monolayer: A first-principles study. FlatChem 2021;28:100257. https://doi.org/10.1016/j.flatc.2021.100257.

[472] Soomro M, Hughes R. The thermal conductivity of porous catalyst pellets. Can J Chem Eng 1979;57:24–8. https://doi.org/10.1002/cjce.5450570104.

[473] Wang S, Luo K, Hu C, Lin J, Fan J. CFD-DEM simulation of heat transfer in fluidized beds: Model verification, validation, and application. Chem Eng Sci 2019;197:280–95. https://doi.org/10.1016/j.ces.2018.12.031.

[474] Aloisi I, Jand N, Stendardo S, Foscolo PU. Hydrogen by sorption enhanced methane reforming: A grain model to study the behavior of bi-functional sorbent-catalyst particles. Chem Eng Sci 2016;149:22–34. https://doi.org/10.1016/j.ces.2016.03.042.

[475] Nardo A Di, Calchetti G, Carlo A Di, Stendardo S. Sorption enhanced steam methane reforming in a bubbling fluidized bed reactor: Simulation and analysis by the CPFD method. Comput Chem Eng 2023;169:108080. https://doi.org/10.1016/j.compchemeng.2022.108080.

[476] Aspen Technology Inc. Aspen Plus® 2022.

[477] Chanburanasiri N, Ribeiro AM, Rodrigues AE, Arpornwichanop A, Laosiripojana N, Praserthdam P, et al. Hydrogen Production via Sorption Enhanced Steam Methane Reforming Process Using Ni/CaO Multifunctional Catalyst. Ind Eng Chem Res 2011;50:13662–71. https://doi.org/10.1021/ie201226j.

[478] Hwang K-R, Lee C-B, Park J-S. Advanced nickel metal catalyst for water–gas shift reaction. J Power Sources 2011;196:1349–52. https://doi.org/10.1016/j.jpowsour.2010.08.084.

[479] Cunha AF, Moreira MN, Mafalda Ribeiro A, Ferreira AP, Loureiro JM, Rodrigues AE. How to Overcome the Water–Gas-Shift Equilibrium using a Conventional Nickel Reformer Catalyst. Energy Technology 2015;3:1205–16. https://doi.org/10.1002/ente.201500175.

[480] Hu Y, Cui H, Cheng Z, Zhou Z. Sorption-enhanced water gas shift reaction by in situ CO2 capture on an alkali metal salt-promoted MgO-CaCO3 sorbent. Chemical Engineering Journal 2019;377:119823. https://doi.org/10.1016/j.cej.2018.08.209.

[481] Chen H, Zhao C, Li Y, Chen X. CO2 Capture Performance of Calcium-Based Sorbents in a Pressurized Carbonation/Calcination Loop. Energy & Fuels 2010;24:5751–6. https://doi.org/10.1021/ef100565d.

[482] Radfarnia HR, Iliuta MC. Hydrogen production by sorption-enhanced steam methane reforming process using CaO-Zr/Ni bifunctional sorbent–catalyst. Chemical Engineering and Processing: Process Intensification 2014;86:96–103. https://doi.org/10.1016/j.cep.2014.10.014.

[483] Kazi SS, Aranda A, Meyer J, Mastin J. High performance CaO-based sorbents for pre- and post-combustion CO2 capture at high temperature. Energy Procedia 2014;63:2207–15. https://doi.org/10.1016/j.egypro.2014.11.240.

[484] Di Giuliano A, Gallucci K, Kazi SS, Giancaterino F, Di Carlo A, Courson C, et al. Development of Ni- and CaO-based mono- and bi-functional catalyst and sorbent materials for Sorption Enhanced Steam Methane Reforming: Performance over 200 cycles and attrition tests. Fuel Processing Technology 2019;195:106160. https://doi.org/10.1016/j.fuproc.2019.106160.

[485] Pistonesi C, Juan A, Irigoyen B, Amadeo N. Theoretical and experimental study of methane steam reforming reactions over nickel catalyst. Appl Surf Sci 2007;253:4427–37. https://doi.org/10.1016/j.apsusc.2006.09.054.

[486] Jokar SM, Parvasi P, Basile A. The performance evaluation of an industrial membrane reformer with catalyst-deactivation for a domestic methanol production plant. Int J Hydrogen Energy 2019;44:25730–9. https://doi.org/10.1016/j.ijhydene.2019.08.062.

[487] Gorji-Kandi S, Alavi-Amleshi SM, Mostoufi N. Experimental investigating the effect of bed geometry on solids mixing in fluidized beds. Particulate Science and Technology 2016;34:127–33. https://doi.org/10.1080/02726351.2015.1054532.

[488] Herce C, Cortés C, Stendardo S. Computationally efficient CFD model for scale-up of bubbling fluidized bed reactors applied to sorption-enhanced steam methane reforming. Fuel Processing Technology 2017;167:747–61. https://doi.org/10.1016/j.fuproc.2017.07.003.

[489] Berruti F, Pugsley TS, Godfroy L, Chaouki J, Patience GS. Hydrodynamics of circulating fluidized bed risers: A review. Can J Chem Eng 1995;73:579–602. https://doi.org/10.1002/cjce.5450730502.

[490] Tu Q, Wang H, Ocone R. Application of three-dimensional full-loop CFD simulation in circulating fluidized bed combustion reactors – A review. Powder Technol 2022;399:117181. https://doi.org/10.1016/j.powtec.2022.117181.

[491] Kim SW, Kim SD, Lee DH. Pressure Balance Model for Circulating Fluidized Beds with a Loop-seal. Ind Eng Chem Res 2002;41:4949–56. https://doi.org/10.1021/ie0202571.

[492] Wang Q, Yang H, Wang P, Lu J, Liu Q, Zhang H, et al. Application of CPFD method in the simulation of a circulating fluidized bed with a loop seal Part II—Investigation of solids circulation. Powder Technol 2014;253:822–8. https://doi.org/10.1016/j.powtec.2013.11.040.

[493] Cheng L, Basu P. Effect of pressure on loop seal operation for a pressurized circulating fluidized bed. Powder Technol 1999;103:203–11. https://doi.org/10.1016/S0032-5910(99)00018-2.

[494] Wang X, Liao L, Fan B, Jiang F, Xu X, Wang S, et al. Experimental validation of the gas–solid flow in the CFB riser. Fuel Processing Technology 2010;91:927–33. https://doi.org/10.1016/j.fuproc.2010.02.020.

[495] Kunii D, Levenspiel O. Fluidization Engineering 2nd Edition 2013:491.

[496] Rüdisüli M, Schildhauer TJ, Biollaz SMA, van Ommen JR. Scale-up of bubbling fluidized bed reactors — A review. Powder Technol 2012;217:21–38. https://doi.org/10.1016/j.powtec.2011.10.004.

[497] Catchpole JP, Fulford George. Dimensionless groups. Ind Eng Chem 1966;58:46–60. https://doi.org/10.1021/ie50675a012.

[498] Glicksman LR. Scaling relationships for fluidized beds. Chem Eng Sci 1988;43:1419–21. https://doi.org/10.1016/0009-2509(88)85118-2.

[499] Bonniol F, Sierra C, Occelli R, Tadrist L. Similarity in dense gas–solid fluidized bed, influence of the distributor and the air-plenum. Powder Technol 2009;189:14–24. https://doi.org/10.1016/j.powtec.2008.05.011.

[500] Van Den Bleek CM, Schouten JC. Can deterministic chaos create order in fluidized-bed scale-up? Chem Eng Sci 1993;48:2367–73. https://doi.org/10.1016/0009-2509(93)81058-4.

[501] Kelkar V V., Ng KM. Development of fluidized catalytic reactors: Screening and scale-up. AIChE Journal 2002;48:1498–518. https://doi.org/10.1002/aic.690480714.

[502] Stein M, Ding YL, Seville JPK. Experimental verification of the scaling relationships for bubbling gas-fluidised beds using the PEPT technique. Chem Eng Sci 2002;57:3649–58. https://doi.org/10.1016/S0009-2509(02)00264-6.

[503] Horio M, Nonaka A, Sawa Y, Muchi I. A new similarity rule for fluidized bed scale-up. AIChE Journal 1986;32:1466–82. https://doi.org/10.1002/aic.690320908.

[504] Glicksman LR. Scaling relationships for fluidized beds. Chem Eng Sci 1984;39:1373–9. https://doi.org/10.1016/0009-2509(84)80070-6.

[505] Glicksman LR, Hyre M, Woloshun K. Simplified scaling relationships for fluidized beds. Powder Technol 1993;77:177–99. https://doi.org/10.1016/0032-5910(93)80055-F.

[506] Kalo L, Pant HJ, Upadhyay RK. Validation of the Glicksman Scaling Law for Gas–Solid Conical Fluidized Beds Using the Radioactive Particle Tracking Technique. Ind Eng Chem Res 2020;59:20943–52. https://doi.org/10.1021/acs.iecr.0c03287.

[507] Roy R, Davidson JF. Similarity between gas-fluidized beds at elevated temperature and pressure. Fluidization VI, Engineering Foundation New York; 1989, p. 293–300.

[508] Fogler HS. Elements of Chemical Reaction Engineering. Prentice-Hall; 1992.

[509] van Ommen JR, Teuling M, Nijenhuis J, van Wachem BGM. Computational validation of the scaling rules for fluidized beds. Powder Technol 2006;163:32–40. https://doi.org/10.1016/j.powtec.2006.01.010.

[510] Wang Q, Zhang K, Brandani S, Jiang J. Scale-up strategy for the jetting fluidized bed using a CFD model based on two-fluid theory. Can J Chem Eng 2009;87:204–10. https://doi.org/10.1002/cjce.20148.

[511] Glicksman LR. Fluidized Bed Scale-up. Fluidization, Solids Handling, and Processing, Elsevier; 1999, p. 1–110. https://doi.org/10.1016/B978-081551427-5.50003-X.

[512] Geldart D. Types of gas fluidization. Powder Technol 1973;7:285–92. https://doi.org/10.1016/0032-5910(73)80037-3.

[513] Kunii D, Levenspiel O. Bubbling bed model: Model for the Flow of Gas through a Fluidized Bed. Industrial and Engineering Chemistry Fundamentals 1968;7:446–52. https://doi.org/10.1021/i160027a016.

[514] Syamlal M, O'Brien TJ. Computer simulation of bubbles in a fluidized bed. AIChE Symp. Ser, vol. 85, Publ by AIChE; 1989, p. 22–31.

[515] Boemer A, Qi H, Renz U. Eulerian simulation of bubble formation at a jet in a two-dimensional fluidized bed. International Journal of Multiphase Flow 1997;23:927–44. https://doi.org/10.1016/S0301-9322(97)00018-9.

[516] Hulme I, Kantzas* A. Validation of Bubble Properties of a Bubbling Fluidized Bed Reactor Using CFD with Imaging Experiments. Polym Plast Technol Eng 2005;44:73–95. https://doi.org/10.1081/PTE-200046041.

[517] Knowlton TM, Karri SBR, Issangya A. Scale-up of fluidized-bed hydrodynamics. Powder Technol 2005;150:72–7. https://doi.org/10.1016/j.powtec.2004.11.036.

[518] Yu S, Yang X, Xiang J, Zhou H, Li Q, Zhang Y. Effects of bed size on the voidage in gas-solid bubbling fluidized beds. Powder Technol 2021;387:197–204. https://doi.org/10.1016/j.powtec.2021.04.035.

[519] Xu G, Sun G, Gao S. Estimating radial voidage profiles for all fluidization regimes in circulating fluidized bed risers. Powder Technol 2004;139:186–92. https://doi.org/10.1016/j.powtec.2003.10.014.

[520] Zhang W, Tung Y, Johnsson F. Radial voidage profiles in fast fluidized beds of different diameters. Chem Eng Sci 1991;46:3045–52. https://doi.org/10.1016/0009-2509(91)85008-L.

[521] Xu G, Sun G, Nomura K, Li J, Kato K. Two distinctive variational regions of radial particle concentration profiles in circulating fluidized bed risers. Powder Technol 1999;101:91–100. https://doi.org/10.1016/S0032-5910(98)00157-0.

[522] Yu S, Yang X, Xiang J, Li Q, Zhou H, Zhang Y. Statistical study of the distribution of voidage in a bubbling fluidized bed with a constant section. Chemical Engineering Research and Design 2021;171:305–16. https://doi.org/10.1016/j.cherd.2021.05.020.

[523] Sobrino C, Ellis N, de Vega M. Distributor effects near the bottom region of turbulent fluidized beds. Powder Technol 2009;189:25–33. https://doi.org/10.1016/j.powtec.2008.05.012.

[524] Wang S, Lu H, Li D, Tang Y. Simulation of the Chemical Looping Reforming Process in the Fuel Reactor with a Bubble-Based Energy Minimization Multiscale Model. Energy & Fuels 2013;27:5008–15. https://doi.org/10.1021/ef401101p.

[525] Abrahamsen AR, Geldart D. Behaviour of gas-fluidized beds of fine powders part II. Voidage of the dense phase in bubbling beds. Powder Technol 1980;26:47–55. https://doi.org/10.1016/0032-5910(80)85006-6.

[526] Knowlton TM. Fluidized bed reactor design and scale-up. In: Scala F, editor. Fluidized Bed Technologies for Near-Zero Emission Combustion and Gasification, Woodhead Publishing; 2013, p. 481–523. https://doi.org/10.1533/9780857098801.2.481.

[527] Yang WC. Handbook of Fluidization and Fluid-Particle Systems. Taylor & Francis; 2003.

[528] Basu P. Design of CFB Components. Circulating Fluidized Bed Boilers, Cham: Springer International Publishing; 2015, p. 229–53. https://doi.org/10.1007/978-3-319-06173-3_8.

[529] Bandara JC, Jayarathna C, Thapa R, Nielsen HK, Moldestad BME, Eikeland MS. Loop seals in circulating fluidized beds – Review and parametric studies using CPFD simulation. Chem Eng Sci 2020;227:115917. https://doi.org/10.1016/j.ces.2020.115917.

[530] Downmore M, Jambgwa SD, Kusaziwa KP. Effect of bed particle size and temperature variation on the minimum fluidisation velocity: A comparison with minimum fluidisation velocity correlations for bubbling fluidised bed designs. Proceedings of the Institution of Mechanical Engineers, Part E: Journal of Process Mechanical Engineering 2019;233:1001–12. https://doi.org/10.1177/0954408918821769.

[531] Said SAM, Simakov DSA, Mokheimer EMA, Habib MA, Ahmed S, Waseeuddin M, et al. Computational fluid dynamics study of hydrogen generation by low temperature methane reforming in a membrane reactor. Int J Hydrogen Energy 2015;40:3158–69. https://doi.org/10.1016/j.ijhydene.2015.01.024.

[532] El-Bousiffi MA, Gunn DJ. A dynamic study of steam-methane reforming. Int J Heat Mass Transf 2007;50:723–33. https://doi.org/10.1016/j.ijheatmasstransfer.2006.07.006.

[533] Sathiyamoorthy D, Horio M. On the influence of aspect ratio and distributor in gas fluidized beds. Chemical Engineering Journal 2003;93:151–61. https://doi.org/10.1016/S1385-8947(02)00257-7.

[534] Werther J. Scale-up modeling for fluidized bed reactors. Chem Eng Sci 1992;47:2457–62. https://doi.org/10.1016/0009-2509(92)87076-3.

[535] Park HC, Choi HS. Influence of cross-sectional aspect ratio on biochar segregation in a bubbling fluidized bed. Sci Rep 2022;12:10600. https://doi.org/10.1038/s41598-022-14282-y.

[536] Rao A, Curtis JS, Hancock BC, Wassgren C. The effect of column diameter and bed height on minimum fluidization velocity. AIChE Journal 2010;56:2304–11. https://doi.org/10.1002/aic.12161.

[537] Blaszczuk A, Nowak W, Krzywanski J. Effect of bed particle size on heat transfer between fluidized bed of group b particles and vertical rifled tubes. Powder Technol 2017;316:111–22. https://doi.org/10.1016/j.powtec.2016.12.027.

[538] Papadikis K, Gu S, Bridgwater AV. A CFD approach on the effect of particle size on char entrainment in bubbling fluidised bed reactors. Biomass Bioenergy 2010;34:21–9. https://doi.org/10.1016/j.biombioe.2009.09.007.

[539] Timsina R, Thapa RK, Moldestad BME, Eikeland MS. Effect of particle size on flow behavior in fluidized beds. International Journal of Energy Production and Management 2019;4:287–97. https://doi.org/10.2495/EQ-V4-N4-287-297.

[540] Warnecke R. Gasification of biomass: comparison of fixed bed and fluidized bed gasifier. Biomass Bioenergy 2000;18:489–97. https://doi.org/10.1016/S0961-9534(00)00009-X.

[541] Wirth K. Axial pressure profile in circulating fluidized beds. Chem Eng Technol 1988;11:11–7. https://doi.org/10.1002/ceat.270110103.

[542] Sánchez-Prieto J, Soria-Verdugo A, Briongos JV, Santana D. The effect of temperature on the distributor design in bubbling fluidized beds. Powder Technol 2014;261:176–84. https://doi.org/10.1016/j.powtec.2014.04.035.

[543] Yang S, Yang H, Zhang H, Li J, Yue G. Impact of operating conditions on the performance of the external loop in a CFB reactor. Chemical Engineering and Processing: Process Intensification 2009;48:921–6. https://doi.org/10.1016/j.cep.2008.12.004.

[544] Wang Q, Yang H, Wang P, Lu J, Liu Q, Zhang H, et al. Application of CPFD method in the simulation of a circulating fluidized bed with a loop seal Part II—Investigation of solids circulation. Powder Technol 2014;253:822–8. https://doi.org/10.1016/j.powtec.2013.11.040.

[545] Dassori CG, Shah YT. Effects of particle characteristics on the performance of a fast fluidized bed reactor. Chem Eng Commun 1991;100:29–45. https://doi.org/10.1080/00986449108911589.

[546] Argyriou DT, List HL, Shinnar R. Bubble growth by coalescence in gas fluidized beds. AIChE Journal 1971;17:122–30. https://doi.org/10.1002/aic.690170126.

[547] Lim CN, Gilbertson MA, Harrison AJL. Bubble distribution and behaviour in bubbling fluidised beds. Chem Eng Sci 2007;62:56–69. https://doi.org/10.1016/j.ces.2006.08.034.

[548] Reay D, Ramshaw C, Harvey A, editors. Process Intensification. Elsevier; 2008. https://doi.org/10.1016/B978-0-7506-8941-0.X0001-6.

[549] Mahabir J, Samaroo N, Janardhanan M, Ward K. Pathways to sustainable methanol operations using gas-heated reforming (GHR) technologies. Journal of CO2 Utilization 2022;66:102302. https://doi.org/10.1016/J.JCOU.2022.102302.

[550] Luis P. Use of monoethanolamine (MEA) for CO2 capture in a global scenario: Consequences and alternatives. Desalination 2016;380:93–9. https://doi.org/10.1016/j.desal.2015.08.004.

[551] Wang Y, Zhao L, Otto A, Robinius M, Stolten D. A Review of Post-combustion CO2 Capture Technologies from Coal-fired Power Plants. Energy Procedia 2017;114:650–65. https://doi.org/10.1016/j.egypro.2017.03.1209.

[552] IEAGHG. Reference data and Supporting Literature Reviews for SMR Based Hydrogen Production with CCS. 2017.

[553] Mudhasakul S, Ku H ming, Douglas PL. A simulation model of a CO2 absorption process with methyldiethanolamine solvent and piperazine as an activator. International Journal of Greenhouse Gas Control 2013;15:134–41. https://doi.org/10.1016/J.IJGGC.2013.01.023.

[554] Oh H-T, Kum J, Park J, Dat Vo N, Kang J-H, Lee C-H. Pre-combustion CO2 capture using amine-based absorption process for blue H2 production from steam methane reformer. Energy Convers Manag 2022;262:115632. https://doi.org/10.1016/j.enconman.2022.115632.

[555] Kum J, Oh H-T, Park J, Kang J-H, Lee C-H. Techno-economic analysis and optimization of a CO2 absorption process with a solvent looping system at the absorber using an MDEA/PZ blended solvent for steam methane reforming. Chemical Engineering Journal 2023;455:140685. https://doi.org/10.1016/j.cej.2022.140685.

[556] Langmi HW, Engelbrecht N, Modisha PM, Bessarabov D. Hydrogen storage. Electrochemical Power Sources: Fundamentals, Systems, and Applications, Elsevier; 2022, p. 455–86. https://doi.org/10.1016/B978-0-12-819424-9.00006-9.

[557] Sdanghi G, Maranzana G, Celzard A, Fierro V. Review of the current technologies and performances of hydrogen compression for stationary and automotive applications. Renewable and Sustainable Energy Reviews 2019;102:150–70. https://doi.org/10.1016/j.rser.2018.11.028.

[558] Valente A, Iribarren D, Dufour J. Harmonised life-cycle global warming impact of renewable hydrogen. J Clean Prod 2017;149:762–72. https://doi.org/10.1016/j.jclepro.2017.02.163.

[559] Equinor ASA. H2H Saltend: The first step to a Zero Carbon Humber 2020.

[560] Salem M, Shoaib AM, Ibrahim AFM. Simulation of a Natural Gas Steam Reforming Plant for Hydrogen Production Optimization. Chem Eng Technol 2021;44:1651–9. https://doi.org/10.1002/CEAT.202100123.

[561] Galletti C, Specchia S, Saracco G, Specchia V. Gold-supported catalysts for medium temperature-water gas shift reaction. Top Catal 2009;52:688–92. https://doi.org/10.1007/S11244-009-9213-5/FIGURES/5.

[562] SIRCAR S, GOLDEN TC. Purification of Hydrogen by Pressure Swing Adsorption. Sep Sci Technol 2000;35:667–87. https://doi.org/10.1081/SS-100100183.

[563] Arias B, Diego ME, Méndez A, Alonso M, Abanades JC. Calcium looping performance under extreme oxy-fuel combustion conditions in the calciner. Fuel 2018;222:711–7. https://doi.org/10.1016/j.fuel.2018.02.163.

[564] Jayarathna CK, Mathisen A, Øi LE, Tokheim L-A. Aspen Plus® Process Simulation of Calcium Looping with Different Indirect Calciner Heat Transfer Concepts. Energy Procedia 2017;114:201–10. https://doi.org/10.1016/j.egypro.2017.03.1162.

[565] French S. The Role of Zero and Low Carbon Hydrogen in Enabling the Energy Transition and the Path to Net Zero Greenhouse Gas Emissions. Johnson Matthey Technology Review 2020;64:357–70. https://doi.org/10.1595/205651320x15910225395383.

[566] Johnson Matthey. LCH^{TM} Process for the production of blue hydrogen. Billingham, UK: 2022.

[567] Zhao B, Liu F, Cui Z, Liu C, Yue H, Tang S, et al. Enhancing the energetic efficiency of MDEA/PZ-based CO2 capture technology for a 650 MW power plant: Process improvement. Appl Energy 2017;185:362–75. https://doi.org/10.1016/J.APENERGY.2016.11.009.

[568] Romano MC, Chiesa P, Lozza G. Pre-combustion CO2 capture from natural gas power plants, with ATR and MDEA processes. International Journal of Greenhouse Gas Control 2010;4:785–97. https://doi.org/10.1016/J.IJGGC.2010.04.015.

[569] Koronaki IP, Prentza L, Papaefthimiou V. Modeling of CO2 capture via chemical absorption processes – An extensive literature review. Renewable and Sustainable Energy Reviews 2015;50:547–66. https://doi.org/10.1016/j.rser.2015.04.124.

[570] Mudhasakul S, Ku H, Douglas PL. A simulation model of a CO2 absorption process with methyldiethanolamine solvent and piperazine as an activator. International Journal of Greenhouse Gas Control 2013;15:134–41. https://doi.org/10.1016/j.ijggc.2013.01.023.

[571] Kum J, Oh H-T, Park J, Kang J-H, Lee C-H. Techno-economic analysis and optimization of a CO2 absorption process with a solvent looping system at the absorber using an MDEA/PZ blended solvent for steam methane reforming. Chemical Engineering Journal 2023;455:140685. https://doi.org/10.1016/j.cej.2022.140685.

[572] Feyzi V, Beheshti M, Gharibi Kharaji A. Exergy analysis: A CO 2 removal plant using a-MDEA as the solvent. Energy 2017;118:77–84. https://doi.org/10.1016/j.energy.2016.12.020.

[573] Bains M, Hill (nee Robinson) L, Rossington P. Fuels: Natural gas. Bristol: 2016.

[574] Martínez I, Grasa G, Meyer J, Di Felice L, Kazi S, Sanz C, et al. Performance and operating limits of a sorbent-catalyst system for sorption-enhanced reforming (SER) in a fluidized bed reactor. Chem Eng Sci 2019;205:94–105. https://doi.org/10.1016/J.CES.2019.04.029.

[575] Lamb JJ, Hillestad M, Rytter E, Bock R, Nordgård ASR, Lien KM, et al. Traditional Routes for Hydrogen Production and Carbon Conversion. Hydrogen, Biomass and Bioenergy, Elsevier; 2020, p. 21–53. https://doi.org/10.1016/B978-0-08-102629-8.00003-7.

[576] Hong J, Field R, Gazzino M, Ghoniem AF. Operating pressure dependence of the pressurized oxy-fuel combustion power cycle. Energy 2010;35:5391–9. https://doi.org/10.1016/j.energy.2010.07.016.

[577] Buhre BJP, Elliott LK, Sheng CD, Gupta RP, Wall TF. Oxy-fuel combustion technology for coal-fired power generation. Prog Energy Combust Sci 2005;31:283–307. https://doi.org/10.1016/j.pecs.2005.07.001.

[578] Garduner M. DOE Hydrogen and Fuel Cells Program Record 9013: Energy requirements for hydrogen gas compression and liquefaction as related to vehicle storage needs. 2009.

[579] Al-Zareer M, Dincer I, Rosen MA. Analysis and assessment of a hydrogen production plant consisting of coal gasification, thermochemical water decomposition and hydrogen compression systems. Energy Convers Manag 2018;157:600–18. https://doi.org/10.1016/j.enconman.2017.11.047.

[580] White CW. ASPEN Plus Simulation of CO2 Recovery Process. Pittsburgh, PA, and Morgantown, WV (United States): 2002. https://doi.org/10.2172/810497.

[581] Patchigolla K, Oakey JE. Design Overview of High Pressure Dense Phase CO2 Pipeline Transport in Flow Mode. Energy Procedia 2013;37:3123–30. https://doi.org/10.1016/j.egypro.2013.06.198.

[582] BEIS. Digest of UK Energy Statistics (DUKES). Department for Business, Energy & Industrial Strategy (BEIS) 2022.

[583] IEAGHG. Toward a Common Method of Cost Estimation for CO2 Capture and Storage at Fossil Fuel Power Plants. Paris: 2013.

[584] IEAGHG. Criteria for Technical and Economic Assessment of Plants with Low CO2 Emissions. 2009.

[585] Christensen P, Dysert LR, Bates J, Burton D, Creese RC, Hollmann J. Cost Estimate Classification system-as applied in engineering, procurement, and construction for the process industries. AACE International Recommended Practices 2005;18:1–9.

[586] Peters MS, Timmerhaus KD, West RE. Plant Design and Economics for Chemical Engineers. 5th ed. McGraw-Hill Education; 2003.

[587] Towler G, Sinnott R. Chemical engineering design: principles, practice and economics of plant and process design. Butterworth-Heinemann; 2021.

[588] BEIS. Hydrogen Production Costs 2021. 2021.

[589] Ofgem. Electricity Prices: Forward Delivery Contracts - Weekly Average (GB). Office of Gas and Electricity Markets 2023. https://www.ofgem.gov.uk/energy-data-and-research/data-portal/wholesale-market-indicators (accessed April 7, 2023).

[590] Department for Energy Security and Net Zero. Prices of fuels purchased by manufacturing industry in Great Britain. Quarterly Energy Prices Publication 2023. https://www.gov.uk/government/statistical-data-sets/prices-of-fuels-purchased-by-manufacturing-industry (accessed April 26, 2023).

[591] Ofgem. Gas Prices: Forward Delivery Contracts - Weekly Average (GB). Office of Gas and Electricity Markets 2023. https://www.ofgem.gov.uk/energy-data-and-research/data-portal/wholesale-market-indicators (accessed April 7, 2023).

[592] Yorshire Water. Wholesale Charges Scheme Non-household 2023/2024. 2023.

[593] Reforming Catalyst Manufacturers 2023. https://www.alibaba.com/products/steam_reforming_catalyst.html (accessed April 9, 2023).

[594] MDEA Price CAS 105-59-9 2023. https://www.made-in-china.com/ (accessed April 9, 2023).

[595] PharmaCompass. Piperazine | Price | Per kg | USD 2023. https://www.pharmacompass.com/active-pharmaceutical-ingredients/piperazine (accessed April 9, 2023).

[596] IndexBox. Chalk and Dolomite Price in the UK - 2023 2023. https://www.indexbox.io/search/chalk-and-dolomite-price-the-uk/ (accessed March 7, 2023).

[597] Pale Blue Dot Energy. Progressing development of the UK's strategic carbon dioxide storage resource. A Summary of Results from the Strategic UK CO 2016;2.

[598] BEIS. UK ETS: Carbon prices for use in civil penalties, 2023 2022. https://bit.ly/4f4TMsS (accessed November 20, 2023).

[599] Leroutier M. Carbon pricing and power sector decarbonization: Evidence from the UK. J Environ Econ Manage 2022;111:102580. https://doi.org/10.1016/j.jeem.2021.102580.

[600] Tsiklios C, Hermesmann M, Müller TE. Hydrogen transport in large-scale transmission pipeline networks: Thermodynamic and environmental assessment of repurposed and new pipeline configurations. Appl Energy 2022;327:120097. https://doi.org/10.1016/j.apenergy.2022.120097.

[601] Briottet L, Batisse R, de Dinechin G, Langlois P, Thiers L. Recommendations on X80 steel for the design of hydrogen gas transmission pipelines. Int J Hydrogen Energy 2012;37:9423–30. https://doi.org/10.1016/j.ijhydene.2012.02.009.

[602] Khan MA, Young C, Mackinnon C, Layzell D. The techno-economics of hydrogen compression. Transition Accelerator Technical Briefs 2021;1:1–36.

[603] Liao L, Zheng J, Li C, Liu R, Zhang Y. Thermodynamic modeling modification and experimental validation of entrained-flow gasification of biomass. Journal of the Energy Institute 2022;103:160–8. https://doi.org/10.1016/j.joei.2022.06.006.

[604] HajiHashemi M, Mazhkoo S, Dadfar H, Livani E, Naseri Varnosefaderani A, Pourali O, et al. Combined heat and power production in a pilot-scale biomass gasification system: Experimental study and kinetic simulation using ASPEN Plus. Energy 2023;276:127506. https://doi.org/10.1016/j.energy.2023.127506.

[605] Oni AO, Anaya K, Giwa T, Di Lullo G, Kumar A. Comparative assessment of blue hydrogen from steam methane reforming, autothermal reforming, and natural gas decomposition technologies for natural gas-producing regions. Energy Convers Manag 2022;254:115245. https://doi.org/10.1016/j.enconman.2022.115245.

[606] Zhao B, Liu F, Cui Z, Liu C, Yue H, Tang S, et al. Enhancing the energetic efficiency of MDEA/PZ-based CO2 capture technology for a 650 MW power plant: Process improvement. Appl Energy 2017;185:362–75. https://doi.org/10.1016/j.apenergy.2016.11.009.

[607] Collodi G, Azzaro G, Ferrari N, Santos S. Techno-economic Evaluation of Deploying CCS in SMR Based Merchant H2 Production with NG as Feedstock and Fuel. Energy Procedia 2017;114:2690–712. https://doi.org/10.1016/j.egypro.2017.03.1533.

[608] Abbas SZ, Dupont V, Mahmud T. Modelling of H2 production via sorption enhanced steam methane reforming at reduced pressures for small scale applications. Int J Hydrogen Energy 2019;44:1505–13. https://doi.org/10.1016/j.ijhydene.2018.11.169.

[609] Bill Cotton. Clean hydrogen: Hydrogen from natural gas through cost effective CO2 capture. 2021.

[610] Alrashed F, Zahid U. Comparative analysis of conventional steam methane reforming and PdAu membrane reactor for the hydrogen production. Comput Chem Eng 2021;154:107497. https://doi.org/10.1016/j.compchemeng.2021.107497.

[611] Keipi T, Tolvanen H, Konttinen J. Economic analysis of hydrogen production by methane thermal decomposition: Comparison to competing technologies. Energy Convers Manag 2018;159:264–73. https://doi.org/10.1016/j.enconman.2017.12.063.

[612] Diglio G, Hanak DP, Bareschino P, Mancusi E, Pepe F, Montagnaro F, et al. Techno-economic analysis of sorption-enhanced steam methane reforming in a fixed bed reactor network integrated with fuel cell. J Power Sources 2017;364:41–51. https://doi.org/10.1016/J.JPOWSOUR.2017.08.005.

[613] Dat Vo N, Kang JH, Oh M, Lee CH. Dynamic model and performance of an integrated sorption-enhanced steam methane reforming process with separators for the simultaneous blue H2 production and CO2 capture. Chemical Engineering Journal 2021;423:130044. https://doi.org/10.1016/J.CEJ.2021.130044.

[614] Khojasteh Salkuyeh Y, Saville BA, MacLean HL. Techno-economic analysis and life cycle assessment of hydrogen production from natural gas using current and emerging technologies. Int J Hydrogen Energy 2017;42:18894–909. https://doi.org/10.1016/j.ijhydene.2017.05.219.

[615] Simbeck D, Beecy D. The CCS paradox: The much higher CO2 avoidance costs of existing versus new fossil fuel power plants. Energy Procedia 2011;4:1917–24. https://doi.org/10.1016/j.egypro.2011.02.071.

[616] Clery D, Gough C. Cluster Mapping Report: The Humber Industrial Cluster. 2022.

[617] BEIS. Guidance on estimating carbon values beyond 2050: an interim approach. 2011.

[618] Environment Agency. Post-combustion carbon dioxide capture: best available techniques (BAT). Guidance 2022. https://www.gov.uk/guidance/post-combustion-carbon-dioxide-capture-best-available-techniques-bat (accessed August 27, 2023).

[619] Matsen JM. Design and scale-up of CFB catalytic reactors. Circulating Fluidized Beds, Dordrecht: Springer Netherlands; 1997, p. 489–503. https://doi.org/10.1007/978-94-009-0095-0_14.

[620] Coker AK. Scale-Up in Reactor Design. Modeling of Chemical Kinetics and Reactor Design, Elsevier; 2001, p. 1034–81. https://doi.org/10.1016/B978-088415481-5/50015-2.

[621] Knowlton T, Reddy Karri SB, Smith JS. Hydrodynamic scale-up of circulating fluidized beds. The 12th International Conference on Fluidization - New Horizons in Fluidization Engineering, ECI Symposium Series; 2007.

[622] Fan LS, Zhu C. Principles of Gas-Solid Flows. Cambridge University Press; 1998.

[623] Khan MA, Young C, MacKinnon C, Layzell D. The Techno-Economics of Hydrogen Compression. Transition Accelerator Technical Briefs 2021;1:1–36.

[624] IEAGHG. Techno-Economic Evaluation of SMR Based Standalone (Merchant) Plant with CCS. 2017.

[625] Woods M, Kuehn N, Shah V, White lll C, Goellner J. Baseline Analysis of Crude Methanol Production from Coal and Natural Gas. 2014. https://doi.org/10.2172/1601964.

[626] Manzolini G, Dijkstra JW, Macchi E, Jansen D. Technical Economic Evaluation of a System for Electricity Production With CO2 Capture Using a Membrane Reformer With Permeate Side Combustion. Volume 4: Cycle Innovations; Electric Power; Industrial and Cogeneration; Manufacturing Materials and Metallurgy 2006:89–99. https://doi.org/10.1115/GT2006-90353.

[627] Rosner F, Chen Q, Rao A, Samuelsen S. Thermo-economic analyses of isothermal water gas shift reactor integrations into IGCC power plant. Appl Energy 2020;277:115500. https://doi.org/10.1016/j.apenergy.2020.115500.

[628] Mays J, Stanis R. Techno-Economic Analysis for GTI's Compact Hydrogen Generator. United States: 2020.

[629] Schmitt T, Zoelle A, Homsy S, Fout T, Shultz T, Woods M, et al. Bituminous Coal and Natural Gas to Electricity: >90% Capture Cases Technical Note. 2021. https://doi.org/10.2172/1837938.

[630] Woods M, Kuehn N, Shah V, White lll C, Goellner J. Baseline Analysis of Crude Methanol Production from Coal and Natural Gas. 2014. https://doi.org/10.2172/1601964.

[631] Rath L, Chou V, Kuehn N. Assessment of Hydrogen Production with CO2 Capture Volume 1: Baseline State-of-the-Art Plants (Final Report). 2011. https://doi.org/10.2172/1767148.

[632] Riva L, Martínez I, Martini M, Gallucci F, van Sint Annaland M, Romano MC. Techno-economic analysis of the Ca-Cu process integrated in hydrogen plants with CO2 capture. Int J Hydrogen Energy 2018;43:15720–38. https://doi.org/10.1016/j.ijhydene.2018.07.002.